Problems in Solid-state Physics

Edited by
A.M.PROKHOROV and A.S.PROKHOROV

Advances in Science and Technology in the USSR

Physics Series

MIR Publishers
Moscow

Problems in Solid-state Physics

Edited by A. M. PROKHOROV, Mem. USSR Acad. Sc., and A. S. PROKHOROV, Cand. Sc. (Phys.-Math.)

This collection of articles has been edited by Academician A. M. Prokhorov, the winner of several Soviet and international awards, including the Hero of Socialistic Labour, Lenin prize, State award, and Nobel prize in Physics. Acad. Prokhorov is an honorary member of the Academies of sciences of many foreign countries, the President of the National Committee of Soviet Physicists, Member-secretary of the General Physics and Astronomy section of the USSR Academy of Sciences, and the Director of the Institute of General Physics of the USSR Academy of Sciences.

The collection contains ten papers devoted to fundamental investigations in various branches of modern solid-state physics. All the results reported in this collection have been obained by Soviet scientists at different institutes of the USSR Academy of Sciences, as well as the Academies of Soviet republics, over the last few years. The authors of these papers are leading scientists in the field of solid-state physics and are well-known not only in the Soviet Union but in other countries as well.

Mir Publishers
2 Pervy Rizhsky Pereulok,
I-110, GSP, Moscow, 129820
USSR

Mir Publishers Moscow

Advances
in
Science
and
Technology
in
the USSR

Physics
Series

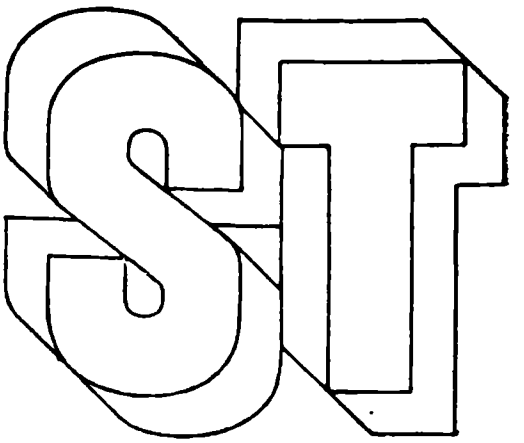

Problems in Solid-state Physics

Edited by A. M. PROKHOROV
Mem. USSR Acad. Sci.
A. S. PROKHOROV
Cand. Sc. (Phys. and Math.)

Translated from the Russian by
Ram S. Wadhwa, Ph. D.

Mir Publishers
Moscow

Проблемы физики твёрдого тела
Под редакцией акад. А. М. Прохорова
И канд. физ.-мат. наук А. С. Прохорова
Издательство «Мир» Москва

First published 1984

На английском языке

© Издательство «Мир», 1984
© English translation, Mir Publishers, 1984

CONTENTS

Preface 8

1. **Submillimetre Dielectric Spectroscopy of Solids** *by G. V. Kozlov, A. M. Prokhorov, and A. A. Volkov* 19
1.1 Introduction 19
1.2 Technique and Methods of Submillimetre BWT Spectroscopy 21
1.3 Investigations of the Dynamics of Crystal Lattice by Submillimetre Dielectric Spectroscopy 37
1.4 Conclusion 53
References 54

2. **Theory of Electric Polarization of Domain Boundaries in Magnetically Ordered Crystals** *by V. G. Baryakhtar, V. A. L'vov, and D. A. Yablonskii* 58
2.1 Introduction 58
2.2 The Phenomenological Theory of Inhomogeneous Magnetoelectric Effect 58
2.3 The Phenomenological Theory of Electric Polarization of Domain Boundaries 61
2.4 Magnetic Symmetry and Electric Polarization of a Crystal with a Plane Domain Boundary 67
2.5 Interdomain Potential Difference 74
2.6 Conclusion 77
Appendix 78
References 79

3. **Ferroelectromagnetics** *by G. A. Smolenskii and I. E. Chupis* 81
3.1 Introduction 81
3.2 The Nature of Magnetoelectric Interactions 87
3.3 Thermodynamic Theory 89
3.3.1 Thermal Phase Transitions 90
3.3.2 Phase Transitions in External Fields 92
3.4 Theory of the High-Frequency Properties of Ferroelectromagnetics 94
3.4.1 Spectrum of Elementary Excitations 94
3.4.2 Behaviour in Alternating External Fields 96
3.5 Experimental Studies of Magnetoelectric Interactions in Ferroelectromagnetics 98
3.6 Possible Applications of Ferroelectromagnetics 103
3.7 Conclusion 105
References 106

4. **High Hydrogen Pressures. Synthesis and Properties of New Hydrides** *by E. G. Ponyatovsky, V. E. Antonov, and I. T. Belash* 109
4.1 Introduction 109
4.2 Methods for Compressing Hydrogen and Obtaining Hydrides 110
4.3 Phase Transformations in Metal-hydrogen Systems 114
4.4 Magnetic Properties of Metal-hydrogen Solutions 133
4.4.1 Magnetic Properties of Ni-Me Alloys 134
4.4.2 Ni-Me-H Solutions 138
4.4.2.1 Ni-Fe-H system 139
4.4.2.2 Ni-Co-H system 143

4.4.2.3 Ni-Mn-H system 144
4.4.2.4 Ni-Cr-H system 145
4.4.2.5 Discussion of properties of Ni-Me-H solutions 146
4.4.3 $Fe_{65}(Ni_{1-x}Mn_x)_{35}$ Solutions 148
4.4.4 Applicability of the Rigid *d*-band Model for Describing the Magnetic Properties of Other Me-H Solutions 154
4.4.4.1 Hydrogen solutions in fcc alloys based on 3*d*-metals 154
4.4.4.2 Hydrogen solutions in 3*d*-metals with hcp lattice 154
4.4.4.3 Hydrogen solutions in 4*d*-metal alloys 158
4.5 Pd-Me-H Systems. Superconductivity and Phase Transformations at High Pressure 158
4.6 Conclusion 168
References 169

5. Dislocations and Physical Properties of Semiconductors *by Yu. A. Ossipyan* 173
5.1 Introduction 173
5.2 The Dislocation Energy Spectrum of Electrons and the Microwave Dislocation Conductivity Mechanism in Semiconductors 174
5.3 Movement of Charged Dislocations in $A^{II}B^{VI}$ Semiconductors 184
5.4 Conclusion 199
References 199

6. InGaAsP Heterojunctions: Preparation, Recombination Processes and Applications in Optoelectronic Devices *by Zh. I. Alferov, D. Z. Garbuzov, and A. T. Gorelenok* 201
6.1 Introduction 201
6.2 Salient Features of Preparation of InGaAsP Solid Solutions and Heterojunctions Based on Them 203
6.3 Recombination Processes in InGaAsP Double Heterojunctions 212
6.4 Lasers 222
6.5 Light-emitting Diodes 227
6.6 Photodetectors 231
6.7 Conclusion 233
References 233

7. Acoustic Instability and Nonlinear Acoustoelectronic Interaction in Semiconductors in an Alternating Electric Field *by Yu. V. Gulyaev and G. D. Mansfel'd* 236
7.1 Introduction 236
7.2 Multitransit Amplification and Generation of Acoustic Waves in Semiconductors under Synchronism 238
7.2.1 The Theory of the Effect 238
7.2.2 Experiment 242
7.3 Current-Voltage Characteristics of Samples and the Generation Spectrum 246
7.4 Interaction of High-intensity Short-wave Sound with Electrons 252
7.5 Amplification and Generation of Acoustic Waves in a Corbino Disc 257
7.6 Semiconductor in an Alternating Electric Field as an Active Medium for the Generation of Acoustic Signals 263
7.6.1 Theory 263
7.6.2 Experiment 264

7.7 Conclusion 265
References 266
8. New Trends in the Physics of Laser Crystals and Glasses *by V. V. Osiko and A. M. Prokhorov* 267
8.1 Introduction 267
8.2 LiF Crystals with Electronic Colour Centres for Tunable Lasers 267
8.3 Active Media for Neodymium Lasers with Nonselective Pumping 275
8.3.1 High-concentration KNFS Glasses with Anomalously Low Concentration Quenching of Neodymium 275
8.3.2 The Use of Sensitization Effect for Increasing the Efficiency of Neodymium Lasers with Nonselective Pumping 282
References 288
9. Etching of Polymers in Quantum- and Particle Flux *by T. M. Makhviladze, A. M. Prokhorov, K. A. Valiev, and L. V. Velikov* 291
9.1 Introduction 291
9.2 Basic Equations of Diffusive Etching 292
9.3 Etching Upon a Uniform Exposure of a Polymer 297
9.4 Etching Upon a Nonuniform Exposure of a Polymer 300
9.5 Etching Rate 306
9.6 Experiments on the Photoetching of Polymers by Soft X-rays 311
9.7 Experiments on Photoetching by VUV-radiation in Vacuum, Nitrogen, and Oxygen-containing Media 320
9.8 Conclusion 327
References 328
10. Coil-globule Transitions in Polymer Systems *by A. Yu. Grosberg and A. R. Khokhlov* 330
10.1 Introduction 330
10.2 Basic Ideas of Lifshitz' Globule Theory 331
10.3 Coil-globule Transitions in the Simplest Linear Uncharged Homopolymers 334
10.4 A Brief Comparison of Theoretical and Experimental Results 339
10.5 Some Results of the Theory of Heteropolymer Globules 341
10.6 Liquid-Crystalline Ordering in Solutions of Rigid Macromolecules 343
10.7 Other Investigated Coil-globule Type Transitions 346
10.8 Conclusion 350
References 351
Author Index 354
Subject Index 361

PREFACE

This is a collection of ten review papers devoted to basic problems of modern solid state physics. All the papers presented in this book have been written by Soviet scientists from different institutes of the Academy of Sciences of the USSR and of Soviet republics, and contain the results of investigations carried out during the last few years. Further developments in these directions in the years to come will undoubtedly help in solving some important scientific technological problems. Because of the lack of space, we were not able to cover all the aspects of modern solid state physics, and had to select just a few of these. We hope to make up for this deficiency in near future.

The first article by Kozlov, Prokhorov, and Volkov is devoted to one of the long-standing problems of spectroscopy, viz. the development of methods of dielectric measurements in the longest infrared wave region (submillimetre range). For a long time, no reliable methods were available for measurements in this region. The paper contains the results of fundamental investigations and original techniques developed at the oscillations laboratory of the Lebedev Institute of Physics of the USSR Academy of Sciences (presently known as the Institute of General Physics of the USSR Academy of Sciences). These studies have helped in solving the problems of submillimetre spectroscopy in solids. At present, special spectrometers for carrying out dielectric measurements in the submillimetre range are being used successfully at this institute. These spectrometers are based on tunable monochromatic oscillators called backward-wave tubes (BWT), which are commercially produced in the USSR. The BWT spectrometers were found to be exceptionally useful instruments, combining the advantages of the microwave techniques and the IR spectroscopy. The dielectric spectra of materials, obtained by BWT spectrometers in the frequency range from 3 to 33 cm^{-1}, are unique and cannot be obtained by any other means in most cases.

The first part of this review by Kozlov *et al.* is devoted to the submillimetre BWT spectroscopic methods and techniques worked out at the Institute of General Physics of the USSR Academy of Sciences. In the second part, the authors have demonstrated the possibilities of the dielectric BWT spectroscopy by citing new original results obtained in the field of solid state physics and dealing with the common problem of phase transitions in crystals. BWT spectrometers were used to study ferroelectrics, semiconductors, superionic conductors, and crystals with an incommensurate phase. In all the crystals, the authors were able to observe and investigate in detail specific lattice vibrations which are either directly responsible for phase

transitions, or are at least closely related to them. In all cases, the experimental results on dispersion of real and imaginary parts of dielectric permittivity of materials are of prime importance for analysis. Such results in the submillimetre range of electromagnetic waves were obtained for the first time, which was not easily accessible to measurements earlier.

The theory of electric polarization of domain boundaries in magnetically ordered crystals has been considered in the review article by Baryakhtar, L'vov, and Yablonskii. The interaction between the magnetic and electric subsystems of a crystal is responsible for several phenomena which are called magnetoelectric effects. These effects began to be investigated thoroughly after the publication of the book "Electrodynamics of Continuous Media" by L.D. Landau and E.M. Lifshitz (1958), in which the linear magnetoelectric effect (a linear relation between the magnetic and electric fields in matter) was predicted for the first time. According to this effect, a linear relation exists between the magnetic and electric fields in matter. The number of magnetic symmetry classes for which the magnetoelectric effect is observed is not large. This is so because a simultaneous existence of an even (in time) polar vector of the electric field **E** and an odd (in time) axial vector of the magnetic field **H** is not possible for a large number of symmetry elements appearing in the magnetic symmetry classes. The latter describe the symmetry of spatially homogeneous ordered media. In real substances, however, some sort of inhomogeneities always exists, and these must affect the nature of magnetoelectric phenomena.

In the article by Baryakhtar *et al.*, it has been predicted that the lowering of the crystal symmetry due to the emergence of some sort of inhomogeneity in a magnetic material should result in its electric polarization. The phenomenological theory of the magnetoelectric effect has been constructed for the case when this inhomogeneity is magnetic in nature. It has been shown that if only the short-range part of the magnetoelectric interactions is significant, the inhomogeneous electric polarization **P** (**r**) is localized in the region of the magnetic inhomogeneity. Domain boundaries (DB) associated with the existence of different types of domain structures are the most prevalent type of magnetic inhomogeneities in magnetically ordered crystals. Baryakhtar *et al.* have paid special attention to the investigation of plane 180° DB's in ferromagnetics and antiferromagnetics. The authors have enumerated for them all possible types of domain boundaries with different types of symmetry, and have obtained a qualitative spatial dependence of the components of the polarization vectors **P** (**r**) for all types of DB's. For uniaxial ferromagnetics and rhombic antiferromagnetics, this dependence has been obtained in an explicit form. The authors have also shown that in all the cases considered by them, there exists an electric charge exchange density in the region

of domain boundaries, which results in an electric field component perpendicular to the DB plane. Besides, an uncompensated surface charge is created in the region where Néel-type DB's emerge on the surface of the sample. Thus, the results of Baryakhtar *et al.* reveal that electric fields can influence the domain structure of magnetically ordered crystals.

The paper by Smolenskii and Chupis is a review of the theoretical and experimental studies conducted so far on ferroelectromagnets. Ferroelectromagnets are a new type of material, predicted and first obtained by Soviet scientists, which are simultaneously ferro- (antiferro-) electrics as well as ferro- (ferri-, antiferro-) magnetics. Special attention has been paid to the magnetoelectric effects arising due to an interaction between the ordered spin subsystem and the ferroelectric subsystem of a crystal. Different mechanisms for this interaction, which contribute to the exchange and relativistic magnetoelectric energy, are discussed. The review also describes the results of theoretical investigations of thermodynamic and high-frequency properties of ferroelectromagnets, including temperature phase transitions, orientational transitions in a magnetic field, spectrum of elementary excitations, and the behaviour of a ferroelectromagnet in alternating external fields. The theoretical investigations explain the results of the basic magnetoelectric measurements of the ferroelectromagnets carried out so far, and also predict the existence of new interesting magnetoelectric effects like the emergence of the first- and second-order phase transitions in the spin subsystem and the ferroelectric subsystem, a strong connection between spin- and polarization waves in ferroelectromagnets, etc.

The authors have analyzed the available experimental data on magnetoelectric measurements in ferroelectromagnets, including the measurement of magnetoelectric susceptibility, dielectric susceptibility anomaly during a magnetic transition, as well as the magnetoelectric measurements in the most widely-investigated ferroelectromagnet, the nickel-iodine boracite. The review also contains a discussion of some aspects of the possible applications of ferroelectromagnets for scientific and practical purposes. The temperatures of the ferroelectric and magnetic ordering, as well as the results of magnetoelectric measurements, have been included in the table of known ferroelectromagnets. The review bears testimony to the leading role of the Soviet scientists in the investigation of ferroelectromagnetic crystals.

The paper by Ponyatovsky, Antonov, and Belash is devoted to the results of investigations of the physical properties of new hydrogenous phases (hydrides) of group VI-VIII transition metals. Most of these metals were earlier considered to be incapable of forming hydrides. In the middle of 1970's, an original method was worked out by Ponyatovsky *et al.* at the High-Pressure Physics Laboratory of the Institute of Solid State Physics of the USSR Academy of Sciences,

according to which hydrogen could be compressed to several gigapascals (tens of kilobars) in volumes allowing the hydrogenation of relatively massive samples. With the help of this method, the authors were able to synthesize and investigate a large number of new hydrides of transition metals. By compressing hydrogen to 2 GPa, they obtained for the first time the hydrides $MnH_{0.96}$, $NiH_{1.25}$, and $TcH_{0.83}$, while a compression up to 6.5 GPa led to the production of the hydrides $FeH_{0.8}$, $CoH_{0.5}$, $MoH_{1.3}$, and $RhH_{0.65}$. Pressures up to 9 GPa were attained by the end of 1981, and this enabled the authors to saturate rhenium up to the composition $ReH_{0.22}$, and to increase the solubility of hydrogen in cobalt and rhodium to the composition $MeH_{1.0}$. Such high parameters have not been obtained anywhere in the world so far. The methods developed for measuring the electrical conductivity and Curie temperatures at high hydrogen pressures over a wide temperature range enabled the authors to construct the T-P phase diagrams of the investigated systems, while the "quenching" of samples under pressure to liquid nitrogen temperatures provided an opportunity of investigating the structure, composition, and physical properties of "quenched" high-pressure phases under atmospheric conditions.

As regards the physical properties, the results of investigation of solid hydrogen solutions in 3*d*- metals and their alloys, which are classical band magnetics, are of utmost interest. Hydrogen was found to affect the magnetic properties of these materials very strongly and in quite different ways. However, an analysis of the available data shows that all the effects are mainly due to an increase in the degree of filling of the *d*-band of the metal by electrons as a result of hydrogenation. This established the physical status of hydrogen as a component of the investigated alloys. The dependence of the magnetic properties of Me-H solutions on concentration was explained with the help of the rigid *d*-band model, which provided an uncontroversial explanation of all the available experimental data, and the prediction of the behaviour of these properties in materials which have not been investigated so far.

Essentially new results were obtained by Ponyatovsky *et al.* during investigations of solid solutions of hydrogen in palladium alloys. The initial interest towards these materials was drawn by a communication reporting an unusually high superconducting transition temperature T_k in such solutions obtained by hydrogen implantation. An investigation of solutions synthesized under high hydrogen pressures in equilibrium conditions showed that these compounds do not possess any anomalous superconducting properties. Thus, the anomalous behaviour of T_k in Pd-Me-H solutions obtained by implantation is not a property of the equlibrium solutions (as was assumed earlier), but is due to the peculiarities of their specific state. However, the authors also observed anomalous properties of Pd-Me-H solutions

formed under high hydrogen pressures. It was found that many Pd-Me-H systems at relatively low temperatures ($\gtrsim 250°C$) undergo phase transitions which are unusual for group VI-VIII *d*-metals and are accompanied by a diffusional redistribution of the atoms of the metallic matrix. This demonstrates the strong effect of hydrogen on the energy of interaction between the atoms of these materials.

Thus, the new experimental results obtained by Ponyatovsky *et al.* with the help of the high-pressure technique have led to a considerable advancement towards answering the important questions concerning the status of hydrogen in transition metals, as well as the processes that may take place during an interaction of the transition metal alloys with hydrogen in an enhanced activity state, i.e. hydrogen which has been compressed to high pressures, both static and dynamic, hydrogen in strong electrolytes, and hydrogen in the plasma state.

The next paper by Ossipyan contains a review of the investigations made during the last few years at the Institute of Solid State Physics of the USSR Academy of Sciences, on the influence of dislocations on the physical properties of semiconductors. A large number of experimental investigations have shown that a considerable interaction takes place between dislocations and the electrons in a semiconductor. There are two aspects to this interaction. Firstly, the presence of dislocations (which are stretches of one-dimensional crystal-lattice defects, capable of moving within the crystal under the influence of an external mechanical force) changes the shape of the electron energy spectrum for a semiconductor as compared to the spectrum of a similar defect-free crystal. This is manifested in the appearance of localized levels or even narrow bands of allowed electron states (connected with dislocation) in the forbidden band gap of the semiconductor. An electron capture to these states from the conduction band or the valence band changes the number and mobility of the charge carriers, thus bringing about significant changes in the electrical properties of semiconductors. The motion of electrons and holes in the narrow dislocation bands under the influence of an electric field leads to a specific quasi-one-dimensional dislocation conductivity, while the transitions among the narrow dislocation bands in the crystal gives rise to dislocation absorption and luminescence. Thus, the electronic properties of semiconductors with dislocations are quite different from those of defect-free crystals.

The second aspect of the electron-dislocation interaction is the effect of the state of an electron subsystem and its variations on the movement of dislocations under the influence of an external force, i.e. the effect on important properties of a crystal like its plasticity and strength. As a result of this, a considerable variation (several hundredths of a per cent) in the flow stress of crystals of $A^{II}B^{VI}$ group semiconductors was observed under the action of light or an

electric field (photoplastic effect and electroplastic effect). In its turn, the movement of dislocations in these crystals led to the appearance of an electric current (dislocation current) in the external circuit containing the crystal being deformed.

All these effects were discovered at the Institute of Solid State Physics of the USSR Academy of Sciences and have considerably changed our concepts about the physical nature of the strength and plasticity of solids.

The paper by Alferov, Garbuzov, and Gorelenok is devoted to new achievements in semiconductor technology and in the fabrication of semiconducting opto-electronic devices. In the end of 1960's, Alferov *et al.* carried out pioneering work at the Ioffe Physico-Technical Institute of the USSR Academy of Sciences on the creation of ideal semiconducting heterojunctions, as well as injection lasers based on them and operating in the CW mode at room temperature. In order to extend the range of semiconducting materials which are suitable for preparing high-quality heterojunctions, Alferov *et al.* proposed in 1971 the use of quaternary solid solutions of a $A^{III}B^{V}$ compounds. After a study of different types of quaternary compounds, the choice ultimately fell on the InGaAsP solid solutions, whose narrow-band compositions could be used to solve the problem of obtaining infrared sources for optical communication systems, and the wide-band compositions could be used for creating light-emitting diodes. In 1974-75, Soviet scientists reported for the first time the creation of low-threshold infrared lasers, and high-efficiency LED's based on InGaAsP/InP heterojunctions. During 1975-76, Alferov *et al.* fabricated first visible injection lasers based on InGaAsP/GaAs and InGaAsP/GaAsP heterojunction lasers. This was followed by the construction of lasers on the shortest wave lengths ($\lambda = 0.637$ μm at $T = 300$ K) based on the same heterojunctions. At present, the number of publications devoted to the preparation and investigation of heterojunctions based on lattice-matched compositions of solid solutions has reached several hundreds. Many optoelectronic devices based on heterojunctions are being commercially produced.

The first part of the review by Alferov *et al.* deals with the technology of obtaining multicomponent solid solutions and heterojunctions based on them. The second part describes the peculiarities of the recombination processes for nonequilibrium carriers in the active region of these heterojunctions, while the third part describes the properties of three main types of optoelectronic devices based on InGaAsP heterojunctions, namely, heterolasers, LED's, and IR photodetectors.

A review of theoretical and experimental investigations of the methods of stimulating acoustic instability in semiconductors by an alternating electric field, first proposed at the Institute of Radioengineering and Electronics of the USSR Academy of Sciences, has been

given in the paper by Gulyaev and Mansfel'd. These include the multitransit amplification of fluctuations under synchronism, amplification in a Corbino disc geometry, and aplification in a high-frequency alternating electric field. The authors have paid special attention to the multitransit amplification and generation of acoustic waves under synchronism, when an alternating electric field (with a half-period equal to the time taken by an acoustic wave to propagate through the crystal) leads to an ultrasonic drift, causing an amplification of acoustic waves or fluctuations. In this case, the faces of the crystal reflect the acoustic wave. Under such conditions, the waves amplified during the first passage through the crystal are amplified again upon reflection, since the drift field also changes sign at the instant of reflection. The amplification process is thus repeated over several periods of the field. A multiple amplification allows longer time delays for a signal represented in the form of acoustic waves excited in a crystal. A multitransit amplification of acoustic fluctuations in a crystal leads to a gradual narrowing of the spectrum of frequencies being amplified, and the emergence of high-intensity acoustic oscillations. In InSb crystals, the oscillation intensity reached 250 W/cm^2 for a 2 kHz width of some spectral components at an oscillation frequency of 2 GHz. A high-intensity, nearly monochromatic acoustic wave is essentially generated under such conditions. With the help of such a powerful source of acoustic waves, it became possible to verify the basic concepts of the theory on nonlinear amplification of acoustic waves, developed in 1969 by Yu. V. Gulyaev. This theory satisfactorily explains the S- and N-shaped current-voltage characteristics obtained experimentally, as well as the dependence of the gain factor on the field and the intensity of acoustic waves. The investigations of the initial stage in the formation of the oscillation spectrum, carried out at the Institute of Radioengineering and Electronics of the USSR Academy of Sciences, led to the first experimental confirmation of the results of the theory of nonlinear interaction of acoustic fluctuations through rapidly damping electron density waves. This theory was developed in 1968 by V. L. Gurevich at the Ioffe Physico-Technical Institute of the USSR Academy of Sciences. The review by Gulyaev and Mansfel'd also describes the work carried out at the Institute of Radioengineering and Electronics, in which the multitransit generation of powerful acoustic flux in the microwave region was obtained for the first time, and the nonlinearity concentration mechanism was investigated under collision-free conditions when the electron mean free path exceeds the acoustic wavelength. It can be confidently stated that the results of investigations described by Gulyaev and Mansfel'd considerably broadens our concepts concerning the interaction of acoustic fluctuations in semiconductors and the nonlinear acoustoelectronic interaction. All this is very important for the creation of acoustoelectronic oscillators and

signal amplifiers, as well as for other data processing devices. The results presented by the authors and the references cited by them indicate the leading role of Soviet scientists in the detailed investigation of nonlinear acoustoelectronic phenomena in semiconductors.

The paper by Osiko and Prokhorov deals with the physics of solid state lasers. Over the last few years, considerable progress has been made in this branch of solid state physics. As a result of theoretical and experimental investigations of the transfer and degradation of electron excitation energy in crystals and glasses with impurities, it became possible to obtain a sharp increase in the efficiency of solid state lasers. Effective solid state lasers with continuous frequency tuning have also been constructed, and this has become possible as a result of new regularities discovered in the spectroscopic and spectro-kinetic properties of crystals with wide vibronic absorption and luminescence spectra. Above all, the crystals and glasses with neodymium impurities are worth mentioning. Until recently, neodymium lasers had a very low efficiency (rarely exceeding 1%), although they are more advantageous in other respects (small size, a high value of average output power or a high pulse energy, and possibility of operation in different modes). The reason behind this low efficiency was a poor utilization of the pumping tube radiation. Over the last few years, neodymium glasses and crystals capable of absorbing a much larger fraction of the pumping tube radiation than the previously known laser materials have been fabricated in the Solid State Physics Laboratory of the Institute of General Physics of the USSR Academy of Sciences under the supervision of V.V. Osiko and A. M. Prokhorov. Crystals with neodymium and chromium impurities, as well as glasses and crystals with the concentration of active neodymium about an order of magnitude higher than in crystals and glasses grown earlier, have been created by this group. All this has led to a sharp increase (two- or three-fold) in the efficiency of Nd lasers. For example, the absolute efficiency of lasers based on concentrated neodymium phosphate glass (KNFS) and on GSGG-Cr^{3+}-Nd^{3+} crystals[1] in the free-generation mode amounts from 5 to 6%, while the slope efficiency exceeds 8%. The pumping energy in this case is about 10-20J.

The considerable progress in the development of solid state lasers with a continuous laser frequency tuning is due, to a large extent, to the development of two new laser crystals during the recent years at the Institute of General Physics of the USSR Academy of Sciences. One of these is a new crystal with chromium ion impurities, viz. GSGG-Cr^{3+}. Continuously tunable lasers in the red and near-infrared spectral regions have been constructed on the basis of these crystals. The parameters of these lasers are better than for lasers based

1 GSGG means of gadolynium-scandium-gallium garnet.

on alexandrite crystals in that they operate efficiently at room temperature, have a higher efficiency and a wider tuning range. The second crystal is that of lithium fluoride with colour centres. The LiF tunable lasers are superior to the dye lasers in two aspects: firstly, they do not require any cooling; and secondly, the tuning range of such lasers is several times wider than for dye lasers so that one LiF crystal element can replace four of five different dyes. The creation of high-efficiency LiF tunable lasers became possible only after the process of transformations of point defects in these crystals were understood, and the methods of accumulating and exciting active centres were worked out.

The paper by Makhviladze, Prokhorov, Valiev, and Velikov is devoted to the experimental and theoretical investigations of the etching processes in polymers by fluxes of quanta and charged particles. A new effect, called the photoetching of polymers, was discovered by the authors during 1980-82 at the Microelectronics Laboratory of the Institute of General Physics of the USSR Academy of Sciences. According to this effect, ionizing radiation like the vacuum ultraviolet and X-rays lead to the destruction of a polymer and the formation of low-molecular fragments which go over to the vacuum or the gaseous medium. The processes occuring in this case can be considered as physico-chemical processes belonging to the field of physical chemistry of solids, and to be more precise, to the radiation- and photochemistry of polymers in a glass-like state. From a practical point of view, the effects discovered by the authors provide a new method for changing the shape and dimensions of polymer materials. The possibility of localizing the etching to regions of size 0.2-0.5 μm during the photoetching by vacuum ultraviolet radiation opens the way for making polymer masks with submicron-sized elements of the pattern. This is extremely important in microelectronics. The authors have worked out original experimental methods for investigating direct etching of polymers and polymer films. The etching kinetics have been investigated in details for many polymer materials. A new theoretical model for this effect has been proposed and developed by the authors by using the concept that the process is of diffusion type. This model is applicable for describing the etching in a flux of electromagnetic radiation and low-intensity particles (nonthermal processes).

On the whole, the results obtained by the authors open new possibilities in the field of vacuum-ultraviolet, X-ray, electron-beam, and ionic-beam lithography, the creation of submicron structures, and the formation of polymers of given dimensions. At present, the processes of photo- and radiational modification of polymers are being investigated all over the world. The discovery of the photoetching of polymers by Makhviladze *et al.* will undoubtedly serve as an important step in the advancement of these efforts.

The paper by Grosberg and Khokhlov deals with the statistical physics of macromolecules. This is a new branch of science, bordering physics, chemistry, and biology. This paper describes the results of the investigations which led to the creation of the theory describing a wide range of phenomena in polymer physics, viz. the coil-globule transition in polymer and biopolymer systems. Following the sad and untimely death of Academician I. M. Lifshitz recently, Grosberg and Khokhlov have developed the ideas emerging from his brilliant and exceptionally fruitful approach (proposed in 1968) in the theoretical physics of polymers. The generalization of this approach and its extension to a wide range of objects in the physics of macromolecules which was started by the authors under the supervision of late Acad. Lifshitz, has led to an explanation of a large number of phenomena, occurring in entirely different polymer systems, within the framework of a single theoretical approach. First of all, the theory of coil-globule transition (collapse) was constructed for the simplest linear uncharged homopolar macromolecule. Such a transition takes place in a diluted solution when the quality of the solvent is made worse. A lot of attention has been paid by the authors to this theory, mainly because the fairly accurate and detailed experimental data on the collapse of separated molecules, which have become available recently, permit a detailed comparison between the theory and experiment. An important aspect in the further development of the theory of coil-globule transitions is its extension to the case of heteropolymers, i.e. macromolecules comprising chains of several different types. Such a generalization is a necessary step towards the construction of a systematic theory of the collapse of proteins which are the most important type of biological molecules. In this paper, the authors have described the present-day state of the problem of globulization of heteropolymers.

Lifshitz's approach was found to be very useful not only for investigating coil-globule transitions, but also for considering several other phase transitions in macromolecular systems. The application of this approach to the theory of liquid-crystal ordering of polymer solutions led to exceptionally important result: it was found that an LC phase transition can be interpreted as a special case of globulization which takes place in the space of link orientations rather than in the ordinary three-dimensional space. This permitted the construction of the theory of orientational ordering of a solution of partially flexible rigid-chain macromolecules. The main points of this theory and its important results are also included in this article by Grosberg and Khokhlov. It was mentioned above that a wide range of phenomena in the physics of polymers and biopolymers can be described as coil-globule transitions. These include, in particular, the collapse of polymer networks, the formation of intramolecular liquid crystals of different types, avalanche-type condensation of counterions

in solutions of weakly-charged polyelectrolytes, the formation of a compact form of DNA (called Ψ-condensation), and the denaturation of proteins. The last section of the review by Grosberg and Khokhlov is devoted to a brief description of the theory which was constructed for these phenomena with the help of Lifshitz' approach.

In conclusion, it can be stated that this approach in the statistical physics of macromolecules, which was initiated by the pioneering work of I.M. Lifshitz, has led to a large number of results of prime importance, and offers great promises for further development and application to new problems in the polymer physics.

A. M. Prokhorov, *Mem. USSR Academy of Sciences*
A. S. Prokhorov, *Cand. Sc.* (*Phys. and Math.*)

1 Submillimetre Dielectric Spectroscopy of Solids

G. V. Kozlov, A. M. Prokhorov, and A. A. Volkov

1.1. INTRODUCTION

The dielectric spectroscopy involves the investigation of the dielectric permittivity of materials as an experimental method for solving different types of physical problems. Besides the Raman effect and neutron scattering, the dielectric measurements offer the most effective means of investigating the dynamics of a crystal lattice. They are used for investigating the vibrational spectra of crystals, phonon-phonon interaction, behaviour of soft modes, relaxation and ordering processes, polarization and conductivity mechanism, migration of domains and impurities, etc.

As a single experimental method, the dielectric spectroscopy covers a huge interval of frequencies, from 10^{-5} to 10^{15} Hz. In view of this, quite different techniques are employed for measuring the permittivity of crystals. These include standard capacitors, bridge- and electronic circuits, waveguide lines, and infrared spectroscopy. In spite of the wide array of methodical equipment available for dielectric spectroscopy, however, the spectral region between microwave and the far-infrared, i.e. the submillimetre wave region ($\nu \sim 10^{11}$-10^{12} Hz) was practically unavailable for a long time. The main reason behind this was the absence of a suitable source of radiation, which held up the fabrication of instruments and the development of measuring techniques.

By the middle of the sixties, the problem of "submillimetre barrier" in spectroscopy lost its edge. Concerted efforts toward improving the microwave and infrared technology made it possible to steadily encroach upon the region of submillimetre waves. Valuable spectroscopic investigations were carried out in the submillimetre region with the help of infrared spectrometers using thermal radiation sources, as well as from monochromatic radiation obtained through generation of submillimetre harmonics in microwave vacuum-tube oscillators. This method of mastering the submillimetre region continues to be developed even today. It cannot be denied, however, that the results for the submillimetre spectroscopy are obtained by using the microwave and infrared techniques with great difficulty, and any large-scale investigations in the submillimetre range continue to be a very complicated process indeed.

Under these conditions, the number of unsolved problems which are directly associated with the submillimetre waves continues to rise. In the solid state physics, for example, the traditional problems of far-infrared and submillimetre spectroscopy, such as the energy gap in superconductors, soft modes in ferroelectrics, magnetic resonance in antiferromagnetics, and bound states of charge carriers in semiconductors, have been supplemented by quite new problems like the dynamics of crystal lattice with incommensurate phases, superionic conductivity, metal-insulator phase transitions, central peak in systems with displacement-type phase transitions, etc.

This review is devoted to the description of a method for dielectric measurements in the submillimetre range, based on the application of a special source of submillimetre radiation called the backward wave tube (BWT). Although this method is not widely used at present, it will be shown that it offers great promises. The BWT oscillators, which are commercially produced in the USSR [1.1, 2], have been successfully used in scientific research for a long time. They serve as the source of radiation in spectrometers constructed in various institutions, including the Lebedev Physical Institute of the USSR Academy of Sciences, the Institute of Radioengineering and Electronics of the USSR Academy of Sciences, the State Pedagogical Institute (Moscow), the Institute of Applied Physics (Gorky), the Institute of Radioengineering and Electronics of the Ukrainian Academy of Sciences (Kharkov), for investigating the properties of solids, liquids, and gases at frequencies $\sim$3-30 cm^{-1}.

The first part of this review deals with the problem of mastering the submillimetre range especially for dielectric spectroscopy. The submillimetre BWT spectrometers, which are being designed in the oscillations laboratory of the Lebedev Physical Institute (now the Institute of General Physics of the USSR Academy of Sciences) for the past twenty years or so [1.3-5], were found to be extremely effective instruments for dielectric measurements, combining the most significant achievements of the infrared spectroscopy and the microwave technology. They make it possible to measure precisely and independently the real (ε') and imaginary (ε'') parts of the permittivity at different points on the frequency scale, and to record the spectra of the quantities being measured over a wide frequency range by using a unified approach. The results obtained with the help of BWT spectrometry, viz. the $\varepsilon'(\nu)$ and $\varepsilon''(\nu)$ spectra with values right up to 10^3, have an average accuracy of $\pm 5\%$ and a frequency resolution $\Delta\nu/\nu \sim 10^{-4}$. These results are unique and practically unattainable by any other method of measurements in most cases.

The second part of the review deals with the applications of submillimetre dielectric spectroscopy for solving some actual problems of solid state physics.

1.2. TECHNIQUE AND METHODS OF SUBMILLIMETRE BWT SPECTROSCOPY

All investigations were carried out by using frequency-tuned monochromatic submillimetre radiation of average power 10 MW, generated by BWT oscillators. In their working principle, the submillimetre BWT's are similar to the well-known microwave vacuum tube oscillators and bear a certain resemblance to the latter in their construction. In this type of instrument, the electrons emitted by an electron gun fly in vacuum over a decelerating system in the form of a fine metallic comb which creates a periodic potential in the path of electrons. The radiation generated in this case is emitted into the free space through an oversized waveguide. Usually, 90% or more of the radiation is linearly polarized along the shorter wall.

An important property of BWT's from a spectroscopic point of view is that the frequency of the radiation generated by them can be

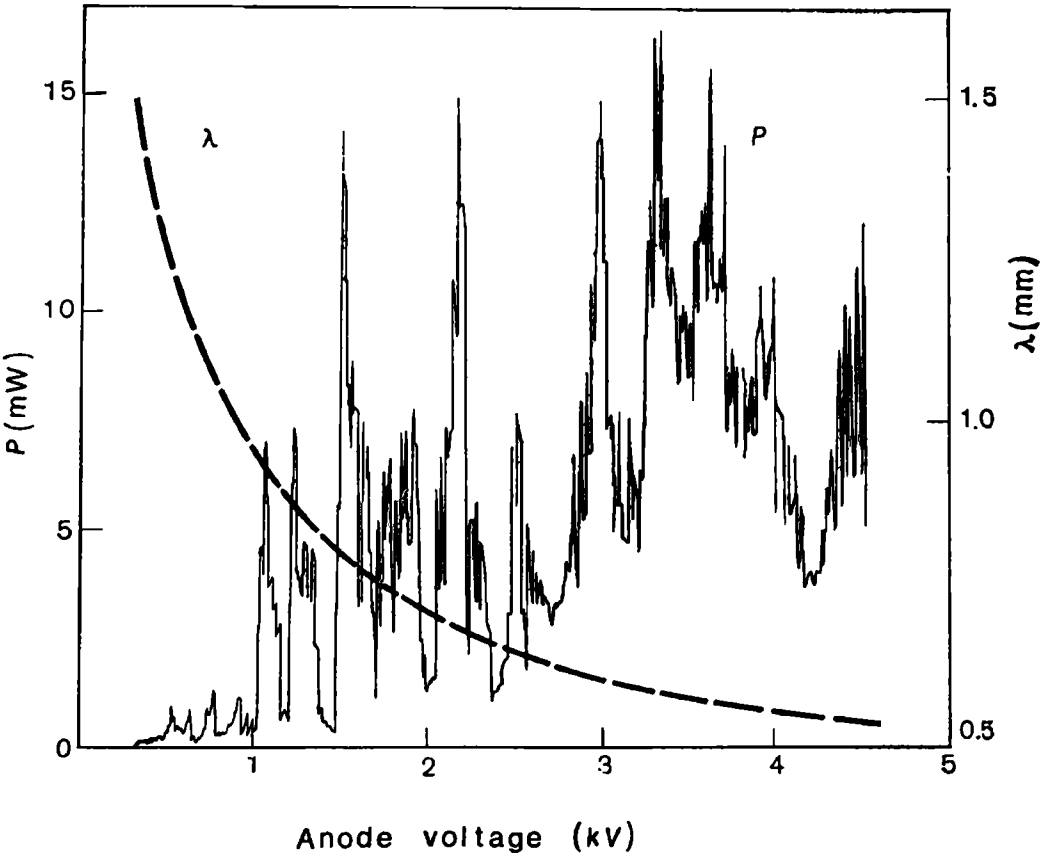

Fig. 1.1. Dependence of the output power P and the radiation wavelength λ on supply voltage for a submillimetre BWT.

continuously tuned over a wide range, viz. up to 50%, and sometimes even up to 100%. Another useful property of BWT's is that the frequency and power of radiation are uniquely related to the magnitude of the supply voltage, and this relation remains unchanged throughout the life of a tube.

Figure 1.1 shows the basic characteristics of typical submillimetre BWT's. The operating range of the present-day BWT's extends right up to frequencies ~ 40 cm^{-1}, and hence a set of 5-6 oscillators is required for spectroscopic investigation of the entire submillimetre range.

The underlying idea in the dielectric measurements by BWT spectrometers is quite simple: the radiation with strictly regulated parameters (frequency, phase, intensity, and polarization) is directed at the sample and is then received by an infrared detector after reflection from or transmission through the sample. The change in the parameters (amplitude and phase) of the operating wave occurring as a result of this interaction gives information about the dielectric properties of the sample. In all the methods worked out by us, the radiation is normally incident on the sample which is prepared in the form of a plane-parallel plate. Depending on the choice of the method used, the measurable quantities can either be the transmission coefficient T of the sample and the phase shift φ of the wave in the sample, or the parameters R and ψ, the reflectivity and the phase shift, corresponding to the case of bulk reflection. The mathematical relations connecting these measurable quantities with the dielectric parameters of a material are well-known in optics [1.6]:

$$T = e^{-\frac{4\pi kd}{\lambda}} \frac{(1-R)^2 + 4R\sin^2\psi}{\left(1 - Re^{-\frac{4\pi kd}{\lambda}}\right)^2 + 4Re^{-\frac{4\pi kd}{\lambda}}\sin^2\left(\frac{2\pi nd}{\lambda} + \psi\right)},$$

$$\varphi = \frac{2\pi nd}{\lambda} - \arctan\frac{k(n^2+k^2-1)}{(k^2+n^2)(2+n)n} + \arctan\frac{Re^{-\frac{4\pi kd}{\lambda}}\sin 2\left(\frac{2\pi nd}{\lambda} + \psi\right)}{1 - Re^{-\frac{4\pi nd}{\lambda}}\cos 2\left(\frac{2\pi nd}{\lambda} + \psi\right)}, \tag{1.1}$$

$$R = \frac{(n-1)^2+k^2}{(n+1)^2+k^2}, \quad \psi = \arctan\frac{2k}{n^2+k^2-1},$$

$$\varepsilon' = n^2 - k^2, \quad \varepsilon'' = 2nk,$$

where d is the sample thickness, and n and k are the refractive index and the absorption index, i.e. the optical constants of the material.

Obviously, any pair of quantities from T, φ, R, and ψ can be used to calculate n and k. Besides, transmission data obtained for

samples with different thicknesses T_1 and T_2 are often used for dielectric measurements. This gives another couple of equations for calculating n and k. In far-infrared spectroscopy, where transmission measurements are difficult, the quantities R and ψ are used as a rule. In general, the choice of experimental methods is frequently quite limited and is almost always uniquely determined by the actual possibilities of measuring T, φ, R, and ψ. It is, however, clear that different pairs of measurable quantities are far from being equivalent in providing the maximum accuracy in the values of n and k. In view of the considerable nonlinearity of Eqs. (1.1), the uncertainty in the values of n and k depends to a large extent on the errors in the measurement of T, φ, R, and ψ, as well as on the absolute magnitude of n and k themselves.

While developing the methods of dielectric measurements by using BWT spectrometers according to their potentialities, we have analyzed the effectiveness of various methods of determining n and k depending on the errors in the measurement of T, φ, R, and ψ [1.7]. It turned out that under nearly identical conditions, the T and φ method gives the best results in versatility and accuracy of measurement of n and k. Figure 1.2 underlines the potentialities of this method as compared to the method of two thicknesses (T_1 and T_2) using a BWT spectrometer. It can be seen that the T and φ method provides a higher accuracy (of about an order of magnitude) than the T_1 and T_2 method of determining n and k over a considerable range of variation of these quantities. The T and φ method is of basic importance in our dielectric measurements and is always used when the radiation power is sufficient to penetrate the sample.

Before describing the design and operation of the BWT spectrometers, let us consider two very important principles which form the basis of their construction. These are the single-channel method of recording spectra and the use of a computer for this purpose.

It can be easily seen from Fig. 1.1 that the output power of a BWT is a strongly nonmonotonic function of frequency. Obviously, this creates certain difficulties in spectroscopic measurements. However, the entire fault does not lie with the BWT's. These difficulties are in principle inherent in submillimetre spectroscopy using monochromatic oscillators. Strictly speaking, Fig. 1.1 shows the frequency dependence not of the power of a BWT oscillator, but of the signal intensity at the detector recording this power. In this figure, the generation zone of a BWT, the transfer function of the channel in which the radiation propagates, and the frequency dependence of the transmissivity of the input window of the detector are superimposed on each other. As in the microwave technique, the standing waves in the measuring channels play a significant role in submillimetre spectroscopy. Besides, parasitic diffraction effects at the apertures restricting the radiation beam also play an important part. The compatibility

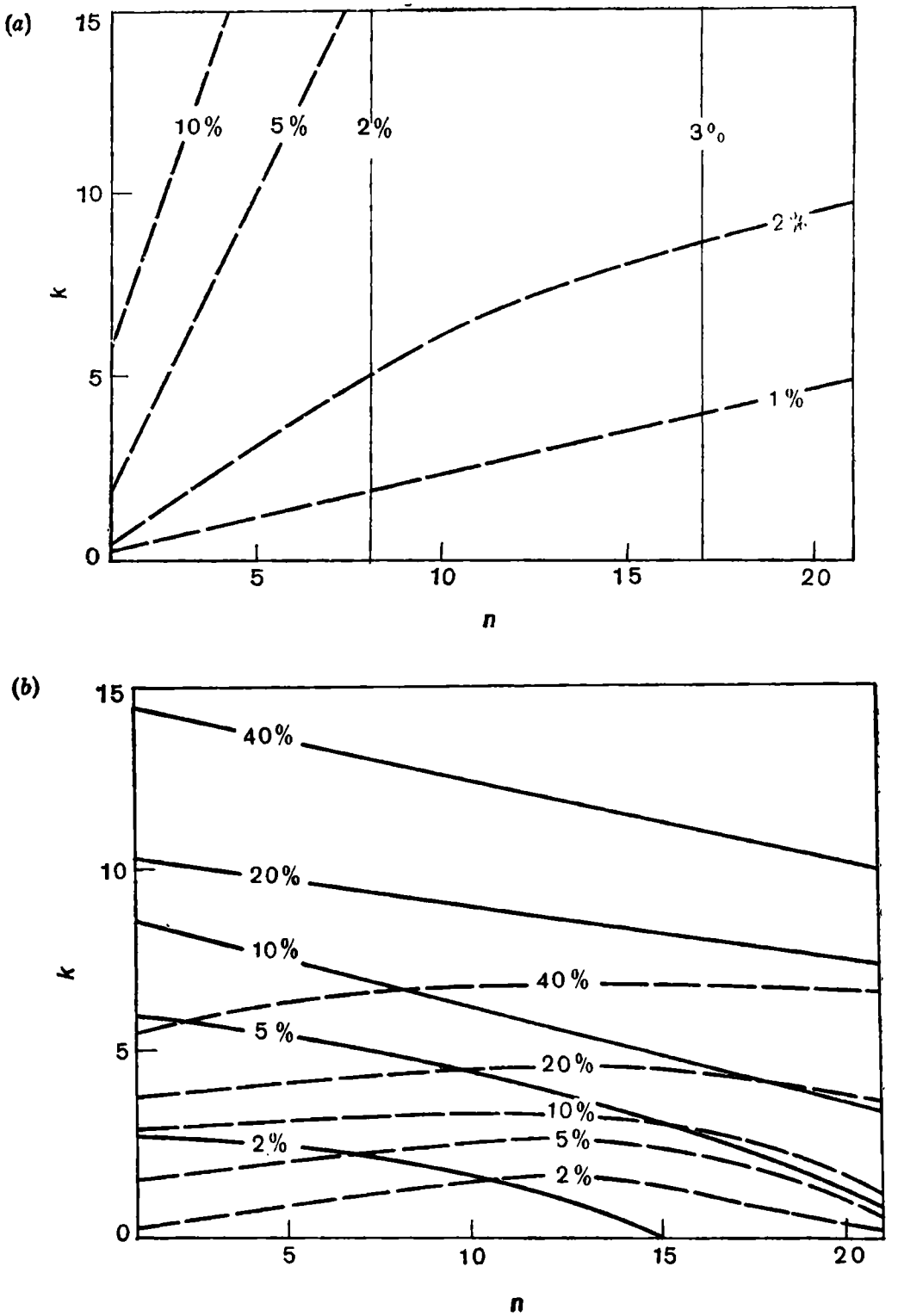

Fig. 1.2 Accuracy of measurement of optical constants n and k on a BWT spectrometer by using two different methods: (*a*) T and φ method; (*b*) the method of two thicknesses (T_1 and T_2). The dashed lines correspond to $\Delta n/n$, while the solid lines denote $\Delta k/k$

of the radiation wavelength with the characteristic parameters of the sectional elements like lenses, windows, diaphragms, etc., together with the monochromaticity of radiation and a high reflectivity of all materials in the submillimetre range, imparts a certain degree of resonance properties to almost any equipment used in the submillimetre technique, including generators, detectors, and radiation control units. Hence, for any radiation source, we always have to deal with complex and quite individual instrument functions in the measuring channels in the submillimetre spectroscopy.

The problem of quantitative measurements at submillimetre wavelengths, however, can be successfully solved and, to our mind, its

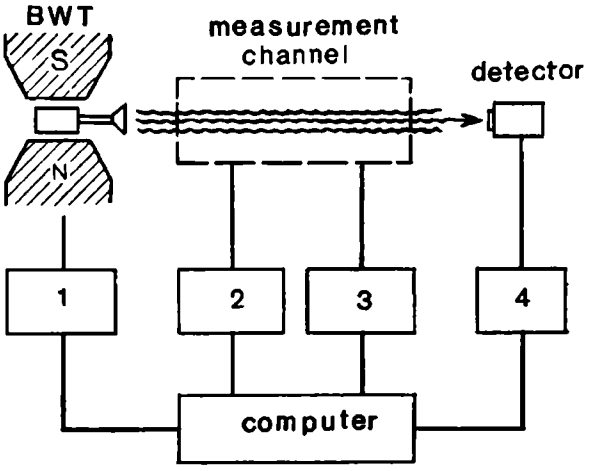

Fig. 1.3. Block diagram of the submillimetre BWT spectrometer *Epsilon*. *1*—BWT power supply; *2*—control system for the measuring channel elements; *3*—system of thermal stabilization of the samples; *4*—recording system.

solution is in line with Chantry's remark [1.8] about the Fourier spectroscopy. According to Chantry, it is advantageous to solve the methodical problems with the help of computer technology rather than by using more and more complex measuring instruments. In other words, the centre of gravity of methodical problems should be shifted from the field of instrumentation towards a mathematical analysis of the results.

The block diagram of a BWT spectrometer of the type *Epsilon* is shown in Fig. 1.3. The spectrometer consists of five main subsystems: (*1*) generator, (*2*) recording system, (*3*) optical measuring channel, (*4*) unit for holding, adjusting, and thermostatic control of samples, and (*5*) control system.

The first subsystem contains replaceable radiation generators, the electromagnet which is required for such generators, and the power supply for the BWT. The high voltage for the BWT is supplied by

a highly stabilized computer-operated transducer which ensures a stabilized voltage between 100 and 6500 V with an accuracy $\Delta U/U$ of not less than 5×10^{-5}. This quantity, which indicates the stability of the power supply, uniquely determines the maximum monochromaticity of radiation: $\Delta\nu/\nu \sim 10^{-5}$. The monochromaticity of radiation can be regulated if required. For this purpose, a high-voltage sawtooth modulator with frequency $\sim$ 1 kHz is included in the BWT power supply.

The recording unit consists of an opto-acoustic Golay cell, a 25 Hz radiation modulator, an amplifier with a synchronous detector, and a sampling-storage-reset circuit. Like the BWT power supply control, the operation of this unit is also synchronized with the modulation frequency. The dynamic range of the recording unit is 10^{-4}.

The measuring section of the spectrometer is similar to an optical measuring channel. While the specific form of this unit depends on the choice of the experimental technique, the basic principles of its construction remain the same: the radiation propagates in free space, a beam of 40 mm cross section is formed by Teflon lenses or metallic parabolic mirrors, plane one-dimensional wire grids with a period $l \ll \lambda$ [1.9] are used as polarizers of radiation and beam dividers; the sample is placed in a channel tightly pressed against a metallic diaphragm.

The sample temperature can be varied from liquid helium temperature to several hundreds degrees centigrade. For this purpose, we use optical cryostats and thermostats which employ thin polymer films as windows in order to avoid the formation of standing waves in the channel.

A computing device based on the computer *Elektronika-60* is used for controlling the operation of the spectrometer.

Figure 1.4 shows the basic measuring system of *Epsilon* for T and φ measurements. The T vs. ν and φ vs. ν spectra are recorded separately in two stages. The T vs. ν spectrum is recorded with the help of a simple "transmission" system, and the sections isolated in Fig. 1.4 by dashed lines are not used. The generator is operated in the frequency scanning mode. The scanning is carried out at different points by varying the BWT supply voltage in steps. The signal at the detector is recorded as a function of the radiation frequency. In order to eliminate the instrumental functions of the spectrometer, the entire procedure is repeated twice, with the sample in the channel and without it.

The second stage involves the recording of the φ vs. ν spectrum. All the elements of the channel are now used, and the system represents a Rozhdestvenskii two-beam polarization interferometer (Mach-Zehnder interferometer). The interferometer operates in such a way that during frequency scanning, one of its mirrors is displaced all the

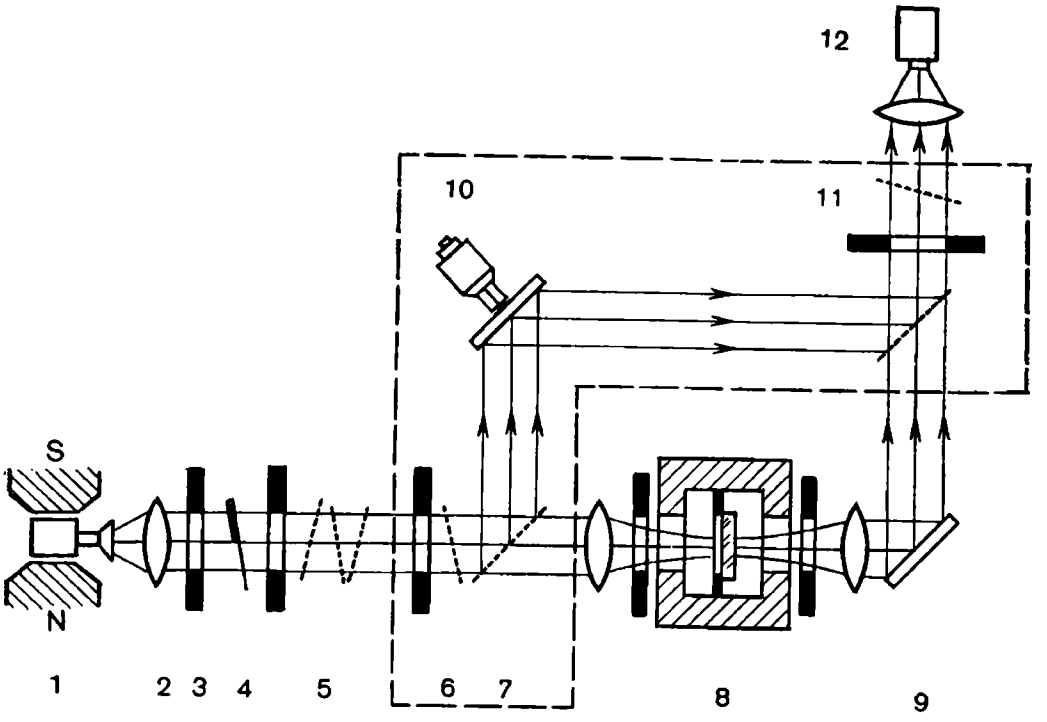

1. Fig.4. Measuring channel of the spectrometer *Epsilon*. *1*—radiation generator (BWT); *2*—Teflon lenses; *3*—absorbing diaphragms; *4*—modulator; *5*—grid attenuator; *6*—polarizer; *7*—dividing grids; *8*—thermostat with the sample; *9*—mirror (phase modulator); *10*—phase-shift compensator: *11*—analyzer; *12*—radiation detector.

time with the help of a servo system in order to sustain the interferometer in a balanced state. The measurable quantity in this case is the displacement $\Delta(\nu)$ of this mobile mirror. In other words, we practically register the change in the optical thickness of the sample with frequency. As in the case of recording T vs. ν spectrum, the basic measurement in this case (with the sample in the channel) is also preceded by gauge measurement, i.e. by the measurement of $\Delta_0(\nu)$ in an empty channel.

The transmission spectrum $T(\nu)$ is calculated by a termwise division of two data files, i. e. the division of the basic file by the gauge file. The phase spectrum $\varphi(\nu)$ of the sample is determined from the difference $\Delta(\nu) - \Delta_0(\nu)$. Clearly, because of the complex instrumental function of the BWT spectrometer, the accuracy of T vs. ν and φ vs. ν measurements depends strongly on the frequency matching of the basic and the gauge spectra. The reproducibility of results in our spectrometers is 1-0.1% (depending on the scanning rate) for $T(\nu)$ measurements and $\sim 1\mu m$ for $\Delta(\nu)$ measurements. These values represent the typical dispersion of the data on T and Δ at an individual point on the frequency scale upon a comparison of several successively recorded spectra.

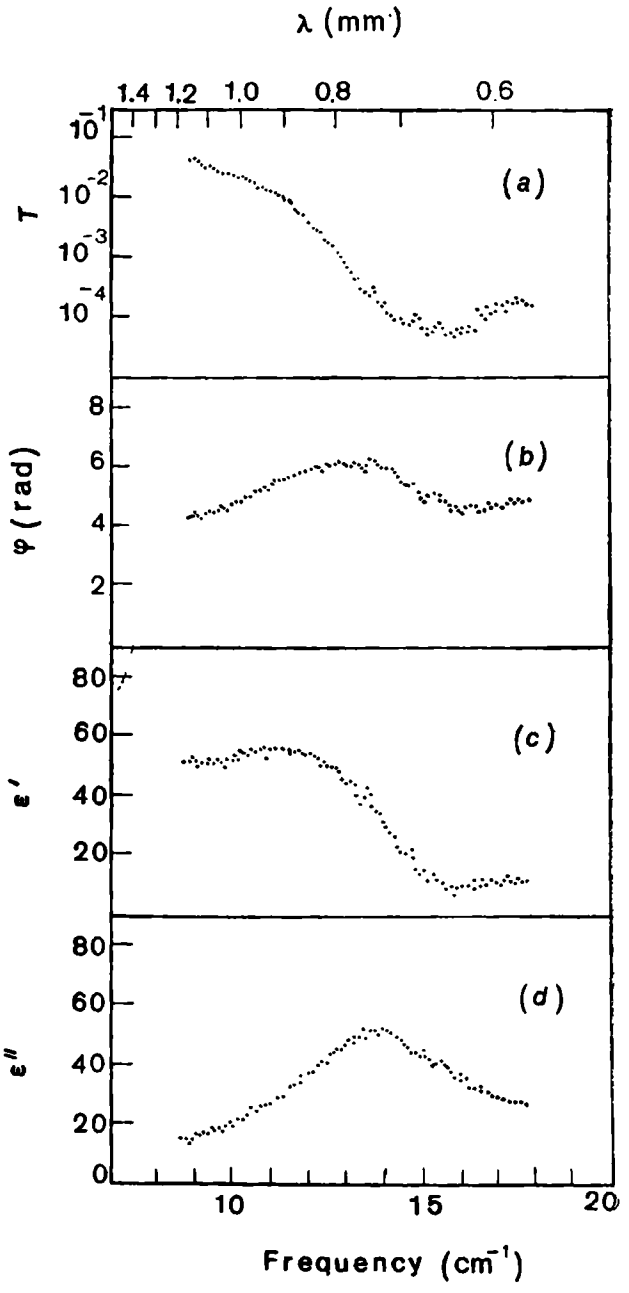

Fig. 1.5. Results of a complete cycle of measurements on the spectrometer *Epsilon*. (*a*) and (*b*) T (ν) and φ (ν) spectra of a 0.11 mm thick $TlGaSe_2$ plate, recorded in the tuning range of one of the BWT's; (*c*) and (*d*) ε′ (ν) and ε″ (ν) dielectric spectra calculated according to the formula (1.1) on the basis of the two previous T (ν) and φ (ν) spectra.

The speed of measurements on *Epsilon* is as follows: a spectrum of 100 points for a retuning of one BWT is registered in 10 to 30 sec for $T(\nu)$ and ~ 30 sec for $\varphi(\nu)$. The calculation of $\varepsilon'(\nu)$ and $\varepsilon''(\nu)$ takes another few minutes.

Figure 1.5 illustrates the main stages in obtaining the $\varepsilon'(\nu)$ and $\varepsilon''(\nu)$ spectra. These measurements were carried out on semiconducting $TlGaSe_2$ samples. It can be seen that in view of a considerable absorption in $TlGaSe_2$ at frequencies $\sim$ 12-16 cm^{-1}, even a very thin sample significantly weakens the radiation ($T \simeq 10^{-4}$). In most cases, however, a BWT spectrometer with opto-acoustical detectors can be confidently used even for transmissivities $T \simeq 10^{-5}$, and this limit can be lowered further by about two orders of magnitude by using cooled detectors. Assuming that the sample thickness can be reduced to tens of microns, the values of ε' and ε'', which can be measured on a BWT spectrometer with the help of the simple universal systems described above, can be estimated at ~ 1000.

Figure 1.6 illustrates the measurements with a quite transparent sample. It also demonstrates the potentialities of a BWT spectrometer for investigating narrow absorption lines on the frequency scale. The $T(\nu)$ and $\varphi(\nu)$ curves in Fig. 1.6 show the antiferromagnetic resonance in yttrium orthoferrite ($YFeO_3$). The smooth oscillations in the $T(\nu)$ and $\varphi(\nu)$ curves are caused by interference of waves in the sample.

It should be noted that the interference of waves inside a sample is a frequently encountered phenomenon in weakly absorbing samples. This gives rise to the additional possibility of determining the dielectric parameters of the material: $\varepsilon'(\nu)$ and $\varepsilon''(\nu)$ can be obtained by fitting the theoretical dependence (1.1) for $T(\nu)$ to the experimental curve. In this case, the frequency dependences of n and k are specified in the form of second- or third-degree polynomials in frequency. There is no need to measure the $\varphi(\nu)$ spectrum. Figure 1.7 describes the case considered above. It should also be noted that in this case, the assumptions contained in Eqs. (1.1) that the wave is plane, is normally incident on the sample, and that the sample has infinite transverse dimensions are satisfied quite well.

In general, however, the monochromatic spectroscopy in the submillimetre range is characterized by the fact that different types of parasitic diffraction and interference effects associated with it are manifested quite clearly in the spectra. They give rise to certain periodic variations on the experimental curves which usually cannot be described by Eqs. (1.1) under reasonable assumptions about the behaviour of n and k. Hence, as a rule, the reliability of submillimetre spectra can be scanned quite well just by a cursory inspection of the experimental curves. Another reliable way of revealing undesired instrument effects consists in repeating the measurements several times with different geometries of the measuring channel. The distor-

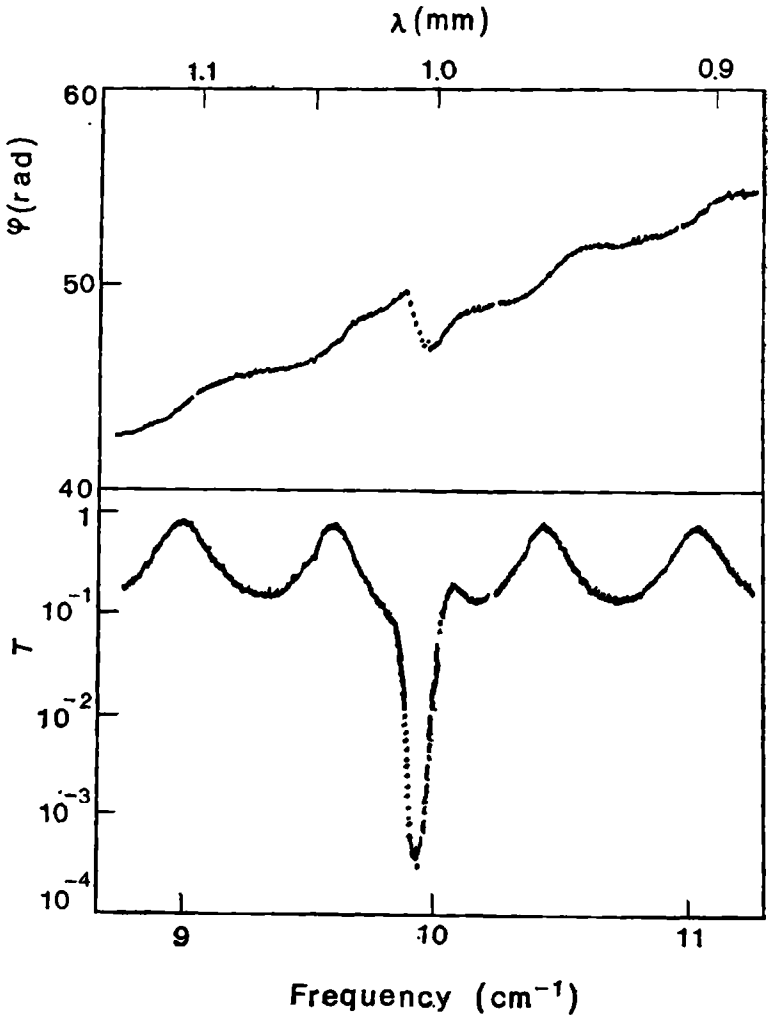

Fig. 1.6. Phase spectrum $\varphi(\nu)$ and transmissivity spectrum $T(\nu)$ of a 1.517 mm thick plate of the $YFeO_3$ crystal. The absorption line at the 10 cm^{-1} frequency corresponds to the antiferromagnetic resonance (no external magnetic field was applied; the measurements were carried out at room temperature).

tions are extremely sensitive to the position of channel elements, and a change in the experimental conditions can convert the systematic instrument errors into random errors.

Figure 1.8 shows some typical distortions of the T vs. ν spectra.

The average accuracy of the dielectric measurements using *Epsilon* spectrometers over a wide frequency range is 1-5% for ε' and 5-10% for ε''. The use of resonator methods gives record values for results in the microwave and infrared regions. For example, ε' can be measured to within 0.01% and errors $\sim 10^{-4}$ in ε'' can be conveniently registered.

Speaking of the application of resonator methods in the submillimetre BWT spectroscopy, it should be mentioned that open resonators are the ones frequently used in this range. Moreover, our experience has shown that for dielectric measurements we can use the simplest form of such resonators, viz. the plane sandwich media with the sample under investigation as one of the layers. The above case of measurement of ε' and ε'' in weakly absorbing materials (Fig. 1.7)

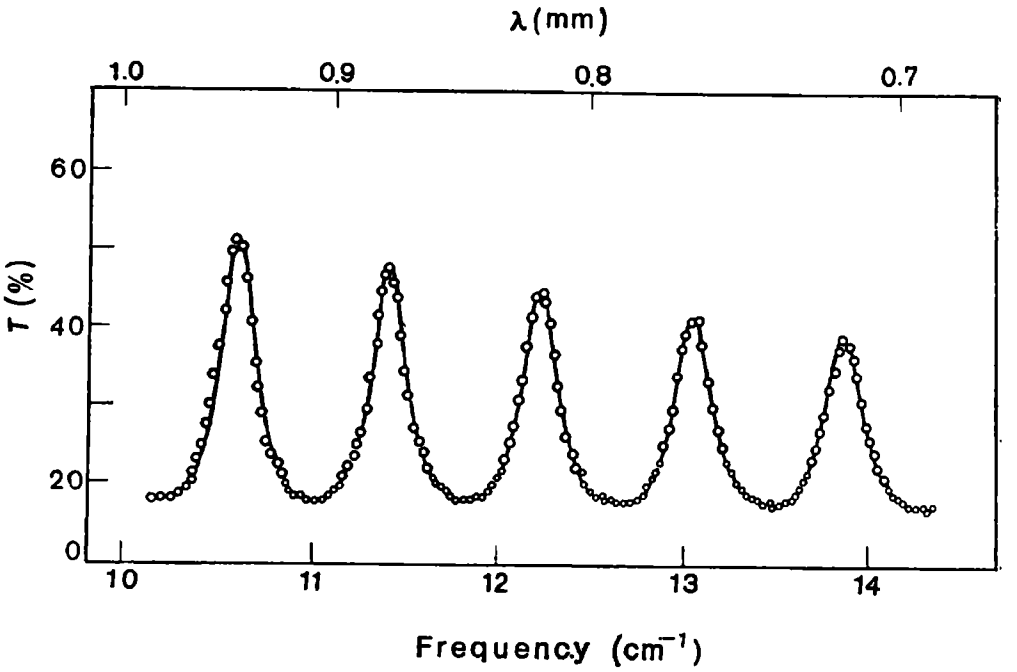

Fig. 1.7. Frequency dependence T (ν) of the transmission coefficient of 0.916 mm thick plate of $LiNbO_3$. The circles denote the experimental points, while the solid line represents the results of the calculations made for T (ν) according to formula (1.1) with $n = 6.7$, $k = 0.01 + 0.0015\nu$ (ν in cm^{-1}). The experimental spectrum is ideally described by the theory.

is nothing but the well-known dielectric resonator method in microwave technology. The sample faces serve as mirrors in this case. The quality of such a resonator, and hence the accuracy of measurements can be easily increased by pressing (or spraying) a metallic grating to the sample faces, thereby increasing the reflectivity of the sample surfaces. In the exactly opposite case, when the transmissivity of the sample is extremely small, the radiation losses due to reflection can be eliminated by applying to the sample resonance-matching dielectric plates. The sandwich systems used in these versions are easy to prepare. Of no less importance is the fact that these systems allow calculations with the help of computers without any sort of simplifications.

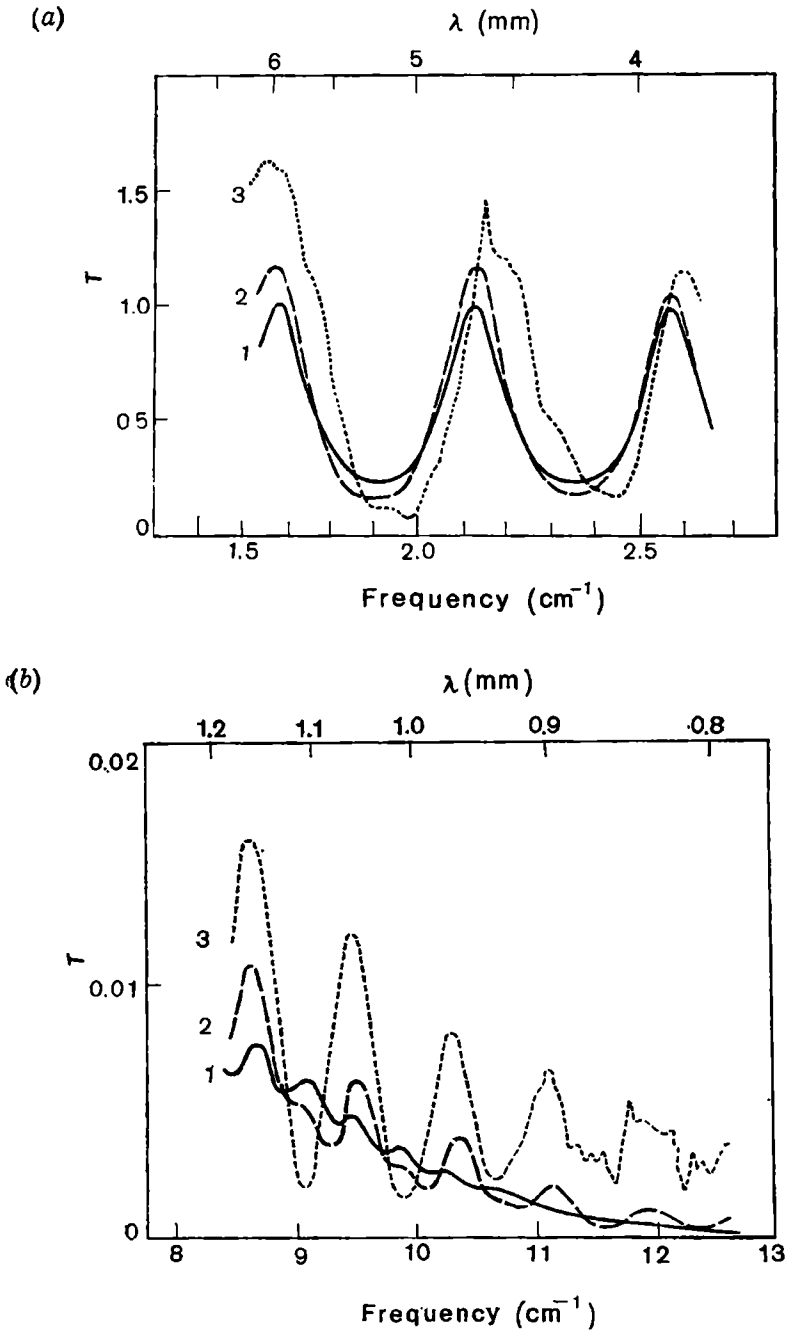

Fig. 1.8. Typical destortions of the submillimetre transmission spectra T (ν): (a) Transmission T (ν) of a 3.24 mm thick plate of a GaAs crystal. The spectra *1*, *2*, and *3* correspond to three different diaphragm sizes, viz. the diameters 30, 12, and 5 mm respectively. The spectra *2* and *3* are clearly distorted, the transmission coefficient T (ν) at the maxima is greater than unity (the distortion of the spectra is due to the diffraction of the radiation at the diaphragm edge). (*b*) Transmission T (ν) of a 0.975 mm thick plate of the ceramic $SrTiO_3$ with an artificially created crack at the centre (the width of the crack can be varied). The electric field vector E is perpendicular to the crack. Spectra *1*, *2*, and *3* correspond to the crack widths of 0.0, 300 and 400 μm. Spectra *2* and *3* are distorted, the period of the interference oscillations in spectrum *3* is doubled in comparison to spectrum *1* (the distortion of spectra is due to the interference of the fundamental wave (passing through the sample) with the parasitic wave arriving at the detector bypassing the sample).

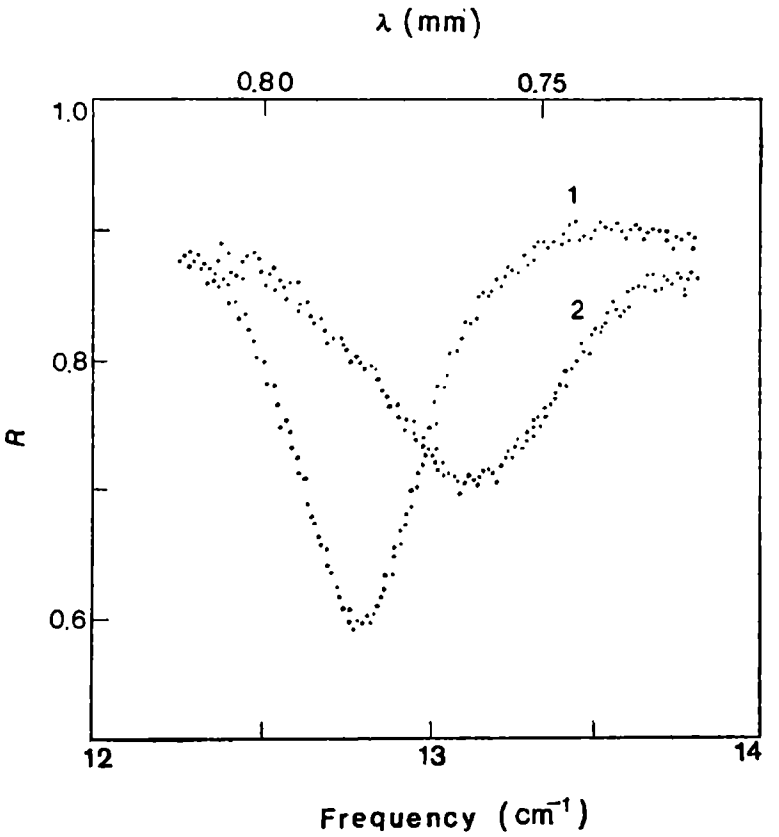

Fig. 1.9. R vs. ν reflection spectra for a 0.174 mm plate of a $SrTiO_3$ crystal (*1*), and for the same $SrTiO_3$ plate with a SbSI plate pressed to its hind face (*2*). Here, SbSI is a texture, the electric field vector **E** is directed parallel to the fibre, and the measurements are carried out at room temperature.

In short, in submillimetre BWT spectroscopy, where the field has a simple structure and the radiation is sufficiently strong and monochromatic to allow a registration of intense and sharp resonance frequency response of the system under investigation, the application of sandwich systems is the most natural and promising way for developing the plane-parallel layer method which is traditionally used for infrared spectroscopy.

By way of an example, Fig. 1.9 shows the reflection spectrum of a plane-parallel $SrTiO_3$ plate, recorded on a BWT spectrometer (curve *1*). It can be seen that in view of the high transparency of $SrTiO_3$ and a high reflectivity of the sample faces, this plate or, in other words, the air-$SrTiO_3$-air system works as a Fabri-Perot interferometer. A resonance minimum in reflectivity is observed at a frequency $\sim 12.8\ cm^{-1}$. The position of this resonance peak on the frequency scale and its height are extremely sensitive to the reflection conditions at the system boundaries (the air-$SrTiO_3$ interface

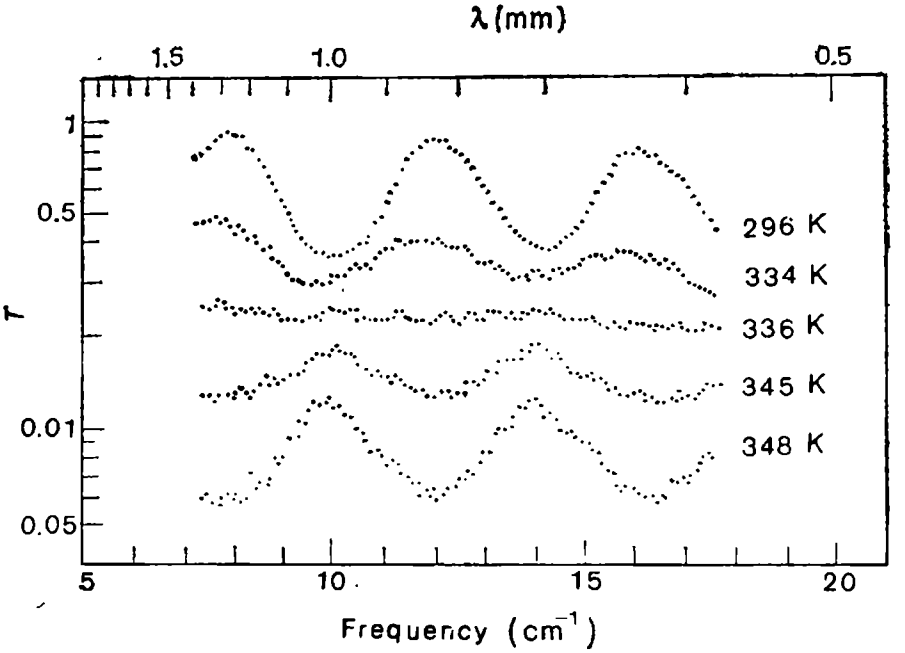

Fig. 1.10. Transmission spectra T (ν) of a polycrystalline VO_2 film deposited on a sapphire substrate. The thickness of the film and the substrate is 0.1μm and 0.383 mm respectively. The shape of the T (ν) spectra depends strongly on the values of n and k for the film. These values, in their turn, vary with the temperature. The data were obtained by B. P. Gorshunov.

in this case). Simple calculations carried out on the basis of formulas for a monolayer give $n = 17.9$ and $k = 0.29$ for $SrTiO_3$ at $\nu \simeq 13$ cm^{-1}.

If it is required to measure the dielectric parameters of, say, a strongly absorbing material with n_x and k_x, we just have to press its surface to the back face of $SrTiO_3$ plate and re-record the reflection spectrum. Curve *2* in Fig. 1.9 represents the reflection spectrum of the air-$SrTiO_3$-SbSI system. SbSI is a semiconducting ferroelectric material with very high dielectric losses in the submillimetre wave range. Knowing n and k for $SrTiO_3$, we can easily calculate the optical constants for SbSI from curve *2*: $n_x = 8.6$ and $k_x = 12.1$ at $\nu \simeq 13$ cm^{-1}. No other method for determining these parameters in SbSI is so simple to use.

Let us consider another example to illustrate the possibilities of application of layered media in the submillimetre range for studying the properties of thin films. Figure 1.10 shows the transmission spectra of a sapphire plate on which a polycrystalline film of vanadium dioxide (VO_2) has been deposited. These spectra have been recorded at different temperatures. Vanadium dioxide, which is an insulator at comparatively low temperatures, changes its properties at 336 K

and becomes a metal. An insulator-metal phase transition takes place in this case.

The transition of VO_2 from one state to another can be seen clearly from its spectra: the transmissivity of the sapphire-VO_2 system sharply decreases upon heating above the transition temperature and its interference pattern shifts by π. It is interesting to note that at a certain point ($T = 336$ K), the wave impedances of sapphire and free

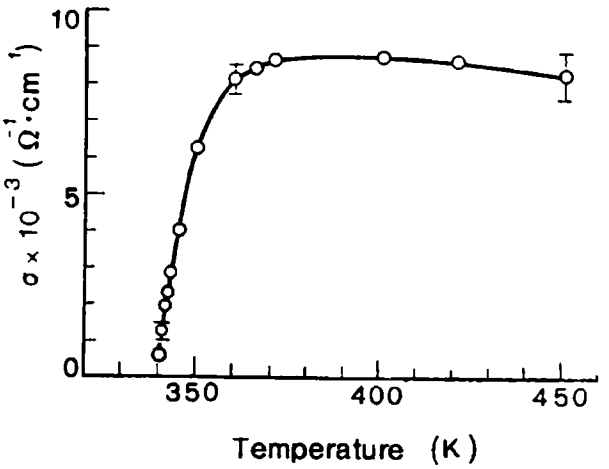

Fig. 1.11. Temperature dependence of the conductivity σ of a VO_2 thin film for frequencies ~10-15 cm^{-1}, calculated on the basis of the T (ν) spectra (see Fig. 1.10).

space are matched in the VO_2 layer, and the reflection at this interface becomes equal to zero. The interference pattern completely disappears.

Figure 1.11 shows the conductivity of VO_2 vs. temperature, calculated from the above T (ν) spectra by fitting them to the corresponding formulas with known values of n and k for sapphire. Note the large values of σ typical of metals, which could be measured by using this method.

Before concluding this section, let us consider the investigation of dielectric properties of low-symmetry crystals. This problem is quite complicated for any dielectric measurements, although it is somewhat simpler to solve in the case of submillimetre BWT spectroscopy. The difficulties in carrying out dielectric measurements in monoclinic and triclinic systems are associated with the fact that we have to completely take into account the tensor nature of the dielectric permittivity. The principal axes of the ellipsoids ε'_{ij} and ε''_{ij} do not necessarily coincide in such crystals. Besides, their orientation may depend on the working frequency and a change in the crystal lattice under the influence of external agencies like temperature, pressure, etc.

Under such conditions, a linearly polarized wave directed at the sample becomes elliptically polarized in it, and relations (1.1) describing the passage of a wave through an isotropic layer are no longer valid. The number of required parameters considerably increases and accordingly, the number of measurable quantities and of equations required for calculations also increases.

One of the possible ways to solve this problem is to measure T and φ for two polarizations of the transmitted wave, obtained by de

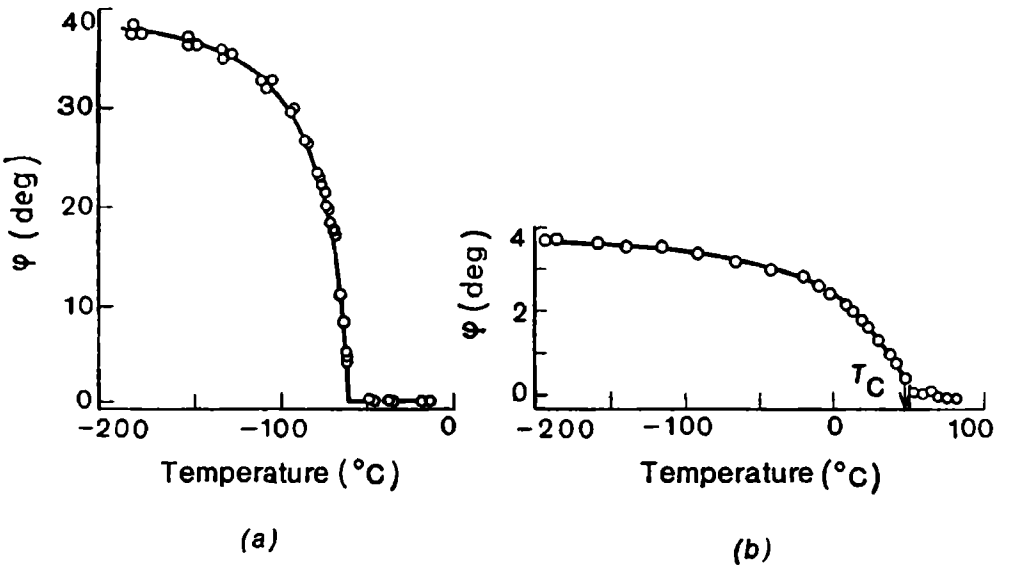

Fig. 1.12. Temperature dependence of the angles of turning of the optical indicatrices around the Y-axis, corresponding to the frequencies $\sim$10 cm^{-1}, for $KH_3(SeO_3)_2$ (*a*) and TGS (*b*) crystals.

composing the elliptical polarization into two mutually orthogonal linear components. By carrying out such measurements for several different orientations of the vector E of the incident wave with respect to crystallographic axes, we can collect sufficient information for calculating the required parameters—six principal values for the ellipsoids, ε'_{ij} and ε''_{ij}, and four polar angles characterizing their orientation. In the general case, the entire set of such measurements must be repeated at each point on the frequency scale.

In view of the application of optical systems involving a high polarization of the radiation, the submillimetre BWT spectroscopy has a considerable advantage over microwave waveguide methods and infrared Fourier spectroscopy and is comparable to the classical crystal optics in its potentialities. A somewhat specific feature of low-symmetry crystals in submillimetre region is that the angles of rotation of permittivity ellipsoids are quite large and in some cases may be equal to tens of degrees. This is due to the fact that the main con-

tribution to the dielectric properties of a crystal comes from its lattice rather than the electron subsystem. From a methodical point of view, the turning of axes (or the bisectrix dispersion, as it is sometimes called) is quite important in the sense that neglecting it may lead to serious experimental errors. From the point of view of crystal physics, it is important because of its close connection with many electrical properties of crystals, like the dependence of the permittivity on electric field, deformation, etc., and can be used as an effective method for studying these properties.

Figure 1.12 shows the temperature dependences of the angles of rotation for optical indicatrices in ferroelectric TGS and ferroelastic $KH_3(SeO_3)_2$. Calculations of the coefficients of spontaneous nonlinear effects, viz. the electric dielectric coefficient M_{52} in TGS and the elastic dielectric coefficient p_{55} in $KH_3(SeO_3)_2$ on the basis of these dependences give the following results: $M_{52} = 38 \cdot 10^{-12}$ CGSE units [1.10] and $p_{55} = 1.5$ [1.11]. It is interesting to note that these values are higher than the corresponding values in the optical region.

Summing up the results of the first part of this review, we can state that with the advent of the BWT spectroscopy in the submillimetre range, the problem of "submillimetre barrier" can be treated as solved with even more justification than in 1925 and 1971 [1.8]

1.3. INVESTIGATIONS OF THE DYNAMICS OF CRYSTAL LATTICE BY SUBMILLIMETRE DIELECTRIC SPECTROSCOPY

Among various problems facing the BWT spectroscopy in the submillimetre range, the investigation of structural phase transitions in crystals occupies a special place on account of its general nature and the clarity of approach towards its solution. All such investigations are based on the concept of soft mode, which was first put forward in the beginning of the sixties [1.12-14]. According to this concept, the instability of the crystal lattice with respect to one of its natural vibrations, viz. the soft mode, is the sole cause of all structural phase transitions. This discovery opened a new and extremely useful branch in the solid state physics, called the investigation of soft modes in crystals. This involves the search for thermally unstable lattice vibrations and an analysis of the dependence of their behaviour on chemical composition, crystal structure, temperature, and other external factors.

A characteristic feature of the soft modes, which is important from the point of view of their spectroscopic analysis, is that the energies of soft modes are considerably lower than of ordinary phonons, and

in most cases their frequencies correspond to the submillimetre spectral region.

In the investigation of the classical soft modes, the submillimetre BWT spectroscopy takes over from the far-infrared spectroscopy where this branch has been occupying an important position for the past twenty years or so. It is clear that not all types of phase transitions can be investigated with the help of infrared spectroscopy or the BWT spectroscopy which is the same as IR spectroscopy in its physical sense. Only such crystals whose soft modes are either polar excitations or are at least closely connected to them can be subjected to investigation. In this respect, the ferroelectric crystals were, and still are, the most conducive objects for investigating soft modes. In intrinsic ferroelectrics, the soft modes are always IR-active both in paraelectric and ferroelectric phases, i.e. at all temperatures.

Let us now consider a typical example of soft mode which was discovered with the help of the BWT spectrometer *Epsilon*.

Figure 1.13 shows the dielectric submillimetre spectra of the complex organic crystal tris-sarcosine calcium chloride (TSCC) [1.15], which is a classical example of the ferroelectric resonant soft mode. Even a cursory glance at the spectra clearly indicates the anomalous decrease in the frequency and increase in the intensity of this vibration upon a lowering of temperature. One can clearly see that the crystal "prepares" for the phase transition long before the temperature for this transition is attained. The completeness and the accuracy of the experimental results enables us to make a strict comparison of these results with the theory. Calculations carried out with the help of the least-square method show that at any temperature, the dependences $\varepsilon'(\nu)$ and $\varepsilon''(\nu)$ can be described, to within experimental errors, by the following relation for resonant dispersion:

$$\varepsilon(\nu) - \varepsilon_\infty + \frac{\Delta\varepsilon\nu_0^2}{\nu_0^2 - \nu^2 + i\gamma\nu}. \tag{1.2}$$

The temperature dependences of ν_0, γ, $\Delta\varepsilon$, and ε_∞, obtained by us by selecting these quantities as the variable parameters in the above formula, are shown in Fig. 1.14. As is typical of soft modes, the square of the soft-mode frequency, ν_0^2, varies almost linearly with temperature. The $\nu_0^2(T)$ dependence is extrapolated to the point $T = 127$ K which coincides with the temperature of the phase transition. An anomaly is observed in the dielectric contribution in this case.

It is not surprising that we began this review of the results of soft-mode spectroscopy with TSCC, a crystal which has a complex structure and is not very well known. The dynamics of the phase transition in this crystal began to be investigated quite recently. Actually, it may seem paradoxical, but the fact is that the soft modes are not clearly manifested in the canonical and undistorted forms shown in Fig. 1.13 even in comparatively simple and thoroughly investigated

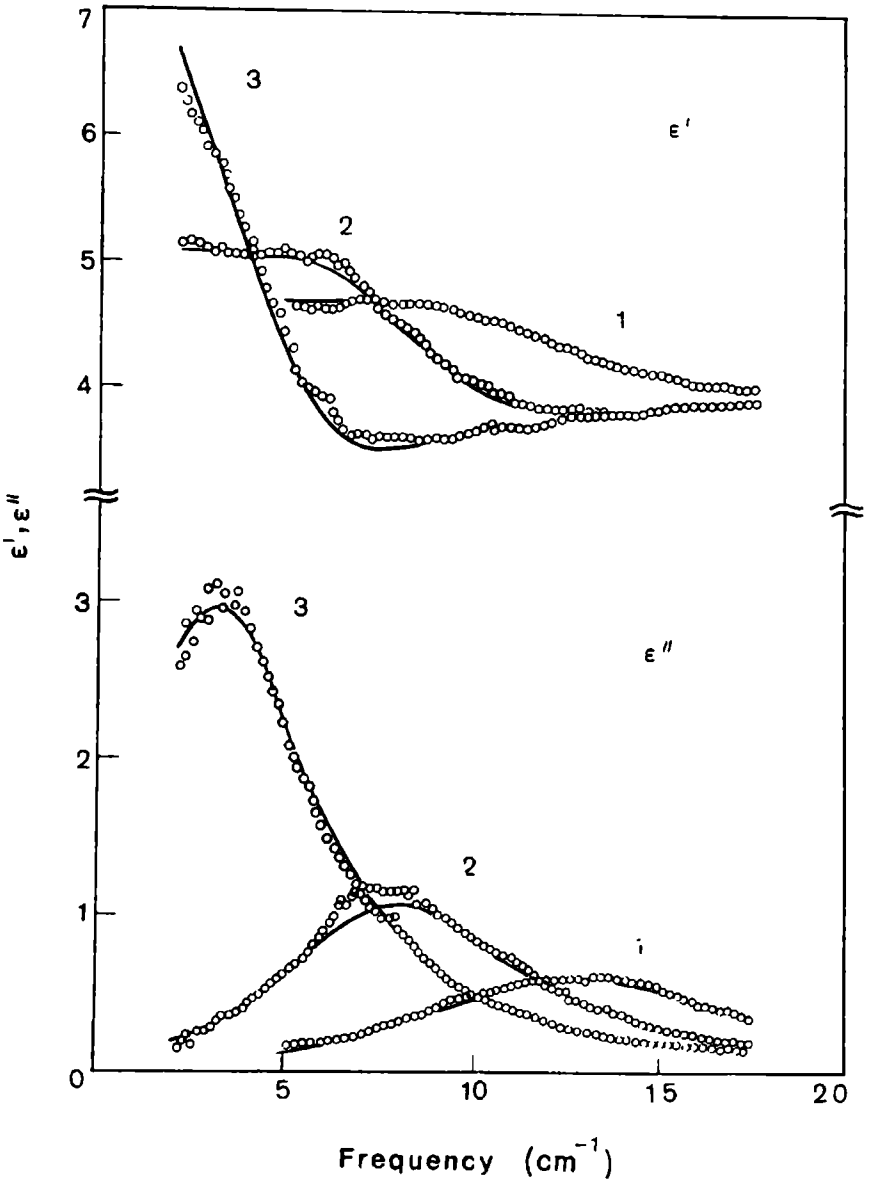

Fig. 1.13. Dielectric submillimetre spectra of a TSCC crystal for the ferroelectric axis. The circles correspond to the experimental results, while the solid line shows the results of calculations of $\varepsilon'(\nu)$ and $\varepsilon''(\nu)$ from the oscillator formula (1.2) using the parameters shown in Fig. 1.14.

crystals with the displacement-type phase transitions, e.g. $BaTiO_3$ and SbSI. In fact, the soft-mode theory was first developed for describing phase transitions in these compounds. Investigations carried out during recent years show that the soft modes in the simplest form, as in the case of TSCC, are manifested extremely rarely. It was found that in $BaTiO_3$, SbSI, and several other crystals with displacement-

type transitions, the soft-mode frequency which varies with temperature does not vanish at the phase transition point but is simply reduced to an anomalously low value. Near the phase-transition point, the soft-mode energy due to nonlinear interactions begins to be pumped to other degrees of freedom. Consequently, a still lower frequency excitation, called the central peak, appears in the crystal spectra.

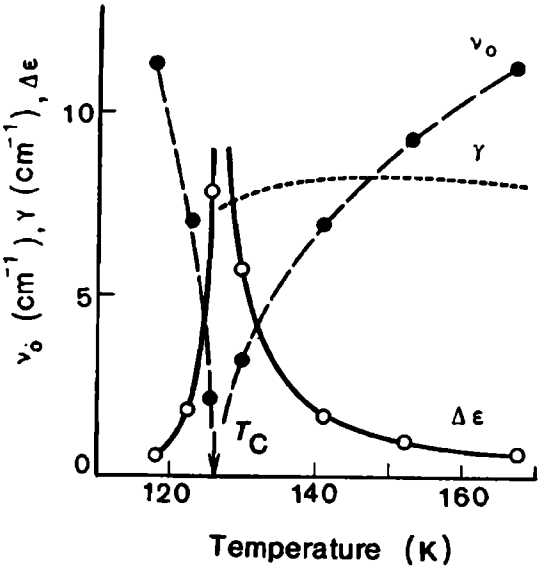

Fig. 1.14. Soft mode parameters in TSCC, calculated on the basis of the submillimetre dielectric spectra (Fig. 1.13); ν_0, γ, and $\Delta\varepsilon$ denote the frequency, damping, and the dielectric contribution of the oscillator respectively.

It is interesting to note that this effect frequently takes place just in the region of submillimetre frequencies.

The interaction between the soft mode and the low-frequency lattice excitations has already been observed by us for many crystals, including $Gd_2(MoO_4)_3$, SbSI, $SC(NH_2)_2$, and $Sn_2P_2S_6$.

Figure 1.15 shows the dielectric spectra of gadolinium molybdate $Gd_2(MoO_4)_3$ which is an improper ferroelectric with a displacement-type phase transition. It can be seen that as the temperature of the crystal approaches the phase-transition point (T_C = 432 K), the soft-mode frequency of the ferroelectric phase in it decreases until the soft mode meets the rigid mode having a frequency $\sim$ 10 cm^{-1}. The interaction between these two lattice excitations leads to an increase in the dipole moment of the rigid mode. Although this mode does not even appear at low temperatures, it now dominates the spectra near the phase-transition point. Figure 1.16 shows, by way of an example, the behaviour of the soft-mode frequency in SbSI. It

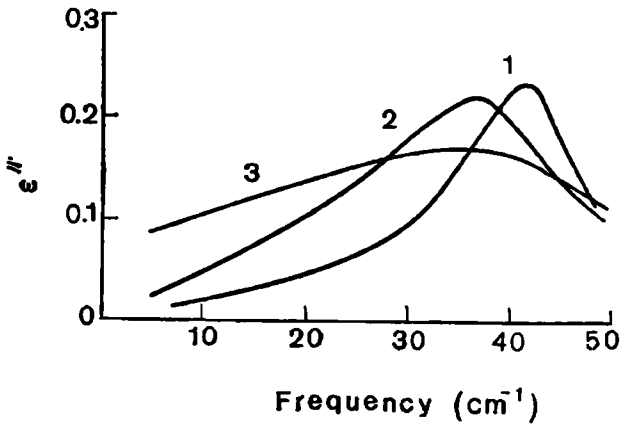

Fig. 1.15. Submillimeter $\varepsilon''(\nu)$ spectra of a $Gd_2(MoO_4)_3$ crystal for the ferroelectric axis, corresponding to 300, 375, and 422 K (curves *1*, *2*, and 3 respectively). The results at frequencies above ~30 cm^{-1} were obtained by J. Petzelt on a Fourier spectrometer.

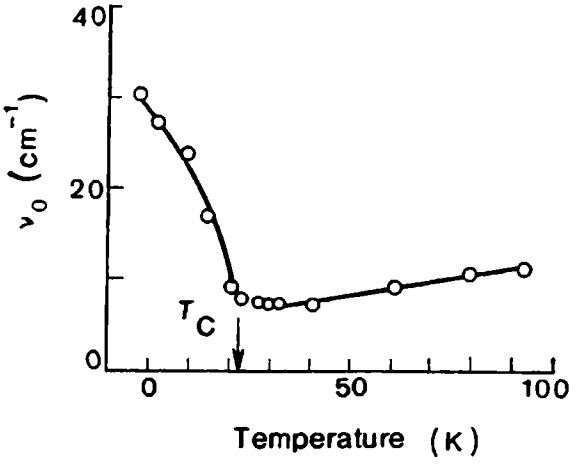

Fig. 1.16. Temperature dependence of the soft mode frequency in an SbSI crystal (grown from the melt).

can be seen that it does not fall below the submillimetre frequency range even at the phase-transition point ($T = 295$ K).

The concept of soft modes has been considerably extended in the last decade, and now covers crystals with the order-disorder-type phase transitions. Until recently, it was disputed whether the soft-mode theory can be applied to such crystals. The soft modes in these crystals are due to the collective motion (ordering and disordering) of the available dipole moments in the lattice, which form the ferroelectrically active subsystem of the crystal. A peculiar property of soft modes in order-disorder systems is that these excitations are essentially anharmonic and supplement the $3N$ normal lattice vibra-

tions. If the unit cell of a crystal contains several ferroelectrically active particles, several additional modes corresponding to different versions of mutual ordering of particles may appear in the spectra.

This situation was investigated by us for a large group of crystals belonging to the KH_2PO_4 (KDP) family [1.16-19]. The ferroelectrically active particles in such crystals are protons which form hydrogen bonds oriented in a direction perpendicular to the ferroelectric

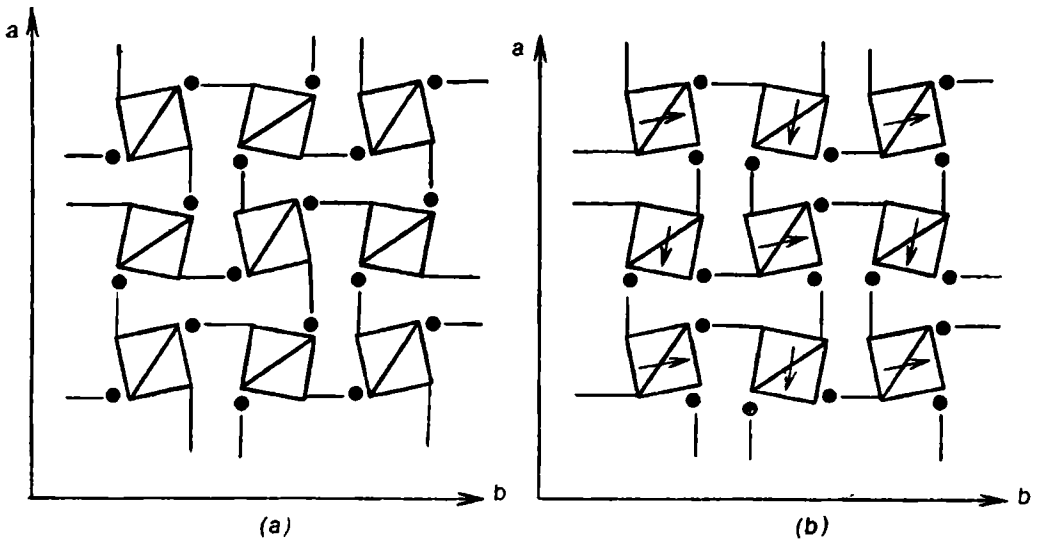

Fig. 1.17. Projections of the proton subsystem of the KDP-type crystals onto the *ab*-plane, corresponding to two types of ordering in hydrogen bond particles: (*a*) ferroelectric ordering; (*b*) ordering resulting in polarization in the *ab*-plane.

axis (the *xy*-plane). The unit cell contains four protons. Two different versions of mutual ordering are shown in Fig. 1.17. In the first case, the dipole moments compensate one another in the *xy*-plane, but cause a displacement of the heavy ions from their equilibrium positions along the *z*-axis, thus creating a dipole moment in this direction. In the second case, a polarization appears in the *xy*-plane. Two modes correspond to these two types of collective motion of the particles: the B_2-symmetry mode (polarized along the *z*-axis) and the E-symmetry mode (polarizationally degenerate in the *xy*-plane).

Typical temperature dependences of the dielectric permittivity of KDP-type crystals in the submillimetre range are shown in Fig. 1.18. The data on the temperature behaviour of B_2- and E-modes, obtained on the basis of these and similar dependences, is presented in Fig. 1.19.

It was found that both types of modes in KDP-type crystals are thermally unstable to some extent. However, the ferroelectric phase

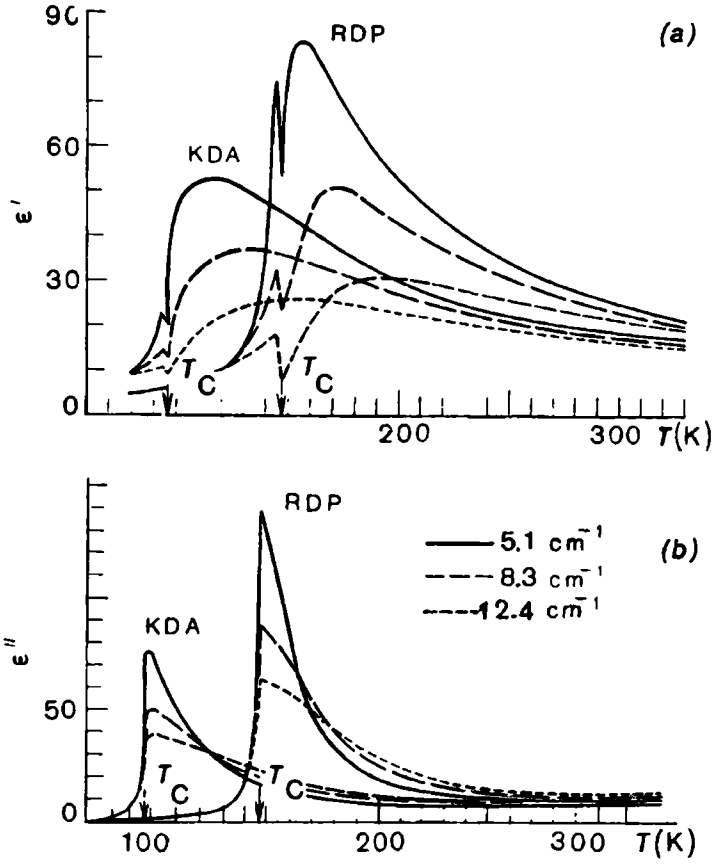

Fig. 1.18. Temperature dependence of the permittivity of KDA and RDP crystals for the ferroelectric axis.

transitions always occur through the B_2-mode, since it makes the lattice unstable faster than the E-mode.

The study of isomorphically substituted KDP-type crystals with the help of the BWT submillimetre spectroscopy proved so fruitful that after describing the properties of such crystals with the help of phenomenological models, it became possible to go over to a qualitatively new stage, viz. the description of their dynamics by using microscopic models. The most important result in this direction was that the cluster model for deuterized crystals could be used to simultaneously describe the thermodynamic and dielectric properties (both static and dynamic) with the same set of variable parameters. In the framework of a unified approach, the cluster energy levels, the long-range interaction constants, the relaxation time of individual particles, as well as the magnitudes of the dipole moments were calculated.

Investigations carried out by us have shown that the study of the behaviour of soft modes at temperatures away from the phase-tran-

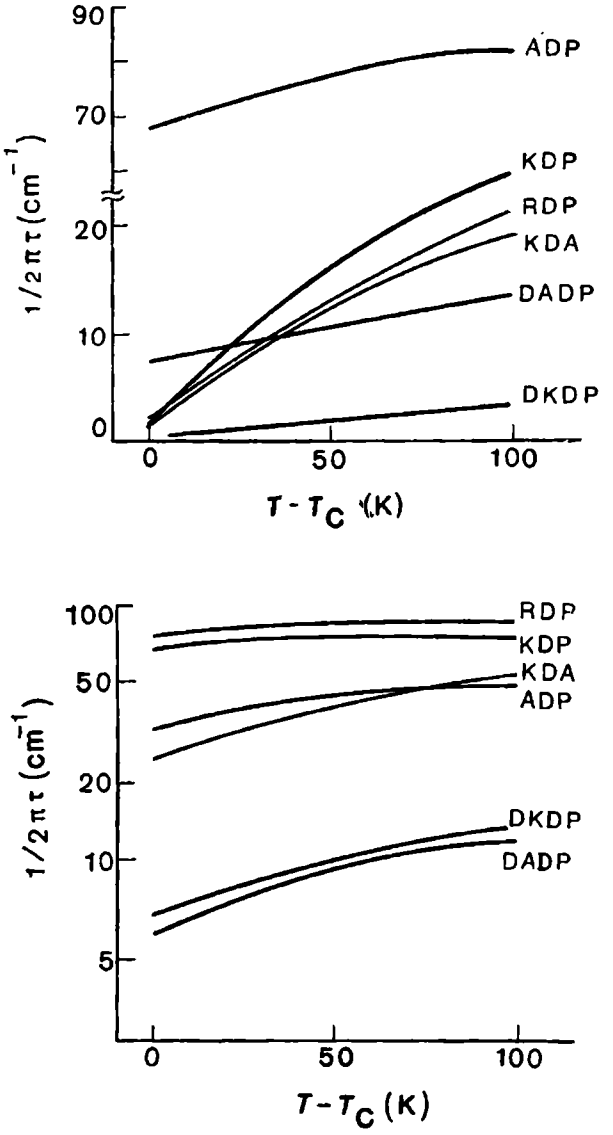

Fig. 1.19. Temperature dependences of (*a*) B_2 and (*b*) E excitation frequencies in KDP type crystals, calculated on the basis of the data similar to those presented in Fig. 1.18.

sition point offer interesting prospects. Under these conditions, when a crystal is away from its critical state and the most general laws governing the phase transition are considerably weakened, the behaviour of soft modes becomes highly peculiar. Thus, it was found that soft-mode frequencies in displacement- and order-disorder-type systems may vary with temperature in quite different ways.

It has been known for long that near the phase transition, the temperature dependence of the reciprocal of the relaxation time in order-

disorder-type systems is quite similar to the temperature dependence of the square of the soft-mode frequency for the displacement-type systems. This analogy is a direct consequence of the close analogy of the ferroelectric excitations in these two types of systems. However, while the frequency of a classical soft mode attains saturation as we move away from the phase-transition point on the temperature scale,

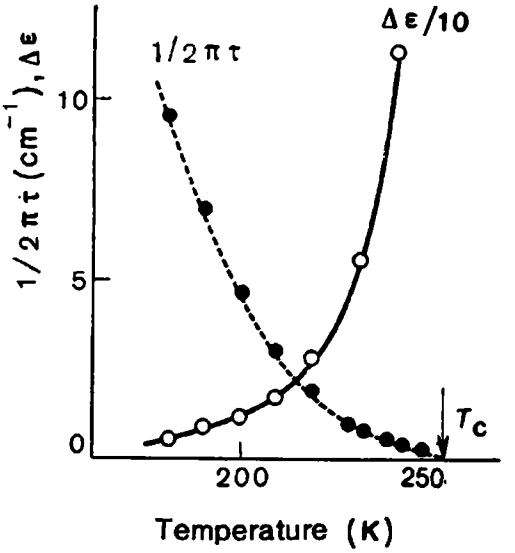

Fig. 1.20. Temperature dependence of the parameters (frequency and dielectric contribution) of the ferroelectric soft mode in a Rochelle salt crystal.

and the soft mode remains in the spectra and continues to make a finite dielectric contribution, the behaviour of $1/(2\pi\tau)$ may be quite different.

Figure 1.20 shows the temperature dependences, obtained from submillimetre dielectric spectra, of the ferroelectric excitation parameters in Rochelle salt which is a classical crystal with an order-disorder phase transition [1.20]. A very peculiar feature of these dependences is that the rate of increase of $1/(2\pi\tau)$ with temperature becomes higher as we go away from T_C. Unlike the usual method of describing the temperature dependence of the typical soft modes, we cannot confine ourselves in this case to the linear approximation in the expansion of $1/(2\pi\tau)$ in powers of temperature,

$$1/[2\pi\tau(T)] = A_1(T - T_C) + A_2(T - T_C)^2 + A_3(T - T_C)^3 + \ldots$$

An analysis of our experimental results concerning $1/(2\pi\tau)$ showed that in Rochelle salt the quadratic and cubic terms start dominating in the above expression as we deviate from T_C by just 10°. The reciprocal of the dielectric contribution of a mode to static dielectric permittivity, $(1/\Delta\varepsilon)$, varies with temperature in a similar way. In

a situation typical of ferroelectrics, the temperature dependence of $1/\Delta\varepsilon$ would obey the Curie-Weiss law according to which the function $1/\Delta\varepsilon\ (T)$ is linear.

Further studies have shown [1.21] that the above anomalies in the behaviour of the ferroelectric mode in Rochelle salt can be explained by the theoretical model developed by Mitsui for systems with the asymmetric potential having two minima. It was revealed that the

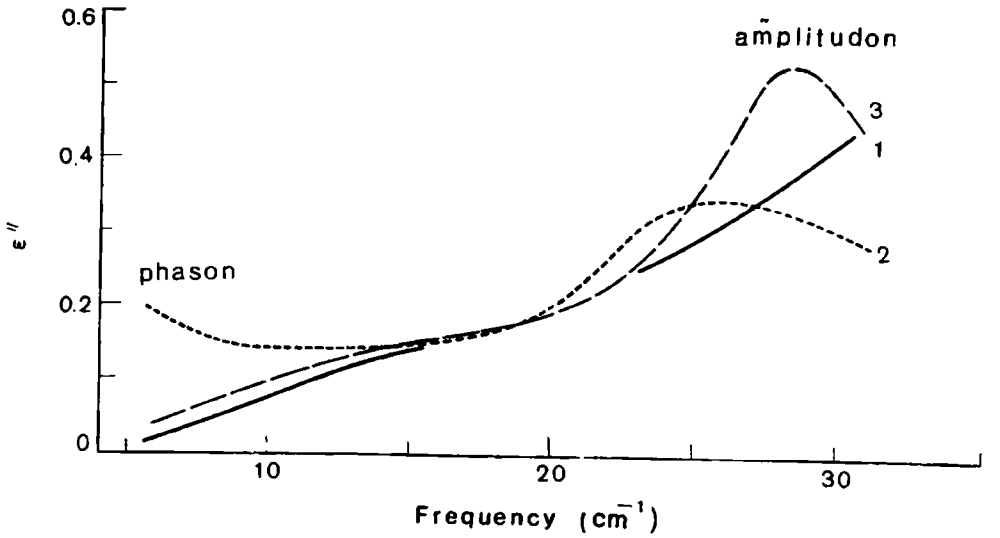

Fig. 1.21. Submillimetre $\varepsilon''(\nu)$ spectra of a K_2SeO_4 crystal for the ferroelectric axis, recorded in the para-phase (*1*), in the incommensurate phase (*2*), and in the ferroelectric phase (*3*) at temperatures 117, 94, and 83 K respectively.

Mitsui model allows for different relations between expansion coefficients $A_1, A_2, A_3, \ldots$. These relations are determined in terms of the relative width of the ferroelectric phase $\delta = (T_1 - T_2)/(T + T_2)$. Thus, it is possible that the nonlinear behaviour of soft-mode parameters is a typical feature of all systems in which the ferroelectric phase is restricted by nonpolar phases on both sides on the temperature scale. This conclusion is confirmed by the results of our studies of two more crystals with an asymmetric two-minimum potential. These materials, deuterated Rochelle salt [1.22] and rubidium hyposulphate $RbHSO_4$ [1.23], have quite different widths of the ferroelectric phase region. In the former case, $\delta = 0.1$, and as in Rochelle salt, $1/(2\pi\tau)$ has a roughly cubic dependence on temperature. In the latter case, $\delta = 1$ and even upon a deviation of about 100 K from T_C, the linear dependence of $1/(2\pi\tau)$ on temperature is preserved.

Besides the investigations of classical soft modes, another similar (and very promising for submillimetre BWT spectroscopy) approach consists in the study of effects accompanying phase transitions in crystals with incommensurate phases. In such crystals, a spatial structural

modulation incommensurate with the lattice period is known to appear at a certain temperature interval. The phase transitions to the incommensurate phase are caused by nonuniform soft modes whose wave vectors lie at the common point in the Brillouine zone: $\mathbf{k}=a\mu$, where a is the inverse lattice vector and μ is an irrational number. Since nonuniform modes do not appear in the IR and Raman spectra, there is no need to consider them here. A theoretical analysis shows that the important factor in this case is the possibility of the appearance of specific low-frequency uniform excitations in the spectra of crystals with an incommensurate phase. These excitations are called phasons and amplitudons and are caused by nonuniform fluctuations of the phase and amplitude of an incommensurate order-parameter wave, and in particular, a polarization wave.

The first observations of the IR-active amplitudon and phason were made by us in a potassium selenate K_2SeO_4 crystal [1.24, 25]. This material is an improper ferroelectric whose properties have been thoroughly and intensively investigated, at present. This crystal undergoes two phase transitions: a transition from the paraphase to an incommensurate phase at $T_i = 128$ K, and a transition from the incommensurate phase to a ferroelectric phase at $T_C = 93$K. Below T_i, an incommensurate structure-modulation wave with $\mu \simeq 1/3$ appears in the crystal. Upon a further cooling of the crystal, the amplitude and the period of modulation increase, and the form of modulation changes from sinusoidal to rectangular. At the T_C point, the entire crystal undergoes a uniform spontaneous polarization, and a transition to the ferroelectric phase takes place.

Figure 1.21 shows the submillimetre dielectric spectra of K_2SeO_4. It can be seen that at room temperature, these curves represent the low-frequency part of the absorption line in the IR region. In the incommensurate phase, two new lines appear in this part (see spectra at $T \cdot \cdot 94$ K). These lines were interpreted by us as an amplitudon ($\nu \simeq 25$ cm^{-1}) and a phason ($\nu < 5$ cm^{-1}). The intensity of the first (amplitudon) line increases as we approach the temperature T_C, where it is abruptly doubled, and the amplitudon is transformed into a soft mode of the ferroelectric phase.

The phason is a lower-frequency oscillation having relaxation properties ($1/(2\pi\tau) \simeq 1$ cm^{-1} at $T \cdot 104$ K). The spectra in Fig. 1.21 show only its high-frequency part. Upon cooling, the phason frequency decreases and becomes equal to zero at the point T_C, thus causing an anomaly in the static permittivity. In the ferroelectric phase, phasons are not observed in dielectric spectra.

All the above-mentioned peculiarities in the behaviour of the phason and amplitudon in the dielectric spectra of a K_2SeO_4 crystal are in good agreement with the available theoretical predictions [1.26].

It should be observed that the phasons in crystals with an incommensurate phase are not the Goldstone waves (which are also called

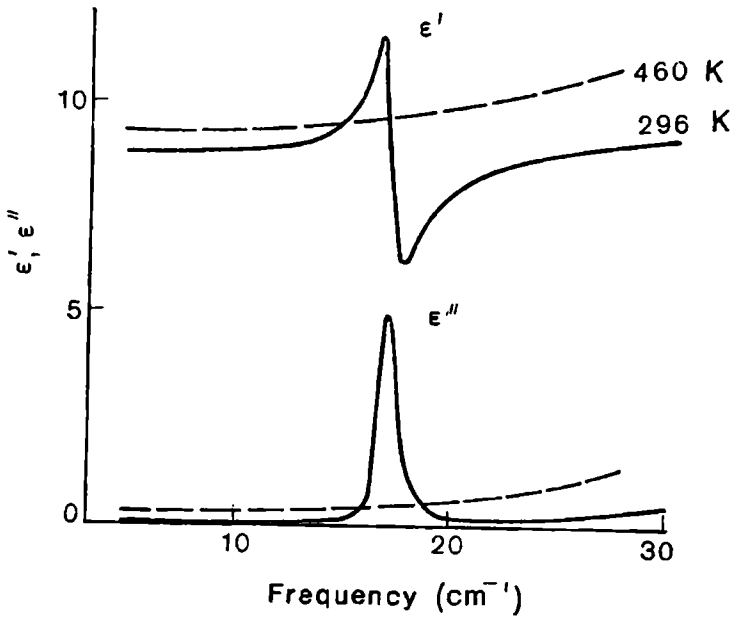

Fig. 1.22. Submillimetre dielectric spectra of a $CsCuCl_3$ crystal ($\mathbf{E} \parallel c$), recorded at temperatures above (dashed line) and below (solid line) the phase transition temperature.

phasons), although both types of excitations are similar in nature and are caused by the fluctuations of structural modulation wave. The former correspond to nonuniform fluctuations, and the latter to uniform fluctuations. Unlike the Goldstone waves, the nonuniform phasons have a nonzero energy and can also exist in systems with a commensurate structure modulation.

Perhaps the only example of such an effect so far is a phason observed by us in a $CsCuCl_3$ crystal [1.27]. The submillimetre dielectric spectra of $CsCuCl_3$ are shown in Fig. 1.22. At $T_C = 423$ K, this crystal undergoes a phase transition with a trebling of the unit cell in the low-temperature phase and the formation of a helicoidal structural modulation wave. In can be seen that below T_C, a high-quality resonance absorption line appears in the spectra. Its parameters, and above all the damping factor, depend on temperature. It was assumed by us that the phase fluctuations of the helicoidal structural modulation wave constitute the microscopic mechanism for the observed mode. According to the group-theory analysis, the Raman spectra must contain, besides this phason, an amplitudon of the A_1-symmetry and a doubly degenerate mode of the E-symmetry. These oscillations were actually observed in specially conducted experiments [1.28].

The low-frequency dynamics of the crystal lattice becomes quite complicated as we go over to proper ferroelectrics with an incommen-

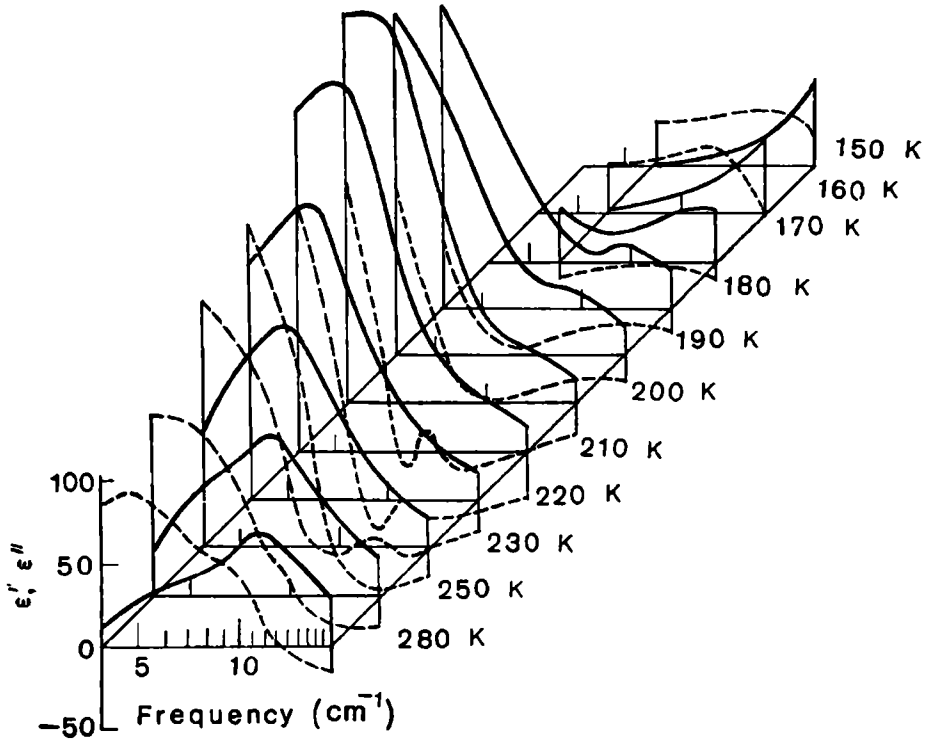

Fig. 1.23. Submillimetre dielectric spectra of a $SC(NH_2)_2$ crystal for the ferroelectric axis. The dashed lines correspond to $\varepsilon'(\nu)$, while the solid lines represent $\varepsilon''(\nu)$.

surate phase. The IR-active excitations which are directly connected with phase transitions may now appear in all the three phases ($T < T_C$, $T_C < T < T_i$, $T_i < T$). Figure 1.23 shows the submillimetre dielectric spectra of a thiourea SC $(NH_2)_2$ crystal [1.29] having transition temperatures $T_i = 202$ K and $T_C = 169$ K. At temperature above T_i, the submillimetre spectra of thiourea are similar to those for ordinary ferroelectrics with a displacement-type phase transition: the high-intensity resonance-type mode, whose frequency decreases as we approach T_i (while the dielectric contribution increases), can be clearly seen in the spectra. As in the case of gadolinium molybdate, the soft mode creeps onto the rigid mode near the phase-transition temperature (T_i in the present case) and considerably increases its intensity. The phase transition at T_i radically changes the situation with the appearance of an incommensurate structural modulation. The soft mode splits into two components at the transition temperature T_i. The actual dielectric dispersion pattern becomes very complicated, but the main aspects of this phenomenon can be easily understood by following the simple diagram shown in Fig. 1.24. The frequency of only one of the branches (the low-frequency branch) tends to zero. It is this branch that determines the main dielectric

contribution from the soft mode to the static permittivity. The higher-frequency branch is an amplitudon which transforms into a soft mode of the ferroelectric phase at $T < T_C$.

So far, we have considered cases in which the submillimetre spectra were used for investigating phenomena, including phase transitions, whose existence was already known. However, it is quite clear that as soon as soft modes appear in the submillimetre spectra, they may serve as a reliable indication of the fact that a crystal is likely to undergo phase transitions. Significantly, such indications

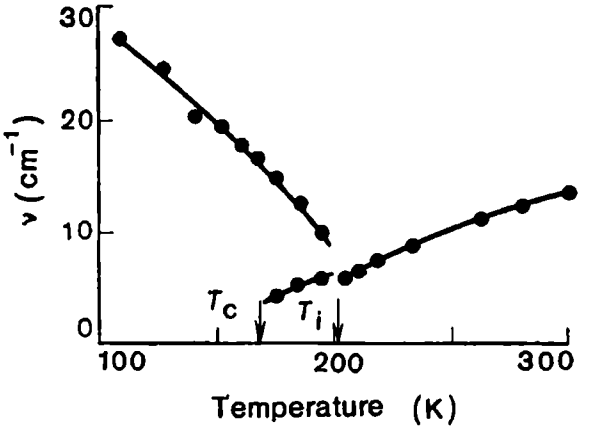

Fig. 1.24. Behaviour of the soft mode in the $SC(NH_2)_2$ crystal, obtained on the basis of the submillimetre dielectric spectra in the approximation of two coupled oscillators [1.25].

correspond to temperatures quite far from the critical temperature, i.e. in the regions where no other anomalies in physical properties have been observed as yet.

Figure 1.25 shows the submillimetre dielectric spectra of a semiconducting $TlGaSe_2$ crystal. These spectra have several peculiarities which point toward the existence of such phenomena in $TlGaSe_2$ that were hitherto unknown [1.30]. In the first place, a high-intensity resonance absorption line can be observed in the spectra (at room temperature and at a frequency ~ 14 cm^{-1}), with all the features of a ferroelectric soft mode: its frequency decreases while the dielectric contribution increases as the temperature is lowered. A highly unusual feature of these spectra is that below $T \sim 120$ K, the mode suddenly begins to lose its resonance properties which were clearly manifested so far: at frequencies ~ 10 cm^{-1}, the value of ε' gradually changes sign from negative to positive with decreasing temperature (curves *3* and *4*), and the derivative $\partial\varepsilon'/\partial\nu$ also changes sign. At $T = 107$ K, the dielectric dispersion abruptly changes to an even greater extent (curves *4* and *5*): the intensity of the soft mode decreases, and the mode shifts toward high frequencies. At $\nu \sim 14$ cm^{-1}, a high-quality

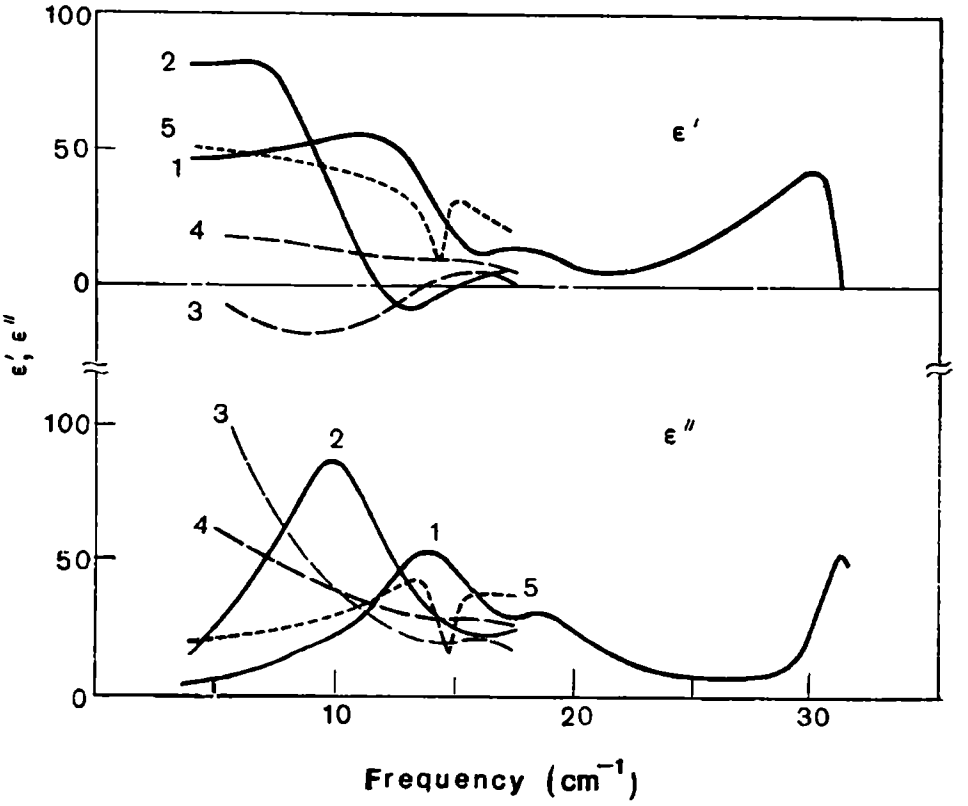

Fig. 1.25. Submillimetre dielectric spectra of a $TlGaSe_2$ crystal (the electric field vector E is parallel to the cleavage plane). Curves *1*, *2*, *3*, *4*, and *5* correspond to the process of monotonic cooling, the temperatures for these curves being $T = 298$ (*1*), 201 (*2*), 123 (*3*), 108 (*4*), and 100 K (*5*).

rigid mode appears in the spectra. It can be seen that this mode effectively interferes with the soft mode which now is considerably broadened (Fano effect).

It is almost certain that structural phase transitions occur in $TlGaSe_2$ at 120 and 107 K. But does the soft mode "freeze" and does $TlGaSe_2$ consequently become a ferroelectric below 107 K? Why does the nature of dispersion $\varepsilon'(\nu)$ change betwen 120 and 107 K? Does an incommensurate phase exist in $TlGaSe_2$ in this temperature interval, or is the central peak due to some critical phenomena?

So far, there is no answer to these questions. Statical measurements, X-ray diffraction studies, the second optical harmonic generations experiments, etc. might provide some clues to these problems.

Before concluding this discussion, let us consider another type of problems which bear a direct relation to the submillimetre dielectric spectroscopy. These problems concern the investigation of dynamic properties of crystals with free carriers, such as an insulator-metal, -superconductor, and -superionic conductor. The investiga-

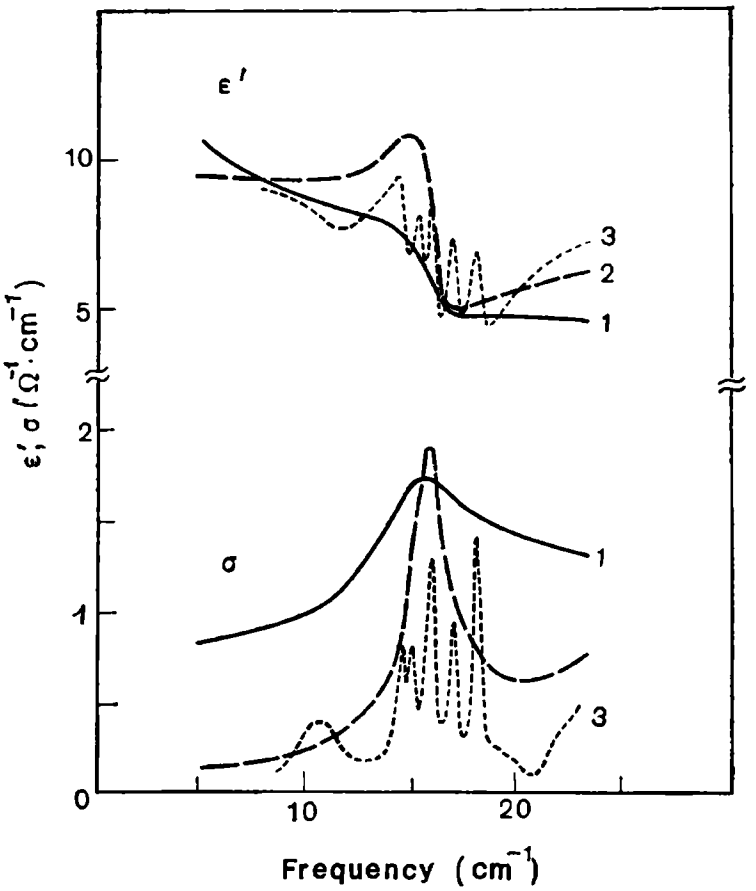

Fig. 1.26. Submillimetre $\varepsilon'(\nu)$ and conductivity $\sigma(\nu) = 0.5\nu\varepsilon''(\nu)$ spectra of the superionic conductor $RbAg_4I_5$, recorded in α-, β-, and γ-phases (curves *1*, *2*, and *3* respectively, the corresponding temperatures being 298, 123, and 40 K).

tion of such systems occupies a special place in submillimetre spectroscopy due to the fact that the energy of submillimetre radiation quanta falls in the region where the phonon spectrum of the lattice is close to the spectrum of free charge carriers. This offers a rare possibility of directly observing effects arising from the interaction of two subsystems, viz. the rigid lattice skeleton and the mobile ions or electrons.

Figure 1.26 represents the submillimetre dielectric spectra for one of the best studied superionic conductors, viz. a $RbAg_4I_5$ crystal [1.31]. Above 122 K, this crystal has a high ionic conductivity which has a record value at room temperature even for superionic conductors, i.e. $\sigma = 0.12$ $(\text{ohm}\cdot\text{cm})^{-1}$. A first-order phase transition in $RbAg_4I_5$ at 122 K changes the conductivity by two orders of magnitude. Another phase transition is observed in this material at 208 K.

However, it affects the crystal properties to a much smaller extent, viz. just the nature of disordering of silver ions in the lattice.

It can be seen from the figure that above 122 K, the submillimetre dielectric spectra consist of a wide band of diffusive absorption by free carriers $\nu < 10$ cm^{-1} and an absorption line in the vicinity of $\nu \simeq 15$ cm^{-1}. The intensity of diffusive absorption decreases with temperature, while the mode at 15 cm^{-1} becomes sharper. An abrupt change is observed in the submillimetre spectra at $T = 122$ K: the diffusive absorption completely disappears, while the absorption line region acquires a structure which is transformed into a whole set of separate narrow lines upon a further cooling of the crystal.

To our mind, the low-energy excitations of this type may be due to the vibrational motion of Ag^+ ions about their local equilibrium positions. In this case the splitting of the absorption lines around 15 cm^{-1} at low temperatures is probably caused by the fact that Ag^+ ions have several nonequivalent allowed positions in the lattice, differing in the height of the barrier separating them as well as in their mutual separation.

It can be seen from the $\varepsilon'(\nu)$ spectra that at frequencies ~ 10 cm^{-1}, the dielectric permittivity remains practically unchanged during the rearrangement of spectra in the region of 15 cm^{-1}. In other words, the dielectric contribution of the mode remains the same during its splitting at 15 cm^{-1}. This means that in all probability, the splitting of a mode into separate lines is not associated with a change in their microscopic mechanism. Apparently, all these lines exist at high temperatures also. However, due to very short durations for which Ag^+ ions exist in their localized states, these lines are considerably broadened. The high mobility of Ag^+ ions neutralizes the nonequivalence of their positions in the crystal lattice.

1.4. CONCLUSION

Table 1.1 contains a complete list of crystals investigated by us during the last five years. A large number of these investigations was carried out in collaboration with leading Soviet scientists from the Istitute of Crystallography (Moscow), Physico-Technical Institute (Leningrad), Institute of Physics (Krasnoyarsk), Institute of Theoretical Physics (Kiev), Institute of Semiconductor Physics (Vil'nius), Institute of Physics (Baku), Institute of Radiophysics and electronics (Yerevan), Universities of Moscow, Dnepropetrovsk, Uzhgorod, Vil'nius as well as with scientists from other countries, especially from the Institute of Physics of the Czechoslovakian Academy of Sciences (Prague), and Universities of Tokyo, Waseda, Nagoya (Japan), Colorado (USA), Paris and Nancy (France).

Such a wide range of collaboration enabled us to use the existing facilities in the field of submillimetre BWT spectroscopy to the ful-

Table 1.1

Classical ferroelectrics with phase transitions of the type		Crystals with incommensurate phase	Crystals, close to ferroelectrics	Conducting materials
"order-disorder"	"displacement"			
KH_2PO_4	SbSI	K_2SeO_4	$NH_4H_2PO_4$, $ND_4D_2PO_4$	$Na-\beta-Al_2O_3$
$KH_{2(1-x)}D_{2x}PO_4$	$Pb_5Ge_3O_{11}$	Rb_2ZnCl_4		AgI
KH_2AsO_4,	$Gd_2(MoO_4)_3$	$(NH_4)_2BeF_4$		$(AgI)_x(Ag_2WO_4)_{(1-x)}$
PbH_2PO_4				
Rochelle salt	$BaTiO_3$	$SC(NH_2)_2$	$KH_3(SeO_3)_2$, $KD_3(SeO_3)_2$	VO_2
TGS, DTGS	$Sn_2P_2S_6$	$Sr_2Nb_2O_7$		$RbAg_4I_5$
$PbHPO_4$		$BaMnF_4$	$CsCuCl_3$	$MTPP(TCNQ)_2$
$RbHSO_4$, $RbDSO_4$	TSCC	$NaNO_2$	$NaNO_3$	
	Benzil		$TlGaSe_2$,	
			$TlGaS_2$	
			$TlInSe_2$,	
			$TlInS_2$	

lest extent and to ensure a rapid progress in our investigations. The friendly relations established with scientists from different countries also played a significant role.

We are indebted to our closest colleagues S. P. Lebedev and J. Petzelt for their continued cooperation. Most of the studies reviewed in this artcile were undertaken jointly with them. The authors also express their gratitude to all those who helped in conducting these experiments.

References

1.1. M. B. Golant, R. L. Vilenskaya, E. A. Zyulina, Z. F. Kaplun, A. A. Negirev, V. A. Parilov, T. B. Rebrova, and V. S. Savel'ev, *Pribory i Tekhnika Eksp.*, No. 4, 136 (1965).
1.2. M. B. Golant, Z. T. Alekseenko, Z. S. Korotkova, L. A. Lunkina, A. A. Negirev, O. P. Petrova, T. B. Rebrova, and V. S. Savel'ev, *Pribory i Tekhnika Eksp.*, No. 3, 231 (1965).
1.3. E. M. Dianov and N. A. Irisova, *Fiz. Tverd. Tela*, 8, 2265 (1966); E. M. Dianov, N. A. Irisova, and V. N. Timofeev, *Fiz. Tverd. Tela*, 8, 2643 (1966).
1.4. E. A. Vinogradov, N. A. Irisova, T. S. Mandel'shtam, and T. A. Shmaonov, *Pribory i Tekhnika Eksp.*, No. 5, 192 (1967).
1.5. V. P. Bystrov, N. A. Irisova, G. V. Kozlov, A. V. Kutsenko, B. A. Polos'yants, and S. A. Terekhin, *Elektronika SVCh*, Ser. 1, 11, 83 (1975).

1.6. L. M. Brekhovskikh, *Waves in Stratified Media*, Izd. Akad. Nauk SSSR, Moscow, 1957 (in Russian).
1.7. A. A. Volkov, G. V. Kozlov, and S. P. Lebedev, *Radiotekhnika i Elektronika*, **24**, 1405 (1979).
1.8. G. W. Chantry, *Submillimeter Spectroscopy*, Acad. Press., London-New York, 1971.
1.9. N. A. Irisova, *Vestnik Akad. Nauk SSSR*, **10**, 63 (1968).
1.10. A. A. Volkov, G. V. Kozlov, I. M. Chernyshev, and L. A. Shuvalov, *Izv. Akad. Nauk SSSR*, Ser. Fiz., **43**, 1726, (1979).
1.11. N. R. Ivanov, G. V. Kozlov, I. M. Chernyshev, and L. A. Shuvalov, *Izv. Akad. Nauk SSSR*, Ser. Fiz., **47**, 485 (1983).
1.12. V. L. Ginzburg, *Zs. Eksp. Teor. Fiz.*, **19**, 36 (1949).
1.13. P. Anderson, *Proc. 2nd All-Union Conf. on Physics of Dielectrics*, Moscow, 1958.
1.14. W. Cochran, *Adv. Phys.*, **9**, 387 (1960); ibid., **10**, 401 (1961).
1.15. G. V. Kozlov, A. A. Volkov, J. F. Scott, G. E. Feldkamp, and J. Petzelt, *Phys. Rev.*, **28**, 255 (1983).
1.16. A. A. Volkov, G. V. Kozlov, and S. P. Lebedev, *Fiz. Tverd. Tela*, **20**, 2021 (1978); ibid., **21**, 1715 (1979); **22**, 2851 (1980); **22**, 3064 (1980); *Kratkie Soobshch. po Fizike*, **9**, 37 (1979).
1.17. A. A. Volkov, G. V. Kozlov, S. P. Lebedev, and I. M. Velichko, *Fiz. Tverd. Tela*, **21**, 3304 (1979).
1.18. A. A. Volkov, G. V. Kozlov, S. P. Lebedev, and A. M. Prokhorov, *Ferroelectrics*, **25**, 531 (1980).
1.19. G. V. Kozlov, S. P. Lebedev, A. M. Prokhorov, and A. A. Volkov, *J. Phys. Soc. Jpn., Suppl, B*, **49**, 188 (1980).
1.20. A. A. Volkov, G. V. Kozlov, and S. P. Lebedev, *Zh. Eksp. Teor. Fiz.*, **79**, 1430 (1980).
1.21. A. A. Volkov, G. V. Kozlov, E. B. Kryukova, and S. P. Lebedev, *Izv. Akad. Nauk SSSR*, **47**, 679 (1983).
1.22. A. A. Volkov, G. V. Kozlov, and S. P. Lebedev, *Fiz. Tverd. Tela*, **23**, 555 (1982).
1.23. V. S. Ambrazyavichene, A. A. Volkov, G. V. Kozlov, V. S. Krasikov, and E. B. Kryukova, *Fiz. Tverd. Tela*, **25**, 1605 (1983).
1.24. J. Petzelt, G. V. Kozlov, A. A. Volkov, Y. Ishibashi, *Z. Physik*, **B33**, 369 (1979).
1.25. A. A. Volkov, Y. Ishibashi, G. V. Kozlov, S. P. Lebedev, J. Petzelt, and A. M. Prokhorov, *J. Phys. Soc. Jpn., Suppl.* B, **49**, 78 (1980).
1.26. V. Dvorak and J. Petzelt, *J. Phys.* C., **11**, 4827 (1978).
1.27. A. A. Volkov, G. V. Kozlov, S. P. Lebedev, J. Petzelt, B. Brzhezina, *Pis'ma v Zh. Eksp. Teor. Fiz.*, **31**, 107 (1980).
1.28. J. Petzelt, I. Gregora, V. Verlochek, J. Fousek, B. Brzhezina, A. A. Volkov, and G. V. Kozlov, *J. Raman Spectroscopy*, **10**, 187 (1981).
1.29. A. A. Volkov, G. V. Kozlov, S. P. Lebedev, J. Petzelt, and Y. Ishibashi, *Ferroelectrics*, **45**, 157 (1982).
1.30. A. A. Volkov, Yu. G. Goncharov, G. V. Kozlov, S. P. Lebedev, A. M. Prokhorov, R. A. Aliev, and K. R. Allakhverdiev, *Pis'ma v Zh. Eksp. Teor. Fiz.*, **37**, 517 (1983).
1.31. A. A. Volkov, G. V. Kozlov, G. I. Mirzoev, and V. G. Hoffman, *Pis'ma v Zh. Eksp. Teor. Fiz.*, 38, 182 (1983).

2 Theory of Electric Polarization of Domain Boundaries in Magnetically Ordered Crystals

V. G. Baryakhtar, V. A. L'vov, and D. A. Yablonskii

2.1. INTRODUCTION

Magnetoelectric (ME) effect is said to take place in a homogeneous magnetic crystal whose equilibrium density of electric polarization **P** depends on the state of the magnetic sybsystem (see, for example, [2.1, 2]). This phenomenon is closely related to the magnetic symmetry of the system [2.3]. A list of magnetic symmetry classes for which ME effect is possible is given in [2.4].

In case a magnetic crystal becomes magnetically inhomogeneous for certain reason, the magnetic symmetry class is reduced (right up to unitary group in the case of a general type inhomogeneity). Besides, the crystal becomes translationally invariant in certain directions. All this results in an electric polarization **P** (r) in the magnetic inhomogeneity region. The polarization depends on the magnetic state of the material, and the symmetry of its spatial distribution is determined by the symmetry of the magnetic inhomogeneity. This effect can be called the inhomogeneous ME effect [2.5], in contrast to the usually observed homogeneous ME effect [2.1-4]. It should be emphasized that this effect must take place in magnetic crystals of any symmetry (including crystals in which the homogeneous ME effect does not occur). The electric polarization caused by inhomogeneity (not necessarily of magnetic origin) is a quite general effect. (In particular, the flexoelectric effect in liquid crystals [2.1, 6] is well known). Note that defects such as impurities and dislocations in a crystalline solid may also be responsible for the inhomogeneous polarization.

2.2. THE PHENOMENOLOGICAL THEORY OF INHOMOGENEOUS MAGNETOELECTRIC EFFECT

If the characteristic dimensions λ of magnetic inhomogeneity appreciably exceed the dimensions of a magnetic unit cell, the inhomogeneous ME effect can be described phenomenologically. To begin with, let us consider ferromagnetic (FM) crystals for which the magnetic inhomogeneity is described by the coordinate-dependent magnetization density **M** (r). Since, generally speaking, the ME in-

teractions have short-range as well as long-range components, the energy of a ferromagnetic crystal can be written in the form

$$W=\int w\,d\mathbf{r}-\frac{1}{2}\int(\mathbf{M}\cdot\mathbf{H}^{(\mathrm{m})}+\mathbf{P}\cdot\mathbf{E}^{(\mathrm{p})})\,d\mathbf{r}-\int(\mathbf{M}\cdot\mathbf{H}+\mathbf{P}\cdot\mathbf{E})\,d\mathbf{r}. \qquad (2.1)$$

Here, the "short-range" contribution to the energy density w depends on the polarization $\mathbf{P}$, magnetization $\mathbf{M}$, and their derivatives; $\mathbf{E}^{(\mathrm{p})}$ and $\mathbf{H}^{(\mathrm{m})}$ are the respective fields of the bound electrostatic and magnetostatic charges, $\mathbf{E}$ and $\mathbf{H}$ being the external electric and magnetic fields. The equilibrium values of the quantities $\mathbf{M}(\mathbf{r})$ and $\mathbf{P}(\mathbf{r})$ are determined by a system of magnetostatic equations and the variational equations for the functional w, obtained under the assumption that the expression for w includes only homogeneous terms and terms containing the first derivatives $\partial\mathbf{M}/\partial x_k$ and $\partial\mathbf{P}/\partial x_k$:

$$\begin{aligned}&\operatorname{curl}\ \mathbf{E}^{(\mathrm{p})}=\operatorname{div}\ (\mathbf{E}^{(\mathrm{p})}+4\pi\mathbf{P})=0,\\&\operatorname{curl}\ \mathbf{H}^{(\mathrm{m})}=\operatorname{div}\ (\mathbf{H}^{(\mathrm{m})}+4\pi\mathbf{M})=0,\end{aligned}$$

$$H_\alpha+H_\alpha^{(\mathrm{m})}-\frac{\partial w}{\partial M_\alpha}+\frac{\partial}{\partial x_k}\frac{\partial w}{\partial\left(\frac{\partial M_\alpha}{\partial x_k}\right)}=0, \qquad (2.2)$$

$$E_i+E_i^{(\mathrm{p})}-\frac{\partial w}{\partial P_i}+\frac{\partial}{\partial x_k}\frac{\partial w}{\partial\left(\frac{\partial P_i}{\partial x_k}\right)}=0$$

(i and k are vector indices, while the subscript α denotes the number of the components of the axial vectors $\mathbf{M}$ and $\mathbf{H}$). In general, the solution of this system is hard to obtain. However, most of the general properties of the inhomogeneous ME effect can be analyzed without solving the system of equation (2.2). For this purpose, we can write the relation between the polarization and the magnetization in a general form, confining to the terms of not higher than the second order in M_α:

$$\begin{aligned}&P_i(\mathbf{r})=P_i^{(0)}(\mathbf{r})+P_i^{(M)}(\mathbf{r})\\&=P_i^{(0)}(\mathbf{r})+\int D_{i,\alpha\gamma}(\mathbf{r}-\mathbf{r}',\ \mathbf{r}-\mathbf{r}'')\,M_\alpha(\mathbf{r}')\,M_\gamma(\mathbf{r}'')\,d\mathbf{r}'\,d\mathbf{r}''.\end{aligned} \qquad (2.3)$$

In this paper, we shall be considering only such cases where the contribution from the long-range forces to the inhomogeneous ME effect is negligibly small. Then, the series expansion of $\mathbf{M}(\mathbf{r}')$ and $\mathbf{M}(\mathbf{r}'')$ in terms of the parameter a/λ in the vicinity of the point $\mathbf{r}$ (a is the ra-

dius of the ME interaction) gives [2.5]

$$P_i^{(M)}(\mathbf{r}) = \delta_i^{(0,M)}\mathbf{M}^2 + \beta_{i,\alpha\gamma}^{(0,M)} M_\alpha M_\gamma + \delta_{ik}^{(1,M)} \frac{\partial}{\partial x_k}\mathbf{M}^2$$

$$+ d_{ik,\alpha\gamma}^{(1,M)}\left(M_\alpha \frac{\partial M_\gamma}{\partial x_k} - M_\gamma \frac{\partial M_\alpha}{\partial x_k}\right) + \beta_{ik,\alpha\gamma}^{(1,M)} \frac{\partial}{\partial x_k} M_\alpha M_\gamma$$

$$+ \delta_{ikj}^{(2,M)} \frac{\partial \mathbf{M}}{\partial x_k}\frac{\partial \mathbf{M}}{\partial x_j} + d_{ikj,\alpha\gamma}^{(2,M)}\left(\frac{\partial M_\alpha}{\partial x_k}\frac{\partial M_\gamma}{\partial x_j} - \frac{\partial M_\gamma}{\partial x_k}\frac{\partial M_\alpha}{\partial x_j}\right) \qquad (2.4)$$

$$+ \beta_{ikj,\alpha\gamma}^{(2,M)} \frac{\partial M_\alpha}{\partial x_k}\frac{\partial M_\gamma}{\partial x_j} + \bar{\delta}_{ikj}^{(2,M)} \frac{\partial}{\partial x_k}\mathbf{M}\frac{\partial \mathbf{M}}{\partial x_j}$$

$$+ \bar{d}_{ikj,\alpha\gamma}^{(2,M)} \frac{\partial}{\partial x_k}\left(M_\alpha \frac{\partial M_\gamma}{\partial x_j} - M_\gamma \frac{\partial M_\alpha}{\partial x_j}\right)$$

$$+ \bar{\beta}_{ikj,\alpha\gamma}^{(2,M)} \frac{\partial}{\partial x_k}\frac{\partial}{\partial x_j} M_\alpha M_\gamma.$$

Tensors $\hat{\beta}^{(0)}$, $\hat{\beta}^{(1)}$, $\hat{\beta}^{(2)}$, and $\hat{\bar{\beta}}^{(2)}$ are symmetric, while $\hat{d}^{(1)}$, $\hat{d}^{(2)}$, and $\hat{\bar{d}}^{(2)}$ are antisymmetric with respect to a transposition of indices α and γ. Their specific structure is determined by the crystallographic group of the paramagnetic phase of the crystal[1].

It follows from (2.4) that the contribution to the electric polarization is made by exchange interaction, relativistic exchange interactions, and relativistic interactions. The constants $\delta_i^{(0,M)} \sim a\delta_{ik}^{(1,M)} \sim a^2\delta_{ikj}^{(2,M)} \sim a^2\bar{\delta}_{ikj}^{(2,M)}$ corresponding to the exchange interaction have the highest values. However, the terms $\delta_i^{(0,M)}\mathbf{M}^2$ and $\delta_{ik}^{(1,M)}\frac{\partial}{\partial x_k}\mathbf{M}^2$ affect the magnitude of the electric polarization only if the magnetization changes in the region of magnetic inhomogeneity. Such a situation may arise either in the vicinity of the Curie point or when an elementary magnetic cell contains more than one magnetic atom. The relativistic exchange constants $d_{ik,\alpha\gamma}^{(1,M)}$, $d_{ikj,\alpha\gamma}^{(2,M)}$, and $\bar{d}_{ikj,\alpha\gamma}^{(2,M)}$ are the next in order of magnitude. All the remaining constants are relativistic in nature.

An expansion similar to (2.4) is obtained for antiferromagnetics (AFM) as well. Thus, for an AFM with two effective magnetic sublat-

---

[1] This statement is always valid except for the rare case when the magnetic symmetry group of the magnetically ordered phase is not a subgroup of the magnetic symmetry group of the paramagnetic phase.

tices, we get

$$P_i(\mathbf{r}) = P_i^{(0)} + P_i^{(L)} + P_i^{(ML)} + P_i^{(M)},$$

$$P_i^{(L)} = f_{i,\alpha\gamma}^{(0,L)} L_\alpha L_\gamma + f_{ik,\alpha\gamma}^{(1,L)} L_\alpha \frac{\partial L_\gamma}{\partial x_k}$$

$$+ \frac{1}{2} \bar{f}_{ikj,\alpha\gamma}^{(2,L)} \frac{\partial L_\alpha}{\partial x_k} \frac{\partial L_\gamma}{\partial x_j} + \frac{1}{2} f_{ikj,\alpha\gamma}^{(2,L)} \frac{\partial}{\partial x_k} L_\alpha \frac{\partial L_\gamma}{\partial x_j},$$

$$P_i^{(ML)} = f_{i,\alpha\gamma}^{(0,ML)} L_\alpha M_\gamma + f_{ik,\alpha\gamma}^{(1,ML)} L_\alpha \frac{\partial M_\gamma}{\partial x_k} + f_{ik,\alpha\gamma}^{(1,ML)} M_\alpha \frac{\partial L_\gamma}{\partial x_k} \qquad (2.5)$$

$$+ f_{ikj,\alpha\gamma}^{(2,ML)} \frac{\partial L_\alpha}{\partial x_k} \frac{\partial M_\gamma}{\partial x_j} + \bar{f}_{ikj,\alpha\gamma}^{(2,ML)} \frac{\partial}{\partial x_k} L_\alpha \frac{\partial M_\gamma}{\partial x_j} + \bar{f}_{ikj,\gamma\alpha}^{(2,ML)} \frac{\partial}{\partial x_k} M_\gamma \frac{\partial L_\alpha}{\partial x_j}.$$

Here, **L** is the antiferromagnetism vector, while the symbol $P_i^{(M)}$ denotes the expansion (2.4). In the same way as in (2.4), we can isolate the exchange, relativistic exchange, and relativistic parts in the coefficients of expansion of $P_i^{(L)}$ and $P_i^{(ML)}$.

As in the case of a ferromagnetic crystal, the structure of the tensors appearing in $P_i^{(M)}$ and $P_i^{(L)}$ is determined exclusively by the crystallographic symmetry class of the paramagnetic phase of the magnetic crystal. The coefficients appearing in the expansion of $P_i^{(ML)}$, on the other hand, can be determined only if we know the crystallographic class, as well as the specific structure of the AFM. This is due to the fact that the transformational properties of the vector **L** are different for operations which transpose or do not transpose the magnetic sublattices (see [2.7]).

The expression (2.5) can be considerably simplified in the isotropic magnetic approximation, where

$$\mathbf{P}^{(M)} = \delta^{(1,M)} \operatorname{grad} \mathbf{M}^2 + d_1^{(1,M)} \mathbf{M} \times \operatorname{curl} \mathbf{M} + d_2^{(1,M)} \mathbf{M} \operatorname{div} \mathbf{M}, \quad (2.6)$$

$$\mathbf{P}^{(L)} = \delta^{(1,L)} \operatorname{grad} \mathbf{L}^2 + d_1^{(1,L)} \mathbf{L} \times \operatorname{curl} \mathbf{L} + d_2^{(2,L)} \mathbf{L} \operatorname{div} \mathbf{L}.$$

This means that at least six of the phenomenological constants in the expansion (2.5) are always nonzero. Here, the first terms are of exchange origin, while the second and third terms are related to the relativistic and relativistic-exchange interactions. It should be noted that a similar expansion, describing the emergence of electric polarization for a nonuniform distribution of the normal vector $\mathbf{n}_0$, takes place in the case of liquid crystals [2.6]. The coefficients which are similar to $d_1^{(1)}$ and $d_2^{(1)}$ are called flexoelectric coefficients. Since, as a rule, the inequality $|\mathbf{M}| \ll |\mathbf{L}|$ is satisfied for AFM's in the absence of an external magnetic field, the major contribution to the electric polarization is made by $P_i^{(L)}$.

The prevalent microscopic theories of magnetoelectric interactions permit only an approximate estimation of the values of the parameters appearing in the phenomenological theory. Moreover, the result

considerably depends on the specific structure of the material. Two types of contributions can be distinguished in the part of the electric polarization which depends on the magnetic state. One of these contributions is due to the lattice deformation caused by the magnetoelastic forces, while the other is associated with the dependence of the electron wave functions on the spin state of the system.

In accordance with [2.8] the spin-dependent electric dipole moment can be represented in the form

$$\mathbf{P}=\sum_l \mathbf{P}_l+\sum_{l,\,m} \mathbf{P}_{lm}+\ldots. \tag{2.7}$$

Here, $\mathbf{P}_l$ is the electric dipole moment associated with the spin of the l-th atom, while $\mathbf{P}_{lm}$ is the moment connected with the l-th and m-th atoms.

The dipole moment $\mathbf{P}_l$ is caused by the Stark effect, which owes its origin to the electric field of the crystal.

According to [2.8], we have

$$P_i^l=\sum_l K^l_{i,\,\alpha\gamma}\, s^l_\alpha\, s^l_\gamma,$$

$$P_i^{lm}=\pi_i^{lm}\mathbf{s}^l\cdot\mathbf{s}^m+\sum_\beta d_{i\beta}^{lm}\,[\mathbf{s}^l\times\mathbf{s}^m]_\beta+\frac{1}{2}\sum_{\beta,\,\gamma}\Gamma^{lm}_{i,\,\beta\gamma}\,(s^l_\beta s^m_\gamma+s^l_\gamma s^m_\beta). \tag{2.8}$$

The first term in P_i^{lm} has an exchange origin and is associated with the dependence of the coordinate part of the electron wave functions on the spin state of the system, in accordance with Pauli's principle. The last term is relativistic in nature and is caused by the spin-orbit interaction. Finally, the second term has a relativistic-exchange character and is due to the interference of the exchange and relativistic interactions. Estimates for the constants appearing in these expressions for some materials are given in [2.8]. The maximum values attained by the constants are:

$$\pi^{lm}\sim\frac{I}{E}(ea_0),\quad d^{lm}\,\frac{v}{c}\,\pi^{lm},\quad \Gamma^{lm}\sim\left(\frac{v}{c}\right)^2\pi^{lm}, \tag{2.9}$$

where e is the electron charge, a_0 a quantity of the order of interatomic distance, v the characteristic velocity of an electron in an atom, c the velocity of light, I the exchange integral, and $E\sim e^2/a_0$. However, the values of these constants are much smaller in known materials. Thus, for example, π is of the order of 10^{-5}-$10^{-4}\ ea_0$ in MnF_2 and FeF_2 [2.8].

The parameters of the expansion (2.8) are connected with the parameters of the phenomenological expansions (2.4) and (2.5) through the following relation:

$$\delta^{(0)}\sim\frac{\pi^{lm}a^3}{\mu_B^2},\quad \beta^{(0)}\sim\frac{\Gamma^{lm}a^3}{\mu_B}.$$

In order to analyze the contribution of magnetoelastic forces to the electric polarization of a magnetic crystal, we must consider the fact that the coefficients of expansion (2.8) depend on the arrangement of atoms in the lattice. This dependence may turn out to be quite significant in highly magnetostrictive crystals. Estimates of contribution from magnetostriction can be found in [2.2]. It can be seen from [2.9] that the maximum effect should be expected in materials with a high magnetic ordering temperature and with strong relativistic interactions.

2.3. THE PHENOMENOLOGICAL THEORY OF ELECTRIC POLARIZATION OF DOMAIN BOUNDARIES

Domain boundaries (DB's) constitute one of the most important and frequently encountered types of magnetic inhomogeneities. Hubert [2.9] has given a detailed review of articles on the DB structure in magnetically ordered crystals.

It is well known [2.1] that the domain structure in ferromagnetics is mainly caused by the magnetic dipole interaction. The situation is quite different in antiferromagnetics where, besides thermodynamically stable domain structure (AFM with a weak ferromagnetism), a nonequilibrium domain structure also exists due to the kinetics of the phase transition to a magnetically ordered state (see [2.10]). The thermodynamically stable domain structure appearing as a result of a first-order phase transition in a magnetic field (the so-called intermediate stage) is also investigated extensively [2.11-17].

The nonuniform polarization in the region of domain boundaries may influence some of their properties. This effect is more pronounced for smaller DB thicknesses and larger values of the magnetoelectric coupling constants. Hence, it is important to calculate the value of the electric polarization.

By way of an example, let us first consider plane 180° domain boundaries in uniaxial ferromagnetics with a centre of inversion [2.1]. In the quadratic magnetization approximation the energy density w_{M} of the magnetic subsystem has the standard form:

$$w_{\mathrm{M}} = -\frac{1}{2}\beta M_z^2 + \frac{1}{2}\alpha_{\parallel}\left(\frac{\partial \mathbf{M}}{\partial z}\right)^2 + \frac{1}{2}\alpha_{\perp}\left[\left(\frac{\partial \mathbf{M}}{\partial x}\right)^2 + \left(\frac{\partial \mathbf{M}}{\partial y}\right)^2\right]. \quad (2.10)$$

For $\beta > 0$, the magnetic moment in domains is directed along the z-axis. Let $\mathbf{n}$ be a unit vector normal to the DB-plane. Since the condition $\mathbf{M}^2 = M_0^2 = \mathrm{const}$ is satisfied at low temperatures, a transition from one domain to another leads to a rotation of the vector $\mathbf{M}$ through the angle θ relative to the z-axis. The magnitude of this an-

gle is determined by the equation

$$\sin\theta(\xi) = \pm(\cosh \xi/\xi_0)^{-1}, \tag{2.11}$$

where ξ is the coordinate along the vector **n**. The $\pm$ signs correspond to two possible equivalent rotations of the vector **M**: the plus sign indicates a variation of θ from 0 to π, while the minus sign indicates a variation from 0 to $-\pi$. The quantity ξ_0 determines the DB thickness. Two types of DB's are possible: the Bloch type and the Néel type. While only the Bloch-type DB domain is stable in the uniaxial model (2.10), a consideration of anisotropy in the basis plane may lead to the stabilization of the Néel DB as well. Hence, we shall be considering both types of boundaries. If $\mathbf{n} \parallel x$, we get for the Bloch-type DB

$$\mathbf{M} = M_0[\mathbf{e}_z\cos\theta(x) + \mathbf{e}_y\sin\theta(x)], \quad \xi_0 = \sqrt{\frac{\alpha_\perp}{\beta}}, \tag{2.12}$$

and for the Néel-type DB

$$\mathbf{M} = M_0[\mathbf{e}_z\cos\theta(x) + \mathbf{e}_x\sin\theta(x)], \quad \xi_0 = \sqrt{\frac{\alpha_\perp}{\beta+4\pi}}. \tag{2.13}$$

Here, $\mathbf{e}_x$, $\mathbf{e}_y$, and $\mathbf{e}_z$ are unit vectors along the x-, y-, and z-axes respectively. The constant 4π in the expression for ξ_0 in (2.13) is due to the magnetic dipole energy in (2.1).

Using the expansion (2.4), we get the following expressions for the electric polarization:

$$P_x = (\beta_{xx,\,yy}^{(1,\,M)} - \beta_{xx,\,zz}^{(1,\,M)}) M_0^2 \frac{d}{dx}\sin^2\theta, \quad P_y = P_z = 0 \tag{2.14}$$

for the Bloch DB, and

$$P_x = (\beta_{xx,\,xx}^{(1,\,M)} - \beta_{xx,\,zz}^{(1,\,M)}) M_0^2 \frac{d}{dx}\sin^2\theta, \quad P_y = 0,$$

$$P_z = d_{zx,\,zx}^{(1,\,M)} M_0^2 \frac{d\theta}{dx} + \frac{1}{2}\beta_{zx,\,zx}^{(1,\,M)} M_0^2 \frac{d}{dx}\sin 2\theta \tag{2.15}$$

for the Néel DB. It should be noted that for a uniaxial crystal, $\beta_{xx,\,yy}^{(1,\,M)} = \beta_{xx,\,xx}^{(1,\,M)}$, while for an isotropic crystal, $\beta_{xx,\,zz}^{(1,\,M)} = \beta_{xx,\,yy}^{(1,\,M)} = \beta_{xx,\,xx}^{(1,\,M)}$. Hence, the component P_x is due to anisotropy only. It is clear from Eqs. (2.14) and (2.15) that the polarization is nonzero only in the nonuniformity region whose dimensions are given by $x \sim \xi_0$.

The presence of the P_x component leads to the appearance of an electric potential in the region of a DB, which is symmetric with respect to the DB centre:

$$\varphi(x) = 4\pi M_0^2 (\beta_{xx,\,yy}^{(1,\,M)} - \beta_{xx,\,zz}^{(1,\,M)}) \left(\cosh\frac{x}{\xi_0}\right)^{-2} \tag{2.16}$$

for a Bloch DB, and

$$\varphi(x) = 4\pi M_0^2 (\beta_{xx,\,xx}^{(1,\,M)} - \beta_{xx,\,zz}^{(1,\,M)}) \left(\cosh \frac{x}{\xi_0}\right)^{-2} \tag{2.17}$$

for a Néel DB. Depending on the sign of the phenomenological parameters, this may be either a potential well or a potential barrier for electrons. In either case, the potential difference between domains is equal to zero.

The component P_z in a Néel DB is responsible for the surface electrostatic charges in the region where it emerges on the surface of the magnetic perpendicular to the z-axis, the surface charge density σ being equal to P_z. Integrating the function $P_z(\xi)$ over the thickness of the DB, we obtain the total electric charge per unit length of the boundary:

$$\pm q_z = \pm \pi M_0^2 d_{zx,\,zx}^{(1,\,M)}. \tag{2.18}$$

If $\theta(\xi)$ varies from 0 to π, a charge $+q_z$ is formed at the sample surface whose outward normal is parallel to the unit vector $\mathbf{e}_z$, while for the rotation of the vector $\mathbf{M}$ in the reverse direction (from 0 to $-\pi$) a charge $-q_z$ is formed. Vertical Néel lines may exist in a Bloch DB (see, for example, [2.18, 19]). Electrostatic charges (2.18) must also appear in the regions where these lines emerge on the sample surface.

For our second example, we consider a DB in a rhombic AFM with the Dzyaloshinskii interaction. We shall confine the discussion to materials which can be described by a model with two effective sublattices (orthoferrite structure).

At low temperatures, the magnitudes of the magnetic moment vectors of the sublattices are constant and hence the condition $\mathbf{L}^2 + \mathbf{M}^2 = M_0^2$ is satisfied. If the exchange interactions are considerably stronger than the relativistic interactions, then $|\mathbf{L}| \gg |\mathbf{M}|$. In this case, the energy of a magnetic subsystem can be approximated according to the standard expression [2.7]:

$$w_{\mathbf{M}} = \frac{1}{2}\delta \mathbf{M}^2 + \frac{1}{2}\alpha_x \left(\frac{\partial \mathbf{L}}{\partial x}\right)^2 + \frac{1}{2}\alpha_y \left(\frac{\partial \mathbf{L}}{\partial y}\right)^2 + \frac{1}{2}\alpha_z \left(\frac{\partial \mathbf{L}}{\partial z}\right)^2$$
$$- d_y M_x L_y - d_x M_y L_x - \frac{1}{2}\beta_x L_x^2 - \frac{1}{2}\beta_y L_y^2 - \frac{1}{2}\beta_z L_z^2. \tag{2.19}$$

From the expansion (2.5) for the electric polarization, we get the following expressions to within the first derivatives:

$$P_x = \delta_x \frac{\partial}{\partial x}\mathbf{M}^2 + d_{xy}\left(L_x \frac{\partial L_y}{\partial y} - L_y \frac{\partial L_x}{\partial y}\right) + d_{xz}\left(L_x \frac{\partial L_z}{\partial z} - L_z \frac{\partial L_x}{\partial z}\right)$$
$$+ \frac{\partial}{\partial x}(\beta_{x,\,x}L_x^2 + \beta_{x,\,y}L_y^2 + \beta_{x,\,z}L_z^2) + \beta_{xy}\frac{\partial}{\partial y}L_x L_y + \beta_{xz}\frac{\partial}{\partial z}L_x L_z,$$
$$P_y = \delta_y \frac{\partial}{\partial y}\mathbf{M}^2 + d_{yx}\left(L_y \frac{\partial L_x}{\partial x} - L_x \frac{\partial L_y}{\partial x}\right)$$

$$+ d_{yz}\left(L_y\frac{\partial L_z}{\partial z}-L_z\frac{\partial L_y}{\partial z}\right)+\frac{\partial}{\partial y}(\beta_{y,x}L_x^2+\beta_{y,y}L_y^2+\beta_{y,z}L_z^2)$$

$$+\beta_{yx}\frac{\partial}{\partial x}L_yL_x+\beta_{yz}\frac{\partial}{\partial z}L_yL_z,$$

$$P_z=\delta_z\frac{\partial}{\partial z}\mathbf{M}^2+d_{zx}\left(L_z\frac{\partial L_x}{\partial x}-L_x\frac{\partial L_z}{\partial x}\right)+d_{zy}\left(L_z\frac{\partial L_y}{\partial y}-L_y\frac{\partial L_z}{\partial y}\right)$$

$$+\frac{\partial}{\partial z}(\beta_{z,x}L_x^2+\beta_{z,y}L_y^2+\beta_{z,z}L_z^2)+\beta_{zx}\frac{\partial}{\partial x}L_zL_x+\beta_{zy}\frac{\partial}{\partial y}L_zL_y, \quad (2.20)$$

where

$$\delta_i=\delta_{ii}^{(1,M)}-\delta_{ii}^{(1,L)}, \quad d_{ij}=d_{ij,ij}^{(1,L)},$$
$$\beta_{ij}=\beta_{ii,jj}^{(1,L)}, \quad \beta_{ij}=\beta_{ij,ij}^{(1,L)}.$$

Depending on the relation between the phenomenological parameters appearing in (2.19), three homogeneous phases are possible in zero magnetic field [2.7]:

$$\text{(I)}\ \mathbf{L}=\pm L_0\mathbf{e}_z, \quad \mathbf{M}=0,$$
$$\text{(II)}\ \mathbf{L}=\pm L_0\mathbf{e}_x, \quad \mathbf{M}=\pm\frac{d_x}{\delta}L_0\mathbf{e}_y, \quad (2.21)$$
$$\text{(III)}\ \mathbf{L}=\pm L_0\mathbf{e}_y, \quad \mathbf{M}=\pm\frac{d_y}{\delta}L_0\mathbf{e}_x.$$

The $\pm$ signs correspond to different domains of the same phase. Phase I is antiferromagnetic, while phases II and III are weakly ferromagnetic. Domain boundaries in orthoferrites have been extensively investigated (see [2.20-22]). In each phase, a DB may be situated in three different crystallographic planes. For each of these planes there are two corresponding planes in which the vector **L** rotates. Thus, 18 different types of DB's are possible. For all DB's in the main approximation concerning the ratio of the relativistic and exchange forces, the angle θ of rotation of the vector **L** inside a DB is determined, as before, by Eq. (2.11).

Let us first consider a DB in phase I. As mentioned above, six different types of DB's are possible in this phase.

Phase I

a_{I}. $\mathbf{n}\parallel x$, $\xi_0^2=\alpha_x/(\beta_z-\beta_y^*)$.

$$\mathbf{L}=\mathbf{L}_0(\mathbf{e}_z\cos\theta+\mathbf{e}_y\sin\theta), \quad \mathbf{M}=\frac{d_x}{\delta}L_0\mathbf{e}_x\sin\theta,$$

$$P_x=\left(\delta_x\frac{d_x^2}{\delta^2}+\beta_{x,y}-\beta_{x,z}\right)L_0^2\frac{d}{dx}\sin^2\theta, \quad P_y=P_z=0.$$

b_{I}. $\mathbf{n}\parallel x$, $\xi_0^2=\alpha_x/(\beta_z-\beta_x^*)$.

$$\mathbf{L} = L_0(\mathbf{e}_z \cos\theta + \mathbf{e}_x \sin\theta), \quad \mathbf{M} = \frac{d_y}{\delta} L_0 \mathbf{e}_y \sin\theta,$$

$$P_x = \left(\delta_x \frac{d_x^2}{\delta^2} + \beta_{x,x} - \beta_{x,z}\right) L_0^2 \frac{d}{dx} \sin^2\theta, \quad P_y = 0,$$

$$P_z = d_{zx} L_0^2 \frac{d\theta}{dx} + \frac{1}{2} \beta_{zx} L_0^2 \frac{d}{dx} \sin 2\theta.$$

a_{I}', $\mathbf{n} \parallel y$, is obtained from a_{I} by interchanging x and y in all the formulas.

b_{I}', $\mathbf{n} \parallel y$, is obtained from b_{I} by interchanging x and y.

c_{I}, $\mathbf{n} \parallel z$, $\xi_0^2 = \alpha_z/(\beta_z - \beta_x^*)$.

$$\mathbf{L} = L_0(\mathbf{e}_z \cos\theta + \mathbf{e}_x \sin\theta), \quad \mathbf{M} = \frac{d_y}{\delta} L_0 \mathbf{e}_y \sin\theta,$$

$$P_z = \left(\delta_z \frac{d_y^2}{\delta^2} + \beta_{z,x} - \beta_{z,z}\right) L_0^2 \frac{d}{dz} \sin^2\theta, \quad P_y = 0,$$

$$P_x = d_{xz} L_0^2 \frac{d\theta}{dz} + \frac{1}{2} \beta_{xz} L_0^2 \frac{d}{dz} \sin 2\theta.$$

c_{I}', $\mathbf{n} \parallel z$, is obtained from c_{I} by interchanging x and y.

Phase II

a_{II}, $\mathbf{n} \parallel z$, $\xi_0^2 = \alpha_z/(\beta_x^* - \beta_y^*)$.

$$\mathbf{L} = L_0(\mathbf{e}_x \cos\theta + \mathbf{e}_y \sin\theta),$$

$$\mathbf{M} = \frac{L_0}{\delta}(d_x \mathbf{e}_y \cos\theta + d_y \mathbf{e}_x \sin\theta),$$

$$P_z = \left(\delta_z \frac{d_y^2 - d_x^2}{\delta^2} + \beta_{z,y} - \beta_{z,x}\right) L_0^2 \frac{d}{dz} \sin^2\theta, \quad P_y = P_x = 0.$$

b_{II}, $\mathbf{n} \parallel z$, $\xi_0^2 = \alpha_z/(\beta_x^* - \beta_z)$.

$$\mathbf{L} = L_0(\mathbf{e}_x \cos\theta + \mathbf{e}_z \sin\theta), \quad \mathbf{M} = \frac{L_0}{\delta} d_y \mathbf{e}_y \cos\theta,$$

$$P_z = \left(\delta_z \frac{d_y^2}{\delta^2} + \beta_{z,z} - \beta_{z,x}\right) L_0^2 \frac{d}{dz} \sin^2\theta, \quad P_y = 0,$$

$$P_x = d_{xz} L_0^2 \frac{d\theta}{dz} + \frac{1}{2} \beta_{xz} L_0^2 \frac{d}{dz} \sin 2\theta.$$

a_{II}', $\mathbf{n} \parallel y$, $\xi_0^2 = \alpha_y/(\beta_x^* - \beta_z)$.

$$\mathbf{L} = L_0(\mathbf{e}_x \cos\theta + \mathbf{e}_z \sin\theta), \quad \mathbf{M} = \frac{d_x}{\delta} L_0 \mathbf{e}_y \cos\theta,$$

$$P_y = \left(-\delta_y \frac{d_x^2}{\delta^2} - \beta_{y,x} + \beta_{y,z}\right) L_0^2 \frac{d}{dy} \sin^2\theta,$$

$$P_x = P_z = 0.$$

b_{II}', $\mathbf{n} \parallel y$, $\xi_0^2 = \alpha_y/(\beta_x^* - \beta_y^*)$.

$$\mathbf{L}=L_0(\mathbf{e}_x\cos\theta+\mathbf{e}_y\sin\theta),\quad \mathbf{M}=\frac{L_0}{\delta}(d_x\mathbf{e}_y\cos\theta+d_y\mathbf{e}_x\sin\theta),$$

$$P_y=\left(\delta_y\frac{d_x^2-d_y^2}{\delta^2}+\beta_{y,y}-\beta_{y,x}\right)L_0^2\frac{d}{dy}\sin^2\theta,\quad P_z=0,$$

$$P_x=d_{xy}L_0^2\frac{d\theta}{dy}+\frac{1}{2}\beta_{xy}L_0^2\frac{d}{dy}\sin 2\theta.$$

c_{II}, $\mathbf{n}\parallel x$, $\xi_0^2=\alpha_{x'}/(\beta_x^*-\beta_z)$.

$$\mathbf{L}=L_0(\mathbf{e}_x\cos\theta+\mathbf{e}_z\sin\theta),\quad \mathbf{M}=\frac{d_x}{\delta}L_0\mathbf{e}_y\cos\theta,$$

$$P_x=\left(-\delta_x\frac{d_x^2}{\delta^2}-\beta_{x,x}+\beta_{x,z}\right)L_0^2\frac{d}{dx}\sin^2\theta,\quad P_y=0,$$

$$P_z=d_{zx}L_0^2\frac{d\theta}{dx}+\frac{1}{2}\beta_{zx}L_0^2\frac{d}{dx}\sin 2\theta.$$

c'_{II}, $\mathbf{n}\parallel x$, $\xi_0^2=\alpha_x/(\beta_x^*-\beta_y^*)$.

$$\mathbf{L}=L_0(\mathbf{e}_x\cos\theta+\mathbf{e}_y\sin\theta),\quad \mathbf{M}=\frac{L_0}{\delta}(d_x\mathbf{e}_y\cos\theta+d_y\mathbf{e}_x\sin\theta),$$

$$P_x=\left(\delta_x\frac{d_y^2-d_x^2}{\delta^2}+\beta_{x,y}-\beta_{x,x}\right)L_0^2\frac{d}{dx}\sin^2\theta,$$

$$P_y=d_{yx}L_0^2\frac{d\theta}{dx}+\frac{1}{2}\beta_{yx}L_0^2\frac{d}{dx}\sin 2\theta,$$

$$P_z=0.$$

The domain boundary in phase III is obtained from the expression for the DB in phase II by interchanging x and y. In all these formulas, the following notation has been used:

$$\beta_x^*=\beta_x+\frac{d_x^2}{\delta},\quad \beta_y^*=\beta_y+\frac{d_y^2}{\delta}.$$

In the boundaries of the type a and a', a rotation of the vector $\mathbf{L}$ is accomplished in the DB plane, and for the boundaries of the type b, b', c, and c', in a plane perpendicular to the DB plane.

As in the case of ferromagnetics, a volume charge density $\rho(\xi)=-dP_n(\xi)/d\xi$ appears in all DB's considered above and results in an electrostatic potential which is defined by the formula

$$\varphi(\xi)=4\pi\tilde{\beta}\left(\cosh\frac{\xi}{\xi_0}\right)^{-2}.$$

The coefficient $\tilde{\beta}$ in this formula coincides with the coefficient of $(d/d\xi)\sin^2\theta$ in the expression for P_n. Besides, in all regions where the boundaries, b, b', c, and c' emerge on the η-th surface of the sample, bound surface charges $q_\eta=\pm\pi L_0^2 d_{\eta\xi}$ are formed, $\eta\xi$ being the plane in which the vector $\mathbf{L}$ rotates.

The boundaries a, a', just like in a ferromagnetic, may have vertical lines dividing boundary regions with different directions of rotation of the vector **L**. Surface electrostatic charges must also appear at such regions on the surface of the sample where these lines emerge.

2.4. MAGNETIC SYMMETRY AND ELECTRIC POLARIZATION OF A CRYSTAL WITH A PLANE DOMAIN BOUNDARY

This section aims at providing a complete classification of all possible types of distribution **P** (**r**) in the DB's of ferromagnetic (FM) and antiferromagnetic crystals.

The distribution of the electric polarization **P** (**r**) for any FM and AFM can be found with the help of the formulas (2.4) and (2.5). The qualitative behaviour of the polarization vector in a crystal with DB's can, however, be described on the basis of symmetry alone. For this purpose, we must know the magnetic symmetry group of the crystal. Naturally, this group will depend on the specific crystal and the type of domain boundaries.

If the radius of curvature r_0 of the boundary is much larger than its thickness, the regions whose dimensions are much smaller than r_0 can be approximately treated as planes. Hence, it is worthwhile to study the symmetry of plane DB's. As in the previous section, we introduce a unit vector **n** perpendicular to the DB plane. The corresponding coordinate will be denoted by ξ. Besides, we introduce two mutually perpendicular unit vectors τ_1 and τ_2 in the DB plane.

Ferromagnetics. To begin with, let us consider a plane DB separating the FM domains. The magnetic symmetry group of a crystal with such a DB is a subgroup of the (Shubnikov) magnetic group of the paramagnetic phase (see footnote 1) and is a set of all operations which do not change the spatial arrangement of the magnetic moments of the atoms. If all translations in this group are put identically equal to a unitary operation, we arrive at the concept of the magnetic symmetry class of a crystal with a DB (the symmetry class of the DB, to be more precise).

Let us enumerate all possible magnetic symmetry classes $G^{(k)}$ of a DB in FM crystals with a plane 180° DB. In this case, the magnetic moments of domains away from the boundary are antiparallel, i.e. $\mathbf{M}(\xi = \infty) = -\mathbf{M}(\xi = -\infty)$. Obviously, the magnetic class of a DB in a crystal can contain only such operations which do not change the conditions at $\xi = \pm\infty$. These operations can be of two types. Operations $g^{(1)}$ of the first type change neither the direction of the axial t-odd vectors $\mathbf{M}(\pm\infty)$ nor the direction of the vector **n** normal to the wall. Operations $g^{(2)}$ of the second type reverse both these directions ($g^{(2)}\mathbf{M}(\infty) = \mathbf{M}(-\infty)$, $g^{(2)}\mathbf{n} = -\mathbf{n}$). The to-

tality of operations $g^{(1)}$ and $g^{(2)}$ forms a certain group. This group corresponds to the highest possible symmetry class of the DB in a given crystal for a chosen direction of the normal **n**. All the remaining symmetry classes are obtained for a given crystal and a fixed **n** by simply enumerating its subgroups.

Four different orientations of the vectors $\mathbf{M}(\pm\infty)$ are possible with respect to the normal to the wall.

(1) $\mathbf{M}(\pm\infty) \parallel \boldsymbol{\tau}_1$. The magnetic symmetry classes for DB's in crystals can comprise the following elements: 1, 2_2, $\bar{2}_1$, $\bar{2}_n$, $\bar{1}'$, $\bar{2}_2'$, $2_1'$, and $2_n'$. In the notation chosen by us, 2_1, 2_2, and 2_n are the second-order rotations about the axes $\boldsymbol{\tau}_1$, $\boldsymbol{\tau}_2$, and **n** respectively, $\bar{1}$ denotes the inversion, while $\bar{2}_1 = 2_1 \cdot \bar{1}$, $\bar{2}_2 = 2_2 \cdot \bar{1}$, and $\bar{2}_n = 2_n \cdot \bar{1}$ are the reflection planes perpendicular to the axes $\boldsymbol{\tau}_1$, $\boldsymbol{\tau}_2$ and **n** respectively. As usual, the prime over a symmetry element indicates a simultaneous time reversal operation. The primed rotations are called antirotations, while $1'$ is called antiinversion.

Sixteen symmetry groups can be formed with the help of these elements. Table 2.1 contains a list of these groups under the numbers k from 1 to 16 (the numbers are given in the first column of the table). It can be seen that the groups from $G^{(2)}$ to $G^{(16)}$ are subgroups of the $G^{(1)}$ group.

(2) $\mathbf{M}(\pm\infty) \parallel \mathbf{n}$. In this case, the following operations may appear in the magnetic classes of a DB in a crystal:

$$1,\ 2_\perp,\ 2_n,\ 3_n,\ 4_n,\ 6_n,\ \bar{1}',\ \bar{2}_\perp',\ \bar{2}_n',\ \bar{3}_n',\ \bar{4}_n',\ \bar{6}_n' \qquad (2.22)$$

where 3_n, 4_n and 6_n are rotations of the third, fourth, and sixth order respectively about the normal **n**, and $2_\perp$ are the second-order rotations about the axes perpendicular to **n**. With the help of the elements (2.22), we can form 42 different groups which cannot be reduced to each other by an interchanging the axes $\boldsymbol{\tau}_1 \leftrightarrow \boldsymbol{\tau}_2$.

All possible magnetic classes of DB's corresponding to the above-mentioned boundary conditions and not containing operations 3_n, 4_n, 6_n, $\bar{3}_n'$, $\bar{4}_n'$, and $\bar{6}_n'$ are given in the rows $k = 12, 13, \ldots, 23$ in Table 2.1. There is no need to enumerate the remaining symmetry classes as far as this paper is concerned.

(3) $\mathbf{M}(\pm\infty) = M_{\tau_1}(\pm\infty)\,\boldsymbol{\tau}_1 \pm M_n(\pm\infty)\,\mathbf{n}$. The DB symmetry is described by one of the classes $G^{(k)}$ with $k = 12, 13, 14$.

(4) $\mathbf{M}(\pm\infty) = M_{\tau_1}(\pm\infty)\,\boldsymbol{\tau}_1 + M_{\tau_2}(\pm\infty)\,\boldsymbol{\tau}_2 + M_n(\pm\infty)\,\mathbf{n}$. The DB symmetry is described by the classes $G^{(15)}$ and $G^{(16)}$.

In order to describe the symmetry of microscopic properties of crystals with plane 180° DB's, we must construct magnetic groups for the classes obtained above. A knowledge of these groups is essential for investigating boundaries whose thickness is comparable with the dimensions of the unit magnetic cell. In this paper, however, we shall

Table 2.1.

k	Symmetry classes	M (∞)	M_{τ_2}	M_{τ_1}	M_n	P_{τ_2}	P_{τ_1}	P_n
1	$(1, \bar{2}_1, 2_2, \bar{2}n) \times (1, \bar{1}')$	τ_1	0	A	0	0	0	A
2	$1, \bar{2}_1 \bar{2}'_2, 2'_n$	τ_1	0	A, S	0	0	0	A, S
3	$1, \bar{2}_1, 2_2, \bar{2}_n$	τ_1	0	A	0	S	0	A
4	$1, \bar{1}', 2'_1, \bar{2}_1$	τ_1	0	A	0	A	0	A
5	$1, \bar{1}, 2'_n, \bar{2}_n$	τ_1	A	A	0	0	0	A
6	$1, \bar{2}_1$	τ_1	0	A, S	0	A, S	0	A, S
7	$1, 2'_1, 2_2, 2'_n$	τ_1	S	A	0	0	0	A
8	$1, 2'_n$	τ_1	A, S	A, S	0	0	0	A, S
9	$1, 2'_1, \bar{2}'_2, \bar{2}_n$	τ_1	0	A	S	0	S	A
10	$1, 2'_1$	τ_1	S	A	S	A	S	A
11	$1, \bar{2}_n$	τ_1	A	A	S	S	S	A
12	$1, \bar{2}'_2$	τ_1, n	0	A, S	A, S	0	A, S	A, S
13	$1, 2_2$	τ_1, n	S	A	A	S	A	A
14	$1, \bar{1}', 2_2, \bar{2}'_2$	τ_1, n	0	A	A	0	A	A
15	$1, \bar{1}'$	τ_1, τ_2, n	A	A	A	A	A	A
16	1	τ_1, τ_2, n	A, S	A, S	A, S	A, S	A, S	A, S
17	$1, \bar{2}'_1, 2_2, \bar{2}'_n$	n	S	0	A	S	0	A
18	$1, \bar{2}'_n$	n	S	S	A	S	S	A
19	$1, 2_n$	n	0	0	A, S	0	0	A, S
20	$1, \bar{1}', 2_n, \bar{2}'_n$	n	0	0	A	0	0	A
21	$1, 2_1, 2_2, 2_n$	n	0	0	A	0	0	A
22	$1, \bar{2}'_1, \bar{2}'_2, 2_n$	n	0	0	A, S	0	0	A, S
23	$(1, 2_1, 2_2, 2_n) \times (1, \bar{1}')$	n	0	0	A	0	0	A

Remark: The first column of the table shows the serial number of the magnetic symmetry classes of domain boundaries in FM's. The second column gives the symmetry elements appearing in these classes, while the third column contains the nonzero components of the vectors $\mathbf{M}(\pm\infty)$. The last two columns show qualitatively the coordinate dependence of the magnetization vector $\mathbf{M}(\xi)$ and the polarization vector $\mathbf{P}(\xi)$ (ξ is the coordinate along the normal to the domain boundary; the symbols A and S denote the antisymmetric and symmetric parts of the function with respect to the substitution $\xi \to -\xi$).

confine ourselves to investigation of DB's whose thickness is much more than the dimensions of the elementary magnetic cell of a crystal. Such DB's can be described with the help of the macroscopic magnetization density $\mathbf{M}(\xi)$ and the macroscopic polarization density $\mathbf{P}(\xi)$. The averaging of spatial disribution of atomic magnetic

and dipole moments is carried out over distances much larger than the interatomic distances but much smaller than the DB thickness. Hence, in order to know the types of distributions of **M** (ξ) and **P** (ξ) that may be realized, in principle, in a particular crystal, it is sufficient to indicate the $G^{(k)}$ classes which are subgroups of the magnetic class of the paramagnetic phase of a given crystal.

Each magnetic symmetry class $G^{(k)}$ has a specific type of coordinate dependence of the components M_α (ξ) of the magnetization density and P_i (ξ) of the polarization density. The exact type of this dependence can be determined by analyzing the action of the operations $g^{(1)}$ and $g^{(2)}$ appearing in the classes $G^{(k)}$ on components of the t-odd axial vector and the t-even real vector. The following rules apply in this case.

If $g^{(1)} M_\alpha = - M_\alpha$ then $M_\alpha (\xi) = 0$; if $g^{(1)} M_\alpha = M_\alpha$, then $g^{(1)}$ does not impose any restrictions on the type of this magnetization component.

If $g^{(2)} M_\alpha = - M_\alpha$, then M_α is an antisymmetric (A) function of the coordinate ξ; if $g^{(2)} M_\alpha = M_\alpha$, M_α is a symmetric (S) function of ξ.

Naturally, these rules are applicable to the functions P_i (ξ) as well. The last two columns of Table 2.1 give the types of dependences M_α (ξ) and P_i (ξ) corresponding to the $G^{(k)}$ classes obtained with the help of these rules. The classes containing the elements 3_n, 4_n, 6_n, $\bar{3}'_n$, $\bar{4}'_n$, and $\bar{6}'_n$ are not included in this table, since they correspond to pulsating DB's in which $M_{\tau_1}(\xi) = M_{\tau_2}(\xi) = P_{\tau_1}(\xi) = P_{\tau_2}(\xi) = 0$. The existence of any of the operations $2_\perp$, $\bar{1}'$, $\bar{2}'_n$, $\bar{3}'_n$, $\bar{4}'_n$, $\bar{6}'_n$ in these classes imposes the following restrictions on the only nonzero components of polarization and magnetization: $P_n (\xi) = - P_n (-\xi)$, $M_n (\xi) = - M_n (-\xi)$.

If the symmetry class of DB contains elements which transpose the magnetic domains, we can determine the centre of the DB. These elements may be $2_\perp$, $2'_\perp$, $\bar{2}_n$, $\bar{2}'_n$, $\bar{3}'_n$, $\bar{4}'_n$, $\bar{6}'_n$. The plane passing through the point of intersection of these elements with the coordinate axis ξ is the centre of the DB. In boundaries which do not have a centre, each nonzero component of magnetization and polarization has a symmetric part, as well as an antisymmetric part. It can be seen from Table 2.1 that in DB's corresponding to classes with $k = 1$ to 6, 14, 15, 19 to 23, there exists a plane $\xi = \xi^*$ such that **M** (ξ^*) = 0. Since the magnetic moment depends on the exchange forces, such DB's can only exist either at temperatures close to the magnetic ordering temperature, or in the magnetics in which the relativistic interactions are comparable to or even exceed the exchange interactions.

In the preceding section, we considered the polarization of Bloch and Néel DB's in FM's. The symmetry of these boundaries is described

by $G^{(17)}$ and $G^{(9)}$ classes respectively. Consequently, a Bloch DB may be formed only in magnetics whose crystallographic symmetry class contains the D_2 class as a subgroup. For the formation of a Néel DB, it is essential that the class C_{2v} be present among the subgroups of the crystallographic class of the magnetic. If these conditions are not satisfied, the DB will have a more complex structure and will be described by a class having not more than two elements. It should be noted that the expressions (2.14) and (2.15) are in agreement with the data given in Table 2.1. The DB's with $k = 8$ and 12 are called quasi-Bloch and quasi-Néel boundaries respectively.

Note that the $G^{(17)}$ class describes highly symmetric Néel-type DB's but with different conditions for $\mathbf{M}$ ($\pm\infty$).

Usually, the inhomogeneity due to the DB's in magnetically ordered crystals has a finite size $\sim \xi_0$ and decreases exponentially with the distance (see Eq. (2.11)). Hence, the classes indicated in Table 2.1 describe the crystal symmetry only in the region of a DB. At distances $\xi \gg \xi_0$, the crystal symmetry is described by the magnetic class of the spatially homogeneous state.

Antiferromagnetics. The above symmetry analysis of ferromagnetics with plane 180° DB's can also be extended to the case of AFM's with two effective magnetic sublattices.[2] Once again, we should first construct the symmetry groups for conditions at infinity. However, in order to stipulate these conditions, we must fix away from the wall the direction of the magnetic moments of the atoms of both sublattices or, in other words, the direction of the antiferromagnetism vector $\mathbf{L}(\infty)$ and the ferromagnetism vector $\mathbf{M}(\infty)$. These vectors have different transformational properties, since unlike $\mathbf{M}(\infty)$, $\mathbf{L}(\infty)$ changes sign upon a transposition of the magnetic sublattices. Taking this fact into consideration, we can divide all the operations in the crystallographic class of the paramagnetic phase into even (+) and odd (—) operations with respect to a given AFM structure [2.7]. The odd operations interchange the atoms of different sublattices, while the even operations interchange only the atoms of the same sublattice.

Since the magnetic symmetry classes of an AFM crystal with DB's are the subgroups of the magnetic classes of its paramagnetic phase, their operations can be also even and odd with respect to a given AFM structure.

To start with, let us consider *AFM structures which are even relative to all translations.* In this case, the magnetic symmetry classes of DB's in an AFM actually consist of the same elements as the DB's in ferromagnetics. However, depending on the parity, the elements for

---

[2] A detailed explanation of the term "effective magnetic sublattices" used here is given in the Appendix (see also [2.23]).

an AFM may be supplemented by the time reversal operation. We shall first consider *classes containing even elements only*. Since **L** and **M** are identically transformed in this case, these classes coincide with those given in Table 2.1. Moreover, column 4 defines the type of coordinate dependence of the vector **M** as well as **L**. As before, we shall not elaborate the classes containing axes of higher than the second order along **n**. All other magnetic symmetry classes for any specific AFM with DB's can be obtained as follows from the classes mentioned in Table 2.1.

(a) The parity of every symmetry operation appearing in $G^{(k)}$ for a given antiferromagnetic is determined.

(b) All odd elements are supplemented by the time-reversal operation.

Table 2.2 gives all the possible parity combinations for elements appearing in $G^{(k)}$. Henceforth, we shall designate the magnetic classes of DB's in an AFM by the symbol $G_m^{(k)}$. The index k enumerates the classes in accordance with Table 2.1, while the subscript m denotes the parity combination of operations appearing in $G_m^{(k)}$ in accordance with Table 2.2. Naturally, with the exception of $G_m^{(1)}$ and $G_m^{(23)}$,

Table 2.2.

m	1	$\bar{1}$	2_1	2_2	2_n	$\bar{2}_1$	$\bar{2}_2$	$\bar{2}_n$
1	+	+	+	+	+	+	+	+
2	+	+	−	−	+	−	−	+
3	+	+	+	−	−	+	−	−
4	+	+	−	+	−	−	+	−
5	+	−	+	+	+	−	−	−
6	+	−	−	−	+	+	+	−
7	+	−	+	−	−	−	+	+
8	+	−	−	+	−	+	−	+

Remark: Possible parity combinations for the elements appearing in the symmetry groups of domain boundaries in antiferromagnetics (m is the number of parity combination, signs plus and minus indicate even and odd elements respectively).

several values of m correspond to the same group in all classes if we use this form of notation. This, however, does not cause any confusion.

The type of distribution of **P** (ξ) in $G_m^{(k)}$ classes is defined, as before, by the last column of Table 2.1 for any value of m. The type of distribution of **L** (ξ) will be defined by the fourth column of this ta-

ble for any m. As far as the dependence $\mathbf{M}(\xi)$ is concerned, it is mainly defined by the number k, as well as m, and is not given in Table 2.1.

Table 2.3 shows the magnetic classes corresponding to highly symmetric rotational domain boundaries in an AFM. It also contains the

Table 2.3.

k	m	Symmetry classes	M_{τ_2} M_{τ_1} M_n	L_{τ_2} L_{τ_1} L_n	P_{τ_2} P_{τ_1} P_n
7	1, 5	$1, 2_2(+), 2_1'(+), 2_n'(+)$	S A 0	S A 0	0 0 A
	2, 6	$1, 2_2'(-), 2_1(-), 2_n'(+)$	A S 0	S A 0	0 0 A
	3, 7	$1, 2_2'(-), 2_1'(+), 2_n(-)$	0 0 S	S A 0	0 0 A
	4, 8	$1, 2_2(+), 2_1(-), 2_n(-)$	0 0 A	S A 0	0 0 A
9	1, 7	$1, \bar{2}_2'(+), 2_1'(+), \bar{2}_n(+)$	0 A S	0 A S	0 S A
	2, 8	$1, \bar{2}_2(-), 2_1(-), \bar{2}_n(+)$	A 0 0	0 A S	0 S A
	3, 5	$1, \bar{2}_2(-), 2_1'(+), \bar{2}_n'(-)$	S 0 0	0 A S	0 S A
	4, 6	$1, \bar{2}_2'(+), 2_1(-), \bar{2}_n'(-)$	0 S A	0 A S	0 S A
17	1, 8	$1, 2_2(+), \bar{2}_1'(+), \bar{2}_n'(+)$	S 0 A	S 0 A	S 0 A
	2, 7	$1, 2_2'(-), \bar{2}_1(-), \bar{2}_n'(+)$	0 S 0	S 0 A	S 0 A
	3, 6	$1, 2_2'(-), \bar{2}_1'(+), \bar{2}_n(-)$	A 0 S	S 0 A	S 0 A
	4, 5	$1, 2_2(+), \bar{2}_1(-), \bar{2}_n(-)$	0 A 0	S 0 A	S 0 A

Remark: Magnetic symmetry classes of highly symmetric rotational DB's and the qualitative form of the functions $\mathbf{M}(\xi)$, $\mathbf{L}(\xi)$, and $\mathbf{P}(\xi)$.

types of dependences $\mathbf{P}(\xi)$, $\mathbf{L}(\xi)$, and $\mathbf{M}(\xi)$. These classes are constructed from the $G^{(7)}$ class (Bloch DB), $G^{(9)}$ class (Néel DB) and $G^{(17)}$ by the method described above. It is clear from this table that each class splits into four classes. To each quartet, there corresponds one type of functions $\mathbf{L}(\xi)$ and $\mathbf{P}(\xi)$ and four different distributions of the magnetization $\mathbf{M}(\xi)$. Of special interest is the fact that in all DB's, a nonzero nouniform magnetization appears irrespective of whether or not the initial AFM phases are weakly ferromagnetic. Thus, for example, $\mathbf{M}(\xi)$ appears in all structures with even as well as with odd inversion. Since an odd inversion precludes the existence of homogeneous, L-linear components in free energy (in particular, the Dzyaloshinskii term), the magnetization nonuniformity in such structures must be caused by invariants containing spatial derivatives, for example, the invariant $\mathbf{M} \cdot \mathrm{curl}\, \mathbf{L}$.

The DB's for a rhombic AFM considered by us in the previous section are distributed over magnetic classes as follows:

$a_{\mathrm{I}}, a_{\mathrm{I}}'$	$b_{\mathrm{I}}, b_{\mathrm{I}}'$	$c_{\mathrm{I}}, c_{\mathrm{I}}'$	a_{II}	b_{II}	a_{II}'	b_{II}'	c_{II}	c_{II}'
$G_{3,7}^{(7)}$	$G_{3,5}^{(9)}$	$G_{2,7}^{(17)}$	$G_{2,6}^{(7)}$	$G_{2,8}^{(9)}$	$G_{4,8}^{(7)}$	$G_{4,6}^{(9)}$	$G_{4,5}^{(17)}$	$G_{3,6}^{(17)}$

Let us now consider *AFM structures which are odd with respect to any translation t* (—). In this case, the magnetic class of a homogeneous AFM contains the operation $1'$ (—). This operation also remains in the magnetic group of the inhomogeneous state if the inhomogeneity dimensions considerably exceed the dimensions of a unit cell. It follows hence that the magnetic symmetry classes of a DB in an AFM with odd translation t (—) are a direct product of the classes $G_m^{(k)}$ and the group consisting of a unitary element 1 and the time inversion operation $1'$ (—): $\bar{G}_m^{(k)} = G_m^{(k)} \times (1, 1'$ (—)). The presence of the operation $1'$ (—) in the symmetry class of a DB in an AFM does not affect the form of **L** (r) and **P** (r), but forbids the existence of nonzero components of magnetization in the entire crystal. In this case, the **L** (r) and **P** (r) dependences are identical in $\bar{G}_m^{(k)}$ and $G_m^{(k)}$ groups for the same values of k and m.

2.5. INTERDOMAIN POTENTIAL DIFFERENCE

If any component of the polarization vector P_i (ξ) has a symmetric part (S), there exists a nonzero value of this component, averaged over the thickness of the DB:

$$\langle P_i \rangle = \frac{1}{\xi_0} \int_{-\infty}^{\infty} P_i(\xi)\, d\xi \tag{2.23}$$

In most of the classes investigated by us, the transverse components P_{τ_1} (ξ) and P_{τ_2} (ξ) of the polarization contain a symmetric part. As mentioned above, this leads to the appearance of an uncompensated electric charge q_τ at the point of emergence of the DB on the appropriate surface (τ_1 or τ_2) of the magnetic. This charge is equal to

$$q_\tau = \pm \int_{-\infty}^{\infty} P_\tau(\xi)\, d\xi \tag{2.24}$$

per unit length of the DB.

To our mind, the investigation of DB's in which the quantity $\langle P_n \rangle$ is nonzero is of special interest since the existence of such a boundary in a crystal leads to an electric potential difference be-

tween the magnetic domains:

$$\varphi_1 - \varphi_2 = 4\pi \int_{-\infty}^{\infty} P_n(\xi)\, d\xi. \tag{2.25}$$

This difference is caused by the volume charge density $\rho(\xi) = -dP_n \cdot d\xi$. Obviously, this effect takes place in all cases when the magnetic class does not contain operations $g^{(2)}$ which change the direction of the vector **n** (since the vectors **n** and $\langle \mathbf{P}_n \rangle$ are transformationally equivalent). Such a property is exhibited by classes with numbers $k = 2, 6, 8, 12, 16, 19$ and 22. It has been mentioned above that the absence of $g^{(2)}$ operation indicates the absence of a centre in the DB. Strictly speaking, the appearance of such DB's makes the magnetic domains inequivalent.

The magnetic classes with $k = 2, 6, 19$, and 22 are less interesting, since they describe pulsating DB's. The most interesting DB's are of rotational type: quasi-Bloch boundaries ($k = 8$), quasi-Néel boundaries ($k = 12$), and completely asymmetric boundaries ($k = 16$).

Since $\mathbf{M}(+\infty) = -\mathbf{M}(-\infty)$, only such terms from (2.4) and (2.5) which cannot be reduced to total derivatives contribute to the integral (2.25). Thus, in pyroelectric and magnetoelectric types of magnetics, the emergence of interdomain potential difference is mainly due to terms without derivatives in Eqs. (2.4) and (2.5) (exchange terms with derivatives may also give a similar contribution). The interdomain potential difference in other magnetics is caused by inhomogeneous exchange-relativistic terms in Eqs. (2.4) and (2.5). For example, for FM's belonging to the pyroelectric class $\mathbf{C}_{2v}$, we have

$$P_z = \beta_{z,xx}^{(0,\mathrm{M})} M_x^2 + \beta_{z,yy}^{(0,\mathrm{M})} M_y^2 + \sum_i \delta_{z,ii}^{(2,\mathrm{M})} \left(\frac{\partial \mathbf{M}}{\partial x_i}\right)^2. \tag{2.26}$$

This gives the following expression for a Bloch-type rotational DB with $\mathbf{n} \parallel z$:

$$\varphi_1 - \varphi_2 = 4\pi (\beta_{z,xx}^{(0,\mathrm{M})} - \beta_{z,yy}^{(0,\mathrm{M})}) M_0^2 \int \sin^2\theta\, dz$$
$$+ \delta_{z,zz}^{(2,\mathrm{M})} M_0^2 \int \left(\frac{d\theta}{dz}\right)^2 dz. \tag{2.27}$$

In FM's belonging to the class $\mathbf{C}_{2h}$, the electric polarization components are given by the expression

$$P_n(\xi) = d_{nn,xy}^{(1,\mathrm{M})} \left(M_x \frac{\partial M_y}{\partial \xi} - M_y \frac{\partial M_x}{\partial \xi}\right). \tag{2.28}$$

Substituting (2.28) into (2.25), we get

$$\varphi_1 - \varphi_2 = 4\pi^2 M_0^2 d_{zz,xy}^{(1,\mathrm{M})} \tag{2.29}$$

or a Bloch-type DB with $\mathbf{n} \parallel z$, and

$$\varphi_1 - \varphi_2 = 4\pi^2 M_0^2 \begin{cases} d_{xx,\,yy}^{(1,\,M)}, & \mathbf{n} \parallel x, \\ d_{yy,\,xy}^{(1,\,M)}, & \mathbf{n} \parallel y, \end{cases} \tag{2.30}$$

for a Néel-type DB. Expressions similar to (2.27), (2.29), and (2.30) are also valid for DB's in AFM's belonging to these classes. $TiCr_2Se_4$, $TiCr_2Te_4$, and Cr_3Te_4 are examples of magnetics belonging to the class $\mathbf{C}_{2h}$ [2.24].

As mentioned above, interdomain potential difference does not appear when a DB has a centre. If an external field (magnetic, electric, mechanical, etc.) is applied to a crystal so that all the $g^{(2)}$ operations are eliminated, this results in a potential difference. It is not difficult to indicate the required type of external field in each particular case if the symmetry group of a DB is known. For example, such a field may be an external magnetic field **H** whose direction is different for different symmetry classes of a DB. For highly symmetric rotational DB's, the direction of this field can be determined by using Table 2.4. For other directions of the external field, uncompensated electric charges q_τ may also appear on the surface of the sample. These directions are also given in Table 2.4.

Table 2.4.

k	m	(0, 0, 0)	$(H_{\tau_1}, 0, 0)$	$(0, H_{\tau_2}, 0)$	$(0, 0, H_n)$
7	1, 5	—	n	—	τ_1
	2, 6	—	—	n	τ_2
	3, 7	—	τ_2	τ_1	—
	4, 8	—	τ_1	τ_2	n
9	1, 7	τ_1	τ_1, n	τ_1	τ_1
	2, 8	τ_1	τ_1	τ_1, n	τ_1, τ_2
	3, 5	τ_1	τ_1, τ_2	τ_1	τ_1
	4, 6	τ_1	τ_1	τ_1, τ_2	τ_1, n
17	1, 8	τ_2	τ_2, τ_1	τ_2	τ_2, n
	2, 7	τ_2	τ_2	τ_2, τ_1	τ_2
	3, 6	τ_2	τ_2	τ_2, n	τ_2
	4, 5	τ_2	τ_2, n	τ_2	τ_2, τ_1

Remark: The table contains all nonzero components of the vector $\langle \mathbf{P} \rangle$, appearing in highly symmetric DB's upon switching on an external magnetic field **H**.

A comparison of Tables 2.3 and 2.4 shows that $\langle P_n \rangle$ (and hence the interdomain potential difference also) appears only when an ex-

ternal magnetic field is applied along the magnetization of the domains. For this reason, in order to observe the effect, the DB's must be fixed.

To conclude this section, note that the interdomain potential difference must exist in all cases when the symmetry of a DB do not contain operations $g^{(2)}$ which make the domains exchange places. This statement is valid for any type of the domain structure (and not only for 180° DB's considered in this section). In particular, it will be valid for DB's separating different phases of a magnetic and appearing during a first-order phase transitions.

2.6. CONCLUSION

In this paper, we have considered some aspects of the emergence of a volume charge density in the magnetic inhomogeneity region of magnetically ordered crystals. In particular, we have carried out a detailed investigation of the electric polarization of 180° DB's in ferromagnetics and antiferromagnetics.

At present, there is probably only one experimental verification of the inhomogeneous magnetoelectric effect. Newnham *et al.* [2.25] observed that electric polarization takes place upon magnetic ordering of the rhombic antiferromagnetic Cr_2BeO_4 whose principal state has a helical magnetic structure. In this case, the polarization **P** may be caused by the exchange relativistic terms in the expansion (2.20). It should be noted that the electric polarization must appear in almost all helical structures, since the general phenomenological theory developed in the first section of this article is applicable, in particular, to this type of inhomogeneities as well.

Besides the electric polarization appearing in magnetics with inhomogeneities, the opposite effect, viz. the appearance of magnetic inhomogeneities when an electric field is applied, is also possible. Vitebskii [2.26, 27] was the first to predict this effect. In his works, he obtained general symmetry criteria for a thresholdless (with respect to the magnitude of the electric field) induction of long-periodic magnetic structures. The possibility of a threshold induction of long-period magnetic structures in rhombic and rhombohedral AFM's was predicted in [2.28].

We briefly list certain problems which, in our opinion, require further investigation.

(a) The electric polarization of domain boundaries other than 180° DB's.

(b) The electric polarization of crystalline solids, which is initiated by nonmagnetic inhomogeneities.

(c) The reverse effect of nonuniform electric polarization on the properties of magnetic subsystem of a magnetic (both static and dynamic).

(d) The effect of an external electric field on the statics and dynamics of the domain structure of magnetics.

(e) The effect of the domain boundaries on the electronic properties of semiconductors and metals.

(f) Phase transitions in magnetics, associated with a change in the magnetic symmetry class of a DB upon a change in thermodynamic parameters. The possibility of such phase transitions arises, generally speaking, due to the existence of several symmetry classes in a DB for the same symmetry class of the homogeneous phase.

APPENDIX

While studying the nonuniform electric polarization of antiferromagnetics it was assumed that the magnetic symmetry of a crystal can be completely characterized by specifying the magnitude, direction, and transformational properties of two vectors, the antiferromagnetism vector **L** and the magnetic moment **M**. We shall now discuss the limits of applicability of such a model.

Any operation g from the Fedorov symmetry group **G** of the paramagnetic phase of a crystal corresponds to a certain rearrangement $\mathcal{T}_g$ of crystallographically equivalent magnetic atoms, and a rotation U_g of the magnetic moments of all the atoms by the same angle. The set of operations $\mathcal{T}_g$ forms a group $\mathcal{T}$ of rearrangement of magnetic atoms. Since each nonunitary operation in **G** has a certain (always nonunitary) rearrangement of magnetic atoms corresponding to it, the group **G** is isomorphic to the group $\mathcal{T}$. Hence, the matrices of irreducible representations of these groups are equivalent. The basic functions of the irreducible representations of the group $\mathcal{T}$ are certain linear combinations of the magnetic moment vectors of the atoms [2.29], which are equivalent to spin densities first introduced in [2.30]. One of these combinations, which is transformed according to unitary representation of the group $\mathcal{T}$, is the ferromagnetism vector **M** of the crystal. If magnetic atoms in a crystal occupy several systems of equivalent positions, we must introduce the vectors $\mathbf{M}_n$ for each of these systems. The remaining vectors which are transformed according to nonunitary respresentations of the group $\mathcal{T}$ are antiferromagnetism vectors $\mathbf{L}_{in}^{(\mu)}$, where μ is the number of an irreducible representation, i is the number of the row of an irreducible representation, and the index n takes into account the possible repetition of irreducible representations in the overal rearrangement representation.

In the exchange approximation, these quantities determine the type of magnetic ordering [2.29]. In particular, the transition from paramagnetic to antiferromagnetic state is characterized by the appearance of nonzero antiferromagnetism vectors $\mathbf{L}_{in}^{(\mu)}$. If the group **G** has nonunitary one-dimensional real irreducible representations, an

AFM ordering may take place in a given crystal for a certain relation between the exchange integrals. In the exchange approximation, this ordering is characterized by the only antiferromagnetism vector **L** which either reverses its direction or does not change at all under any rearrangements in $\mathcal{P}$. This means that the set of all crystallographically equivalent magnetic atoms of an antiferromagnetic can be divided into two equal subsets such that each operation from the rearrangement group either interchanges the atoms from the same subset, or interchanges completely different subsets. These subsets are effective magnetic sublattices of a crystal.

The AFM structures characterized by antiferromagnetism vectors which are transformed by multidimensional irreducible representations of rearrangement groups require a special consideration.

References

2.1. L. D. Landau and E. M. Lifshitz, *Electrodynamics of Continuous Media*, Pergamon Press, Oxford, 1965.
2.2. G. A. Smolenskii and I. E. Chupis, *Uspekhi Fiz. Nauk*, 137, 415 (1982).
2.3. I. E. Dzyaloshinskii, *Zh. Eksp. Teor. Fiz.*, 37, 881 (1959).
2.4. N. N. Neronova and N. V. Belov, *Dokl. Akad. Nauk SSSR*, 120, 556 (1959).
2.5. V. G. Baryakhtar, V. A. L'vov, and D. A. Yablonskii, *Pis'ma v Zh. Eksp. Teor. Fiz.*, 37, 12, 565 (1983).
2.6. P. G. de Gennas, *The Physics of Liquid Crystals*, Clarendon Press, Oxford, 1974.
2.7. E. A. Turov, *Physical Properties of Magnetically Ordered Crystals*, Izd. Akad. Nauk SSSR, Moscow, 1963 (in Russian).
2.8. Tôru Moria, *J. Appl. Phys.*, 39, 1042 (1968).
2.9. Alex Hubert. *Theorie der Domänenwände in Geordneten Medien.* Springer Verlag, Berlin, Heidelberg, New York, 1974.
2.10. M. M. Farztdinov, *Uspekhi Fiz. Nauk*, 84, 611 (1964).
2.11. V. G. Baryakhtar, A. E. Borovik, and V. A. Popov, *Pis'ma v Zh. Eksp. Teor. Fiz.*, 9, 634 (1969), *Zh. Eksp. Teor. Fiz.*, 62, 2233 (1972).
2.12. K. L. Dudko, V. V. Eremenko, and V. M. Fridman, *Zh. Eksp. Teor. Fiz.*, 61, 678, 1553 (1971).
A. A. Mil'ner, Yu. A. Popkov, and V. V. Eremenko, *Zh. Eksp. Teor. Fiz.*, 18, 39 (1973).
2.13. A. A. Galkin and S. N. Kovner, *Pis'ma v Zh. Eksp. Teor. Fiz.*, 9, 456 (1969).
2.14. A. I. Mitsek, N. R. Kolmykova, and P. F. Gaydanskii, *Fiz. Tverd. Tela*, 11, 1258 (1969).
2.15. A. R. King and D. Paquette, *Phys. Rev. Lett.*, 30, 662 (1973).
2.16. I. M. Vitebskii and D. A. Yablonskii, *Fiz. Tverd. Tela*, 19, 3388 (1977).
2.17. V. G. Baryakhtar, B. N. Razsukovannyi, and E. P. Stefanovskii, *Fiz. Met. i Metalloved.*, 36, 456 (1973).
2.18. A. H. Bobeck and E. Della-Torre, *Magnetic Bubbles*, North-Holland Publishing Co., Amsterdam, 1975.
2.19. V. K. Raev and G. E. Khodenkov, *Cylindrical Magnetic Domains in Computer Units*, Energoizdat, Moscow, 1981 (in Russian).
2.20. L. N. Bulaevskii and V. L. Ginzburg, *Pis'ma v Zh. Eksp. Teor. Fiz.*, 11, 404 (1970).
2.21. M. M. Farztdinov, S. D. Mal'ginova, and A. A. Khalfina, *Izv. Akad. Nauk SSSR*, Ser. Fiz., 34, 1104 (1979).

2.22. K. P. Belov and A. M. Kadomtseva, *Uspekhi Fiz. Nauk*, **103**, 577 (1971).
2.23. V. A. L'vov and D. A. Yablonskii, *Fizika Nizkikh Temperatur*, **8**, 951 (1982).
2.24. A. Oles, F. Kajzar, M. Kucab, and W. Sicora, *Magnetic Structures Determined by Neutron Diffraction*, Panstwowe Wydawnictwo Naucowe, Warsaw, 1976.
2.25. R. E. Newnham, J. J. Kramer, W. A. Shulze, and L. E. Cross, *J. Appl. Phys.*, **49**, 6088 (1978).
2.26. I. M. Vitebskii, *Fiz. Met. i Metalloved*, **55**, 468 (1983).
2.27. I. M. Vitebskii, *Zh. Eksp. Teor. Fiz.*, **82**, 577 (1982).
2.28. V. G. Baryakhtar and D. A. Yablonskii, *Fiz. Tverd. Tela*, **24**, 2522 (1982).
2.29. D. A. Yablonskii, *Zh. Eksp. Teor. Fiz.*, **77**, 365 (1979).
2.30. I. E. Dzyaloshinskii, *Zh. Eksp. Teor. Fiz.*, **32**, 1547 (1957).

3 Ferroelectromagnetics

G. A. Smolenskii and I. E. Chupis

3.1. INTRODUCTION

The interaction between various subsystems in a crystal formed an important branch of contemporary solid-state physics. The investigation of electron-phonon, magnon-phonon, magnon-electron, and other interactions, as well as their influence on static and dynamic phenomena in a crystal, have led to the discovery of several new effects. Ferroelectromagnetics, which form a new class of materials recently discovered, are of considerable scientific interest. These are compounds in which magnetic and ferroelectric (or antiferroelectric) ordering exists simultaneously. The interaction of these ordered subsystems, hereinafter called the magnetoelectric (ME) interaction, introduces a number of peculiarities in ferroelectric and magnetic phase transitions, the spectrum of elementary excitations, and the response of a system to electric and magnetic fields. Besides, the ME interaction is responsible for many new interesting effects.

The discovery of ferroelectromagnetic compounds was preceded by an intensive and fruitful development of the physics of magnetic phenomena and ferroelectricity. The search for new ferroelectrics led to the discovery of such materials with a perovskite structure and a significant iron ion concentration by a group of Leningrad physicists in 1958 [3.1, 2]. This raised the hopes that compounds with perovskite structure could simultaneously be ferroelectrics and ferro(antiferro)magnetics [3.3]. The possibility of the coexistence of spontaneous magnetic moments and polarization does not contradict the general criteria for the emergence of ferromagnetism and ferroelectricity. The magnetic ordering is determined by the exchange interaction between electron spins, while ferroelectricity is due to redistribution of charge density in the lattice. In perovskite-type compounds ABO_3 (see Fig. 3.1), the angles in the (cation B)-oxygen-(cation B) chains are close to 180°. Hence, the transition element ions occupying octahedral B-positions can become ordered due to an indirect exchange interaction involving oxygen ions. According to the model theories put forth in those years, the ferroelectric (FE) ordering in perovskite lattice appears mainly due to the displacements of A and B ions. The ordering is facilitated

by the presence of X ions with stereochemically active unshared pair of 6*s*-electrons (Pb^{2+}, Bi^{3+}, Tl^{+}) in the A sublattice, and the transition metal ions (Ti^{4+}, Zr^{4+}, Nb^{5+}, Ta^{5+}, W^{6+}, Mo^{6+}) in the B-sublattice, which have a noble gas shell after the removal of *s*- and *d*-electrons [3.4]. These ions, however, do not have a magnetic moment. In order to satisfy the necessary conditions for the emergence of ferroelectricity and magnetism, ferroelectrically active ions as well as magnetic ions were introduced into the octahedral positions. This led in 1961 to the synthesis of the first ferroelectromagnetic

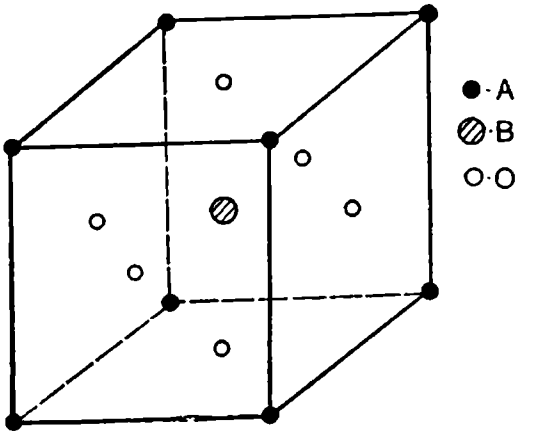

Fig. 3.1. The ideal unit cell of perovskite ABO_3. The B ion is at the centre of the cube, while the oxygen ions are at the centres of the faces.

$Pb(Fe_{2/3}W_{1/3})O_3$ combining ferroelectric and antiferromagnetic properties, as well as the first ferroelectromagnetic solid solutions $(1-x)\,Pb(Fe_{2/3}W_{1/3})O_3 - xPb(Mg_{1/2}W_{1/2})O_3$ (the ions in parentheses occupy octahedral positions) [3.5]. The first measurements of ferroelectromagnetic properties were taken on polycrystalline samples. Later, single crystals of $Pb(Fe_{2/3}W_{1/3})O_3$ and $Pb(Fe_{1/2}Nb_{1/2})O_3$ were used for this purpose [3.6]. In $BiFeO_3$, which was also one of the first ferroelectromagnets, ferroelectric ordering [3.7, 4] and antiferromagnetic ordering [3.8, 9] were observed. About fifty ferroelectromagnetic compounds and dozens of solid solutions combining ferro(antiferro)electric properties with ferro-, ferri-, and antiferromagnetic properties are known at present. A large number of ferroelectromagnets, and especially solid solutions, were synthesized by Moscow physicists [3.10]. The first ferroelectromagnetic crystals were synthesized in the Soviet Union and the theory of these materials was also developed here. It is not surprising, therefore, that the largest number of publications in this field also comes from the USSR. Swiss, French, and Japanese scientists have also made a significant contribution to the synthesis and investigation of ferroelectromagnetics.

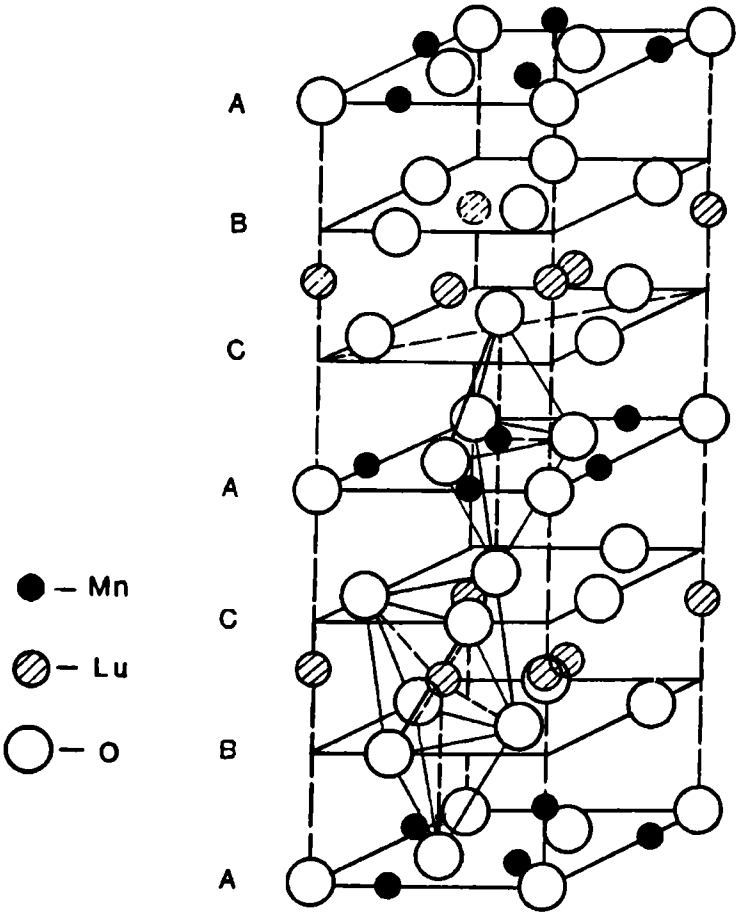

Fig. 3.2. Structure of the hexagonal manganite $LuMnO_3$.

With the exception of three natural crystals (congolite $Fe_3B_7O_{13}Cl$, chambersite $Mn_3B_7O_{13}Cl$, and magnetite Fe_3O_4) [3.11], all ferroelectromagnetic compounds are synthesized. Depending on their structural properties, ferroelectromagnetics can be divided into several basic classes.

1. Compounds with perovskite-type structure $A(B_I, B_{II}, \ldots \ldots)O_3$ (Fig. 3.1) containing magnetic ions which fully (e.g., $BiFeO_3$) or partially occupy the octahedral B-positions (Table 3.1, Nos. 1-15).

2. Hexagonal rare-earth manganites with the general formula $RMnO_3$ (R — Y, Ho, Er, Tm, Yb, Lu, or Sc) discovered by Bertaut *et al.* [3.12]. These compounds are ferroelectrics with antiferromagnetic or weak ferromagnetic properties. Their crystal structure is shown in Fig. 3.2. The trigonal bipiramids, which are connected by their vertices, form layers perpendicular to the six-fold axis. The Mn atoms lie inside the bipiramids, and the rare-earth atoms occupy positions between the bipiramid layers.

Table 3.1. Ferroelectromagnetics

No.	Compound	Type of electric ordering	Type of magnetic ordering	θ_E, K	θ_M, K	Magnetoelectric measurements
1	$Pb(Fe_{2/3}W_{1/3})O_3$	FE	AFM	178	363	Change in the internal magnetic field upon FE transition
2	$Pb(Fe_{1/2}Nb_{1/2})O_3$	FE	AFM	387	143, 155	$M_S(\tilde{E})$
3	$BiFeO_3$	AFE? FE	AFM	1123 ?	≈ 650	$\varepsilon(\theta_M)$, induction of P by spin-flop
4	$Eu_{1/2}Ba_{1/2}TiO_3$	FE	FM	165	4.2	
5	$Pb(Mn_{2/3}W_{1/3})O_3$	AFE?	AFM	473		$\varepsilon(\theta_M)$
6	$Pb(Mn_{1/2}Re_{1/2})O_3$	AFE?	FIM	393	103	
7	$Pb(Mn_{1/2}W_{1/2})O_3$	AFE?	AFM	423	100	
8	$Pb(Fe_{1/2}Ta_{1/2})O_3$	FE	AFM	233	≈ 170	
9	$Pb(Co_{1/2}Re_{1/2})O_3$	AFE?	FIM	403	< 77	
10	$Pb(Ni_{1/2}Re_{1/2})O_3$	AFE?	FIM	343	< 77	
11	$Pb(Co_{1/2}W_{1/2})O_3$	AFE FE	AWFM	305	9	
12	$BiMnO_3$	AFE?	FM	773	103, 110	
13	$Cd(Fe_{1/2}Nb_{1/2})O_3$	AFE?	AFM	753	48	
14	$Bi_6Fe_2Ti_3O_{18}$	FE	FM?	θ_{EI}=1171 θ_{EII}=1025	723?	χ^{ME}?
15	$Bi_9Ti_3Fe_5O_{27}$	FE	AWFM	1103, 1073	363, 403	Induction of electrical signal by the magnetic field
16	$YMnO_3$	FE	AFM	913, 933	≈ 80	
17	$YbMnO_3$	FE	AFM AWFM	983, 993	87,3 3,8	
18	$HoMnO_3$	FE	AFM AWFM	873	76 5	
19	$ErMnO_3$	FE	AFM	833	79	
20	$TmMnO_3$	FE	AFM	> 573	86	
21	$LuMnO_3$	FE	AFM		91	
22	$ScMnO_3$	FE	AFM		120	
23	$Cr_3B_7O_{13}Cl$	FE	AFM	≈ 260	25	
24	$Cr_3B_7O_{13}Br$	FE	AFM	4	50	
25	$Cr_3B_7O_{13}J$	FE	AFM	4	95	
26	$Mn_3B_7O_{13}Cl$	FE	AFM	680	≈ 6	
27	$Mn_3B_7O_{13}Br$	FE	AFM	566	6	

Continued

No.	Compound	Type of electric ordering	Type of magnetic ordering	θ_E, K	θ_M, K	Magnetoelectric measurements
28	$Mn_3B_7O_{13}J$	FE	AWFM	412	26	$m(\widetilde{E})$
29	$Fe_3B_7O_{13}Cl$	FE	AWFM	≈ 609	≈ 11	$m(\widetilde{E})$
30	$Fe_3B_7O_{13}Br$	FE	AWFM	≈ 495	≈ 17	$m(\widetilde{E})$
31	$Fe_3B_7O_{13}J$	FE	AWFM	349	≈ 30	
32	$Co_3B_7O_{13}Cl$	FE	AWFM	623	11, 5, 15 22	χ^{ME}, $m(\widetilde{E})$
33	$Co_3B_7O_{13}Br$	FE	AWFM	458	20	
34	$Co_3B_7O_{13}J$	FE	AWFM	≈ 197	38	$m(\widetilde{E})$, $\varepsilon(\theta_M)$
35	$Cu_3B_7O_{13}Cl$	FE	AFM AWFM	365	20 8, 4	χ^{ME}
36	$Cu_3B_7O_{13}Br$	FE	AWFM	226	24	$\varepsilon(\theta_M)$
37	$Ni_3B_7O_{13}Cl$	FE	AFM AWFM	610	25 9	χ^{ME}
38	$Ni_3B_7O_{13}Br$	FE	AWFM	398	30, 40	$m(\widetilde{E})$
39	$Ni_3B_7O_{13}J$	FE	AWFM	64	64	χ^{ME}, ε (H), P (H), m (E)
40	$BaNiF_4$	FE	AFM	1593	70	Pyroelectric signal anomaly at $T=\theta_M$
41	$BaMnF_4$	PE	AWFM		25	$\varepsilon(\theta_M)$
42	$BaCoF_4$	FE	AFM	1153	≈ 70	
43	$BaFeF_4$	PE	AFM		≈ 54	
44	$Li(Fe_{1/2}Ta_{1/2})O_2F$	PE	AFM	853	883	Induction of electric current by magnetic field
45	Cr_2BeO_4	PE	AFM	28	28	
46	$PbMn_2O_4$	FE?	AWFM		63?	$m(\widetilde{E})$
47	$Cu(HCOO)_2 \cdot 4H_2O$	AFE?	AWFM	≈ 235	17	
48	β-$Tb_2(MoO_4)_3$	FE	AFM		2	
49	β-$Gd_2(MoO_4)_3$	FE	AFM	432	0.3	
50	β-$NaFeO_2$	FE	AWFM	723	723	
51	Fe_3O_4	FE	FIM		858	χ^{ME}

Remarks: The data with a question mark are unconfirmed.
Notation: FE — ferroelectric; AFE — antiferroelectric; PE — pyroelectric; FM — ferromagnetic; AFM — antiferromagnetic; AWFM — antiferromagnetic with weak ferromagnetism; FIM — ferrimagnetic; χ^{ME} — statistical ME susceptibility; M_s — spontaneous magnetization; $\widetilde{E}$ — amplitude of the alternating electric field; ε — permittivity.

3. Boracites, viz. the compounds having the general formula $M_3B_7O_{13}X$, where M is a bivalent metal ion (M = Cr, Mn, Co, Fe, Cu, or Ni and X = Cl, Br, or I). These compounds are ferroelectric-antiferromagnetics (some of them are weak ferromagnetics). The first ferroelectromagnetic boracites were synthesized and subsequently investigated extensively by Swiss physicists. In the high-temperature phase, all boracites have the cubic symmetry $\bar{4}3m$. A decrease in temperature results in phase transitions in the sequence $\bar{4}3m \rightarrow mm2 \rightarrow m \rightarrow 3m$. The $3m$- and/or m-phases do not appear in some compounds. The transition to the $mm2$ orthorhombic phase in all boracites (with the exception of Ni-I) is accompanied by the appearance of FE properties. The magnetic ordering in boracites takes place at temperatures considerably below the room temperature. In the Ni-I boracite, the temperatures of FE and magnetic transitions coincide, and an improper FE transition takes place [3.13].

4. The $BaMF_4$ (M = Mn, Fe, Co or Ni) with an orthorhombic crystal structure in the high-temperature phase. These compounds are pyro- or ferroelectrics with antiferromagnetic or weak ferromagnetic properties, appearing at sufficiently low temperatures. Some of them may exhibit antiferroelectric properties [3.14].

In addition to the compounds listed above, ferroelectromagnetics with other structures are also known to exist. The ferroelectric ferrite Fe_3O_4 with an inverted spinel structure and the oxide ferroelectric-antiferromagnetic $Li(Fe_{1/2}\ Ta_{1/2})O_2F$ with a pseudoilmenite structure are examples of such compounds [3.15]. Antiferromagnetic helical-type ordering appears in the triclinic Cr_2BeO_4 below 28 K. Apparently, this is accompanied by the emergence of FE properties [3.16].

Table 3.1 contains a list of the ferroelectromagnetic compounds known at present and indicates the temperatures of electric (θ_E) and magnetic (θ_M) transitions. A detailed bibliography on the crystal structure, the history of the discovery of ferroelectromagnetic properties, and some physical properties of the listed compounds can be found in the earlier reviews [3.10, 17-20]. The classification presented in this table characterizes the ferroelectric and magnetic properties of the materials. However, it must be borne in mind that a transition to the FE state is nothing but a special case of the transitions occurring as a result of lowering the crystal lattice symmetry. Such transitions may be accompanied, for example, by a transition to the ferroelastic state, viz. the emergence of a spontaneous deformation due to mechanical stresses [3.21]. The magnetic, ferroelectric and ferroelastic ordering can take place simultaneously, for example, in boracites, $BaMF_4$, and in rare-earth molybdates β-$Tb_2(MoO_4)_3$ and β-$Gd_2(MoO_4)_3$ [3.22].

In this review, we shall confine ourselves to an analysis of magnetic and ferroelectric properties of spontaneously polarized dielectric crystals only, paying special attention to the ME interaction.

3.2. THE NATURE OF MAGNETOELECTRIC INTERACTIONS

Landau and Lifshitz indicated the possibility of the existence of an equilibrium electric polarization in magnetically ordered crystals, proportional to the magnetic field strength, as well as an equilibrium magnetization proportional to the electric field strength (the linear ME effect) [3.23]. The linear ME effect was studied by Dzyaloshinskii [3.24] from the point of view of magnetic symmetry. Magnetically ordered crystals showing a linear ME effect are commonly called magnetoelectrics. A large number of articles has been devoted to the investigation of linear (and in the recent years, nonlinear) ME effects in magnetoelectrics. Nonlinear ME effects can occur in any materials, even if they are not magnetically ordered. A ferroelectromagnetic differs from other materials in that besides the ME effects induced by external fields, it also exhibits spontaneous ME effects due to strong electric and magnetic internal fields. This may give rise to qualitatively new ME effects which do not have an analogue in other crystals. Interesting ME effects can also be expected in ferroelectromagnetics in external fields. Ferroelectromagnetics have an important advantage over magnetoelectrics and other crystals in that the ME effects in these materials are the strongest (see below).

The ME effects in ferroelectromagnetics take place due to the interaction of the spin- and FE subsystems of the crystal. In order to characterize the ME interactions, it is convenient to divide them into two parts, viz. the magnetoisotropic (exchange) and the anisotropic parts.

The exchange magnetoisotropic ME energy describes the change in the exchange interaction due to an electric polarization, as well as the effect of the spin-exchange field on the magnitude of the crystal polarization. As a rule, the unit cell of a ferroelectromagnetic is quite complicated. The magnetic cations are separated by nonmagnetic ions, and the exchange interaction is indirect. During an FE transition, the lattice ions are displaced, thus changing the equilibrium distance between the magnetic ions and hence the exchange integral. Besides, the change in the electric field due to the Stark effect upon an FE transition in the crystal perturbes the wave functions of the magnetic electrons as well as the electrons of the intermediate atoms participating in the indirect exchange. Consequently, the overlapping of the electron wave functions changes, thus changing the value of the transport integral of magnetic electrons, as

well as the strength of the indirect exchange interaction. Conversely, the change in the polarization due to magnetic ordering can be considered as a result of the Zeeman splitting of levels due to the exchange field. In turn, this splitting accompanied by the displacement of ions as a result of the electron-phonon interaction.

The anisotropic ME energy characterizes the change in the energy of magnetic anisotropy due to the electric polarization and the effect of the anisotropic magnetic spin field on the magnitude of the polarization. As a result of the FE ordering, the internal electric field causes a Stark splitting of the electron levels of the magnetic ions, changing the spin-orbit and spin-spin interactions, and hence the energy of magnetic anisotropy as well. On the other hand, the magnetic anisotropy field changes the electron states of ions due to the Zeeman effect. Consequently, the electric dipole moment also changes. Besides, electromagnetic elastic interaction can also serve as a source of the ME energy. The existence of an elastic subsystem in the crystal leads to the emergence of electrostriction which accompanies the FE ordering and changes the crystal size. This, in turn, changes the magnetic state due to magnetostrictive interaction, and vice versa.

These mechanisms of ME interactions in a ferroelectromagnetic correspond to the free energy density which can be represented as a power series in the projections of the electric moment $\mathbf{P}$ (r) and the magnetic moment $\mathbf{M}_s$ (r) (s is the number of the magnetic sublattice):

$$\mathbf{F}_{\mathrm{ME}} = -\left(\Gamma^{j}_{ss'} P^{j} + \frac{1}{2}\gamma^{jj'}_{ss'} P^{j} P^{j'}\right) \mathbf{M}_s \cdot \mathbf{M}_{s'} - \left(\Lambda^{jll'}_{ss'} P^{j} + \frac{1}{2}\lambda^{jj'll'}_{ss'} P^{j} P^{j'}\right) M^{l}_{s} M^{l'}_{s'} + \ldots \quad (3.1)$$

In this formula, j, j', l, l' are the indices of the projections. The terms containing odd powers of polarization can exist only in ferroelectromagnetics with a paraelectric phase without a central symmetry. The energy of the exchange ME interaction in such crystals (the first term in (3.1) with the coefficient Γ) has been obtained in [3.25]. The calculations of the exchange ME energy resulting from the interaction of spins with optical phonons [3.26, 27] give the value $\gamma \simeq 10^{-7}$ dyne^{-1} cm^2 for the parameter of the exchange ME interaction. For $P^2 \simeq 10^9$ CGS units and $M^2 \simeq 10^5 \mathrm{Gs}^2$, the exchange ME energy is equal to $F^{\mathrm{ex}}_{\mathrm{ME}} \simeq 10^7$ erg·cm^{-3}. The contribution of electromagnetic elastic interaction to the ME energy [3.28] can be estimated by putting $F^{\mathrm{el}}_{\mathrm{ME}} \sim c u_{\mathrm{E}} u_{\mathrm{M}}$, where c is the elastic constant, u_{E} the electrostriction, and u_{M} the magnetostriction. Assuming $c \simeq 10^{12}$ erg·cm^{-3}, $u_{\mathrm{E}} \simeq 10^{-3}$-$10^{-2}$, and $u_{\mathrm{M}} \simeq 10^{-5}$-$10^{-4}$, we get $F^{\mathrm{el}}_{\mathrm{ME}} \simeq 10^4$-$10^6$ erg·cm^{-3}. This quantity may assume values of the order of 10^7 erg·cm^{-3} for compounds with rare-earth ions, where

magnetostriction may attain the values $u_M \simeq 10^{-3}$. In other words, the electromagnetic elastic energy may play a significant role in materials with large values of electrostriction and magnetostriction.

The exchange ME interaction is electrostatic in nature, while the anisotropic ME energy (the last two terms in (3.1)) appears only if we take into account the spin-orbit and magnetic dipole couplings. Hence, in crystals where the exchange energy prevails over the magnetic anisotropy energy, the exchange ME energy considerably exceeds the anisotropic ME energy.

3.3. THERMODYNAMIC THEORY

The theoretical investigations of the equilibrium properties of ferroelectromagnetics have been carried out within the framework of the Landau theory of second-order phase transitions by using the expansion of the free energy in powers of the FE and magnetic moments. The presence of any invariants in the expression for the free energy is determined by the symmetry group of the paraphase (i.e. the phase with $\mathbf{P} = 0$ and $\mathbf{M}_s = 0$). The classes and special groups allowing for ferroelectromagnetic structures with different mutual orientations of **P** and **M** are given in [3.29-32]. The cases when the crystal symmetry permits exchange ME invariants which are linear in polarization are indicated in [3.33].

In addition to the magnetic and dielectric susceptibilities, the concept of magnetoelectric susceptibility is frequently employed in ferroelectromagnetics. This quantity characterizes the change in the magnetization under the action of an electric field, as well as the change in the polarization under the action of a magnetic field. The response of the system to the action of an external electric field **E** and a magnetic field **H** is described by the generalized susceptibility tensor

$$\hat{\chi} = \begin{pmatrix} \hat{\chi}^{E} & \hat{\chi}^{EM} \\ \hat{\chi}^{ME} & \hat{\chi}^{M} \end{pmatrix},$$

where $(\hat{\chi}^{E})_{ik} = \chi^{E}_{ik}$, χ^{M}_{ik} and $\chi^{EM}_{ik} = \chi^{ME}_{ki}$ are the second-rank tensors of dielectric, magnetic, and magnetoelectric susceptibilities respectively:

$$\chi^{E}_{ik} = \frac{\partial P_i}{\partial E_k}, \quad \chi^{EM}_{ik} = \frac{\partial P_i}{\partial H_k}, \qquad \chi^{ME}_{ik} = \frac{\partial M_i}{\partial E_k}, \quad \chi^{M}_{ik} = \frac{\partial M_i}{\partial H_k} \quad (i, k = 1, 2, 3). \tag{3.2}$$

The components of the generalized susceptibility tensor can be expressed in terms of the derivatives of the thermodynamic potential $\Phi = \Phi(\mathbf{P}, \mathbf{M}_s)$ with respect to the components of FE and magnetic

moments [3.34]. From the condition that Φ (**P**, **M**) have its minimum value in the simplest isotropic case, we get the inequality

$$(\chi^{ME})^2 < \chi^E \chi^M \tag{3.3}$$

which determines the upper bound for the absolute magnitude of the ME susceptibility. It can be seen from this inequality that the largest value of the ME susceptibility, and hence of ME effects, should be expected in crystals having large values of χ^E and χ^M, i.e. in ferroelectric ferro(ferri)magnetics [3.35].

3.3.1. Thermal Phase Transitions

Generally speaking, a ferroelectromagnetic possesses two transition temperatures: the ferroelectric transition temperature θ_E and the magnetic transition temperature θ_M. If the FE transition is improper and induced by the magnetic transition, these two temperatures coincided. In this case, the ME interaction energy contains terms that are even in magnetic moments and odd in the components of a polarization vector. This means that **P** may become of the order of $\mathbf{M}^2$ at a temperature below θ_M (improper FE transition). Such a transition takes place in nickel-iodine boracite. In particular, an improper FE transition can take place during a helical-type magnetic ordering, if the ME energy contains terms of the type $P_i M_s^l (\partial M_{s'}^{l'}/\partial x_k)$. Probably, such a transition takes place in the ferroelectric-antiferromagnetic Cr_2BeO_4 which has a helical magnetic structure and a centrally-symmetric D_{2h}^{16} paraphase [3.16].

If the ME energy does not contain invariants which are linear in **P**, the FE and magnetic transition temperatures may coincide for a sufficiently large value of the ME interaction. In this case, a first-order phase transition takes place [3.36].

The following results were obtained from investigations of second-order thermal phase transitions in a ferroelectromagnetic [3.28, 34, 37]: (1) the "twinning law" is satisfied for $T - \theta_E < \theta_M$, just as in the case of an ordinary FE transition; (2) the temperature dependence of the magnetic (FE) susceptibility shows a break at the temperature of the FE (magnetic) transition; and (3) the magnetic (FE) susceptibility undergoes a jump at the temperature of the FE (magnetic) transition. The last effect is analogous, for example, to the jumps in the heat capacity and the elastic moduli during second-order phase transitions.

The break in the temperature dependence of susceptibility is a first-order effect in the ME interaction, while the jump in the susceptibility is a second-order effect. Owing to a break in the temperature dependence $\chi^M(T)$ at $T = \theta_E$, the magnetic susceptibility below θ_E will differ from the values obtained by extrapolation of

the temperature dependence $\chi^{M}(T)$ from the paraelectric phase to the region $T < \theta_E$. This difference, which we shall denote by $\Delta\chi^{M}(\Gamma)$, will increase in its absolute magnitude with decreasing temperature in direct proportion to the square of the spontaneous polarization, if the temperatures θ_E and θ_M are widely separated, so that the dependence of the magnetic parameters on temperatures near θ_E can be neglected:

$$\Delta\chi^{M} \propto P^2\ (T) \quad (T \leqslant \theta_E).$$

Similarly, the change in the dielectric permittivity $\Delta\varepsilon = 4\pi\Lambda\,\chi^{E}$ at $T \leqslant \theta_M < \theta_E$ will be proportional to the square of the magnetic order parameter M:

$$\Delta\varepsilon \propto M^2\ (T) \quad (T \leqslant \theta_M).$$

The sign of $\Delta\chi^{M}$ ($\Delta\varepsilon$) depends on the sign of the ME interaction constant and can be either positive or negative.

As mentioned above, the appearance of $\Delta\chi^{M}$ ($\Delta\varepsilon$) below θ_E, (θ_M) is a first-order effect with respect to the ME interaction. Hence, we should primarily expect an experimental confirmation of this effect rather than the weaker susceptibility jump which is of the second order with respect to the interaction. Indeed, the ferroelectromagnetics show a break rather than a jump in the dielectric permittivity at the magnetic transition temperature (see Sec. 3.5). Investigations of the temperature dependence of $\Delta\chi^{M}(\Delta\varepsilon)$ at $T \leqslant \theta_E(\theta_M)$ can give information about the critical index of the emergent order parameter.

An analysis of the temperature dependence of the ME susceptibility near the temperatures of the second order phase transitions within the framework of the Landau theory shows that for $\theta_E < \theta_M$, $\chi^{ME} \propto (\theta_E - T)^{-1/2}$ in the vicinity of θ_E [3.34, 37]. For $\theta_M < \theta_E$ [3.38], we have

$$\chi^{ME} \propto (\theta_M - T)^{k-1},$$

where $k \geqslant 1\ 2$ is the exponent in the temperature dependence of the magnetization $\mathbf{m} = \sum_s \mathbf{M}_s$ (s is the number of the magnetic sublattice) and $m \propto (\theta_M - T)^{k}$. The exponent k is equal to 1/2 for a ferromagnetic transition or a transition to a weakly ferromagnetic phase whose magnetization is due to the second-order invariants in the thermodynamic potential. In this case, the ME susceptibility has an anomalously high value in the vicinity of the second phase-transition temperature θ_M: $\chi^{ME} \propto (\theta_M - T)^{-1/2}$. If however, the small ferromagnetic moment is due to fourth-order invariants, we have $k = 3/2$ and $\chi^{ME} \propto (\theta_M - T)^{1/2}$.

3.3.2. Phase Transitions in External Fields

One of the manifestations of the ME interaction is a shift in the magnetic transition temperature due to an electric field, and in the FE transition temperature due to a magnetic field. In ferroelectromagnetics with $\theta_M < \theta_E$, the shift $\Delta\theta_M$ in the magnetic transition temperature is proportional to the electric field strength [3.28], i.e. $\Delta\theta_M \propto E$, irrespective of the crystal symmetry. The shift in the temperature of the FE ordering in ferroelectromagnetics with $\theta_E < \theta_M$ is proportional to the magnetic field, i.e. $\Delta\theta_E \propto H$, if the crystal symmetry allows a linear ME effect (in other words, if the ferroelectromagnetic is simultaneously a magnetoelectric). In ferroelectromagnetics of any symmetry, the shift $\Delta\theta_E$ is proportional to the square of the magnetic field H. Thus, if we neglect the paraprocesses, the ME exchange interaction in a ferroelectric antiferromagnetic leads to the following change in the FE transition temperature in a magnetic field:

$$\Delta\theta_E = \theta_E - \theta_E^0 = \gamma H^2 C \pi^{-1} (2\Delta_0)^{-2}. \qquad (3.4)$$

Here, θ_E^0 is the FE transition temperature in the absence of a magnetic field, Δ_0 is the exchange constant, and C is the Curie-Weiss constant.

The ME interaction may change the order of a phase transition, or induce additional phase transitions in magnetic and FE subsystems due to a change in temperature or magnetic field [3.39-43]. We shall illustrate this by considering the simplest example of the phase diagrams of a uniaxial ferroelectric-ferromagnetic ($\mathbf{P}_0 \parallel \mathbf{M}_0$) in a magnetic field perpendicular to the spontaneous magnetic moment $\mathbf{M}_0$ (Fig. 3.3). In these diagrams, F denotes ferroelectric ordering, while FM denotes ferromagnetic ordering. The lower index shows the orientation of magnetization relative to the external magnetic field. The dash-and-dot lines indicate the phase boundaries with numbers from *1* to *4* denoting FM_{11}, FFM_{11}, FM, and FFM transitions respectively. The second-order phase transition lines H_{ik} between i-th and k-th phases are shown by solid lines, while dashed lines indicate the first-order phase transitions. For a weak ME interaction, $2\lambda^2 M_0^2 < \beta\delta$, $\lambda > 0$ ($\beta > 0$ is the magnetic anisotropy constant, and δ is the coefficient in the anharmonic term $\left(\frac{1}{4}\delta P^4\right)$ in the FE energy) the phase diagram is characterized by a tetra-critical point K for second-order transitions (Fig. 3.3*a*). In the absence of the ME interaction, the spin subsystem contains one line $H_{13} = H_\beta$ corresponding to a second-order transition to the state in which the magnetization is directed along the field. Correspondingly, the FE subsystem also contains one line indicating the second-order thermal phase transitions H_{12}. As the spontaneous polarization sets in, the

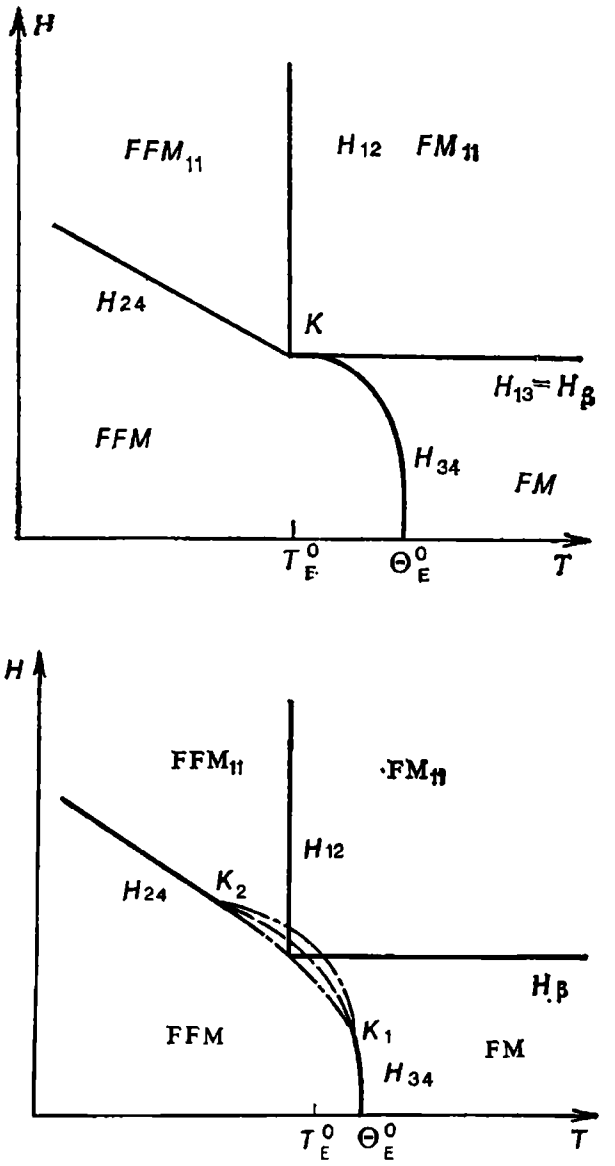

Fig. 3.3. Phase diagrams of an easy-axis ferroelectric-ferromagnetic for the case $\lambda > 0$: (a) $\beta\delta > 2\lambda^2 M_0^2$; (b) $\beta\delta < 2\lambda^2 M_0^2$.

ME interaction leads to a change in the slope of the line of the orientation magnetic transition ($H_\beta \to H_{24}$) as well as to a bending of the FE transition line ($H_{12} \to H_{34}$). Besides, additional second-order transitions with respect to temperature (curves H_{24} and H_{34}) and magnetic field (H_{34}) also take place. Thus, in a spin system the thermal transition H_{34} indicates a change in the direction of magnetization due to the FE ordering. With respect to the magnetic field, the same transition line H_{34} means that in the temperature interval

$[T_E^0, \theta_E^0]$, the reorientation of magnetization from an "easy axis" to the direction of the magnetic field takes place through two second-order phase transitions (instead of one transition in ordinary ferromagnetics with $P = 0$). The ME interaction caused a displacement of the FE transition temperature $T = T_E^0$ in fields weaker than the magnetic anisotropy field H_β, as well as to the possibility of a second-order FE transition with respect to the magnetic field (line $H_{34}(T)$). In the case of a strong ME interaction (Fig. 3.3*b*), the second-order transition line undergoes a discontinuity in the vicinity of the tetra-critical point, and two triple points K_1 and K_2 for phase transitions, as well as two triple-phase points appear. Consequently, the phase transition on the segment K_1-K_2 becomes a first-order transition. In particular, the thermal FE transition and the orientation of the magnetization along the magnetic field are first-order transitions in the vicinity of T_E^0.

The influence of the ME interaction is manifested most clearly during orientation transitions in ferroelectric-antiferromagnetics with $\theta_E \ll \theta_M$ [3.42, 43]. In this case, the second-order "spin-flip" transition from the antiferromagnetic to ferromagnetic states in a magnetic field is replaced by a first-order transition [3.43, 44]. As the temperature decreases to $T < \theta_E$, the spin-flop of magnetic sublattices, can be replaced by a metamagnetic-type transition between collinear antiferromagnetic and ferromagnetic states. Both spin-flop and metamagnetic transition are accompanied by a jump in the polarization. In other words, they induce a first-order transition between two FE phases. The possibility of an "easy magnetic axis—easy magnetic plane" transition upon the emergence of polarization in ferroelectric-antiferromagnetic due to a renormalization of the magnetic anisotropy constant by the ME interaction energy has also been indicated [3.45].

3.4. THEORY OF THE HIGH-FREQUENCY PROPERTIES OF FERROELECTROMAGNETICS

3.4.1. Spectrum of Elementary Excitations

At low temperatures ($T \ll \theta_M, \theta_E$), small oscillations of electric and magnetic moments relative to equilibrium positions propagate in the form of spin waves and polarization waves, which are found to be interrelated through the ME interaction. The quanta of these coupled oscillations are called ferroelectromagnons [3.46]. The ferroelectromagnon spectrum has been investigated to a greater extent than other properties of ferroelectromagnetics. Without going into the explicit expressions for the spectrum, we shall just present the basic results here.

The spin waves are coupled very weakly with the polarization waves in ferroelectric-ferromagnetics [3.46-48]. Here, the ME interaction takes place through the relativistic interactions, and the homogeneous ferromagnetic resonance frequency is much smaller than the optical frequency so that the non-interacting branches can intersect only in the vicinity of the Brillouin zone boundary.

In ferroelectromagnetics with two (or more) magnetic sublattices, the coupling between the spin waves and the polarization waves can be stronger than in a ferroelectric-ferromagnetic, since it is due to stronger ME exchange interaction [3.49-51]. The coupling of spin and polarization oscillations exists only in the case of a noncollinear orientation of spins in the ground state.

In uniaxial ferroelectric-antiferromagnetics without weak ferromagnetism, the noncollinear orientation of spins may be caused by an external electric field which controls the coupling of waves. If the magnetic field is directed along the easy axis or in the basis plane, the polarization waves are coupled only with the lower spin branch ω_{1s}, whose relative frequency variation due to the ME interaction is given by $(\Delta\omega_{1s}\ \omega_{1s}) \sim (H\ H_0)^2$, H_0 being the exchange field. Unlike a ferromagnetic, where $\Delta\omega_s$ is always much smaller than ω_s, $\Delta\omega_s$ in antiferromagnetic can be of the order of ω_s but only in very strong fields of the order of exchange fields. As a result of the ME interaction, the low-frequency branch is no longer of purely spin origin and an admixture of a few FE oscillations appears in it. An analysis [3.49] shows that the polarization amplitude in the lower branch of the spectrum may be of the order of magnetization amplitude even for magnetic fields that are considerably weaker than the exchange fields.

A ferroelectric-antiferromagnetic with a weak ferromagnetism is subjected to the Dzyaloshinskii relativistic ME interaction, for example, with energy in the form $\Lambda\,[\mathbf{M}_1 \times \mathbf{M}_2]\cdot\mathbf{P}$ [3.52] or $\lambda_i\,[\mathbf{M}_1 \times \mathbf{M}_2]_i P^2$. This interaction couples the polarization oscillations with the upper spin branch ω_{2s} even in the absence of a magnetic field [3.53]. A comparison of the Dzyaloshinskii ME energy with the exchange ME energy depending on the magnetic field shows that the Dzyaloshinskii ME interaction gives for $H < H' = \sqrt{\lambda'\gamma}\,H_s \sim \sim \sqrt{\beta'/\Delta_0}\,H_s \simeq 10^2$ Oe (H_s is the spin-flop field) the main contribution to the dynamic coupling of spin and polarization waves in ferroelectrics which are weak ferromagnetics. For stronger magnetic fields, the ME exchange interaction predominated. The fact that the ME exchange interaction and the Dzyaloshinskii ME interaction link the polarization oscillations with different branches of the spin spectrum can be employed for investigating these interactions separately.

The strongest coupling between the spin and polarization waves should be expected in ferroelectric-ferrimagnetics [3.50]. Here, the

polarization oscillations at a frequency ω_E are coupled by exchange interaction with the lower as well as upper branch ω_{2s} of the spin waves. The magnitude of this coupling is larger than in a ferroelectric-antiferromagnetic by a factor of $\Delta_0/\beta \simeq 10^2$. This strengthening of the coupling is due to the fact that the interacting branches become closer, and just like ω_E, ω_{2s} also lies in the IR region. This means that a resonant interaction between FE wave and the upper spin wave is possible, for example, when they approach one another upon a decrease in ω_E near the FE transition temperature. In ferroelectric-ferro(antiferro)magnetics, a resonant interaction between the frequencies ω_E and ω_s seems unlikely owing to their considerable separation.

In ferroelectric-antiferromagnetics with an "easy magnetic plane" anisotropy, the ME interaction may create a gap in the activationless spin branch [3.54, 55]. This effect is similar to the appearance of activation frequency in the magnetic spectrum of antiferromagnetics due to a magnetoelastic or ME interactions [3.56]. Unlike antiferromagnetics, for which the ME gap is proportional to the external electric field strength, the ferroelectric-antiferromagnetics have an ME gap even in the absence of an electric field. According to the estimates given in [3.54], the contribution from the ME interaction to the magnitude of the gap in a ferroelectric-antiferromagnetic may exceed the contribution from the magnetoelastic interaction by an order of magnitude or more.

The spin- and polarization waves in a ferroelectromagnetic interact not only with each other, but also with other elementary excitations in a crystal. Owing to the electro- and magnetoelastic interactions, a coupling arises between the ferroelectromagnons and acoustic phonons [3.57, 58]. The former also interact with electromagnetic waves due to electric and magnetic dipole interactions [3.57, 59].

The idea about the role of ME interactions in relaxation effects is of considerable importance for an experimental investigations of the spectrum and other high-frequency properties of ferroelectromagnetics. The available results of relaxation processes in ferroelectromagnetics [3.60, 61] show that the ME interaction may play a significant (and in some cases decisive) role in them.

3.4.2. Behaviour in Alternating External Fields

The ME interactions influence the spectrum and the nature of spin and FE oscillations, thereby introducing peculiarities in the behaviour of a ferroelectromagnetic in alternating external fields. A resonant absorption of the energy of an alternating magnetic field at the FE frequency and a resonant absorption of the electric energy at the spin wave frequency become possible [3.46-48, 50, 51]. The maximum absorption of the energy of an electric (magnetic)

field at the spin (FE) frequency is possible in strong exchange fields or when the frequencies ω_E and ω_s are close enough for resonance. In a ferroelectric-ferrimagnetic with $\theta_M > \theta_E$ and $\omega_E > \omega_{2s}$, the FE frequencies can approach the frequency of the upper spin branches, for example, in the vicinity of the Curie temperature θ_E, where the frequency of the soft FE mode decreases considerably. Near the resonance, the amount of the electric field energy absorbed by the spin oscillations is of the same order as the energy absorbed by the FE oscillations.

Besides the resonance effects, various nonlinear processes have been theoretically investigated for ferroelectromagnetics in alternating external fields. The possibility of the ME frequency doubling has been indicated, viz. the onset of polarization (magnetization) oscillations at twice the frequency of the magnetic (electric) field [3.25, 62]. Various methods of investigating the spectrum of elementary excitations of a ferroelectromagnetic by creating an instability in it with the help of external fields have been considered. The parametric excitation of spin waves in a ferroelectric-antiferromagnetic by an alternating electric field seems to be the most effective approach [3.63, 64]. Owing to the ME exchange interaction, the threshold field for exciting spin waves in a ferroelectric-antiferromagnetic is small and can be easily attained experimentally. The threshold field e_{th} is defined by the expression

$$e_{th} = \frac{4\eta_s}{\gamma} \frac{\delta P_0}{\Delta_0} \left(\frac{\omega}{gM_0} \right)^2, \tag{3.5}$$

where $\omega = \omega_{1s} + \omega_{2s}$ is the electric field frequency, g is the gyromagnetic ratio, and η_s is the relative decrement of damping of spin waves. Assuming that $(\omega/gM_0) \simeq 10$, $\eta_s \simeq 10^{-2}$, $\gamma \simeq 10^{-7}$ dyne^{-1} cm^2, $\delta \simeq 10^{-11}$dyne^{-1}cm^2, $\Delta_0 \simeq 10^2$, $P_0 \simeq 10^4$-10^5 CGS units, we get $e_{th} \simeq 10$ V/cm. This value is two or three orders lower than the threshold field induced by the Dzyaloshinskii ME interaction [3.64]. The values of the threshold excitation fields in ferroelectric-ferromagnetics [3.65] and ferroelectric-ferrimagnetics are also several orders higher than those obtained from formula (3.5).

The frequency of the alternating electric field in the case of parametric excitation (3.5) is of the order of spin frequencies. Under certain conditions, an electric field with a much higher frequency can also excite spin waves, although much stronger excitation fields are required for this purpose. A rapidly oscillating electric field which varies slowly in space can excite spin waves in a ferroelectric-antiferromagnetic at values of the field exceeding the threshold value (3.5) by several orders of magnitude [3.66, 67].

Ferroelectromagnetic oscillations can also be excited by an electric current in semiconductors [3.52] or by an electron beam passing through a dielectric in a narrow cylindrical channel [3.68]. The elec-

trons moving through a crystal produce Čerenkov excitation of oscillations. In magnetic materials, the spin waves are excited as a result of the interaction of an electron beam with the electromagnetic field of the magnetic and is of a relativistic dynamic nature. The rate of growth of the spin waves is proportional to $(v/c)^{2/3}$ (v and c are the electron velocity and the velocity of light), and the excitation is effective at sufficiently high velocities of the beam electrons [3.69]. A different situation arises in ferroelectromagnetics where an electrostatic interaction takes place between the electrons of the beam and the electric dipole moment of the crystal. Owing to the ME coupling, this interaction can lead to an instability of the spin waves. This method of excitation is electrostatic, and the rate of growth of the waves does not contain the small factor $(v/c)^{2/3}$. Both spin and FE oscillations are excited. However, this method cannot be used to excite the soft FE mode which is characterized by the absence of an electrostatic field.

3.5. EXPERIMENTAL STUDIES OF MAGNETOELECTRIC INTERACTIONS IN FERROELECTROMAGNETICS

In spite of the large number of effects predicted theoretically, the experimental investigation of ferroelectromagnetic crystals is still at its initial stage. Most of the experimental studies are devoted to the synthesis of ferroelectromagnetics and to the determination of the type of electric and magnetic ordering. The investigation of the nature and magnitude of the ME interactions presumes the existence of sufficiently perfect single crystals with a low electric conductivity. Only a few such ferroelectromagnetics are known so far. The investigation of the linear ME effect requires that the samples must not only be single crystals, but also have preferably a single domain character, since the ME susceptibility of the linear effect in 180° domains has the opposite sign. A preferential orientation of magnetic moments in crystals is created by applying an electric and a magnetic field near the phase transition temperatures.

Ni-I boracite ($Ni_3B_7O_{13}I$) is the most thoroughly investigated compound. The interest to this compound was provoked by the work of Ascher *et al.* [3.70], who clearly demonstrated for the first time the connection between the polarization and magnetization in ferroelectromagnetics. This compound occupies a special place among ferroelectromagnetics, since the FE and magnetic ordering temperatures coincide for it: $\theta_E = \theta_M = \theta$. The electric polarization is induced by the antiferromagnetic ordering with a weak ferromagnetism, which arises below $\theta = 64$ K. The vector **P** is directed along the [001] axis, while the spontaneous magnetic moment is in a plane

perpendicular to **P** [3.70]. If the direction of the magnetic moment is taken as the y-axis, the magnetic point group for such a state is given by $m'm2'$. Ascher *et al.* [3.70] observed a clearly marked interrelation between the directions of spontaneous polarization and magnetization: a rotation of **P** through 180° is accompanied by a rotation of $\mathbf{M}_s$ through 90°, and vice versa. This phenomenon was explained from the point of view of the group theory [3.71], as well as thermodynamically [3.13]. Using the simplest model of two magnetic sublattices, it can be shown that the thermodynamic potential of Ni-I boracite contains the term $P_z(L_x^2 - L_y^2)$ (**L** is the antiferromagnetism vector) which gives rise to a polarization $P_z \sim (L_x^2 - L_y^2)$ upon an antiferromagnetic transition. This term also indicates that a rotation of $\mathbf{M}_s$ from the y-axis to the x-axis, corresponding to the $L_x \to L_y$ transformation, reverses the sign of polarization.

In the state $m'm2'$ under consideration, the nonzero components χ^{EM} for the linear ME effect are given by $\alpha_{yz}^{EM} = \alpha_{zy}^{ME}$ and $\alpha_{zy}^{EM} = \alpha_{yz}^{ME}$. In other words, the following relations hold:

$$p_z = \alpha_{zy}^{EM} H_y, \quad m_y = \alpha_{yz}^{ME} E_z,$$
$$p_y = \alpha_{yz}^{EM} H_z, \quad m_z = \alpha_{zy}^{ME} E_y. \tag{3.6}$$

In these formulas, **p** (**m**) is the change in the electric (or magnetic moment induced by a magnetic (electric) field. This change is much smaller than the spontaneous moment and is described by a term of the form **P** [**L** × **M**] in the thermodynamic potential. If the magnetic field is directed along the y-axis ($y \parallel \mathbf{M}_s$), a polarization $p_z \sim L_x M_y \sim L_x H_y$ is induced, i.e. the ME susceptibility of the linear effect is given by $\alpha_{zy}^{EM} = \alpha \sim L_x$. The p_z vs H_y dependence obtained experimentally in [3.70] during the remagnetization of the crystal in the direction $y \parallel \mathbf{M}_s$ has a bowtie-shaped ME hysteresis loop (Fig. 3.4). The initial state (segment *1*) for $\mathbf{H} \parallel -y$ is a single-domain state with $\mathbf{M} \parallel \mathbf{H}$ and $\alpha > 0$. A decrease and reorientation of the field, which reverses the direction of the magnetization without altering the direction of L_x, leave α unchanged ($\alpha \sim L_x$) (segments *2* and *3*). In a field which reverse the direction of L_x, α changes sign abruptly, and segment *4* corresponds to the values of α in stronger fields. A repeated reversal of magnetization is accompanied by a change in the ME signal along the segments $5 \to 6 \to 7 \to 8$. The value of α at 15 K is 3.8×10^{-4}. The ME susceptibility has an unusual temperature dependence: in the vicinity of θ, α changes sign and has a small negative peak (Fig. 3.5). Such a form of the α vs T dependence may be due to the contribution of the antiferromagnetism vector to the linear ME effect caused by weak rhombic distortions of the cubic lattice in the paramagnetic phase [3.72]. The finite value of the negative peak is due to nonlinear ME effects

and decreases with the increasing magnetic field strength [3.72, 73]. Other anomalous effects are also observed in Ni-I boracite. These include the asymmetry of the FE hysteresis loop [3.70, 74], the ex-

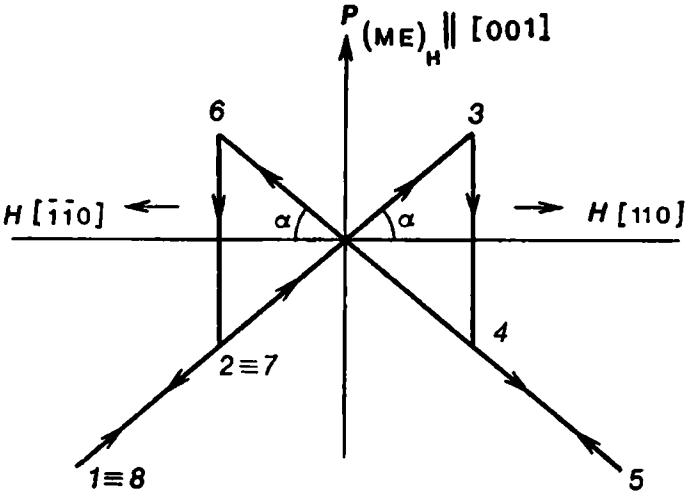

Fig. 3.4. ME hysteresis loop for Ni-I boracite at 46 K [3.70]. The magnetic field is directed along the ± [110] direction (in pseudocubic indices).

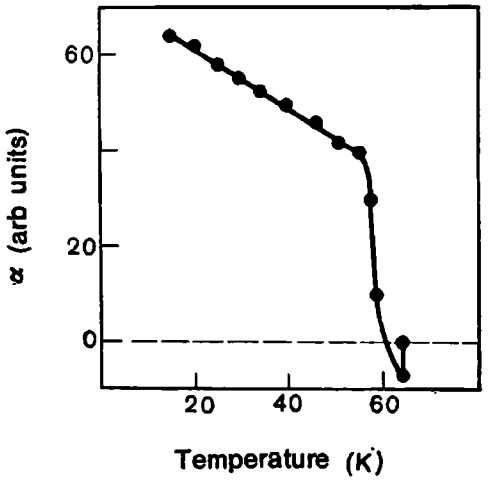

Fig. 3.5. ME susceptibility of the Ni-I boracite as a function of temperature [3.70]. The measurements were carried out after cooling from a temperature above 65 K in the fields $H = 7.6$ kOe parallel to [110] and $E =$ $= 10$ kW/cm parallel to [001].

istence of a maximum in the temperature dependence of spontaneous magnetization in the vicinity of θ [3.75], and a return of the polarization to its original direction after the magnetic field which has worsed its direction is switched off [3.73]. All these effects were ex-

plained [3.72] by taking into account the rhombic distortion of the cubic lattice in the paramagnetic phase [3.76], and the fact that these distortions are very small, and hence the second- and fourth-order magnetic moment invariants in the thermodynamic potential are comparable. The ME interaction in Ni-I boracite is manifested in a strong dependence of the dielectric permittivity on the magnitude and direction of the magnetic field [3.77]. The largest variation of $\varepsilon_{zz}(H)$ was observed in the vicinity of θ, where a 90° rotation of

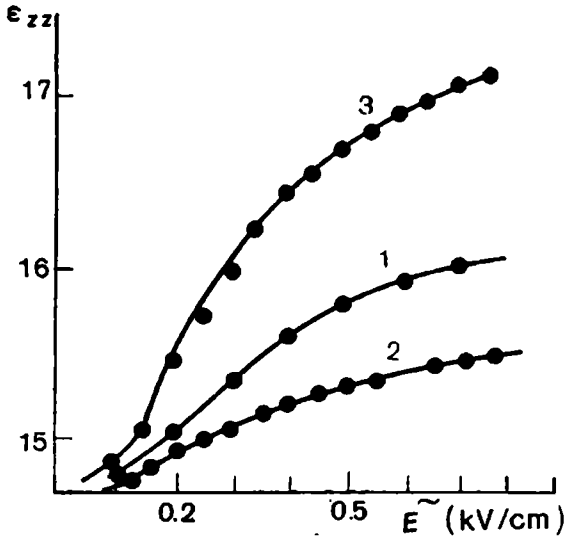

Fig. 3.6. Dependence of the permittivity of Ni-I boracite on the amplitude of the alternating electric field E at 62 K in a magnetic field $H = 12.5$ kOe [3.77]: *1*—$H = 0$; *2*—$\mathbf{H} \parallel \mathbf{M}_s$; *3*—$\mathbf{H} \perp \mathbf{M}^2$.

the magnetic field H = 12.5 kOe led to a 30% change in the value of ε_{zz} as compared to its value at $H = 0$ (Fig. 3.6). This effect indicates a strong interaction between the FE and magnetic subsystem of Ni-I boracite near the phase transition temperature. Subsequent investigations of the linear ME effect in Ni-I boracite show the presence, besides α_{zy} and α_{yz}, of other nonzero components of the ME susceptibility, connected with different magnetic ion groups in the unit cell [3.78] (the unit cell of Ni-I boracite contains 12 magnetic ions). This indicates a lower magnetic class than $m'm2'$ [3.79].

The **linear ME effect** was also studied in other boracites: in single crystals Ni-Cl [3.20], Co-Cl [3.80], Cu-Cl [3.81], and in polycrystals Co-I, Ni-Br and Mn-I [3.82]. In Ni-Cl boracite, a peak in the ME susceptibility is observed near 9K during a transition to the weak ferromagnetic state (Fig. 3.7) [3.20]. This peak is in accord with the concepts [3.38] on the anomalous behaviour of the ME susceptibility near the temperature of transition to the weak ferromagnetic state in a ferroelectric rhombic crystal. The linear ME effect was also

studied in the ferroelectric-ferrimagnetic semiconductor Fe_3O_4 [3.83]. The magnetization induced by an alternating electric field was observed in $Pb(Fe_{1/2}Nb_{1/2})O_3$ [3.84], $PbMn_2O_4$ [3.85], and Fe-Br, Co-Cl, Co-I, and Fe-Cl boracites [3.87, 86].

A break in the temperature dependence of dielectric permittivity during magnetic ordering, which had been predicted earlier [3.37], was observed in $BiFeO_3$ [3.88, 89], in Cu-I and Cu-Br boracites

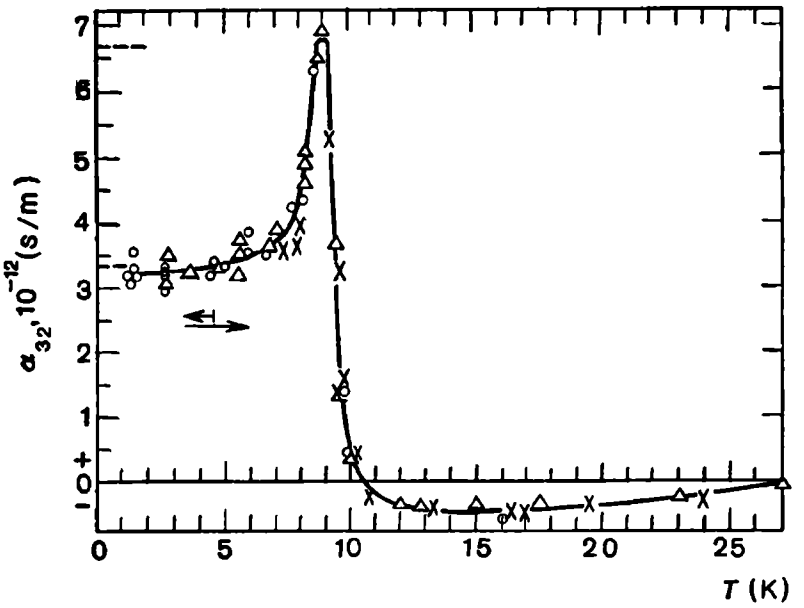

Fig. 3.7. Temperature dependence of the ME susceptibility $\alpha_{zy} = \alpha_{32}$ in Ni-Cl boracite [3.20].

[3.90], $BaMnF_4$ [3.91, 92], as well as in certain ferroelectromagnetic solid solutions. Figure 3.8 shows the temperature dependence of the dielectric permittivity $\varepsilon(T)$ in the pyroelectric-antiferromagnetic $BaMnF_4$ [3.92], indicating a break in ε at the magnetic ordering temperature $\theta_M \simeq 30$ K. Fox *et al.* [3.93] attribute the break in $\varepsilon(T)$ at $T = \theta_M$ to a weak ferromagnetism and an anisotropic ME interaction of the type $F_{anis} = \lambda_{ik} L_i M_k P^2$. However, it follows from the general theoretical concepts (see Sec. 3.3) that a break in $\varepsilon(\theta_M)$ appears even in the isotropic case and does not impose any additional restrictions on the crystal symmetry. In any ferroelectric-antiferromagnetic there exists an exchange energy of the form $F_{ex} = \gamma P^2 L^2$ which considerably exceeds the anisotropic energy F_{anis}. The exchange ME energy causes a change in the dielectric permittivity

$$\Delta\varepsilon \sim \gamma L^2 \sim \gamma M_0^2 \sim \gamma\,(\theta_M - T)^{2\beta} \quad (T \leqslant \theta_M), \tag{3.7}$$

where M_0 is the magnetic moment of the sublattice. The theoretically calculated value of $\Delta\varepsilon$ for $BaMnF_4$ at $T = 0$ with the help of the expression for the ME exchange interaction parameter γ in terms of microscopic constants [3.27] leads to values which are in agreement with the experimentally observed results for $\Delta\varepsilon$. The value of the

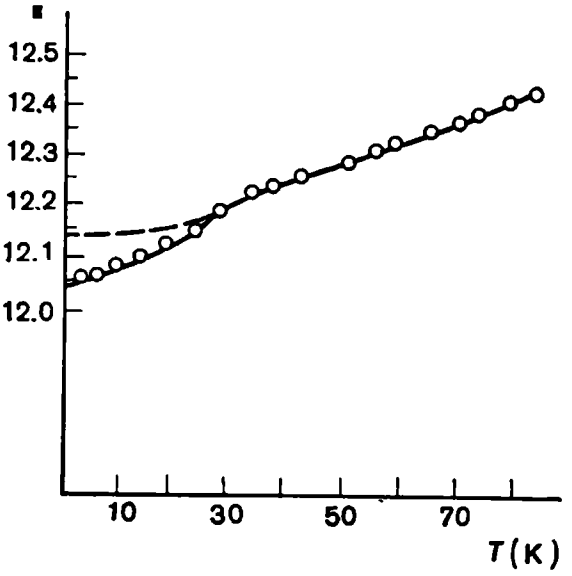

Fig. 3.8. Permittivity along the pyroelectric axis as a function of temperature in $BaMnF_4$ [3.92].

magnetic critical index β, estimated from the ε (T) dependence shown in Fig. (3.8), is found to be of the order of 0.35. Neutron diffraction measurements [3.94] yield the value $\beta \simeq 0.32$.

Among other ME measurements in ferroelectromagnetics, the visual observation of narrow-band ferromagnetic domains inside the FE domains in Ni-Cl and Ni-Br boracites [3.95] and the observation of the maximum in the electric signal induced during a reversal of the magnetic sublattice in $BiFeO_3$ [3.96] are worth mentioning. The latter effect is in agreement with the theoretical concepts on the jump in electric polarization as a result of a spin-flop.

3.6. POSSIBLE APPLICATIONS OF FERROELECTROMAGNETICS

The above digression shows that the studies of ferroelectromagnetics have just begun. However, the existence of new magnetoelectric effects that can be used in technology is already becoming obvious. Experimental proof has been obtained for the interaction of magnetization and polarization, and for the possibility of controlling the magnetization by an electric field or the electric

polarization by a magnetic field. A significant ME interaction is also observed in heterophase systems [3.97]. Therefore, we can assume that just like the ferroelectromagnetic crystals, heterophase systems will also find applications in technology. Let us consider some possible uses of ferroelectromagnetics for scientific and practical purposes.

The dependence of the ME susceptibility on the orientation of the moments in the domains makes it possible to exercise a magnetoelectric control over spin- and FE states. An investigation of the temperature and field dependence of the ME susceptibility may provide information on the orientation (spin-flop, spin-flip) and thermal phase transitions. The magnetic critical index can be determined from the temperature dependence of the dielectric permittivity. Similarly, the FE index can be determined from the temperature dependence of the magnetic susceptibility.

In order to use ferroelectromagnetics for practical purposes, it is desirable to have compounds with low losses, low electric conductivity, a considerable magnetic moment and ME susceptibility, as well as sufficiently high values of the electric and magnetic transition temperatures (above room temperatures). There are no ferroelectromagnetics satisfying these requirements at present, although some of these are satisfied by some individual compounds.

The devices based on ferroelectromagnetic crystals can be divided into three types: (1) devices using the FE or magnetic properties separately, (2) devices which simultaneously employ the FE and magnetic properties, but without any ME interaction, and (3) devices whose action is based on ME effects. We shall not be considering the first type of devices, since the use of FE crystals, as well as magnetically ordered crystals, is quite common. The review by Wood and Austin [3.98] contains a detailed table of the possible applications of magnetoelectric crystals as well as the characteristics of 15 different devices whose operation range varies from audio to optical frequencies and which include modulators, phase inverters, switches, rectifiers, stabilizers, etc. We shall consider only some of these devices here.

The second type of devices includes the Faraday phase inverter operating in the microwave region. The quality of its operation is determined by the quality $\varepsilon' M_z/\varepsilon''$, where M_z is the component of the magnetization in the direction of propagation of electromagnetic waves, and ε' and ε'' are the real and imaginary components of the dielectric permittivity. The observed small values of M_z in ferroelectromagnetics may not affect the quality of the device for large values of the dielectric permittivity ε'. Such values of ε' are observed, for example, in perovskite compounds and heterophase systems [3.99]. It seems possible to use ferroelectromagnetics in reversing optical modulators and optical processors whose operation is based on the

electro-optic and magneto-optical Kerr, Pockels, and Faraday effects, as well as on birefringence.

The application of the ME interaction (devices of the third type), for example, switching or modulation of electric polarization by a magnetic field, makes it possible to obtain a magnetically operated optical device in the visible and infrared spectral regions. The operation of this device is based on the variation of the linear birefringence by changing the polarization under the action of the magnetic field. The magnetic field required to switch the polarization may not be very high and is just a few kilooersteds for Ni-I boracite. This type of P-switching would have required strong electric fields of the order of several kilovolts per centimeter. Samples in the form of thin plates are required to produce such fields, while in the magnetic method of polarization switching, massive samples can be used.

The predicted ease with which the spin waves can be parametrically excited by an alternating electric field in ferroelectric-antiferromagnetics makes it possible to use them for creating UHF spin wave oscillators in spin-wave electronics. Ferroelectric-ferrimagnetic crystals also seem to be effective for inducing spin oscillations in the IR region with the help of an electric field. A considerable admixture of FE oscillations in the low-frequency branch of the spectrum of ferroelectromagnetics also indicates the possibility of generation of new type of coupled waves called the ferroelectromagnetic waves. Nonlinear ME interaction, which is manifested especially strongly near the transition temperatures, can be used to produce a nonlinear ME optical device for, say, frequency doubling.

Ferroelectromagnetic crystals can also be used as thin-film waveguides in integral optics and fibre communication technology.

3.7. CONCLUSION

This review demonstrates that the ME interactions give rise to several new and interesting effects in ferroelectromagnetics. A connection has been established between the spontaneous electric and magnetic moments. The influence of a magnetic field on the electric moment and of an electric field on the magnetization has also been observed. It has been shown theoretically that the ME interaction leads to additional first and second order phase transitions in the spin and FE subsystems, to the excitation of the spin waves by an alternating electric field, and of FE oscillations by a magnetic field, as well as to a gap in the spin-wave spectrum in the absence of external fields. Most of these effects are yet to be confirmed experimentally.

At present, the experimental data are mainly qualitative in nature. Further studies of the values of the ME constants and ME energies in different crystals are required. Unlike the magnetoelec-

trics with weak induced ME effects, the ferroelectromagnetic crystals exhibit a strong spontaneous ME effect which is manifested most clearly near the phase-transition temperatures. For measurements and possible practical applications, it is preferable to use ferroelectromagnetics with large values of θ_E and θ_M, and with clearly manifested magnetic and FE properties, i.e. ferro- and ferrimagnetics with an intrinsic FE ordering. The synthesis of such ferroelectromagnets will open new prospects for their application in technology.

References

3.1. G. A. Smolenskii and A. I. Agranovskaya, *Zh. Eksp. Teor. Fiziki*, **28**, 1491 (1958).
3.2. G. A. Smolenskii, A. I. Agranovskaya, S. N. Popov, and V. A. Isupov, *Zh. Eksp. Teor. Fisiki*, **28**, 2152 (1958).
3.3. G. A. Smolensky and V. A. Ioffe, *Communications de Colloque International de Magnetism de Grenoble* (France), 2-6 Jullet, Communication No. 1 (1958).
3.4. G. A. Smolenskii, V. A. Isupov, A. I. Agranovskaya, and N. N. Krainik, *Fiz. Tverd. Tela*, **2**, 2982 (1960).
3.5. G. A. Smolenskii, V. A. Isupov, N. N. Krainik, and A. I. Agranovskaya, *Izv. Akad. Nauk SSSR*, Ser. Phys., **25**, 1333 (1961).
3.6. V. A. Bokov, I. E. Myl'nikova, and G. A. Smolenskii, *Zh. Eksp. Teor. Fiziki*, **42**, 643 (1962).
3.7. Yu. N. Venevtsev, G. S. Zhdanov, and S. P. Solovjev, *Kristallografiya*, **5**, 520 (1960).
3.8. G. A. Smolenskii, V. M. Yudin, E. S. Sher, and Yu. E. Stolypin, *Zh. Eksp. Teor. Fiziki*, **43**, 877 (1962).
3.9. S. V. Kiselev, R. P. Ozerov, and G. S. Zhdanov, *Dokl. Akad. Nauk SSSR*, **145**, 1255 (1962).
3.10. Yu. N. Venevtsev, V. V. Gagulin, and V. N. Lyubimov, *Ferroelectromagnetics*, Nauka, Moscow, 1982 (in Russian).
3.11. Kato Koichi, Iida Shuichi, *J. Phys. Soc. Japan*, **51**, 1335 (1982).
3.12. F. Bertaut, F. Forrat, and P. Fang, *Compt. Rend. Acad. Sci.*, **256**, 1958 (1963).
3.13. Yu. M. Gufan, *Pis'ma Zh. Eksp. Teor. Fiziki*, **8**, 271 (1968).
3.14. E. T. Keve, S. C. Abrahams, and I. L. Bernstein, *Journ. Chem. Phys.*, **51**, 4928 (1969); *ibid.*, **53**, 3279 (1970).
3.15. I. H. Ismailzade, N. I. Nesterenko, and F. A. Mirishli, *Abstr. of the Commun. of the Seventh Intern. Congr. of Union of Crystallogr.*, Moscow, 1966, A207.
3.16. R. E. Newnham, J. J. Kramer, W. A. Shulze, and L. E. Cross, *J. Appl. Phys.*, **49**, 6088 (1978).
3.17. G. A. Smolenskii, V. A. Bokov, V. A. Isupov, N. N. Krainik, and G. M. Nedlin, in: *Ferroelectrics*, Izd. Rostov Univ., Rostov, 1968, p. 129.
3.18. Yu. N. Venevtsev. L. I. Zhdanov, Yu. E. Roginskaya, Yu. Ya. Tomashpol'skii, V. N. Lyubimov, L. I. Shvorneva, K. P. Mitrofanov, and A. S. Viskov, in: *Ferroelectrics*, Izd. Rostov. Univ., Rostov, 1968, p. 155.
3.19. S. M. Skinner, *IEE Trans. Parts. Mater. Packaging*, PMP-6, 68 (1970).
3.20. H. Shmid, in: *Magnetoelectric Interaction Phenomena in Crystals*, London, New York, Paris, 1975, p. 121.
3.21. A. Keitsiro, *Phys. Rev. B: Solid State*, **2**, 754 (1970).
3.22. R. A. Fisher, E. W. Hornung, G. E. Brodale, and W. F. Giangue, *J. Chem. Phys.*, **56**, 193 (1972).

3.23. L. D. Landau and E. M. Lifshitz, *Electrodynamics of Continuous Media*, Pergamon Press, Oxford, 1960.
3.24. I. E. Dzyaloshinksii, *Zh. Eksp. Teor. Fiziki*, **37**, 881 (1959).
3.25. L. N. Bulaevskii and V. M. Fain, *Pis'ma v Zh. Eksp. Teor. Fiziki*, **8**, 268 (1968).
3.26. Yu. I. Balkarei and V. A. Nikitov, *Fiz. Tverd. Tela*, **17**, 2089 (1975).
3.27. I. E. Chupis, in: *Proc. of Conf. on Low Temperature Physics*, Kharkov, 1980, Part II, p. 173 (in Russian).
3.28. A. I. Mitsek and G. A. Smolenskii, *Fiz. Tverd. Tela*, **4**, 3581 (1962).
3.29. V. A. Koptsik, *Kristallografiya*, **5**, **7**, 932 (1960).
3.30. N. N. Neronova and N. V. Belov, *Dokl. Akad. Nauk SSSR*, **129**, 556 (1959); *Kristallografiya*, **4**, 807 (1959).
3.31. L. A. Shuvalov and N. V. Belov, *Kristallografiya*, **7**, 192 (1962).
3.32. V. N. Lyubimov, *Fiz. Tverd. Tela*, 5, 951 (1963); *Kristallografiya*, 8, 699, (1963).
3.33. O. V. Kovalev, *Fiz. Tverd. Tela*, **14**, 961 (1972); *Kristallografiya*, **18**, 221 (1973).
3.34. G. M. Nedlin, *Fiz. Tverd. Tela*, **4**, 3568 (1962).
3.35. W. E. Brown, R. M. Hornreich, and S. Strikman, *Phys. Rev.*, **168**, 574 (1968).
3.36. J. Holakowsky, *Phys. St. Solidi*, **56 (b)**, 615 (1973).
3.37. G. A. Smolenskii, *Fiz. Tverd. Tela*, **4**, 1095 (1962).
3.38. G. M. Nedlin, *Izv. Akad. Nauk SSSR, Ser. Phys.*, **29**, 890 (1965).
3.39. I. E. Chupis, in: *Solid State Physics*, Vladivostok, 1972 (in Russian); *Proc. of 1st Int. Conf. on Magnetism MCM-73*, Moscow, 1973, **1**, 1, Nauka, Moskow, 1974, p. 354.
3.40. V. G. Baryakhtar and I. E. Chupis, in: *Magnetoelectric Interaction Phenomena in Crystals*, London-New York-Paris, 1975, p. 57.
3.41. I. E. Chupis and N. Ya. Plyushko, *Fiz. Tverd. Tela*, **14**, 3444 (1972).
3.42. I. E. Chupis, in: *Some Questions in the Physics of Thin Ferromagnetic Films*, Vladivostok, 1974, p. 3.
3.43. I. E. Chupis, *Fizika Nizkikh Temperatur*, **2**, 762 (1976); ibid., **1**, 183 (1975); **7**, 203 (1981).
3.44. M. A. Savchenko, A. V. Stefanovich, and M. A. Khabakhpashev, *Fiz. Met. i Metalloved*, **47**, 1320 (1979).
3.45. I. A. Akhiezer and Z. A. Spol'nik, *Fiz. Tverd. Tela*, **15**, 220 (1973).
3.46. V. G. Baryakhtar and I. E. Chupis, *Fiz. Tverd. Tela*, **11**, 3242 (1969).
3.47. V. G. Baryakhtar and I. E. Chupis, *Fiz. Tverd. Tela*, **10**, 3547 (1968); *Ukr. Fiz. Zh.*, **17**, 652 (1972).
3.48. V. G. Baryakhtar and I. E. Chupis, *Intern. Journ. Magnet.*, 5, 337 (1974).
3.49. I. E. Chupis, *Fiz. Nizkikh Temp.*, **2**, 622 (1976).
3.50. I. E. Chupis and N. Ya. Aleksandrova, *Fiz. Tverd. Tela*, **21**, 3166 (1979).
3.51. I. E. Chupis, *Fiz. Nizkikh Temp.*, **6**, 771 (1980).
3.52. A. I. Akhiezer, I. A. Akhiezer, *Zh. Eksp. Teor. Fiz.*, 39, 1009 (1970).
3.53. L. N. Davydov, Z. A. Spol'nik, *Ukr. Fiz. Zh.*, **18**, 1368 (1973).
3.54. M. A. Khabakhpashev, *Fiz. Tverd. Tela*, **20**, 238 (1978).
3.55. M. A. Savchenko and M. A. Khabakhpashev, *Fiz. Tverd. Tela*, **26**, 39 (1978).
3.56. V. G. Shavrov, *Fiz. Tverd. Tela*, **7**, 328 (1965).
3.57. N. Ya. Plyusko and I. E. Chupis, *Ukr. Fiz. Zh.*, **19**, 826 (1974).
3.58. M. A. Savchenko and M. A. Khabakhpashev. *Fiz. Tverd. Tela*, **18**, 2699 (1976).
3.59. I. A. Akhiezer and L. N. Davydov, *Fiz. Tverd. Tela*, **12**, 3171 (1970).
3.60. I. E. Chupis and N. Ya. Plyushko, *Fiz. Tverd. Tela*, **13**, 2522 (1971).
3.61. M. A. Savchenko and M. A. Khabakhpashev, *Fiz. Tverd. Tela*, 20, 1845 (1978).
3.62. E. Ascher, *Phil. Mag.*, **17**, 149 (1968).

3.63. I. E. Chupis and N. Ya. Aleksandrova, *Ukr. Fiz. Zh.*, **27**, 300 (1982).
3.64. I. A. Akhiezer and L. N. Davydov, *Ukr. Fiz. Zh.*, **15**, 1747 (1970); *Pis'ma v Zh. Eksp. Teor. Fiz.*, **13**, 380 (1971).
3.65. I. E. Chupis and V. N. Savchenko, in: *Some Questions in the Physics of Thin Ferromagnetic Films*, Vladivostok, 1974 (in Russian), p. 93.
3.66. I. A. Akhiezer and L. N. Davydov, *Fiz. Tverd. Tela*, **13**, 1795 (1971).
3.67. V. A. Nikitov, *Trudy MFTI, Ser. Radiotekhnika i Elektronika*, No. 9, 118 (1975).
3.68. A. S. Bakay and I. E. Chupis, *Fiz. Nizkikh Temp.*, **3**, 1153 (1977).
3.69. A. I. Akhiezer, V. G. Baryakhtar, and S. V. Peletminskii, *Spin Waves*, Nauka, Moscow, 1967 (in Russian), Sec. 14.
3.70. E. Ascher, H. Rieder, H. Schmid, and H. Stössel, *J. Appl. Phys.*, **37** 1404 (1966).
3.71. O. V. Kovalev, *Fiz. Tverd. Tela*, **14**, 307 (1972).
3.72. I. E. Chupis, *Fiz. Nizkikh Temp.*, **9**, 56 (1983).
3.73. H. Schmid, in: *Crystal Growth*, Nauka, Moscow, 1967 (in Russian), Vol. 7, p. 32.
3.74. M. Tadashi and M. Tashiaki, *J. Phys. Soc. Japan*, **29**, 1092 (1970).
3.75. L. N. Baturov, R. V. Zorin, B. I. Al'shin, and Yu.N.Yarmukhamedov, *Fiz. Tverd. Tela*, **22**, 279 (1980).
3.76. A. V. Kovalev and G. T. Andreeva, *Fiz. Tverd. Tela*, **21**, 1744 (1979).
3.77. L. N. Baturov, B. I. Al'shin, and Yu.N. Yarmukhamedov, *Fiz. Tverd. Tela*, **20**, 2254 (1978).
3.78. L. N. Baturov and B. I. Al'shin, *Fiz. Tverd. Tela*, **21**, 3 (1979).
3.79. J. P. Rivera and H. Schmid, *Ferroelectrics*, **36**, 447 (1981).
3.80. J. P. Rivera, H. Schmid, J. M. Moret, and H. Bill, *Intern. J. Magnet.*, **6**, 211 (1974).
3.81. H. Minetaka, K. Kay, and K. Jinzo, *J. Phys. Soc. Japan*, **39**, 1625 (1975).
3.82. L. N. Baturov, B. I. Al'shin, and R. V. Zorin, in: *Abstracts of Papers to the All-Union Conf. on Magnetic Phenomena Physics*, Kharkov, 1979, p. 165.
3.83. G. T. Rado and J. M. Ferrari, *Phys. Rev. B. Solid State*, **15**, 290 (1977).
3.84. D. N. Astrov, B. I. Al'shin, R. V. Zorin, and L. A. Drobyshev, *Zh. Eksp. Teor. Fiz.*, **55**, 2122 (1968).
3.85. B. I. Al'shin, D. N. Astrov, and L. N. Baturov, *Pis'ma v Zh. Eksp. Teor. Fiz.*, **22**, 444 (1975).
3.86. L. N. Baturov, B. I. Al'shin, and D. N. Astrov, *Fiz. Tverd. Tela*, **19**, 916 (1977).
3.87. L. N. Baturov, R. V. Zorin, B. I. Al'shin, and V. I. Bugakov, *Fiz. Tverd. Tela*, **23**, 908 (1981).
3.88. N. N. Krainik, N. P. Khuchua, and V. V. Zhdanova, in: *Proc. of Intern. Meeting of Ferroelectrics*, Prague, 1966, V. 1, p. 377.
3.89. Yu. E. Roginskaya, Yu. Ya. Tomashpol'skii, Yu.N. Venevtsov, V. M. Petrov, and G. S. Zhdanov, *Zh. Eksp. Teor. Fiz.*, **50**, 69 (1966).
3.90. S. N. Drozhdin, B. G. Bochkov, N. D. Gavrilova, T. V. Popova, V. A. Koptsik, and V. K. Novik, *Kristallografiya*, 20, 854 (1975).
3.91. G. A. Samara and P. M. Richards, *Phys. Rev. Ser. B*, **14**, 5073 (1976).
3.92. G. A. Samara and I. F. Scott, *Solid State Comm.*, **21**, 167 (1977).
3.93. D. L. Fox, D. R. Tilley, I. F. Scott, and H. I. Guggenheim, *Phys. Rev. Ser. B*, **21**, 2926 (1980).
3.94. D. E. Cox, S. M. Shapiro, R. A. Cowley, I. M. Eibschütz, and M. I. Guggenheim, *Phys. Rev. Ser. B*, **19**, 5754 (1979).
3.95. J. H. Brunskill and H. Schmid, *Ferroelectrics*, **36**, 395 (1981).
3.96. I. H. Ismailzade and R.Y.Yakupov, *Phys. Stat. Sol., Ser.(a)*, **32**, K161 (1975).
3.97. I. Van den Boomgaard and R.A.I.A. Born, *J. Mater. Sci.*, **13**, 1538 (1978).
3.98. E. Wood and A. E. Austin, *Intern. J. Magnet.*, **5**, 303 (1974).
3.99. K. Leibler, V. A. Isupov, and H. Bielska-Landowska, *Acta Phys. Polon., Ser. A*, **40**, 815 (1971).

4 High Hydrogen Pressures. Synthesis and Properties of New Hydrides

E. G. Ponyatovsky, V. E. Antonov, and I. T. Belash

4.1. INTRODUCTION

For many years, the properties of transition metal-hydrogen systems have drawn the attention of researchers working in diverse fields of physics and material science. There are several reasons for the growing interest in the problem "hydrogen in metals". These include the unusual physical properties of metal-hydrogen systems caused by the unique nature of hydrogen as a component, the profound effect of hydrogen on mechanical, physical, and chemical properties even at extremely low concentrations, and a wider range of practical applications of metal-hydrogen systems (purification and accumulation of hydrogen, separation of its isotopes, designing new types of heat exchangers, catalyzers, and so on). The intensive studies on the interaction of hydrogen with metals were largely stimulated by investigations in the field of hydrogen power engineering and thermonuclear fusion. The possibility of using hydrogen as a universal power source has shed a new light on the question of developing structural materials that are stable to hydrogen. The construction of apparatus using plasma requires a knowledge of the peculiarities of the interaction of reactor materials with hydrogen in the state of enhanced thermodynamic activity.

In spite of the extensive investigations that have been conducted throughout the world to study the metal-hydrogen systems, the data on the physical properties of solutions of hydrogen even in such important and interesting transition metals as Fe, Co, Ni, Cr, Mn, and Mo has remained scarce so far. As a matter of fact, the solubility of hydrogen in these metals is extremely low at atmospheric pressures, and a huge amount of experimental data concerning the influence of hydrogen on the properties of these metals and their alloys was obtained for hydrogen concentrations usually not exceeding the H-to-metal atomic ratio $n \approx 10^{-5}$-10^{-7}. Such concentrations are comparable with those of various defects (hydrogen traps), and this complicates the physical interpretation of the accumulated experimental data.

In order to isolate the role of hydrogen as an alloying element in forming physical properties of a system under consideration and to analyze the important question about the physical status of hydrogen

in transition metals, we must be able to freely vary the hydrogen content over a wide interval. This may be accomplished by varying the chemical potential of hydrogen. An increase in the chemical potential of hydrogen shifts the thermodynamic equilibrium in the metal-excess hydrogen systems towards higher concentrations of Me-H solid solutions right up to the formation of hydrides of stoichiometric compositions. For example, it was observed in [4.1] that the interaction of hydrogen plasma with molybdenum leads to the formation of hydrogen-saturated phases with compositions up to MoH_2.

Earlier, the increase in the hydrogen content of transition metals was mainly attained by electrochemical methods which were first used to obtain hydrides of nickel and chromium. Later, hydrogen implantation and diverse methods of plasma synthesis were used for this purpose. However, the use of these methods imposes severe limitations on the geometrical dimensions and the quality of the samples obtained. In the case of electrochemical saturation and implantation, the samples are usually thin films of a few microns thickness, while for plasma synthesis we obtain fine powders with numerous defects. The high density of defects in hydrogenated films and powders may be the reason behind specific physical properties which are not inherent in the bulk samples of the same composition. By way of an example, we refer the reader to communication [4.2] about the transition of thin palladium films to the superconducting state upon irradiation by alpha-particles.

4.2. METHODS FOR COMPRESSING HYDROGEN AND OBTAINING HYDRIDES

All these drawbacks can be directly eliminated if hydrides are synthesized by placing the metal in an atmosphere of hydrogen whose thermodynamic potential is raised by compression to high pressures. The work with high-pressure gases, however, involves many experimental difficulties, and even for inert gases the upper limit of pressures attainable with the help of more or less assimilated techniques does not exceed 2-3 GPa. These difficulties are considerably enhanced in the case of hydrogen due to its high compressibility, extremely low viscosity, and chemical corrosiveness which greatly increases with temperature and pressure. For this reason, until the last decade, the investigation of metal-hydrogen systems was restricted to pneumatic pressures (10-15 MPa) and in individual cases to a few hundred MPa. This range of pressures was first exceeded in the middle of 1960s by Polish scientists who designed a system in which a bronze bomb containing hydrogen was placed in a hydrostatic high-pressure chamber [4.3]. This made it possible to isolate the chamber walls from the direct influence of hydrogen and to use

steel chambers for compressing hydrogen up to $P_{H_2} \approx 2.5$-3 GPa at room temperature and to $P_{H_2} \approx 1.5$ GPa at $T \leqslant 450$°C.

The significant increase in the pressure and temperature range permitted synthesizing nickel- and chromium hydrides under equilibrium conditions and obtaining for the first time manganese hydride and hydrogen-saturated phases based on a series of nickel and palladium alloys, as well as studying their crystal structure and thermal stability, and investigating of their magnetic and superconducting properties (a detailed review of research conducted during this period is given in [4.4-6]).

The abilities of "piston-cylinder" type hydrostatic chambers are practically exhausted by pressures of the order of 3 GPa. By using the method proposed in [4.7] for obtaining high hydrogen pressures, we were able to overcome this barrier. The method consists in the following. A condensed hydrogen-containing compound is introduced into an ampoule-type container. The container is placed into a high-pressure chamber, preliminary compression is performed, and hydrogen is freed by decomposing the compound by any known means. The temperature and pressure in the operating zone of the high-pressure chamber and, hence, of hydrogen in the container are then brought up to the required values. With the help of this method, a series of high pressure cells was created at the Institute of Solid State Physics of the USSR Academy of Sciences. This allowed an investigation of the behaviour of the Curie points and electrical resistance of specimens under hydrogen pressure from ~3 MPa to 9 GPa at $-150 \leqslant T \leqslant 500$°C.

Thermal decomposition is the simplest way to release hydrogen from a compound. The block diagram of cells for measuring the electrical resistance of samples in which this method is used is shown in Fig. 4.1. No external source is required for filling the ampoule with hydrogen, since hydrogen is released during thermally activated decomposition of the hydride (*03*, *14*) placed beforehand in the lower part of the ampoule. Elimination of the appropriate filling system from the scheme permits complete utilization of the potentialities of ordinary hydrostatic high-pressure chambers, while the appreciable simplification of the construction permits production of cells of quite small dimensions (Fig. 4.1, cell *11-17*) which can be placed into the operation zone of the existing quasihydrostatic chambers. It is the use of the quasihydrostatic chambers that made it possible to overcome the limit ~3 GPa and to compress hydrogen to 9 GPa. It should be noted that even this limit of 9 GPa is set by the chambers at our disposal and not by the method proposed in [4.7]. Readers interested in details of the application of this method are referred to the articles listed in [4.8].

By the middle of 1970s, there remained twelve transition elements in the Periodic Table for which hydrides were not obtained:

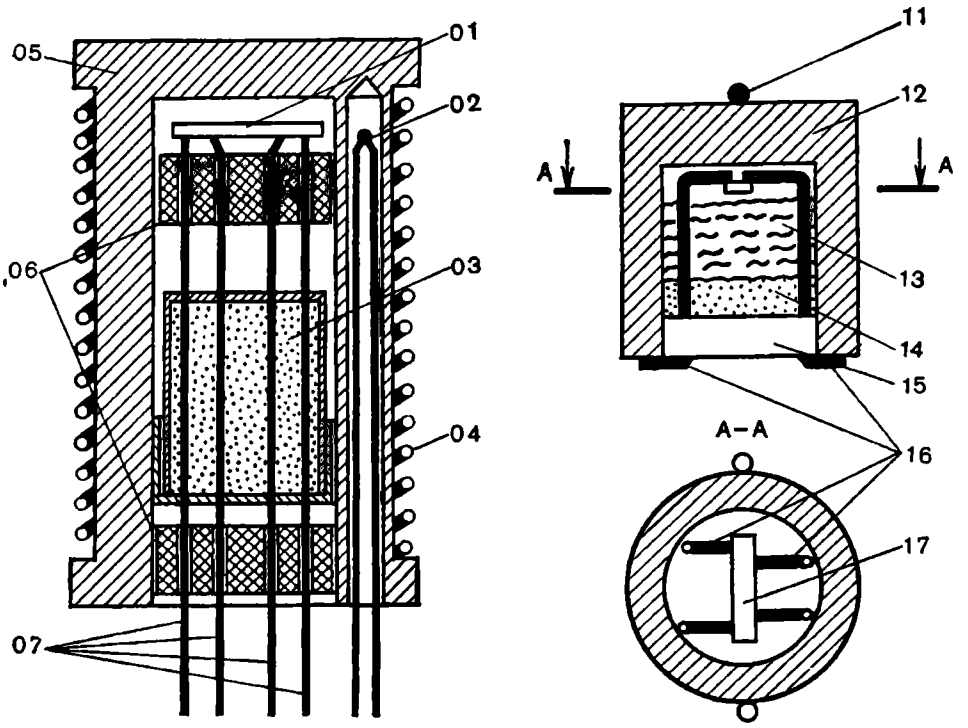

Fig. 4.1. Block diagram of cells for measuring the electrical resistance of samples in hydrogen atmosphere using hydrostatic (*01-07*) and quasi-hydrostatic (*11-17*) chambers.
01, *17*—sample; *02*, *11*—thermocouple junction; *03*, *14*—hydride (hydrogen source); *04*—heater; *05*—ampoule (brass); *06*—clamps (pyrophyllite); *07*, *16*—electrical leads; *12*—ampoule (Teflon); *13*—glass wool; *15*—ampoule cap (Teflon); all free space in the ampoules *05* and *12* is filled with silicone or petrol.

Mn, Fe, Co, Mo, Tc, Ru, Rh, W, Re, Os, Ir, and Pt. The application of the new method for compressing hydrogen reduced the number of such elements to six. We synthesized hydrides of manganese (simultaneously with Polish scientists), iron, cobalt, molybdenum, technetium, and rhodium. Significant quantities of hydrogen were introduced into Re and Ru. Gold hydride, the first member of the family of noble metal hydrides, was also synthesized by using the high-pressure technology [4.9].

The structure and limiting compositions of hydrogen solutions in group VI-VIII transition metals synthesized so far are shown in Table 4.1. All hydrides are formed only on the basis of one of the two closest packings of metal atoms, namely fcc (face-centred cubic, γ) or hcp (hexagonal close-packed, ε). It should be mentioned that here and subsequently we shall be dealing only with massive samples. Apparently, if the samples are in the form of thin films, hydrides with other compositions and structures can be formed. For example, it is reported in [4.10] that heating a 500-1000 Å thick film of palla-

Table 4.1. Hydrides of Transition Metals

VI	VII	VIII		
ε $CrH_{1.0}$	ε $MnH_{0.96}$	ε $FeH_{0.8}$	ε, γ $CoH_{1.0}$	γ $NiH_{1.25}$
ε $MoH_{1.3}$	ε $TcH_{0.83}$	ε $RuH_{0.03}$	γ $RhH_{1.0}$	γ $PdH_{1.0}$
W	ε $ReH_{0.22}$	Os	Ir	Pt

Remark: The maximum attained hydrogen concentration is indicated; ε are solutions with hcp metal lattice; γ are solutions with fcc metal lattice.

dium up to $T \gtrsim 600$°C in a hydrogen atmosphere at $P_{H_2} = 0.1$ MPa results in the formation of $PdH_{1.33}$ with a tetragonal lattice having the parameters $a = 2.896$ Å and $c = 3.330$ Å at room temperature (such a hydride was initially obtained by the same authors by implantation of hydrogen into palladium). A similar treatment of massive samples led to the formation of ordinary Pd-H solutions with fcc metal sublattices.

All the investigated hydrides of transition metals are characterized by a metallic conductivity of the order of the conductivity of the starting metal. The kinetics of hydrogen absorption (hydride formation) varies from metal to metal over an extremely wide interval: at $T = 250$°C, from several minutes for palladium [4.11, 12] and nickel [4.12, 13] to tens of hours for technetium [4.14] (the samples are foils of 0.1-0.2 mm thickness). A similar diversity is also observed in the kinetics of thermal decomposition of hydrides into metal and molecular hydrogen under atmospheric conditions: hydrides of manganese [4.15, 16] and technetium [4.17] are metastable at 20°C, while hydrides of iron [4.18] and rhodium [4.19] rapidly decompose at $T \approx -100$°C onwards. In liquid nitrogen, all hydrides without exception last indefinitely. Taking into account such kinetics of formation and decomposition of hydrides, systems for "quenching" the samples were developed. The sample is first saturated with hydrogen at high pressure and temperature. After this, the sample is rapidly cooled (down to −180°C, if necessary) without changing the pressure. The pressure is then brought down to the atmospheric level, and the sample is taken out of the chamber for

a subsequent study of its physical properties. The investigation of these metastable (relative to decomposition into metal and molecular hydrogen) hydrides under atmospheric pressure considerably supplemented the results of measurements under high hydrogen pressure.

In the following sections, we shall describe the results of investigation of phase diagrams of metal-hydrogen systems, crystal structure, thermal stability, as well as magnetic and superconducting properties of recently obtained hydrides.

4.3. PHASE TRANSFORMATIONS IN METAL-HYDROGEN SYSTEMS

Cr-H. Chromium can be electrolytically saturated with hydrogen to compositions close to CrH [4.20]. Depending on the conditions of electrolysis, hydrides thus obtained can either have an fcc or an hcp lattice of the metal.

Baranowski and Bojarski [4.21] were the first to synthesize chromium hydride through a direct interaction of the metal with hydrogen at high pressures. A noticeable solubility of hydrogen in bcc (body-centered cubic) chromium (α-phase) was not observed. Chromium hydride (ε-phase) is formed on the basis of an hcp lattice whose parameters at $T = -190°C$ and under atmospheric pressure are $a = 2.717$ Å, $c = 4.436$ Å, and $c/a = 1.633$ [4.21]. Our measurements have shown that the composition of the hydride is close to the CrH stoichiometry over the entire investigated stability range on the T-P_{H_2} diagram right up to $T = 400°$ C and $P_{H_2} = 7$ GPa.

The formation of chromium hydride is accompanied by a considerable (several tens per cent) increase in the sample resistance, the decomposition—by its decrease. Figure 4.2 shows the T-P_{H_2} phase diagram of the Cr-H system, constructed mainly on the basis of resistometric data [4.22]. It can be seen from the phase diagram that the considerable hysteresis in the $\alpha \rightleftarrows \varepsilon$ transformation persists at all temperatures right up to 400 °C. Apparently, this hysteresis is caused by the elastic stresses which are close to the yield stress and appear in the sample due to an abrupt increase in the volume ($\approx 19\%$) upon hydride formation. In this case, the curve of thermodynamic equilibrium between the α- and ε-phases must be much closer to the hydride decomposition curve than to the hydride formation curve, since the removal of even a small amount of hydrogen leads to a relaxation of the elastic stresses [4.4]. For the Cr-H system, such an assumption is confirmed by a satisfactory agreement between the calculated value of the thermodynamic equilibrium pressure at room temperature [4.23] and the experimental curve for the $\varepsilon \rightarrow \alpha$ transition (Fig. 4.2.).

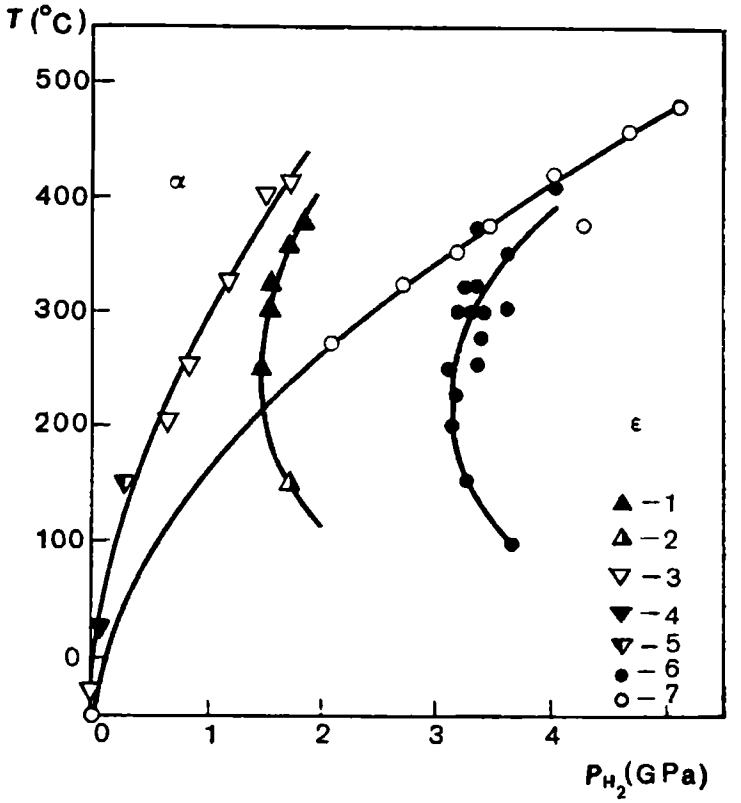

Fig. 4.2. T vs. P_{H_2} phase diagrams for the Cr-H (*1-5*) and Mo-H (*6*, *7*) systems [4.25].
1, *6*—pressure corresponding to $\alpha \rightarrow \varepsilon$ transitions; *3*, *7*—pressure corresponding to $\varepsilon \rightarrow \alpha$ transitions; *2*, *5*—results of [4.21] and [4.23]; *4*—calculated equilibrium pressure for $2Cr + H_2 \rightleftharpoons 2CrH$ [4.23].

Mo-H. Molybdenum hydride was first synthesized under a high hydrogen pressure [4.24]. Figure 4.2 shows the T-P_{H_2} phase diagram of the Mo-H system, constructed on the basis of resistometric data [4.25]. Typical isotherms for the electrical resistivity of molybdenum in a hydrogen atmosphere, clearly indicating the jumps caused by the formation and decomposition of hydride, are shown in Fig. 4.3.

It can be seen from Fig. 4.2 that the T-P_{H_2} diagram for the Mo-H system is analogous to the diagram for the Cr-H system, and the curves corresponding to the formation and decomposition of molybdenum hydride are merely displaced towards the region of higher pressures. As in the case of bcc chromium, the solubility of hydrogen in bcc molybdenum is quite low. As to the ε-solutions, our recent measurements have shown that in the investigated stability region of molybdenum hydride on the T-P_{H_2} diagram (right up to $T = 400°$ C and $P_{H_2} = 7$ GPa), its composition is close to $n \approx 1.2$-1.3 and de-

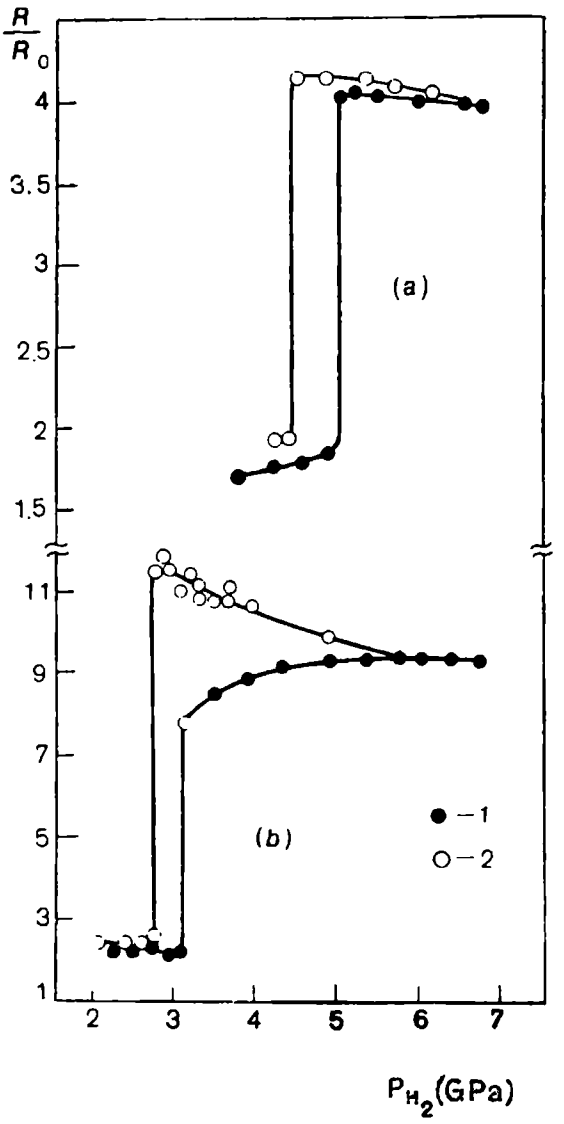

Fig. 4.3. Electrical resistivity isotherms for rhodium (*a*, $T = 300$°C) [4.47] and molybdenum (*b*, $T = 325$°C) [4.25] in hydrogen atmosphere.
1—with increasing pressure; *2*—with decreasing pressure. R_0 is the sample resistance at room temperature and under atmospheric pressure.

pends only slightly on the temperature and pressure of hydrogen. Under atmospheric pressure and at T . — 145° C, the parameters of the hcp metallic sublattice of hydride are $a = 2.92$ Å, $c = 4.74$ Å, and $c/a = 1.63$ [4.24]. A transition of molybdenum hydride into superconducting state was not observed at $T \geqslant 2$ K.

W-H. No noticeable solubility of hydrogen in tungsten was observed at $T \leqslant 400$°C and $P_{H_2} \leqslant 9$ GPa.

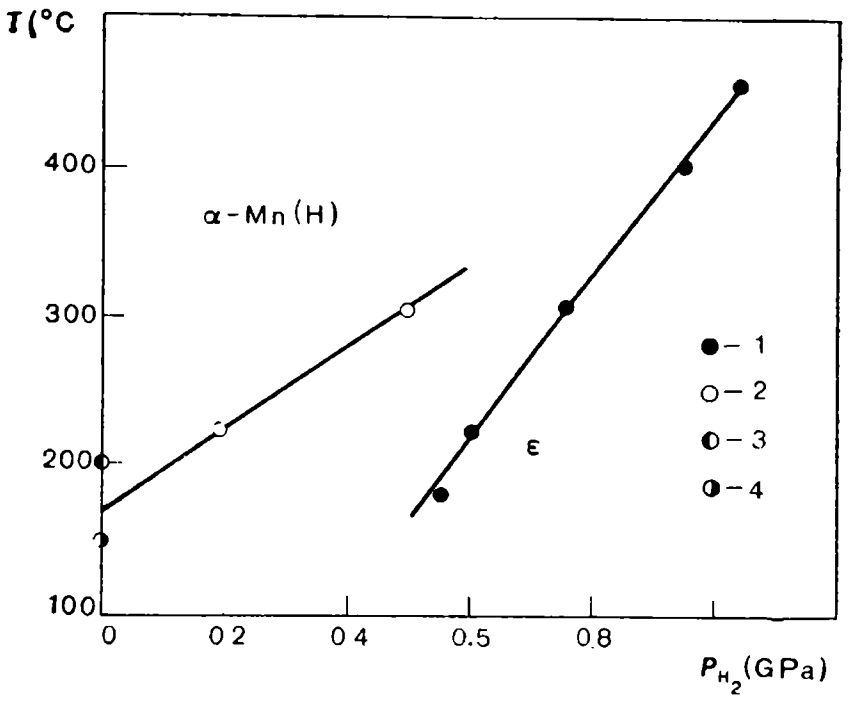

Fig. 4.4. T **vs.** P_{H_2} **phase diagram for the Mn-H system.** *1*—points corresponding to the onset of hydride formation [4.26]; *2* [4.6], *3* [4.15], and *4* [4.16] are the points corresponding to the decomposition of the hydride.

Mn-H. Manganese hydride was first obtained under a high hydrogen pressure [4.15, 16]. The phase diagram of the Mn-H system is shown in Fig. 4.4. The values of pressures corresponding to the hydride formation have been obtained from the position of jumps in the electrical resistivity isotherms [4.26], while the pressures corresponding to its decomposition are determined from the hydrogen content in the Mn-H samples obtained by exposure to hydrogen atmosphere [4.6].

It can be seen from Fig. 4.4 that manganese hydride is stable under normal conditions. Figure 4.5 shows the dependence of the parameters of the hcp metallic lattice of manganese hydride on composition at room temperature [4.27]. A reduction in the hydrogen content of the samples to $n \approx 0.65$ leads to a monotonic decrease in the value of the parameters a and c of the hydride. In the concentration range $0 < n \leqslant 0.65$, where the parameters a and c remain practically unchanged, the samples consist of a mixture of the hydride and initial α-Mn. Thus, the region of existence of the continuous solid ε-solutions Mn-H (hydrides) at atmospheric pressure has a lower concentration limit $n_\varepsilon^{\min} \approx 0.65$ for which clear bends are observed in the a

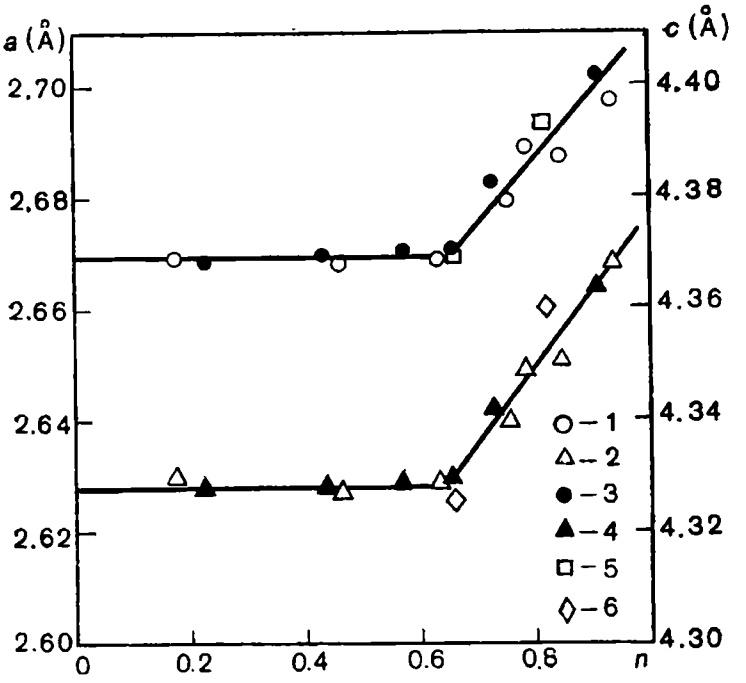

Fig. 4.5. Dependence of the parameters of the hcp metal lattice on n for Mn-H (light symbols) and Mn-D (dark symbols) solutions at room temperature [4.27].
1, *3*—parameter *a*; *2*, *4*—parameter *c*; *5*, *6*—results of [4.15].

vs. n and c *vs.* n curves. It is interesting to note (see Fig. 4.5) that the a (n) and c (n) dependences, as well as the value of $n_\varepsilon^{\min}$ for Mn-D solutions, are close to those for Mn-H solutions. Neutronographic studies of the deuteride $MnD_{0.65}$ at $T \geqslant 80$ K have shown [4.28] that deuterium atoms occupy the octahedral interstices in the hcp lattice of the metal.

Tc-H [4.17, 14]. In the investigated range of hydrogen pressures up to $\sim$ 2.2 GPa, the Tc-H solutions are formed on the basis of the initial hcp lattice of the metal. The T-P_{H_2} diagram for the Tc-H system, however, turned out to be rather complicated: two isomorphic (at least so far as the metal lattice is concerned) phase transitions, $\varepsilon_0 \rightarrow \varepsilon_1$ and $\varepsilon_1 \rightarrow \varepsilon_2$, take place in the system and are accompanied by an abrupt increase in the solubility of hydrogen in technetium. It is interesting to note that in the hydrogen solubility isotherm for technetium at 300° C (Fig. 4.6), two regions of supercritical anomalies (near $P_{H_2} = 0.3$ and 1.3 GPa) are clearly seen for these transitions, terminating at the critical points at $T < 300°$ C.

The Tc-H solutions are kinetically stable under normal conditions. A rapid decomposition of the Tc-H hydrides takes place upon heating in vacuum to $T \geqslant 80°$ C. At room temperature and atmospheric

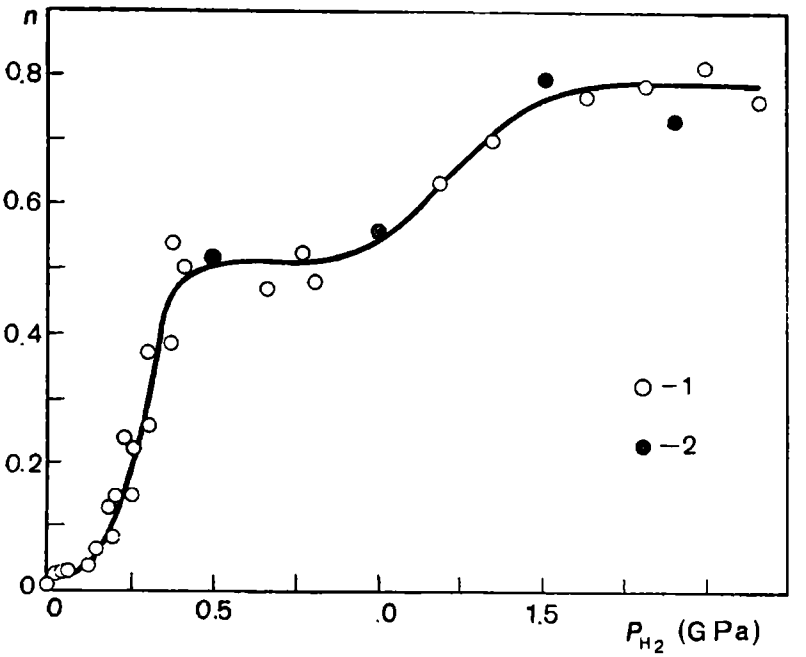

Fig. 4.6. Solubility of hydrogen in technetium at $T = 300°C$. *1*—results of [4.14]; *2*—results of [4.17].

pressure, the maximum hydrogen solubility in the ε_0-phase amounts to $n \approx 0.04$; the samples with $0.04 \leqslant n \leqslant 0.39$ consist of a mixture of the ε_0-phase and ε-hydride, while from $n \approx 0.39$ to $n \approx 0.78$ the region of continous ε-solutions stretches[1]. Parameters of the metal lattice of the ε-hydride ($a = 2.805$ Å, $c = 4.455$ Å, and $c/a = 1.588$) remain unchanged, within experimental errors, for the entire concentration range $0.39 \leqslant n \leqslant 0.78$. The dissolution of hydrogen in the ε_0-phase decreases the superconducting transition temperature of technetium from $T_k = 7.85$ K for $n = 0$ to $T_k \approx 7.35$ K for $n \approx 0.04$. The Tc-H solutions in the ε-phase with $n \geqslant 0.39$ possess no superconductivity at $T \geqslant 2$ K.

Re-H [4.30]. At $T = 250°$ C, the solubility of hydrogen in rhenium increases monotonically with pressure, thus causing a smooth deviation of the pressure dependence of the electrical resistance of the

1 It should be noted that the *T-c* diagram for the metastable equilibria in the Tc-H solutions under atmospheric pressure apparently differs considerably from the *T-c* projection of the equilibrium T-P_{H_2}-c diagram of the Tc-H system onto the plane $P_{H_2} \approx 0.1$ MPa. This difference is a quite common feature of Me-H systems (see [4.29]). In particular, this results in a need for reliable data on the phase composition of Me-H solutions for different values of external parameters, since only part of the investigations of physical properties of such solutions can be carried out directly at high hydrogen pressure, while other studies have to be conducted on samples in the metastable state.

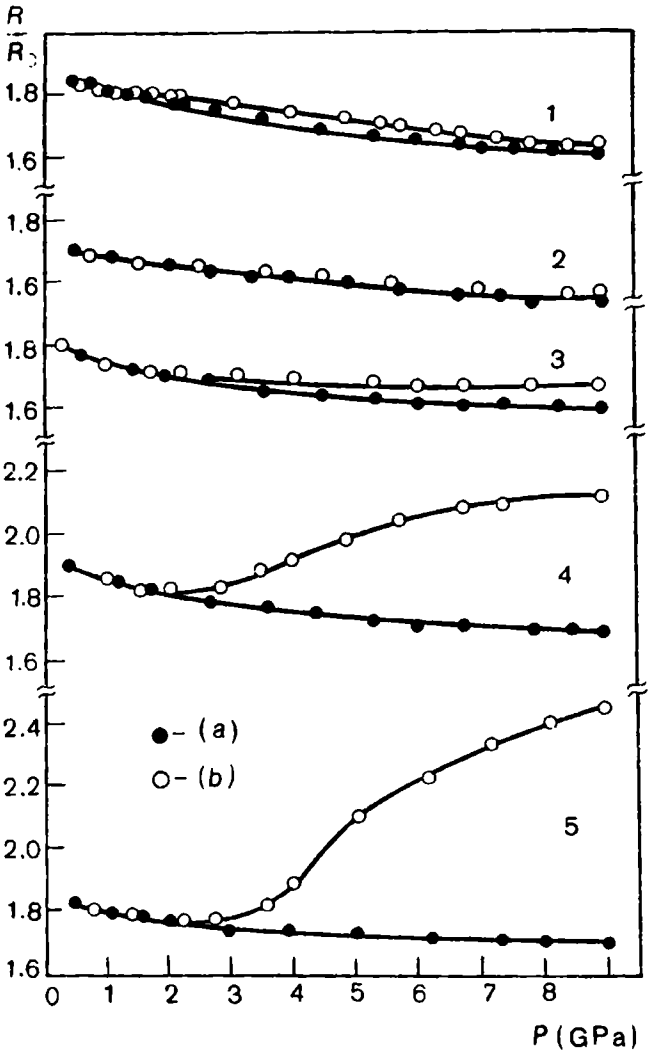

Fig. 4.7. Electrical resistance isotherms in an inert medium (*a*) and in hydrogen (*b*) at $T = 250°C$, obtained through a stepwise increase in pressure.
1—Pt; *2*—Ir; *3*—Os; *4*—Ru (results of the present paper); *5*—Re, results of [4.30]. R_0 is the same as in Fig. 4.3.

sample from the analogous dependence for rhenium in an inert atmosphere (Fig. 4.7). At this temperature and the pressure $P_{H_2} = 9$ GPa, the concentration of the Re-H solid solution attains the value $n = 0.13 \pm 0.03$. At $P_{H_2} = 9$ GPa, the equilibrium concentration of hydrogen in rhenium increases with decreasing temperature, reaching $n = 0.22 \pm 0.03$ at $T = 170°$ C. Under atmospheric pressure, a noticeable evolution of hydrogen from Re-H samples begins at $T \geqslant 0°$ C.

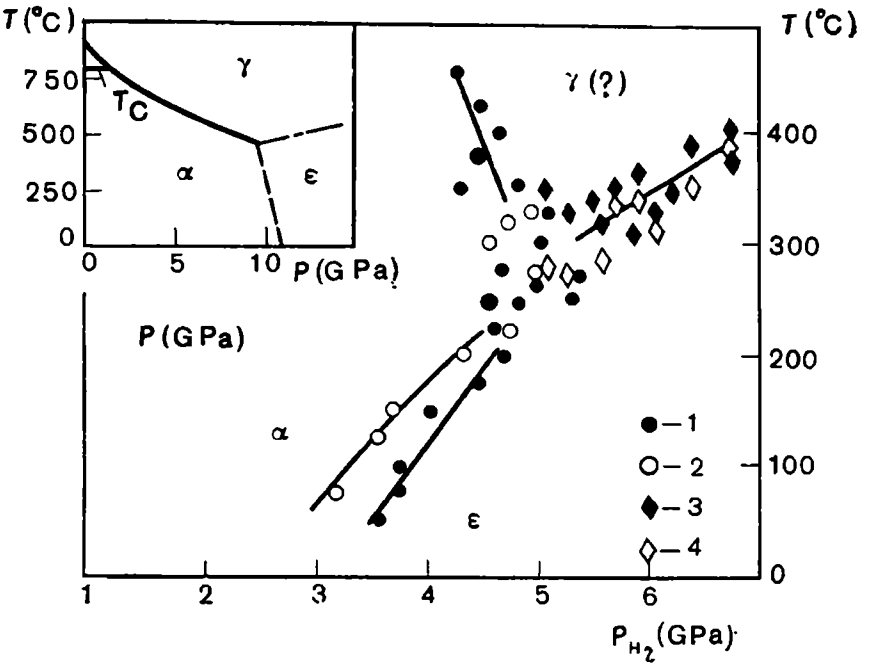

Fig. 4.8. T vs. P_{H_2} phase diagram for the Fe-H system [4.31]. *1*, *2*—position of anomalies on the electrical resistance isotherms (Fig. 4.9) for increasing and decreasing pressures respectively; *3*, *4*—position of anomalies on the electrical resistance isobars and initial magnetic susceptibility (Fig. 4.10) upon heating and colling respectively. The inset shows the T vs. P diagram for iron [4.32]; T_C is the line corresponding to Curie temperatures.

X-ray investigations at $T \approx -180$ C have shown that the introduction of hydrogen does not change the symmetry of the hcp lattice of rhenium, and leads only to a monotonic increase in the value of its parameters. The parameter a increases more rapidly than c, and the ratio c/a decreases from 1.615 for the initial rhenium to 1.591 for a sample with $n = 0.22$. The increase in V_a, the volume per rhenium atom, amounts to $\partial V_a/\partial n \approx 2.6$ Å^3 per H atom.

Dissolution of hydrogen causes a decrease in the value of T_k for Re from 1.87 K for $n = 0$ to 1.66 K for $n = 0.03 \pm 0.01$. For $n = 0.07 \pm 0.02$, the superconducting transition temperature falls to below 1.4 K.

Fe-H. Iron hydride was first synthesized at $P_{H_2} = 6.7$ GPa and $T = 250°$ C [4.18]. The hydride had a composition $n \approx 0.8$. Under atmospheric pressure and $T = -120$ °C, the hydride decomposed into the initial bcc iron and molecular hydrogen. According to X-ray investigations, iron hydride at $T = -190°$ C has an hcp metal lattice with the parameters $a = 2.686$ Å, $c = 4.380$ Å, and $c/a = 1.631$.

Figure 4.8 shows the T-P_{H_2} diagram for the Fe-H system, wherein the locations of anomalies of temperature (Fig. 4.9) and baric (Fig.

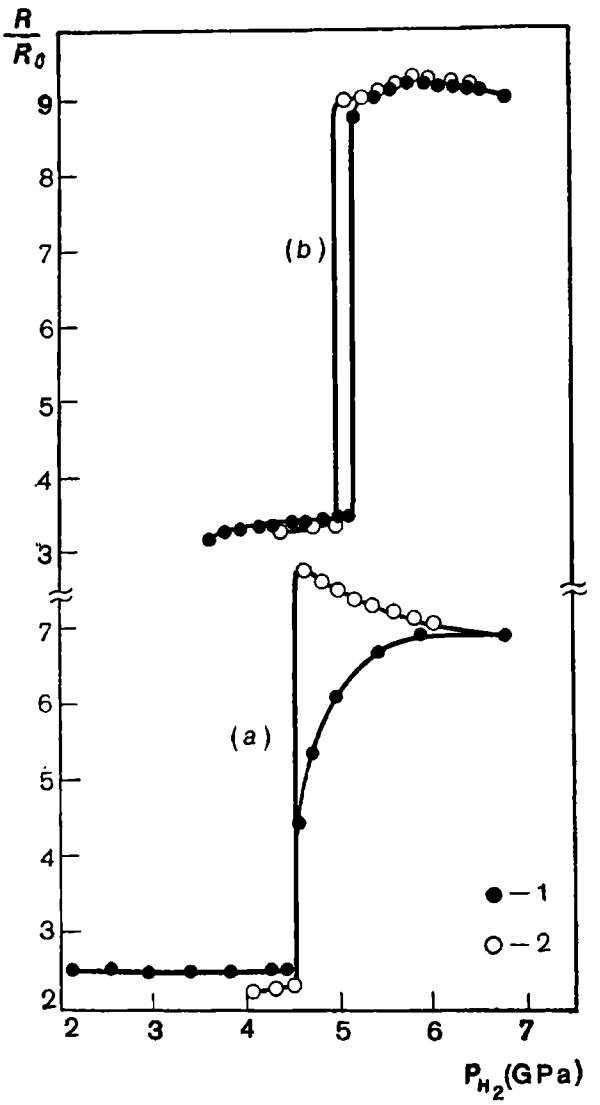

Fig. 4.9. Electrical resistance isotherms for iron in hydrogen atmosphere at $T = 250°C$ (*a*) and 330°C (*b*) [4.31].
1—with increasing pressure; *2*—with decreasing pressure. R_0 is the same as in Fig. 4.3.

4.10) dependences of electrical resistance of iron in a hydrogen atmosphere are indicated [4.31]. The lines of phase transformations divide the T-P_{H_2} plane of the diagram into three regions (α, ε, and γ), the coordinates of the triple point being $T \approx 280°$ C and $P_{H_2} \approx$ ≈ 5 GPa. In the α-region, solutions having a bcc lattice for iron are thermodynamically stable (the concentration of these solutions does not exceed $n \approx 0.01$), while in the ε-region, concentrated hydrogen solutions with an hcp iron lattice are stable.

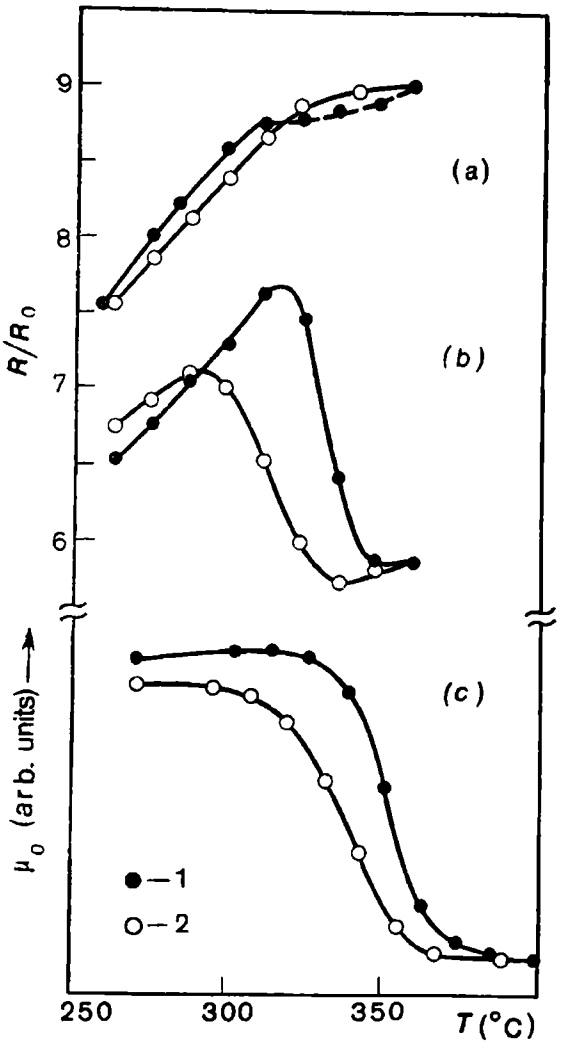

Fig. 4.10. Isobars for the electrical resistance (*a*, *b*; P_{H_2} = 6.1 GPa) and initial magnetic permeability (*c*; P_{H_2} = 5.7 GPa) in the vicinity of the $\varepsilon \rightleftarrows \gamma$ transformation in the Fe-H system [4.31].
1—upon heating; *2*—upon cooling; *a*—first cycle of heating and cooling; *b*—fifth cycle; *c*—fourth cycle. R_0 is the same as in Fig. 4.3.

The composition and crystal structure of the γ-solutions have not been investigated so far. It is possible, however, to argue in favour of the fact that the γ-phase must be an interstitial hydrogen solution on the basis of an fcc iron lattice. (1) The inset in Fig. 4.8 shows the *T-P* diagram for iron [4.32], where α, ε, and γ denote the regions of stability of the phases with bcc, hcp, and fcc lattices respectively. The effect of hydrogen on the polymorphic transformations in iron can be estimated from the data for alloys of iron with other transition metals whose addition shifts these transformations to the temperature and pressure regions convenient for measurements. Inves-

tigations of iron-rich Fe-Ni alloys [4.33] and $Fe_{78}Mn_{22}$ alloy have shown [4.34] that temperatures of the $\alpha \rightarrow \gamma$ and $\gamma \rightarrow \alpha$ transitions decrease, while the temperatures of the $\varepsilon \rightarrow \gamma$ and $\gamma \rightarrow \varepsilon$ transitions increase in a hydrogen atmosphere relative to their values at the same pressure in an inert medium. It can be easily seen that if these tendencies are retained for pure iron as well, the T-P_{H_2} diagram of the Fe-H system must have the same topology as the T-P diagram of iron, albeit with a lower pressure at the triple point ($\alpha + \varepsilon + \gamma$). The experiment yields just this type of diagram, see Fig. 4.8. (2) All hydrides of the group VI-VIII transition metals obtained so far are interstitial hydrogen solutions on the basis of just two closest packings of metal atoms, either hcp or fcc (see Table 4.1). (3) The $\varepsilon \rightarrow \gamma$ and $\gamma \rightarrow \varepsilon$ transitions in the Fe-H solutions are accompanied by the resistance anomalies (Fig. 4.10) of the same type as for hcp $\rightleftarrows$ fcc transformations in iron [4.35], Fe-Ru alloys [4.36], Fe-Mn alloys and hydrogen solutions based on them [4.34]. Such transformations in these materials are also characterized by the so-called "training" effect observed in the Fe-H system, consisting in a considerable increase in the amplitude of the resistivity anomalies accompanying the $\varepsilon \rightarrow \gamma$ and $\gamma \rightarrow \varepsilon$ transitions upon transferring the sample several times from the ε- to the γ-state and vice versa (see Fig. 4.10).

The ε-hydride of iron is a ferromagnet with a spontaneous magnetization $\sigma_0 \approx 2.2\ \mu_B$ per Fe atom at atmospheric pressure and $T = 0$ K [4.37], which is close to the σ_0 value for the initial α-Fe. Measurements of magnetic permeability have shown that at $P_{H_2} \leqslant 6.7$ GPa, the ε-solutions Fe-H remain ferromagnetic at all temperatures right up to the temperature of the $\varepsilon \rightarrow \gamma$ transition (typical isobars of the magnetic permeability of the Fe-H solutions in the vicinity of the $\varepsilon \rightleftarrows \gamma$ transformation are shown in Fig. 4.10).

Co-H. Cobalt has two allotropic modifications at atmospheric pressure. At low temperatures, the phase with an hcp lattice is stable, while upon increasing the temperature to $T_\gamma \approx 450°$ C, a transition to the phase with an fcc lattice takes place. In an inert atmosphere, T_γ increases with pressure with a slope $(dT_\gamma/dP)_{in} \approx 33°\ C \cdot GPa^{-1}$ [4.38, 39]. Measurements in a hydrogen atmosphere have shown that at $P_{H_2} \leqslant 2.5$ GPa, the dissolution of hydrogen in cobalt results in a higher $\varepsilon \rightarrow \gamma$ transition temperature as compared to its value in an inert atmosphere at the same pressure [4.39]. At $P_{H_2} \leqslant 6.5$ GPa and $T < T_\gamma$ (P_{H_2}), hydrogen forms with cobalt continuous ε-solutions whose concentration reaches $n \approx 0.5$ at $P_{H_2} = 6.5$ GPa and $T = 225°$ C. An extension of the range of investigation of the Co-H system to P_{H_2} 9 GPa revealed that at $250° \leqslant T \leqslant 350°$ C and $P_{H_2} \approx 7$GPa, this system undergoes the $\varepsilon \rightarrow \gamma$ transorfmation accompanied by an abrupt increase in the solubility of hydrogen in cobalt (Fig. 4.11) and the appearance of an anomaly in the electrical resistance isotherms (Fig. 4.12).

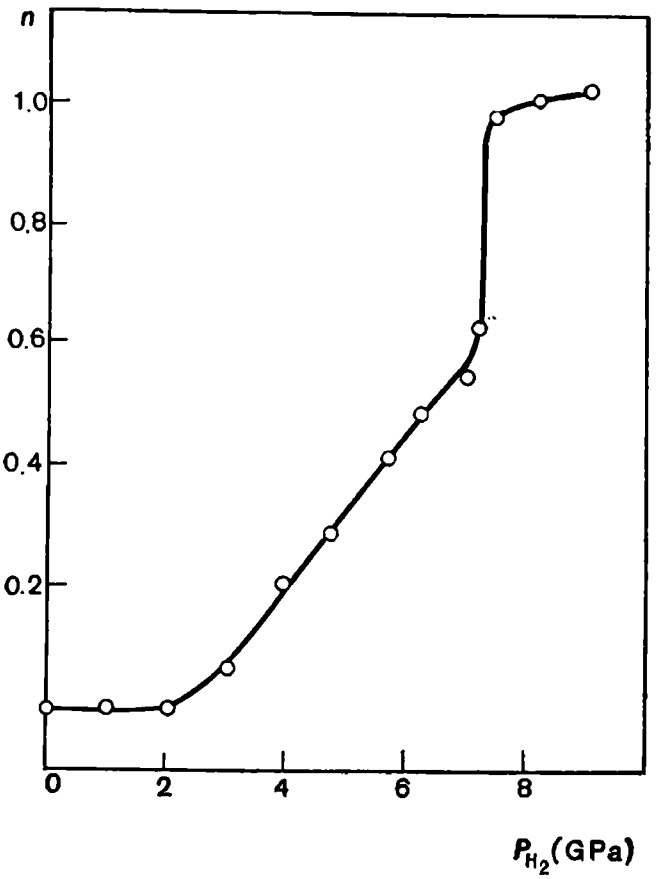

Fig. 4.11. Solubility of hydrogen in cobalt at $T = 350$°C (results of the present paper).

Figure 4.13 depicts the data of X-ray investigations of the Co-H samples saturated with hydrogen at high pressure and $250° \leqslant T \leqslant 350°$ C over a period of 24 hours. Extrapolation of approximately linear $a_\varepsilon(n)$ and $c_\varepsilon(n)$ dependences from $n < 0.6$ to $n = 1$ gives the value $\Delta V_\varepsilon \approx 1.82$ Å^3 per Co atom for the increase in the volume of the ε-solutions Co-H upon hydrogenation. It is interesting to note that if the obtained γ-hydride with $n \approx 1$ is treated as a solution of hydrogen in the γ-phase of Co, the increase in the volume upon its formation will have approximately the same value $\Delta V_\gamma \approx 1.8$ Å per Co atom. Since the specific volumes of the ε- and γ-phases of cobalt are also nearly the same, the data obtained on the solubility of hydrogen in these phases permits an analysis of the possible shape of the T-P_{H_2} diagram for the Co-H system.

Indeed, in view of the large specific volume of molecular hydrogen, the formation of the Co-H solid solutions is accompanied by a decrease in the volume of the system. Hence, for given T and P_{H_2}, the thermodynamic equilibrium will shift towards the formation of such

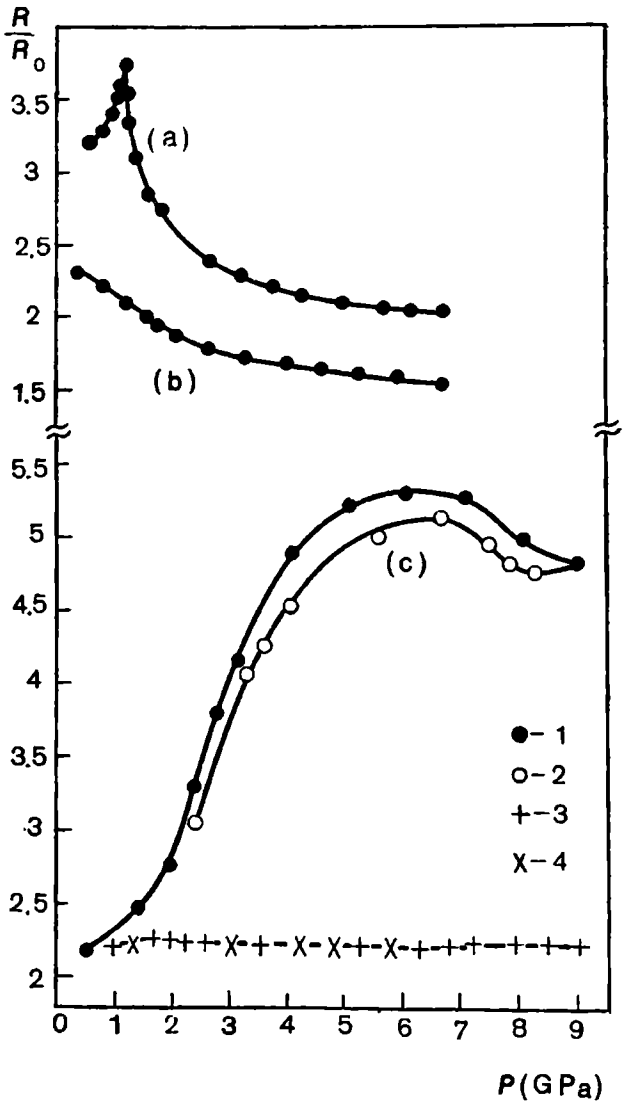

Fig. 4.12. Electrical resistance isotherms for nickel (*a*; T = 300°C), palladium (*b*; T = 200°C); and cobalt (*c*; T = 250°C) (results of the present paper).
1, *2*—with increasing and decreasing pressure in hydrogen atmosphere; *3*, *4*—the same in an inert medium.

solid solutions in which the hydrogen concentration is higher. According to the data given in [4.40], the γ-solutions of hydrogen based on the Ni-Co alloys containing up to 60 at.% Co undergo the isomorphic $\gamma_1 \rightarrow \gamma_2$ transition accompanied by an abrupt increase in the solubility of hydrogen (the T-P_{H_2} diagram for the $Ni_{40}Co_{60}$-H system is presented in Fig. 4.15). An extrapolation to pure cobalt shows that for the γ-solutions Co-H, the line of this transition on the virtual

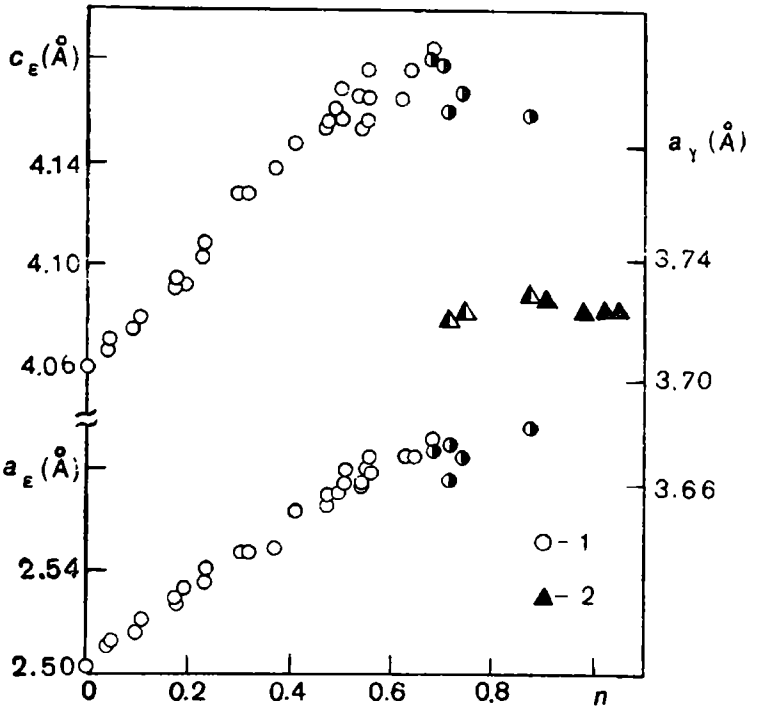

Fig. 4.13. Dependence of the parameters of an hcp (ε) and fcc (γ) metal lattice for Co-H solutions under atmospheric pressure and $T = -190°C$ (results of the present paper).
1—ε-solutions; *2*—γ-solutions. The half-filled symbols correspond to the two-phase (ε + γ) samples.

T-P_{H_2} diagram should be close to the vertical $(P_{H_2})_{\gamma_1 \to \gamma_2} \approx$ 6-8 GPa. Thus, while for $P_{H_2} \geqslant 7$ GPa the solubility of hydrogen in γ-Co is higher than in ε-Co (see Fig. 4.11), the situation will most probably be reversed at lower pressures. The following pattern for the $\varepsilon \to \gamma$ transition temperature in cobalt with increasing hydrogen pressure can therefore be expected: for $P_{H_2} \ll 7$ GPa, the transition temperature should initially increase relative to its value in an inert medium at the same pressure (in other words, the temperature range for the stability of the ε-solutions Co-H should become wider), attain a maximum value, and then rapidly fall at $P_{H_2} \to (P_{H_2})_{\gamma_1 \to \gamma_2} \approx 7$ GPa. The available experimental data confirm such a trend in the T_γ (P_{H_2}) dependence.

Ni-H. Nickel hydride was first obtained by electrochemical methods [4.41]. Later, it was also synthesized under equilibrium conditions, i.e. at a high hydrogen pressure [4.42]. At room temperature, nickel hydride is formed through the isomorphic $\gamma_1 \to \gamma_2$ transition accompanied by an abrupt increase in the solubility of hydrogen in nickel from $n \leqslant 0.01$ to $n \approx 1$. Under normal conditions, nickel hydride is unstable and completely decomposes over a period of a few days.

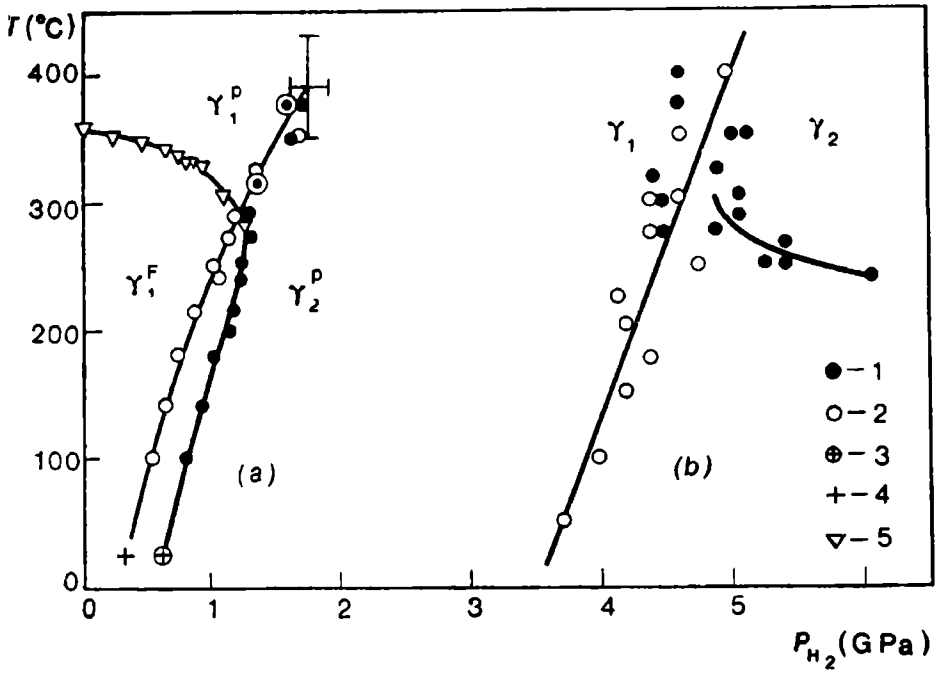

Fig. 4.14. T vs. P_{H_2} phase diagrams for Ni-H [4.43, 13] (*a*) and Rh-H [4.47] (*b*) systems.
1, *2*—pressures corresponding to $\gamma_1 \rightarrow \gamma_2$ and $\gamma_2 \rightarrow \gamma_1$ transitions respectively; *3*, *4*—the same (results of [4.53, 114]); *5*—Curie points; γ^F and γ^P represent the ferromagnetic and paramagnetic phases, respectively.

The T-P_{H_2} phase diagram for the Ni-H system [4.43, 13] is shown in Fig. 4.14. The values of pressures corresponding to the $\gamma_1 \rightarrow \gamma_2$ and $\gamma_2 \rightarrow \gamma_1$ transitions were obtained from the position of anomalies on the electrical resistance isotherms (a typical R vs. P_{H_2} isotherm is presented in Fig. 4.12). It can be seen from Fig. 4.14 that the hysteresis in the $\gamma_1 \rightleftarrows \gamma_2$ transformation declines with a rise in temperature and completely disappears at $T \gtrsim 270°$ C. In turn, the maximum solubility of hydrogen in the γ_1-phase increases while its minimum solubility in the γ_2-phase decreases with temperature [4.13], and at $T_{cr} \approx 390°$ C and $(P_{H_2})_{cr} \approx 1.75$ GPa, the line of the $\gamma_1 \rightleftarrows \gamma_2$ phase transformation terminates at a critical point of the liquid-vapour type (the coordinates of the critical point are obtained by extrapolating the data for Ni-Fe-H solutions [4.44]).

Nickel is a ferromagnet with its Curie point at $T_C \approx 354°$ C, and in the region of existence of the γ_1-phase on the T-P_{H_2} diagram for the Ni-H system, an additional curve of Curie points appears [4.43], above which the γ_1-solutions are paramagnetic and below which they are ferromagnetic (the γ_2-solutions are paramagnetic down to liquid-helium temperatures [4.45]). A considerable lowering of Curie points (by $\sim 76°$ C at $P_{H_2} = 1.25$ GPa) for the γ_1-solutions Ni-H with in-

creasing pressure is due to an increase in the equilibrium solubility of hydrogen in nickel, since in an inert medium the Curie point of nickel rises by about 4° C at $P = 1.25$ GPa, see [4.46]. The high sensitivity of Curie points to the hydrogen content of the γ_1-solutions Ni-H is worth noting: at $P_{H_2} = 1.25$ GPa and $T = 270°$ C, the hydrogen concentration in the solution is just $n \approx 0.02$.

Under atmospheric pressure and at $T \leqslant -20°$ C (when the samples are hindered from exchanging hydrogen with the surroundings), the maximum solubility of hydrogen in the γ_1-phase of the Ni-H solutions amounts to $n_{\gamma_1}^{max} \leqslant 0.02$. At $n_{\gamma_1}^{max} < n < n_{\gamma_2}^{min} \approx 0.7$, the samples consist of a mixture of the γ_1- and γ_2-phases with compositions $n_{\gamma_1}^{max}$ and $n_{\gamma_2}^{min}$, while at $n_{\gamma_2}^{min} \leqslant n \leqslant 1.25$, the γ_2-phase is stable [4.45]. At atmospheric pressure and $T = -190°$ C, the parameter a for the fcc metal lattice of the γ_2-solutions Ni-H is approximately equal to 3.72 Å and remains practically unchanged over a wide range of concentrations ($0.7 \leqslant n \leqslant 1.25$). Experimental investigations have revealed that nickel hydride with $n = 1.18$ is not superconducting at temperatures above 1.2 K [4.13].

Ru-H. Ruthenium has an hcp lattice. At $T = 250°$ C, the solubility of hydrogen in ruthenium monotonically increases with pressure and attains the value $n \approx 0.03$ at $P_{H_2} = 9$ GPa. The electrical resistance isotherms for ruthenium in hydrogen and in an inert medium are shown in Fig. 4.7. Under normal conditions, the Ru-H samples are unstable with respect to decomposition into the metal and molecular hydrogen.

Rh-H. Rhodium hydride was first synthesized under high hydrogen pressure [4.19]. The T-P_{H_2} phase diagram for the Rh-H system was constructed in [4.47] from a location of abrupt changes in the electrical resistance isotherms (typical isotherms are shown in Fig. 4.3) and is presented in Fig. 4.14. Our recent measurements have revealed that the $\gamma_1 \rightarrow \gamma_2$ transition is accompanied by an abrupt increase in the solubility of hydrogen in fcc rhodium from $n \approx 0.01$ to $n \approx 1$.

The decomposition of the hydride into the metal and molecular hydrogen begins under atmospheric pressure at $T \geqslant -100$ to $-60°$ C. At $T = -190$ °C, the period of the fcc metal lattice of rhodium hydride with $n = 1.02 \pm 0.03$ is $a = 4.020$ Å. A superconducting transition in rhodium hydride was not observed at temperatures down to 2 K.

Pd-H. Palladium hydride was first synthesized through a direct interaction of the metal with hydrogen and was fairly widely investigated even in the 19th century [4.48]. Like nickel, palladium forms a wide range of interstitial solid solutions with hydrogen on the basis of an fcc lattice of the metal. The T-c diagram of the Pd-H system shows a hump of stratification into the isomorphic γ_1- and γ_2-phases

(depleted and enriched in hydrogen). The parameters of the critical point are given by $T_{cr} = 292°$ C, $(P_{H_2})_{cr} = 1.97$ MPa, and $n_{cr} = 0.25$ [4.11]. Above room temperature and at hydrogen pressures up to 6.7 GPa, other transformations in the Pd-H system do not take place and the solubility of hydrogen in palladium simply increases monotonically with pressure [4.12]. Figure 4.12 demonstrates a typical isotherm for the electrical resistance of the γ_2-solution Pd-H. It is interesting to note that while a hydrogen pressure of just 1 kPa (at room temperature) is sufficient to obtain a Pd-H solution with $n \approx 0.6$, solutions with $n > 1$ cannot be synthesized even at $P_{H_2} = 7$ GPa.

During the last decades, the Pd-H system has attracted the attention of a large number of research workers due to the discovery of the so-called "55 K anomaly" in the temperature dependence of the specific heat of the γ_2-solutions with $n \lesssim 0.8$ [4.49], as well as the discovery of superconductivity in the solutions with $n \gtrsim 0.8$ [4.50]. A detailed description and discussion of the results of investigations in the Pd-H system can be found in the review articles [4.11, 51].

Os-H. This system is completely analogous to the Ru-H system, the only difference being that at $T = 250°$ C and $P_{H_2} = 9$ GPa, the solubility of hydrogen in osmium is about ten times lower than in ruthenium and constitutes $n \approx 0.003$.

Ir-H and Pt-H. Iridium and platinum are metals with an fcc lattice. The concentration of hydrogen in samples obtained by keeping 0.1 mm thick foils of these metals under a hydrogen pressure of 9 GPa at $T = 250$ °C attained the value $n \approx 0.005$. Under atmospheric pressure and at room temperature, all the hydrogen is liberated from the samples over a few minutes. It should, however, be noted that the electrical resistivity of iridium and platinum in hydrogen at 250° C behaved practically in the same manner as in an inert atmosphere (see Fig. 4.7). In this respect, it remains unclear whether hydrogen was actually dissoluted in the bulk of the metal or whether there was, say, just an adsorption of hydrogen over macroscopic defects in the course of the experiment.

Ni-Me-H systems. The main body of data on the magnetic properties of hydrides of transition metals, which are described and analysed in Sec. 4.4, was obtained from an investigation of the solutions of hydrogen in the alloys of nickel with Cu, Co, Fe, Mn, and Cr. Hence, it is expedient to briefly describe the changes introduced in the structure and phase composition of the solutions as a result of replacing nickel by these metals.

Nickel forms a wide range of disordered substitutional solid solutions with these metals on the basis of an fcc lattice [4.52]. During the formation of the Ni-Me-H solutions, hydrogen occupies the interstices in this lattice. Substitution of nickel by other metals leads to a smooth deformation of the T-P_{H_2}-c diagram of the Ni-H system, the

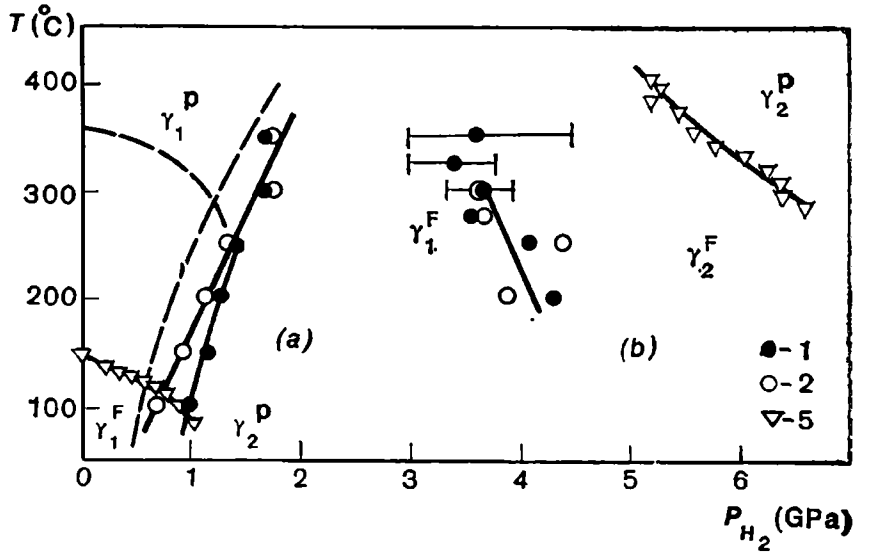

Fig. 4.15. T vs. P_{H_2} phase diagrams for the $Ni_{95}Cr_5$-H system (results of the present paper) (*a*), and $Ni_{40}Co_{60}$-H system [4.40] (*b*). The notation is the same as in Fig. 4.14. The dashed lines show the curve for $\gamma_2 \rightarrow \gamma_1$ transitions and the Curie temperature line for the system Ni-H [4.43, 13].

critical temperature of stratification into the γ_1- and γ_2-phases decreasing in all cases. By way of an illustration of the observed effects, Fig. 4.15 shows the variation of the T-P_{H_2} diagram of the Ni-H system when nickel is replaced by cobalt and chromium. In particular, it can be seen from Fig. 4.15 that doping by these metals shifts the line of the $\gamma_1 \rightleftarrows \gamma_2$ phase transformation towards the region of higher pressures. The addition of iron has a similar effect on the pressure of the $\gamma_1 \rightleftarrows \gamma_2$ transformation [4.44, 53], while a substitution of nickel by copper [4.54, 55] or manganese [4.56, 57] practically does not change the position of the line of the $\gamma_1 \rightleftarrows \gamma_2$ transformation on the T-P_{H_2} diagram. If nickel contains more than $\sim$ 40 at. % Cu, $\sim$ 15 at. % Fe, or $\sim$ 20 at. % Mn, the critical temperature of phase separation in the corresponding Ni-Me-H systems falls below room temperature and at $T \geqslant 25°$ C, the solubility of hydrogen in alloys with a larger concentration of the doping element becomes a continuous function of pressure. Investigations of the Ni-Me-H samples, which were preliminarily saturated with hydrogen at high pressures and which were metastable at atmospheric pressure, showed that at $P \approx 0.1$ MPa, the critical temperature falls below the room temperature at lower concentrations of the doping metal (for example, a separation into the γ_1- and γ_2-phases in the case of Ni-Fe-H solutions [4.58] was not observed even in $Ni_{90}Fe_{10}$-H samples).

The dependences of increase in the volume of an elementary cell on hydrogen concentration are similar for the γ-alloys Ni-Me. For

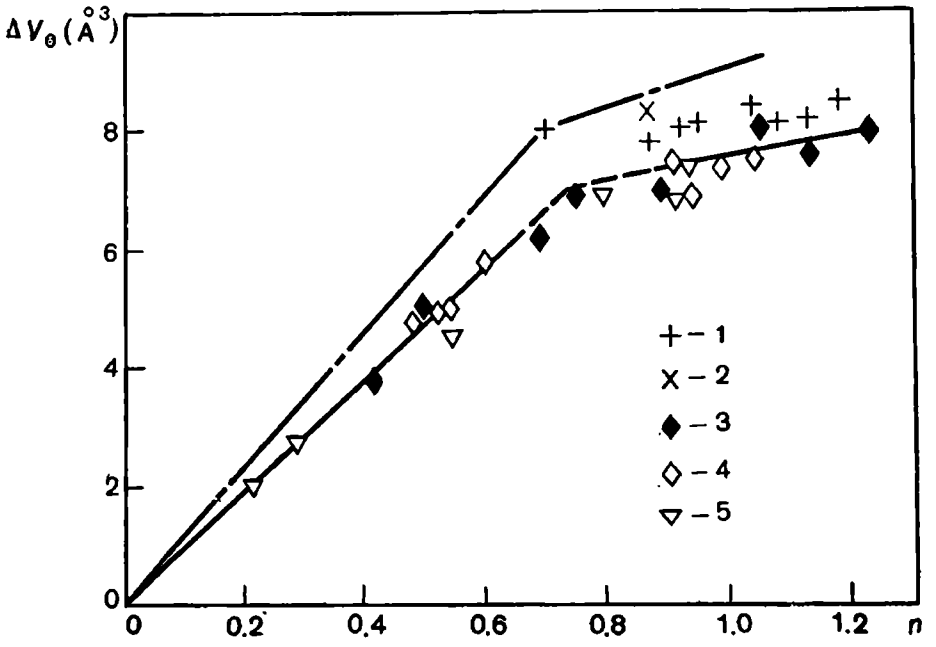

Fig. 4.16. ΔV_0 vs. n dependence for the increase in the volume of unit cell for fcc metals and alloys.
1—Ni, $T = 293$ K [4.13]; *2*—Ni, $T = 293$ K [4.115]; *3* and *4*—Ni-Fe alloys with 20 and 67.6 at. % Fe respectively, $T = 83$ K [4.58]; *5*—$Fe_{65}Ni_6Mn_{29}$, $T = 83$ K [4.83]; the dot-and-dash line shows the ΔV_0 (n) dependence for palladium-based alloys at room temperature [4.59].

most of the alloys, these dependences have a common feature: at $n \gtrsim 0.7$-0.8, a decrease in their slope $\beta = (\partial/\partial n)\, \Delta V_0$ (n) is observed. For example, the slope for the $Ni_{80}Fe_{20}$ and $Ni_{32.5}Fe_{67.5}$ alloys changes from $\beta \approx 9.5$ Å^3 for $n < 0.8$ to $\beta \approx 2.5$ Å^3 for $n > 0.8$, see Fig. 4.16 (for the sake of clarity, the ΔV_0 vs. n dependence for $n < 0.8$ and $n > 0.8$ is approximated by straight line segments). A similar trend was earlier observed for the ΔV_0 vs. n dependence for palladium-based alloys [4.59]. The nature of this effect is not yet understood. Some possibilities for explaining it are opened up by the investigations of hydrogen solutions in nickel and nickel-based alloys, for which the concentrations $n > 1$ has been obtained. Indeed, for $n \approx \approx 0.6$ and at room temperature, hydrogen in nickel occupies octahedral interstices [4.60] whose number in an fcc lattice is equal to the number of lattice points. When all these interstices are filled in, the γ-hydride will have a concentration $n = 1$. Consequently, γ-solutions with $n > 1$ must be different in structure as compared to solutions with $n \approx 0.6$. The only anomaly in the ΔV_0 vs. n dependences for the Ni-H and Ni-Me-H γ-solutions at hydrogen concentrations up to 1.23 (for the $Ni_{80}Fe_{20}$-H solution) is observed at $n \approx \approx 0.8$, and it is logical to assume that this anomaly is due to the on-

set of a structural rearrangement. As to the rearrangement, it may involve, for example, the occupation of a part of the tetrahedral interstices for $n > 0.8$, whose number in an fcc lattice is equal to two per lattice point (although in this case, due to the smaller dimensions of the tetrahedral pores, the partial volume of hydrogen, characterized by the value of β, is more likely to increase than decrease). It also cannot be excluded that even for $n > 0.8$, hydrogen continues to occupy only octahedral interstices whose number per lattice point increases due to an increase in the number of vacancies in the fcc lattice of the metal for $n > 0.8$.

In conclusion of this section, it is worth noting that upon a decrease in temperature even down to $T \leqslant 4.2$ K, none of the investigated samples of nonstoichiometric solid solutions Ni-Me-H revealed an ordering or a separation into phases of stoichiometric (with respect to hydrogen) composition. Generally speaking, such phenomena could be expected from the requirement of minimum configurational entropy. This is probably due to the fact that the corresponding critical temperatures are very low and thermodynamically equilibrium states are not attained for kinetic reasons.

4.4. MAGNETIC PROPERTIES OF METAL-HYDROGEN SOLUTIONS

The 3*d*-metals of VI-VIII groups and alloys based on these metals are characterized by the existence of a magnetic order. Experiments have shown that in the case of transition metals, hydrogenation does not lead to a unique variation of their magnetic properties, for example, to a decrease in the temperature of transition to the magnetically ordered state, which is a dominating trend in the case of hydrogenation of rare-earth metals [4.61]. On the contrary, the effects have turned out to be very diverse. In particular, the following phenomena are observed upon hydrogenation of pure metals.

Chromium, which has a bcc lattice, is an antiferromagnet with the Néel temperature $T_N = 312$ K; the ε-hydride $CrH_{0.97}$ is paramagnetic down to helium temperatures [4.62, 63]. The low-temperature modification of manganese (α-Mn) is an antiferromagnet with $T_N = 100$ K; in the concentration range of $0.65 \leqslant n \leqslant 0.94$, the ε-solutions Mn-H possess a spontaneous magnetization which increases monotonically with concentration of hydrogen in the solution, but even at $n = 0.94$ remains very small ($\leqslant 0.02$-$0.05\mu_B$ per Mn atom at $T = 82$ K; μ_B is the Bohr magneton), while the Curie point attains quite high values $T_C > 280$ K [4.27]. Iron with a bcc structure is a ferromagnet with $T_C = 1043$ K, which has at $T = 0$ K a spontaneous magnetization $\sigma_0 = 2.22\ \mu_B$ per atom; the ε-hydride $FeH_{0.8}$ is also

a ferromagnet with nearly the same value of $\sigma_0 = 2.2\mu_B$ per Fe atom [4.37] and with $T_C > 670$ K [4.31, 37]. Dissolution of hydrogen in the hcp modification of cobalt (ferromagnet with $\sigma_0 = 1.72$ μ_B per atom) leads to a slight decrease in the spontaneous magnetization (see [4.64], and also Fig. 4.26). Fcc nickel is a ferromagnet with $T_C = 627$ K and $\sigma_0 = 0.616$ μ_B per atom. Introduction of hydrogen causes a decrease in the value of T_C (see Fig. 4.14) and also lowers the magnetization σ_0; in the concentration range $0.7 \leqslant n \leqslant 1.18$, the γ_2-solutions Ni-H are paramagnetic at $T \geqslant 4.2$ K [4.45].

A simple listing of the above facts already indicates that it is, in any case, not easy to construct a consistent picture of the effect of hydrogen on the magnetic properties of transition metals, limiting the study to the properties of Me-H solutions based on the elements only. In this connection, it was very fruitful to investigate the hydrogen solutions in fcc alloys of 3*d*-metals, and, primarily, in the nickel-based alloys. Nickel-based alloys have for a long time been the subject of intensive experimental investigations, and the large body of experimental data accumulated over the years provides an exact picture of the effect of the doping substitution elements on the magnetic properties of materials (see [4.65, 66]). The alloys form a wide range of continuous γ-solutions with hydrogen, which permits a systematic investigation of the effect of the addition of hydrogen on these properties. Finally, the magnetic properties of fcc alloys based on nickel are correctly described by the band theory of magnetism, thus creating a proper base for the interpretation of the effects arising as a result of hydrogenation.

4.4.1. Magnetic Properties of Ni-Me Alloys

In the band theory of magnetism, the electrons, which partially fill the conduction band, are the carriers of the magnetic moment. The exchange interaction leads to the dependence of the energy of the electrons on the orientation of their magnetic moment which, in the first approximation, can be represented as the relative shift of the electron subbands for opposite directions of spins by the energy $\Delta = I\sigma$, where I is the effective exchange interaction parameter. Usually, it is assumed that the Fermi level in transition metals intersects the overlapping narrow *d*-band (with a high density of electron states) and the wide *s*-band (with a low density of states), the magnetic properties of the material being mainly determined by the structure of the *d*-band and the degree to which it is filled. It should be noted that in spite of the evident roughness of these approximations, such an approach permits a quantitative description of the temperature, field, pressure, and concentration dependences of the macroscopic magnetic characteristics in the case of fcc alloys based on 3*d*-metals (see, for example, [4.65-68]).

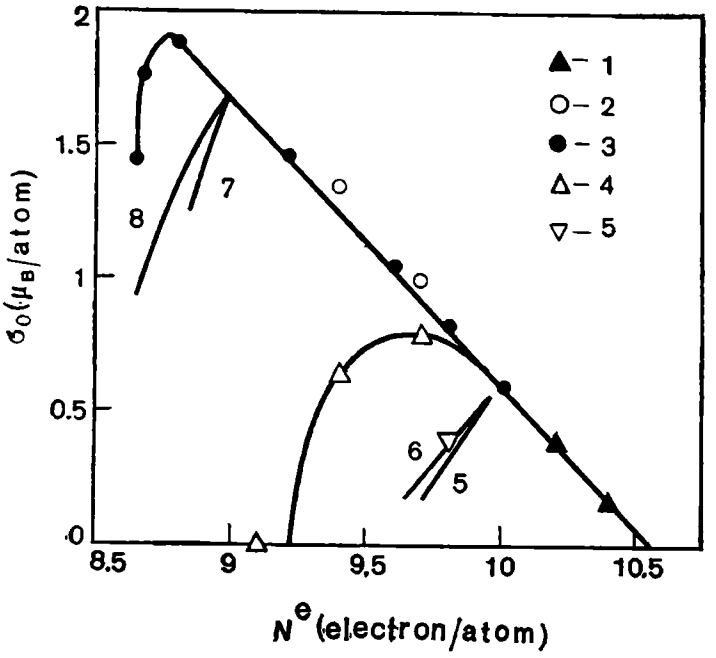

Fig. 4.17. Spontaneous magnetization σ_0 at $T = 0$ K as a function of the average number N^e of $(3d + 4s)$ electrons per atom in binary fcc alloys (see [4.65, 66]).
1—Ni-Cu; *2*—Ni-Co; *3*—Ni-Fe; *4*—Ni-Mn; *5*—Ni-Cr; *6*—Ni-V; *7*—Co-Cr; *8*—Co-Mn.

The dependence of spontaneous magnetization σ_0 on concentration at 0 K for fcc alloys of *3d*-metals is customarily represented in the form of the Pauling-Slater curve (Fig. 4.17) as a function of the average number N^e of $3d + 4s$ electrons (present in an isolated atom) per atom of the alloy. Figure 4.17 shows the experimental values of σ_0 for Ni-Me alloys serving as a basis for obtaining the solid hydrogen solutions considered in this paper.

The following characteristic property of the Pauling-Slater curve is worth noting: the values of σ_0 for the alloys of nickel with cobalt, copper and iron (for atomic fraction of iron $x_{Fe} \leqslant 0.6$) fall on a single straight line with a slope $\partial\sigma_0/\partial N^e \approx -1.05\ \mu_B$ per electron. Nickel is well described by the band theory of ferromagnetism, and near 0 K it can be considered as a strong itinerant ferromagnet for which one half of the *d*-band ($d\uparrow$ with spins pointing up) is filled completely, while the other half ($d\downarrow$ with spins pointing down) is only partially filled [4.68]. This is shown schematically in Fig. 4.18*a*. The magnitude of σ_0 is related to the number of electrons with uncompensated spin, i.e., in this case, simply to the number of holes $p\downarrow$ in the $d\downarrow$-subband, through the relation $\sigma_0 = (1/2)g\mu_B \cdot p\downarrow \approx \mu_B p\downarrow$, since for nickel (and for alloys based on nickel) the spectroscopic factor $g \approx 2.2 \sim 2$, see [4.66] (which indicates the smallness of the or-

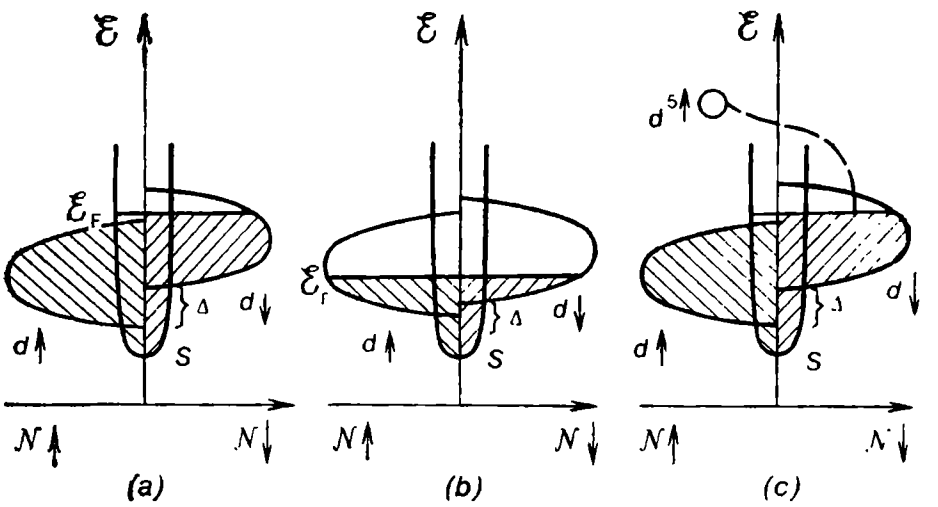

Fig. 4.18. Band structure diagrams for itinerant ferromagnets at $T = 0$ K.
a—strong ferromagnet; *b*—weak ferromagnet; *c*—diagram illustrating the flow of electrons from the virtual impurity bound state $d^5\uparrow$ to the $d\downarrow$-subband of a strong ferromagnet. $\mathscr{E}$ is the energy of states; $\mathscr{N}\uparrow$ and $\mathscr{N}\downarrow$ represent the density of states with upward and downward spins; $\mathscr{E}_F$ is the Fermi energy; $\Delta = I\sigma_0$.

bital contribution, i.e. nearly pure spin origin of magnetization in these materials). The linear dependence of σ_0 on N^e with a slope $\partial\sigma_0/\partial N^e \approx -1\mu_B$ per electron for the alloys of nickel with Cu, Co, and Fe are well explained if it is assumed [4.65] that alloying nickel with these elements (1) does not lead to deformation of the curves for the density of electron states $\mathscr{N}\uparrow(\mathscr{E})$ and $\mathscr{N}\downarrow(\mathscr{E})$, only shifting them in energy, relative to one another, as a single entity (this approximation is called the rigid band approximation for ferromagnets; the physical significance of this approximation and the limits of its applicability are discussed in [4.66]). (2) The alloys remain strong ferromagnets (with completely filled $d\uparrow$-subband). Indeed, in this case, the changes in σ_0 upon doping will stem primarily from the change in the number of holes in the $d\downarrow$-subband and, hence,

$$\sigma_0(x_{Me}) \approx \sigma_0^{Ni} + \Delta Z \mu_B x_{Me}, \tag{4.1}$$

where $\Delta Z = Z_{Ni} - Z_{Me}$ is the difference in the nuclear charges of nickel and the impurity. This is what as actually observed in experiments.

As can be seen from Fig. 4.17, the behaviour of the dependence of σ_0 on N^e for many alloys deviates from that predicted by the rigid band model for strong itinerant ferromagnets. For Ni-Fe alloys with $x_{Fe} \gtrsim 0.63$, this deviation is apparently related to the appearance of a significant number of holes in the $d\uparrow$- as well as in the $d\downarrow$-subbands [4.70]. The corresponding band scheme is shown in Fig. 4.18*b*.

The fact that the spontaneous magnetization may decrease rather than increase with increasing number of holes in the d-band in itinerant ferromagnets with holes in both d-subbands at $T = 0$ K (such ferromagnets are called weak) can be illustrated in the following manner. Let, as in Fig. 4.18*b*, $\mathcal{N}\uparrow(\mathcal{E}_F) > \mathcal{N}\downarrow(\mathcal{E}_F)$, where $\mathcal{E}_F$ is the Fermi level. Then, with a decrease in the occupancy of the d-band by electrons, the number of holes in the $d\uparrow$-subband will rise more rapidly than in the $d\downarrow$-subband, and $\sigma_0 = (1/2)\, g\mu_B\,(p\downarrow - p\uparrow) \approx \mu_B\,(p\downarrow - p\uparrow)$ will decrease.

The "anomalous" dependences of σ_0 on N^e, like those observed for Ni-Cr and Ni-V alloys, when the strong deviation from the straight line with a slope $\partial\sigma_0/\partial N^e \approx -1\mu_B$ per electron appears already at low concentrations of the doping element, were explained by Friedel [4.69] by using the concept of "virtual bound states". According to Friedel, when an atom of a transition impurity appears in a metal, the d-level of this atom, which is higher in energy than the bottom of the conduction band, becomes delocalized. However, in the space of coordinates and energy there remains a "virtual d-level", viz. the region where (1) the amplitude of the spherical component of the wave function with $l = 2$ is anomalously large, and (2) this amplitude corresponds to the excess charge density, which, being summed over the entire region, is approximately equal to the charge of the initial bound d-state (which is $2l + 1 =$ five-fold degenerate). This virtual level may split into sublevels with opposite spins due to the intra-atomic exchange interaction, if the metal-solvent has a sufficiently narrow conduction band (and more so, if it is a ferromagnet).

In the case of nickel, as long as the virtual $d^5\uparrow$-sublevel lies below the Fermi level, alloying will lead to changes as in the rigid band model for strong itinerant ferromagnets (see (4.1)). This is due to the fact that screening of the excess impurity charge is mainly ensured by a part of the d-band with a high density of states at the Fermi level, i.e. by the $d\downarrow$-subband, the characteristic screening radius being less than or of the order of the interatomic distance [4.69]. Therefore, the magnetic moments of the nickel matrix and of the impurity must be independent of the impurity concentration:

$$\begin{cases} \mu_{matr} = \text{const}, \\ \mu_{imp} = \mu_{matr} + \Delta Z \mu_B. \end{cases}$$

This leads to the formula (4.1) for the average magnetic moment $\bar{\mu} = \sigma_0$ of the alloy.

The larger the difference ΔZ (i.e. the farther the impurity element is to the left of nickel in the Periodic Table), the higher the perturbing potential (repulsive in nature) introduced by the impurity. It may be expected that for a certain value of ΔZ, this potential will be large enough to take the virtual $d^5\uparrow$-state out of the filled half of

the *d*-band and to shift it in energy above the Fermi level. This situation is schematically shown in Fig. 4.18*c*. The electrons from such a state pour out into the conduction band and mainly fall into the $d\downarrow$-subband with opposite spin due to its high density of states at the Fermi level (dotted line in Fig. 4.18*c*). The state with $l = 2$ is five-fold degenerate. Consequently, when the virtual $d^5\uparrow$-level crosses the Fermi level, five electrons from the states with upward spin go over into the states with downward spin, thus changing the spontaneous magnetization by $\sim 10\ \mu_B$. This leads to the following formula for the average magnetic moment of the alloy:

$$\sigma_0 (x_{Me}) \approx \sigma_0^{Ni} + (\Delta Z - 10)\ \mu_B x_{Me}, \qquad (4.2)$$

which is in good agreement with the slopes of the σ_0 vs. N^e dependences for alloys of nickel with chromium, vanadium, and titanium.

Thus, if the impurities are listed in order of decreasing atomic numbers, the following picture is observed when Ni is alloyed with other 3*d*-metals. Copper, cobalt, iron, and (partially) manganese do not change the band structure of nickel very much, and over a wide range of the alloy compositions, the σ_0 vs. x_{Me} dependences are determined mainly by changes in the electron concentration N^e. With alloying by elements with $Z < Z_{Cr}$, both changes in N^e and in the band structure play an important role.

4.4.2. Ni-Me-H Solutions

Friedel's analysis of the proton screening conditions in transition metals [4.71] showed that the state of hydrogen in metals at the beginning of the *d*-series must be closer to H^-, and in metals at the end of these series, to H^+. In recent years, a series of quantum-mechanical calculations of the band structure of hydrides of 3*d*- and 4*d*-metals, among which the seminal work by Switendick deserves special mention [4.72], have been performed. The results of all the calculations, which were carried out by using different methods (APW method [4.72-75], model Hamiltonian method [4.76]), with a different choice of crystal potentials and self-consistent calculations [4.73, 74], are in good agreement with each other and give for γ- and ε-solutions with $n \leqslant 1$ the following pattern for the effect of hydrogen on the band structure of the metals at the end of the 3*d*- and 4*d*-series of the Periodic Table. A new hydrogen band below the Fermi level is not formed in such hydrides, i.e the hydrogen states are actually close to H^+ and the hydrogen atoms are electrons donors in the conduction band of the host metal. At the same time, the dissolved hydrogen strongly deforms the band structure of the metal, both the H-Pd and H-H interaction playing an important role. This deformation, however, has a selective character. The *d*-type states, especially in the upper part of the *d*-band (which is responsi-

ble for the magnetic properties of a material), change only slightly, while the energy of the *s*-states decreases significantly. The latter leads to an increase in the number of states below the Fermi energy of the host metal with increasing number of protons in its interstices. Thus, only a part of the electrons ($\eta \approx 0.4$-0.1 electron per proton for Pd and Ni [4.72]), supplied by hydrogen atoms to the conduction band, occupies states above the Fermi level, while another part goes into these additional levels below it. Qualitatively, this effect can be illustrated with the help of the diagrams shown in Fig. 4.18, assuming that with increasing hydrogen concentration in the metal, the curve for the density of the *s*-states is shifted down in energy with respect to the curves for the density of the $d\uparrow$- and $d\downarrow$-states. It should be noted that in view of the high density of the *d*-states at the Fermi level, nearly all the electrons with energy $\mathscr{E} > \mathscr{E}_F$ of the host metal must occupy just these states, i.e. each hydrogen atom is a donor of η electrons into the *d*-band of the metal.

Calculations of the band structure of hydrides of transition metals have explained (in many cases quantitatively) the results of the experimental investigation of the electron heat capacity, magnetic susceptibility, photoemission spectra, and other physical properties, including superconductivity, for a number of Me-H systems (see [4.72-74, 76, 11]). For the Ni-Me-H solutions, these calculations have served as a theoretical basis for justifying the use of the "rigid *d*-band model" to describe their magnetic properties [4.56]. According to this model, the change in these properties upon hydrogenation is mainly caused by the increase in the degree of filling of the *d*-band of the host metal, hydrogen being considered as the donor of a fractional number of electrons $\eta \leqslant 1$ electron per atom to the *d*-band. It should, however, be emphasized that such a model is not a direct consequence of band calculations, since the magnetic properties are also affected by a variation in the exchange interaction which is not yet possible to estimate correctly; the strong volume effects accompanying dissolution of hydrogen in Ni-Me alloys must also be kept in mind.

The diversity of the magnetic properties of Ni-Me alloys make them convenient model objects for clarifying various aspects of the influence of hydrogen. We shall now describe the most significant results of experimental investigations of the magnetic properties of a number of Ni-Me-H systems and show that the behaviour of these properties can be unambiguously explained within the framework of the rigid *d*-band model.

4.4.2.1. Ni-Fe-H system. Figure 4.19 shows the σ_0 vs. n dependences for γ-solutions of hydrogen in nickel [4.45] and Ni-Fe alloys [4.58]. The γ_2-phase of Ni-H solutions is paramagnetic at $T \geqslant 4.2$ K, the minimum solubility of hydrogen in this phase at $T < 250$ K being $n_{\gamma_2}^{\min} = 0.7$ [4.45]. Samples with $n < 0.7$ consist of a mixture of γ_1- and γ_2-phases, while their magnetization is proportional to the

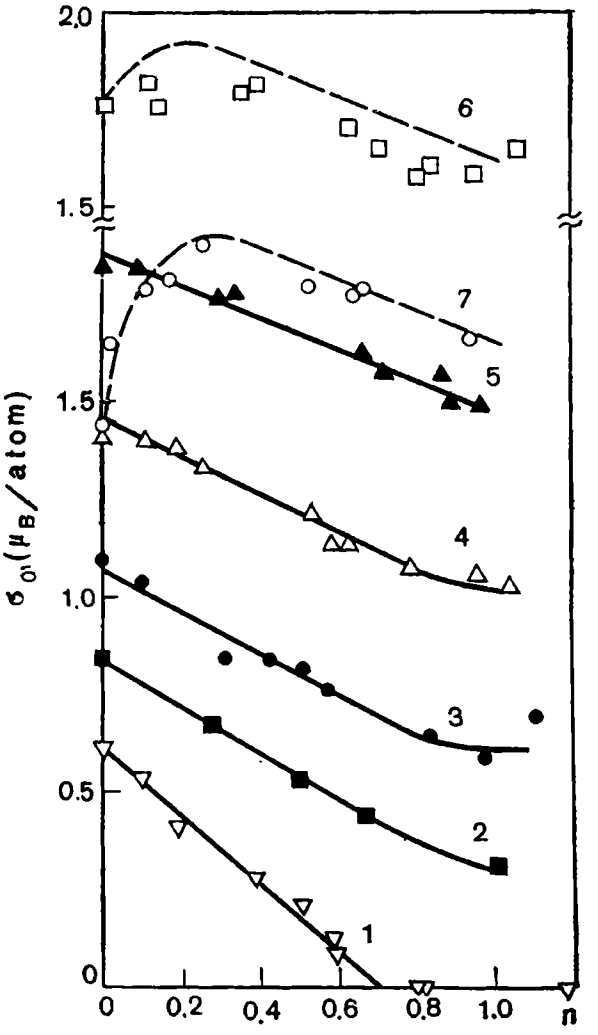

Fig. 4.19. Dependence of the spontaneous magnetization σ_0 at $T = 0$ K and under atmospheric pressure on the hydrogen concentration n in Ni-Fe alloys with different iron contents [4.58].
At. % Fe: *1*—0; *2*—10; *3*—20; *4*—40; *5*—60; *6*—66.1; *7*—67.5. The dashed lines show the σ_0 (n) dependences for alloys with 66.1 and 67.5 at. % Fe, calculated by using the relation (4.4.3). σ_0 is given in μ_B/atom of the Ni-Fe alloy.

content of the γ_1-phase with $\sigma_0\,(n_{\gamma_1}^{max}) \approx \sigma_0^{Ni}$. A separation into γ_1- and γ_2-phases was not observed in hydrogen solutions in Ni-Fe alloys with $x_{Fe} \geqslant 0.1$.

The first thing that draws attention in the σ_0 vs. n dependences for the alloys with $0.1 \leqslant x_{Fe} \leqslant 0.6$ is the presence of a linear section for $n \leqslant 0.8$ and deviation from linearity for $n > 0.8$. It should be recalled that the composition $n \approx 0.7$-0.8 is singular for all investigated γ-solutions of hydrogen in nickel- (and palladium-) based alloys:

the nature of the ΔV_0 vs. n dependences changes for $n > 0.8$ (see Fig. 4.16). The reasons behind the appearance of this anomaly are not clear, so it is expedient to confine the discussion to the magnetic properties of Ni-Fe-H solutions with $n \leqslant 0.8$. The values of the slopes $\partial\sigma_0/\partial n$ obtained with a linear approximation to the experimental σ_0 vs. n dependences at $n \leqslant 0.8$ for alloys containing $\leqslant 60$ at. % Fe, decrease monotonically and nearly linearly in absolute magnitude with increasing iron content in Ni-Fe alloys (and, correspondently, with decreasing electron concentration N^e of these alloys) from $\sim 0.6\mu_B$ per H atom for $x_{Fe} = 0.1$ to $\sim 0.4\mu_B$ per H atom for $x_{Fe} = 0.6$.

Ni-Fe alloys with $x_{Fe} \leqslant 0.6$ are strong itinerant ferromagnets. It should be noted that as long as the ferromagnet remains strong (i.e., at $T = 0$ K, holes are present only in its $d\downarrow$-subband), the value $\sigma_0 \propto p\downarrow = p$, viz. the total number of holes in the d-band. So, σ_0 is independent of the change in the exchange interaction and of the deformation of the bands if it does not cause a change in p. In the rigid band approximation ("proton" model), the hydrogenation of such ferromagnets should, therefore, lead to a decrease in their magnetization with a slope $\partial\sigma_0^r/\partial n \approx -1\mu_B$ per H atom. If, as a result of hydrogenation, holes appear both in the $d\downarrow$- and $d\uparrow$-subbands, this will cause a decrease in σ_0 with $|\partial\sigma_0/\partial n| > |\partial\sigma_0^r/\partial n|$, since the lowering of σ_0 due to filling of the $d\downarrow$-subband by the hydrogen electrons will be supplemented by the effect of the transfer of the electrons from $d\uparrow$-subband to $d\downarrow$-subband. For hydrogen solutions in Ni-Fe alloys with $x_{Fe} \leqslant 0.6$, the slopes $|\partial\sigma_0/\partial n| \approx 0.5\ \mu_B$ per H atom are less than $|\partial\sigma_0^r/\partial n|$. It is reasonable to ascribe this to the changes in the band structure of the Ni-Fe alloys occurring upon hydrogenation and accompanied by an increase in the number p of holes in the d-band. In the framework of the rigid d-band model, the experimental values of $\partial\sigma_0/\partial n$ may be explained by considering hydrogen as a donor of a fractional number of electrons $\eta \approx 0.5$ electron per H atom to the d-band of Ni-Fe alloys.

Let us go back to Fig. 4.19. A comparison with Fig. 4.17 shows that for all Ni-Fe alloys with $x_{Fe} \leqslant 0.675$, the concentration dependences of σ_0 with the introduction of hydrogen into the alloys and with the substitution of iron by nickel are similar: for a certain concentration, σ_0 attains its maximum value $\sigma_0^{max} \approx 1.86\text{-}1.9\mu_B$ per atom, and then begins to decrease. The similarity between σ_0 vs. n dependences for the alloys with 66.1 and 67.5 at. % Fe and the σ_0 vs. x_{Ni} dependence in the Ni-Fe system is even more complete, as can be shown in the following way. For alloys with $x_{Fe} \leqslant 0.6$, the magnetization decreases linearly both when Fe is replaced by Ni and when the hydrogen concentration is increased. Following [4.58], let us introduce for each specific Ni-Fe alloy with $x_{Fe} \leqslant 0.6$, the coefficient ξ, relating the changes in the composition of the binary Ni-Fe alloys

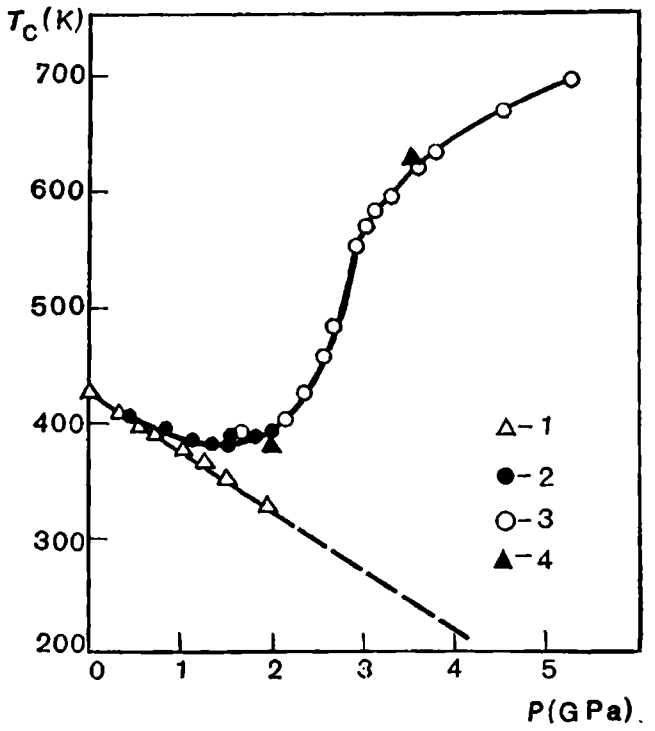

Fig. 4.20. Pressure dependence of the Curie temperatures of $Ni_{67.5}Fe_{32.5}$ alloy in an inert medium (*1*) (results of [4.87]) and in hydrogen (*2*) (results of [4.87]); *3*—results of [4.58]; *4*—values of T_C (n) calculated by using the relations (4.4.3) and (4.4.4).

and changes in n, leading to the same changes in σ_0:

$$\Delta x_{Fe} = \frac{(\partial\sigma_0/\partial n)}{(\partial\sigma_0/\partial x_{Fe})}\, n = -\xi n. \tag{4.3}$$

Extrapolation of the approximately linear ξ vs. x_{Fe} dependence to alloys with $x_{Fe} = 0.661$ and 0.675 gives $\xi \approx 0.185$. The σ_0 vs. n dependences for these alloys constructed with such a value of the scaling factor ξ are shown by the dotted lines in Fig. 4.19. It is seen that they are in agreement with the experimental data.

A similar correspondence occurs between the Curie points of the Ni-Fe alloys and hydrogen solutions based on them. The experimental dependences of the Curie points for the alloy with 67.5 at. % Fe on pressure in an inert medium and in hydrogen are shown in Fig. 4.20. It can be seen that in an inert medium, T_C of the alloy decreases linearly with a slope $(dT_C/dP)_{in} \approx -50$ K·GPa^{-1} with pressure up to 2 GPa. In a number of papers (for example, in [4.77]), it is shown that for Ni-Fe Invars the T_C vs. P dependence in an inert medium is nearly linear (dotted line in Fig. 4.20) at higher pressures as well. When measurements are carried out in a hydrogen atmosphere,

the hydrogen concentration in the alloy increases with pressure (right up to $n \approx 1$ at $P_{H_2} = 5.1$ GPa and $T = T_C$ of the $Ni_{32.5}Fe_{67.5}$-H solution at this pressure). This results in a significant deviation in the T_C vs. P_{H_2} dependence from that in an inert medium toward higher temperatures.

Assuming that the correspondence established by formula (4.3) between σ_0 of alloys with and without hydrogen is also valid for T_C and $(dT_C/dP)_{in}$, we get the following relation for Ni-Fe-H solutions:

$$T_C(P_{H_2}) = T_C(x_{Fe} - \xi n) + \left(\frac{dT_C(x_{Fe} - \xi \cdot n)}{dP}\right)_{in} P_{H_2}. \quad (4.4)$$

The values of T_C (P_{H_2}) for the $Ni_{32.5}Fe_{67.5}$-H solutions, calculated in [4.58] by using formula (4.4), are shown in Fig. 4.20 by solid triangles and are in good agreement with the experimental dependence. It was also shown in [4.58] that the relations (4.3) and (4.4) satisfactorily describe the behaviour of the T_C vs. P_{H_2} dependence for the non-Invar $Ni_{90}Fe_{10}$ alloy as well.

Thus, over the entire investigated concentration range $0.1 \leqslant x_{Fe} \leqslant 0.675$ for the Ni-Fe alloys, the $\sigma_0(n)$ and $\sigma_0(\Delta x_{Fe})$ dependences, as well as the $T_C(n)$ and $T_C(\Delta x_{Fe})$ dependences are similar and, in addition, have the same similarity factor ξ. Formally, this can be represented as a similarity in the dependences of σ_0 and T_C on electron concentration upon hydrogenation and upon replacement of Fe by Ni, respectively. The coefficients of such similarity, $\zeta = (Z_{Ni} - Z_{Fe})\xi = 2\xi$, will then give the "effective" number of electrons supplied by hydrogen to the conduction band of the metal. The existence of this similarity for Ni-Fe alloys with $x_{Fe} > 0.6$, which are weak itinerant ferromagnets (i.e. which have holes both in the $d\downarrow$- and $d\uparrow$-subbands at 0 K), is a strong argument in favour of the fact that in fairly wide ranges of concentration, the rigid band model is a good approximation for describing the magnetic properties of all fcc Ni-Fe alloys as well as the fact that the rigid d-band model can be used for hydrogen solutions based on these alloys.

4.4.2.2. Ni-Co-H system. In [4.40], we have investigated hydrogen solutions in fcc $Ni_{70}Co_{30}$ and $Ni_{40}Co_{60}$ alloys which are strong itinerant ferromagnets. As in strong itinerant Ni-Fe ferromagnets with $x_{Fe} \leqslant 0.6$, dissolution of hydrogen in these alloys decreases σ_0 and T_C. The linear approximation to the experimental σ_0 vs. n dependences for $n < 0.8$ gives slopes $\partial\sigma_0/\partial n = -0.76\mu_B$ and $-0.71\mu_B$ per H atom for the single-phase $Ni_{70}Co_{30}$-H and $Ni_{40}Co_{60}$-H solutions respectively, which agrees with the predictions of the rigid d-band model. An attempt to describe the $\sigma_0(n)$ and $T_C(n)$ dependences for the Ni-Co alloys with the same coefficients of similarity ξ (introduced through relations analogous to (4.3)) did

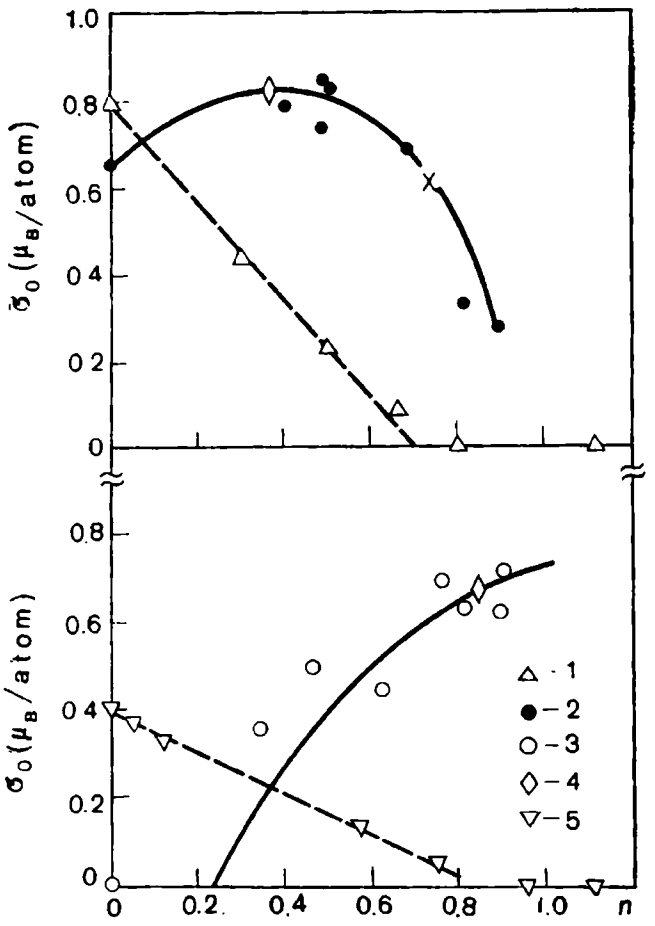

Fig. 4.21. Dependence of the spontaneous magnetization σ_0 at $T = 0$ K on the hydrogen concentration n in disordered Ni-Mn alloys [4.56] (*1*—10, *2*—20, *3*—30 At. % Mn; *4*—values of σ_0 used for calculating ξ), and in the $Ni_{95}Cr_5$ alloy (*5*—results of the present paper).

not lead to such a good agreement between the calculated and experimental values of $T_C(P_{H_2})$ as for the Ni-Fe alloys, but the sign and order of magnitude of the effect were found to be correct.

4.4.2.3. Ni-Mn-H system. The σ_0 vs. x_{Mn} dependence for disordered fcc Ni-Mn alloys is not monotonic (see Fig. 4.17). The spontaneous magnetization of nickel ($N^e = 10$ electrons per atom) is given by $\sigma_0^{Ni} \approx 0.616\ \mu_B$ per atom. Upon substituting manganese for nickel, σ_0 increases, attains its maximum value $\sigma_0^{max} \approx 0.8\mu_B$ per atom at $x_{Mn} \approx 0.1$, and then begins to decrease [4.66]. The Curie points decrease monotonically from 627 K for pure nickel to helium temperatures for the alloy with $x_{Mn} \approx 0.26$. The σ_0 (n) dependences obtained by us in [4.56] for hydrogen solutions in disordered Ni-Mn alloys with 10, 20, and 30 at. % Mn are shown in Fig. 4.21. Just as in the Ni-H system, a separation into γ_1- and γ_2-phases is observed

in the $Ni_{90}Mn_{10}$-H system at atmospheric pressure and $T \leqslant 150$ K. The γ_2-phase is paramagnetic at $T \geqslant 4.2$ K, and a nearly linear decrease in σ_0 in the range of hydrogen concentrations $0 \leqslant n \leqslant 0.7$ is caused by the decrease in the content of the ferromagnetic γ_1-phase in the two-phase mixture ($\gamma_1 + \gamma_2$) with increasing n. A separation of the $Ni_{80}Mn_{20}$-H and $Ni_{70}Mn_{30}$-H solutions into γ_1- and γ_2-phases was not observed.

The magnetization of the Ni-Mn-H solutions at room temperature was also investigated in [4.78] (for samples which were electrolytically saturated with hydrogen under atmospheric pressure) and in [4.79] directly under high hydrogen pressure. The results of these measurements are in accord with the data given in [4.56].

A comparison of Figs. 4.21 and 4.17 shows that as for Ni-Fe and Ni-Co alloys, the σ_0 (n) and σ_0 (Δx_{Mn}) dependences for Ni-Mn alloys are similar. Let us introduce the coefficients $\zeta = \Delta N^e/n$ relating the changes in composition and, correspondingly, electron concentration N^e in the initial alloys with the changes in n leading to identical changes in σ_0. A comparison of the values of σ_0 (n) for $Ni_{80}Mn_{20}$-H and $Ni_{70}Mn_{30}$-H solutions, shown in Fig. 4.21 by diamond-shaped symbols, with the values of σ_0 (x_{Mn}) presented in [4.66] for Ni-Mn alloys, gives $\zeta = 0.81$ and 0.48 electron per H atom, respectively. The σ_0 vs. n curves calculated for these values of ζ for the $Ni_{80}Mn_{20}$ and $Ni_{70}Mn_{30}$ alloys are shown in Fig. 4.21 by solid lines. It can be seen that they satisfactorily agree with the experimental σ_0 vs. n dependences.

Thus, the effect of dissolved hydrogen on σ_0 of Ni-Mn alloys is completely analogous to the effect of substituting nickel for manganese. There is no such analogy for the Curie points for alloys with 10 and 20 at.% Mn: an increase in the nickel content in Ni-Mn alloys increases T_C, while injection of hydrogen decreases T_C. The T_C vs. n and T_C vs. Δx_{Ni} dependences again become similar for the alloy with 30 at.% Mn: a saturation of this alloy with hydrogen up to $n = 0.85$ (the value of σ_0 for this composition of the solution is indicated by the diamond-shaped symbol in Fig. 4.21) leads to a monotonic increase in its Curie point to ~250 K, while for the $Ni_{83.5}Mn_{16.5}$ alloy (which has the same value of σ_0), $T_C \approx 400$ K [4.52].

4.4.2.4. Ni-Cr-H system. Summing up the results described in subsections 4.4.2.1-3, it can be stated that the σ_0 vs. n dependences for γ-solutions based on alloys of nickel with iron, cobalt, and manganese are analogues to the corresponding σ_0 vs. x_{Ni} dependences for the initial binary alloys. Such an analogy also holds for the Curie points, the only exception being Ni-Mn alloys with 10 and 20 at.% Mn. An entirely different behaviour of the magnetic properties was observed in the case of Ni-Cr alloys. A replacement of chromium by nickel in these alloys leads to the increase both in σ_0 (Fig. 4.17) and T_C

[4.52]. Our measurements have shown that an increase in the hydrogen concentration in the γ_1-phase of the $Ni_{95}Cr_5$-H solution results in a significant lowering of T_C (Fig. 4.15), while the γ_2-phase of this solution is paramagnetic at $T \geqslant 4.2$ K; see Fig. 4.21 (for $n \leqslant n_{\gamma_2}^{\min} \approx 0.8$, the samples consisted of a mixture of γ_1- and γ_2-phases; so, the magnetization of the samples was proportional to the content of the ferromagnetic γ_1-phase). A decrease in σ_0 and T_C for Ni-Cr alloys containing up to 7 at. % Cr was also observed upon electrolytic saturation by hydrogen [4.80].

4.4.2.5. Discussion of properties of Ni-Me-H solutions. Earlier, we discussed in detail one limiting case: hydrogen solutions in strong itinerant ferromagnets (Ni-Co and Ni-Fe with $x_{Fe} \leqslant 0.6$), when the concentration dependence of the magnetic properties of the initial alloys was mainly determined by the degree to which the *d*-band is filled and not by its deformation.

The other limiting case, when a change in the alloy composition strongly deforms the band structure, is realized, for example, for Ni-Cr and Ni-V alloys. In these alloys, the perturbing potential introduced by the Cr and V atoms is large enough to shift the virtual $d^5\uparrow$-levels of the impurity atoms above the Fermi level (see Fig. 4.18*c*). The electrons from these states go over into the conduction band, increasing the degree of filling of the *d*-states of nickel, which decreases T_C and σ_0. Upon hydrogenation of such alloys, the electrons supplied by the hydrogen atoms will also mainly fill the *d*-band of nickel in view of its high density of states at the Fermi level, thus decreasing T_C and σ_0. It is exactly this situation that is observed upon saturation of Ni-Cr alloys with hydrogen.

Thus, in both limiting cases, the band theory of ferromagnetism can explain the observed dependences $\sigma_0(n)$ and $T_C(n)$ under the assumption that it is the degree of filling of the *d*-band of the metal by electrons that has a dominating effect on the magnetic properties upon hydrogenation. The situation is more complicated in the case of alloys for which the σ_0 vs. N^e dependences deviate from the straight line with the slope $\partial\sigma_0/\partial N^e \approx -1\mu_B$ per electron only for a large impurity concentration. Such magnets include Ni-Fe alloys with $x_{Fe} > 0.6$ and Ni-Mn alloys with $x_{Mn} \geqslant 0.1$ (see Fig. 4.17). These itinerant ferromagnets are weak, i.e. at 0 K they have a considerable number of holes in the $d\downarrow$- as well as $d\uparrow$-subband. The role of band structure deformation in the $\sigma_0(x_{Ni})$ dependences for these alloys is at present the subject of controversy, especially for the Ni-Fe alloys which exhibit anomalous physical properties (Invar nature) in this concentration range. Here the converse is true: the observed analogy in the behaviour of σ_0 (and of T_C in most cases) with increasing Ni concentration and with hydrogenation indicates that the magnetic properties of the initial alloys (without hydrogen) are to be mainly determined by the degree of filling of the *d*-band rather than its defor-

mation, over a fairly wide range of concentrations ($\Delta N^e \leqslant \zeta\, n \leqslant 0.5$ electron per atom). Indeed, let us assume that for values of N^e smaller than a certain limiting value N^e_{lim}, the deviations from the straight line

$$\sigma_0 (N^e) \approx \sigma_0^{Ni} + (N^e - N^e_{Ni})\, \mu_B \qquad (4.6)$$

(which describes the behaviour of spontaneous magnetization of strong itinerant ferromagnets with an fcc lattice) in Ni-Fe and Ni-Mn alloys are caused by sharp (taking place in the interval $\Delta N^e \ll 0.5$ electron per atom) and qualitatively different changes in the band structure. Experiments show that for both groups of alloys, the effect of hydrogen on σ_0 of alloys with $N^e < N^e_{lim}$ is completely equivalent to the effect of increasing their electron concentration. This equivalence is illustrated especially clearly by the coincidence of the maximum values σ_0^{max} in the σ_0 vs. n dependences for the solutions $Ni_{32.5}Fe_{67.5}$-H (Fig. 4.19, $\sigma_0^{max} \approx 1.85\mu_B$ per atom) and $Ni_{80}Mn_{20}$-H (Fig. 4.21, $\sigma_0^{max} \approx 0.8\mu_B$ per atom) with the maximum values in the corresponding σ_0 vs. N^e dependences for Ni-Fe and Ni-Mn alloys (Fig. 4.17). Consequently, the effect of hydrogen on the band structure of Ni-Fe alloys is opposite to the effect of substituting Fe for Ni in Ni-Fe alloys and Mn for Ni in Ni-Mn alloys. In other words, according to our starting assumption, these two effects are qualitatively different. This, however, is extremely unlikely: the entire body of the experimental and theoretical data shows that hydrogen must slightly deform the *d*-band of the metals and should only increase the degree of filling of this band by electrons.

Thus, the analysis of the effect of hydrogen on the magnetic properties of the Ni-Fe and Ni-Mn alloys leads to the conclusion that the deviation of the dependences for these alloys from (4.6) is due not to a sharp change in the *d*-band structure or in the nature of the exchange interaction in the region of the "anomalous" behaviour of the σ_0 vs. N^e dependences, but at the very least due to the changes gradually accumulating over a wide concentration range of the order of the total content of Fe and Mn in the alloys. It should be noted that the concentration dependence of these changes is much weaker when nickel is alloyed with iron (in this case, a value $\Delta N^e = (Z_{Ni} - Z_{Fe})\, x_{Fe} \approx 2.0 \times 0.6 = 1.2$ electron per atom is required for the σ_0 vs. N^e dependence to begin deviating from (4.6)) than in the case of alloying with manganese (here, ΔN^e is equal to $3 \times 0.1 = 0.3$ electron per atom). Probably, the stronger deformation of the band structure of nickel when it is alloyed with manganese rather than iron is responsible for the fact that, in contrast to all the investigated Ni-Fe alloys, no analogy is observed for Ni-Mn alloys with 10 and 20 at. % Mn in the change of the Curie points with the alloy composition and with saturation by hydrogen.

4.4.3. $Fe_{65}(Ni_{1-x}Mn_x)_{35}$-H Solutions

The $Fe_{65}(Ni_{1-x}Mn_x)_{35}$ alloys (percent by weight) are a classical system which has served for many years as a model for investigating the problems of the competition between ferromagnetic and antiferromagnetic ordering in fcc metals. These alloys provided a rare opportunity to systematically observe the effect of hydrogen on both types of magnetic ordering for the same group of objects.

The substitution of Mn for Ni in the $Fe_{65}(Ni_{1-x}Mn_x)_{35}$ system decreases the Curie temperature from $T_C = 467$ K for the $Fe_{65}Ni_{35}$ alloy to helium temperatures for the alloy containing ~10% Mn. For higher manganese concentrations, antiferromagnetic ordering takes place in the system, and the Néel temperature increases monotonically up to $T_N = 442$ K for the $Fe_{65}Mn_{35}$ alloy. Both ferromagnetically and antiferromagnetically ordered alloys exhibit anomalous physical properties characteristic of Invars (see [4.81, 82]).

Using the technique developed by the authors for compressing hydrogen to 7 GPa, γ-solutions with concentrations up to $n \sim 1$ were obtained for alloys over the entire concentration range from $Fe_{65}Ni_{35}$ to $Fe_{65}Mn_{35}$ [4.83]. The σ_0 vs. n and T_C vs. n dependences for the Fe-Ni-Mn-H solutions are shown in Fig. 4.22. The following is observed when the $Fe_{65}(Ni_{1-x}Mn_x)_{35}$ alloys are saturated with hydrogen. The Néel temperatures of the antiferromagnetic alloys decrease, and a ferromagnetic ordering sets in for a certain concentrations n_t of hydrogen. After this, the Curie temperatures of the ferromagnetic solutions increase monotonically. Therefore, the change in the magnetic properties of the $Fe_{65}(Ni_{1-x}Mn_x)_{35}$ alloys as a result of hydrogenation turned out to be analogous to their change upon substituting Ni for Mn (which increases the electron concentration N^e). As shown in [4.84], the shape of the Mössbauer spectrum of hydrogen-saturated alloy $Fe_{66}Ni_{31}Mn_3$ (atomic percent) also approaches the shape of the spectrum for the $Fe_{65}Ni_{35}$ alloy.

Let us introduce the similarity coefficients ζ for the dependences of the magnetic properties of the alloys with and without hydrogen. If we assume that the concentration dependence of the magnetic properties of the pseudo-binary $Fe_{65}(Ni_{1-x}Mn_x)_{35}$ system, as well as the dependence of these properties on the hydrogen content of these alloys, is mainly determined by the change in the degree of filling of the d-band, then for all these alloys and hydrogen solutions based on them, one and the same effective concentration N_f^e of electrons should exist, at which ferromagnetic ordering sets in. Assuming that the values of ζ do not differ much for the investigated alloys, we get $\langle\zeta\rangle = 0.7$ electron per H atom and $N_f^e = 8.35$ electrons per atom from the equation

$$N^e + \langle\zeta\rangle n_f = N_f^e$$

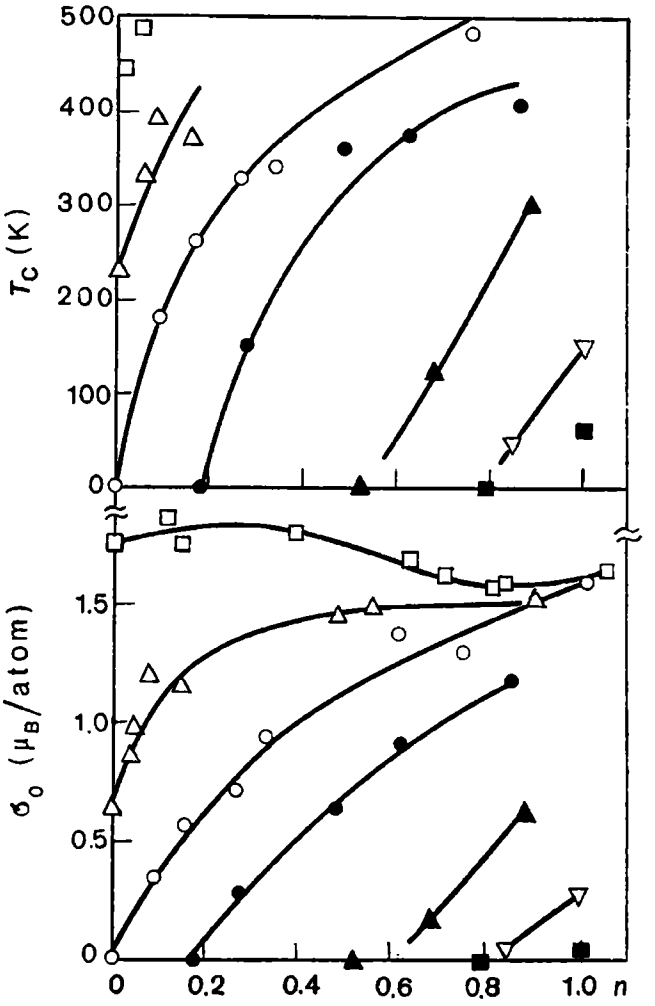

Fig. 4.22. T_C vs. n and σ_0 vs. n dependences for hydrogen solutions in fcc alloys $Fe_{65}(Ni_{1-x}Mn_x)_{35}$ [4.83]. The notation is the same as in Fig. 4.23.

by using the method of least squares and the values of N^e and n_f given in Table 4.2. The values of $N_f^e - N^e$ and $\zeta = (N_f^e - N^e)/n_f$ are also given in this table. It is seen that the sign and the order of magnitude of the ζ's obtained in this way are in agreement with the assumption that the degree of filling of the d-band plays a dominating role in the formation of the dependences of the magnetic properties of the investigated alloys on nickel and hydrogen concentration.

The results of investigations of hydrogen solutions in $Fe_{65}(Ni_{1-x}Mn_x)_{35}$ alloys not only confirm the earlier notions about the nature of the influence of hydrogen on the magnetic properties of transition metals, but also reveals new aspects of this influence. As a matter of fact, the magnetic properties of the $Fe_{65}(Ni_{1-x}Mn_x)_{35}$ alloys [4.81, 82] and hydrogen solutions based on them [4.83] are

Table 4.2. Parameters for Hydrogen Solutions in $Fe_{65}(Ni_{1-x}Mn_x)_{35}$ Alloys [4.83]

Mn wt.%	T_C, K	T_N, K	N^e el/atom	$N_f^e - N^e$ el/atom	n_f	ζ el/atom
0	467	—	8.68	−0.33	—	—
4.5	228	—	8.54	−0.19	—	—
10	—	—	8.38	−0.03	0	—
17	—	160	8.17	0.18	0.18	1.00
24	—	253	7.97	0.38	0.58	0.66
29	—	341	7.82	0.53	0.81	0.65
35	—	442	7.62	0.70	0.94	0.74

Remark: $\zeta = (N_f^e - N^e)/n_f$; $N_f^e = 8.35$ el/atom in the Fe-Ni-Mn alloy.

well described by the equations of the theory of very weak itinerant ferromagnetism [4.85]. In particular, it follows from these equations that

$$\frac{T_C}{\sigma_0} = \frac{1}{2\pi k_B \mathscr{N}(\mathscr{E}_F)} \left[\frac{3\nu_1^2 - \nu_2}{\nu_1^2 - \nu_2} \right]^{1/2} \tag{4.7}$$

for weak itinerant ferromagnets (k_B is the Boltzmann constant, $\mathscr{N}(\mathscr{E}_F)$ is the density of states at the paramagnetic Fermi level $\mathscr{E}_F$, while $\nu_m = \mathscr{N}^{(m)}(\mathscr{E}_F)/\mathscr{N}(\mathscr{E}_F)$). In fcc ferromagnets, the Fermi level seems to pass near the maximum of the density of states curve $\mathscr{N}(\mathscr{E})$ [4.66], which gives $\nu_2 \leqslant 0$. For $\nu_2 \leqslant 0$, the values of the factor in square brackets in Eq. (4.7) depend slightly on the magnitudes of the parameters entering into it, changing from 3 for $\nu_2 = 0$ to 1 for $\nu_2 \to -\infty$. For a parabolic band, this factor is equal to 2. Thus, the density of states at the paramagnetic Fermi level for a weak itinerant ferromagnet can be roughly estimated if T_C and σ_0 are known:

$$\frac{T_C}{\sigma_0} \approx \frac{1}{\sqrt{2}\,\pi k_B \mathscr{N}(\mathscr{E}_F)}. \tag{4.8}$$

The T_C vs. σ_0 dependence for the $Fe_{65}(Ni_{1-x}Mn_x)_{35}$ system is shown in Fig. 4.23. It can be seen that for the investigated samples, the values of T_C as a function of σ_0 lie nearly on a single curve (in order to show how strongly the T_C vs. σ_0 dependences can deviate from one another for different itinerant ferromagnets, the point for Ni is indicated in Fig. 4.23 by the diamond-shaped symbol). It follows from Eq. (4.8) that a common dependence of T_C on σ_0 for all Fe-Ni-Mn alloys and hydrogen solutions based on them is indicative of a unique relation between the values of T_C and σ_0 for these materials and $\mathscr{N}(\mathscr{E}_F)$ at the paramagnetic Fermi level.

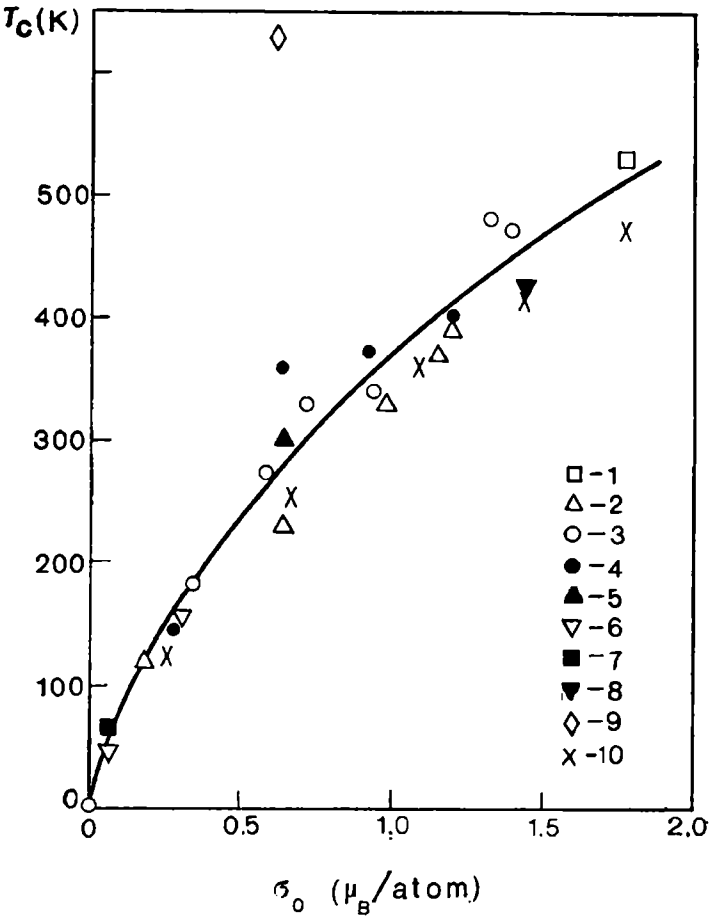

Fig. 4.23. Dependence of Curie points T_C on spontaneous magnetization at $T = 0$ K.
1-7—γ-solutions of hydrogen in the alloys $Fe_{65}(Ni_{1-x}Mn_x)_{35}$ [4.83] (*1*—0; *2*—4.5; *3*—10; *4*—17; *5*—24; *6*—29; *7*—35 wt. % Mn); *8*—Ni-Fe alloy containing 67.5 at. % Fe [4.58, 87]; *9*—nickel; *10*—$Fe_{65}(Ni_{1-x}Mn_x)_{35}$ alloys [4.81].

This result correlates well with all the facts indicating a weak deformation of *d*-bands and small changes in the dependences of the exchange interaction as a function of the degree of filling of the *d*-band, accompanying hydrogenation of fcc nickel alloys, including the Ni-Fe Invars. Indeed, if the possibility of random coincidences is neglected, several conditions must be satisfied simultaneously in order that the weak itinerant ferromagnets with the same density of states $\mathscr{N}(\mathscr{E}_F)$ at the paramagnetic Fermi level have the same Curie temperatures and the same values of spontaneous magnetization over a wide range of values of $\mathscr{N}(\mathscr{E}_F)$. Firstly, the form of the *d*-band must be the same for all these ferromagnets. Secondly, the degree of filling of their *d*-bands must be the same. Finally, the relative shift of the $d\uparrow$- and $d\downarrow$-subbands, $\Delta = I\sigma$, must also be the same at all

temperatures, i.e. the effective exchange interaction parameters I must be equal. Hence, the data for the $Fe_{65}(Ni_{1-x}Mn_x)_{35}$ alloys shown in Fig. 4.23 indicate that the change in the magnetic properties upon substituting nickel for manganese in this pseudo-binary system, as well as upon a saturation of these alloys by hydrogen, is mainly due to the increase in the degree of filling of the d-band and, in addition, the phenomenological coefficients $\zeta < 1$ electron per H atom for the Fe-Ni-Mn-H solutions are close to the number η of electrons supplied by the hydrogen atoms above the Fermi level.

Such conclusions also provide a certain clarification for one of the most complicated questions arising in the discussion of the influence of hydrogen on the magnetic properties of transition metals, namely, the role of volume effects: the $Fe_{65}(Ni_{1-x}Mn_x)_{35}$ alloys, just as the Ni-Fe alloys with $x_{Fe} \gtrsim 0.6$, are Invars whose characteristic feature is a strong dependence of the magnetic properties on volume.

The solid line in Fig. 4.24 shows the σ_0 vs. N^e dependence for fcc Ni-Fe alloys under atmospheric pressure. The dotted lines show the analogous dependences for $P = -5$ and $+5$ GPa, calculated by assuming that σ_0 depends linearly on volume and by using the experimental values of $(1/\sigma_0)\,(\partial\sigma_0/\partial P)_{1n}$ obtained under hydrostatic compression [4.46, 86]. For $N^e \lesssim 9$ electrons per atom, the slope of the σ_0 vs. N^e dependence for $P = -5$ GPa increases sharply. For example, when N^e decreases from 8.9 to 8.7 electrons per atom, σ_0 increases by $\sim 0.9\mu_B$ per atom. If the itinerant ferromagnet is strong [and the number of holes in the d-bands of nickel-based fcc alloys is such that these alloys must become strong ferromagnets when the magnetization attains the value $\sigma_0\,(N^e) \sim \sigma_0^{Ni} + (N^e - 10)\,\mu_B$], a change in the degree of filling of the d-band by $\Delta N^e = 8.9 - 8.7 = 0.2$ electron per atom increases σ_0 by only $\sim 0.2\mu_B$ per atom. The increase in σ_0 by the remaining amount $\sim (0.9 - 0.2) = 0.7\mu_B$ per atom can take place only as a result of an additional decrease in the number of electrons in the d-band due to another mechanism, for example, on account of a transfer of ~ 0.7 electron per atom to the s-band. This is unlikely, since this number of electrons is comparable to the total number of occupied states in the s-band.

Thus, in order for the σ_0 vs. N^e dependence at $P = -5$ GPa shown in Fig. 4.24 to be realized, this pressure must lead to catastrophic changes in the band structure (and exchange interaction) in Invar alloys. The dissolution of $n \sim 1$ of hydrogen in such alloys causes an increase in the volume that is equivalent to the action of a negative pressure ~ 15 GPa and, at the same time, as we have seen, it slightly changes the shape of the d-band and the dependence of the exchange interaction parameter on the degree of filling of the band. It should be recalled that hydrogenation of the Ni-Fe Invars with 66.1 and 67.5.% Fe does not increase their spontaneous magne-

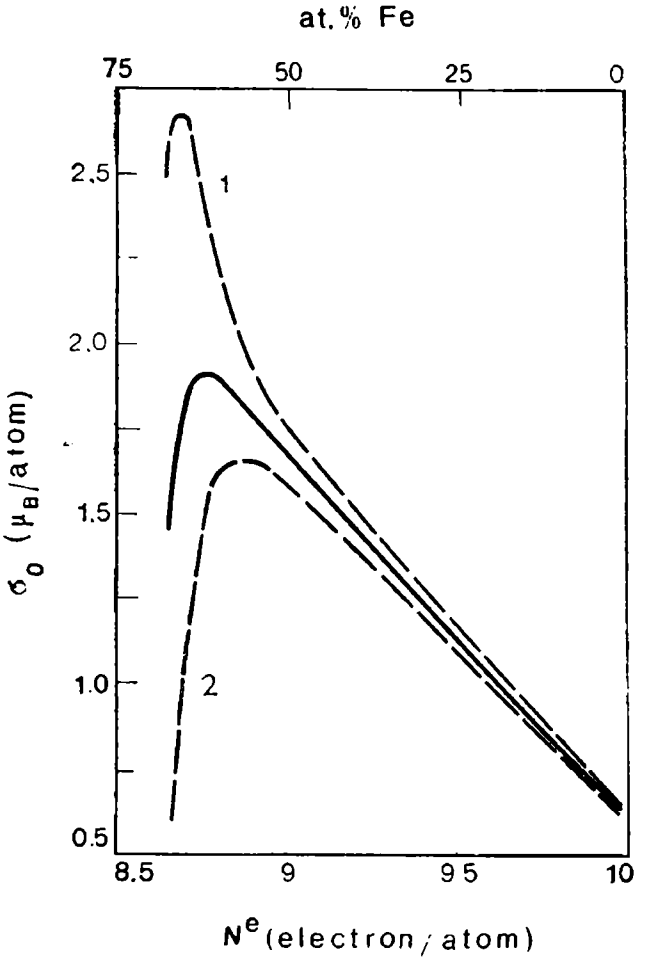

Fig. 4.24. Concentration dependences of σ_0 or Ni-Fe alloys. The solid line shows the curve obtained under atmospheric pressure [4.65, 66]; *1* and *2* represent the curves for $P = -5$ and $+5$ GPa, respectively.

tization beyond the value $\sigma_0^{max} \approx 1.9\mu_B$ per atom, the maximum value for Ni-Fe alloys without hydrogen (see Fig. 4.19). Since the compression of Invars leads to a sharp decrease in σ_0 (see Fig. 4.24, curve *2*), this suggests that the σ_0 vs. V dependence is asymmetric with respect to the volume V_0 under atmospheric pressure: for $V < V_0$, the magnetization increases with increasing V, while for $V \sim V_0$, it reaches a stationary value and subsequently remains practically unchanged.

It is interesting that in contrast to the σ_0 vs. n dependences, the T_C vs. n dependences for the investigated Ni-Fe alloys can be explained by considering the increase in volume during hydrogenation to be the main effect and by using the T_C vs. V dependences obtained under conditions of compression [4.87, 58]. However, such facts

like the possibility of describing the T_C vs. n dependence within the scope of the rigid d-band model with reasonable values of η, and unduly high estimates for values of σ_0 for hydrogen solutions in Invar alloys while taking into account the volume effects (using the values of $\partial\sigma_0/\partial V$ obtained under compression), cast doubts over the physical content of estimates of the effect of variations of volume on the Curie temperatures as well.

Summing up the above presentation, it can be stated that the problem of the role of volume effects in the change in the magnetic properties of transition metals upon hydrogenation is nontrivial and is an interesting field for further research.

4.4.4. Applicability of the Rigid d-band Model for Describing the Magnetic Properties for Other Me-H Solutions

4.4.4.1. Hydrogen solutions in fcc alloys based on 3d-metals. The concept of hydrogen as a donor of a fractional number of electrons in a weakly deformed d-band of the host metal, which is one of the most significant results of the investigations of magnetic properties of γ-solutions Ni-Me-H, allows at least a qualitative prediction of the behaviour of these properties for a number of systems. For example, an increase in n should lower σ_0 and T_C of strong itinerant ferromagnets (Ni-Cu, Ni-Zn, Co-Fe; for Ni-Cu alloys, this fact is confirmed experimentally, see [4.88, 89]) and alloys for which $\partial\sigma_0/\partial N^e > 0$ for low impurity concentrations (Ni-V, Co-Mn, Co-Cr). Owing to the high density of states at the Fermi level of nickel and cobalt, the electrons of the dissolving hydrogen must fill the d-band in fcc alloys of these metals with nontransition elements (Ni-Al, Ni-Ge, Co-Sb, etc.) as well, again lowering σ_0 and T_C. An increase in σ_0 with hydrogen concentration should apparently be observed only for those alloys with $\partial\sigma_0/\partial N^e > > 0$, for which the σ_0 vs. N^e dependences deviate from (4.6) only for a large impurity concentration, i.e. this deviation is to a large extent due to the degree of filling of the d-band (Ni-Fe alloys with $x_{Fe} > 0.6$ and Ni-Mn alloys with $x_{Mn} > 0.1$).

4.4.4.2. Hydrogen solutions in 3d-metals with hcp lattice. A necessary condition for using the rigid d-band model to describe the magnetic properties of Me-H solutions is a knowledge of the dependence of these properties on the occupancy of the d-band in the starting materials (without hydrogen). For fcc metals, such information can be obtained, for example, from the σ_0 (N^e) and T_C (N^e) dependences for alloys of 3d-metals closely positioned in the Periodic Table, whose properties are described well by the rigid band model. The concentration dependences of the magnetic properties of alloys with an hcp lattice have been investigated to a much lesser extent,

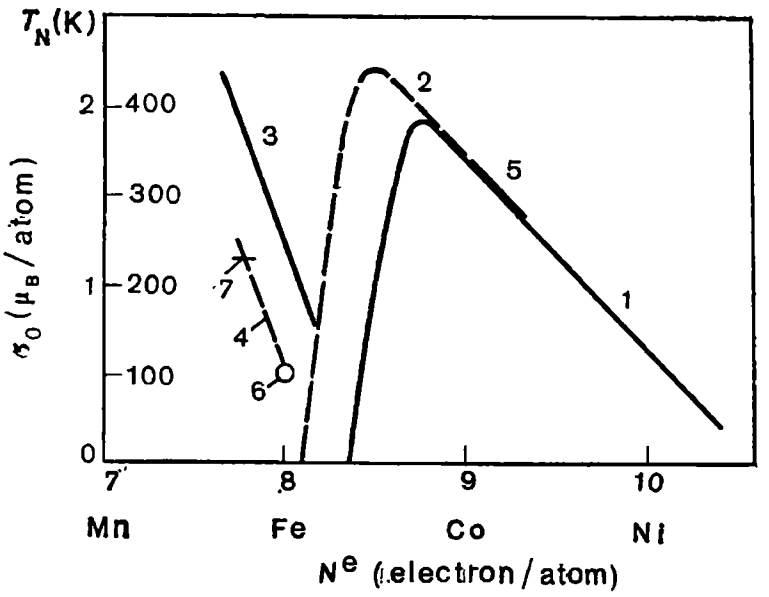

Fig. 4.25. Concentration dependences of spontaneous magnetization σ_0 at $T = 0$ K and of Néel temperatures T_N for the alloys of 3d-metals that are nearest neighbours in the periodic table.
γ—fcc alloys; ε—hcp alloys. *1*—σ_0^γ; *2*—σ_0^ε; *3*—T_N^γ; *4*—T_N^ε; *5*—σ_0^ε for Co-Ni alloys; *6*—T_N^ε for Fe; *7*—T_N^ε for Fe-Mn alloys.

primarily due to relatively narrow intervals of the mutual solubility of 3*d*-metals in hexagonal phases. However, for $N^e \gtrsim 7.7$ electrons per atom, these dependences are apparently similar for hcp and fcc alloys.

Indeed, for fcc alloys of 3*d*-metals closely positioned in the Periodic Table, the values of σ_0 as a function of N^e lie on a single curve (see Fig. 4.25). With decreasing N^e to ~8.8 electrons per atom, σ_0 increases almost linearly with a slope $\partial\sigma_0/\partial N^e \approx -\mu_B$ per electron (Ni-Cu, Ni-Co, and Ni-Fe alloys), reaches a maximum, and then begins to decrease. For $N^e \approx 8.35$ electrons per atom, the alloys become paramagnetic down to helium temperatures. Then antiferromagnetic ordering sets in, and the Néel temperature monotonically increases up to $T_N \approx 440$ K at $N^e = 7.65$ electrons per atom ($Fe_{65}(Ni_{1-x}Mn_x)_{35}$ alloys).

As regards the magnetic properties of hcp metals and alloys, it is known that the σ_0 vs. N^e dependence for hcp Co-Ni alloys is nearly linear (segment of the solid line in Fig. 4.25), has a slope $\partial\sigma_0/\partial N^e \approx -\mu_B$ per electron and is close to the σ_0 vs. N^e dependence for fcc alloys [4.90, 91] (the slope $\partial\sigma_0/\partial N^e \approx -\mu_B$ per electron indicates that like the fcc alloys in the same interval of values of N^e, the hcp Co-Ni alloys are strong itinerant ferromagnets). Extrapolation from the Fe-Ru and Fe-Os alloys [4.92] shows that the

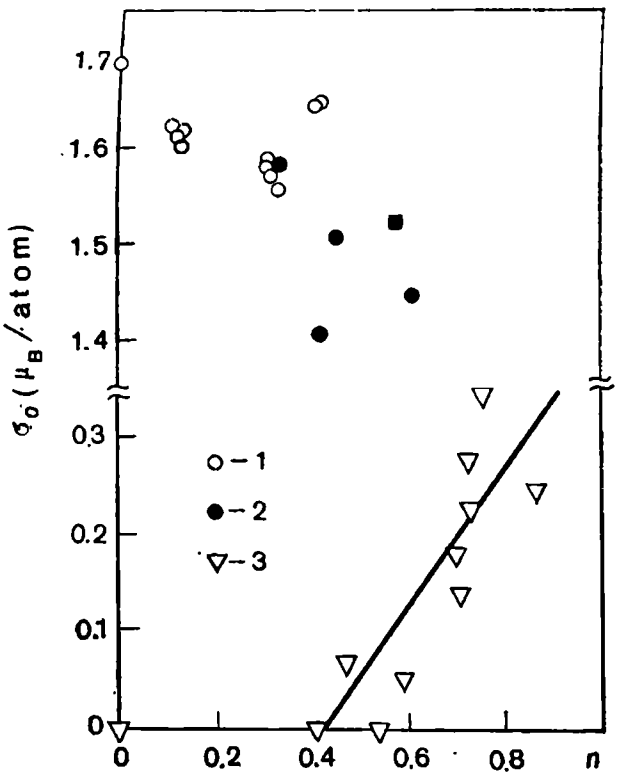

Fig. 4.26. σ_0 vs. n dependence for ε-solutions Co-H (*1*—results of [4.64]; *2*—results of the present paper), and $Fe_{77.6}Mn_{22.4}$-H (*3*—results of [4.94]).

virtual hcp phase of iron ($N^e = 8$ electrons per atom) is an antiferromagnet with $T_N \approx 100$ K (the circle in Fig. 4.25). The hcp Fe-Mn alloys ($7.71 \leqslant N^e \leqslant 7.82$ electrons per atom) are antiferromagnets with $T_N \approx 230$ K [4.93] (the horizontal segment of the solid line in Fig. 4.25). Sufficiently correct data on the magnetic properties of hcp alloys with $8 < N^e < 9$ electrons per atom are unavailable in the literature. One can, however, expect that in this range of electron concentration as well, the σ_0 vs. N^e and T_N vs. N^e dependences for hcp alloys are similar to those for fcc alloys (the dotted line in Fig. 4.25).

As is seen from the above, the objects of interest to us from the point of view of investigating the effect of hydrogen on the magnetic properties of hcp alloys are basically exhausted by cobalt, iron, and Fe-Mn alloys in which the hcp phase is metastable at atmospheric pressure in the concentration range between 18 and 30 at. % Mn [4.52]. The results of investigations of the σ_0 vs. n dependence for the ε-solutions Co-H are shown in Fig. 4.26. The experimental data show a considerable spread in values, but the general tendency is a lowering of spontaneous magnetization with increasing hydrogen

concentration (at present, we are engaged in a more accurate determination of the σ_0 vs. n dependence for the ε-solutions Co-H and the investigation of magnetic properties of the γ-solutions). This is exactly how σ_0 should behave upon hydrogenation of a strong itinerant ferromagnet according to the rigid d-band model.

If the rigid d-band model is also valid for the ε-solutions of hydrogen in iron and Fe-Mn alloys, and if our conjectures concerning the dependence of magnetic properties of these materials on the degree of filling of the d-band (Fig. 4.25) are true, the dissolution of hydrogen must convert them from antiferromagnets to ferromagnets. Experiments have shown that this is actually the case. The ε-solution Fe-H for $n \approx 0.8$ was found to be a ferromagnet with $\sigma_0 \approx 2.2\mu_B$ per Fe atom [4.37]. At $n \gtrsim 0.4$, the appearance of spontaneous magnetization was observed for $Fe_{77.6}Mn_{22.4}$-H as well [4.94] (the σ_0 vs. n dependence for these solutions is shown in Fig. 4.26; the investigated samples were single-phase materials).

It is interesting to note that the results of investigations of Fe-H and Fe-Mn-H ε-solutions, confirming the identical character of the σ_0 vs. N^e dependences for hcp and fcc alloys of 3d-metals with $N^e \gtrsim 8$ electrons per atom on the whole, reveal, at the same time, a certain difference between them (like the one shown in Fig. 4.25). Indeed, according to the rigid d-band model, the value of $\sigma_0 \approx \approx 2.2\mu_B$ per Fe atom for the ε-hydride of iron cannot, as a function of the effective electron concentration $N^e + \eta n$, lie above the continuation of the σ_0 (N^e) straight line for hcp Co-Ni alloys, since for the alloys having values of σ_0 lying on this straight line, the holes must be only in the d_γ-subband, and hence the magnetization has its maximum possible value for the given degree of filling of the d-band. As is easily seen from Fig. 4.25, the maximum of the σ_0 vs. N^e dependence for hcp alloys shifts noticeably due to these restrictions to the left along the N^e-axis with respect to its position on the dependence for fcc alloys (for the ε-solutions Fe-H, such restrictions lead to the condition $\zeta \lesssim 0.6$ electron per H atom, which is a reasonable estimate [4.37]). Further, for the ε-solutions $Fe_{77.6}Mn_{22.4}$-H, ferromagnetism appears for $n \approx 0.4$. Even if we assume that $\eta = 1$ electron per H atom for the $Fe_{77.6}Mn_{22.4}$ alloy (the value of η for the Me-H solutions investigated to date is found to be lower), the appearance of ferromagnetism in hydrogen solutions on its base will correspond to the effective electron concentration $N^e + \eta n \approx \approx 7.8 + 0.4 = 8.2$ electrons per atom, which is less than the electron concentration $N^e \approx 8.35$ electrons per atom corresponding to the appearance of ferromagnetic ordering in fcc alloys.

Thus, under the above assumptions, we get a consistent picture describing unambiguously all the available data on concentration dependence of the magnetic properties of 3d-metals with an hcp lattice and their alloys as well as hydrogen ε-solutions based on them.

It should, however, be emphasized that the applicability of the proposed model is, for the time being, limited to metals and alloys whose electron concentration lies in the interval $7.7 \leqslant N^e \leqslant 9.3$ electrons per atom. Beyond this interval, certain effects which cannot be explained within the scope of the model could be observed. The spontaneous magnetization observed for the ε-solutions Mn-H [4.27] may serve as an example of this kind. The nature of magnetism in these solutions is not clear so far and requires further investigations.

4.4.4.3. Hydrogen solutions in *4d*-metal alloys. In contrast to metals at the end of the *3d*-series, *4d*-metals do not have properties which are simply and uniquely related to the degree of filling of the *d*-band, which makes if difficult to study experimentally the problem of the status of hydrogen in solutions based on them. It can, however, be stated that all available experimental data on the effect of hydrogen on the physical properties of these metals and their alloys (electron heat capacity, magnetic susceptibility, shape of the Mössbauer spectra, etc.) can be consistently explained by treating hydrogen as a donor contributing ~1 electron per H atom to the weakly deformed conduction band of the metal-solvent. A detailed discussion of these problems and references to the original papers are given, for example, in [4.72, 76, 11, 95].

4.5. Pd-Me-H SYSTEMS. SUPERCONDUCTIVITY AND PHASE TRANSFORMATIONS AT HIGH PRESSURE

Soon after the discovery of superconductivity in the Pd-H solutions with $n \geqslant 0.8$ [4.50], Stritzker [4.96] discovered that implantation of hydrogen in alloys of palladium with noble metals (Cu, Ag, and Au) may make them superconductors with critical temperature T_c up to 13-17 K, which is much higher than $T_c \approx 9$ K attained for the Pd-H solutions [4.51]. Stritzker's discovery provided a strong impetus for the development of experimental and theoretical investigations of superconducting properties of hydrogen solutions in alloys of palladium with various metals (a review and analysis of the most significant results of these investigations are given in [4.51]). It should, however, be noted that most of the experimental results on the superconductivity of Pd-Me-H solutions were obtained on samples which were saturated with hydrogen under nonequilibrium conditions (mainly through implantation), since the equilibrium solubility of hydrogen in the investigated alloys is not sufficiently high at pressures usually employed for hydrogenation. Samples obtained by implantation have rather peculiar properties: hydrogen is contained only in a narrow layer and is

distributed nonuniformly along its thickness, the metal lattice is known to be seriously damaged during implantation, and so on.

Using the technique for compressing hydrogen to high pressures, we were able to synthesize (under near-equilibrium conditions) macroscopic hydrogen-saturated samples of several palladium alloys. We began our investigations with hydrogen solutions in the alloys of palladium with Cu, Ag, Au, Ni, and Pt, which, according to the available data [4.51], possess the most interesting superconducting properties. Already the first experiments on the palladium-noble metal-hydrogen solutions have shown that the superconducting properties of homogeneous massive samples may radically differ from those of the samples obtained by hydrogen implantation.

The following is observed during implantation of hydrogen into the Pd-Cu, Pd-Ag, and Pd-Au alloys [4.96]. For a certain irradiation dose, the thin ($\sim$1500 Å) hydrogen-containing layer formed in the metal becomes superconducting. With further irradiation, T_c increases, reaches a maximum value T_c^m, and then begins to decrease. In its turn, the dependence of T_c^m on the concentration of the alloying element in palladium for each of the binary systems Pd-Cu, Pd-Ag, Pd-Au is also a curve with a maximum, the maximum values being $T_c^{mm} \approx 16.6$, 15.6, and 13.6 K respectively, for the $Pd_{55}Cu_{45}$, $Pd_{70}Ag_{30}$ and $Pd_{84}Au_{16}$ alloys. The typical T_c vs. n dependence upon hydrogen implantation in the $Pd_{55}Cu_{45}$ alloy is shown in Fig. 4.27. Similar dependences were observed for the $Pd_{70}Ag_{30}$-H and $Pd_{84}Au_{16}$-H solutions, the only difference being in the optimum hydrogen concentration for which the maximum value of T_c was observed ($n_{opt} \approx 0.7$, 0.8, and 0.9 respectively for the alloys with Cu, Ag, and Au).

The investigation of the $Pd_{60}Cu_{40}$ and $Pd_{80}Ag_{20}$ alloys (the compositions are close to optimum for obtaining the maximum T_c values for hydrogen implantation), saturated with hydrogen at $P_{H_2} \leqslant 7$ GPa, showed [4.97] that the $Pd_{60}Cu_{40}$-H solutions for $n \leqslant 0.6$ and at $T \geqslant 2$ K are not superconducting, while the T_c vs. n dependence for the $Pd_{80}Ag_{20}$-H solutions at $n \leqslant 1$ is close to that for the Pd-H solutions (see Fig. 4.27). The T_k vs. n dependences for the γ-solutions $Pd_{97}Au_3$-H, $Pd_{91}Au_9$-H [4.98], and $Pd_{90}Cu_{10}$-H (see Fig. 4.28), saturated with hydrogen at $P_{H_2} \leqslant 8$ GPa, were found to be approximately the same as for the Pd-H and $Pd_{80}Ag_{20}$-H solutions as well, which also disagrees with the data of [4.96].

Thus, our results show that the anomalously high values of T_c obtained with hydrogen implantation in alloys of palladium with noble metals are due to the peculiarities of metastable states arising upon implantation. It should be noted that at present there is no unified point of view as to how the alloying of palladium with noble metals should affect the superconducting transition tempera-

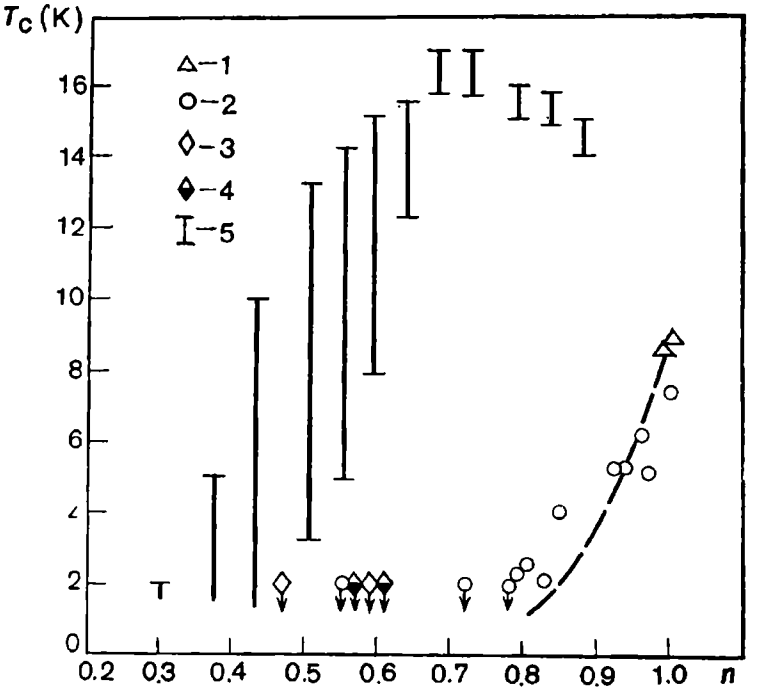

Fig. 4.27. Dependence of the superconducting transition temperature T_c on the hydrogen concentration n.
1—for the Pd-H solutions (results of the present paper); *2*—for γ-solutions $Pd_{80}Ag_{20}$-H [4.97]; *3*—for γ-solutions $Pd_{60}Cu_{40}$-H (results of the present paper); *4* -for γ'-solutions $Pd_{60}Cu_{40}$-H solutions [4.97] (symbols with arrows show that the samples are not superconducting at $T \geqslant 2$ K); *5*—for $Pd_{55}Cu_{45}$-H solutions [4.96] (the intervals in which the sample resistance changes from 90 to 10% of the value of residual resistance of the normal phase have been indicated). The dotted line shows the T_c vs. n dependence for the Pd-H solutions [4.51].

ture. For example, according to the theoretical estimates in [4.74, 99], this alloying should increase T_c, while the theoretical data in [4.100] and the estimates made in [4.101] on the basis of the experimental investigation of the low-temperature specific heat of nonsuperconducting $Pd_{80}Ag_{20}$-H solid solutions indicate that this temperature should decrease. The possibility that the instability of the crystal lattice (due to a softening of some phonon modes and a corresponding increase in the electron-phonon interaction constant) can play an important role in obtaining high T_c upon hydrogen implantation in palladium alloys with Cu, Ag, and Au was noted by Stritzker [4.96, 51] who discovered an interesting feature in the dependence of their T_c on the dose ψ of implanted hydrogen. For the Pd-Cu and Pd-Ag alloys with compositions close to optimum ($T_k^m \gtrsim 15$ K), the monotonic rise in T_c with increasing ψ was sometimes replaced by its sudden fall and vanishing of superconductivity for $T \geqslant 1$ K, while the residual resistance R_{res} decreased discontin-

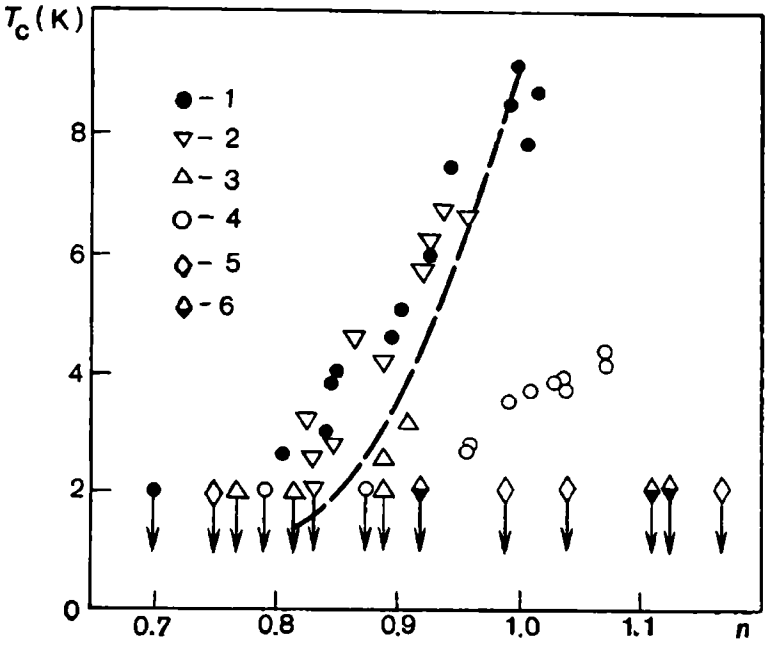

Fig. 4.28. T_c vs. n dependence for γ-solutions of hydrogen in the alloys.
1—$Pd_{90}Cu_{10}$ (results of the present paper); *2*, *3*—$Pd_{97}Au_3$ and $Pd_{91}Au_9$ [4.98]; *4*, *5*—$Pd_{95}Ni_5$ and $Pd_{80}Ni_{20}$ [4.110]; *6*—results for $Pd_{80}Ni_{20}$-H solutions consisting of a mixture of palladium-enriched and depleted phases. The arrows at the symbols and the dashed lines are the same as in Fig. 4.27.

uously by 10-20%. Further increase in ψ led to a monotonic decrease in R_{res}, but the appearance of superconductivity for $T \geqslant 1$ K was no longer observed. Stritzker explained this by the formation of a new nonsuperconducting phase with a smaller value of R_{res}.

The above discussion suggests that the appearance of superconductivity with anomalously high values of T_c accompanying implantation of hydrogen into palladium alloys with noble metals may be closely related just to the structural peculiarities of these systems. So, although according to the data available in the literature only ordinary γ-solutions of hydrogen on the basis of disordered metal lattice must be formed in the Pd-Cu-H [4.102], Pd-Ag-H [4.103, 104], and Pd-Au-H [4.105, 106] systems, we considered it expedient to carry out a structural analysis of such solutions. It turned out that under high hydrogen pressures, the Pd-Me-H systems may actually undergo new phase transformations which were never observed earlier upon hydrogenation of alloys of group VI-VIII transition metals and which are followed by a diffusion rearrangement of the atoms of the metallic matrix.

$Pd_{60}Cu_{40}$-H system [4.107]. The study of the isobars of the electrical resistance for the $Pd_{60}Cu_{40}$ alloy in a hydrogen atmosphere and

in the pressure interval of 0.5-2 GPa showed that an irreversible phase transition occurs in the samples upon heating above $T^* \approx \approx 200°C$, the resistance of the samples sharply decreasing during the phase transition. The transition proceeds quite slowly: even at 350° C, the drift in the resistance continues for tens of hours. X-ray studies revealed that the metallic sublattice of the $Pd_{60}Cu_{40}$-H samples obtained by exposing at $T = 200°C < T^*$ under hydrogen pressure $0.5 \leqslant P_{H_2} \leqslant 2$ GPa and having the composition $n \leqslant 0.47$ retains fcc symmetry and, in addition, the value of ΔV_0 of the jump in the unit cell volume of the $Pd_{60}Cu_{40}$ alloy accompanying hydrogenation agrees satisfactorily with the ΔV_0 vs. n dependence presented in [4.59] (see Fig. 4.16) for γ-solutions of hydrogen in palladium and its alloys. The $Pd_{60}Cu_{40}$-H samples obtained by exposing at $250 \leqslant T \leqslant 350°C$ (i.e. at $T > T^*$) had a metallic sublattice whose symmetry can be described on the basis of an fct (face-centered tetragonal) pseudocell (hereafter called the γ'-phase) with the axial ratio $0.94 \lesssim c/a \lesssim 0.97$. The hydrogen concentration in these specimens lay in the range $0.3 \leqslant n \leqslant 0.5$, and the volume per metal atom was nearly the same as for γ-solutions $Pd_{60}Cu_{40}$-H with similar values of n.

Further investigations revealed that the tetragonal structure of $Pd_{60}Cu_{40}$ alloys was retained even after quenching of γ'-samples in vacuum at 300° C, which led to *complete* liberation of hydrogen from the samples. The volume per metal atom decreased in this case to values close to those for the initial $Pd_{60}Cu_{40}$ alloy, while the tetragonality of the lattice grew. After quenching at $T \gtrsim 350°$ C, the structure of the alloy returned to the starting fcc one. The return to the fcc structure occurred also after plastic deformation of the sample at room temperature. These results show that at atmospheric pressure and $T \gtrsim 20°$ C, the γ'-structure of the $Pd_{60}Cu_{40}$ alloys is not a thermodynamically equilibrium one. At the same time, the metastability of this structure after complete evolution of hydrogen and even a certain increase in its degree of tetragonality support the proposition that the observed tetragonal distortions are mainly related not to the possible phase transformation in the hydrogen sublattice (for example, its ordering), but rather to a restructuring of the metal sublattice itself in the $Pd_{60}Cu_{40}$-H solution.

One of the possibilities of such restructuring is atomic ordering. The presence of wide regions with ordered atomic positioning in T vs. c diagrams is characteristic of the Cu-Pd system as well as a number of related systems. In particular, ordering in the region of compositions close to Cu_3Pd leads precisely to tetragonal distortion of the fcc lattice of Cu-Pd alloys [4.108, 109]. With ordering of this type, in addition to the main (structural) lines of the fct lattice, superstructural lines appear whose position is close to that for reflections from planes with mixed indices. For γ'-samples, in

addition to the main lines, 11 weak and broad lines were observed, and mixed indices could be attributed to all of them.

Thus, the results of investigations [4.107] allows us to assert with quite a high degree of reliability that the formation of the γ'-phase in the $Pd_{60}Cu_{40}$-H system is accompanied by ordering of the metallic sublattice (although an incomplete one, which is indicated by the large width of the superstructural lines compared to that of the main lines). As regards the superconducting properties of $Pd_{60}Cu_{40}$-H solutions, it is hard to estimate at present the role of the instability of solutions with respect to ordering in obtaining anomalously high values of T_c reported in [4.96], since the structural investigations cannot be carried out for the samples saturated with hydrogen through implantation. If hydrogenation of the samples is performed under high pressures, superconductivity is absent at $T \geqslant 2$ K in both the γ- and γ'-solutions $Pd_{60}Cu_{40}$-H with $n \leqslant 0.6$ (see Fig. 4.27).

Pd-Ag-H system. We studied solutions formed on the basis of the alloys with 20, 50, and 78 at.% Ag at hydrogen pressures up to 6.7 GPa and temperatures up to 400° C. The $Pd_{50}Ag_{50}$-H system was found to be most interesting. At $P_{H_2} = 6.7$ GPa, phenomena completely analogous to those occurring in the $Pd_{60}Cu_{40}$-H system were observed for this system. At $T = 200°$ C, the system underwent an irreversible phase transition accompanied by a decrease in the sample resistance and a tetragonal distortion of its metal lattice. Tetragonality of the sample lattice was retained after complete liberation of hydrogen from the samples by quenching at $T \approx 250°$ C and disappeared after quenching at $T \geqslant 375°$ C or a plastic deformation of the samples without hydrogen at room temperature. The γ'-solutions $Pd_{50}Ag_{50}$-H differ from $Pd_{60}Cu_{40}$-H only in that the lattice of the former has $c/a < 1$. From the analogy between the properties of the Pd-Ag-H and Pd-Cu-H systems, it is reasonable to conclude that as in the $Pd_{60}Cu_{40}$-H system, the new phase transition observed in the $Pd_{50}Ag_{50}$-H system is accompanied by ordering of the metallic matrix (although superstructural lines were not observed in the X-ray photographs for the ordered $Pd_{50}Ag_{50}$-H solutions due to the nearly equal atomic scattering factors for palladium and silver).

On the basis of the data of resistometric and structural study of the samples obtained at high hydrogen pressures (see Table 4.3), the T vs. P_{H_2} phase diagram was constructed for the $Pd_{50}Ag_{50}$-H system (Fig. 4.29). Besides the lower limit of the temperature interval for the formation of the ordered γ'-phase (whose position is apparently determined by the kinetics of the process), the phase diagram also shows the line of the $\gamma' \rightleftarrows \gamma$ transformation which is the upper boundary of the temperature range for the thermodynamical stability of the γ'-solutions. Note that in the investigated range

Table 4.3. Data of X-ray Investigations at Atmospheric Pressure and $T = -190°$ C for $Pd_{50}Ag_{50}$-H Samples Obtained by Exposing for 24 Hours at T and P_{H_2} Indicated in Fig. 4.29

No.	n	a, Å	c, Å	c/a	ΔV_0, Å^3
1	0.38	4.042	—	—	3.7
2	0.52	3.995	4.249	1.064	5.5
3	0.50	3.985	4.259	1.069	5.3
4	0.48	3.986	4.271	1.073	5.5
5	0.51	3.985	4.283	1.075	5.7
6	0.44	4.062	—	—	4.7
7	0.44	3.987	4.242	1.064	5.1
8	0.44	3.991	4.228	1.059	5.0
9	0.43	3.996	4.217	1.055	5.0
10	0.43	3.989	4.224	1.059	4.9
11	0.44	4.007	4.193	1.046	5.0
12	0.39	4.049	—	—	4.1
13	0.29	4.043	—	—	3.8

Remark: We draw the reader's attention to the fact that the magnitudes of parameters for the γ'-solutions $Pd_{50}Ag_{50}$-H listed in the table are not the thermodynamically equilibrium values for given T and P_{H_2}, since a 24-hours exposure was obviously insufficient to bring the samples to the equilibrium state.

of hydrogen pressures, the temperature T_0 corresponding to disordering of the $Pd_{50}Ag_{50}$-H solutions was found to be much lower than that for the $Pd_{60}Cu_{40}$-H solutions for which $T_0 \gg 350°$ C at $0.5 \leqslant P_{H_2} \leqslant 2$ GPa [4.107].

As to the $Pd_{80}Ag_{20}$-H system, only ordinary γ-solutions based on disordered fcc metal lattice are formed in it at $P_{H_2} \leqslant 6.7$ GPa and $T \leqslant 400°$ C. According to the data of X-ray analysis, the $Pd_{22}Ag_{78}$-H solutions ($n \leqslant 0.09$) also have an fcc metal lattice.

The T_c vs. n dependence for the $Pd_{80}Ag_{20}$-H solutions is shown in Fig. 4.27. The investigated $Pd_{50}Ag_{50}$-H and $Pd_{22}Ag_{78}$-H solutions were not found to be superconducting for $T \geqslant 2$ K.

Pd-Au-H system. Investigations of hydrogen solutions in the alloys with 3, 9, 22.5, 50, and 75 at.% Au showed that at $P_{H_2} \leqslant 6.7$ GPa and $200 \leqslant T \leqslant 350°$ C, only ordinary γ-solutions on the basis of disordered lattice of the alloys are formed in the Pd-Au-H system [4.98]. Thus, if γ'-solutions are formed in the Pd-Au-H system at all, their disordering temperatures is below 200° C.

The dependence of the superconducting transition temperature on hydrogen concentration in the $Pd_{97}Au_3$ and $Pd_{91}Au_9$ alloys is

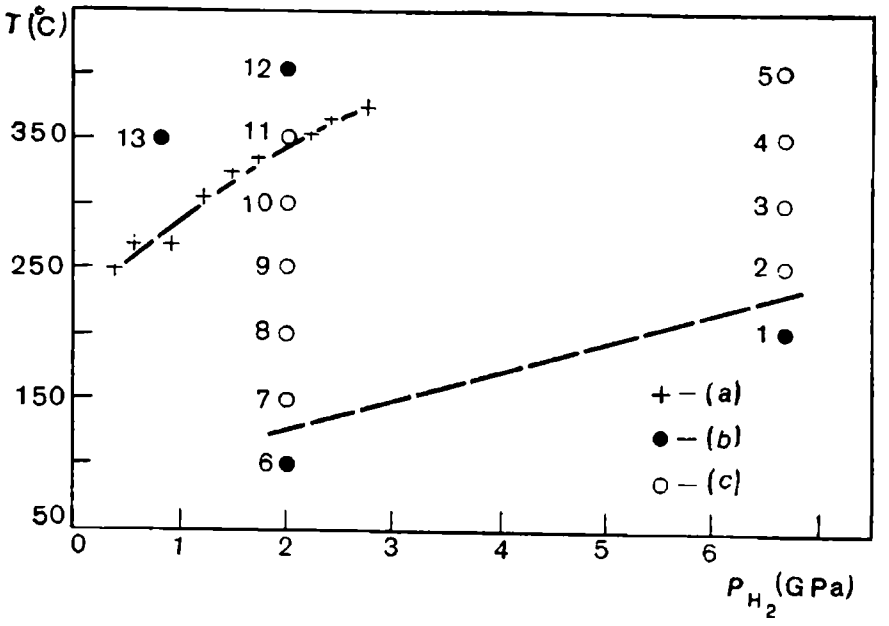

Fig. 4.29. T vs. P_{H_2} phase diagram for the $Pd_{50}Ag_{50}$-H system (results of the present paper).
a—values of the $\gamma' \rightleftarrows \gamma$ transition temperature. The dotted line is the lower limit of the temperature range in which the γ'-phase is formed. The numbers *1* to *13* indicate the conditions for obtaining the $Pd_{50}Ag_{50}$-H samples for investigations at normal pressure; data are shown in Table 4.3 (*b*—γ-solutions, *c*—γ'-solutions).

shown in Fig. 4.29. No superconducting transition was observed at $T \geqslant 2$ K for hydrogen solutions in alloys containing $\geqslant$22.5 at. % Au (the maximum hydrogen concentration attained for the alloys with 22.5, 50, and 75 at. % Au was $n = 0.61$, 0.25, and 0.03 respectively).

Pd-Ni-H system [4.110]. The alloys with 5, 20, 40, 60, and 80 at. % Ni were investigated. The measurements showed that at $P_{H_2} \leqslant$ $\leqslant 7$ GPa and $T \leqslant 250°$ C, only ordinary γ-solutions are formed in the Pd-Ni-H system, the line of the isomorphic $\gamma_1 \rightleftarrows \gamma_2$ transformation shifting monotonically towards higher pressures with increasing nickel content of the alloys. At $T > 250°$ C, the γ_2-solutions based on the alloys with 20, 40, 60, and 80 at. % Ni dissolute into hydrides of almost pure nickel and of palladium with a few atomic percent of Ni. The two-phase state of such samples is retained even after complete removal of hydrogen by annealing in vacuum at $T \leqslant 350°$ C. Quenching in vacuum at $T \geqslant 400°$ C or plastic deformation of hydrogen-free samples at room temperature returns the alloys to the starting homogeneous state. Hence, separation into phases enriched and depleted in palladium is not an equilibrium property of Pd-Ni solutions themselves under normal conditions.

It is the triple Pd-Ni-H solutions with a high hydrogen concentration which are found to dissolute.

Substitution of nickel for palladium leads to a suppression of superconductivity in the γ-solutions Pd-Ni-H (see Fig. 4.28), and γ-solutions based on the alloys with ⩾20 at. % Ni are not superconducting for $T \geqslant 2$ K [4.110]. Actually, it is just the behaviour of the superconducting properties that one should expect during alloying with a ferromagnetic metal. An unexpected result was the absence of superconductivity at $T \geqslant 2$ K for solutions based on the alloys with ⩾20 at. % Ni, dissoluted into palladium-enriched and depleted phases. This effect might be due to the suppression of superconductivity in particles of the palladium-enriched phase, precipitated from the Pd-Ni-H solid solution under the influence of the surrounding paramagnetic medium (the dimensions of the particles did not, in any case, exceed 0.5 μm). It is worth noting here that while the data on the superconductivity of Pd-Ni-H solutions obtained in samples saturated with hydrogen through implantation at helium temperature [4.51] and through electrolysis at $T \approx 200$ K [4.111] were in accord with our data [4.110], the hydrogenation of Pd-Ni alloys at a high hydrogen pressure and room temperature [4.112] led to different results: most of the samples based on alloys with ~20 and even 43 at. % Ni had rather high values of T_c. Crystal structure of the samples was not investigated in [4.112], but it is quite possible that samples with ⩾20 at. % Ni might consist of a mixture of palladium-enriched and depleted phases, and the palladium-enriched phase was superconducting.

Pd-Pt-H-system. The study of samples based on the alloys with 2.8, 10, 15, 20, 25, 40, and 60 at. % Pt showed that only ordinary γ-solutions are formed in the Pd-Pt-H system at $P_{H_2} \leqslant 6.5$ GPa and $T < 250°$ C, the solubility of hydrogen in the Pd-Pt alloys decreasing monotonically with increasing platinum concentration. At $T \geqslant 250°$ C, solutions based on the alloys containing ⩾15 at. % Pt dissolute into the hydride of palladium with a few atomic percent of Pt and the alloy with composition close to $Pd_{25}Pt_{75}$ in which hydrogen solubility at $P_{H_2} \leqslant 6.5$ GPa is negligible. After removal of the hydrogen through quenching in vacuum at 300° C, all the Pd-Pt samples return to their initial homogeneous state.

Figure 4.30 shows the data on the superconductivity of the Pd-Pt-H samples. The change in the T_c vs. n dependence for the γ-solutions with increasing platinum concentration in the alloys turned out to be nonmonotonic. The T_c vs. n dependence for the $Pd_{97.2}Pt_{2.8}$-H solutions is more gently sloping than that for the Pd-H solutions, and though at low values of n, the $Pd_{97.2}Pt_{2.8}$-H solutions possess higher values of T_c, the maximum T_c value reached for these solutions is lower than that for Pd-H. At $T \geqslant 2$ K, no superconductivity was observed for the $Pd_{90}Pt_{10}$-H solutions with

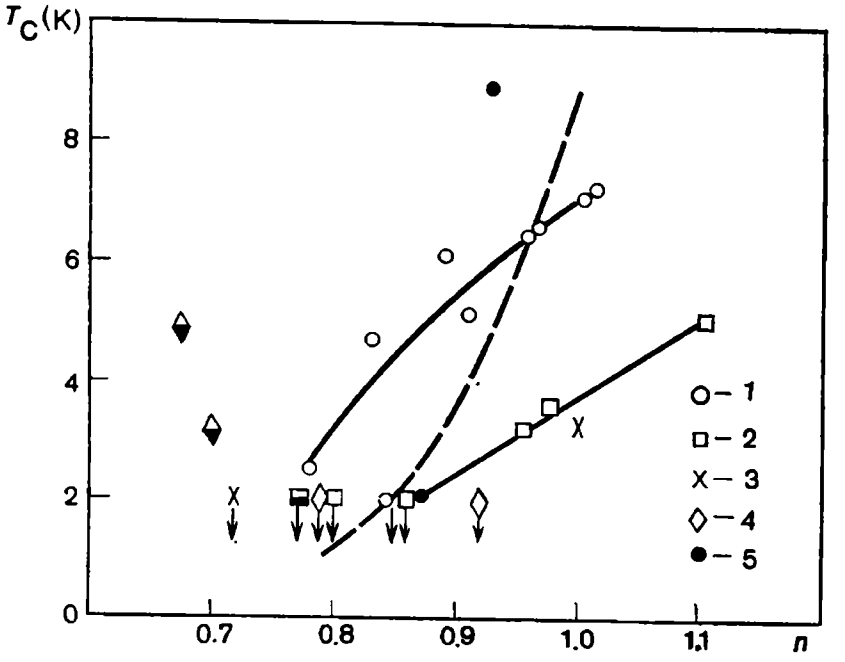

Fig. 4.30. Dependence of the superconducting transition temperature T_c on the hydrogen concentration n in Pd-Pt alloy containing: *1*—2.8; *2*—15; *3*—20; *4*—25 at. % Pt (results of the present paper); *5*—2.8 at. % Pt (results of [4.113]). Half-blackened symbols refer to the samples in which a separation into palladium-enriched and depleted phases are observed. The arrows and the dashed line are as in Fig. 4.27.

$n \leqslant 0.97$. Superconductivity reappeared in the $Pd_{85}Pt_{15}$-H and $Pd_{80}Pt_{20}$-H solutions, then vanished again, and the $Pd_{75}Pt_{25}$-H, $Pd_{60}Pt_{40}$-H, and $Pd_{40}Pt_{60}$-H solutions turned out to be nonsuperconducting at hydrogen concentrations up to $n = 0.92$, 0.51, and 0.11 respectively. In general, it should be remarked that the superconducting properties of the Pd-Pt-H system are found to be quite astonishing: our results on the behaviour of T_c differ from the results of [4.51] for the samples with implanted hydrogen (according to [4.51], $T_c^m \approx 9.5$ K for the alloys containing $\leqslant$30 at.% Pt, and then decreases rapidly), as well as from the data of [4.113] for the $Pd_{97.2}Pt_{2.8}$ alloys saturated with hydrogen at high pressure and room temperature (see Fig. 4.30).

A gratifying result was the discovery of superconductivity in the two-phase $Pd_{75}Pt_{25}$-H samples (half-blackened diamond-shaped symbols in Fig. 4.30), which is in line with the inference that the Pd-Pt-H solutions dissolute into palladium-enriched and depleted phases at high hydrogen pressure and $T \gtrsim 250°$ C.

4.6. CONCLUSION

As is seen from the results described in this paper, the technique for compressing hydrogen to high pressures turned out to be quite a valuable tool for investigating the metal-hydrogen systems. With the help of this technique, over a relatively short period of time, hydrides were obtained for most of the group VI-VIII transition metals which were earlier considered to form no hydrogen-saturated phases. The crystal structure and composition of these new hydrides were studied and the diagrams of phase transformations were constructed. It seems now that there are no transition metals which do not form hydrides at all, and one can expect that a further extension of the pressure range will result in the injection of considerable amounts of hydrogen even in metals like tungsten, osmium, iridium, and platinum, the most inert metals with respect to hydrogen.

The possibility of varying the hydrogen concentration in 3*d*-metals of VI-VIII groups over a wide range led to a lot of new experimental results which helped in constructing a systematic picture of the effect of hydrogen on the magnetic properties of transition metals. An analysis of the accumulated experimental data shows that all the observed effects stem primarily from the increase in the degree of filling of the weakly deforming *d*-band of the metal-solvent by electrons, the hydrogen supplying a fractional number of electrons ($\eta < 1$ electron per proton) to the *d*-band (the rigid *d*-band model). It is worth mentioning that the concept of the hydrogen as a donor of a fractional number of electrons to the *d*-band of the metal-solvent agrees with the theoretical calculations carried out by other authors on the band structure of the hydrides of transition metals.

The study of the Pd-Me-H solutions showed that homogeneous thick samples saturated with hydrogen under pressure and in near-equilibrium conditions do not reveal anomalous superconducting properties which were earlier observed in the experiments on hydrogen implantation. Therefore, the unusual behaviour of T_c for the Pd-Me-H solutions obtained by implantation is not a property of the equilibrium solutions but is due to the peculiarities of the metastable state of thin and defect-saturated hydrogen-containing layers formed in the process of implantation. The fact that the Pd-Me-H solutions obtained by implantation possess considerably higher values of T_c as compared to those for the equilibrium solutions throws a new light on the possibilities of improving the superconducting properties by using various metastable states of a material, including an adjustment of its defect structure.

An interesting result of our investigations of the Pd-Me-H systems is the discovery of new phase transformations accompanied by

a diffusion rearrangement of atoms of the metal matrix and occurring at comparatively low temperature. The discovery of such transformations is yet another convincing proof of the extremely strong influence of hydrogen on the interatomic interaction and diffusion mobility of the metallic components of the hydrogenated alloys.

Thus, the new experimental results obtained with the help of the high pressure technique have significantly contributed toward clarifying the important problems concerning the physical status of hydrogen in transition metals and the processes that can occur when the alloys of transition metals interact with hydrogen in the state of enhanced activity, i.e. with hydrogen compressed to high static and dynamic pressures, hydrogen in strong electrolytes, and hydrogen plasma.

References

4.1. V. Kh. Alimov, A. E. Gorodetsky, A. P. Zakharov, V. M. Sharapov, *Dokl. Akad. Nauk SSSR*, **241**, 595 (1978).
4.2. B. Stritzker, *Phys. Rev. Lett.*, **42**, 1769 (1979).
4.3. B. Baranowski, R. Wiśniewski, *Bull. Akad. Polon. Sci.*, **14**, 273 (1966); R. Wiśniewski. In: *III Krajowa Narada Techniki Wysokich Ciśnień*, Warszawa, 1969; B. Baranowski, W. Bujnowski, *Roczn. Chem.*, **44**, 2271 (1970).
4.4. B. Baranowski, *Ber. Bunsenges. phys. Chem.*, **76**, 714 (1972).
4.5. B. Baranowski, *Topics in Appl. Phys.*, **29**, 157 (1978).
4.6. B. Baranowski, *Z. phys. Chem.* N. F., **114**, 59 (1979).
4.7. I. T. Belash, E. G. Ponyatovsky, Patent No. 741105 (USSR).
4.8. V. E. Antonov, I. T. Belash, E. G. Ponyatovsky. In: *Fizika i Tekhnika Vysokikh Davleny*, 9, 65 (1982), Naukova Dumka, Kiev; *Proc. 8th AIRAPT/19th EHPRG Conf.* **1**, 80 (1981), Uppsala, Sweden.
4.9. V. E. Antonov, T. E. Antonova, I. T. Belash, A. E. Gorodetsky, E. G. Ponyatovsky, *Dokl. Akad. Nauk SSSR*, **266**, 376 (1982).
4.10. S. A. Semiletov, R. V. Baranova, Yu. P. Khodyrev, R. M. Imamov, *Kristallografiya*, **25**, 1162 (1980).
4.11. E. Wicke, H. Brodowsky, *Topics in Appl. Phys.*, **29**, 73 (1978).
4.12. V. E. Antonov, I. T. Belash, E. G. Ponyatovsky, V. I. Rashupkin, *Fiz. Metallov i Metallovedenie*, **48**, 75 (1979).
4.13. V. E. Antonov, I. T. Belash, E. G. Ponyatovsky, *Dokl. Akad. Nauk SSSR*, **223**, 1114 (1977).
4.14. V. I. Spitsyn, V. E. Antonov, O. A. Balakhovsky, I. T. Belash, E. G. Ponyatovsky, V. I. Rashupkin, V. Sh. Shekhtman, *Dokl. Akad. Nauk SSSR*, **260**, 132 (1981).
4.15. M. Krukowski, B. Baranowski, *Roczn. Chem.*, 49, 1183 (1975).
4.16. E. G. Ponyatovsky, I. T. Belash, *Dokl. Akad. Nauk SSSR*, **224**, 607 (1975).
4.17. V. I. Spitsyn, E. G. Ponyatovsky, V. E. Antonov, I. T. Belash, O. A. Balakhovsky, *Dokl. Akad. Nauk SSSR*, **247**, 1420 (1979).
4.18. V. E. Antonov, I. T. Belash, V. F. Degtyareva, E. G. Ponyatovsky, V. I. Shiryaev, *Dokl. Akad. Nauk SSSR*, **252**, 1384 (1980).
4.19. V. E. Antonov, I. T. Belash, V. F. Degtyareva, E. G. Ponyatovsky, *Dokl. Akad. Nauk SSSR*, **239**, 342 (1978).
4.20. A. Knödler, Metaloberfl, **17**, 161 (1963); A. D. Stock, K. I. Hardcastle, *J. Inorg. Nucl. Chem.*, **32**, 1183 (1970); G. Wolf, *Z. phys. Chem.* (Leipzig), **246**, 403 (1971); H. R. Khan *et al.*, *Math. Res. Bull.*, 9, 1191 (1974).

4.21. B. Baranowski, K. Bojarski, *Roczn. Chem.*, **46**, 525 (1972).
4.22. E. G. Ponyatovsky, I. T. Belash, *Dokl. Akad. Nauk SSSR*, **229**, 1171 (1976).
4.23. B. Baranowski, K. Bojarski, *Roszn. Chem.*, **46**, 1403 (1972).
4.24. I. T. Belash, V. E. Antonov, E. G. Ponyatovsky, *Dokl. Akad. Nauk SSSR*, **235**, 379 (1977).
4.25. V. E. Antonov, I. T. Belash, E. G. Ponyatovsky, *Dokl. Akad. Nauk SSSR*, **248**, 635 (1979).
4.26. M. Krukowski, B. Baranowski, *J. Less-Common Metals*, **49**, 385 (1976).
4.27. I. T. Belash, B. K. Ponomarev, V. G. Thiessen, N. S. Afonikova, V. Sh. Shekhtman, E. G. Ponyatovsky, *Fiz. Tverd. Tela*, **20**, 422 (1978).
4.28. V. P. Zhebelev, V. A. Somenkov, E. G. Ponyatovsky, S. Sh. Shilshtein, I. T. Belash, *Neorgan. Mater.*, **14**, 1620 (1978).
4.29. E. G. Ponyatovsky, V. E. Antonov, I. T. Belash, *Uspekhi Fiz. Nauk*, **137**, 663 (1982).
4.30. V. E. Antonov, I. T. Belash, V. Yu. Malyshev, E. G. Ponyatovsky, N. A. Tulina, *Dokl. Akad. Nauk SSSR*, **269**, 617 (1983).
4.31. V. E. Antonov, I. T. Belash, E. G. Ponyatovsky, *Scripta Metal.*, **16**, 203 (1982).
4.32. J. F. Cannon, *J. Phys. Chem. Ref. Data*, **3**, 781 (1974).
4.33. E. G. Ponyatovsky, V. E. Antonov, I. T. Belash, *Fiz. Metallov i Metallovedenie*, **44**, 1038 (1977); **46**, 1090 (1978).
4.34. E. G. Ponyatovsky, V. E. Antonov, I. T. Belash, *Fiz. Metallov i Metallovedenie*, **46**, 1090 (1978).
4.35. F. P. Bundy, *J. Appl. Phys.*, **36**, 616 (1965).
4.36. L. D. Blackburn, L. Kaufmann, M. Cohen, *Acta Metal.*, **13**, 533 (1965).
4.37. V. E. Antonov, I. T. Belash, E. G. Ponyatovsky, V. G. Thiessen, V. I. Shiryaev, *Phys. Stat. Sol.* (a), **65**, K43 (1981).
4.38. G. C. Kennedy, R. C. Newton, In: *Solids under Pressure*, N.Y.-London, 1963, p. 163-178.
4.39. I. T. Belash, V. E. Antonov, E. G. Ponyatovsky, *Dokl. Akad. Nauk SSSR*, **235**, 128 (1977).
4.40. V. E. Antonov, I. T. Belash, B. K. Ponomarev, E. G. Ponyatovsky, V. G. Thiessen, *Phys. Stat. Sol.* (a), **57**, 75 (1980).
4.41. B. Baranowski, M. Smialowski, *J. Phys. Chem. Solids*, **12**, 206 (1959); *Bull. Acad. Polon. Sci.*, **7**, 663 (1958).
4.42. B. Baranowski, R. Wiśniewski, *Bull. Acad. Polon. Sci.*, **14**, 273 (1966).
4.43. E. G. Ponyatovsky, V. E. Antonov, I. T. Belash, *Dokl. Akad. Nauk SSSR*, **229**, 391 (1976).
4.44. E. G. Ponyatovsky, V. E. Antonov, I. T. Belash, *Dokl. Akad. Nauk SSSR*, **230**, 649 (1976).
4.45. V. G. Thiessen, V. E. Antonov, I. T. Belash, B. K. Ponomarev, E. G. Ponyatovsky, *Dokl. Akad. Nauk SSSR*, **242**, 1390 (1978).
4.46. D. Bloch, *Ann. de Phys.*, **1**, 3 (1966).
4.47. V. E. Antonov, I. T. Belash, V. M. Koltygin, E. G. Ponyatovsky, *Dokl. Akad. Nauk SSSR*, **248**, 131 (1979).
4.48. T. Graham, *Proc. Roy. Soc.*, **16**, 422 (1868); *Phil. Mag.*, **36**, 63 (1868); *C. R. Ac. Sci.*, **66**, 1014 (1868); *Ann. Chim. Phys.* (Paris), **14**, 315 (1868).
4.49. D. M. Nace, J. G. Aston, *J. Am. Soc.*, **79**, 3623, 3627 (1957).
4.50. T. Skośkiewicz, *Phys. Stat. Sol.* (a), **11**, K123 (1972).
4.51. B. Stritzker, H. Wühl, *Topics in Appl. Phys.*, **29**, 243 (1978).
4.52. M. Hansen, K. Anderko. *Constitution of Binary Alloys*, McGraw-Hill Book Company, N. Y./Toronto/London, 1958.
4.53. B. Baranowski, S. Filipek, *Roczn. Chem.*, **47**, 2165 (1973).
4.54. V. E. Antonov, I. T. Belash, V. F. Degtyareva, E. G. Ponyatovsky, V. G. Thiessen, *Fiz. Metallov i Metallovedenie*, **53**, 677 (1982).
4.55. B. Baranowski, M. Tkacz, *Europhys. Conf. Abstr.*, **1A**, 108, (1975).

4.56. V. E. Antonov, I. T. Belash, V. G. Thiessen, *Phys. Stat. Sol.* (a), **59**, 673 (1980).
4.57. M. Krukowski, B. Baranowski, *J. Less-Common Metals*, **49**, 385 (1976).
4.58. V. E. Antonov, I. T. Belash, V. F. Degtyareva, B. K. Ponomarev, E. G. Ponyatovsky, V. G. Thiessen, *Fiz. Tverd. Tela*, **20**, 2680 (1978).
4.59. B. Baranowski, S. Majchrzak, T. B. Flanagan, *J. Phys. F: Metal Phys.*, **1**, 258 (1971).
4.60. E. O. Wollan, J. W. Cable, W. C. Koehler, *J. Phys. Chem. Sol.*, **24**, 1141 (1963).
4.61. W. E. Wallace, *Ber Bunsenges. phys. Chem.*, **76**, 832 (1972).
4.62. M. Hanson, H. R. Khan, A. Knödler, Ch. J. Raub., *J. Less-Common Metals*, **43**, 93 (1975).
4.63. H. R. Khan, Ch. J. Raub, *J. Less-Common Metals*, **49**, 399 (1976).
4.64. V. G. Thiessen, V. E. Antonov, I. T. Belash, B. K. Ponomarev, E. G. Ponyatovsky, *Phys. Stat. Sol.* (a), **48**, K185 (1978).
4.65. J. Crangle, G. C. Hallam, *Proc. Roy. Soc.*, **272A**, 119 (1963).
4.66. S. V. Vonsovsky, *Magnetizm*, Nauka, Moskva, 1971 (in Russian).
4.67. M. J. Besnus, Y. Gottehrer, G. Munschy, *Phys. Stat. Sol.* (b), **49**, 597 (1972).
4.68. B. K. Ponomarev, V. G. Thiessen, *Zh. Eksper. Teor. Fiz.*, **73**, 332 (1977).
4.69. J. Friedel, *J. Phys. et Rad.*, **19**, 573 (1958); **23**, 692 (1962); *Nuovo Cimento Suppl.*, **7**, 287 (1958).
4.70. G. T. Dubovka, *Phys. Stat. Sol.*, (a), **24**, 375 (1974).
4.71. J. Friedel, *Ber. Bunsenges. phys. Chem.*, **76**, 828 (1972).
4.72. A. C. Switendick, *Sol. State Comm.*, **8**, 1463 (1970); *Ber. Bunsenges. phys. Chem.*, **76**, 535 (1972); *Topics in Appl. Phys.*, **28**, 101 (1978).
4.73. D. A. Papaconstantopoulos, B. M. Klein, *Phys. Rev. Lett.*, **35**, 110 (1975); D. A. Papaconstantopoulos, B. M. Klein, J. S. Faulkner, L. L. Boyer, *Phys. Rev.*, **B18**, 2784 (1978).
4.74. D. A. Papaconstantopoulos, B. M. Klein, E. N. Economou, L. L. Boyer, *Phys. Rev.*, **B17**, 141 (1978); D. A. Papaconstantopoulos, E. N. Economou, B. M. Klein, L. L. Boyer. In: *Proc. Intern. Meeting on Hydrogen in Metals.* Münster, 1979, p. 733; *Phys. Rev.*, **B20**, 177 (1979).
4.75. M. Gupta, A. J. Freeman, *Phys. Rev.*, **B17**, 3029 (1978).
4.76. N. I. Kulikov, V. N. Borzunov, A. D. Zvonkov, *Phys. Stat. Sol.* (b), **86**, 83 (1978).
4.77. J. M. Leger, C. Loriers-Susse, B. Vodar, *Phys. Rev.*, **B6**, 4250 (1972).
4.78. H. J. Schenk, H. J. Bauer. In: *Proc. Intern. Meeting on Hydrogen in Metals.* Münster, 1979, p. 350.
4.79. H. J. Schenk, H. J. Bauer, B. Baranowski, *Phys. Stat. Sol.* (a), **52**, 195 (1979).
4.80. G. J. Zimmermann, H. J. Bauer, *Z. Phys.*, **229**, 154 (1969).
4.81. B. K. Ponomarev, S. V. Alexandrovich, *Zh. Eksper. Teor. Fiz.*, **67**, 1965 (1974).
4.82. G. T. Dubovka, E. G. Ponyatovsky, I. Ya. Georgieva, V. E. Antonov, *Phys. Stat. Sol.* (a), **32**, 301 (1975).
4.83. V. E. Antonov, I. T. Belash, B. K. Ponomarev, E. G. Ponyatovsky, V. G. Thiessen, *Phys. Stat. Sol.* (a), **52**, 703 (1979).
4.84. T. Sohmura, F. E. Fujita, *Sol. State Comm.*, **25**, 43 (1978).
4.85. D. M. Edwards, E. P. Wohlfarth, *Proc. Roy. Soc.*, **303A**, 127 (1968); E. P. Wohlfarth, *J. Appl. Phys.*, **39**, 1061 (1968).
4.86. V. E. Antonov, G. T. Dubovka, *Fiz. Metallov i Metallovedenie*, **40**, 645 (1976).
4.87. E. G. Ponyatovsky, V. E. Antonov, I. T. Belash, *Fiz. Tverd. Tela*, **18**, 3661 (1976).
4.88. H. J. Bauer, G. Berninger, G. Zimmermann, *Z. Naturforsch.*, **23a**, 2023 (1968); H. J. Bauer, *Z. angew. Phys.*, **26**, 87 (1968).

4.89. V. E. Antonov, I. T. Belash, V. F. Degtyareva, E. G. Ponyatovsky, V. G. Thiessen, *Fiz. Metallov i Metallovedenie*, 53, 677 (1982).
4.90. P. Weiss, R. Forrer, *Ann. de Phys.*, **12**, 279 (1929).
4.91. R. M. Bozorth, *Ferromagnetism*. D. van Nostrand, Toronto/New York/London, 1951.
4.92. H. Ohno, *J. Phys. Soc. Japan*, **31**, 92 (1971).
4.93. H. Ohno, M. Mekata, *J. Phys. Soc. Japan.*, **31**, 102 (1971).
4.94. V. E. Antonov, I. T. Belash, I. Ya. Georgieva, V. F. Degtyareva, V. G. Thiessen, A. V. Shalimova, *Fiz. Tverd. Tela*, **24**, 975 (1982).
4.95. E. Wicke, *J. Less-Common Metals*, **74**, 185 (1980).
4.96. B. Stritzker, *Z. Phys.*, **268**, 261 (1974).
4.97. V. E. Antonov, I. T. Belash, E. G. Ponyatovsky, V. I. Rashupkin, *Zh. Eksper. Teor. Fiz., Pis'ma*, **31**, 451 (1980).
4.98. V. E. Antonov, T. E. Antonova, I. T. Belash, E. G. Ponyatosky, V. I. Rashupkin, *Phys. Stat. Sol.* (a), **77**, K 23 (1983).
4.99. B. N. Ganguly, *Z. Phys.*, **B22**, 127 (1975).
4.100. K. H. Bennemann, J. W. Garland, *Z. Phys.*, **260**, 367 (1973).
4.101. G. Wolf, J. Yanke, K. Bohmhammel, *Phys. Stat. Sol.* (a), **36**, K125 (1976).
4.102. T. B. Flanagan, D. M. Chisdes, *Sol. State Comm.*, **16**, 529 (1975); D. Fisher, D.M. Chisdes, T. B. Flanagan, *J. Sol. State Chem.*, **20**, 149 (1977).
4.103. H. Brodowsky, E. Poeschel, *Z. Phys. Chem. N.F.*, **44**, 143 (1965).
4.104. A. W. Szafrański, B. Baranowski, *Phys. Stat. Sol.* (a), **9**, 435 (1972).
4.105. A. Maeland, T. B. Flanagan, *J. Phys. Chem.*, **69**, 3575 (1965).
4.106. B. Baranowski, R. Wiśniewski, *Phys. Stat. Sol.*, **35**, 593 (1969).
4.107. V. F. Degtyareva, V. E. Antonov, I. T. Belash, E. G. Ponyatovsky, *Phys. Stat. Sol.* (a), **66**, 77 (1981).
4.108. W. B. Pearson, *A Handbook of Lattice Spacings and Structures of Metals and Alloys*. Pergamon Press, London, 1964.
4.109. K. Schubert, B. Kiefer, M. Wilkens, R. Haufler, *Z. Metallkunde*, **46**, 692 (1955); D. M. Jones, E. A. Owen, *Proc. Phys. Soc.*, **67A**, 297 (1954).
4.110. V. E. Antonov, T. E. Antonova, I. T. Belash, E. G. Ponyatovsky, V. I. Rashupkin, V. G. Thiessen, *Phys. Stat. Sol.* (a), **77**, 71 (1983).
4.111. L. Sniadower, L. Dumoulin, P. Nedellec, J. P. Burger. In: *Metall-Hydrogen Systems*, Ed. T.N. Veziroğlu, Pergamon Press, Oxford, 1982.
4.112. T. Skośkiewicz, *High Temp.-High Pressures*, **7**, 684 (1975); *Phys. Stat. Sol.* (a), **48**, K165 (1978).
4.113. T. Skośkiewicz, A. W. Szafrański, B. Baranowski, *Phys. Stat. Sol.* (b), **59**, K135 (1973).
4.114. B. Baranowski, K. Bocheńska, *Roczn. Chem.*, 38, 1419 (1964); *Z. Phys. Chem. N.F.*, **45**, 140 (1965).
4.115. S. Majchrzak, *Bull. Acad. Polon. Sci.*, **15**, 485 (1967).

5 Dislocations and Physical Properties of Semiconductors

Yu. A. Ossipyan

5.1. INTRODUCTION

The main concepts about the influence of dislocations on the electric properties of semiconductors are based on the model in which a dislocation chain is treated as a line of atoms with dangling chemical bonds. These atoms may capture electrons from the conduction band or, conversely, give away unpaired electrons to other centres, thus acting as acceptors or donors. Consequently, the dislocations in semiconductors possess an electric charge. This leads to a sharp anisotropic change in the carrier mobility upon introduction of dislocations into a crystal. Investigations of the energy spectrum of electrons directly involved in dislocation states are also of considerable interest. It is found that these electrons account for such properties of plastically deformed semiconductors as dislocation electric conductivity and dislocation EPR.

All this indicates that the electron properties of semiconductors with dislocations are quite different from the properties of defect-free crystals.

However, the electron-dislocation interaction in semiconductors is not confined to just these properties. It has been experimentally shown that the state of the electron subsystem and its variation have a considerable effect on the movement of dislocations under the action of mechanical loads, i.e. on the strength and plasticity of semiconductors. This has been confirmed by the discovery of photoplastic effect, electroplastic effect, dislocation current and dislocation luminescence, and several other effects during the last few years. The essence of these phenomena lies in the fact that when an electron subsystem is excited by light or an electric field, the dislocation levels as well as the levels of other local centres are occupied nonuniformly by the electrons. Under these conditions, an excess electric charge is created on the dislocations, thus ensuring the hardening of the crystal. A moving dislocation sweeps the electrons from the local centres into the conduction band. It is the return of these electrons to lower energy states that causes dislocation luminescence.

In this review, we shall be considering both the above-mentioned aspects of the electron-dislocation interaction. We shall present

the latest experimental results, as well as the model concepts formed to this date regarding the dislocation spectrum of electrons and the mechanism of movement of charged dislocations in semiconductors.

5.2. THE DISLOCATION ENERGY SPECTRUM OF ELECTRONS AND THE MICROWAVE DISLOCATION CONDUCTIVITY MECHANISM IN SEMICONDUCTORS

The experimental results which led to an understanding of the mechanism of interaction between moving electrons and dislocations in simple semiconductors were obtained mainly during the last 20-25 years. A review of these results and analysis of the possible mechanisms of electron-dislocation interaction are given in [5.1].

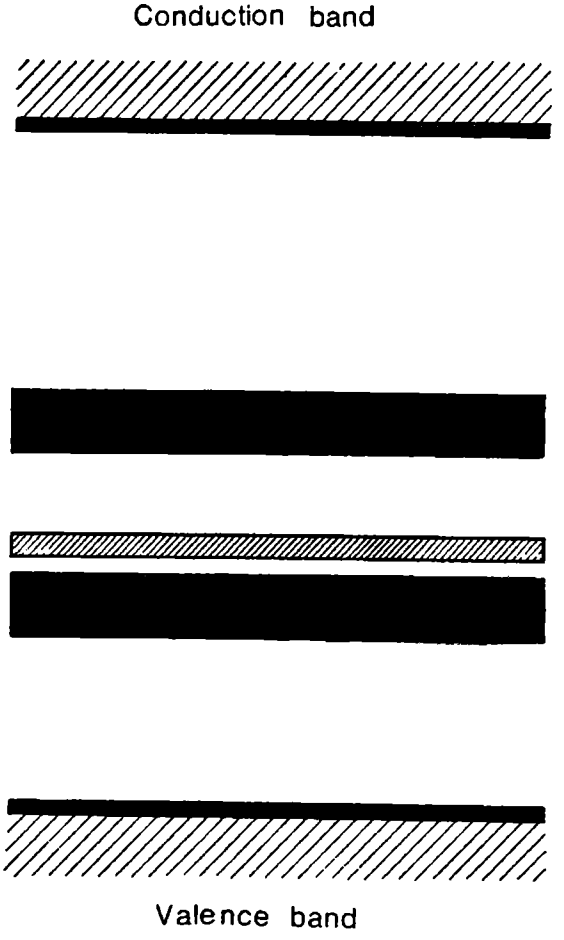

Fig. 5.1. Dislocation bands diagram following from the experimental results of [5.4].

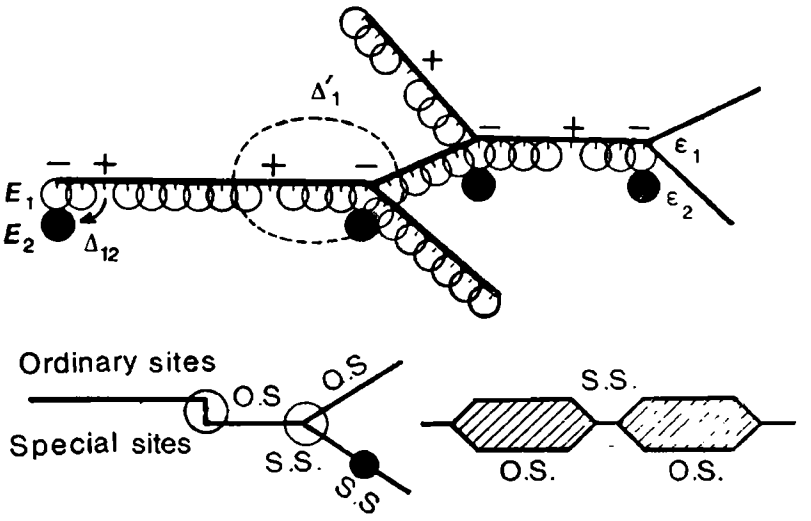

Fig. 5.2. Dislocation energy spectrum of electrons in Ge and Si. Δ_1—distance between the top of the valence band and the donor dislocation band E_1; $\Delta_1 = 0.07$ eV for Ge and 0.42 eV for Si; Δ_2 is the distance between the bottom of the conduction band and the acceptor dislocation band E_2; $\Delta_2 = 0.5$ eV for Ge and 0.52 eV for Si; Δ_{12} is the Mott-Habbard gap between the donor (E_1) and the acceptor (E_2) dislocation bands; $\Delta_{12} = 0.18$ eV for Ge and 0.20 eV for Si; Δ_1' is the gap between the donor dislocation band and the detached hole band E_1'; $\Delta_1' < 0.03$ eV for Ge and Si; ε_1 and ε_2 are the local defect states.

Without repeating the detailed material contained in [5.1], we shall consider in this article some aspects of this problem, which have been explained successfully only during the last few years.

The general diagram of the dislocation electron energy spectrum in basic semiconductors was earlier obtained by us from an analysis of the results of investigations of the microwave dislocation conductivity of silicon and germanium crystals with dislocations, as well as from photo-EPR studies [5.2, 3]. It was found that the experimental results on the dislocation conductivity of *p*- and *n*-type crystals can be explained by assuming that the forbidden band contains at least three dislocation bands for electrons. Moreover, the upper and the lower band were assumed to have a very high carrier mobility, while the mobility in the central band was assumed to be quite low (see Fig. 5.1) [5.4].

The results of photo-EPR studies led us to be conclusion that during plastic deformation, the creation of the main dislocation states for electrons is accompanied by the creation of certain acceptor states which are filled in dark by electrons. Upon illumination, electrons from these acceptor levels go over to a main dislocation band, thus increasing the dislocation EPR signal [5.3].

On the basis of the above considerations, the spectral diagram shown in Fig. 5.2 was proposed. Before discussing the specific

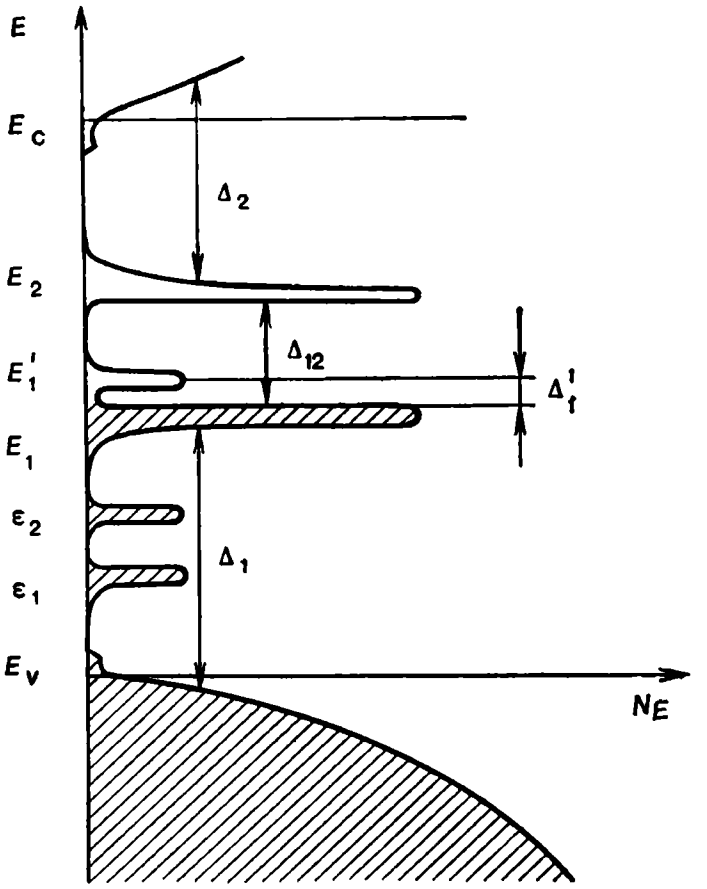

Fig. 5.3. Electron states at dislocation chains. The same notation as in Fig. 5.2 has been used.

structure of the spectrum in detail, let us consider certain aspects of the model of dislocation chains (Fig. 5.3).

As before, we assume that the dangling bond electrons of atoms belonging to a dislocation core form a narrow one-dimensional donor band whose width depends on the extent of overlapping of the wave functions of the electrons of the dangling bonds along the dislocation chain. The dangling dislocation bonds may capture extra electrons which are available in the crystal due to the presence of a chemical donor or other defects, or due to an excitation of electrons, say, by light or by a strong electric field. These extra electrons may be captured at the dislocation acceptor levels, thus forming a narrow dislocation acceptor band E_0. The Coulomb interaction between two electrons at one site between the above-mentioned one-dimensional bands gives rise to a gap whose existence indicates that a dislocation chain with dangling bonds may be described as a Mott-Habbard insulator.

Investigations of the dislocation structure in real crystals show that the regular regions of a dislocation line are quite short (a few tens or a few hundreds interatomic distances), and that the regular regions of the dislocation line alternate with the local defects like steps, intersections with other dislocations, cleavages, etc. Besides, the impurity atoms like oxygen may give rise to defects in the vicinity of a dislocation centre. Such local defects on or near a dislocation line may form additional acceptor and donor electron states. The number of these states depends on the number of local defects. We shall assume that both types of these local levels ε_1 and ε_2 are below the fundamental dislocation donor band. Then, in the case of a pure (undoped by shallow impurities) semiconductor with dislocations, a part of dangling band electrons is transferred to the acceptor levels of these local defects, thereby creating holes in the donor dislocation band. These holes are mobile and must move, on account of Coulomb forces, toward the electrons captured at the local defects. When the holes approach these defects, they come to a stop and cease to be mobile.

Since the gap between E_1 and E_1' bands does not exceed 0.05 eV [5.2, 3], the mean distance between a hole in E_1' and an electron in E_1 must be of the order of 5 lattice constants. Such a dislocation "exciton" may be stable, for example, due to the existence of an energy barrier at the dislocation, or due to a spatial separation if the local defect is not exactly in the dislocation core. Thus, a narrow band of holes (which are involved in a Coulomb interaction with the electrons captured at the acceptor levels of the local defects in a dislocation) gets separated from the fundamental dislocation donor band. Obviously, these holes have a lower mobility in comparison to the ordinary holes created in the dislocation donor band due to the electron capture from the dangling bonds in the dislocation by the chemical acceptors. If a semiconductor is undoped, or if the number of acceptor or donor impurities is small, both ε_1 and ε_2 bands are always completely filled in dark.

An analysis of the results on photo-EPR measurements on the basis of the spectrum described above is given in [5.3]. Let us now turn to the dislocation conductivity (DC).

In spite of the considerable progress made in the investigation of DC, the available experimental results [5.4-7] have proved to be insufficient for arriving at a definite conclusion on the DC mechanism. The dislocation mechanism appears to be the most probable one: the microwave conduction is due to the motion of carriers (electrons or holes) captured by dislocations along the dislocation centres. In this case, dislocations can be considered as one-dimensional conductors distributed within the crystal volume. However, the data given in [5.4-7] do not allow us to completely exclude another DC mechanism according to which dislocations play a different

role from the one mentioned above. The plastic deformation of a crystal and its subsequent annealing (at temperatures 460 and 700°C respectively in the case of Ge) may be accompanied by a diffusion of shallow doping impurities in the dislocation elastic fields. Thus, it cannot be ruled out that (at least in principle) certain regions can appear in the vicinity of dislocations, where the impurity concentration is higher than its average value by several orders of magnitude. (In our experiments, we used crystals of *n*- and *p*-type Ge with a shallow impurity concentration of 10^{13} cm^{-3}.) In this case, the charge carriers could be degenerate in such heavily doped regions, thus leading to microwave conductivity. It is clear from the above discussion that if we could prepare samples with dislocations and with a deliberate homogeneous distribution of shallow impurities, it could be possible to made a choice between these two alternative mechanisms of DC.

We tried to solve this problem with the help of neutron doping [5.8, 9]. Upon irradiation by thermal neutrons, some isotopes of Ge can become unstable by absorbing neutrons and decay into III and V group elements (see Table 5.1). The following reactions take place upom irradiation of Ge by thermal neutrons:

Table 5.1. Isotopic Composition of Natural Ge

Isotope	Ge^{70}	Ge^{72}	Ge^{73}	Ge^{74}	Ge^{76}
Percentage in natural Ge	21.2	27.3	7.9	37.1	6.5

captured neutrons (%)

30.4 $Ge^{70}(n, \gamma)Ge^{71} \xrightarrow{\text{K-capture}} Ga^{71}$ (5.1)

8.5 $Ge^{74}(n, \gamma)Ge^{75} \xrightarrow{\beta\text{-decay}} As^{75}$ (5.2)

0.52 $Ge^{76}(n, \gamma)Ge^{77} \xrightarrow{\beta\text{-decay}} As \xrightarrow{\beta\text{-decay}} Se^{77}$ (5.3)

The other isotopes remain stable after capturing neutrons.

The first of these expressions describes the appearance of acceptors, while the next two expressions correspond to the appearance of donors.

The isotope Ge^{70} is transformed into the unstable isotope Ge^{71} after capturing a neutron. In turn, this isotope is transformed into Ga^{71} as a result of K-capture. The time variation of the concentration of acceptors in Ga^{71} is described by the radioactive decay equation for the Ge^{71} isotope:

$$N_{Ga} = N_0 \left\{1 - \exp\left(\frac{t \ln 2}{\tau}\right)\right\}, \tag{5.4}$$

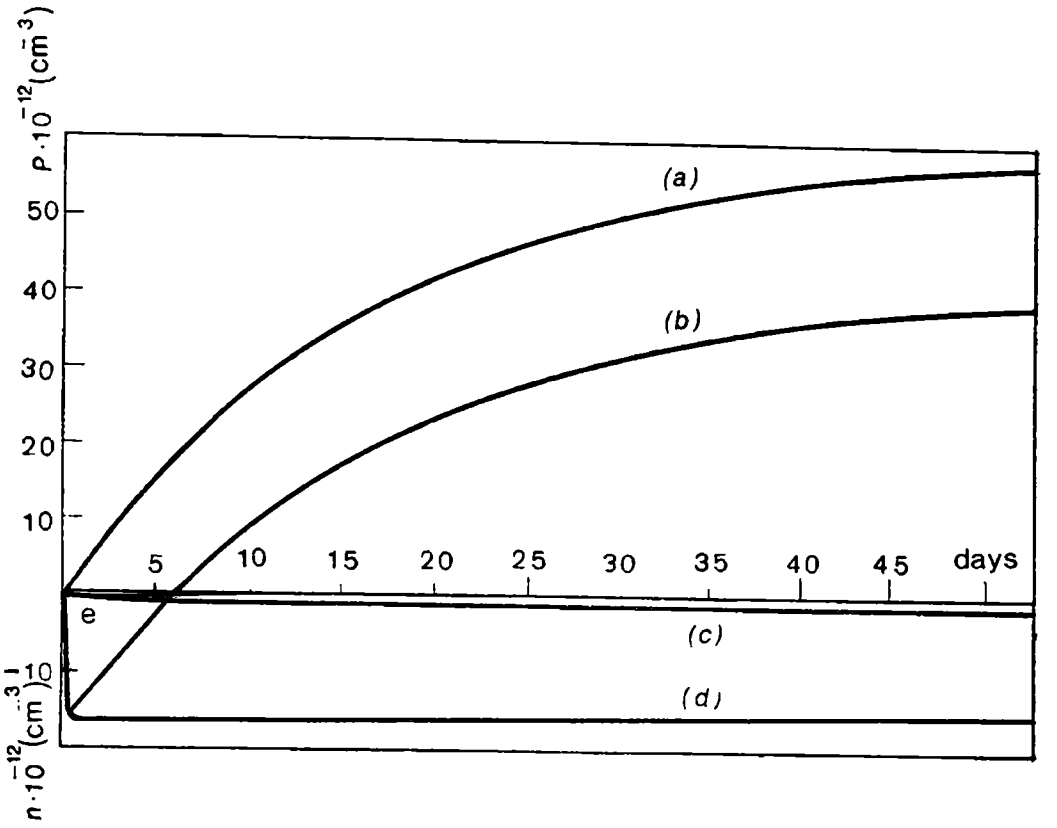

Fig.5.4. Kinetics of the isotope conversion in natural germanium (calculated).

where N_0 is the concentration of Ge^{70} atoms capturing neutrons, t is the time elapsed after the irradiation, and τ is the half-life (12 days). The curve showing this dependence is represented in Fig. 5.4*a*.

The transformation of Ge^{74} into As^{75} takes place as follows. After capturing a neutron, the Ge^{74} isotope decays into the radioactive isotope Ge^{75}, which in turn is transformed into the isotope As^{75} (with a half-life 82 min) as a result of β-decay.

After capturing a neutron, the Ge^{76} isotope is transformed into the unstable isotope Ge^{77} which decays into the unstable isotope As^{77}. In turn, As^{77} decays with a half-life of 38.8 hours into the stable isotope Se^{77}. The formula describing the kinetics of the appearance of Se^{77} is more complicated than the corresponding formulas for Ga^{71} and As^{75}. This is due to the fact that the concentration of the isotope (from which Se^{77} itself is "obtained") also depends on time.

Figure 5.4 (curves *a*, *c*, *d*, *e*) shows the kinetics of the transformation of all the above-mentioned isotopes, i.e. the kinetics of the accumulation of donor and acceptor centres.

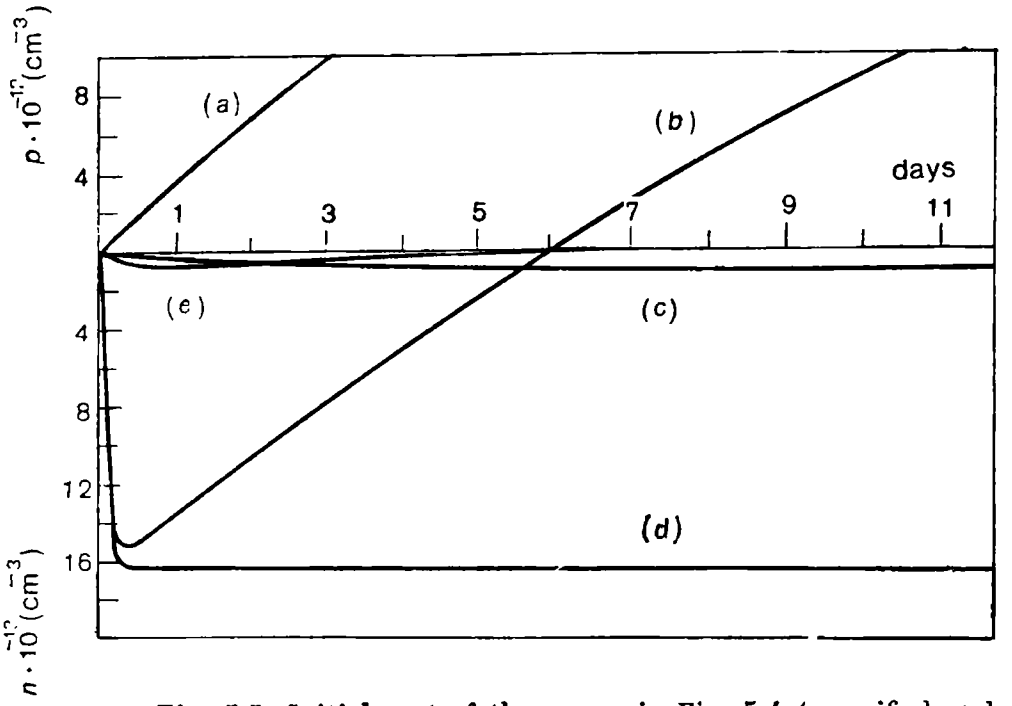

Fig. 5.5. Initial part of the curves in Fig. 5.4 (magnified scale.(

Curve *b* in Fig. 5.4 shows the time dependence of the difference in the concentrations of the donor and acceptor centres (taking into account the fact that Se^{77} is a double donor). The degree of compensation is the donor to acceptor concentration ratio:

$$K = \frac{\sum N_d}{N_a}.$$

Since the donor and acceptor impurities are created as a result of irradiation, and their concentration does not change in the same way with time, the degree of compensation will naturally change as well. When the concentration of acceptor impurities becomes equal to the total concentration of donor impurities, the degree of compensation becomes equal to unity. This happens in 5.85 days after the irradiation. By this time, the Ge isotopes which are transformed into donor centres completely decay (Figs. 5.4 and 5.5), and the change in the compensation is determined by the appearance of acceptor impurities. After a nearly complete decay, the degree of compensation attains a constant value and does not change any more. The final value of the compensation is given by the formula

$$K = \frac{N_{As} + 2N_{Se}}{N_{Ga}} \simeq 30\%.$$

The coefficient 2 appearing before the selenium concentration is due to the fact that each selenium atom contributes two electrons to the conduction band. The magnitude of K does not depend on the radiation dose and is determined just by the concentration of $Ge^{70,74,76}$ isotopes in natural Ge and by the probabilities of capture of a thermal neutron by these isotopes.

We shall now describe in detail the samples and the measuring technique.

Samples for deformation were cut in the form of a parallelepiped of dimensions $3 \times 6 \times 30$ mm^3 along $[1\bar{1}0]$, [001], and [110] directions respectively, from a single crystal of high-purity n-Ge (with a 2×10^{11} cm^{-3} concentration difference between donors and acceptors). The bending axis was directed along $[1\bar{1}0]$. The samples were deformed by four-point flexure at a temperature of 460°C. After deformation, the samples were covered by ultrapure tin by vacuum coating and were annealed at 700°C in an atmosphere of ultrapure argon for ten minutes. Crystals prepared in this way were cut along the neutral plane and parallelepipeds perpendicular to the bending axis were cut from each half. The dislocation density was calculated from the etching pits on [110] faces and was found to be $N_D = 3 \times 10^6$ and 6×10^6 cm^{-2} in the samples investigated by us.

After deformation, the samples did not exhibit a microwave dislocation conductivity. This is explained by an extremely low donor concentration in the original samples.

The samples were then coated with a protective layer of tin (as a heterocoating for subsequent annealing) and were irradiated in a reactor (with a 300 : 1 ratio between thermal neutrons and fast neutrons). The irradiation time of 8 min was chosen in such a way that the final concentration of the introduced acceptors was 4×10^{13} cm^{-3}. Besides the deformed samples, control samples were also irradiated. After irradiation, the samples were annealed at 500°C for 7-8 hours. This was followed by a slow cooling in order to eliminate the structural defects introduced during irradiation mainly due to the presence of fast neutrons in the reactor beam. At first glance, this forced annealing seems to nullify the advantage of the neutron doping method, since there is a danger of the shallow impurities being attracted towards the dislocations during annealing. However, these apprehensions are justified only for the donors. The acceptors are practically not even created till the end of the annealing process. Thus, we started our measurements with samples in which the donor concentration was 10^{13} cm^{-3} (it is not possible to make any statement about the uniform distribution of these donors in the sample after annealing). Every day, 10^{12} new acceptors were created per cubic centimeter of the sample, and these acceptors were distributed uniformly over the bulk of the sample.

Let us now consider the measuring technique.

The sample was placed in a cylindrical passthrough cavity in which TE_{111} vibrations were excited at a frequency 9500 MHz. The upper part of the cavity had slots for connecting it to a microwave oscillator and to a detector from which the signal was fed to an oscilloscope.

The oscillator operated in the FM mode, and a resonance curve was observed on the oscilloscope screen. A thin metallic platelet parallel to the slots for connections was soldered at the bottom of the cavity. This platelet removed the degeneracy in the oscillations and also served to fix the direction of the electric field inside the cavity.

A hole for introducing the sample was drilled in the upper part of the cavity. The sample was in the form of a disc and was mounted on a thin Teflon insert at the centre of the cavity. The insert, together with the sample, could be rotated with respect to the cavity. In this case, naturally, the direction of the electric field was not altered. Only the angle between the field and the dislocations changed. By rotating the sample, we can find the orientation corresponding to the lowest Q-factor of the resonator. It was found that the lowest Q (highest conductivity) always corresponds to the position when the electric field is directed along the dislocations (i.e. along the [110] direction). The cavity frequency remained practically unchanged as a result of rotation. The temperature of the resonator and the sample was maintained at 4.2 K. In order to control the change in the concentration of doping impurities with time, we measured the Hall effect at a constant current and at 77 K in samples which were irradiated by the same neutron flux as the samples used for microwave measurements.

Figure 5.6 shows the results of measurements of the change in carrier concentration with time after the Ge samples were irradiated in a reactor. Curve *a* corresponds to the control sample, while curve *b* corresponds to the sample which was first subjected to plastic deformation ($N_D = 3 \times 10^6$ cm^{-2}).

It can be seen that according to the calculations for the kinetics of transformation of different isotopes mentioned above, the sample remained *n*-type for the first few days, although the concentration of the conduction electrons in it steadily decreased. The compensation factor became equal to unity after 5.85 days; beyond this, the hole concentration began to increase.

A noticeable concentration of conduction electrons was not observed in the sample with dislocations even during the first days after irradiation. This is due to the fact that all donor electrons generated at this temperature are captured by dislocations and escape from the conduction band [5.10].

After compensation, when the conductivity is hole-type, both samples behave in an identical manner, the only difference being

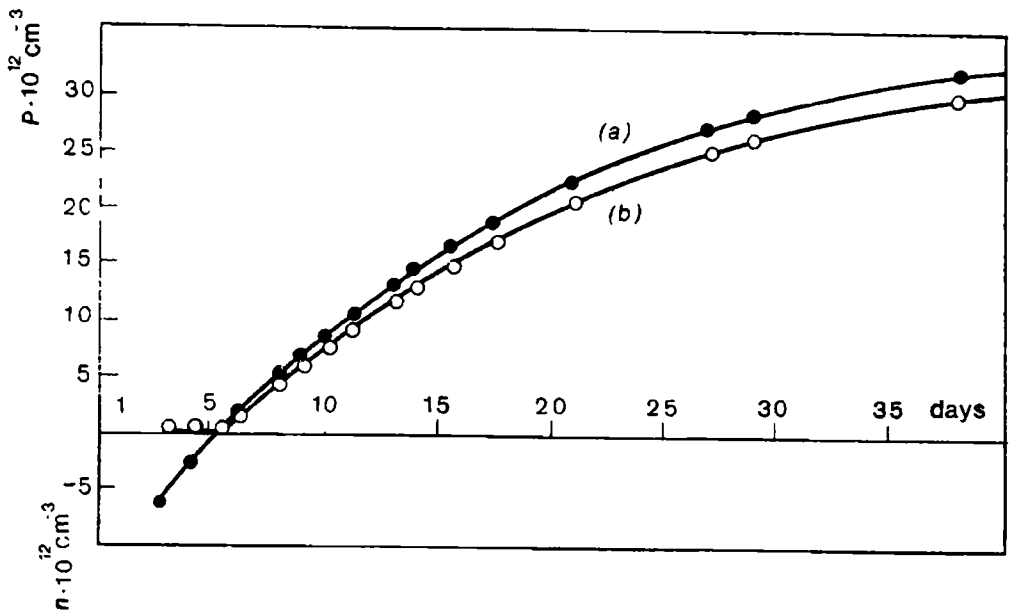

Fig. 5.6. Change in the carrier concentration in Ge after neutron irradiation: (*a*) control sample; (*b*) sample with $n_D = 3 \times 10^6$ cm^{-2}.

that the concentration of free holes in the control sample is somewhat higher.

Figure 5.7 shows the results of measurements of microwave DC as a function of time elapsed after irradiation.

It can be seen that (curve *1*) the DC first decreases and attains its minimum value after 5 days. After this, it begins to increase and reaches saturation after about 12 days. This can be explained as follows. At first, the number of electrons captured by a dislocation (and hence the DC) decreases with decreasing number of donors and increasing degree of compensation. The conductivity has its lowest value when the compensation is close to unity. Later, it begins to increase (as hole conductivity now) as the number of acceptors increases with time. When a dislocation has captured all the holes that it is capable of (if we take into consideration the occupancy factor), and the hole concentration at dislocations does not change any more, DC also attains a saturation value. It should be noted that during this time, the total concentration of holes in the sample continues to rise (Fig. 5.6). If the dislocation concentration is somewhat higher (Fig. 5.7, curve *2*), then in accordance with the spectral structure (Figs. 5.1 and 5.2) we arrive at a situation (just after irradiation) in which the carriers (holes) are situated in the low-mobility band (i.e. in the E_1' band, Fig. 5.2), and no conductivity is observed along the dislocations. Beyond this, as the number of acceptors increases with time, the holes go over to the E_1 band and the conductivity increases. After the moment of

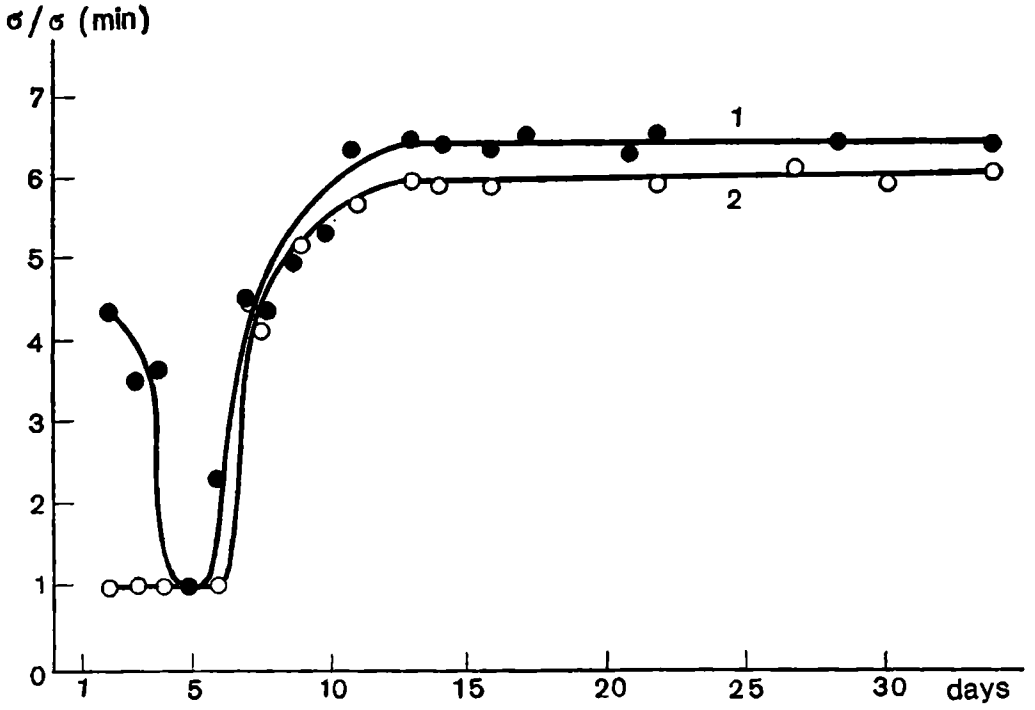

Fig. 5.7. Microwave DC in plastically deformed germanium after neutron irradiation: N_D (in cm^{-2}) = 3×10^6 (*1*); 6×10^6 (*2*).

compensation, curves *1* and *2* in Fig. 5.7 practically coincide. Thus, it can be stated on the basis of the experimental results presented above that we have been able to observe microwave dislocation conductivity under the conditions when the doping impurity (Ga^{71}) is uniformly distributed deliberately. This, in turn, is a decisive argument in favour of the electric conductivity mechanism along the dislocation centres.

Before concluding this section, we would like to mention another experimental result which is in agreement with the dislocation spectrum model. While measuring the dislocation Hall effect, we were able to show [5.11] that in *n*-type Ge crystals, the conductivity along the dislocations is hole-type when the dislocations capture electrons from donors and become negatively charged.

5.3. MOVEMENT OF CHARGED DISLOCATIONS IN $A^{II}B^{VI}$ SEMICONDUCTORS

After the discovery of the photoplastic effect (PhPE) in cadmium sulphide [5.12], it became clear that dislocations in $A^{II}B^{VI}$ semiconductors actively interact in their motion with the electron subsystem of the crystal. It was found that this interaction strongly affects

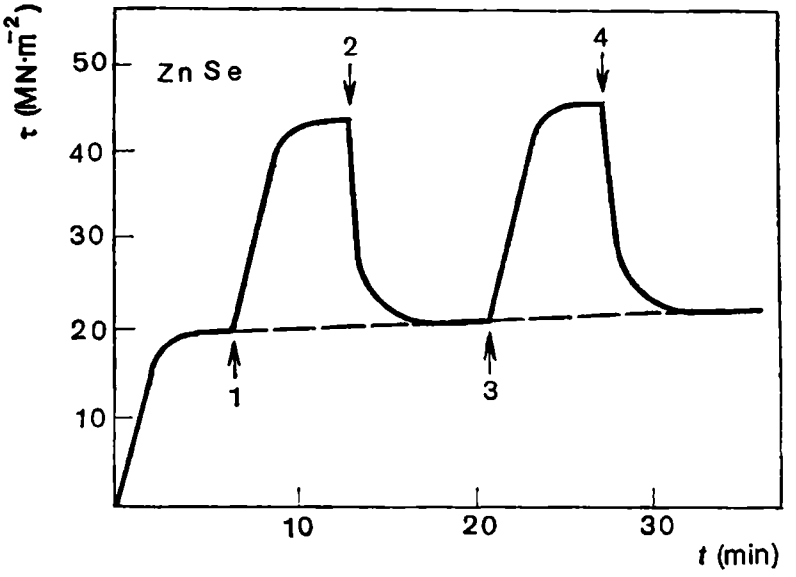

Fig. 5.8. Photoplastic effect in ZnSe. The sample was irradiated with visible light at the instants *1* and *3*; the light was switched off at the moments *2* and *4*. Temperature $T = 20°C$.

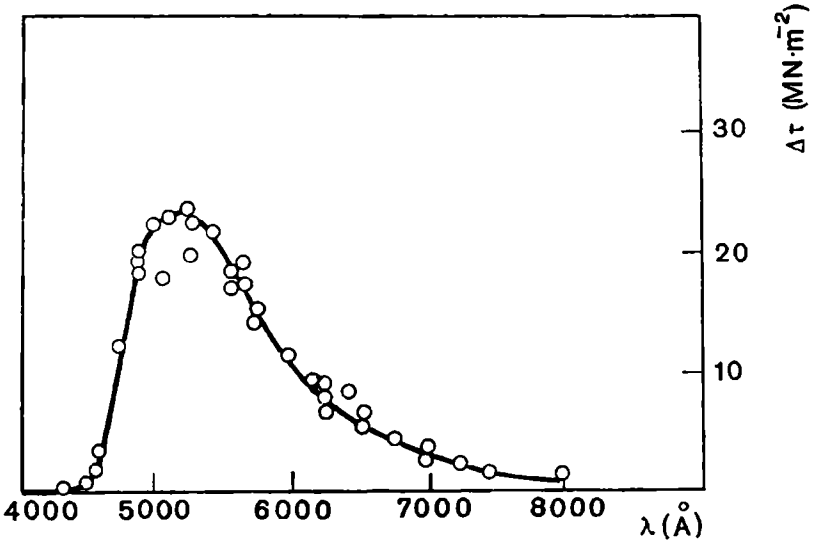

Fig. 5.9. Photoplastic effect spectrum in ZnSe; $\Delta\tau$ is the difference in the resolved shear stresses under illumination and in dark. Temperature $T = 20°C$.

the ability of a crystal to undergo plastic deformation when external mechanical stresses are applied to it.

Figure 5.8 shows the diagram of plastic deformation of a ZnSe crystal which exhibits PhPE. When the crystal being deformed is irradiated by visible light, the flow stress τ is doubled, but returns to its previous value as the irradiation is discontinued. The spectral dependence of PhPE is shown in Fig. 5.9. It is characterized by

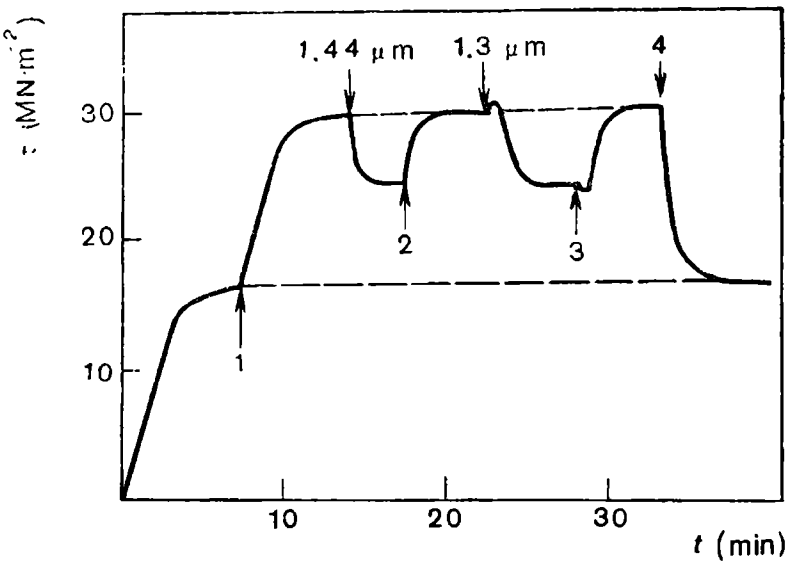

Fig. 5.10. IRQPhPE in CdS. Visible light was switched on and off at the instants *1* and *4* respectively, while the additional infrared illumination was switched off at the moments *2* and *3*; $T = 100°C$.

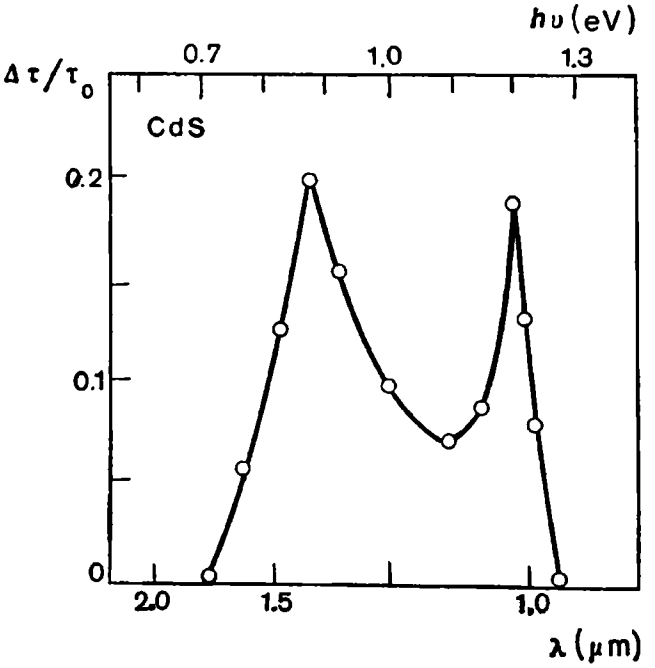

Fig. 5.11. IRQPhPE spectrum in CdS; $\Delta\tau$ is the IR quenching, τ_0 is the magnitude of the PhPE, $T = 100°C$.

a maximum in the region of the fundamental absorption edge and a smooth fall towards higher wavelengths.

Investigation of PhPE in different $A^{II}B^{VI}$ crystals led us to the conclusion that the PhPE mechanism involves a change in the conditions of the electrical interaction between moving dislocations and the point centres overcharged under the action of light and having localized levels for electrons in the forbidden gap.

This was confirmed by our subsequent discovery of the effects like the infrared quenching (IRQ) of PhPE [5.13], impurity photoplastic effect (IPhPE) [5.14], deformation luminescence (DL), as well as the injection plastic effect (IPE) [5.15]. Figure 5.10 shows the IRQPhPE, while its spectral dependence is shown in Fig. 5.11. It can be seen that the maximum quenching occurs in the region around 1.3 eV, which corresponds to the position of the local level of R-centres for CdS [5.16].

However, further investigations of the plastic deformation in $A^{II}B^{VI}$ semiconductors have shown that the electric charge of dislocations plays a very significant role in the deformation process. We have observed effects which owe their origin to the motion of charged dislocations and bring the electric charge to the crystal surface. Figures 5.12-5.14 illustrate the experimentally observed effects associated with a change in the electrical conditions at the boundary of a crystal during its deformation.

Short-circuiting effect (ShCE) [5.17] (Fig. 5.12) means that if during plastic deformation, the opposite faces of a crystal are short-circuited through an external circuit, the flow stress may considerably decrease. This fact is explained by assuming that the electric charge accumulated near the surface during plastic deformation interferes with the motion of charged dislocations and prevents them from appearing at the surface. In other words, this leads to a hardening of the crystal. The removal of this charge through an external circuit eliminates this factor and decreases the flow stress.

Dislocation current in the external circuit (Fig. 5.13) can be easily measured during plastic deformation when charged dislocations move inside the crystal. The method of dislocation current measurement for $A^{II}B^{VI}$ crystals is much more sensitive than any other method involving mechanical measurements.

Electroplastic effect (EPE) means that the application of an external electric field to a crystal being deformed may increase or decrease the flow stress, depending on the magnitude and sign of the applied field (Fig. 5.14). The EPE mechanism is associated with the influence of the external field on the charged dislocations and is clear from the above explanation. The factors described above convincingly prove that the electric charge of dislocations plays a very important role in the process of plastic deformation of semi-

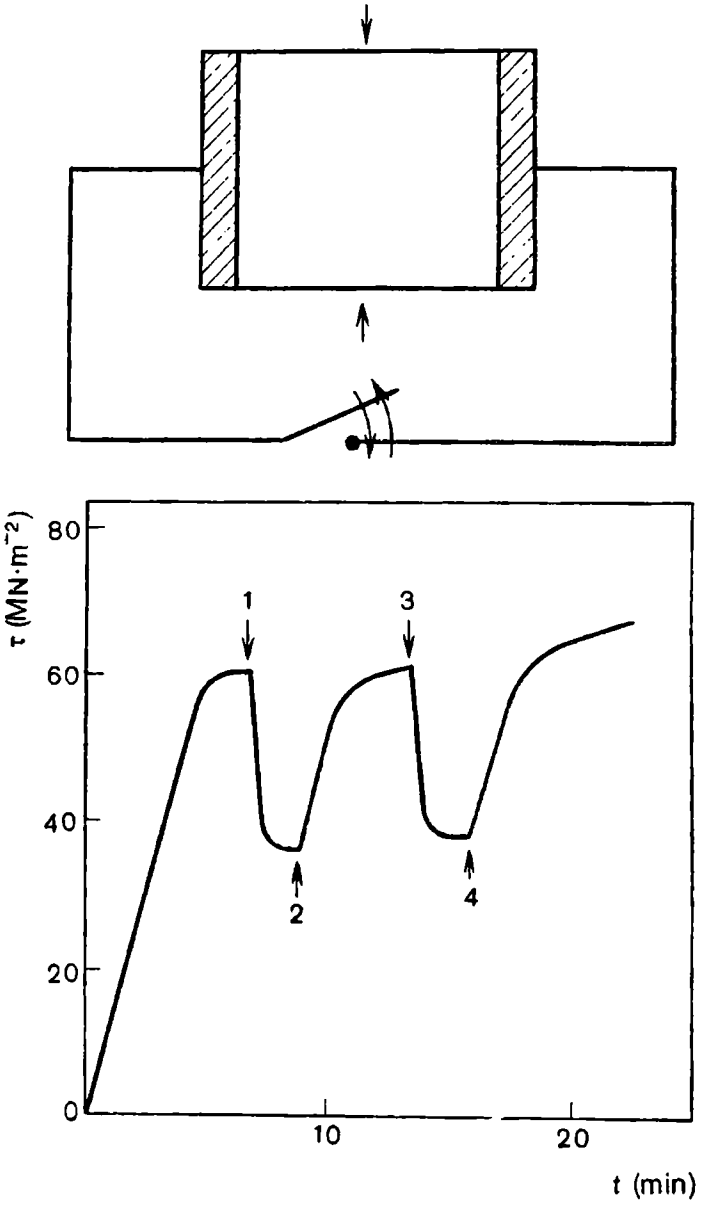

Fig. 5.12. Diagram for obtaining ShCE in ZnS. The sample faces were short-circuited at the instants *1* and *3*, and were disconnected at the instants *2* and *4*; $T = 20°C$.

conductors. Naturally, this leads to the problem of quantitatively determining the charge corresponding to different types of dislocations, and an investigation of the influence of different factors (temperature and rate of deformation, illumination, electric field, etc.) on this quantity. For this purpose, we have developed and applied several experimental methods.

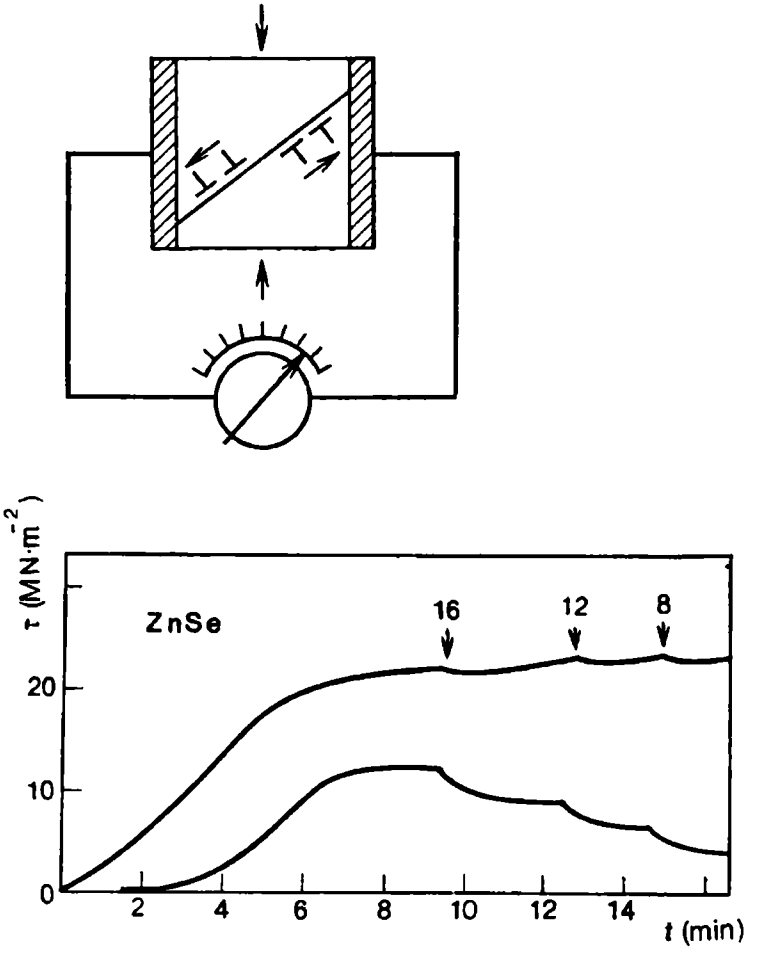

Fig. 5.13. Schematic diagram of the dislocation currents method and diagrams of deformation (upper curve) and dislocation current (lower curve). The arrows indicate the moments of changing of loading rate (indicated in μm/min); $T = 20°C$.

The Dislocation Current Method. In the general case, the dislocation current density is given by the relation

$$j_D = \sum_i q_i \langle \rho_i v_i \rangle, \qquad (5\ 5)$$

where q_i is the linear density of the electric dislocation charge and ρ_i and v_i are the density and velocity of a moving dislocation. The summation is carried out over all types of charged dislocations. Here, we should mention the considerable difference between $A^{II}B^{VI}$ semiconductors and alkali halide crystals (AHC) in which certain electric effects were also observed [5.18]. In crystals having a centre of symmetry (such as AHC), the dislocations of opposite mechanical sign moving in the opposite directions are physical equivalent, and even have the same electric charge. According to

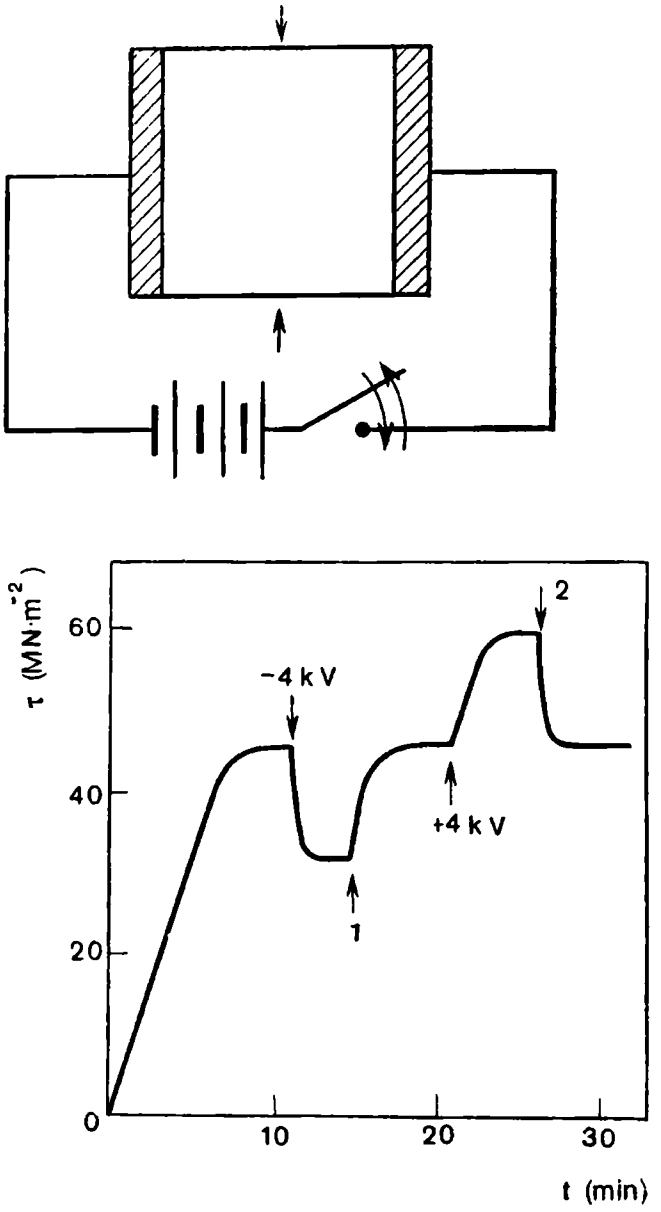

Fig. 5.14. Diagram for obtaining odd EPE in ZnS samples placed in silicone oil. The applied electric voltage was switched off at the instants *1* and *2*; $T = 20°C$.

formula (5.5), this means that $\langle j_D \rangle = 0$ in the case of a uniform deformation. Dislocation current in AHC can be experimentally measured only when space- or time fluctuations appear in the dislocation flux $(\rho_i v_i)$ of the same mechanical sign [5.18]. As has been mentioned above, an entirely different situation was observed by us during the plastic deformation of $A^{II}B^{VI}$ compounds. Electric

currents of constant magnitude and direction, proportional to the strain rate were observed. By measuring the dislocation current on mutually perpendicular faces of the samples, we can determine the direction of the dislocation current density vector $\mathbf{j}_D$. During the motion of the dislocations in the basal plane of hexagonal crystals (CdSe, CdS, ZnO), as well as in the [111] plane of cubic crystals (CdTe, ZnSe, ZnS, ZnTe), this direction coincides with the direction of motion of 60° dislocations. In other words, it lies in the slip plane and is perpendicular to the 60° dislocations lines. Hence it is natural to assume that the charge is transferred by just these dislocations. It was found that the mobilities of 60° dislocations of different polarities (α- and β-dislocations) differ very strongly for all $A^{II}B^{VI}$ compounds. Hence, the main contribution to the dislocation current in this case always comes from the same type of dislocation. This allows us to determine the linear density q of the electric charge of dislocations from the measurements of the dislocation current I_D and the rate $\dot{l}_p$ of plastic flow.

In the simplest case when dislocations of the same type move parallel to the current contacts, the charge passing through the external circuit upon a displacement of one dislocation by dx is given by

$$dQ = \frac{qL_D\,dx}{H} = q\,dS/H, \tag{5.6}$$

where L_D is the length of the dislocation, dS the area swept by it upon a displacement through dx, and H the distance between contacts along the slip plane.

The decrease in the length l_p of the sample in the direction of the compression is given by

$$dl_p = b_z\,dS/S_1,$$

where b_z is the projection of the Burgers vector on the compression axis, $S_1 = DH$ the area of the slip plane, and D the width of the contacts. For the motion of any arbitrary number of dislocations per unit time, we have

$$Q = \frac{qD\sum dx_i}{H}, \quad l_p = \frac{b_z\sum dx_i}{H}, \tag{5.7}$$

$$\frac{Q}{l_p} = \frac{I_D}{\dot{l}_p} = \frac{qD}{b_z}, \quad q = \frac{I_D b_z}{\dot{l}_p D}. \tag{5.8}$$

It can be seen from Eq. (5.8) that the ratio of the dislocation current I_D and the rate $\dot{l}_p$ of the plastic flow does not depend on the density or the velocity of dislocations. This allows us to determine the linear density q of the dislocation charge from measurements of I_D

and $\dot{l}_p$. A consideration of the more general case, when the dislocation loop expands in the slip plane shows that if the mobility of one type of components of the loop is assumed to be higher than the mobility of the other components, for example, if $v_\alpha > v_\beta$, v_{scr}, we obtain the following formula for determining the linear charge density for the most mobile type of dislocations:

$$\frac{dQ}{dl_p} \approx q_\alpha \frac{D}{b_z}.$$

However, it should be noted here that as the plastic deformation is stored in the crystal, the slow-moving components of the loops may also be stored (L_β/L_α increases) and the ratio dQ/dl_p decreases with time. Under these conditions, we can no longer use formula (5.8) for determining q. Hence, we consider the independence of I_D/l_p on the extent of deformation during the experiment as the criterion for applying formula (5.8). We can mention two more limitations concerning the application of the dislocation current method. In the steady state, when the current I_{meas} through the measuring instrument is constant, a potential difference $U = R_{in}I_{meas}$ appears on the sample faces, R_{in} being the input resistance of the instrument. This potential difference leads to a conductivity (electronic) current $I_{el} = U/R_s$ (where R_s is the sample resistance), since if

$$I_{meas} = I_D - I_{el}, \text{ then } I_D = I_{meas}\left(1 + \frac{R_{in}}{R_0}\right). \qquad (5.9)$$

It can be seen from (5.6) that the dislocation current I_D is equal to I_{meas} only when $R_{in} \ll R_s$. This relation should be always satisfied during measurements.

The other limitation concerns the possibility of screening of the dislocation charge by free carriers and charged point-defects. In the case of a complete screening, there are only neutral objects (dislocation + screening charge) moving over the bulk of the sample and the dislocation current disappears. Further investigations of the electronic properties of the crystals showed that for dislocation velocities between 10^{-3} and 1 cm/sec, such a screening does not take place.

The dislocation band method [5.19] can be used to determine the charge of even less mobile dislocations. It has been shown experimentally that at least during the initial stages of plastic deformation, the main source of dislocations in $A^{II}B^{VI}$ compounds is the crystal surface. Removing certain stress concentrators from the sample surface by polishing, we can load the crystal to a stress τ, such that $\tau_m > \tau > \tau_s$, τ_s being the operating stress from the surface dislocation sources, and τ_m the stress corresponding to the actuation of surface dislocation sources. If the surface is now pricked or scratched, a slip band will proceed from it to the bulk of the crystal. This slip

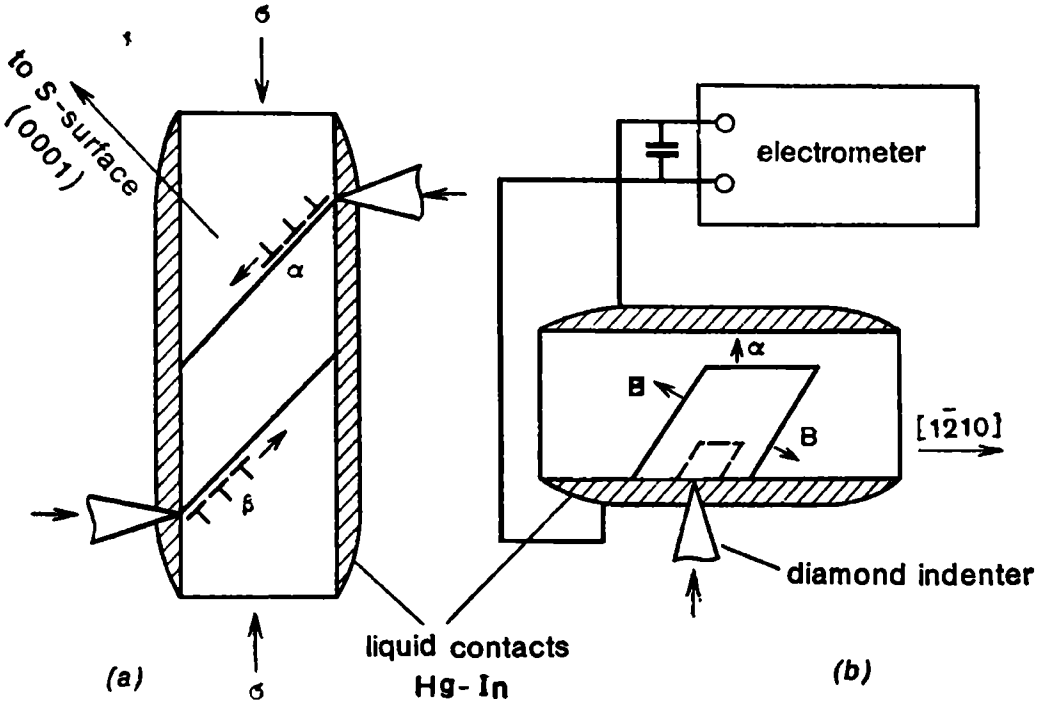

Fig. 5.15. (*a*) Diagram illustrating the creation of α- and β-slip bands in CdS (σ is the compressive stress); (*b*) sample cross section in the slip plane [0001]; B denotes a screw dislocation.

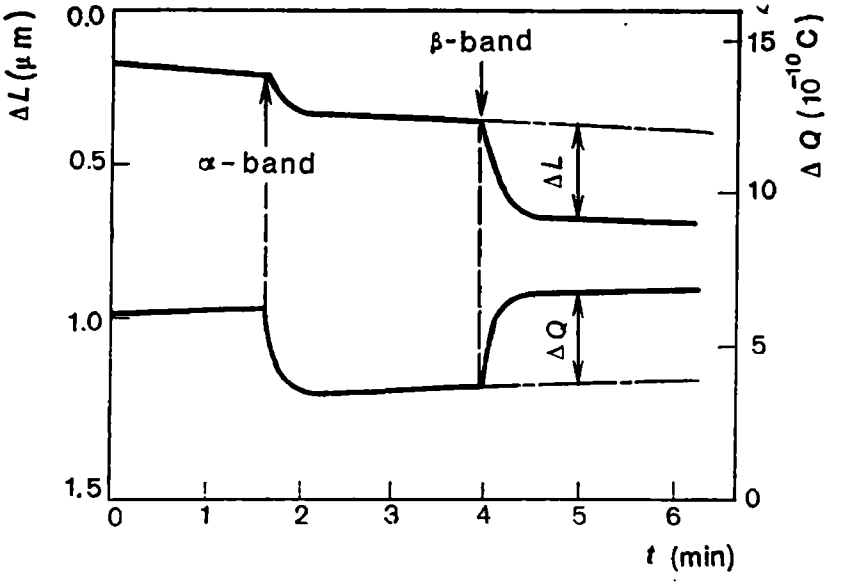

Fig. 5.16. Time dependence of ΔQ and Δl during the passage of α- and β-slip planes through a CdS sample. The arrows indicate the moments at which the scratches were inflicted on the sample surface.

band consists of dislocations whose type will depend on the type of the surface. Figures 5.15 and 5.16 illustrate this method in which we measure the charge ΔQ passing through the external circuit and the sample deformation ΔL as a slip band originated at the surface passes through it. As before, $q = \alpha\ (\Delta Q/\Delta L)\ b_z$ in this case, α being a geometrical factor determined by the type of dislocation loops. Figure 5.16 shows an example of the measurement of ΔQ and ΔL as α- and β-slip bands pass through a CdS sample. Quite low values of ΔL (from 0.01 to 1 μm) were measured with the help of a movable electrode tube (mechanotron).

Method of application of a compensating field. This method is based on the idea of the compensating action of the elastic stresses on dislocations upon loading from the side of the external electric field E. In other words, this method is based on the electroplastic effect (Fig. 5.14). The force F acting on a unit length of the charged dislocation is given by

$$F = qE + b\tau. \tag{5.10}$$

If during the experiment the force F remains unchanged as a result of the application of an external field E (this can be verified by checking the strain rate $\dot{l}_p$, which should remain unchanged in this case), we obtain

$$q = \alpha b \frac{\Delta\tau}{E}. \tag{5.11}$$

Here, $\Delta\tau$ is the change in the flow stress required for keeping the value of $\dot{l}_p$ unchanged when the external field E is applied. Identical results were obtained by us from all the three methods described above for determining the dislocation charge density in $A^{II}B^{VI}$ crystals. These results are compiled in Table 5.2. They correspond to dark measurements at room temperature and are averaged over a large number of ingots. All the values of q given in the table correspond to dislocations with an edge component. The charge density in the case of screw dislocations is so low that it was not possible to measure it with the help of any of the methods described above. All dislocations in n-type materials were found to be negatively charged, while in p-ZnTe crystals, they were positive. It is worth noting that the polar dislocations (α and β) in CdS have the same sign of the charge (but different magnitudes). It was observed that illumination affects the dislocation charge in ZnS [5.20], CdS, CdSe, and CdTe [5.21]. In all these materials, the charge increased as a result of illumination. The spectral dependence of the amount of charge is shown in Fig. 5.17. In order to study the dependence of q on the deforming rate $\dot{l}_p$ and on temperature, we used a special method in which the deforming rates were reversed. In this case,

Table 5.2. Types of Mobile Dislocations and Their Charge

Material	Type of conductivity, structure	Type of dislocation	Mean value of charge in darkness (qb/e)	Maximum charge under illumination (qb/e)
ZnO	*n* wurtzite	60° complete dislocation Zn (B)	−0.54	
		screw dislocation	uncharged	uncharged
ZnS	*n* sphalerite	edge partial dislocation S (B)	−0.80	−1.15
		screw dislocation (B)	uncharged	uncharged
ZnSe	*n* sphalerite	60° complete dislocation Se (B)	−0.50	−0.92
		screw dislocation (B)	uncharged	uncharged
ZnTe	*p* sphalerite	60° complete dislocation Te (B)	+0.42	+0.78
		screw dislocation (B)	uncharged	uncharged
CdS	*n* wurtzite	60° complete dislocation Cd (B)	−0.36	−0.54
		60° complete dislocation S (B)	−0.7	
		screw dislocation (B)	uncharged	uncharged
CdSe	*n* wurtzite	60° complete dislocation Cd (B)	−0.17	−0.35
		screw dislocation (B)	uncharged	uncharged
CdTe	*n* sphalerite	60° complete dislocation Te (B)	−0.12	
		screw dislocation (B)	uncharged	uncharged

conditions were created under which the dislocation density could be treated as constant during the course of measurements [5.22]. In other words, the deforming rate is proportional to the dislocation

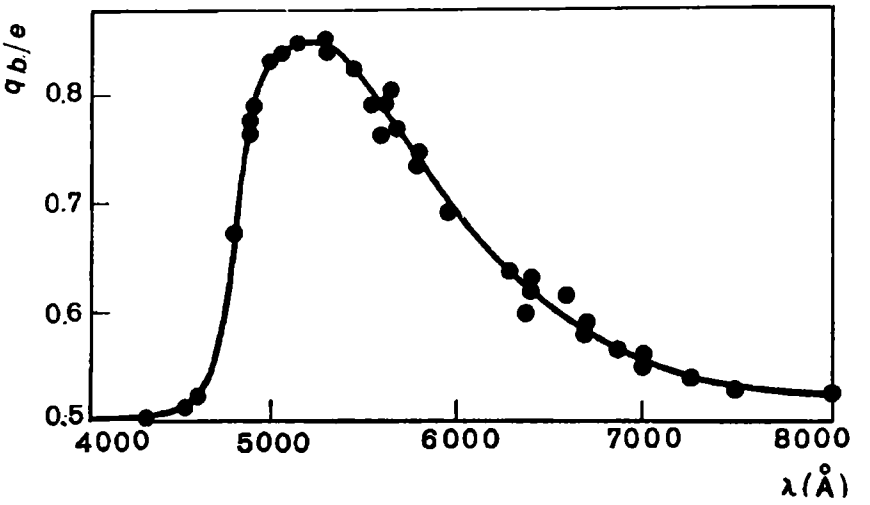

Fig. 5.17. Spectral dependence of the dislocation charge in ZnSe on the wavelength of the incident light. The deformation rate was 10μm/min, and the temperature $T = 20°C$.

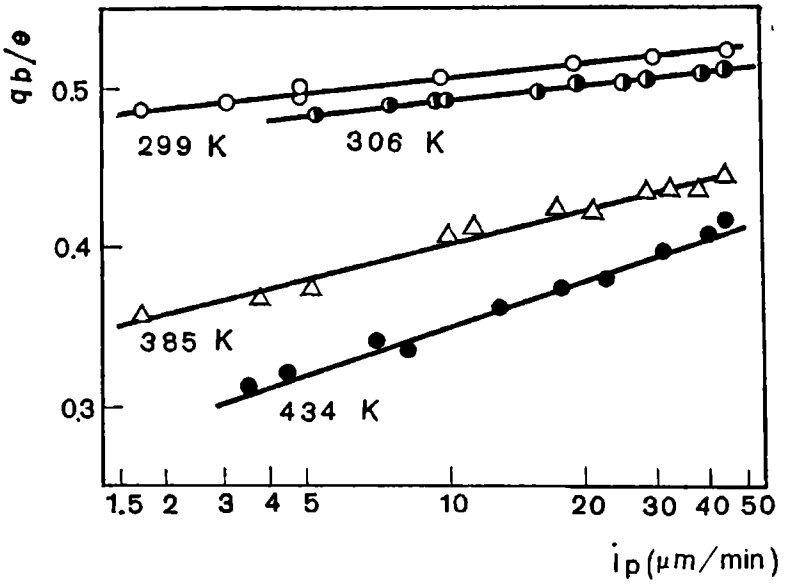

Fig. 5.18. Dependence of the dislocation charge in ZnSe on the deformation rate.

velocity. Under these conditions, the increase in q with velocity is proportional to the logarithm of the deforming rate, the proportionality factor increasing with temperature (see Fig. 5.18). With

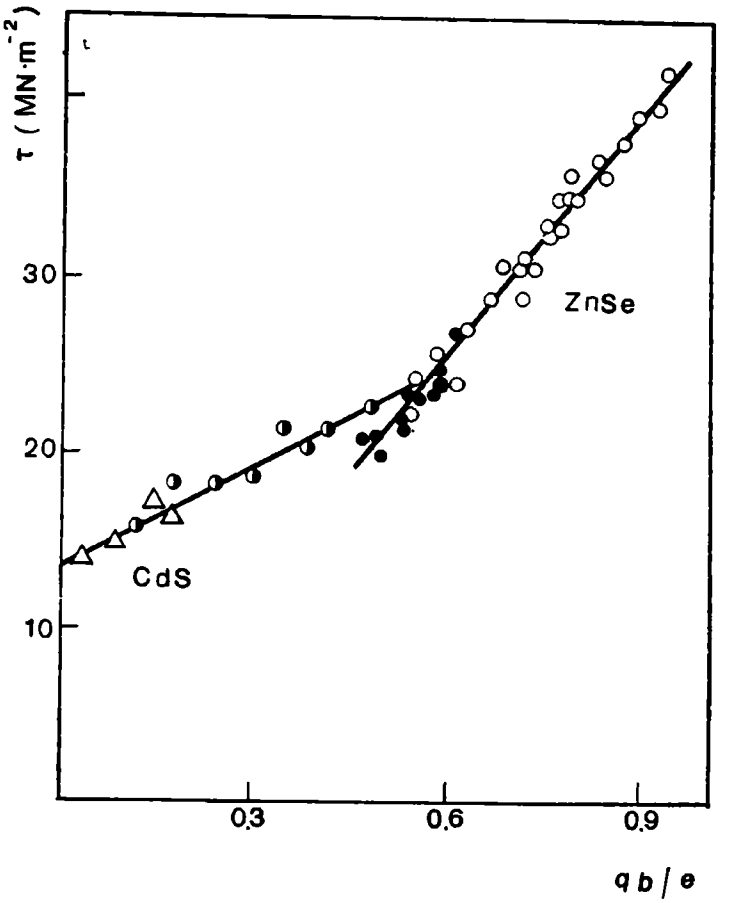

Fig. 5.19. Dependence of the shear flow stress τ at $\dot{l}_p = 10$ μm/min on the dislocation charge in CdS and ZnSe; *1*, *2*—in dark; *3*, *4*—under illumination; $T = 20$°C.

the help of such a method, successively changing the loading rate, temperature, and the dislocation charge (by illumination or injection of charge carriers), and analyzing the curves obtained in this way [5.23], we were able to show that the following relation is satisfied in all cases involving the investigation of $A^{II}B^{VI}$ compounds:

$$\dot{l}_p = \dot{l}_0 \exp\left\{-\frac{E_0 - \gamma\tau + aq}{T}\right\}, \tag{5.12}$$

where a is parameter proportional to the ionic lattice charge. The coefficient γ (activation volume) does not change upon illumination and remains constant to within 10-15% when the extent of plastic deformation is changed. For ZnSe, it is equal to $(20 \pm 2)\ b^3$, while for ZnS and CdS, it is equal to $(25 \pm 4)\ b^3$ and $(50 \pm 10)\ b^3$ respectively [5.22]. On the basis of these results, we can conclude that the

motion of dislocations in $A^{II}B^{VI}$ takes place according to the Peierls mechanism. This is also confirmed by electron micrographs showing long uniform segments of dislocations, lying in the directions of Peierls contour valleys. Figure 5.19 shows the experimental dependence of the resolvent shear stress for CdS and ZnSe on the dislocation charge.

It can be seen that this dependence is significant for CdS, while for ZnSe, it is even more significant. This leads to the conclusion

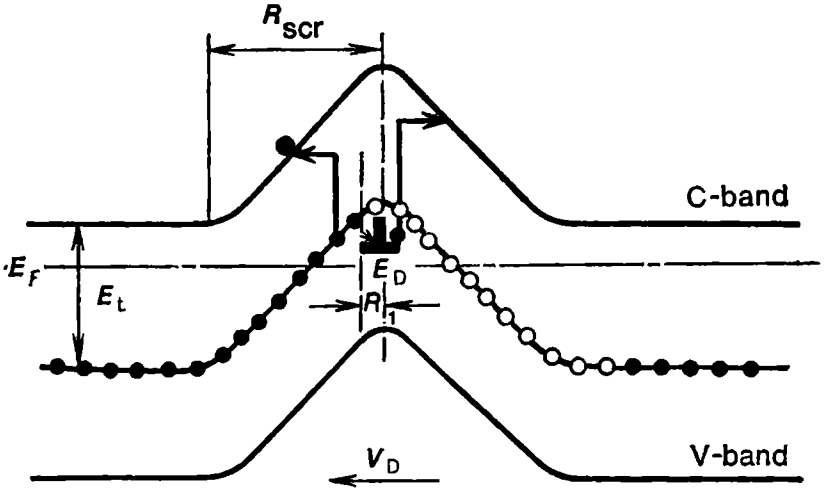

Fig. 5.20. Bending of allowed bands near a dislocation and schematic diagram of electronic transitions.

that the process of plastic deformation in $A^{II}B^{VI}$ compounds cannot be described accurately without considering the magnitude and variation of the dislocation charge.

In conclusion, let us consider the nature of such a large dislocation charge. Results of our investigations, including those described in this review, show that the magnitude, and especially the sign of dislocation charge in $A^{II}B^{VI}$ compounds cannot be explained on the basis of the ionic nature of the interatomic bonds in these crystals. The magnitude of the charge is dynamic in nature and changes with the motion of dislocations through the crystal in which a large number of electrically charged point centres exist. The interaction of moving dislocations with local centres results in the capture of a part of their charge by a dislocation. At the same time, a part of the local centres is ionized and a certain number of electrons are released into the conduction band, where they recombine (deformation luminescence). As a result, a crystal with moving dislocations has an unequilibrium electron distribution between bands, local centres, and dislocations. This distribution strongly differs from the case when the dislocations are at rest [5.24]. Some of these processes are shown schematically in Fig. 5.20, which represents

the change in the band structure around a dislocation moving at a velocity v_D. Here, R_1 is the radius within which the charge from a point centre can be captured by a dislocation, R_{scr} the screening radius of the cylinder, E_F the Fermi level, E_D the dislocation level and E_t the position of the local centres away from the dislocation. Transitions of electrons from centres to the dislocation and to the conduction band are shown by arrows. The filled circles represent centres with electrons, while hollow circles show empty centres.

On the basis of this diagram, we can explain the processes of redistribution of electric charges between dislocations, local centres, electron- and hole bands, occurring when dislocations move during plastic deformation. We can also explain the effect of illumination injection of carriers, temperature, deformation rate, etc. on these processes. All the phenomena described by us in this review can be explained in this way.

5.4. CONCLUSION

The results of the investigations of interaction of dislocations with electrons in semiconductors (a part of the results presented in this review was published elsewhere) have shown that the dislocations have a considerable, and sometimes decisive effect on many physical properties of real semiconducting crystals.

The peculiar electronic properties and their evolution in a number of technologically important crystals cannot be explained without taking into account the effect of dislocations. Thus, dislocation studies are essential for solid state electronics.

On the other hand, a dislocation as a chain of atoms in a crystal, each of which has a peculiar electronic structure, is an exceptionally convenient object for experimental investigations of a number of one-dimensional and quasi-one-dimensional phenomena in solid crystals. There is no need to repeat that the study of one-dimensional phenomena remains one of the key problems both in theoretical and experimental solid state physics.

All this indicates that the investigation of dislocations and their interaction with electrons is still one of the problems of solid state physics, important from the theoretical as well as practical point of view.

References

5.1. Yu. A. Ossipyan, *Soviet Scientific Reviews*, Sec., A, 4, 219 (1982).
5.2. Yu. A. Ossipyan, *Crystal Res. and Techn.*, 16, 239 (1981).
5.3. V. V. Kveder and Yu. A. Ossipyan, *Zh. Eksp. Teor. Fiz.*, 53, 618 (1981).
5.4. Yu. A. Ossipyan, V. I. Tal'yanskii, A. A. Kharlamov, and S. A. Shevchenko, *Zh. Eksp. Teor. Fiz.*, 76, 1655 (1979).
5.5. Yu. A. Ossipyan, V. I. Tal'yanskii, and S. A. Shevchenko, *Zh. Eksp. Teor. Fiz.*, 72, 1543 (1977).

5.6. V. A. Grazhulis, V. V. Kveder, V. Yu. Mukhina, and Yu. A. Ossipyan, *Pis'ma v Zh. Eksp. Teor. Fiz.*, **24**, 164 (1976).
5.7. Yu. A. Ossipyan, V. M. Prokopenko, V. I. Tal'yanskii, A. A. Kharlamov, and S. A. Shevchenko, *Pis'ma v Zh. Eksp. Teor. Fiz.*, **30**, 123 (1979).
5.8. A. G. Zabrodskii, *Pis'ma v Zh. Eksp. Teor. Fiz.*, **33**, 258 (1981).
5.9. Yu. A. Ossipyan, V. M. Prokopenko, and V. I. Tal'yanskii, *Pis'ma v Zh Eksp. Teor. Fiz.*, **36**, 69 (1982).
5.10. W. Schröter, *Phys. Stat. Sol.*, **21**, 211 (1967).
5.11. Yu. A. Ossipyan and S. A. Shevchenko, *Pis'ma v Zh. Eksp. Teor.. Fiz.*, **33**, 218 (1981).
5.12. Yu. A. Ossipyan and I. B. Savchenko, *Pis'ma v Zh. Eksp. Teor. Fiz.*, **7**, 130 (1968).
5.13. Yu. A. Ossipyan, V. F. Petrenko, and I. B. Savchenko, *Pis'ma v Zh. Eksp. Teor. Fiz.*, **13**, 622 (1971).
5.14. Yu. A. Ossipyan, V. F. Petrenko, and M. Sh. Shikhsaidov, *Pis'ma v. Zh. Eksp. Teor. Phys.*, **20**, 363 (1974).
5.15. Yu. A. Ossipyan and V. F. Petrenko, *Pis'ma v Zh. Eksp. Teor. Fiz.*, **17**, 555 (1973).
5.16. R. H. Bube, *Physics and Chemistry of II-VI Compounds*, ed. by M. Aven and T. S. Prener, North Holland, Amsterdam, 1967, p. 659.
5.17. Yu. A. Ossipyan and V. F. Petrenko, *Zh. Eksp. Teor. Fiz.*, **69**, 1362 (1975).
5.18. R. W. Whitworth, *Adv. Phys.*, **24**, 203 (1975).
5.19. A. V. Zaretskii, Yu. A. Ossipyan, V. F. Petrenko, and G. K. Stukova, *Fiz. Tverd. Tela*, **19**, 418 (1977).
5.20. Yu. A. Ossipyan and V. F. Petrenko, *Dokl. Akad. Nauk SSSR*, **226**, 803 (1976).
5.21. V. F. Petrenko and R. W. Whitworth, *Phil Mag.* A, **41**, 681 (1980).
5.22. Yu. A. Ossipyan and V. F. Petrenko, *Zh. Eksp. Teor. Fiz.*, **75**, 296 (1978).
5.23. Yu. A. Ossipyan and V. F. Petrenko, *J. de Phys.* C-6, **40**, 161 (1979).
5.24. L. G. Kirichenko, V. F. Petrenko, and G. V. Uimin, *Zh. Eksp. Teor. Fiz.*, **74**, 742 (1978).

6 InGaAsP Heterojunctions: Preparation, Recombination Processes and Applications in Optoelectronic Devices

Zh. I. Alferov, D. Z. Garbuzov, and A. T. Gorelenok

6.1. INTRODUCTION

The difficulties encountered during attempts to obtain high-quality heterojunctions in the Ga-As-P system [6.1] and the brilliant success achieved in this direction by going over to the Al-Ga-As system [6.2] demonstrated experimentally by the end of the sixties that heterojunctions with properties similar to those of the ideal model [6.3] can be obtained if their components are materials with close lattice constants. The prospects of practical applications of heterojunctions, associated mainly with the fabrication of optoelectron devices, also revealed two other requirements which pioneered the search for suitable materials for creating new types of heterojunctions. In the first place, these new compounds must lead to the construction of devices with a wider spectral range than that provided by the AlGaAs/GaAs system. Secondly, like GaAs and $Al_xGa_{1-x}As$ ($x < 0.3$), these compounds must have a direct band structure.

In the light of these requirements, we presented at the International Conference on Semiconducting Heterojunctions at Budapest in 1970, an analysis of the possible means of obtaining new types of heterojunctions in $A^{III}B^{V}$ compounds [6.4]. In this report, we drew attention to the prospects of going over from ternary to quaternary compounds $A_x^{III}B_{1-x}^{V}C_y^{III}D_{1-y}^{V}$ for the first time, especially picking out the solid solutions InGaAsP for this purpose. It was also shown that in order to create heterojunctions on the basis of quaternary compounds, we should use lattice-matched series of their compositions, all the compounds in each series having the same lattice constant owing to a proper choice of the parameters x and y. The other physical parameters of these compounds especially the values of E_g, however, are different for different compounds in a series. The greatest advantage of using the InGaAsP solid solutions lies in that different compositions of this compound with a direct forbidden bandgap may have values of E_g ranging between 0.4 and 2.0 eV at 300 K, thus ensuring a considerable broadening of the range of "direct" E_g's as compared with the AlGaAs/GaAs system both toward higher and lower values of energy. Indeed, high-quality heterojunctions produced between 1973 and 1976 in the systems

of lattice-matched compositions of the InGaAsP solid solutions formed the basis for developing optoelectronic devices for infrared (λ = 1.7-1.1 μm) as well as visible (λ = 0.75-0.62 μm) regions of the spectrum.

The first lattice-matched InGaAsP/InP heterojunctions for narrow-band compositions were experimentally obtained in 1973 by Antypes and Moon [6.5]. On the basis of single InP-InGaAsP heterojunctions, they fabricated avalanche photodiodes with an infrared threshold of 1.15 eV. A year later, the Soviet scientists Bogatov *et al.* [6.6] reported the attainment of coherent radiation with λ = 1.02 μm at 77 K in injection lasers based on InP-InGaAsP-InP double heterojunctions (DH) (DH-lasers). Later, in 1975-76, the same authors created the first low-threshold InGaAsP/InP DH-lasers (λ = 1-1.1 μm) operating in the pulsed mode at room temperature [6.7] and high-efficiency light-emitting diods (LED) on similar structures [6.8]. Hsieh *et al.* [6.9] in 1976 obtained CW InGaAsP/InP DH-lasers (λ = 1.1 μm) at 300 K. This triggered an avalanche of research activity in this direction primarily due to the fact that silica fibres used in optical communication systems have minimum losses at λ = 1.3 μm and λ = 1.55 μm, i.e. within the spectral range of InGaAsP/InP DH lasers. At present, InGaAsP/InP DH structures not only form the basis of commercial spontaneous and coherent light sources for optical communication, but also lie at the root of several perspective versions of photodetectors for these systems.

The attempts at creating narrow-band heterojunctions in the InGaAsP/InP systems were accompanied in 1974-75 by efforts to obtain wide-band lattice-matched structures in InGaAsP-GaAs and InGaAsP-GaAsP systems. The interest toward wide-band compositions of InGaAsP was mainly caused by the fact that by this time the short-wave limits of the operation of AlGaAs/GaAs heterolasers had been established. It was found that on account of the influence of indirect minima in the conduction band of AlGaAs, the threshold values in AlGaAs DH lasers rapidly increase from λ = 0.73 μm onwards [6.10] and for the limiting values λ = 0.67 μm and T = 300 K, the value of J_{th} exceeds 100 kA/cm^2 [6.10]. In InGaAsP solid solutions, a transition from direct to indirect band structure takes place at E_g = 2.2 eV (at 300 K), which is 0.35 eV higher than for the AlGaAs system and can therefore be expected to considerably broaden the operating range of injection heterolasers based on these solutions towards shorter wavelengths. The investigations carried out by the group of scientists at the University of Illinois under the supervision of Prof. Holonyak gave a considerable impetus to the overall research activity on this field. During the years 1973-75, Holonyak's group reported the growth of high-quality epitaxial layers of InGaAs and InGaAsP, which are lattice-matched with the substrates GaAs and GaAsP [6.11]. Optical excitation of

laser samples formed by these layers enabled Holonyak *et al.* [6.11] to obtain $A^{III}B^{V}$ laser in a record low shortwave region, including the green region of the spectrum ($\lambda = 0.557$ μm at 77 K). Holonyak and his coworkers [6.12] were also the first to fabricate visible injection lasers based on single GaAsP-InGaAsP heterojunctions (the active region in this case is GaAsP).

However, the basic success in the creation of shortwave injection lasers was attained only after perfecting the technology for preparation of DH structures based on InGaAsP solid solutions which are lattice-matched with GaAs [6.13] or with GaAsP solid solution [6.14]. After a slackening of the pace of investigations in the end of the seventies, the interest in this field was revived recently as a result of the studies of light sources in optical information systems and a surge of activity was noticed in the development of CW injection lasers in the visible range. Besides the work on the improvement of parameters of red AlGaAs DH lasers, the creation of lasers based on InGaAsP/GaAs double heterojunctions and operating in the region of 0.7 μm with comparable or even lower thresholds than for the AlGaAs/GaAs system [6.15] has been reported. These lasers are also known to operate in the CW mode at 300 K [6.16].

The authors of this review were a part of the group of scientists at the Ioffe Physico-Technical Institute of the USSR Academy of Sciences who carried out the work reported in [6.4] and [6.13-15]. In addition to these studies, a wide range of investigations was carried out at the same institute on obtaining the InGaAsP/InP DH structures, the recombination processes for nonequilibrium carriers (NC), and the creation of coherent and spontaneous light sources based on these heterojunctions and operating at the wavelengths $\lambda = 1.3$ and 1.55 μm. The main aim of this review is to give a brief description of all the results obtained in this field at the Physico-Technical Institute of the USSR Academy of Sciences. The authors are grateful to the other members of the group without whose active cooperation it would not have been possible to carry out most of the works reported in this review.

6.2. SALIENT FEATURES OF PREPARATION OF InGaAsP SOLID SOLUTIONS AND HETEROJUNCTIONS BASED ON THEM

In spite of the rapid progress made in the field of liquid-phase epitaxy (LPE) of InGaAsP solid solutions, no reliable theoretical or experimental data were available in literature till the end of the seventies, concerning the dependence of E_g on composition, the phase equilibrium data and the effect of the lattice mismatch on the luminescence properties of the solid solutions, etc. Likewise,

the question of doping was still unresolved and no data was available on the coefficient of thermal expansion.

Usually, the values of E_g and the lattice constant a are predicted by interpolation of the data known for binary compounds (InAs, GaAs, GaP, InP) and the ternary solid solutions (InGaAs, InGaP, InAsP, GaAsP) based on them [6.17-20]. In [6.18-20], the depen-

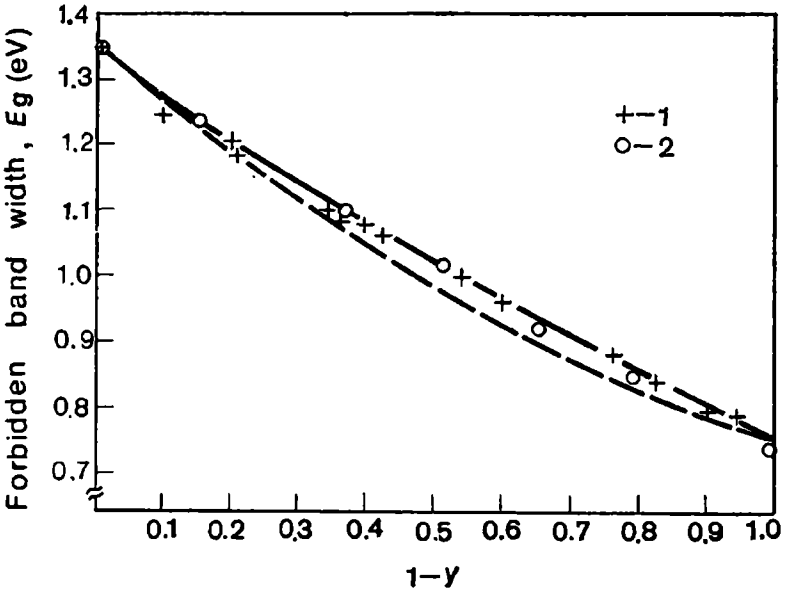

Fig. 6.1. Dependence of E_g for $In_{1-x}Ga_xAs_{1-y}P_y$ solid solutions lattice-matched to InP, on concentration of As in solid phase. The solid curve is based on calculations according to Eq. (6.1), while the dotted curve is based on calculations that do not take into account the mixing effects. Curve *1*: experimental results of [6.17]; curve *2*: data from [6.20].

dences of E_g on composition were described by a third-degree interpolation polynomial. None of these dependences, however, was in good agreement with the experimental results. This is so because the cubic dependence does not take into account the mixing effects which are inherent in quaternary compounds. In order to consider the mixing effects, we used a dependence described by a fourth-degree interpolation polynomial [6.17]:

$$E_g\ (x, y) = 0.356 + 0.995y + 1.072x + 0.357xy - y\ (1 - y)\ (0.23 - 0.02x) - x\ (1 - x)\ (0.42 + 0.282y) + 0.912x\ (1 - x)\ y\ (1 - y). \qquad (6.1)$$

This led to a good agreement between the theoretical and experimental results, as shown in Fig. 6.1 for the $In_{1-x}Ga_xAs_{1-y}P_y$ solid solutions which are lattice-matched to InP. The dotted curve represents the results of calculations carried out by neglecting the mixing

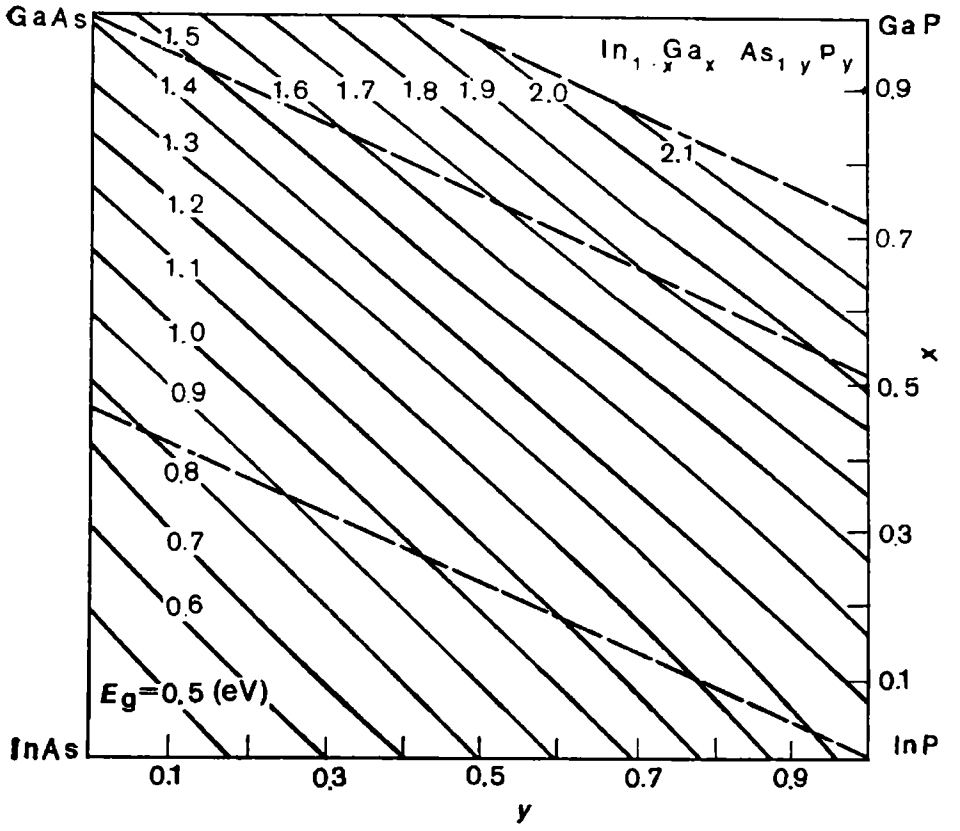

Fig. 6.2. Dependence of E_g for $In_{1-x}Ga_xAs_{1-y}P_y$ on composition, calculated according to (6.1). The dotted curves correspond to compositions which are lattice-matched to GaAs and InP (T = 300 K).

effects, i.e. by neglecting the last term in (6.1). It should be noted that the expression (6.1) provides a correct interpretation for the change in the direct energy gap not only in the InGaAsP solid solutions, but also in the four ternary systems bordering it on the quadratic phase composition diagram. The shape of the constant E_g line has been determined more precisely in the system under analysis with the help of this expression. The results of calculations are shown in Fig. 6.2.

The lattice-matched substitution condition for InGaAsP solid solutions with respect to InP has the following form [6.21]:

$$y = (0.1896 - 0.40519x)/(0.1896 + 0.0127x), \quad T = 300 \text{ K},$$

$$y = (0.1931 - 0.40264x)/(0.1931 + 0.00157x), \quad T = 923 \text{ K}.$$

The analogous condition for solid solutions lattice-matched to GaAs can be written as follows:

$$y = 0.40519\ (1 - x)/(0.1896 + 0.0127x), \quad T = 300 \text{ K}.$$

The study of phase equilibria in In-Ga-As-P quaternary system is stimulated by the requirement of an accurate control of the solid solution composition. The most useful approach in this direction is based on the simple solution theory in its regular approximation. A detailed discussion of phase equilibria in III-V ternary compounds was given in [6.22]. By using a known set of thermodynamic parameters, the authors obtained a satisfactory agreement between the calculated results and the experimental data available for a number of III-V compounds. Nevertheless, this set of parameters is not suitable for describing the In-Ga-As-P quaternary systems [6.23]. As can be seen from the experimental data obtained at low temperatures (600-650°C is a typical temperature range for In-Ga-As-P epitaxial growth), there are large discrepancies between the calculated and experimental results. A good agreement between theory and experiment has been obtained in [6.24]. However, for this purpose the authors not only resorted to an arbitrary variation of the thermodynamic parameters used in [6.22], but also introduced an interaction parameter which depends on the solid phase composition. Clearly, this is in contradiction to the simple solution theory. The proposed thermodynamic parameter may be used only within a small temperature range for solid solution compositions lattice-matched to InP and cannot describe the phase equilibrium over the entire phase diagram.

A satisfactory agreement between the calculated results and the experimental data on phase equilibrium in InGaAsP quaternary solid solutions was obtained in [6.21]. The thermodynamic analysis was based on the simple solution theory with linear temperature-dependent interaction parameter for the liquid and solid phases. The temperature dependences of the interaction parameters were obtained by a processing of experimental data on liquidus and solidus isotherms of ternary systems in accordance with the equations of the simple solution theory. Figure 6.3 shows the experimental and calculated data for the phase equilibrium of In-Ga-As-P system for the solid solution InGaAsP lattice-matched to InP [6.21], together with the experimental and calculated values of E_g of the same solutions as functions of the liquid phase composition [6.17]. A satisfactory agreement between theory and experiment can be clearly seen.

It should, however, be noted that even an exact knowledge of the phase diagram does not help in obtaining layers with a given composition. Under real conditions, of epitaxial growth, the unavoidable supercooling of the liquid phase disturbs the thermodynamic equilibrium of the system. The situation is worsened by the thermodynamic instability of the binary substrate in contact with the multicomponent liquid phase.

The absence of equilibrium in LPE leads to a mass transfer through

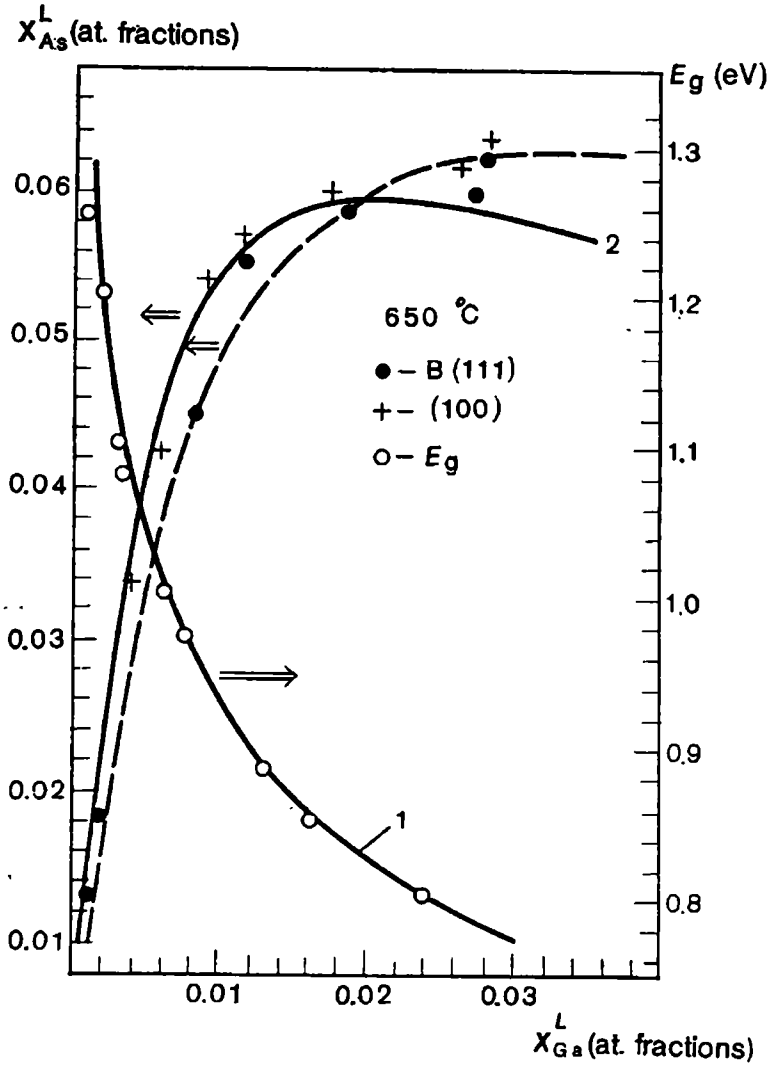

Fig. 6.3. Dependence of As concentration in the liquid phase and E_g for InGaAsP on concentration of Ga in the liquid phase. Solid curves have been obtained theoretically, curve *1* takes into account the mixing effect, while curve *2* represents the quasiregular approximation. The dotted curve corresponds to the regular approximation.

the interface, accompanied by a dissolution of the substrate or the precipitation of a new phase. As a result, the system may go over to the quasiequilibrium state after forming on the substrate surface a transition layer which is in equilibrium with the initial liquid phase. The existence of a transition layer was experimentally established for ternary systems [6.25], and was observed by the authors in quaternary systems as well. It has been shown theoretically [6.26, 27] that the formation of the transition layer may be described by using the model of diffusive mass transfer in both phases. For

the quaternary InGaAsP solid solutions, a kinetic analysis of the growth of layers from supercooled melt-solutions under isothermal conditions was carried out by one of the authors of [6.27]. It was shown that for an exact determination of the liquid phase composition, which is essential for deposition of layers with a given composition under selective conditions, we should use the effective distribution coefficients rather than their equilibrium values (Fig. 6.4).

Four different modifications of LPE, which were developed earlier for the AlGaAs/GaAs system [6.28], are used at present for obtaining

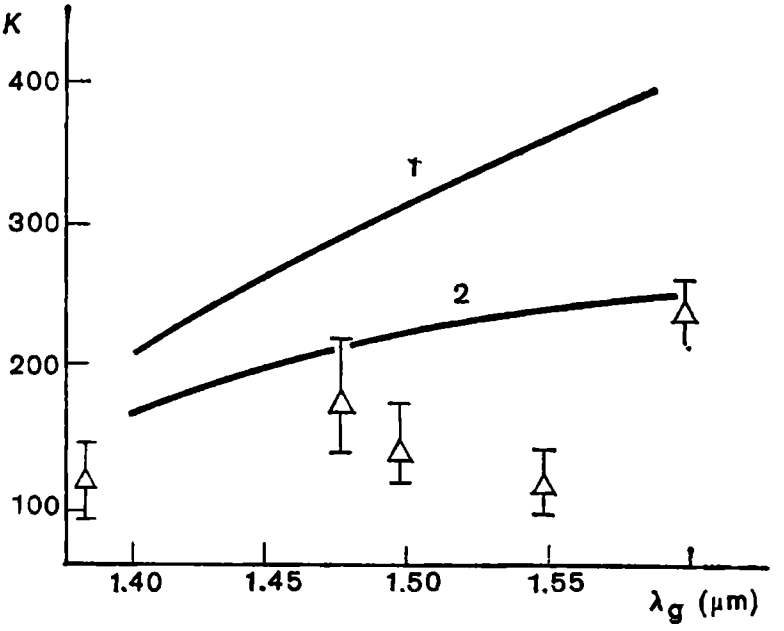

Fig. 6.4. Dependence of equilibrium (*1*) and effective (*2*) distribution coefficients K on emission wavelength in InGaAsP/InP heterojunctions. Solid curves correspond to calculated values, while the experimental values are marked by triangles [6.27].

heterojunctions based on quaternary InGaAsP solid solutions. These include the equilibrium cooling from the saturated solutions [6.23, 29], cooling from the supersaturated solutions [6.30, 31], the two-phase solution technique [6.32], and the step-cooling technique [6.21]. Typical temperatures for epitaxial growth are 650-600°C for InGaAsP/InP and 750-700°C for InGaAsP/GaAs (GaAsP) DH's. The main drawback of the first three LPE techniques is that they cannot be used to obtain 1-2 μm thick layers of solid solutions with a constant composition over the entire thickness of the layer. The isothermal growth method does not suffer from this drawback and is, therefore, the most widely used method for LPE.

While creating InGaAsP/InP DH's, special attention must be paid to the problem of lattice matching between the LPE layer and

the substrate. This system is extremely sensitive to temperature variations, and a deviation of 1°C from the liquidus temperature leads to a mismatching of ~0.02% [6.30] in the lattice parameters ($\Delta a/a$) of the solid solution for a solid phase composition corresponding to $\lambda \simeq 1.15$ μm. The corresponding mismatching for $\lambda \simeq 1.3$ μm and $\lambda \simeq 1.55$ μm amount to ~0.04% [6.27] and ~0.1% respectively. While doping a solid solution, we must also consider the variation of $\Delta a/a$ depending on the type of the doping impurity [6.33]. At a certain critical mismatching of the lattice parameters, misfitting dislocations (MD) may appear in the epitaxial layer [6.34]. These dislocations may serve as the centres for nonradiative recombination; their presence is indicated by the dark lines [6.35] in the luminescence pattern of the material and decreases the quantum yield of luminescence (see Fig. 6.5). MD's are generated much more easily at higher temperatures than at room temperature [6.34]. Hence, in order to obtain layers free from MD's lattice matching is essential at the temperature at which epitaxy is carried out. The dislocation-free layers will in this case have negative values of $\Delta a/a$ at 300 K, corresponding to the difference in the thermal expansion coefficients of the solid solution layer and InP [6.36] (see Fig. 6.6). The lattice mismatching has a very strong influence on the heterointerface profiles. It is shown by the Auger analysis that the interface region width between InGaAsP and InP is more than that between InP and InGaAsP [6.37]. The greater the lattice mismatching between layers, the wider the heterointerface profiles. Apparently, this is due to an increase in the diffusion coefficients of the components in the field of mechanical stresses caused by the lattice mismatching. For this reason, and in order to decrease the lattice mismatching due to the difference in the thermal expansion coefficients for the materials in contact at the heterojunction boundary, it is preferable to use, wherever possible, InGaAsP solid solutions as wide-band emitters.

In order to determine the lattice mismatching between layers, X-ray diffraction methods are often used. In our investigations also, we employed the method based on the measurement of the spectral dependence of the linear polarizability of luminescence [6.38]. The advantage of this method lies in that it can be used to determine the internal stresses and lattice mismatching in devices already fabricated (lasers, LED's, etc.) and to predict the device lifetime.

It will be shown in the next section that in the InGaAsP/InP DH structures with an undoped active layer, the internal quantum efficiency of luminescence is higher than that in a structure with a deliberately doped active layer. Hence, while fabricating light sources, one faces the problem of combining a *p-n* junction with a heterojunction. Unfortunately, however, there is no technologi-

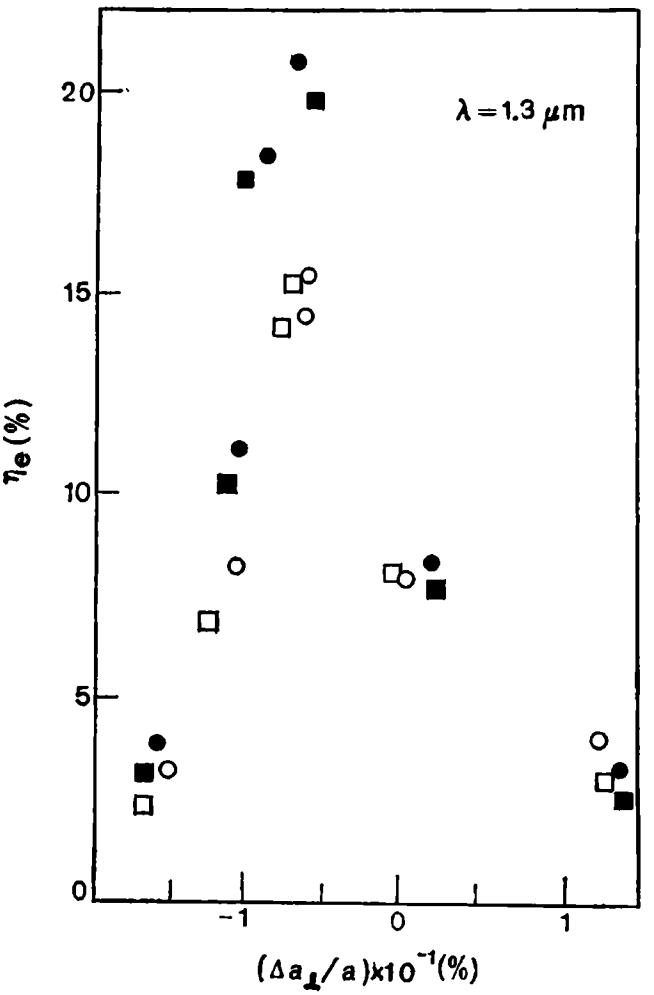

Fig. 6.5. Dependence of the external quantum efficiency of radiation in InGaAsP/InP DH's on the mismatching of lattice parameters at 300 K.

cally effective acceptor impurity for the InGaAsP/InP system like germanium in the AlGaAs/GaAs system. Zinc, which is used most frequently as an acceptor, has a high partial pressure at the temperature of epitaxy and a high diffusion coefficient in InP and InGaAsP [6.39], leading to a displacement of the *p-n* junction in the active region and to a deterioration of the properties of light sources [6.40]. Magnesium, which was proposed by us as an acceptor [6.41], has a lower (by an order of magnitude) partial pressure and a smaller diffusion coefficient. However, even the use of Mg as dopant for growing *p-n* junctions results in a displacement of the junction from the heterointerface, thus lowering the efficiency of radiation [6.42]. Hence, it was suggested by us that in order to prevent the acceptors from penetrating the active region, an intermediate layer

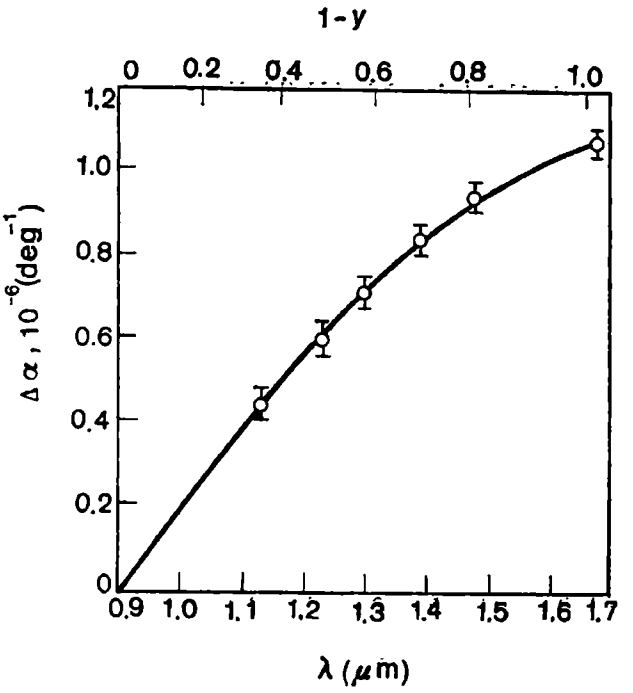

Fig. 6.6. Dependence of the difference in coefficients of thermal expansion of InGaAsP and InP solid solutions on the solid phase composition [6.36].

of undoped wide-band material be grown before the *p*-emitter layer [6.42]. It should be also noted that thermal treatment of heterojunctions with an intermediate layer in phosphorus atmosphere doubles or trebles the external quantum yield of radiation in the same way as for isotypic *N-n-N* heterojunctions [6.43] (*N* indicates the type of electron conductivity of a wide-band emitter).

Before concluding this section, let us briefly consider the method for obtaining pure undoped layers which are necessary for photodetectors. Usually, layers of pure InP and $In_{0.53}Ga_{0.47}As$ ($\leqslant 10^{15}$ cm^{-3}) are obtained as a result of a prolonged annealing (for tens of hours) of the melt in graphite [6.44] or sapphire [6.45] containers. This led to a lowering of the electron concentration in InGaAs to 2×10^{14} cm^{-3} and to a mobility 68 000 cm^2/(V·sec) at 77 K [6.44]. Our recent experiments on obtaining pure layers of InGaAs by adding rare-earth elements to the melt have resulted in a considerably simplified technology and lowered the electron concentration in the layers to $\sim 5 \times 10^{13}$ cm^{-3} with a mobility $\sim$100 000 cm^2/(V·sec) at 77 K. The annealing time in these experiments was just 1-2 hours.

6.3. RECOMBINATION PROCESSES IN InGaAsP DOUBLE HETEROJUNCTIONS

By the end of the seventies, the investigation of the AlGaAs/GaAs DH's had revealed the peculiarities of the recombination processes in $A^{III}B^{V}$ compounds with a direct bandgap, such as GaAs and $Al_xGa_{1-x}As$ ($x < 0.3$) [6.46]. It was shown that in high-quality layers of these compounds, which are a narrow-band active region of DH structures, the bulk processes of nonradiative recombination do not influence the total recombination rate over a wide range of doping levels and temperatures. The lifetimes of the nonequilibrium carriers are determined by the rate of the band-to-band radiative transitions. Moreover, as a result of multiple self-absorption and reradiation of intrinsic luminescence in the active region, the observed effective lifetimes (τ_{eff}) may be more than the quantum-mechanical radiative lifetimes (τ_0) by an order of magnitude, while the measured values of the external quantum efficiency η_e may exceed by the same amount the upper limit of the external quantum efficiency ($\eta_{e0} = 1.5\%$) restricted by the angle of total internal reflection at the semiconductor-air interface [6.46].

The values of the external efficiency of InGaAsP/InP light emitting diodes with $\lambda < 1.2$ μm, obtained from first investigations [6.8], were also found to be higher than η_{e0}, although they were 1.5-2 times lower than the corresponding values for AlGaAs/GaAs LED's of identical construction [6.47]. These results indicate a high internal quantum efficiency of electroluminescence (η_{iel}) in the active region of "short-wave" InGaAsP/InP heterojunctions. However, the ambiguity in the interpretation of the results of electroluminescence experiments prevented an exact evaluation of the quantity η_{iel} in these InGaAsP compounds. The data on this quantity for the most interesting compositions of InGaAsP with $E_g = 0.8$-0.95 eV are even more scarce and no information is available about the effect of doping on the efficiency of radiative transitions in InGaAsP. The necessity of investigating the recombination mechanisms in this material was also dictated by the fact that the temperature dependence of the lasing thresholds for InGaAsP/InP DH lasers was found to be much stronger than for AlGaAs DH lasers. Theoretical estimates [6.48] showed that this may be due to the influence of Auger recombination processes.

The results given below were obtained from photoluminescence (PL) studies of isotypic *N-n-N* and *P-p-P* InGaAsP/InP DH ($\lambda = 1.3$ and 1.55 μm) and InGaAsP/GaAs DH ($\lambda = 0.73$ μm) grown correspondingly on InP ⟨100⟩ and GaAs ⟨111⟩ substrates from indium-rich melts by LPE. The lattice mismatching for the structures investigated in this article did not exceed 0.04%.

The external PL efficiency was measured by using the method developed earlier for AlGaAs DH's [6.49], with the help of a laser whose radiation was absorbed directly in the DH active region. For InGaAsP InP DH's, a YAG:Nd^{+++} laser (λ = 1.06 μm) was used while a Kr^{+} laser (λ = 0.67 μm) was employed for InGaAsP/GaAs DH's. The effective lifetimes of nonequilibrium charge carriers (NCC) were determined for pulse excitation with an AlGaAs DH laser, or a nitrogen laser pumping a dye laser. As in the case of AlGaAs/GaAs DH's [6.46, 49], the measurements of edge absorption in the investigated materials were used [6.50] for calculating the calibrating dependences $\eta_e = f(\eta_i)$ and $\tau_{eff}/\tau = f(\eta_i)$. After an experimental determination of η_e and τ_{eff}, these dependences were used for calculating the internal recombination parameters η_i and τ for the active region material, as well as the radiative and nonradiative lifetimes of NCC's.

Let us first consider the recombination processes in undoped *N-n-N* DH's in which the concentration of residual donors was (1-3) × 10^{17} cm^{-3}. Measurements carried out on a large number of samples showed that for an excitation density 10^2 W/cm^2, typical values of η_e at 300 K were 4-6% for InGaAsP/InP DH's with mirror surfaces (λ = 1.3 and 1.55 μm). This value is somewhat lower than for the corresponding AlGaAs DH's [6.49]. The values of η_e are doubled if one of the surfaces is matted. For InGaAsP, the values of η_i corresponding to these values of the external efficiency amount to 70-80%. The highest values of the external and internal radiative recombination efficiencies observed in some InGaAsP/InP heterojunctions with λ = 1.3 μm (η_e = 15% for mirror surfaces, $\eta_i \simeq 90\%$) are close to typical values of η_e and η_i for AlGaAs DH's [6.51]. For InGaAsP InP heterojunctions, the values of η_e and η_i depend weakly on the excitation level in the 1-10^3 W/cm^2 range (see Fig. 6.7). The values of η_i for InGaAsP/GaAs heterojunctions (λ = 0.73 μm) are also found to be not less than 80% at 300 K [6.52]. However, a higher excitation level is required for obtaining such values of the internal efficiency of radiative transitions in InGaAsP/GaAs DH's (see curve *2* in Fig. 6.7).

Temperature investigations have shown that in the entire range between 80 and 400 K, $\eta_i \geqslant 70\%$ in undoped isotypic InGaAsP DH's, and that the recombination of the NCC mainly takes place through band-to-band radiative transitions. Accordingly, the effective lifetimes of NCC determined from a decay of the edge emission pulse (Fig. 6.8) increase with temperature, following the law $\tau \propto T^{3/2}$ which is valid for radiative transitions occurring with momentum selection [6.53]. The absolute value of τ_{eff} for InGaAsP/InP DH's with λ = 1.3 μm is then 3-4 times higher than the corresponding value for InGaAsP GaAs DH (Fig. 6.8) on account of the dependence of the band-to-band radiative transition probability on E_g [6.53].

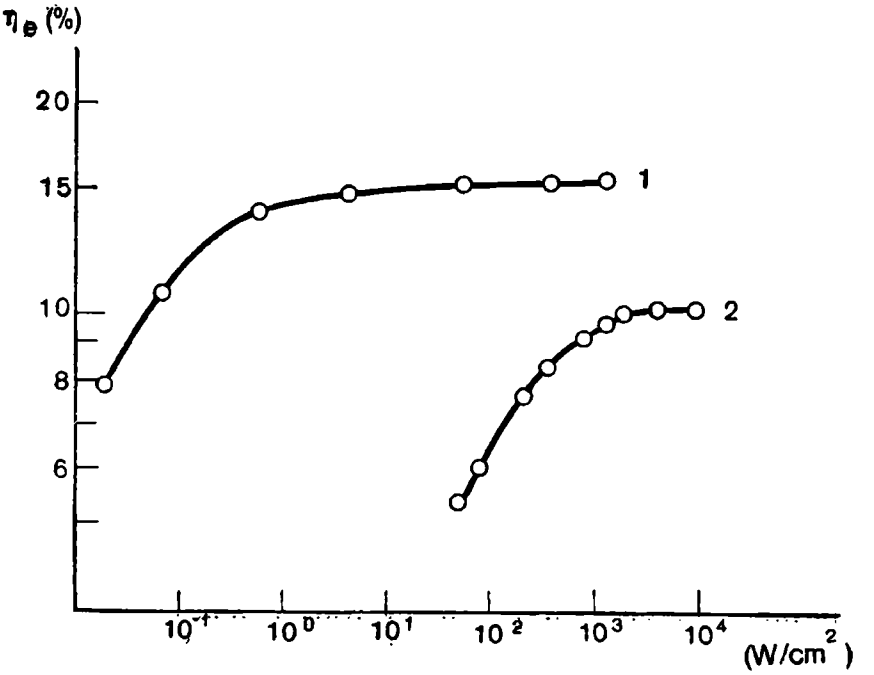

Fig. 6.7. *1*—dependence of the external luminescence efficiency on the density of the exciting radiation for InGaAsP/InP *N-n-N* structure ($\lambda = 1.3$ μm, mirror faces, $d = 1$μm); *2*—similar dependence for InGaAsP/GaAs *N-n-N* structure ($\lambda = 0.73$ μm, mirror faces, $d = 1.1$μm).

It can be seen from Fig. 6.9 that doping of $In_{0.7}Ga_{0.3}As_{0.64}P_{0.36}$ by acceptors (zinc) leads to a decrease in the efficiency of radiative transitions starting from a hole concentration $\sim 3 \times 10^{17}$ cm^{-3} [6.54]. Similar effects were observed for InGaAsP compositions corresponding to narrower ($E_g = 0.8$ eV) as well as wider ($E_g = 1.7$ eV) band gaps [6.55]. It is also well known that InP doped with acceptor impurities has a considerably lower quantum efficiency of luminescence as compared to *n*-InP. In this respect, InP and InGaAsP differ from GaAs and AlGaAs whose doping with acceptors leaves the value of $\eta_i = 90\%$ unchanged right up to $p = 2 \times 10^{18}$ cm^{-3} (curve *2*, Fig. 6.9) [6.46]. An enhancement of nonradiative recombination upon doping InP and InGaAsP by acceptors is obviously due to defect formation processes rather than to Auger recombination. It cannot, however, be ruled out that Auger recombination also contributes to the nonradiative recombination in the narrow-band solid solutions heavily doped with acceptors.

The foregoing explains the growing interest towards the InGaAsP/InP DH structures with an undoped active region, which are used at present for manufacturing LED's and lasers. At effective current densities $\sim 10^3$ A/cm^2, the concentration of NCC's in the

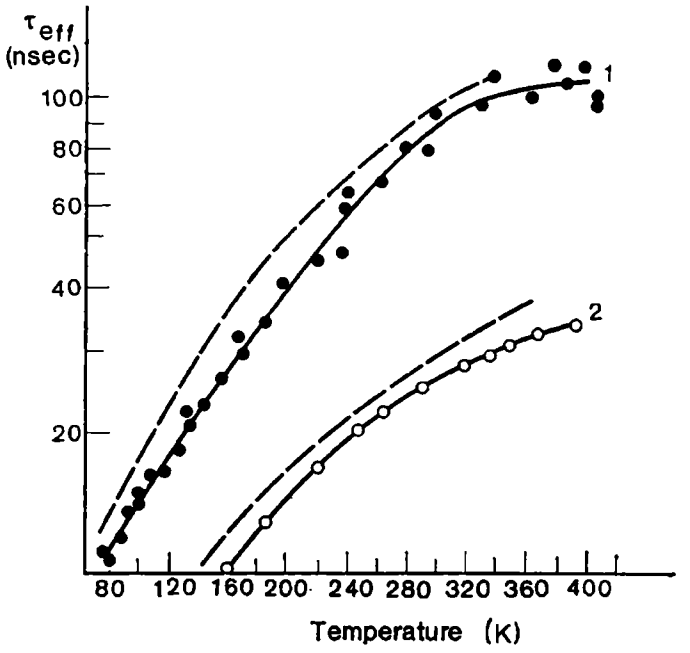

Fig. 6.8. Temperature dependences for effective lifetimes of nonequilibrium carriers in the active regions of the same structures as in Fig. 6.7; *1*—InGaAsP/InP DH, *2*—InGaAsP/GaAs DH. Dotted curves show the $\tau \propto T^{3/2}$ dependence.

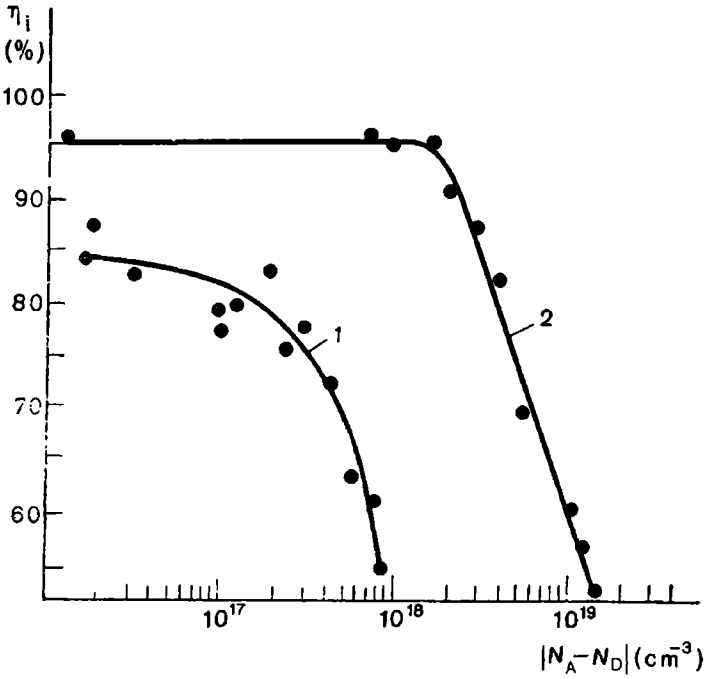

Fig. 6.9. Dependence of the internal efficiency of radiative transitions on acceptor doping level for the active region of Zn-doped InGaAsP/InP DH's ($\lambda = 1.3\mu m$) (curve *1*) and Ge-doped AlGaAs DH's (curve *2*).

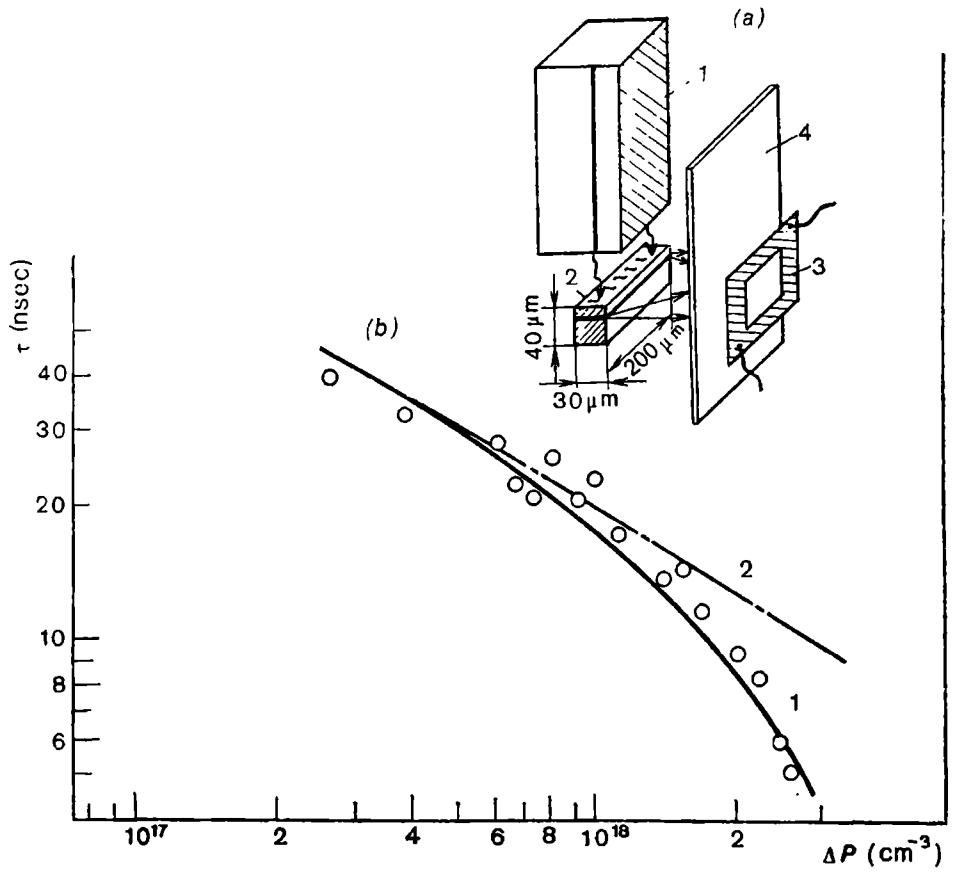

Fig. 6.10. (*a*) Experimental set-up for pulsed photoexcitation of DH's: *1*—AlGaAs DH laser; *2*—DH InGaAsP/InP sample under investigation; *3*—Ge avalanche photodiode; *4*—InP filter.
(*b*) Experimentally determined values of lifetimes as functions of the concentration of nonequilibrium carriers (circles) at $T = 350$ K (InGaAsP/InP, $d = 0.3\mu m$, $\lambda = 1.3\mu m$); curves *1* and *2* are theoretically calculated dependences $\tau = f(\Delta p)$ according to formulas (6.3) and (6.2) respectively.

active region of such light sources exceeds the concentration of majority carriers and bimolecular recombination takes place in the electron-hole plasma. The efficiency of radiative transitions in electron-hole plasma has been the subject of discussion in a number of articles dealing with the investigation of parameters of InGaAsP/InP LED's [6.56-57]. The saturation of electroluminescence intensity caused by a decrease in the quantum efficiency of such LED's at high current densities was ascribed by the authors of [6.56] to the increasing role of Auger recombination. This was disputed by the authors of [6.57], who pointed out that the "saturation effect" was observed in InGaAsP/InP LED's at low temperatures as well, and that such an effect takes place in AlGaAs/GaAs LED's also. Subsequent experiments on LED's also failed to establish

conclusively the physical principle underlying the saturation. The difficulties in interpreting the results of electroluminescence experiments are due to the relatively complex nature of the object under investigation, uncontrollable gradients in the distribution of the doping impurities, and the spatial inhomogeneity in the current density distribution across the p-n junction.

The optical method of exciting NCC's in isotypic DH structures considerably simplifies the investigation of the recombination processes at high excitation levels. In such experiments (see Fig. 6.10*a*), we used an AlGaAs DH laser as the source of pumping radiation. This allowed us to simultaneously measure the luminescence efficiency and the NCC lifetimes as functions of the excitation density [6.58]. The determination of lifetimes enabled us to calculate the concentration Δp of NCC in the active region of the DH under investigation for a given excitation level and to obtain the dependences $\eta_e = f(\Delta p)$ and $\tau_{eff} = f(\Delta p)$, shown in Figs. 6.10*b* and 6.11. These dependences correspond to an InGaAsP/InP DH ($\lambda = 1.3$ μm) with a 0.3 μm thick active layer. The value of η_i for this structure in the low excitation region ($\Delta p = \Delta n < n_0$) was found to be about 75% at 300 K. It can be seen from Fig. 6.11 that an increase in the NCC concentration leads to a decrease in the luminescence efficiency. This decrease is negligible at $T = 295$ K but becomes more significant at $T = 350$ K.

It is well known that for high NCC concentrations ($\Delta n = \Delta p > n_0$), the band-to-band radiative lifetime decreases with increasing Δp according to the relation

$$\tau = \frac{1}{B(n_0 + \Delta p)}, \tag{6.2}$$

where B is a constant independent of the excitation level in the simplest case: $B = B_0 = (\tau_0 n_0)^{-1}$. A comparison of the experimental data for τ_{eff} with the above expression (dot-and-dash curves in Figs. 6.10 and 6.11) shows that with increasing Δp, τ_{eff} decreases more rapidly at 350 K, and more slowly at 295 K, than what should be expected from the simplest model of bimolecular recombination. The slower drop in τ_{eff} at 295 K can be explained if we take into account the dependence of the coefficient B on the NCC concentration. The decrease in the value of B with increasing $\Delta n = \Delta p$ may be due to a transition to the degenerate NCC distribution in the conduction band of the material under investigation. The results of the corresponding calculations for the band-to-band radiative lifetime in InGaAsP taking into account the momentum selection rules are shown by curve *1* in Fig. 6.11. If the calculated values of τ_0 are doubled (curve *2*, Fig. 6.11), the theoretical dependence $\tau = f(\Delta p)$ is found to be in good agreement with the experimental results. The twofold increase in the experimental lifetimes as com-

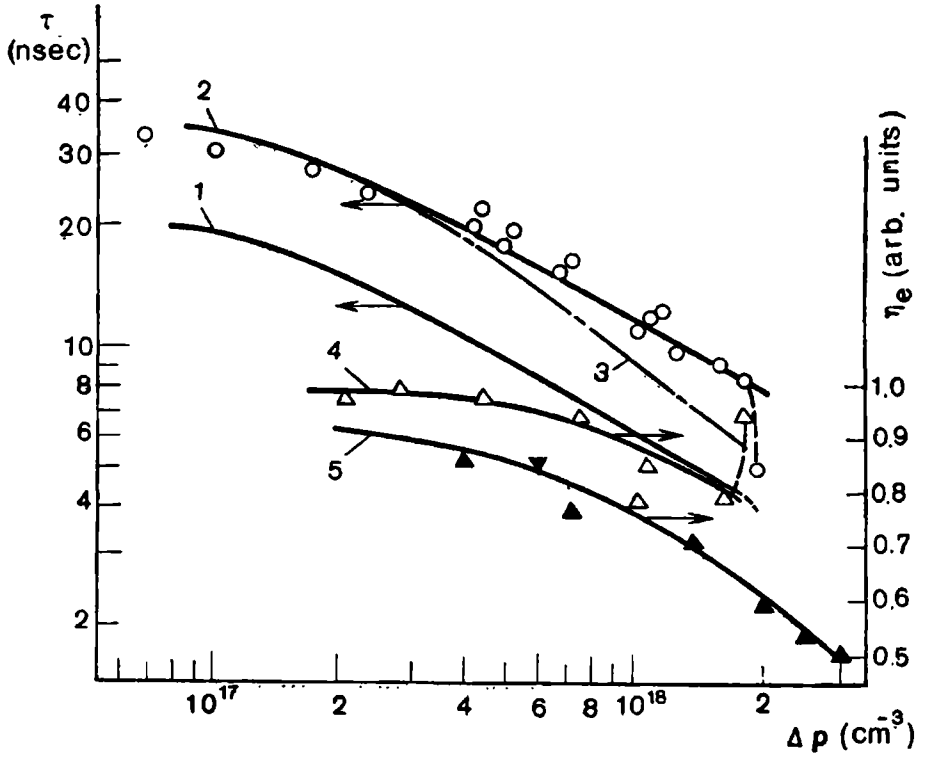

Fig. 6.11. Experimental and theoretical $\tau = f(\Delta p)$ dependences at 350 K and $\eta_e = f(\Delta p)$ at 295 and 350 K for the same DH's as in Fig.6.10. Circles denote the experimental values of τ_{eff} (295 K). Light and dark triangles represent the experimental data on the variation of η_e at 295 and 350 K: *1*—results of quantum-mechanical calculations of the radiative lifetimes taking into account the degeneracy of nonequilibrium carriers; *2*—the same as *1* after introducing corrections for self-absorption; *3*—$\tau_{eff} = [B_{eff}(n_0 + \Delta p)]^{-1}$ dependence at $B_{eff} = \text{const}$; *4* and *5*—theoretical curves for η_e: $\eta_e = \tau_{eff}/\tau$, where τ and τ_{eff} are radiative and total lifetimes of the nonequilibrium carriers.

pared to the theoretical values is in accord with the calculations of the reradiation effects in InGaAsP DH's with appropriate parameters. Thus, it can be concluded on the basis of the above results that for $In_{0.7}Ga_{0.3}As_{0.64}P_{0.36}$, the real values of the coefficient B, which can be interpreted as the spectrally averaged radiative transition probability, are correctly described by the theoretical curve *1* and are equal to $B = 1.7 \times 10^{-10}$ cm^3 sec^{-1} for $\Delta p = 3 \times 10^{17}$ cm^{-3} and $B = 1.2 \times 10^{-10}$ cm^3 sec^{-1} for $\Delta p = \Delta n = 2 \cdot 10^{18}$ cm^{-3} respectively.

In order to explain the experimental dependence $\tau_{eff} = f(\Delta p)$ at 350 K, we must also consider the additional channel for nonradiative recombination. As a result of this, the drop in the value of τ_{eff} with increasing Δp is faster than linear. It is but natural to assume

that the band-to-band Auger process is such a recombination channel. The dependence $\tau_{eff} = f(\Delta p)$ should then have the form

$$\tau_{eff} = \frac{1}{B_{eff}(n_0 + \Delta p) + C(\Delta p)^2}. \tag{6.3}$$

The reradiation effects have been taken into account in this expression by introducing the coefficient B_{eff} which is about half the calculated value of B at 350 K. In the same way as for $T = 295$ K, it is assumed that the magnitude of B_{eff} decreases with increasing Δp in accordance with the calculations for the rate of radiative transitions. The best fit of the theoretical curve to the experimental results for τ_{eff} was obtained by assuming the value 1.1×10^{-29} cm^{6}sec^{-1} for the coefficient C. This value of C was found to be one-fourth of the value obtained from the most accurate calculations of the Auger recombination rate in degenerate electron-hole plasma in $In_{0.7}Ga_{0.3}As_{0.64}P_{0.36}$ [6.59]. These calculations were carried out for the fastest Auger "hole" recombination process in which one of the holes is excited to the split-off valence band. According to the authors of [6.59], the above-mentioned discrepancy is within the accuracy of their calculations which were based on Kane's band theory. By using the values of the radiative and nonradiative recombination coefficients, we can easily calculate the dependence of the radiation efficiency on Δp ($\eta_e = \tau_{eff}/\tau$). The corresponding theoretical curves are in good agreement with the experimental results for 295 and 350 K (see Fig. 6.11, curves *4* and *5*).

It should be emphasized that while comparing the experimental and theoretical results, we have used a simple band-to-band transition model (with momentum selection) to describe the rate of radiative transitions in InGaAsP [6.53]. As in the case of GaAs [6.46], such a theoretical approximation is in good agreement with the experiment for a concentration range of 10^{17}-10^{18} cm^{-3} and for temperatures $T > 80$ K. Naturally, the ratio of the radiative transition probabilities in GaAs (B') and InGaAsP (B) in this case also satisfies the results obtained from this theory:

$$B'/B = (E_g'/E_g)^2 (m_e/m_e') (m_{hh}'/m_{hh})^{3/2} \tag{6.4}$$

Here, B' and B denote the radiative transition probability for low excitation levels, while the rest of the indices correspond to the usual notation for effective masses in GaAs and InGaAsP. Using relation (6.4) for determining the coefficient B and assuming that the value of the Auger recombination coefficient changes with the band parameters in accordance with the theoretical calculations in [6.59], we can determine the efficiency of radiative transitions for other compositions of InGaAsP solid solutions as well. Table 6.1 contains the calculated values of η_i for low NCC concentrations and for NCC concentrations $\sim 2 \times 10^{18}$ cm^{-3} close to the lasing threshold in DH

Table 6.1. Calculation of the Auger Recombination Influence on the Efficiency of Radiative Transitions in InGaAsP/InP DH Structures with Different Compositions of the Active Region

		λ (μm)	1.55	1.3	1.15	1.06
$\Delta n = \Delta p = 10^{17}$ cm^{-3}	η_i	295 K	83	97	99	99
	(%)	373 K	65	94	97	99
$\Delta n = \Delta p = 2 \times 10^{18}$ cm^{-3}	η_i	295 K	28	77	89	95
	(%)	373 K	14	60	81	88

lasers. It can be seen from the data presented in this table that Auger recombination at 300 K should practically have no effect on the parameters of LED's and lasers based on InGaAsP/InP DH's with $\lambda < 1.1$ μm.

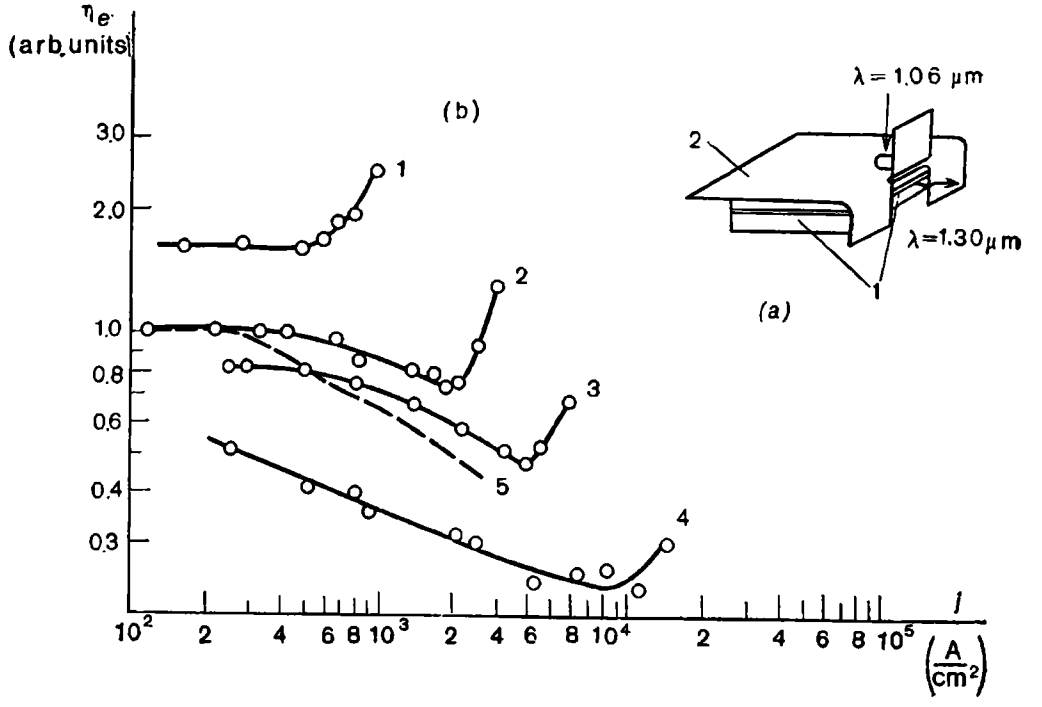

Fig. 6.12. (*a*) Experimental set-up for photoexcitation of DH's: *1*—the structure under investigation; *2*—diaphragm.
(*b*) Curves *1-4*—dependences of η_e on photoexcitation density for InGaAsP/InP *N-n-N* DH's ($\lambda = 1.3$ μm, $d = 0.3$ μm) at different temperatures: *1*—233 K, *2*—293 K, *3*—328 K, *4*—373 K. For the sake of convenience in comparison, the optical excitation density has been converted into current density; curve *5* shows the dependence of η_{eel} on current density according to experimental results of [6.56] on electroluminescence.

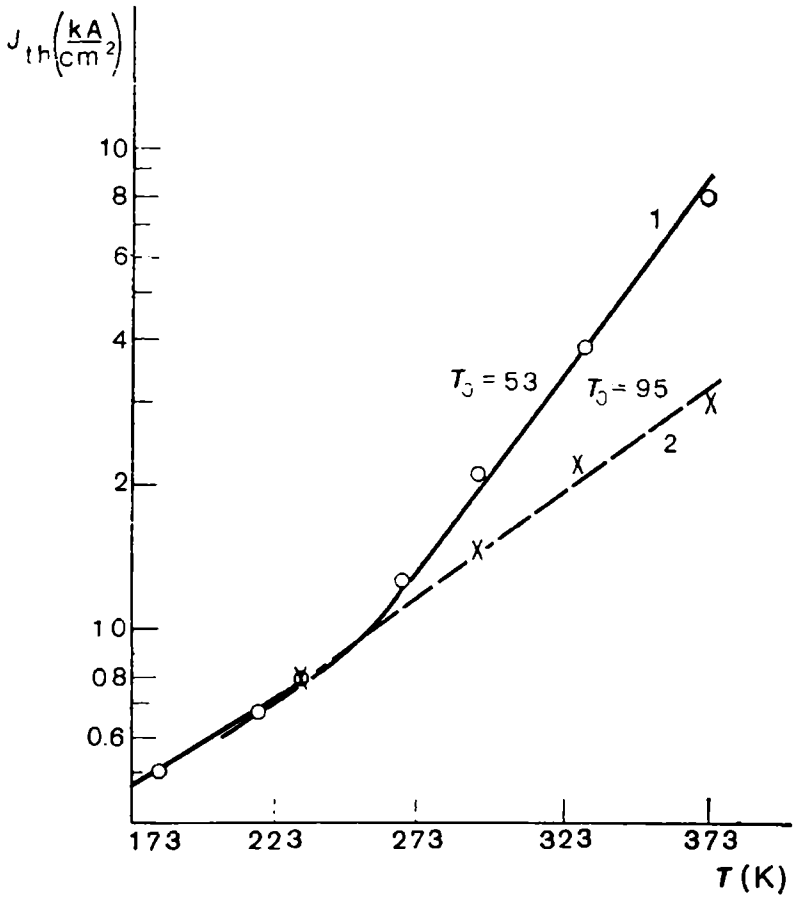

Fig.6.13. *1*—temperature dependence of the lasing threshold in sample of the same DH as in Fig. 6.12; *2*—lasing thresholds after taking into account the correction for drop in J_{th} at threshold excitation densities (see Fig. 6.12). As in Fig. 6.12, the threshold excitation densities are expressed in units of equivalent current density.

A comparison of curves *2* and *5* in Fig. 6.12 shows that the drop in the value of $\eta_{e.el}$ with increasing current density, which is usually observed in InGaAsP/InP LED's with $\lambda = 1.3$ μm [6.56], is much more pronounced than in photoluminescence experiments with similar isotypic samples. Besides, it can be also seen that the saturation of the electroluminescence intensity may be caused mainly by some specific processes which are characteristic of NCC injection in the diodes only. The dependences $\eta_e = f(J)$ for different temperatures, shown in Fig. 6.12 (curves *1-4*), have been obtained by photoexcitation of the sample in the form of a Fabry-Perot resonator [6.60]. The radiation is extracted through one of the resonator faces and the rise in the value of η_e in the region of high excitation densities is associated with a transition to the lasing mode. Figure 6.13 shows the temperature dependence of the lasing threshold (J_{th}) in this sample.

The data presented in Fig. 6.12 can be used to introduce a correction for the increase in the threshold due to Auger recombination. After the introduction of this correction, the sharp bend in the temperature dependence of the threshold almost completely disappears and the temperature dependence of J_{th} becomes the same for the entire temperature region from 80 to 400 K. It should be noted that curve *1* in Fig. 6.13 corresponds to a typical temperature dependence of the threshold in injection lasers with $\lambda = 1.3$ μm [6.48]. The results given in this section indicate that further investigations in this field should be directed at finding the reasons behind the "residual" temperature dependence of J_{th}, which is not connected with the Auger processes.

6.4. LASERS

Most of the communications relating to InGaAsP heterojunction lasers are publications aimed at establishing priority. These works contain reports on creation of lasers with a certain wavelength, the peculiarities of their construction, the operating conditions, and parameters. The first article [6.6] on InGaAsP/InP DH lasers reported about a pulsed laser emitting at the wavelength 1.02 μm at 77 K and having a threshold current density $J_{th} = (0.6\text{-}4)$ kA/cm^2. The next paper [6.7] concerned a pulsed laser of this kind operating at a wavelength 1.02-1.11 μm at 300 K with $J_{th} = 10.4$ kA/cm^2. In [6.61], J_{th} was lowered to 50 A/cm^2 at 77 K and 1.2 kA/cm^2 at 300 K for $\lambda = 1.33$ μm. Subsequent improvements in the technology of preparing DH's led to a progressive lowering of the threshold current density at 300 K and the lowest value of J_{th} for $\lambda = 1.35$ μm has now reached 0.67 kA/cm^2 at 300 K [6.62]. This is comparable with the J_{th} attained for ordinary DH lasers in the AlGaAs/GaAs system. In all the above-mentioned works, different versions of LPE described in Sec. 6.1 were used for preparing heterojunctions.

While fabricating DH's for lasers, two important problems are encountered. These are the lattice matching in the epitaxial layers of a heterojunction and localization of the *p-n* junction in it. Quantitative data on these problems was not available in literature so far.

Figure 6.14 shows the experimental dependence of J_{th} for broad-area lasers ($\lambda = 1.55$ μm) on lattice mismatching between the active layer and the substrate. In this case, the upper wide-band emitter is a InGaAsP solid solution with energy gap ~1.0 eV. It can be seen from Fig. 6.14 that J_{th} attains its minimum value for $\Delta a\, a \simeq$ $\simeq -0.1\%$. For lasers emitting at wavelength 1.3 μm, the J_{th} minimum is found to be at $\Delta a/a \simeq -0.05\%$. If we take into account the thermal expansion coefficients for the corresponding compositions of InGaAsP solid solutions in the active region [6.36], it is found that heterojunctions having $\Delta a/a$ equal to zero at the temperature of

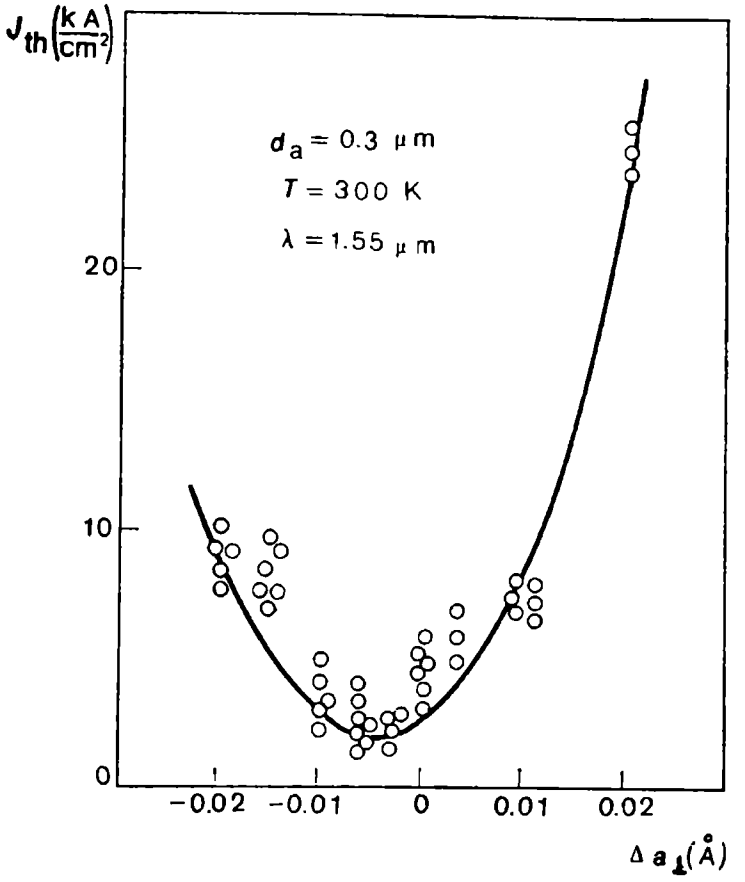

Fig. 6.14. Dependence of J_{th} for broad-band lasers on mismatching of lattice parameters ($T = 300$ K, $\lambda = 1.55$ μm).

epitaxial growth (645° C) have the lowest values of J_{th}. The maximum differential quantum efficiency in this case is also obtained for the minimum value of J_{th}.

Figure 6.15 shows the dependence of J_{th} for broad-area lasers with $\lambda = 1.55$ μm on the thickness of the intermediate undoped layer grown in front of the Mg-doped p-emitter in order to prevent the acceptors from penetrating the active region of thickness 0.5 μm. It can be seen that J_{th} has its minimum value for an intermediate layer of thickness ~0.6 μm. The differential quantum efficiency in this case passes through a maximum. These heterojunctions were prepared by LPE at 645° C by step-cooling technique. In other words, the emitters were grown from supersaturated solutions, while the active region was grown under isothermal conditions from supercooled melt at $\Delta T = 5°$ C.

In order to attain CW operation at room temperatures, stripe-geometry lasers are employed. The first report on CW operation at room temperature in InGaAsP/InP heterojunction lasers appeared

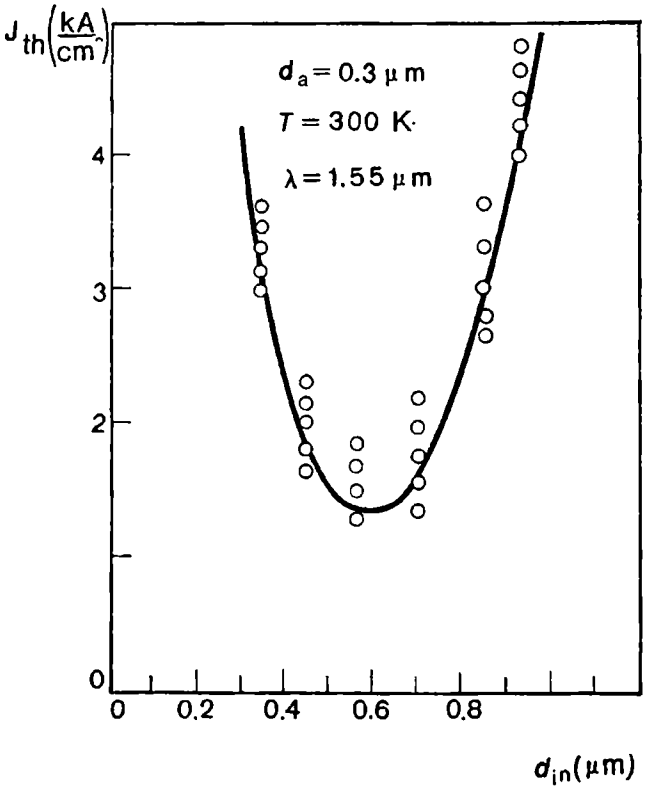

Fig. 6.15. Dependence of J_{th} for broad-band lasers on intermediate layer thickness d_{in} for InGaAsP:Mg structures with a p-emitter.

in 1976 [6.9]. The threshold current in these lasers was equal to 265 mA. Further developments of several different constructions of InGaAsP/InP stripe-geometry lasers, which were earlier tried for the AlGaAs/GaAs system [6.10], brought the threshold current for the CW operation down to ~10 mA at 300 K. The power of best lasers has attained values up to ~20 mW [6.63]. The differential quantum efficiency in pulsed operation is ~70% [6.64].

The most promising laser intended for optical communication systems seems to be some kind of a buried-heterostructure laser with two-dimensional optical and current confinement. This laser can be fabricated in two ways: buried mesastripe lasers [6.65] and the crescent geometry lasers grown in etched V-grooves [6.66] by using a p-n junction or high-resistivity i-InP isolation. Owing to a quite small width of the waveguide, both types of lasers have stable mode radiation patterns and linear characteristics of light output against injection current. At present the best way to fabricate such lasers seems to be the hybrid technology, i.e. a combination of LPE and vapour-phase epitaxy (VPE)

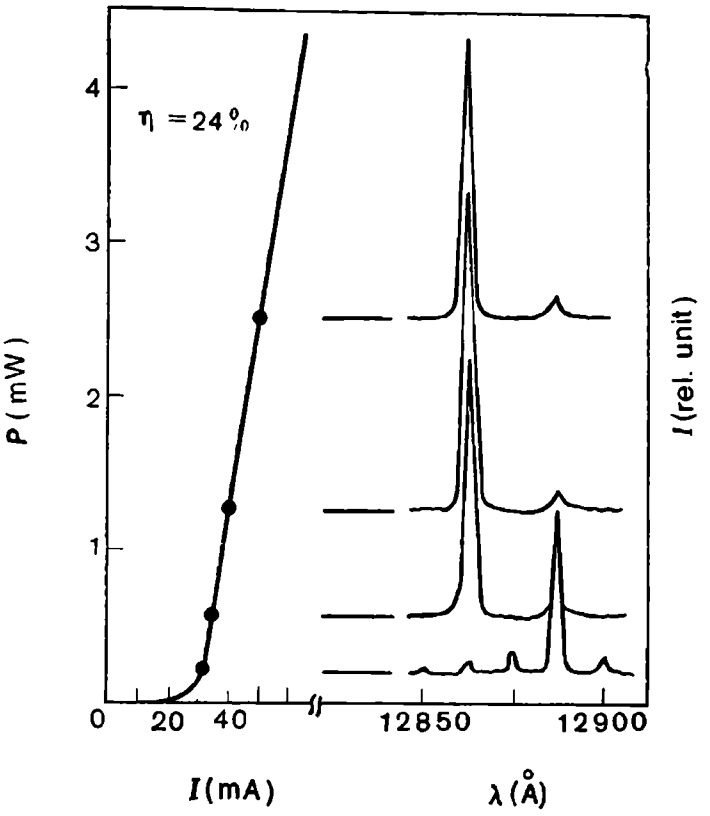

Fig. 6.16. Watt-ampere characteristics and emission spectra in CW buried mesastripe laser ($T = 300$ K).

[6.65]. The DH wafers are obtained by LPE, while after mesa-etching the high resistivity isolating *i*-InP layer is subsequently grown by VPE. Because of the possibility of growing high-resistivity InP by VPE, the hybrid technology of laser fabrication opens a new possibility of better current confinement.

Figure 6.16 shows typical current-power characteristics and CW radiation spectra for one of the buried mesastripe lasers obtained by hybrid technology at 300 K with a waveguide of 8 μm width and a 170 μm long cavity [6.67]. The DH wafers for this laser, which is based on the InGaAsP/InP system with $\lambda \simeq 1.3$ μm, was obtained by LPE using step cooling technique at 645° C. The mesa stripes were buried from high-resistance InP ($\rho \sim 10^5$ ohm·cm) doped with Fe by metal-organic chemical vapour deposition method. The lowest threshold current at 300 K was 30 mA, the differential quantum efficiency on both sides was ~24%, and the radiation power was 3-4 mW at $2J_{th}$. It can be seen from the figure that the emission spectrum at $1.2J_{th}$ and above consists of practically one longitudinal mode. Such lasers are also characterized by one transverse mode with

a divergence $\theta_{\parallel} = 12°$ C in a plane parallel to the heterojunction and $\theta_{\perp} = 50°$ C in a plane perpendicular to it (the active region of this laser is 0.5 μm thick).

While investigating InGaAsP injection lasers operating in the visible spectral region, the main attention was first paid to the possibility of advancing towards the short-wave spectral region.

The technology of growing InGaAsP/GaAsP DH structures developed in the Physico-Technical Institute of the USSR Academy of Sciences led in 1975-76 to the construction [6.13, 14] of injection lasers with record-low wavelengths ($\lambda = 0.637$ μm at 300 K and $\lambda = 0.575$ μm at 77 K in the yellow-green spectral region). The appropriate lattice-matched DH structures were grown by LPE on GaAsP substrates and consisted of two wide-band InGaP emitters and a narrower InGaAsP active region. The important point in this direction was the choice of optimal GaAsP substrates for preparing short-wave lasers. The composition of these substrates ensures the most wideband InGaP and InGaAsP compounds which are lattice-matched to the substrate and still retain their direct band structure (for InGaP, $E_g = 2.2$ eV at 300 K). Lasers based on similar DH structures but operating at somewhat longer wavelengths were constructed at nearly the same time by Prof. Holonyak's group in USA [6.68]. It was only in 1982 that Fujimoto *et al.* [6.69] reported the construction of InGaAsP/GaAsP lasers with shorter wavelengths ($\lambda = 0.621$ μm at 300 K).

It was mentioned in the introduction that interest toward powerful CW lasers in the visible range ($\lambda \simeq 0.7$ μm) has grown over the past few years owing to the possibility of their application in recording and reproducing information on discs. In this spectral region, GaAs substrates can be used to create InGaAsP/GaAs DH lasers, and there are grounds to assume that for this purpose, such lasers can successfully compete with the traditional AlGaAs DH lasers. The validity of these assumptions follows from the data given in [6.52], where it has been shown that the internal efficiency of the radiative transitions in InGaAsP/GaAs DH structures with $\lambda \geqslant \geqslant 0.73$ μm, grown by LPE, may attain the value of 80% at 300 K. Injection DH lasers with low threshold currents ~1.3 kA/cm^2 ($\lambda = 0.78$ μm) have been created for operating in CW mode on the basis of these structures [6.15]. The creation of first InGaAsP/GaAs CW lasers with $\lambda = 0.72$-0.78 μm by using vapour-phase method has also been reported [6.16].

Further investigations on the power characteristics and aging test will ultimately determine the competitiveness of such lasers against the DH AlGaAs visible lasers.

6.5. LIGHT-EMITTING DIODES

InGaAsP/InP DH light-emitting diodes whose active region ensures operation at wavelengths 1.3 and 1.55 μm are of great practical importance. Although commercial production of LED's designed for optical communication systems has started in several countries and dozens of papers have been devoted to them, there is practically no information in the literature about their basic parameter, for example, the efficiency η_{iel} of transformation of electrical energy into light in their active region. The parameter η_{iel} is equivalent to the internal quantum efficiency of radiative transitions, which is determined in the photoluminescence experiments. However, its determination from the measurements of external efficiency of the electroluminescence (η_{eel}) is a much more complicated problem, primarily due to the considerable influence of absorbing ohmic contacts or reflecting metal coatings on the value of η_{eel}. These factors have an especially strong effect on the values of η_{eel} in devices based on structures without passive absorbing regions of semiconducting materials, i.e. structures like AlGaAs/GaAs DH's (in which the GaAs substrate is removed) or the InGaAsP/InP DH's under consideration. In order to eliminate the effect of these factors, a technique was worked out to determine the parameter η_{eel} by using a transparent electrode for investigating DH's that do not have ohmic contacts [6.70]. In order to measure η_{eel} by this method, a direct voltage was applied between a metallic plate on which the sample under investigation lies, and a thin GaP plate pressed to the other face of the sample served as the second transparent electrode. The radiation generated in the active region of the sample passed through the GaP plate and was recorded by using a Ge-photodiode of large area adjoining the GaP plate. Measurements carried out in this way in a large number of InGaAsP/InP DH's have shown that, in order to obtain structures with an injection luminescence efficiency comparable with photoluminescence efficiency of isotopic structures, special technological methods must be worked out to ensure the localization of the p-n junction in one of the emitters near the heteroboundary while conserving the n-type conductivity in the undoped active region. It was only after the development of technological process that values of η_{eel} comparable with the results of the first publication [6.8] on InGaAsP/InP double heterojunction LED's were obtained both for $\lambda = 1.3$ μm and $\lambda = 1.55$ μm; later, values up to twice those reported originally were obtained [6.71, 72]. For DH structures with mat-finished surfaces, measurements by the transparent electrode method gave values of η_{eel} of the order of 10-12% in the best of these samples. Apparently, the high external efficiency of electroluminescence is due to multipass effects in the same way as for photoluminescence experiments with isotypic structures. In accordance with the

corresponding calibration curve $\eta_e = f(\eta_i)$, the internal quantum efficiency of electroluminescence in the active region of these DH's with a *p-n* junction is about 80%. It should be remarked that similar values for the external efficiency of electroluminescence may be obtained for AlGaAs/GaAs DH's only upon removal of the GaAs substrate. This leads to a considerable complication of the device technology [6.47].

The InGaAsP/InP structures considered above were used for the fabrication of surface-emitting diodes whose construction is schematically shown in Fig. 6.17*b*. The diameter of the ohmic contact with the upper *p*-InP emitter was equal to 50 μm. The size of this contact spot was much smaller than the distance (about 200 μm) between the contact stripes on the *n*-InP emitting surface. It can be seen from the figure that the spatial distribution of near-field over the emitting surface is also about 200 μm. Thus, not more than 30% of the total radiation was extracted through the emitting surface corresponding to the size of the ohmic contact. Consequently, the losses associated with the absorption of a part of photons under the ohmic contact are more than compensated by the reflection from the coating on the remaining part of the rear surface of the device, and the external efficiency of the best samples of such LED's rose to 15-16% (see Fig. 6.17*a*). This is about 1.5 times more than the values of η_{eel} obtained for the original structure by transparent electrode method. Calculations carried out in [6.73] show that the blurring of the active region in comparison to the area of the region over which the current flows is a characteristic property of DH LED's with a high internal quantum efficiency. The emission from the peripheral regions of such DH's is due to the self-absorption of the primary electroluminescence radiation by the active region after reflection from the device surfaces.

On the basis of the results presented above, we can analyze the power characteristics of surface-emitting InGaAsP/InP LED's for optical communication considered in a number of latest publications [6.74, 75]. The construction of these LED's differs from the schematic diagram shown in Fig. 6.17*b* mainly in that the window in contact with the emitting surface is smaller than the diameter (100 μm) of the fibre used. In the absence of any special matching equipment, the typical value of radiation power in a fibre with numerical aperture $N_A = 0.2$ is 50 mW for a current 100 mA through the LED [6.74, 75]. The total radiation power extracted through the contact window is $(N_A)^{-2}$ times more ($\sim$2 mW), corresponding to $\eta_{eel} = 2\%$. Such comparatively small values of η_{eel} can be attributed to the uncontrollable doping of the DH active region by acceptors (leading to a decrease in the value of η_{iel}), as well as to a blurring of the emission region to dimensions exceeding the size of the window in contact with the emitting surface.

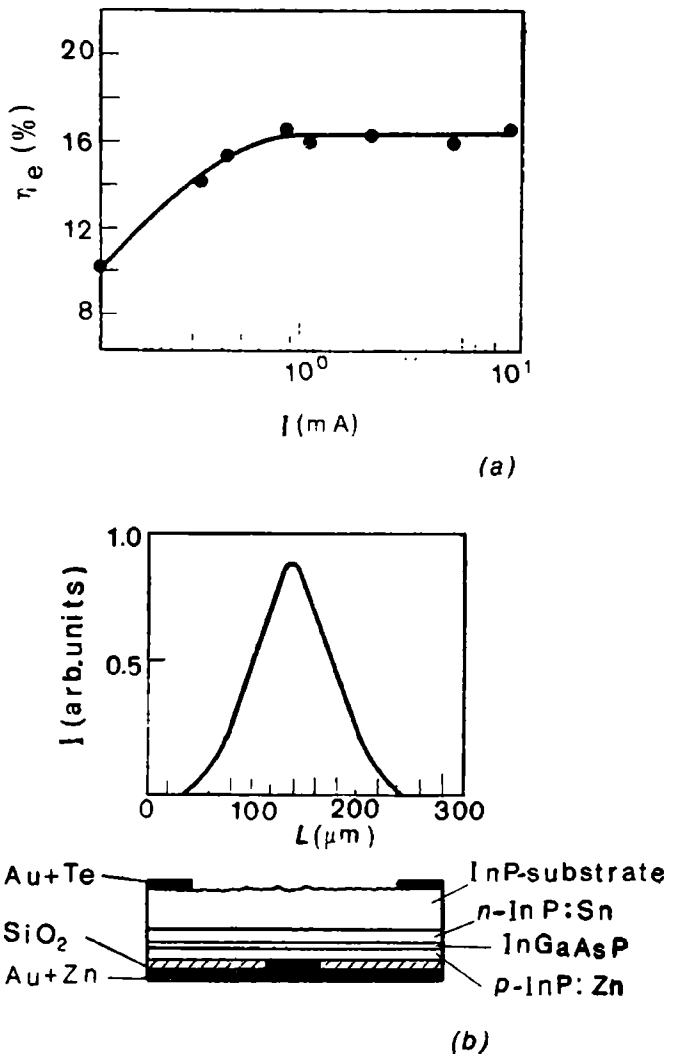

Fig. 6.17. (*a*) Dependence of external quantum yield of radiation on current for an InGaAsP InP DH surface-emitting diode ($\lambda = 1.3\mu m$). (*b*) Construction of a photodiode and distribution of near-field over its emitting surface.

Investigations of AlGaAs/GaAs LED's have shown that besides surface-emitting diodes, edge-emitting diodes from which the radiation is extracted along the heterojunction surface, can also be used successfully. In spite of the large values of η_{eel} obtained in one of the first works [6.76] on edge-emitting InGaAsP/InP LED's, the surface-emitting diodes have continued to dominate so far. It was only recently [6.77] that the potential advantages of edge-emitting InGaAs/InP LED's have been revealed. These advantages are mani-

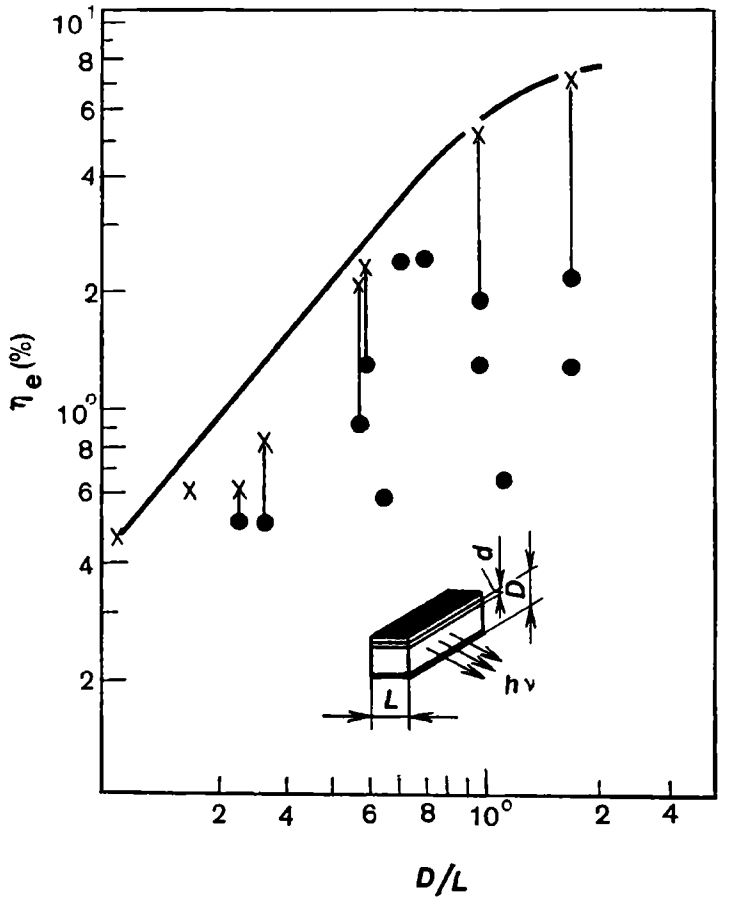

Fig. 6.18. Schematic diagram of an InGaAsP/InP DH edge-emitting diode. Circles and crosses represent the values of η_{eel} for edge-emitting diodes as functions of parameter D/L. Circles correspond to samples with cleaved faces, while crosses represent the values of η_{eel} obtained after matting one of the emitting faces ($T = 300$ K, $\lambda = 1.3\mu$m).

fested most strongly during the fabrication of supershort edge-emitting diodes (see Fig. 6.18), whose length along the output direction is comparable to or less than the thickness of the InP substrate which is transparent to the radiation emitted in the active region. Obviously, for photons propagating over the InP substrate in such sources, the probability of their interaction with the side faces of the crystal is higher than the probability of their absorption under the ohmic contacts. The extraction of the radiation from an edge is facilitated by mat-finishing the other face. The maximum values of η_{eel} for supershort edge-emitting InGaAsP/InP DH diodes are 6% (see Fig. 6.18). The edge-emitting sources are extremely simple in construction and do not have the shortcomings inherent in surface-emitting LED's. The luminescence intensity saturation effect is

much less pronounced in these sources at high current densities, and there are no problems associated with the expansion of the emission region due to the reradiation effect. A decrease in the role of reradiation effects, as compared to the surface-emitting diodes, increases the speed of such LED's. For a current density of 5×10^2 A/cm^2, the speed of edge-emitting sources is not less than 10^{-8} sec, and this ensures a modulation of signals with frequencies up to 50 MHz.

6.6. PHOTODETECTORS

At present, the maximum number of papers on this subject is devoted to the fabrication and analysis of heterojunction photodetectors based on InGaAsP/InP. Mainly, these papers are devoted to the study of three types of photodetectors, viz. the avalanche photodetectors (APD) [6.78-79], *p-i-n* photodetectors [6.80], and phototransistors (HJPT) [6.81, 82].

In view of the fact that the APD's have the highest sensitivity among the photodetectors, their investigation is of great interest. The optimized design of an APD is the one in which the avalanche region is separated from the light-absorption region. In other words, the *p-n* junction is placed in the InP-emitter at a certain distance from the heterointerface [6.78, 79]. The formation of a *p-n* junction in InP helps to reduce the dark currents in an APD due to lower values of diffusion current, generation-recombination current, and tunnel current in InP as compared to InGaAsP or InGaAs.

Figure 6.19 schematically shows an APD of mesa structure. The carrier concentration in *n*-InP with a 2 μm thick layer between the *p-n* junction and heterointerface is 5×10^{15} cm^{-3}, and the carrier concentration in the narrow-band *n*-InGaAsP of thickness 2 μm was 8×10^{15} cm^{-3}. The *p-n* junction was made by diffusing Cd. The diameter of the mesa was about 100 μm. No antireflecting or protective coatings were used [6.79]. The value of capacitance, which was equal to 1 pF in the absence of a bias, decreased to 0.5 pF when a reverse bias was applied. Figure 6.19 shows the dependence of the dark current I_d and of the multiplication M on the applied bias voltage for this APD. The avalanche multiplication appears at a bias voltage $V_B \approx 50$ V, and attains a value of 200 at 86 V. The dark current at a voltage of $0.9V_{br}$ was 1×10^{-5} A/cm^2 (V_{br} is the breakdown voltage). The sensitivity had a typical shape for heterophotodetectors, i.e. varied from 0.5 to 1.0 arb. units in the region 0.9-1.35 μm. The lowest dark current was obtained in an APD of plane construction with an SiO_2 protective coating which decreased the surface leakage current. Its value at $0.9V_{br}$ was found to be $3 \times \times 10^{-6}$ A/cm^2 [6.78]. The highest multiplication factor $M = 5500$ was obtained in [6.83] by using a mesa structure. The dark current in this case was 8×10^{-5} A/cm^2 at $\sim V_{br}$. The sensitivity of such

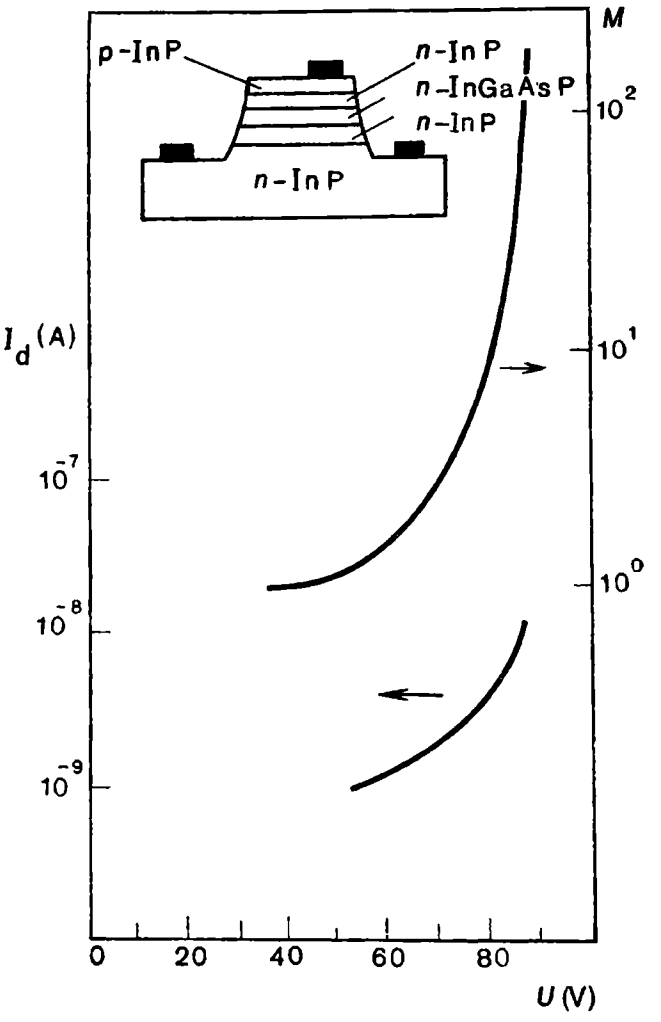

Fig. 6.19. Construction of an APD and the dependence of I_d and M on reverse bias.

APD's varies between 0.5 and 0.7 A/W for $M = 1$. The pulse build-up and decay time of the photoresponse is about 100 psec.

In view of smaller values of dark currents and of capacitances as compared to APD's, the *p-i-n* photodiodes have improved noise characteristics and a faster response [6.80]. The sensitivity of *p-i-n* photodiodes attains the value 0.7 A/W without any anti-reflecting coating. Hence such photodetectors can be used successfully, together with field-effect transistors (FET) in optical communication systems.

Phototransistors based on InGaAsP/InP heterojunction can also be used in optical communications. Although such detectors have a somewhat inferior noise level and a slower response, current amplification up to 1000 has been achieved for them [6.81, 82]. It should

be also mentioned that besides heterophotodetectors, InGaAs-based photoresistors have also been successfully employed in optical communication systems [6.84].

6.7. CONCLUSION

The investigations of lattice-matched heterojunctions in the InGaAsP system form a new independent branch of semiconductor electronics at present. This review did not aim at describing the problem in its entirety, the more so because investigations in this area are far from complete and are being rapidly extended. Apparently, the most promising aspect of this activity in the development of vapour-phase and molecular beam epitaxy methods whose application opens new avenues for construction and practical application of multilayer heterojunctions based on quaternary solid solutions.

References

6.1. Zh. I. Alferov and D. Z. Garbuzov, *Fiz. Tverd. Tela*, 7, 2375 (1965); *ibid.*, 9, 279 (1967).
6.2. Zh. I. Alferov, V. M. Andreev *et al. Int. Conf. Sm. Phys.*, Moscow, 1968, 1, 504, Nauka, Moscow, 1969; Zh. I. Alferov, V. M. Andreev *et al.*, *Fiz. Tekhn. Polupr.* 4, 1826 (1970).
6.3. R. L. Anderson, *Solid State Electron*, 5., 341 (1962).
6.4. Zh. I. Alferov, V. M. Andreev *et al.*, *Proc. Int. Conf. Phys. Chem. Sem. Heterojunc. Layered Struct.* Akad. Tiado. Budapest, 1, 93 (1971).
6.5 G. A. Antypes and R. L. Moon, *J. Electrochem. Soc.*, 120, 1574 (1973).
6.6. A. P. Bogatov, L. M. Dolginov *et al.*, *Kvant. Elektron.*, 1, 2294 (1974).
6.7. A. P. Bogatov, L. M. Dolginov *et al.*, *Fiz. Tekhn. Polupr.* 9, 1956 (1975).
6.8. L. M. Dolginov, N. Ibrakhimov *et al.*, *Fiz. Tekhn. Polupr.*, 9, 1319 (1975); L. M. Dolginov, A. E. Drakin *et al.*, *Kvant. Electron.*, 5, 11, 2488 (1978).
6.9. J. J. Hsieh, J. A. Rossi, and J. P. Donneley, *Appl. Phys. Lett.*, 28, 709 (1976).
6.10. H. C. Casey and M. B. Panish. *Heterostructure Lasers*, Academic Press, New York, San Francisco, London, 1978.
6.11. H. M. Macksey, M. H. Lee, N. Holonyak, Jr. *et al.*, *J. Appl. Phys.*, 44, 5035 (1973); W. R. Hitchens, N. Holonyak, Jr. *et al.*, *J. Cryst. Growth*, 27, 154 (1974).
6.12. J. J. Coleman, W. R. Hitchens, N. Holonyak *et al.*, *Appl. Phys. Lett.*, 25, 725 (1974); J. J. Coleman, N. Holonyak *et al.*, *IEEE J. Quant. Elec.*, QE-11, 471 (1975).
6.13. Zh. I. Alferov, I. N. Arsent'ev, D. Z. Garbuzov, and V. D. Rumyantsev, *Pis'ma v Zh. Tekhn. Fiz.*, 1, 305 (1976); *ibid.*, 1, 406 (1975).
6.14. Zh. I. Alferov, I. N. Arsent'ev, D. Z. Garbuzov *et al.*, *Pis'ma v Zh. Tekhn. Fiz.*, 2, 241 (1976); *ibid*, 2, 481 (1976).
6.15. Zh. I. Alferov, I. N. Arsent'ev, L. S. Vavilova *et al.*, *Fiz. i. Tekhn. Polupr.*, 18, (1984).
6.16. A. Usui, Y. Matsumoto *et al.*, *Ninth Int. Symp. on GaAs and Related Compounds*, Oiso, Japan, 1981 (Bristol, England, 137 (1982)).
6.17. A. T. Gorelenok, A. G. Dzigasov *et al.*, *Fiz. i Tekhn. Polupr.*, 15, 2410 (1981).
6.18. R. L. Moon, G. A. Antypes *et al.*, *J. Elec. Mater.*, 3, 635 (1974).
6.19. L. M. Dolginov, P. G. Eliseev *et al.*, *Kvant. Elektron.*, 3, 1381 (1976).

6.20. R. E. Nahory, M. A. Pollack *et al.*, *Appl. Phys. Lett.*, 33, 659 (1978).
6.21. A. T. Gorelenok, V. N. Mdivani *et al.*, *Cryst. Growth*, 60, 355 (1982).
6.22. M. B. Panish and M. Ilegems, *Progr. in Solid State Chemistry*, Pergamon Press, New York-London, 39, p. 7 (1972).
6.23. K. Nakajima, T. Kusunoki *et al.*, *J. Electrochem. Soc.*, 125, 123 (1978).
6.24. E. H. Perea and C. G. Fonstad, *J. Appl. Phys.* 51, 331 (1980).
6.25. M. B. Small, R. Ghez *et al.*, *Appl. Phys. Lett.*, 35, 209 (1979).
6.26. M. B. Small and R. Ghez, *J. Appl. Phys.* 50, 5532 (1979).
6.27. A. T. Gorelenok, P. P. Moskvin *et al.*, *Proc. 3rd All-Union Conf. on Phys. Processes in Semicond. Heterostructures*, 3, 4, Odessa, 1982 (in Russian).
6.28. J. J. Hsieh, *J. Cryst. Growth*, 27, 49 (1974).
6.29. N. A. Bert, A. T. Gorelenok *et al.*, *Avtometriya*, No. 6, 11 (1980).
6.30. M. Feng, L. W. Cook *et als.*, *Appl. Phys. Lett.*, 34, 292 (1979).
6.31. N. A. Bert, A. T. Gorelenok *et al.*, *J. Cryst. Growth*, 52, 716 (1981)
6.32. K. Sakai, S. Akiba *et al.*, *J. Appl. Phys.*, 16, 2043 (1977).
6.33. M. Feng, H. H. Tashima *et al.*, *Appl. Phys. Lett*, 34, 91 (1979).
6.34. K. Nakajima, S. Komija *et al.*, *J. Electrochem. Soc.*, 127, 1568 (1980).
6.35. N. A. Bert, V. I. Vdovin *et al.*, *Abstracts of Papers to the 3rd All-Union Conf. on Phys. Processes in Semicond. Heterojunctions*, 3, 120, Odessa, 1982.
6.36. N. A. Bert, A. T. Gorelenok *et al.*, *Zh. Tekhn. Fiz.*, 51, 1018 (1981).
6.37. M. Feng, L. W. Cook *et al.*, *Appl. Phys. Lett.*, 34, 697 (1979).
6.38. N. A. Bert, A. T. Gorelenok *et al.*, *Fiz. Tekhn. Polupr.*, 16, 60 (1982).
6.39. O. Wada, A. Mayerfeld *et al.*, *J. Electrochem. Soc.*, 127, 2278 (1980).
6.40. J. J. Coleman and F. R. Nash, *Electron. Lett.*, 14, 558 (1978).
6.41. Zh. I. Alferov, A. T. Gorelenok *et al.*, *Pis'ma v Zh. Tekhn. Fiz.*, 3, 1169 (1977).
6.42. D. Z. Garbuzov, A. T. Gorelenok *et al.*, *Fiz. Tekhn. Polupr.*, 15, 504 (1981).
6.43. V. V. Agaev, K. A. Gatsoev et al., *Abstracts of Papers to 3rd All-Union Conf. on Phys. Processes in Semicond. Heterostructures*, 2, 55, Odessa, 1982.
6.44. L. W. Cook, M. H. Tashima *et al.*, *J. Crystal Growth*, 56, 475 (1982).
6.45. A. A. Bel'skii, A. T. Gorelenok *et al.*, in: *Semiconductor Heterojunctions and Solar Energy Photoconverters*, Yerevan, 1982, p. 6.
6.46. D. Z. Garbuzov, *J. of Luminescence*, 27, 109 (1982).
6.47. Zh. I. Alferov, V. M. Andreev, D. Z. Garbuzov *et al.*, *Fiz. Tekhn. Polupr.*, 9, 1265 (1975); *Pis'ma v Zh. Tekhn. Fiz.*, 3, 657 (1977).
6.48. A. Sugimura, *IEEE J. Quantum Electron.*, QE-17, 627 (1981).
6.49. Zh. I. Alferov, V. G. Agafonov, D. Z. Garbuzov *et al.*, *Fiz. Tekhn. Polupr.*, 10, 1497 (1976).
6.50. V. P. Evtikheev, D. Z. Garbuzov, and A. T. Gorelenok *Fiz. Tekhn. Polupr.*, 17, 1402 (1983).
6.51. V. V. Agaev, D. Z. Garbuzov, A. T. Gorelenok *et al.*, *Fiz. Tekhn. Polupr.*, 15, 2282 (1981).
6.52. I. N. Arsent'ev, L. S. Vavilova, D. Z. Garbuzov *et al.*, *Fiz. Tekhn. Polupr.*, 16, 1615 (1982).
6.53. T. S. Moss, G. J. Burell, and B. Ellis, *Semiconductor Opto-Electronics*, Butterworths, London, 1973.
6.54. V. V. Agaev, D. Z. Garbuzov *et al.*, *Pis'ma v Zh. Tekhn. Fiz.*, 8, 267 (1982).
6.55. I. N. Arsent'ev, D. Z. Garbuzov, and V. D. Rumyantsev, *Proceedings of the 2nd All-Union Conference on Physical Processes in Heterostructures*, 3, 4, Odessa, 1982.
6.56. N. K. Dutta and R. J. Nelson, *Appl. Phys. Lett.*, 38, 407 (1981).
6.57. H. Temkin, A. K. Chin *et al.*, *Appl. Phys. Lett.*, 39, 405 (1981).
6.58. V. V. Agaev, D. Z. Garbuzov *et al.*, *Fiz. Tekhn. Polupr.*, 17, 1557 (1983).
6.59. D. Z. Garbuzov, Z. S. Sokolova, and V. B. Khalfin, *Fiz. Tekhn. Polupr.*, 16, 1105 (1982); B. L. Gel'mont, Z. S. Sokolova, and V. B. Khalfin, *Fiz. Tekhn. Polupr.*, 17, 453 (1983).
6.60. V. V. Agaev, D. Z. Garbuzov *et al.*, *Fiz. Tekhn. Polupr.*, 17, 538 (1983).

6.61. Zh. I. Alferov, A. T. Gorelenok *et al.*, *Pis'ma v Zh. Tekhn. Fiz.*, **4**, 1329 (1978).
6.62. R. J. Nelson, *Appl. Phys. Lett.*, **35**, 654 (1979).
6.63. M. Hirao, S. Tsuji *et al.*, *Opt. Commun.*, **1**, 10 (1980).
6.64. N. Tamari, M. Ozon *et al.*, *Appl. Phys. Lett.*, **41**, 1075 (1982).
6.65. Zh. I. Alferov, M. G. Vasil'ev, A. T. Gorelenok *et al.*, *Pis'ma v Zh. Tekhn. Fiz.*, **8**, 680 (1982).
6.66. H. Imai, H. Ishikawa, and K. Hori, *Appl. Phys. Lett.*, **4**, 583 (1982).
6.67. M. G. Vasil'ev, A. A. Gvozdev, A. T. Gorelenok *et al.*, *Zh. Tekhn. Fiz.*, **51**, 1413 (1983).
6.68. W. R. Hitchens, N. Holonyak, Jr. *et al.*, *Appl. Phys. Lett.*, **27**, 245 (1975); J. J. Coleman, N. Holonyak, Jr. *et al.*, *Appl. Phys. Lett.*, **29**, 167 (1976).
6.69. A. Fujimoto, H. Jashida *et al.*, *Jap. J. Appl. Phys.*, **21**, L488 (1982).
6.70. V. G. Agafonov, D. Z. Garbuzov, N. A. Tupitskaya *et al.*, *Fiz. Tekhn. Polupr.*, **15**, 1498 (1981).
6.71. Zh. I. Alferov, D. Z. Garbuzov *et al.*, *Pis'ma v Zh. Tekhn. Fiz.*, **8**, 1473 (1982).
6.72. Zh. I. Alferov, A. T. Gorelenok *et al.*, *Pis'ma v Zh. Tekhn. Fiz.*, **8**, 257 (1982).
6.73. D. Z. Garbuzov, V. B. Khalfin, and V. P. Chalyi, *Fiz. Tekh. Polupr.*, **12**, 2114 (1978).
6.74. P. D. Wright, Y. G. Chai, and G. A. Antypas, *IEEE Trans. Electron Devices*, **ED-26**, 1220 (1979).
6.75. O. Wada, S. Yamakoshi *et al.*, *IEEE J. Quantum Electron.*, **QE-18**, 368 (1982).
6.76. T. P. Pearsall, B. I. Miller *et al.*, *Appl. Phys. Lett.*, **28**, 499 (1976).
6.77. D. Z. Garbuzov, K. A. Gatsoev, A. T. Gorelenok *et al.*, *Zh. Tekhn. Fiz.*, **51**, 1408 (1983).
6.78. K. Nishida, K. Taguchi *et al.*, *Appl. Phys. Lett.*, **35**, 251 (1979).
6.79. Zh. I. Alferov, M. G. Vasil'ev, A. T. Gorelenok *et al.*, *Pis'ma v Zh. Tekhn. Fiz.*, **8**, 722 (1982).
6.80. T. Lee, C. A. Burrus *et al.*, *IEEE J. Quantum Electron.*, **QE-17**, 232 (1981).
6.81. D. Akhmedov, V. G. Danil'chenko *et al.*, *Fiz. Tekhn. Polupr.*, **16**, 372 (1982).
6.82. J. C. Campbell, A. G. Dentai *et al.*, *IEEE J. Quantum Electron.*, **QE-17**, 264 (1981).
6.83. O. K. Kim, S. R. Forrest *et al.*, *Appl. Phys. Lett.*, **39**, 402 (1981).
6.84. J. C. Gammel, H. Ohno *et al.*, *IEEE J. Quantum Electron.*, **QE-17**, 269 (1981).

7 Acoustic Instability and Nonlinear Acoustoelectronic Interaction in Semiconductors in an Alternating Electric Field

Yu. V. Gulyaev and G. D. Mansfel'd

7.1. INTRODUCTION

The importance of the present work is connected with a search for new methods of creating active acoustic media capable of amplifying and generating acoustic and electromagnetic oscillations in the microwave region, as well as with the necessity of solving some fundamental physical problems in the investigation of nonlinear acoustoelectronic interactions and evolution of the spectrum of amplified acoustic fluctuations. Three methods of stimulating acoustic activity in a semiconductor are considered. These methods are based on the effect of amplification of acoustic waves and fluctuations in an alternating electric field which causes a supersonic drift velocity of carriers. The first method consists in a multitransit (cyclotron) amplification of waves under conditions of synchronism [7.1]. The frequency of the alternating electric drift field (usually of the order of several hundred kilohertz) is chosen according to the condition that the half-period of the field is equal to the time of propagation of the acoustic waves (AW) through the crystal. Consequently, the waves reflected after one transit arrive again in the amplifying phase of the electric field and this process is repeated many times. The multitransit amplification of noise fluctuations leads to an effective generation of acoustic and electromagnetic oscillations in the microwave region. The high-intensity acoustic fluxes created as a result of multitransit generation open new avenues for experimental investigation of a whole range of nonlinear acoustoelectric phenomena which were either investigated scantily or were not investigated at all. Such nonlinear phenomena can occur in the case of a monochromatic signal [7.2], as well as upon an amplification of fluctuations [7.3]. In this paper, we present the results of studies of multitransit generation itself (see Sec. 7.2), and of the nonlinear effects arising due to such a generation, viz. the influence of trapping of carriers by an acoustic wave (concentration nonlinearity) on the shape of the current-voltage characteristics, and the generation spectrum upon amplification of fluctuations (see Sec. 7.3). In the latter case, the multitransit amplification of fluctuations in a semiconducting crystal helps to increase the length of the path over which they interact, thus providing a unique opportunity of directly verifying the results of the theory according to which the interaction of phonons through

rapidly damping free electron density waves dominates. A separate section (see Sec. 7.4) has been devoted to the results of investigations of concentration nonlinearity under collision-free conditions.

In the second method of stimulating acoustic activity, the semiconducting crystal is cut in the form of a disc whose plane contains piezoactive directions. Ohmic contacts are fused to the lateral surface and at the centre of the disc. When such a disc is placed in a transverse magnetic field (Corbino disc), the acoustic waves or fluctuations may be amplified on account of the projection of azimuthal and radial components of the electron drift velocity onto the piezoactive directions [7.4]. Section 7.5 contains results of theoretical investigations of amplification of acoustic waves in an alternating field created in a sample in the shape of a Corbino disc, and the results of experiments on the generation of acoustic oscillations and the observation of strong superlinearity in current-voltage characteristics, caused by acoustic instability [7.5]. This section also describes the results of experiments on the transformation of acoustic flux spectrum due to a nonlinear interaction of the fluctuations being amplified [7.6].

Finally, the third method of creating acoustic instability (see Sec. 7.6) is connected with the acoustoelectron amplification of a high-frequency alternating electric field whose sign changes every half-period. The amplitudes of the positive and negative half-periods are equal (meander), and the change in sign takes place many times during the propagation of acoustic waves through the crystal. In this case, the amplification of waves is independent of the direction of their propagation, and the crystal behaves as an active medium for amplifying AW [7.7]. The results of investigation of the conditions for exciting instability in such a system are presented. The experimental results complement the results of investigations of nonlinear interaction between fluctuations, obtained in the preceding sections.

Experimental investigation of all the effects described above was carried out on n-InSb samples which are piezoelectric semiconductors. The n-type indium antimonide is a convenient model material for studying the peculiarities of the acoustoelectron interaction. At 77 K (the crystal temperature in experiments) the mean free path l of the electrons exceeds the acoustic wavelength λ in the frequency range of several hundred megahertz, which is an experimentally well-studied region. In this case, the condition $ql > 1$ (where $q = 2\pi/\lambda$) is satisfied, and the interaction is collision-free. In a transverse magnetic field H, the nature of interaction changes: if the condition $qR_c \ll 1$ (R_c is the cyclotron radius of electrons) is satisfied, the results of the theory developed for $ql \ll 1$ become applicable. In all the formulas of the theory, the Maxwell time τ_M is now replaced by $\tau \approx \tau_M (\mu H/c)^2$, where μ is the electron mobility and c the velocity of light.

7.2. MULTITRANSIT AMPLIFICATION AND GENERATION OF ACOUSTIC WAVES IN SEMICONDUCTORS UNDER SYNCHRONISM

7.2.1. The Theory of the Effect

Figure 7.1 shows a semiconducting crystal in an alternating electric field whose frequency F satisfies the synchronism condi-

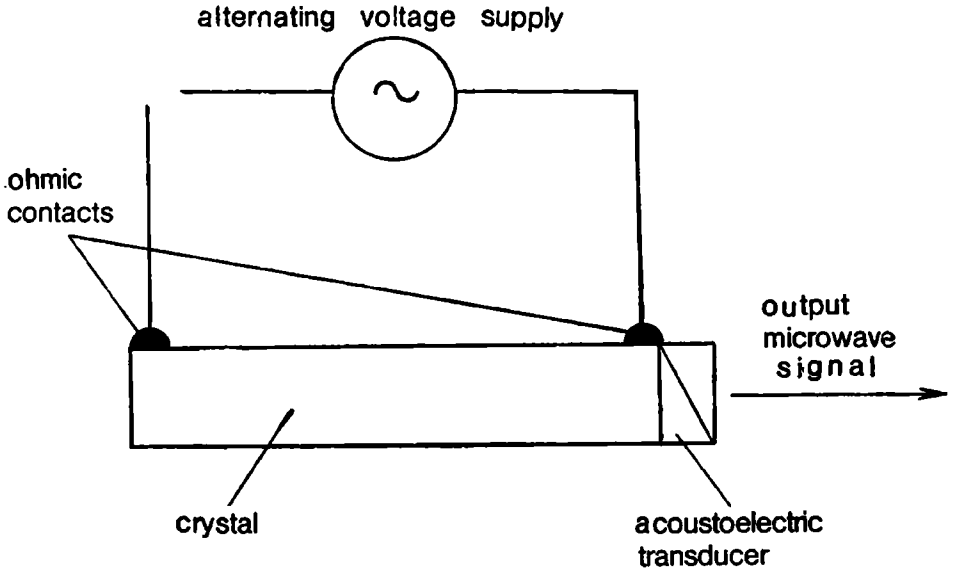

Fig. 7.1. Multitransit generation in semiconductors. An alternating power supply creates the ultrasonic electron drift necessary for amplification. The excited waves are detected by a transducer.

tion $F = F_0 = 1/T = v_{s_0}/2L$. Here L is the length of the crystal, v_{s_0} the velocity of sound averaged over the half-period $T/2$ of the field, and F_0 the synchronism frequency.

In the case of synchronism, the transit time of an acoustic wave along the crystal is exactly equal to the half-period of the electric field. Consequently, an acoustic wave which has been amplified during one path due to ultrasonic drift again encounters an amplifying alternating field after the reflection at the end face of the crystal. The large amplification also leads to a rapid increase in the acoustic noise, and this ultimately leads to the generation of intense acoustic and electromagnetic oscillations in the crystal.

The main peculiarities of the initial stage of the multitransit amplification of acoustic waves in an alternating electric field can

be described by the linear theory of acoustoelectron interaction [7.8, 9]. We introduce the function

$$G(t)=\int_0^t (\alpha_e(E)-\alpha_L)\, v_s\, dt, \tag{7.1}$$

which defines the time variation of the amplitude u (t) of an acoustic wave propagating in a crystal according to the formula

$$u(t)=u_0 e^{G(t)}. \tag{7.2}$$

Here, u_0 is the initial amplitude of the acoustic wave, v_s the velocity of sound, α_e (E) the coefficient of electronic amplification in the linear theory [7.8, 9], and α_L the lattice absorption coefficient. The electric field appearing in the expression for α_e (E) can be expressed in the form

$$E_\sim = E_0 \sin(\Omega t + \varphi)\, \mathrm{sgn} \sin(\Omega_0 t + \theta), \tag{7.3}$$

where E_0 is the amplitude of the alternating electric field, $\Omega = 2\pi F$, and φ the initial phase of the field.

In order to take into account the effect of departure from synchronism, we shall assume that the field frequency F may differ from the synchronism frequency F_0. The factor $\mathrm{sgn} \sin(\Omega t - \theta)$ describes the mutual variation of the directions of propagation of an acoustic wave and the electric field upon reflection from the end faces of the crystal. Here $\Omega_0 = 2\pi F_0$ is the synchronism frequency, and θ the phase whose introduction enables us to investigate the amplification of a wave which at the moment of switching on the field was at the point $x_0 \approx \theta v_s/\Omega_0$, $x \in [0, L]$, L being the length of the crystal.

The following conclusions can be drawn from an analysis of (7.1).

(a) For a fixed value of $E_\sim$, the maximum gain over the shortest duration of time is attained by waves situated near the end face of the crystal ($x = 0$) at the moment of switching on the cocurrent electron drift.

(b) For $F \neq F_0$, each value of $E_\sim$ has a corresponding moment of time t_0 at which G (t) attains the maximum value. At $t > t_0$, the function G (t) is decreasing.

In the same way, we can formulate [7.10] the conditions for the onset of generation in an alternating electric field [7.11]. Suppose that a wave with the amplitude u_0 exists at the front face of the crystal when the field is switched on. After N round transits through the crystal and reflections at its end faces, the wave amplitude be-

comes equal to $u_N = u_0^{G_N + i\varphi_N}$, where

$$G_N = \int_0^{2NL} \alpha_e(E)\, dx - 2NL\alpha_L - N(\delta_1 + \delta_2), \tag{7.4}$$

$$\varphi_N = \int_0^{2NL} q(E)\, dx + N\varphi_{\text{refl}}^{(1)} + N\varphi_{\text{refl}}^{(2)}, \tag{7.5}$$

$$q(E) = \frac{\omega_s}{v_s(E)}, \tag{7.6}$$

$q(E)$ is the wave vector of the acoustic wave, δ_1, δ_2 and $\varphi_{\text{refl}}^{(1)}$, $\varphi_{\text{refl}}^{(2)}$ the coefficients which take into account the change in amplitude and phase upon reflection at the end faces of the crystal, and $\omega_s = 2\pi f_s$ the frequency of sound being amplified.

In the case of exact synchronism, we have

$$G_N = -N\left[2\int_0^L \alpha_e(E)\, dx + 2\alpha_L L + \delta_1 + \delta_2\right] \equiv N\xi, \tag{7.7}$$

$$\varphi_N = N\left[2\int_0^L q(E)\, dx + \varphi_{\text{refl}}^{(1)} + \varphi_{\text{refl}}^{(2)}\right] \equiv N\psi. \tag{7.8}$$

If, as in [7.10], the coefficient K of sound amplification is connected with the summation of wave amplitudes for multiple transits through the expression $K = S/S_0$ (S_0 is the initial intensity of the acoustic wave and S the intensity of the resultant wave at the front face after multiple transits through the crystal), we can write the generation condition for the case when the interference effects enhance the amplification, $\psi = 2\pi N$ ($N = 1, 2, \ldots$) in the following form:

$$K = \left(\sum_{N=0}^{\infty} e^{N\xi}\right)^2. \tag{7.9}$$

Thus, the condition $\xi \geqslant 0$ must be satisfied in the case of generation. The physical meaning of this is quite clear: the amplification for each transit must compensate the losses due to the lattice absorption as well as the losses upon reflection.

Let us try to formulate the conditions for the onset of generation at a detuning $F \neq F_0$ in the simplest case when $\omega_s\tau_M \ll 1$ and $qr_D = 1$ (τ_M is the Maxwell relaxation time and r_D the Debye screening radius). In this case, the electron amplification factor depends linearly on the field, and we can exactly calculate G_N

and φ_N:

$$G_N = 2N\left[\alpha_0 \frac{\gamma v_{s_0} \sin 2\pi Nx}{4\pi N F_0 (1+x) \tan(\pi x/2)} - (\alpha_0 + \alpha_L) L - \delta_1 - \delta_2\right], \quad (7.10)$$

$$\varphi_N = \text{const}(\gamma)\, \omega_s T_0 N \left[1 - \frac{\eta}{4}\left(1 + \frac{\omega_s^2 \tau_M^2}{4}\right) + \frac{\eta}{8} \frac{\gamma \sin 2\pi Nx}{2\pi N (1+x) \tan \pi x/2} \omega_s^2 \tau_M^2 - \frac{\eta}{32} \omega_s^2 \tau_M^2 \gamma^2 \left(1 - \frac{1}{4\pi} \frac{\sin 4\pi Nx}{1+x}\right)\right] + N(\varphi_{\text{ref}}^{(1)} + \varphi_{\text{ref}}^{(2)}). \quad (7.11)$$

Here, $\alpha_0 = \eta q (\omega_s \tau_M/4)$, $x = (F - F_0)/F_0$ is the relative frequency deviation from synchronism, $\gamma = \mu E_0/v_s$, μ the electron mobility, and η the electromagnetic coupling factor. The coefficient K will then have the form

$$K = \left(\sum_{N=0}^{\infty} e^{G_N} \cos \varphi_N\right)^2 + \left(\sum_{N=0}^{\infty} e^{G_N} \sin \varphi_N\right)^2. \quad (7.12)$$

It can be easily shown that this series will be always convergent if the function is given by formula (7.10): for any x and γ we can find N beyond which $G_N < 0$. It can be seen from (7.11) that φ_N is a complicated function of N for $x \neq 0$, and hence we cannot formulate the condition for the enhancement of amplification due to interference effects. Thus, in the case of frequency deviation from synchronism, we cannot write the generation condition in an alternating electric field in the same form as obtained in [7.4]. This conclusion remains valid for any $\omega\tau_M$.

An analysis of formulas (7.9) and (7.12) shows that

(a) The signal being detected must be in the form of a train of amplified noise spikes. If the signal is detected with the help of a transducer on the end face of the crystal, the spike repetition frequency is equal to F. If the signal is detected according to the high-frequency voltage generated in the sample due to the piezoelectric effect and is recorded through ohmic contacts, the noise spike repetition frequency is $2F$.

(b) The signal observed on the screen of an oscilloscope in the case of a detuning ($x \neq 0$) must be a complex superposition of trains of noise pulses amplified over a finite number of transits.

Thus, from an analysis of the generation conditions on the basis of the linear theory, it follows that the generation of acoustic oscillations in the sense of [7.10] is possible only for an exact synchronism $x = 0$. In this case, the semiconducting crystal acts as an acoustic resonator excited on eigen-modes with a large value of the number n. Actually, both for synchronism and deviation from it, the amplitude

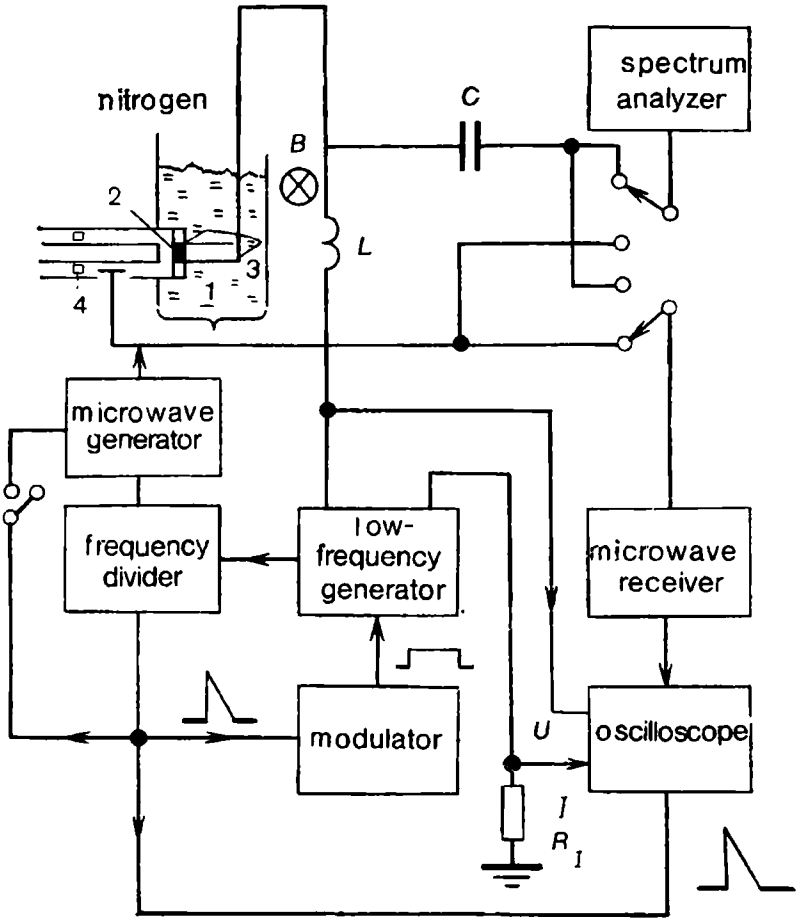

Fig. 7.2. Block diagram of the experimental setup for studying the amplification and generation of acoustic waves. For notation, see text.

and phase of the resultant signal are determined by the nonlinear interaction between acoustic fluctuations in an alternating electric field.

7.2.2. Experiment

The block diagram of the experimental setup for studying the amplification and generation of acoustic waves is shown in Fig. 7.2. The *n*-InSb crystals (1) under investigation were in the form of thin rectangular slabs with plane-parallel end faces and cut along the [110] piezoelectric direction. One of the ends of the sample had an electroacoustic CdS transducer (EAT) (*2*) attached to it. The crystal was soldered to the cover of a coaxial tunable cavity (*4*) in such a way that the transducer was placed in the region of maximum electric field. The alternating electric field was supplied through

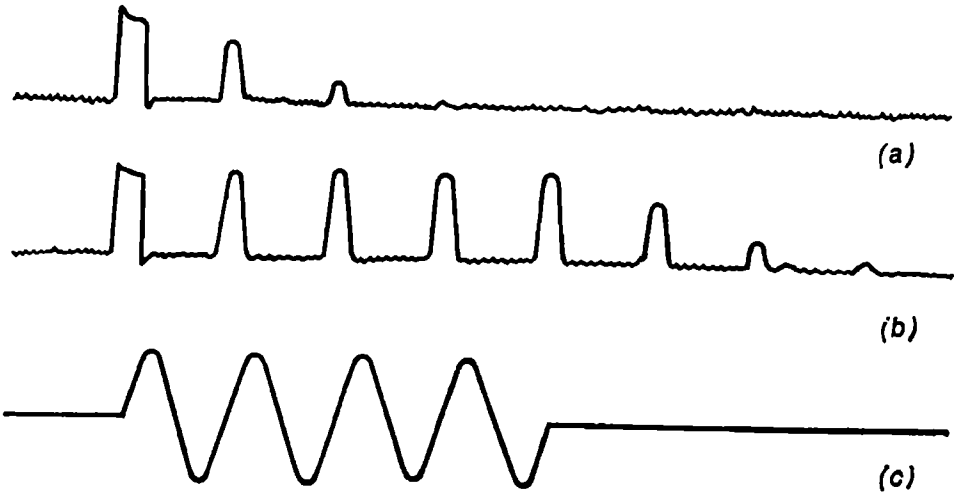

Fig. 7.3. Oscillograms of echo pulses (*a*) without field, (*b*) with field, and (*c*) drift voltage oscillogram.

fused contacts (*3*) made from In and Te. The alternating electric field for creating the ultrasonic drift of electrons was supplied by a generator of voltage in the sinusoidal form or segments of sinusoids, and by unmodulated sinusoidal reference signal supplied to the frequency divider. The modulator and the oscilloscope were synchronized with the help of pulses generated by the frequency divider. Such a method of synchronization enabled the observation of the beginning of multitransit amplification of acoustic waves on the screen of two-beam oscilloscope when an alternating electric field is switched on. When the modulator was switched off, the circuit worked in a continuous regime. An electromagnetic signal corresponding to acoustic vibrations being amplified or generated in the crystal from the cavity or directly from the ohmic contact is fed either at the input of the microwave receiver connected to the oscilloscope or at the spectral analyzer. The microwave generator was used for exciting the monochromatic AW pulses during an investigation of their multitransit amplification.

Figure 7.3 shows the oscillograms of echo pulses corresponding to multiple transits. These pulses are excited from outside with the help of an electroacoustic transducer of acoustic waves of frequency 520 MHz over a crystal of length ~ 1 cm. The oscillograms 7.3*a* and 7.3*b* respectively correspond to the pulses without and with an alternating field (Fig. 7.3*c*) with a frequency $F \simeq 106$ kHz (synchronism frequency). The rise in the amplitude of echo signals and an increase in their number due to multitransit amplification can be clearly seen here. The dependence of the increase in the signal level per transit on the amplitude of the alternating electric field for

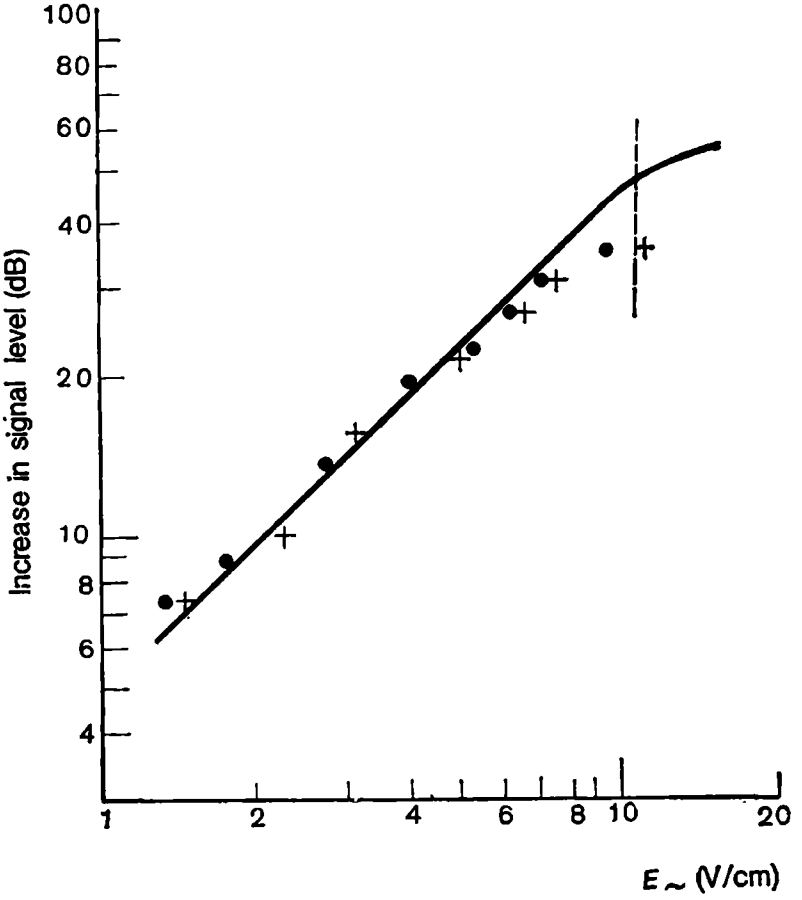

Fig. 7.4. Increase in the signal intensity as a function of the alternating field amplitude.

a sample with electron concentration $n = 6.9 \times 10^{13}$ cm^{-3} is shown in Fig. 7.4. The solid curve is obtained theoretically, while the points correspond to experimental results [7.12]. The increase in the signal level at fields $E_{th} \simeq 11$ V/cm is accompanied by a multitransit generation of waves which takes place at the frequency of maximum electronic gain. This generation continues even when the external supply exciting the acoustic waves is switched off. An example of the oscillogram of the signal being generated is shown in Fig. 7.5. According to the theory, the generated signal is a pulse train with a repetition frequency $F \simeq F_0$.

For fields that are weaker than E_{th}, the multitransit amplification of acoustic waves helps in a considerable compensation of the non-electronic losses in the AW energy and obtain a multitransit delay regime for an acoustic signal introduced from outside. In some experiments, a delay of 0.5 msec is obtained at frequencies up to 1.2 GHz.

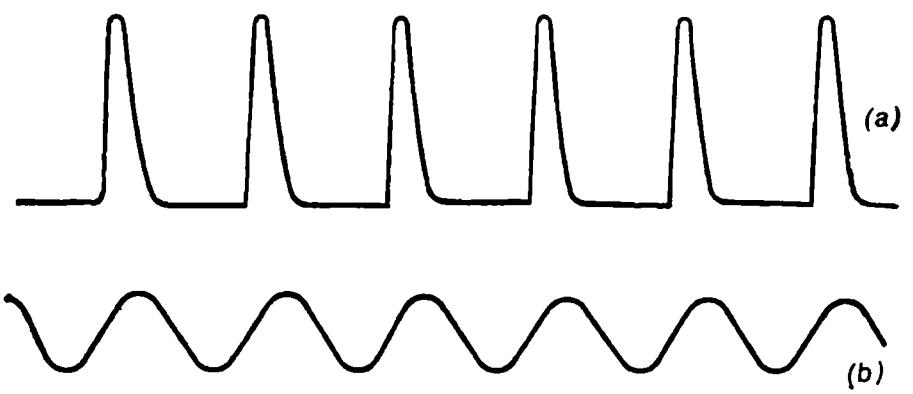

Fig. 7.5. Oscillograms of (*a*) generated signal and (*b*) sample voltage.

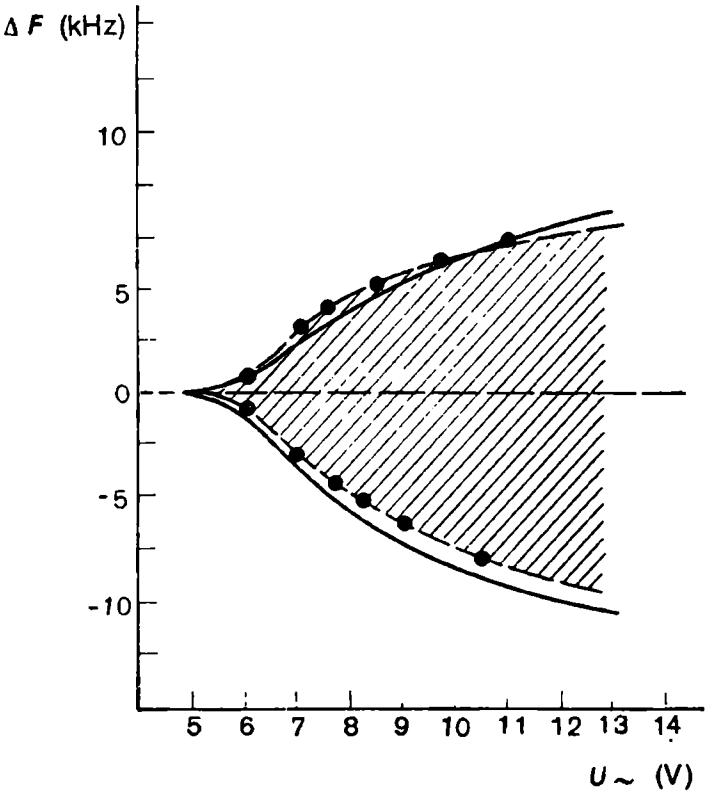

Fig. 7.6. Generation region (ΔF, U), $F_0 = 121.01$ kHz. The solid curve represents the theoretical generation threshold. The shaded area shows the region in which the generation is observed experimentally.

Under steady-state conditions, the frequency of the generated signal depended on the electron concentration and was always somewhat lower than the maximum amplification frequency obtained by the formula $f_m \quad v_s 2\pi r_D$ of the linear theory [7.8]. This fact is quite understandable if we consider that the lattice absorption in a crystal is a function of frequency [7.13]. It was established that generation also takes place when the field frequency is slightly different from the synchronism frequency. However, in this case it was necessary to increase the amplitude of the alternating field in order to attain generation.

Figure 7.6 presents the experimentally obtained ΔF vs. $U_{\sim}$ diagram for one of the samples, showing the boundaries of the region inside which the amplified noises are detected. It can be seen that for strong electric fields the amplified noises are detected over a fairly wide range of frequency F. This region becomes narrower when the electric field is decreased. The same diagram also shows the theoretical boundary of the region of noise generation. The theoretical curve was obtained as an envelope to the family of curves $G_N(x, U) = A$ (where $A = 55$ dB is the amplification for which the acoustic noises start exceeding the noise level of the receiver) for different values of N from 3 to infinity. The following values were used while calculating these curves: $f = 1300$ MHz, $H = 2$ kOe, $\alpha_L = 13$ dB/cm, and $\alpha_0 = 8$ dB/cm. It can be seen from the figure that the theoretical value of the threshold field under synchronism conditions and the boundary of the region of noise generation are in excellent agreement with the experimental values. By measuring the synchronism frequency at the instant of the onset of generation at $E = E_{th}$, we can determine the velocity of acoustic waves from the formula $v_s = 2LF$ with an accuracy up to 10^{-4}.

7.3. CURRENT-VOLTAGE CHARACTERISTICS OF SAMPLES AND THE GENERATION SPECTRUM

In the case of a multitransit generation in an alternating electric field, the acoustic waves attain a high intensity and strongly influence the current-voltage characteristic (CVC) of the sample. This is due to the appearance of an acoustoelectric current which is associated with the waves being amplified and is directed against the ohmic current under the conditions of amplification.

Figures 7.7 *a* and *b* show respectively the oscillograms of the current through the sample and the voltage at the sample. The increase in the amplitude of the sample voltage and the decrease in the current, as well as the distortion of the shape of the voltage and current pulses, coincide in time with the appearance of generated signal detected by the receiver. This means that the slope of CVC of the sample considerably changes when generation sets in. Moreover, it

was found that in the case of a multitransit generation of acoustic waves, the CVC of a semiconductor considerably depends on the number N of the transit of the ultrasonic wave through the crystal, and may be S-shaped or N-shaped depending on the experimental conditions.

Figure 7.8 shows the set of CVC obtained for a sample at a constant current for different numbers of wave transits. A special feature of

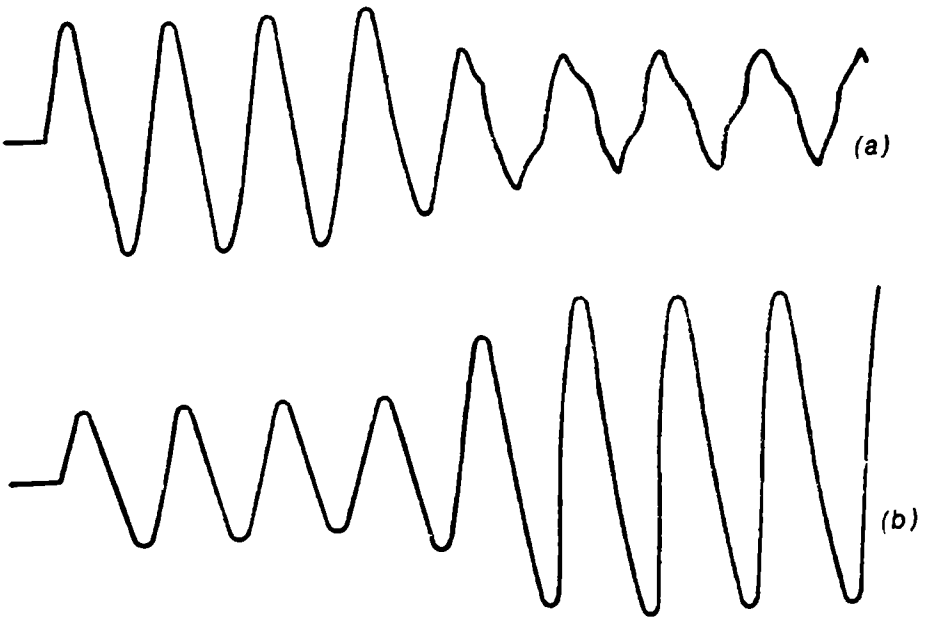

Fig. 7.7. Oscillogram of (*a*) the sample current and (*b*) the sample voltage.

these characteristics is the existence of S-shaped regions which expand with increasing intensity of the amplified noise.

Saturation of CVC and its deviation from linearity are due to the fact that when the electric field attains its threshold value at which the electronic gain exceeds the lattice attenuation, the acoustic noises rapidly increase and the acoustoelectric current associated with them is subtracted from the ohmic current, thus reducing the current passing through the sample. For a large number of transits (in our case, for $2N > 20$), the shape of the CVC no longer depends on N.

The existence of a region with a negative differential conductivity was predicted in the nonlinear theory of acoustic waves amplification [7.2], and is connected with a decrease in the electronic gain for large drift currents.

The change in the CVC slope during generation of acoustic waves was used for estimating the intensity of the generated acoustic flux.

It was shown in [7.14] that for the nonlinear amplification of a wide acoustic noise flux containing waves with different q's, the Weinreich relation connecting the acoustoelectric field with the intensities of these waves is valid:

$$E_{\text{a.e.}} = \sum_q \frac{\alpha_q W_q}{env_s}. \tag{7.13}$$

In our order-of-magnitude estimates, it was assumed that $\alpha_q \to \alpha_L(q)$ in the steady state, $\alpha_L(q)$ being the lattice attenuation at the frequency $\omega_s = qv_s$.

Using the value of the acoustoelectric voltage obtained from the CVC and measuring the field distribution in the samples with the

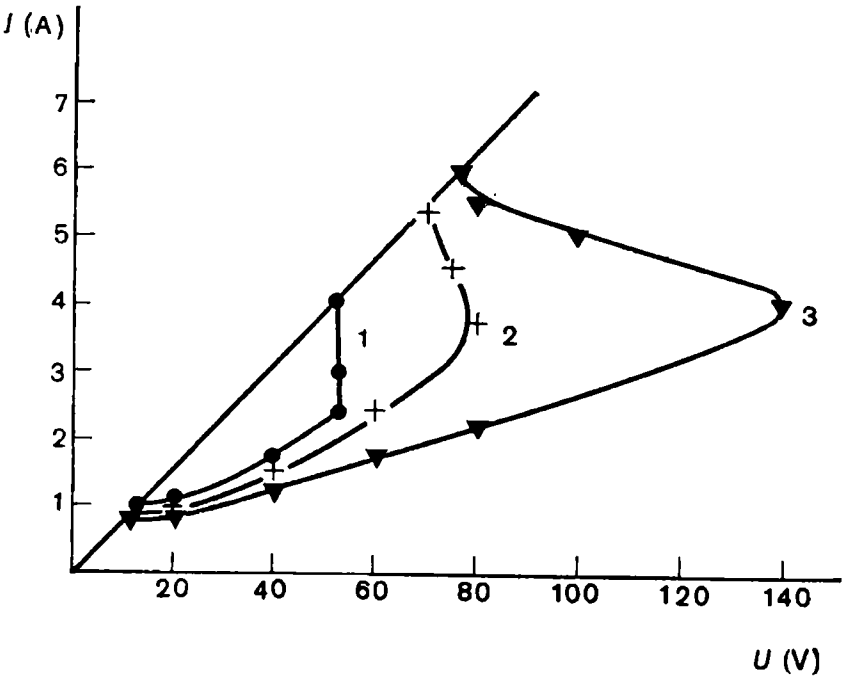

Fig. 7.8. CVC of a sample for a given current and for different double transits $2N$: (1) $N = 5$, (2) $N = 8$, (3) $N = 11$.

help of probes, we were able to estimate the intensity of acoustic waves from their spectral distribution. This value was found to be $W \simeq 250$ W/cm^2 at $I = 3.5$ A for curve 3 in Fig. 7.8.

Figure 7.9 shows the CVC of a sample for a specified voltage applied to it. A peculiar feature of this characteristic is the existence of a region with a decreasing slope. The possibility of an N-shaped CVC for a semiconductor in the case of acoustic instability was discussed in [7.15]. It is associated with a significant lattice absorption which shifts the amplification threshold toward stronger drift fields.

Physically, this phenomenon can be explained as follows. Upon the attainment of a threshold value v_d of the electron drift velocity required for amplification and considerably exceeding v_s, the acoustic noises start getting amplified. This leads to the appearance of potential wells in acoustic waves, which move at a velocity v_s and trap

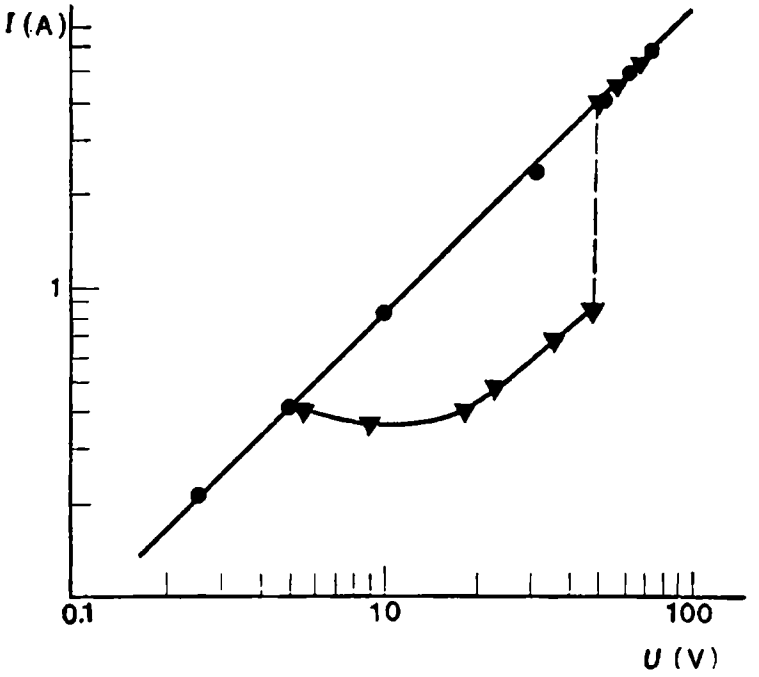

Fig. 7.9. CVC for a sample under a specified voltage.

a significant part of electrons, making them travel at this velocity. As a result, the sample current decreases. The experimentally obtained values are in good qualitative agreement with the results presented in [7.15] and are of the same order of magnitude.

The most important question connected with the generation of acoustic waves concerns the evolution of spectral distribution of oscillations during a nonlinear amplification of fluctuations [7.3].

Figure 7.10*a* shows the oscillogram of an alternating drift current through the sample, while Fig. 7.10*b* represents the signal from a microwave detector tuned to the frequency of acoustic fluctuations being amplified in a crystal of length 0.6 cm and with $n \simeq 3 \times 10^{13}$ cm^{-3} at $H = 3$ kOe. It can be seen that the sample current attains a stationary value in about 50 μsec after the application of the electric field, i.e. after about 20 transits of acoustic waves along the crystal. Attainment of a stationary value of the current, and hence of the CVC, means that a stationary integral intensity of the acoustic fluctuations has been reached during this time. Unlike the CVC, the spectrum of generated oscillations stabilizes over a

much longer time. It can be seen from Fig. 7.10*b* that a strong microwave signal is recorded in a time $t_2 \simeq 500$ μsec after the field has been switched on. The intensity distribution of the acoustic waves over the spectrum was experimentally measured as a function of the time of their transit across the crystal. It was found that a wide spectrum of acoustic waves is generated at the beginning. After the passage of a certain time t_1, when the CVC has already stabilized,

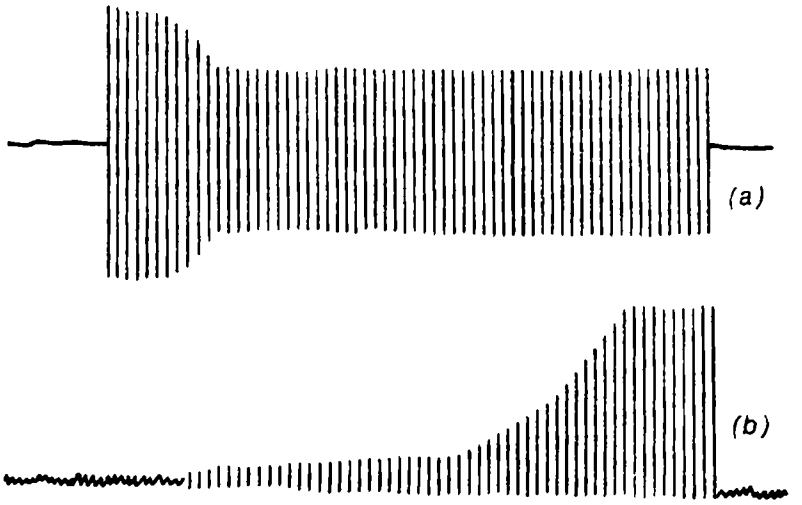

Fig. 7.10. Oscillograms of (*a*) alternating drift current and (*b*) signal from a microwave detector.

the spectral width of the generated signal is a few hundred megahertz It can be seen from Fig. 7.11 that the spectral width then decreases as the acoustic waves accomplish multiple transits across the crystal and are amplified. The integral intensity of the acoustic waves, determined from the CVC, remains the same for all the curves in Fig. 7.11. After a time t_2, only a relatively narrow component remains in the spectrum. Its width and frequency do not change even when the alternating drift-field oscillator starts operating in a continuous mode.

The frequency of the generated oscillations depends on the electron concentration in the crystal and the magnitude of the drift field. In order of magnitude, it is close to the values obtained from the linear amplification theory taking into account the real frequency dependence of lattice absorption. For crystals investigated in this work, this value was found to be 0.6-2.5 GHz.

An increase in the resolving power of the spectrum analyzer shows that the stabilized signal has a complex structure and contains a large number of bright spectral lines which are separated by the alternating drift-field frequency $F \simeq v_s/2L$ (see Fig. 7.12).

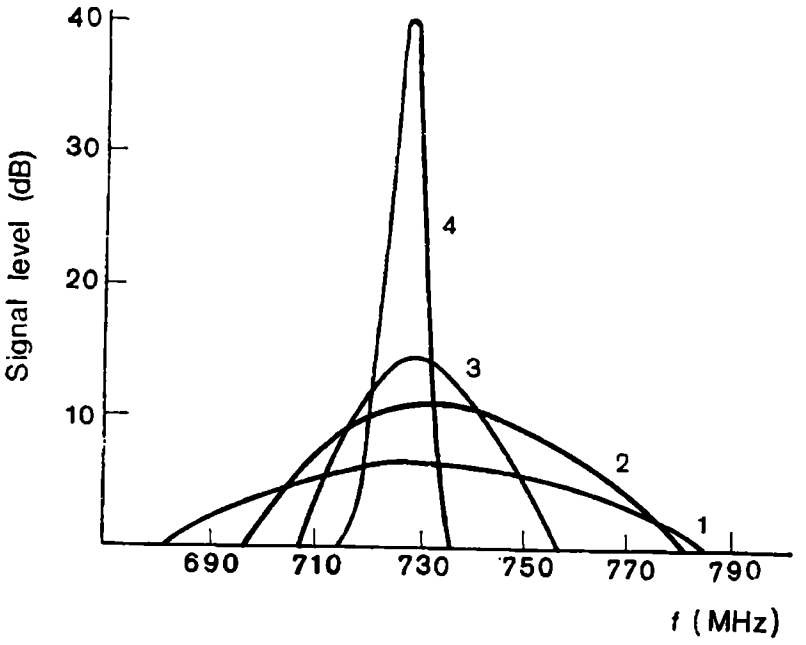

Fig. 7.11. Spectral distribution of amplified fluctuations at different instants after switching on the field: (1) $t_1 = 100$ μsec; (2) $t_2 = 200$ μsec; (3) $t_3 = 400$ μsec; (4) $t_4 = 800$ μsec.

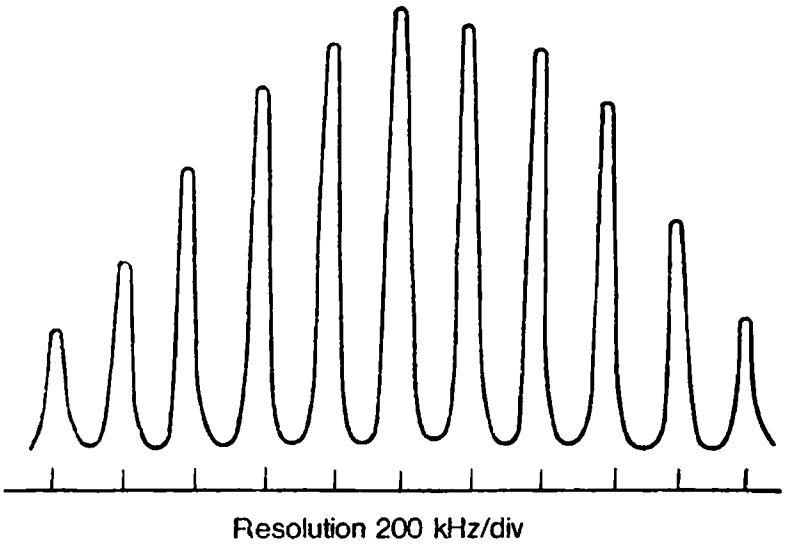

Fig. 7.12. Fine structure of the generation spectrum in one of the samples. The central frequency corresponds to 1580 MHz. The separation between spectral components is equal to the frequency of the alternating drift field generator.

The observed signal spectrum can be fully explained if we consider the Fourrier expansion of a train of radio pulses. It is interesting to note that the width of an individual spectral component is found to be $\sim 10^3$ Hz, and hence the relative width of the generated signal in the steady state is $\sim 10^{-6}$. A very narrow (almost monochromatic) phonon beam is filtered from a wide beam (of several hundred megahertz). The integral intensity of the acoustic waves remains unchanged in this case. In some experiments, harmonics and subharmonics of the fundamental frequency were found after narrowing down the spectrum.

These results justify the application of the conclusion of the nonlinear theory of amplification of acoustic waves [7.2] for a quantitative and qualitative explanation of the above-mentioned S-shaped CVC in the steady-state conditions. Such a strong monochromatization of generated waves also explains the appearance of harmonics and subharmonics in the spectrum [7.2, 14, 16].

The experimental observation of the narrowing of spectrum at the initial stage of its formation may serve as a proof for the existence of the nonlinear interaction of fluctuations through rapidly damping electron density waves (the so-called non-Peierls interaction), proposed in [7.3], where it was expected that this mechanism must dominate over the mechanism of direct interaction between phonons.

According to [7.3], the nature of spectral transformation during a nonlinear interaction between the amplified fluctuations must depend on the sign of the non-Peierls interaction operator $P(q, q')$ appearing in the equation describing their kinetics. In particular, for $P(q, q') < 0$, a narrowing of spectrum can be expected at a constant integral intensity. Under the conditions of our experiments, the operator $P(q, q')$ is negative, and a narrowing of fluctuation spectrum is actually observed upon their amplification at a constant integral intensity.

At present, there is no theory for describing all the stages of the monochromatization process, and it is not possible to explain the width of the spectral lines obtained in our experiments in detail.

7.4. INTERACTION OF HIGH-INTENSITY SHORT-WAVE SOUND WITH ELECTRONS

A peculiar feature of the multitransit generation of acoustic waves in semiconductors under conditions of synchronism is that generation can take place even for a linear field dependence of the amplification factor if the condition $ql > 1$ is satisfied. Such a generation was experimentally realized and investigated by us [7.11, 17]. Quite intense fluxes (up to ~ 120 W/cm^2) were experimentally obtained in a relatively narrow spectral region. This allowed, for

the first time, an investigation of the concentration mechanism of nonlinear amplification under collision-free conditions.

Figure 7.13 illustrates the procedure for measuring the dependence of acoustoelectric amplification on the intensity of acoustic waves. Acoustic waves are generated in the crystal by an alternating electric field whose frequency is equal to the synchronism frequency. The alternating electric field is switched off at a certain instant t_1 (Figure 7.13*a*), when the acoustic flux in the crystal attains an intensity W_1. At subsequent instants of time, the acoustic waves perform transits through the crystal without any field and are attenuated

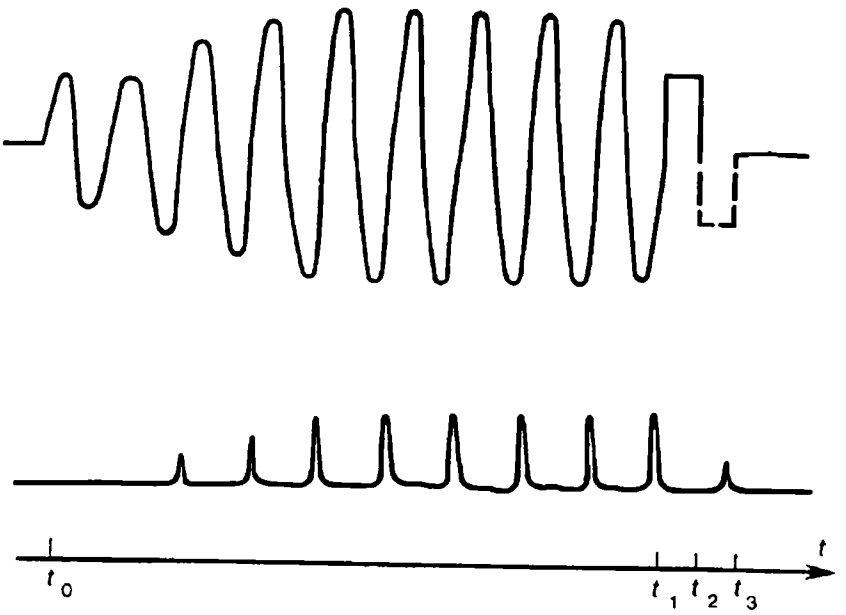

Fig. 7.13. Oscillograms of (*a*) alternating drift voltage and (*b*) the microwave signal generated in the crystal for $ql > 1$.

with the lattice attenuation coefficient α_L. The corresponding echo pulses are shown in Fig. 7.13*b*. After each transit through the sample in the absence of an electric field, the intensity of the acoustic waves changes by a factor of exp $(-\alpha_L L)$. If a rectangular electric field pulse is applied to the sample at the instant t_1, such that the direction of the carrier drift coincides with the direction of propagation of acoustic waves, the latter are amplified. For a fixed amplitude of the alternating electric current (a fixed acoustic intensity W_1 at the front face of the crystal), we can measure the dependence of the acoustic signal level on the magnitude of the applied pulse-drift current. By applying current pulses of proper polarity at t_2, t_3, . . ., we can measure the dependence of the signal level on the drift current for different intensities at the crystal front face, differing from W_1 by a factor exp $(-\alpha_L L)$, exp $(-2\alpha_L L)$, . . . respectively. The

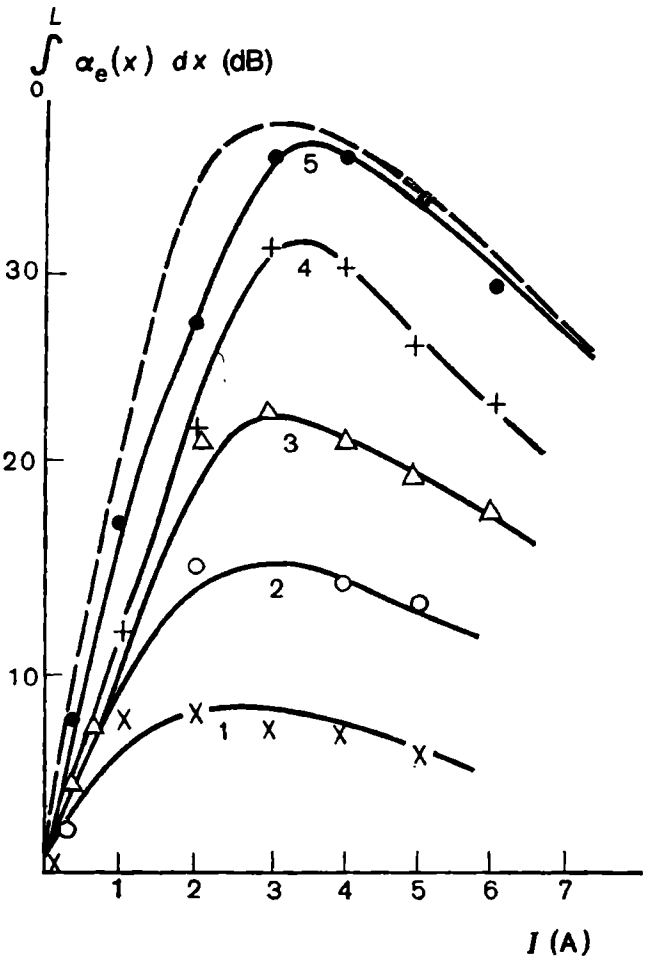

Fig. 7.14. Dependence of the acoustic wave amplification on drift for different values of the AW input intensity W (W/cm²) (*1*) ≃ 45; (*2*) ≃4.5; (*3*) ≃0.45; (*4*) ≃4.5×10^{-2}; (*5*) ≃4.5×10^{-3}.

intermediate power values can be obtained by changing either the number of half-period of the electric field, or its amplitude.

The intensities of acoustic waves were estimated with the help of the acoustoelectric effect. In our experiments, the acoustoelectric effect was measured at a frequency $f_s \sim 1060$ MHz. The wave intensity was known and attained the values up to 45 W/cm².

Figure 7.14 shows the experimental dependences of the acoustic signal amplification on the drift current for different intensities of acoustic waves at the crystal front face. It can be seen that with increasing initial intensity, α_e decreases for any value of the drift current, its amplitude tending to the lattice absorption coefficient α_L at the maximum power value W_1. The value of the parameter $e\varphi/kT$ in this case is equal to ~3.

It is interesting to observe the behaviour of α_e (I) for large drift fields. It can be seen that for all curves, α_e passes through a maximum at a certain value of the drift current and then decreases. For curve 5, the maximum is attained at $v_d = I/env_s = 250v_s$. The existence of such a maximum in α_e is described quite well by the linear theory which is applicable for large values of v_d/v_s. The corresponding formula has the form

$$\alpha_e = \frac{1}{2}\eta q \frac{\sqrt{\frac{\pi}{2}\frac{m^*v_s^2}{kT}}\, q^2 r_D^2 \left(1-\frac{v_d}{v_s}\right)}{(1+q^2r_D^2)^2 + \left[\sqrt{\frac{\pi}{2}\frac{m^*v_s^2}{kT}}\left(1-\frac{v_d}{v_s}\right)\right]^2} \ (\text{cm}^{-1}), \qquad (7.14)$$

where m^* is the electron effective mass.

The dashed curve in Fig. 7.14 shows the theoretical values obtained for our parameters of the semiconductor. It is interesting to compare this curve with the experimental curve 5 which was obtained for a low acoustic intensity at the back face of the crystal. For relatively small drift currents, the experimental curve is considerably lower than the theoretical curve. Apparently, this is due to the emergence of "pulse" nonlinearity which decreases the electronic gain [7.18, 19]. After this, the relative contribution from this nonlinearity mechanism decreases with increasing drift current due to an increase in the drift velocity [7.20, 21], while the intensity of the acoustic waves continues to rise. Upon a further increase in the electron drift velocity, the amplitude of the electron bunches accompanying the waves falls both in the linear and nonlinear amplification regimes, and the amplification decreases.

It should be noted that the theoretical curve has been plotted for a temperature equal to the lattice temperature. Numerical estimates based on a comparison of experimental and theoretical results show that the maximum heating of electrons at the highest fields of ~200 V/cm under our experimental conditions is at least three to four times less than what would be expected from the results of [7.21], and the temperature of electrons does not exceed 100 K. (Moreover, the theoretical curve plotted by taking into account a significant heating in accordance with [7.21] must be much higher and without a maximum. The heating must enhance the amplification.) Apparently, the high-frequency piezoelectric field of an acoustic wave, which is of the same order as the constant field for high intensities, also heats the electron gas to a small extent only and does not influence the electronic gain.

Figure 7.15 shows the electronic gain as a function of the intensity of acoustic waves at the crystal front face for different values of the drift field. It can be seen that the electronic gain sharply drops with increasing W (the regions with $e\varphi/kT < 1$ and $e\varphi/kT > 1$ are separat-

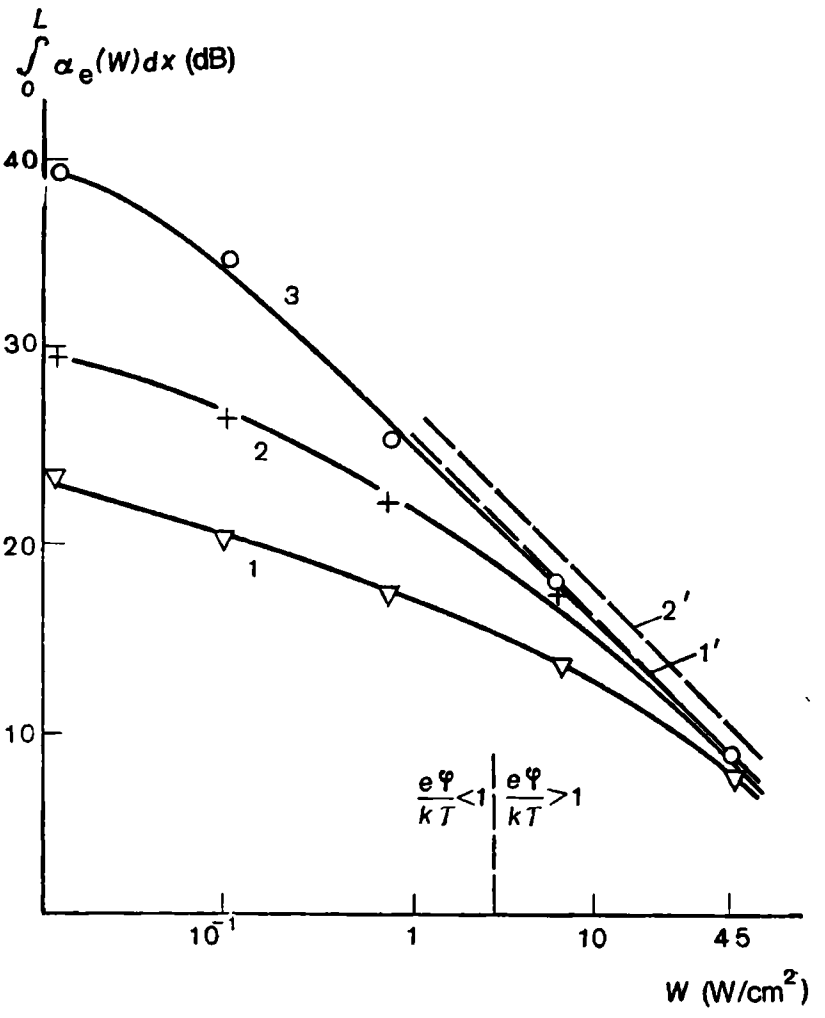

Fig. 7.15. Dependence of the electronic gain on acoustic wave intensity for different values of the current I (A) through the sample. Solid lines represent the experimental results for (*1*) 1.5; (*2*) 2; (*3*) 3 A. Dashed curves correspond to the theoretical values for (*1'*) 1.5 and (*2'*) 2 A.

ed by dashed lines in the figure). It should be remarked that instead of the local value of the electronic gain, the value of $\int_0^L \alpha_e(x)\,dx$ was actually measured in experiment. According to the theory [7.22], the local value of $\alpha_e(W) \sim 1/W$. In order to compare the theoretical and experimental values, the quantity $\int_0^L \alpha_e(x)\,dx$

was calculated by using α_e from [7.22] and the continuity equation for the acoustic flux.

The theoretical dependences obtained in this way are shown in Fig. 7.15 for drift currents $I = 1.5$ A and 2 A, when the heating of electrons is still small and the carrier drift velocity is much lower than their thermal velocity—a condition which must be satisfied in order to use the results of [7.21]. It can be seen that although there is no exact quantitative agreement between theory and experiment, the general trend of the experimental dependences is in accord with the theory. This disagreement is probably due to an error in the experimental determination of the acoustic wave intensity for a large drift velocity at $I = 3$ A (when the approximations of the theory are just valid), the general nature of the experimental dependence is still in good agreement with the theory.

7.5. AMPLIFICATION AND GENERATION OF ACOUSTIC WAVES IN A CORBINO DISC

A Corbino disc is one of the possible models for an "infinite" semiconducting medium in which amplification and generation

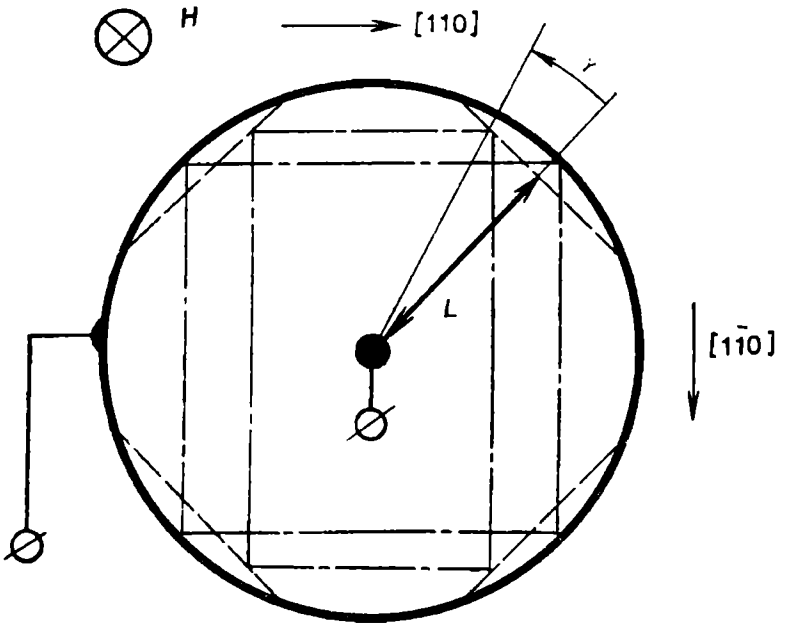

Fig. 7.16. Sample geometry for calculating amplification in a Corbino disc.

of acoustic waves can take place [7.4]. Such a setup is shown in Fig. 7.16. The semiconducting sample in the form of a disc of thickness h is cut in such a way that the piezoactive directions are in the

plane of the disc. Such a situation may arise, for example, when $A^{III}B^{V}$ crystals are used. The dot-and-dash line in the figure shows the path of the propagation of shear acoustic waves along the piezoactive directions [110] and [1$\bar{1}$0] for this type of crystals. The ohmic contacts are located at the centre of the sample and on its lateral surface. When an electric current I and a magnetic field H are switched on, the drifting electrons will have radial and azimuthal components of velocity (and hence the projection of velocities) onto the piezoactive directions. The principle on which a ring oscillator works can be formulated as follows. Upon reflection at the lateral surface of a disc, piezoactive acoustic waves propagate along the perimeter of a square and interact with the drifting electrons. The above discussion is valid for an infinitely narrow acoustic beam. In actual practice, an acoustic beam has a finite width, and hence the real reflecting surface should be in the form of planes shown in Fig. 7.16 by dashed lines. In a ring oscillator, the amplified acoustic waves will in general propagate along the perimeter of a rectangle whose position can be specified by introducing the angle γ shown in the figure. Hence, one of the problems which we are dealing with in this paper is to determine the gain factor and the phase shift of an acoustic wave as a function of the angle γ.

Since the current lines do not coincide with the direction of the wave vector $\mathbf{q}$ of an acoustic wave, the drift velocity of electrons along $\mathbf{q}$ will change from point to point. Consequently, the amplification factor of the acoustic wave (determined with the help of the formula given in [7.8]) and its velocity (and hence the phase advance), which depend on the electron drift velocity, will be complicated functions of the coordinates. The formula for the total electronic gain G upon the passage of a wave along the perimeter of a rectangle has a very cumbersome form [7.4], and we shall only present the results of its analysis. It is found that the magnitude of the drift velocity in the radial direction necessary for amplification is less than the value for the ordinary amplification by a factor of about $\mu H/c$. The shape of the dependence of the total gain on the drift velocity is reminiscent of the curve in the linear theory. However, apart from the changes introduced in it due to the presence of a magnetic field (a displacement of zero and maximum amplification toward lower drift velocities v_d), the gain curve is also not symmetric with respect to the point $v_d = v_s$.

Numerical analysis shows that the gain factor strongly depends on the angle γ, and it is almost impossible to obtain a constant gain in a wide beam (the angles γ for which $\partial G/\partial\gamma \simeq 0$ are restricted to a few degrees).

In order to find the generation conditions, it is also necessary to know the phase shift introduced in an acoustic wave due to one transit through the crystal.

Numerical calculations for the difference in the phase shift $\Delta\varphi = \varphi(\gamma) - \varphi(0)$ as a function of the angle γ for different drift velocities has shown [7.4] that the phase advance strongly depends on the drift velocity and becomes equal to several radians at $\gamma \simeq 10°$. Nevertheless, we can choose the drift velocity in such a way that $\Delta\varphi$ is small for $|\gamma| \leqslant \gamma_{max}$. Thus, for $v_d^{\perp} \simeq 0.82 v_s$ and $\gamma_{max} = 6°$, $\Delta\varphi = 0$. Hence, it is possible to obtain a fairly wide beam of acoustic waves which are amplified in the same phase.

It should be recalled that we have used in our calculations the expression for the current density in a Corbino disc, while the crystal shown in the figure has plane parts of lateral faces. Estimates show that if these faces are bounded by angles $\gamma \simeq \pm 11°$, the error in the value of the drift current will not exceed 1%.

In analogy with [7.10], we can formulate the conditions for the excitation of a cyclic acoustoelectronic generator. For the onset of generation, it is essential that (a) the electronic gain should compensate the lattice energy losses in acoustic waves, losses due to reflection, and losses due to the divergence of the acoustic beam:

$$G \geqslant 4\sqrt{2}\alpha_L L - \sum_m \ln \delta_m + \Delta \tag{7.15}$$

(here, α_L is the lattice absorption coefficient, δ_m the coefficient of reflection of acoustic waves at the m-th face, and Δ the coefficient which takes into account the energy losses due to the beam divergence) and (b) the waves which complete a full transit through the crystal should be added in phase:

$$\Delta\varphi + \sum_m \varphi_m = 2\pi n, \tag{7.16}$$

where φ_m is the phase shift due to reflection at the m-th face and n the integer.

For $v_d^{\perp} = 0.082 v_s$ and $f = 1400$ MHz, the generation condition (7.15) is easily satisfied for an InSb sample in the example considered above. According to (7.16), the sample is an acoustic resonator excited at a mode with a large n. The width of the generated beam in this case is ~ 0.8 mm.

Thus, calculations carried out on the basis of the linear theory show that acoustic waves can be actually generated in a Corbino disc of this type, albeit only in the form of a narrow beam for radial electron drift velocities $v_d^{\perp}$ much lower than the velocity of sound.

In actual experiments on generation, the conditions (7.15) and (7.16) practically cannot be satisfied due to a nonideal geometry of the sample, and above all, due to a considerable rearrangement of the field in the sample as a result of the acoustoelectric effect. It can be expected that the acoustic fluctuations will in fact be amplified in the sample in an electric field that varies from point to point. In this case, the crystal will not act as a resonator.

The peculiarities of acoustic noise amplification were experimentally investigated in a disc of diameter $D = 8$ mm, cut from n-InSb having a mobility $\mu = 5.6 \times 10^5$ cm^2/(V·sec) and a concentration $n = 1.1 \times 10^{14}$ cm^{-3}. A magnetic field $H = 1$ to 3 kOe helped in attaining values between 5 and 15 for the parameter $\mu H/c$. Plane reflecting surfaces forming an angle of 45° with the acoustoactive directions were created on the lateral surface of the disc by optical polishing. In order to register the electromagnetic signal produced

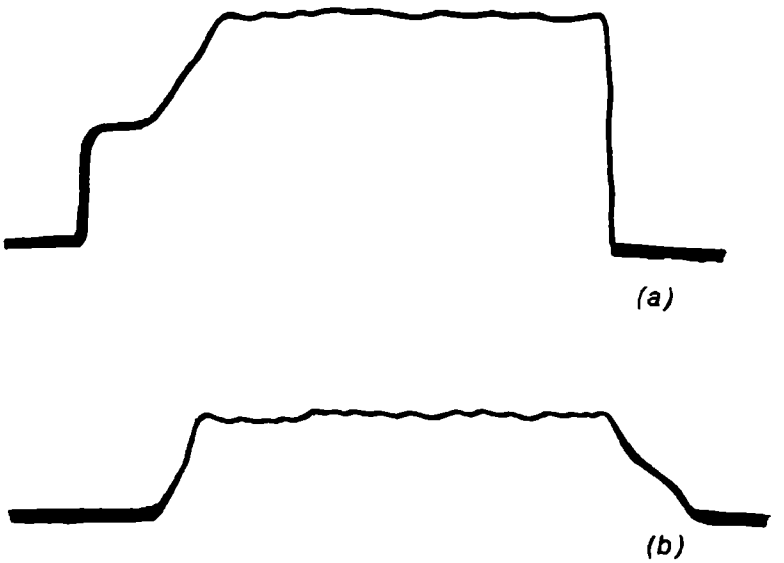

Fig. 7.17. Oscillograms of (*a*) current pulse through a sample cut in the form of a disc and (*b*) noise detected by a wide-band microwave receiver.

by the piezoelectric effect during generation of acoustic noise, a capacitance probe *4* was placed on the plane of one of the reflecting faces and connected to a microwave receiver.

Figure 7.17*a* shows the waveform of the current pulse through the sample, while Fig. 7.17*b* is the oscillogram of the noise registered by a wide-band microwave receiver. It can be seen that a positive step appeares on the current pulse, and the noise becomes significant. The instant when a strong acoustic noise starts being registered coincides with the appearance of the step on the current pulse. It should be noted that after the sample current is switched off, a noise of decreasing amplitude is still registered for some time. Figure 7.18 shows the CVC of the sample, plotted for the initial part of the pulse (*1*) and for the steady-state at the end of the pulse (*2*). It can be seen that curve *2* is superlinear. The observed effects are due to acoustoelectric interaction. This is supported by the following facts.

1. The superlinearity of the CVC. This can be explained by the Hall current due to the acoustoelectric component of the current directed against the flux of the wave being amplified.

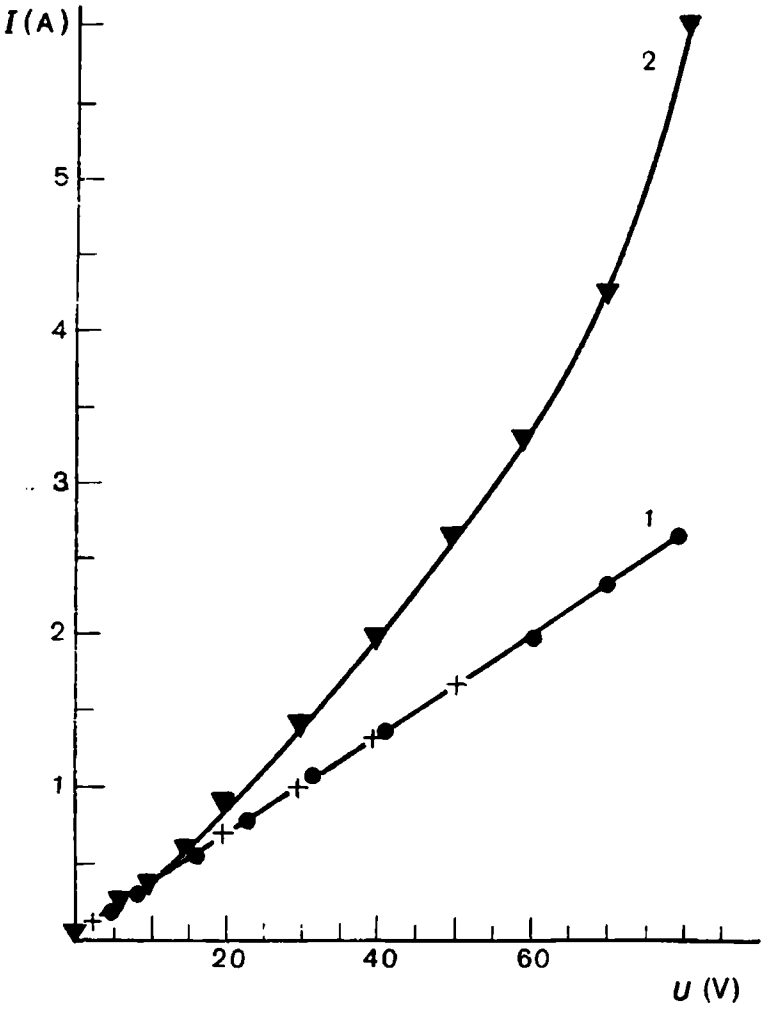

Fig. 7.18. CVC of a Corbino disc: (*1*) at the instant of switching on the current and (*2*) in the steady state.

2. A considerable time delay in the onset of the CVC break. For the acoustoelectric current induced by the amplified noise to become noticeable against the background of the drift current, the total gain in the noise should be large, i.e. ~70 dB. Such a gain can be attained only after a certain time which is of the order of several microseconds.

3. The appearance of an electromagnetic signal just at the instant when a step appears on the current pulse. For a given limited sensitivity of the detector, the electromagnetic signal due to the amplified noise becomes noticeable just at the instant when the noise intensity increases abruptly due to amplification.

4. The presence of an electromagnetic signal of decreasing amplitude when the field is switched off. This is apparently due to the

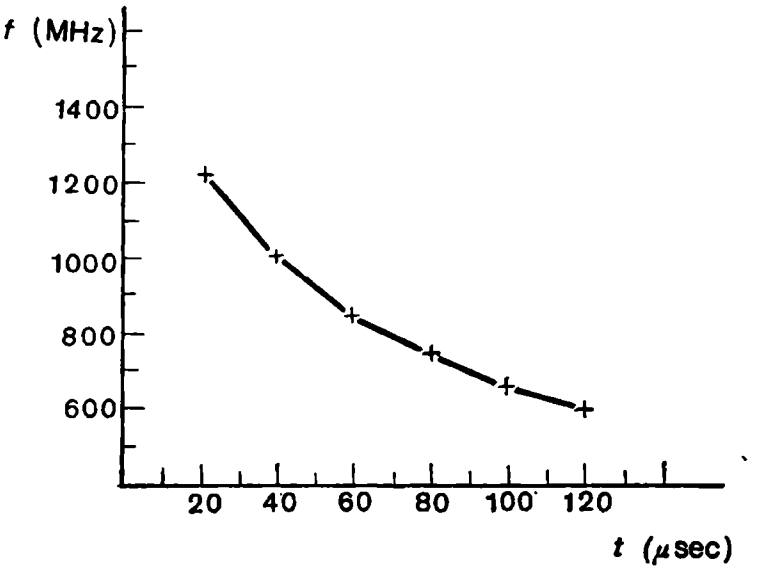

Fig. 7.19. Dependence of the generation frequency on the time elapsed after switching on the current.

fact that the amplitude of the amplified acoustic noise in the crystal cannot be decreased instantaneously.

5. Finally, evidence in favour of the acoustoelectric origin of the effect is provided by a good agreement between the measured drift current required to obtain a sufficient electronic amplification of the acoustic waves and the theory for the amplification in the Corbino disc geometry [7.4].

Thus, the sample under investigation is a medium in which a multitransit amplification of acoustic fluctuations takes place in an electric field which varies in a semiconductor from point to point. Since the resonator properties of a crystal are not manifested in this case and the sample can be used as a model for an "infinite" amplifying medium, it becomes possible to experimentally study the evolution of the spectrum of fluctuations being amplified in a Corbino disc. We have investigated the dependence of the generated signal frequency on the time elapsed after the onset of generation. The results of these experiments are presented in Fig. 7.19. It can be seen that the signal with the highest frequency of 1200 MHz is registered at the initial stage of generation. The frequency 1200 MHz satisfies the condition $\alpha_e(f) - \alpha_L(f) = 0$. The noise intensity at this frequency decreases with time, although it increases at a lower frequency. After 60 μsec. the maximum noise is detected at a frequency $f \sim 850$ MHz, while after 120 μsec, the noise is highest at a frequency of 620 MHz. Thus, as the acoustic fluctuations are amplified as a result of their multiple transits, the frequency corresponding to the

maximum of their intensity decreases. This downward frequency shift in the spectrum takes place smoothly.

The obtained experimental results are in qualitative agreement with the conclusions of the theory of nonlinear interaction between acoustic fluctuations through free electron density waves. This theory was developed in [7.6] for the case when $v_d > v_s$, the interaction operator $P(q, q') > 0$, and a decrease in the generation frequency is predicted. Such a behaviour of the generation spectrum was observed more than once in CdS and GaAs crystals. A spectral transformation due to a nonlinear interaction of waves was also observed in [7.23].

In order to compare the results of our experiments with the theory presented in [7.6], it was essential to determine the sign of $P(q, q')$. For the sample parameters and fields (both electric and magnetic) employed in our experiments, the value of this operator was found to be always positive.

These results considerably supplement the data on the nonlinear interaction between fluctuations during their multitransit amplification under synchronism conditions (see Sec. 7.4). The spectra predicted by the theory of nonlinear interaction of fluctuations were obtained in the same n-InSb semiconducting sample under different experimental conditions.

7.6. SEMICONDUCTOR IN AN ALTERNATING ELECTRIC FIELD AS AN ACTIVE MEDIUM FOR THE GENERATION OF ACOUSTIC SIGNALS

In this section, we shall present the results of investigations of acoustic wave generation in semiconducting crystals placed in a nonsinusoidal alternating periodic field. The field changes its sign every half-period $T/2$, and its shape in the positive and negative half-period is the same, i.e. $E(t) = -E(t + T/2)$. Moreover, the sign change occurs many times during the propagation of the acoustic wave through the crystal [7.7, 24]. In this case, the acoustic waves will be amplified irrespective of the direction of their propagation, and the crystal bounded by surfaces which act as mirrors for reflecting AW will be an active resonator. In this sense, a semiconducting crystal is the acoustic analogue of a laser.

7.6.1. Theory

For a nonsinusoidal electric field, the expression for the mean gain $\bar{\alpha}$ can be obtained by using the standard system of equations in the linear theory of acoustoelectronic interaction. For the

case under consideration, we have

$$\frac{L}{v_s} \gg \frac{T}{2} \gg f_s^{-1},$$

where L is the length of the crystal and v_s the velocity of sound. The mean gain factor has the form

$$\bar{\alpha} = \frac{\eta q}{\omega_s \tau} \frac{1}{T} \int_0^{T/2} \frac{[x^2 - (B^2+1)]\, dt}{(1-x^2)^2 + 2B^2(1+x^2) + B^4}. \qquad (7.17)$$

where $B = (1 + q^2 r_D^2)/\omega_s \tau$.

The maximum gain is attained for rectangular field pulses when $x = \sqrt{(1+B^2) + 2B\sqrt{1+B^2}}$ at a frequency $f_m = (1/2\pi)(v_s/r_D)$. A numerical analysis for specific semiconductors shows that the existence of pulse fronts causes a sharp decrease in the value of $\bar{\alpha}$.

7.6.2. Experiment

Figure 7.20 shows the theoretically obtained values of f_s and x for which the condition $\bar{\alpha} - \alpha_L > 0$ is satisfied, i.e. bidirectional amplification of acoustic waves takes place and generation becomes possible as a result of their multitransit amplification. Calculations were made for two values of magnetic field (6 and 7 kOe) for a material with electron concentration $n = 1.4 \times 10^{13}$ cm^{-3} and mobility $\mu = 6 \times 10^5$ cm^2/(V·sec). The value of α_L was taken from [7.13].

For crystals having such parameters, an intensive generation of acoustic flux was experimentally observed (by measuring the alternating component of the current in the sample circuit). Measurements were made in a crystal of length $L = 4$ to 8 mm. The period of alternating field was $\sim$0.5 μsec, while the total duration of the pulse front was $\leqslant$ 30 nsec. Oscillations were observed in the gigahertz region over a relatively high frequency interval of $\sim$50 MHz. The intensity maxima observed for $H = 6$ and 7 kOe are shown in the figure by the triangles and circles respectively. It can be seen that oscillations are observed in the region of expected values of x and f_s. It is interesting to note that two intensity maxima were observed for every value of the magnetic field, the ratio of their frequencies being $\sim$0.68. Such a frequency ratio for observed oscillations can be associated with spectral transformations due to nonlinear effects, considered in [7.3, 6]. A decrease of about 30% in the frequency from its value at the maximum gain, observed for $P(q, q') > 0$, was pre-

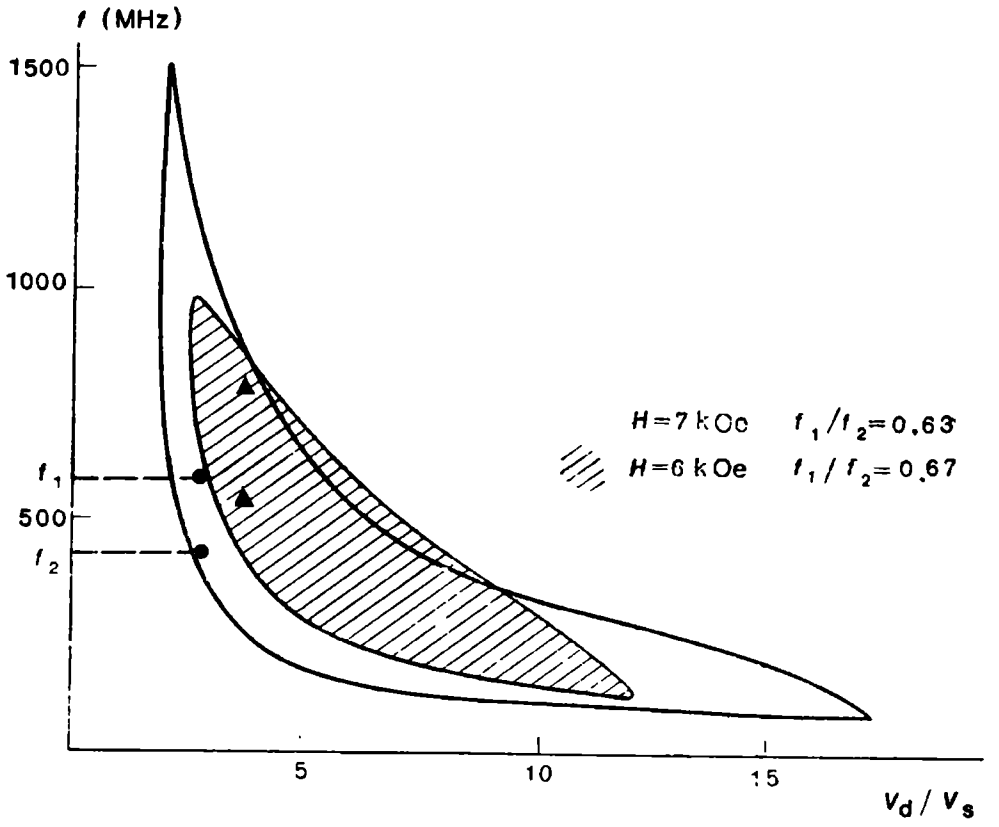

Fig. 7.20. The values of $(f, v_d/v_s)$ for which AW generation is possible.

dicted in [7.6]. In our experiments, the values of $P(q, q')$ in the half-periods corresponding to the counter drift of electrons were actually found to be positive.

7.7. CONCLUSION

This review presents the results of the first theoretical and experimental investigations of new methods of creating active acoustic media capable of amplifying and generating acoustic vibrations in the microwave region. These include multitransit (cyclotron) amplification under synchronism conditions, amplification in an alternating field for Corbino discs, and amplification in a high-frequency alternating field. With the help of the strong acoustic fluxes obtained during the generation of acoustic vibrations, it became possible to investigate for the first time a whole range of nonlinear effects which were either not studied before, or were not subjected to thorough investigations. In addition, the conclusions of the theories of nonlinear amplification of acoustic waves and non-

linear interaction of acoustic fluctuations were confirmed experimentally.

The authors are grateful to N. I. Polzikova, S. V. Boritko, V. S. Veretin, and A. A. Rubtsov, for their assistance in the experimental part of this work, and to A. S. Bugaev for useful discussions.

References

7.1. A. S. Bugaev, Yu. V. Gulyaev, and G. D. Mansfel'd, *Electronics Letters*, **14**, 403 (1978).
7.2. Yu. V. Gulyaev, *Fiz. Tverd. Tela*, **12**, 415 (1970).
7.3. V. L. Gurevich, V. D. Kagan, and B. D. Laikhtman, *Zh. Eksp. Teor. Fiz.*, **54**, 188 (1968).
7.4. Yu. V. Gulyaev, G. D. Mansfel'd, and N. I. Polzikova, *Radiotekhnika i Elektronika*, **25**, 2634 (1980).
7.5. Yu. P. Mukhortov and V. I. Pustovoit, *Zh. Eksp. Teor. Fiz.*, **61**, 1157 (1971).
7.6. L. A. Kulakova and B. D. Laikhtman, *Fiz. Tverd. Tela*, **19**, 1778 (1977).
7.7. S. V. Boritko, Yu. V. Gulyaev, and G. D. Mansfel'd, *Pis'ma v Zh. Tekhn. Fiz.*, **9**, 35 (1983).
7.8. D. L. White, *Journ. Appl. Phys.*, **33**, 2547 (1962).
7.9. H. N. Spector, *Phys. Rev.*, **165**, 562 (1968).
7.10. V. L. Gurevich and B. D. Laikhtman, *Fiz. Tverd. Tela*, **7**, 3218 (1965).
7.11. G. D. Mansfel'd, A. A. Rubtsov, and Yu. V. Gulyaev, *Fiz. Tekhn. Poluprovodnikov*, **14**, 915 (1980).
7.12. V. S. Veretin and G. D. Mansfel'd, *Fiz. Tekhn. Poluprovodnikov*, **12**, 524 (1978).
7.13. S. N. Ivanov, G. D. Mansfel'd, and E. N. Khazanov, *Fiz. Tverd. Tela*, **15**, 317 (1973).
7.14. S. V. Gantsevich, V. D. Kagan, and R. Katilyus, *Zh. Eksp. Teor. Fiz.*, **67**, 1766 (1974).
7.15. Yu. V. Gulyaev, *Fiz. Tekhn. Poluprovodnikov*, **1**, 1712 (1967).
7.16. J. Zucker and S. Zemon, *Appl. Physs Lett.*, 9, 611 (1966); Yu. V. Gulyaev and P. E. Zilberman, *Phys. Lett.*, **30A**, 378 (1969).
7.17. G. D. Mansfel'd and A. A. Rubtsov, *Fiz. Tverd. Tela*, **24**, 1150 (1982).
7.18. Yu. M. Galperin and V. D. Kagan, *Zh. Eksp. Teor. Fiz.*, **59**, 1657 (1970).
7.19. P. E. Zilberman, *Zh. Eksp. Teor. Fiz.*, **60**, 1943 (1971).
7.20. S. N. Ivanov, G. D. Mansfel'd, and E. N. Khazanov, *Fiz. Tverd. Tela*, **15**, 282 (1973).
7.21. M. Gliksman and W. A. Hicinbothen, Jr., *Phys. Rev.*, **129**, 1572 (1963).
7.22. V. D. Kagan, *Fiz. Tverd. Tela*, **16**, 1766 (1974).
7.23. M. K. Balakirev, S. V. Bogdanov, and A. S. Leonov, *Pis'ma v Zh. Tekhn. Fiz.*, **8**, 172 (1982).
7.24. Zh. E. Smbatyan, Yu. V. Gulyaev, and A. S. Bugaev, *Fiz. Tekhn. Poluprovodnikov*, **16**, 1517 (1982).

8 New Trends in the Physics of Laser Crystals and Glasses

V. V. Osiko and A. M. Prokhorov

8.1. INTRODUCTION

Crystal and glass lasers have played and continue to play an important part in laser engineering. The main advantages of these lasers are better output parameters (pulse energy and average radiation power) and their capability to operate in different modes (from ultrashort picosecond pulses to high-power CW oscillations). Besides, such lasers are quite compact. Owing to these properties, crystal and glass lasers find a wide range of applications. They are successfully used in technology for different types of material processing, in communication, detection and ranging, in scientific research, and in high-power installations for investigations in the field of laser fusion. During the last few years, the physics of activated crystals and glasses has advanced significantly. Important regularities in the formation of active centres in laser matrices, the transport and transfer of electron excitation energy between impurity ions, the dependence of the luminescence spectral and laser properties on the composition and structure of laser matrices were investigated and explained. This led to the emergence of a new generation of active media which were used to create lasers with a continuously tunable emission frequency over a wide range of spectrum, and also sharply increased the efficiency of solid state lasers. The present review is devoted to two aspects in the physics of active media, viz. the investigation of LiF crystals with electronic colour centres for room-temperature tunable lasers, and the creation of new active media for high-efficiency lasers in the near infra-red region.

8.2. LiF CRYSTALS WITH ELECTRONIC COLOUR CENTRES FOR TUNABLE LASERS

Fritz and Menke [8.1] were the first to report in 1965 the lasing on colour centres in a KCl-Li crystal pumped by flash lamps. However, this discovery was not developed for the next ten years, and it was only in 1975 that Mollenauer's group in USA reported that tunable lasing was obtained and investigated on colour centers in KCl-Li and RbCl-Li pumped by another laser [8.2]. Later, a group of scientists at the Hannover University reported the creation

of a laser with a different type of colour centres in KCl-Na and RbCl-Na crystals [8.3]. A group of Soviet scientists at the Institute of Thermal Physics at the Siberian Division of the USSR Academy of Sciences observed lasing on three types of colour centres in LiF crystals [8.4, 5]. Since then, the number of papers devoted to such investigations has continued to rise. Comparatively recent reviews [8.6-8] describe the physical processes behind the formation of different types of colour centres in crystals, as well as the results concerning the tunable oscillations obtained in these crystals. From the very beginning, tunable colour centre lasers attracted the attention of scientists due to their unique properties: a wide tuning range (from 0.7 to 3.3 μm, i.e. the wavelengths for which dye lasers either do not exist, or are less efficient), a high frequency stability, small oscillation line widths, ability to operate in the pulse repetition mode or in CW mode, etc.

So far, laser activity has been observed in a number of crystals. These include lithium fluoride, fluorides and chlorides of sodium and potassium, rubidium chloride, and fluorides of calcium and strontium. As grown, these crystals are colourless. Upon irradiation by gamma rays, high-energy electrons, X-rays, or heating in the atmosphere of alkali metal vapours (the so-called additive coloration), the crystals acquire intrinsic point defects which localize electrons or holes. The absorption bands of such charged defects give a characteristic colour to the crystals. The F-centre, which is an anion vacancy capturing one electron is the simplest in structure. The structure of all other colour centres for which lasing has been obtained is derived from the F-centres. Thus, an F_2-centre consists of two F-centres situated at adjoining lattice sites, an F_2^+-centre is a paired centre which has lost an electron, while an F_2^--centre is a paired centre which has captured a third electron. Sometimes, cation impurities are introduced into the crystal lattice. In this case, a colour centre (single or paired) in the vicinity of an impurity cation (for example, Li^+ instead of K^+ in the KCl lattice) has an index A (as in F_A). If two impurity cations are situated near an F-centre, the centre has the index B and is denoted by F_B. Lasing on colour centres takes place in the same manner as in dye lasers (Fig. 8.1). The pumping radiation is absorbed in a wide vibronic band. This is followed by a nonradiative relaxation to the minimum of the potential-energy curve for the excited state over a period of 10^{-12}-10^{-13} sec. After this, a radiative transition to a lower state (with a decay time of 10-100 nsec) and a rapid relaxation to the minimum of the potential-energy curve of the ground state takes place.

There is a considerable difference between the Stokes' shift for F_A and F_B colour centre levels on the one hand, and F_2, F_2^+ and F_2^- centres on the other hand. Thus, for F_A and F_B centres the absorption transition lies in the region 0.5-0.6 μm, while the luminescence

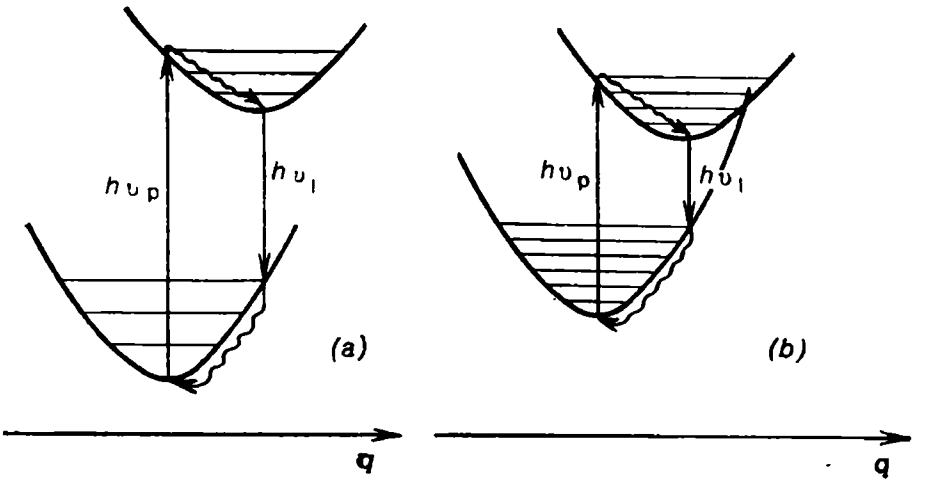

Fig. 8.1. Potential-energy curves for the ground state and the excited state of colour centres in alkali halide crystals: (*a*) F_A and F_B centres; (*b*) F_2, F_2^+, and F_2^- centres.

transition lies around 2-3 μm. This corresponds to a Stokes shift of $\sim 15\,000$ cm^{-1}, which is several times higher than the luminescence transition energy. Consequently, the point of intersection of the potential-energy curves for the excited and ground states lies close to the energy minimum of the excited state. As a result of this, the nonradiative losses are found to be significant, and a laser with F_A and F_B centres can operate only at temperatures much below the room temperature (< 100 K). Scientists in the USA and FRG have developed cryogenic tunable lasers based on F_A and F_B colour centres and operating below 100 K [8.2, 3, 9, 10]. Soviet scientists, on the other hand, have concentrated their attention to the creation of tunable lasers operating at room temperature. Unlike the F_A and F_B centres, the Stokes shifts for F_2, F_2^+, and F_2^- centres are smaller than the luminescence transition energy. This ensures a high quantum yield which weakly depends on temperature even above room temperature. At the same time, the Stokes shifts are sufficiently large to ensure oscillations according to the four-level diagram.

At present, lasers based on colour centres in LiF crystals are technologically the most advanced (Table 8.1). The F_2, F_2^+, and F_2^- centres in LiF have large values of oscillator strength for electronic-vibrational transitions, wide luminescence bands, and a four-level transition diagram at room temperature. Besides, LiF crystals have relatively high mechanical strength, are weakly soluble in water, and can be easily processed.

The acceptor nature of the F_2^+ centre and peculiarities of its electronic structure ensure a fairly high stability to powerful pumping radiation. The main drawback of F_2^+ centres is their low thermal stability. Their half-life at room temperature is just 12 hours. Until

Table 8.1. Parameters of Tunable Lasers on Colour Centres in LiF

Crystal	Type of centre	Pumping wavelength (μm)	Tuning range (μm)	Laser average power (mW)	Power pulse (mW)	Efficiency* (%)	Reference
LiF	F_2	0.45	0.665-0.715	—	0.0012	10 (13)	[8.39]
LiF	F_2	0.53	0.65-0.75	—	—	—	[8.12, 13]
LiF	$F_2 \rightarrow F_2^+$	0.53	0.84-1.1	400	0.4	30	[8.13, 40]
LiF-OH^-	F_2^+	0.69	0.83-1.15	—	0.0015 J	0.3 (1)	[8.11]
LiF	F_2^-	1.06	1.1-1.26	200	0.2	25 (50)	[8.16]

* The values of slope efficiency are given in parentheses.

recently, such a low stability was the main obstacle in the creation of high-efficiency lasers based on these centres, although the lasing effect in them was observed as early as in 1977 [8.4, 5]. An attempt to stabilize the F_2^+ centres by introducing an OH^- impurity into LiF was made in [8.11]. In this case, a small fraction of F_2^+ centres attained a high thermal stability. In spite of this, the basic laser properties of the crystals deteriorated, and their radiation stability also decreased. A new method of accumulating ionized centres, which allowed for a high stability of LiF-F_2^+, was proposed in [8.12,13]. This method combines the high thermal stability of a neutral F_2 centre with the photostability of F_2^+. The absorption spectrum of these centres is shown in Fig. 8.2*a*. When the second harmonic radiation from a neodymium laser (0.53 μm) or a rhodamine 6G laser (0.55-0.58 μm) is used for pumping, pulsed periodic oscillations are excited in F_2 centres. However, in view of the photoinstability in the pumping channel, a two-stage ionization of an F_2 centre to F_2^+ (Fig. 8.3*a*) takes place according to the mechanism $F_2 \rightarrow F_2^* \rightarrow F_2^+$. This leads to a certain drop in the F_2 absorption band and to the appearance of a new F_2^+ band (Fig. 8.2*b*). Since the pumping radiation ionizes the F_2 centre and excites F_2^+ centres equally well, the oscillation of F_2^+ centres smoothly replaces the oscillation of F_2 centres in the pumping channel. The dynamics of accumulation of the F_2^+ centres is shown in Fig. 8.3*b*. It can be seen that shortly after the pumping has been switched on, the transmission in the spectral region corresponding to the maximum of the absorption band of ionized centres sharply decreases at first, and then stabilizes. Accordingly, the generation of the F_2^+ centres also stabilizes. The first pulsed periodic LiF-F_2^+ lasers effectively operating at room temperature were created with the help of the above method. In a non-

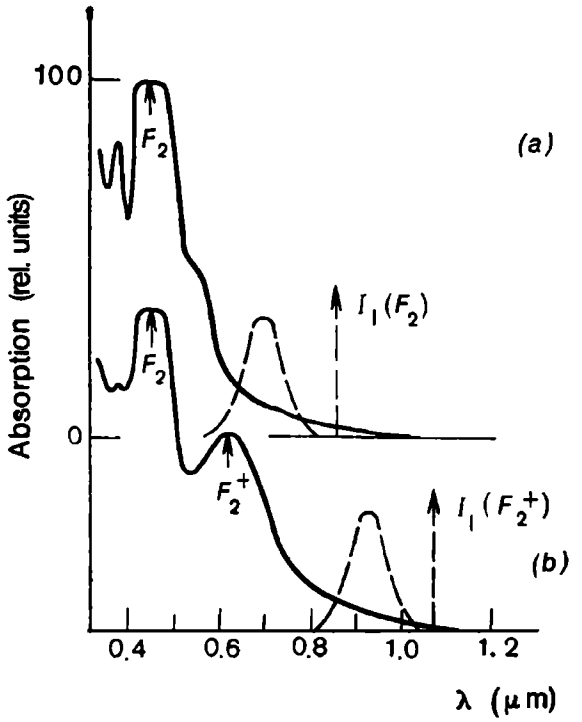

Fig. 8.2. Absorption spectra (solid lines) and luminescence spectra (dashed lines): (*a*) γ-irradiated LiF crystal with F_2 centres; (*b*) in the channel of pumping by the Nd laser second harmonic with $\lambda = 0.53\mu m$ for the same crystal.

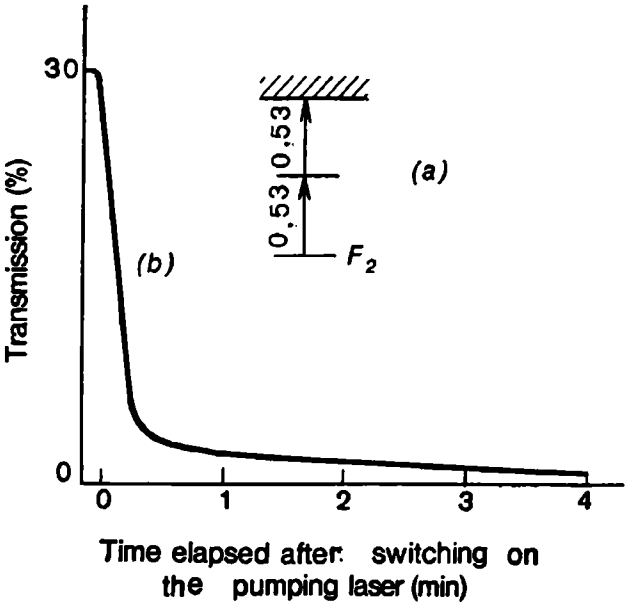

Fig. 8. . The two-step photoionization of F_2 centres in LiF (*a*) and the kinetics of this process (*b*) upon irradiation of LiF-F_2 crystal by the Nd laser second harmonic with $\lambda = 0.53\mu m$. The kinetics of the $F_2 \rightarrow F_2^+$ process was tracked by the transmission of the He-Ne laser radiation with $\lambda = 0.632\mu m$.

selective resonator, the energy efficiency of the laser was found to be 24%, while the quantum efficiency reached 42% (with respect to pumping). The laser operates at a pulse repetition rate up to 100 pps without forced cooling and ensures a beam divergence of 10^{-3} rad, which is close to the diffraction limit [8.13]. Further development of LiF-F_2^+ lasers by using a holographic selector (Fig. 8.4*a*) has been described in [8.14]. Besides the active element, the laser resonator

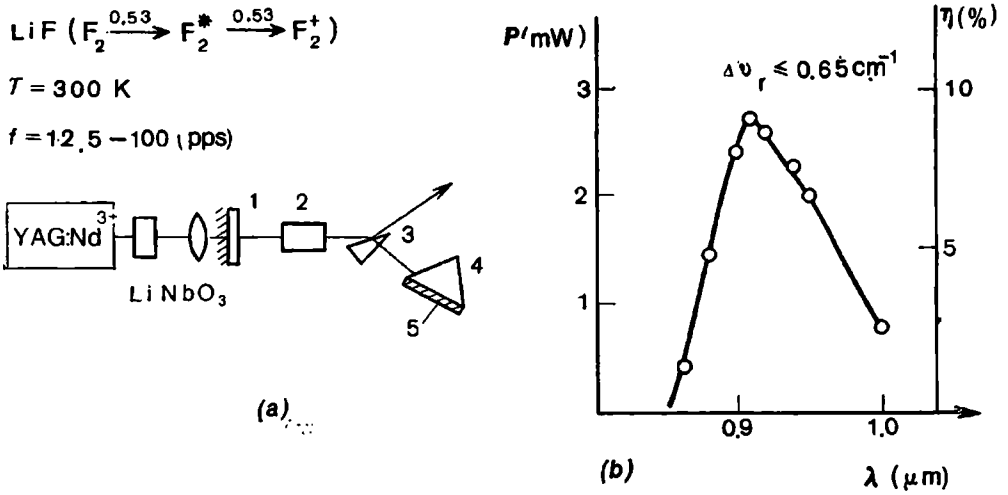

Fig. 8.4. (*a*) Schematic diagram of LiF-F_2^+ tunable laser with a holographic selector: *1*—input mirror (83% transmission at 0.532 μm and 100% reflection in the region 0.8-1.15μm); *2*—LiF-F_2^+ active element; *3*—prism-telescope; *4*—optically transparent wedge; *5*—three-dimensional holographic phase grating. (*b*) The tuning curve for this laser.

contains a telescopic prism which was also used for extracting the radiation, and a holographic grating-selector with 2800 lines per millimetre. The laser operated at a pulse repetition rate up to 100 pps. The absorption energy efficiency was 10% at an oscillation line width below 0.65 cm^{-1}, while the spectral tuning range was more than 1500 cm^{-1} (see Fig. 8.4*b*).

It is very important that a neodymium garnet laser can be used for pumping, since this is essentially the only laser capable of generating pulses whose duration varies from microseconds to picoseconds. A preliminary photoionization of F_2 centres ($F_2 \rightarrow F_2^+$) led to the creation of a tunable room temperature picosecond laser [8.15]. The laser resonator was formed by two opaque mirrors, and contained LiF-F_2 as the active element. A three-prism dispersion element was used for narrowing and tuning of the spectrum. Radiation was extracted from the resonator with the help of a glass stack. A synchronous train of picosecond second-harmonic pulses from a neodymium garnet laser was used for pumping. A bleachable dye No. 3955 dissolved in nitrobenzene was used for mode locking the laser. The resonator

lengths of the tunable and the pumping lasers were matched. The duration of pumping pulses was 45 psec. In this case, the duration of tunable laser pulses reached 10 psec, which is close to the duration of a band-width limited pulse with a spectral width of 3 cm^{-1}.

The F_2^- centres are the other type of colour centres in LiF, which are important for creating tunable room-temperature lasers [8.16]. These centres have a half-life of several years at room temperature and are photostable to the powerful IR pumping radiation. Here, the main problem is to obtain LiF crystals with a sufficiently high concentration of the F_2^- centres and with low inactive losses in the region of oscillation wavelength. Recently, this problem was solved by a group of scientists from the Institute of General Physics of the USSR Academy of Sciences, and active LiF-F_2^- elements with a high F_2^- concentration and low optical losses were obtained. These elements were used to construct lasers with the most favourable parameters for a nonselective resonator. When pumped by the Q-switched fundamental radiation of a neodymium garnet laser, the efficiency is 25%, the absorbed energy efficiency is 32%, while the slope efficiency is 50%. The lasing band has a width of 1000 cm^{-1} and its maximum lies at 1.17 μm. Lasing on F_2^- centres has also been obtained with a pumping efficiency of ~0.5%, when smooth pulses of a free-running laser are used for pumping. The line width for a tunable LiF-F_2^- laser is less than 0.5Å and its tuning range lies between 1.08 and 1.23 μm. At the maximum of the tuning range (λ_{max} = = 1.17μm), the efficiency is 10% with respect to the energy incident on the crystal and 12% with respect to the absorbed energy, while the slope efficiency is equal to 23%. The laser operates at room temperature with a pulse repetition rate of 100 pps.

The development of tunable lasers based on LiF with F_2, F_2^+, and F_2^- colour centres using a single pump source (neodymium laser) makes it possible to cover the wavelength region within 0.65-1.25 μm, which is important for practical applications but is not accessible when we use dye lasers. The tuning curves for LiF colour centre lasers and dye lasers are compared in Fig. 8.5. It can be seen that LiF crystal elements replace at least 10 different dyes. New spectral regions may be covered by doubling and frequency mixing of colour centre laser frequencies using nonlinear processes. Table 8.2 presents the results of a number of nonlinear frequency transformations of the fundamental frequencies of colour centre lasers based on LiF crystals. These transformations are accomplished with the help of $LiIO_3$, $LiNbO_3$, and GaSe crystals. Frequency mixing of tunable lasers pumped by a neodymium laser with λ = 1.06 μm sharply increases the output energy in the blue-green spectral region and covers the far infrared region (5.5-16.5 μm). It should be noted that with the help of the difference frequency technique in GaSe, as proposed in [8.17], we can considerably advance towards longer wavelengths,

Table 8.2. Nonlinear Frequency Conversions for Tunable Lasers on Colour Centres in LiF

Type of Conversion	Nonlinear Crystal	Lasing range (μm)
ωLiF-F_2^-	—	1.08-1.23
ωLiF-F_2^+	—	0.84-1.1
ωLiF-F_2	—	0.65-0.75
2ωLiF-F_2^-	$LiIO_3$, $LiNbO_3$	0.54-0.615
ωLiF-F_2^-+ω1.06	$LiIO_3$, $LiNbO_3$	0.54-0.57
2ωLiF-F_2^+	$LiIO_3$	0.42-0.55
ωLiF-F_2^++ω1.06	$LiIO_3$	0.47-0.54
ωLiF-F_2^+—ω1.06	GaSe	5.5-16.5

the only restriction being imposed by the transparency of the nonlinear crystal. The basic features of colour centre LiF pulsed periodic lasers are presented in Table 8.1. The F_2^+ and F_2^- colour centre lasers are at present the most advanced lasers for practical applications

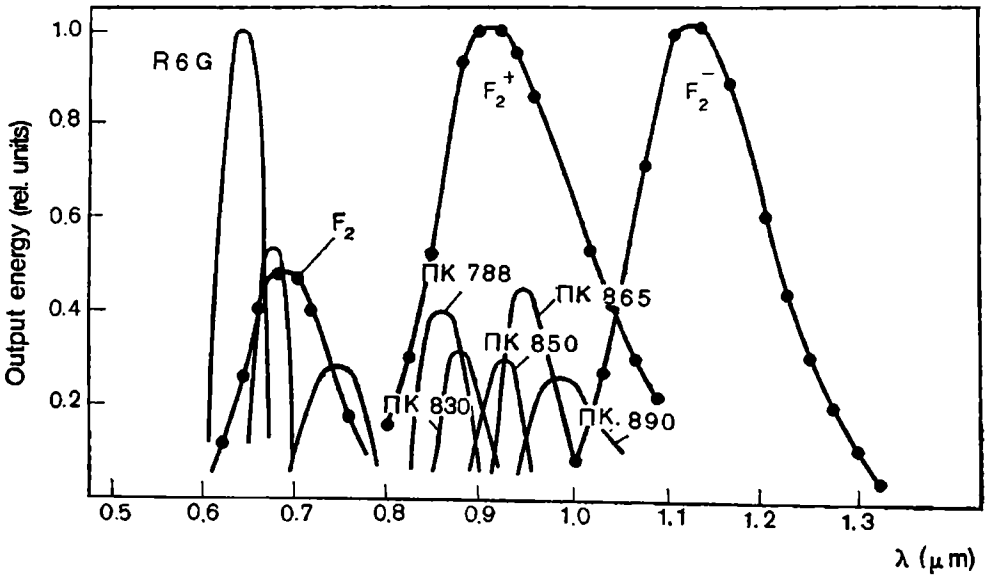

Fig. 8.5. The tuning curve for lasers on LiF with F_2, F_2^+, and F_2^- colour centres compared with the tuning curves for dye lasers (ПК denotes the trade mark of the dye).

(crystals with F_2 centres are not sufficiently photostable so far). A reliable and easily accessible pumping source (the second and the first harmonic of neodymium laser) exists for both crystals. The operating temperatures can exceed the room temperature by 60°.

The wavelength range of LiF-F_2^+ and LiF-F_2^- lasers is inconvenient for dye lasers, while the continuous tuning range is several times broader than for dye lasers. Besides, these lasers have a high efficiency. Their pulse power reaches several megawatts, while the average power is hundreds of milliwatts. It can be assumed that the stability problem for LiF-F_2^+ and Li-F_2^- active elements have been solved. For example, at room temperatures, the decay time for F_2^- centres is about five years. The thermal stability of the active elements for the $F_2 \rightarrow F_2^+$ transformation is even higher, and this ensures a long service life (up to 10^3-10^4 hours) of these elements.

8.3. ACTIVE MEDIA FOR NEODYMIUM LASERS WITH NONSELECTIVE PUMPING

8.3.1. High-concentration KNFS Glasses with Anomalously Low Concentration Quenching of Neodymium

The dependences of the Nd^{3+} luminescence quantum yield from the $^4F_{3/2}$ level is presented in Fig. 8.6 for several laser crystal and glasses [8.18]. A sharp decrease in the quantum yield at Nd^{3+} concentrations above 1-3% is characteristic of most matrices. The quenching is caused by the resonance interaction of transitions shown in Fig. 8.7. This interaction comes into play when the distance between neighbouring Nd^{3+} ions decreases to 3 Å.

However, the first exception to the rule was probably observed in 1967 [8.19]: the luminescence quantum yield in BaF_2-NdF_3 crystals remained high even at the Nd^{3+} concentration of 4×10^{21} cm^{-3}, which is about 10 times higher than in ordinary laser crystals. It was also shown that the weak quenching is due to a shift of the $^4I_{15/2}$ and $^4I_{13/2}$ levels (which are responsible for quenching) with respect to other ground states such that the radiative transition frequencies are much lower than the absorption frequency. The transitions in this case are detuned. An anomalously low quenching was reported in the middle of the seventies for another crystal, viz. NdP_5O_{14} [8.20, 21]. The concentration of Nd^{3+} ions in this crystal is equal to 4×10^{21} cm^{-3}. The low quenching was attributed by the authors to the fact that the neighbouring Nd^{3+} ions in such a crystal are separated by 5.2 Å, while this distance in other matrices is of the order of 3 Å. This difference is of great importance, since the probability of quenching during a dipole interaction is proportional to R^{-6}. It has been shown in [8.22] that as in the case of BaF_2-NdF_3, the anomalous arrangement of the intermediate $^4I_{15/2}$ and $^4I_{13/2}$ levels in NdP_5O_{14} also plays an important role (besides the large distance between neighbouring Nd^{3+} ions). Thus, laser media with

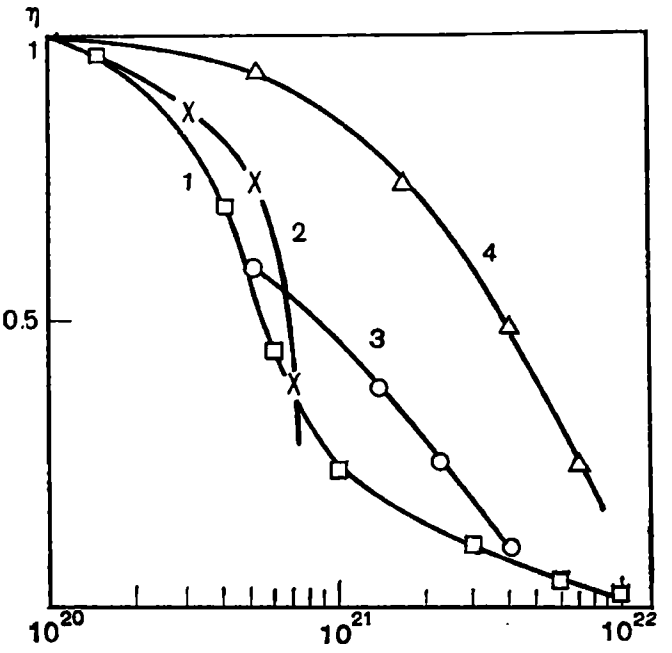

Fig. 8.6. The concentration dependence of the luminescence quantum yield of Nd for different laser matrices: *1*—$La_{1-x}Nd_xF_3$ crystal; *2*—YAG-Nd^{3+} crystal; *3*—GLS-1 glass; *4*—KNFS glass.

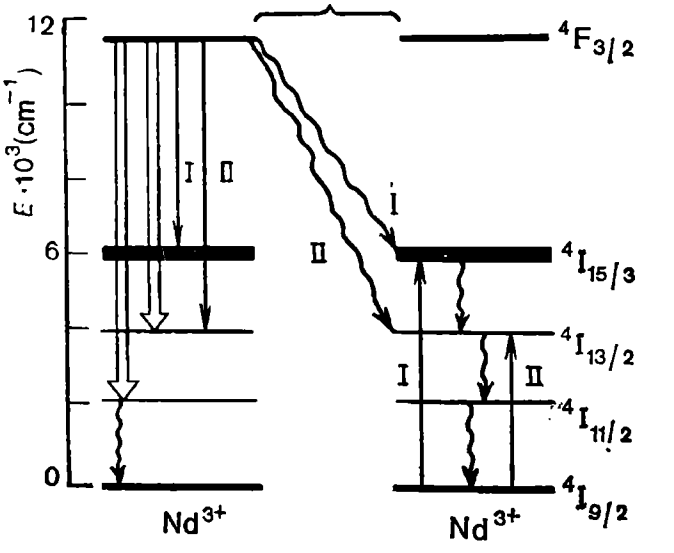

Fig. 8.7. Diagram of lower energy levels of Nd^{3+} and nonradiative energy transfer from the excited (left) to the unexcited (right) Nd^{3+} ion.

a high active ion concentration must have (1) a low probability of the elementary quenching interaction and (2) large minimum distance between active ions, allowed by the matrix structure.

At present, about two dozens of crystals with a high Nd concentra-

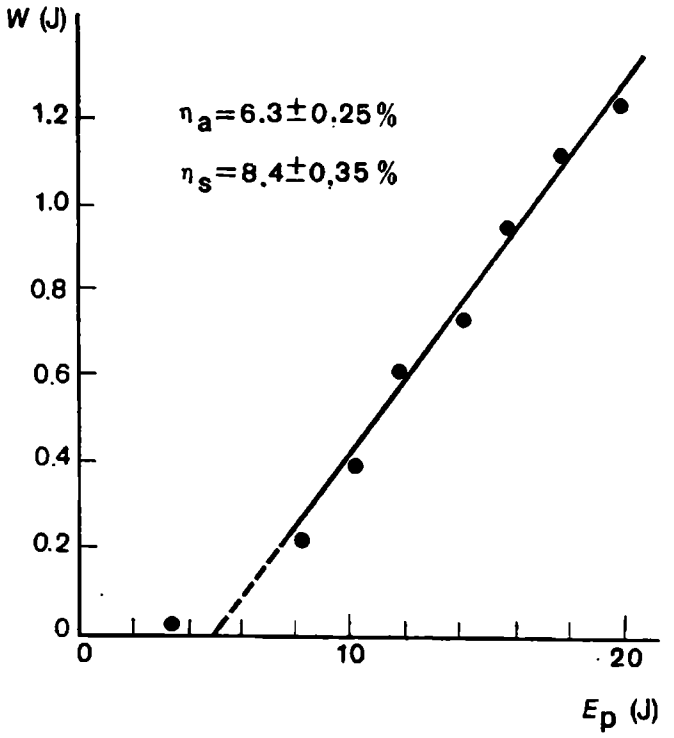

Fig. 8.8. The dependence of the KNFS laser energy on the pumping energy in the free-running mode. Active element size is ⌀ 6.3 × 80 mm; $n_{Nd} = 8 \times 10^{20}$ cm^{-3}, and the resonator is 105 mm in length (plane mirrors are used, the reflection of the output mirror being 85%). η_a and η_d denote the absolute and differential efficiency respectively.

tion have been synthesized all over the world. These crystals are mainly phosphates. Unfortunately, these compounds are unstable and decompose upon heating. Hence, it is difficult to grow crystals whose dimensions are comparable with those used for Ruby or YAG lasers. These materials are used for making minilasers. Another approach was adopted by a group of scientists from the Institute of General Physics of the USSR Academy of Sciences, who fabricated high-concentration neodymium glasses [8.18, 23-25]. It is well known that glasses can be used for making large-size laser elements of any shape and with a high optical homogeneity. It was shown that the following rules must be observed while creating high-concentration glasses. (a) The basic composition of glasses must permit the incorporation of large quantities of neodymium. For this purpose, it was proposed that oxides like Sc_2O_3, Y_2O_3, La_2O_3, and Gd_2O_3 be used as basic oxides instead of alkali- and alkali-earth oxides. In this case, the introduction of large quantities of Nd_2O_3 does not violate the structure of these glasses, since the Nd^{3+} ions have the same chemical nature and dimensions as the La^{3+} and Gd^{3+} ions. (2) The composition and structure of the glass must be such that the interaction

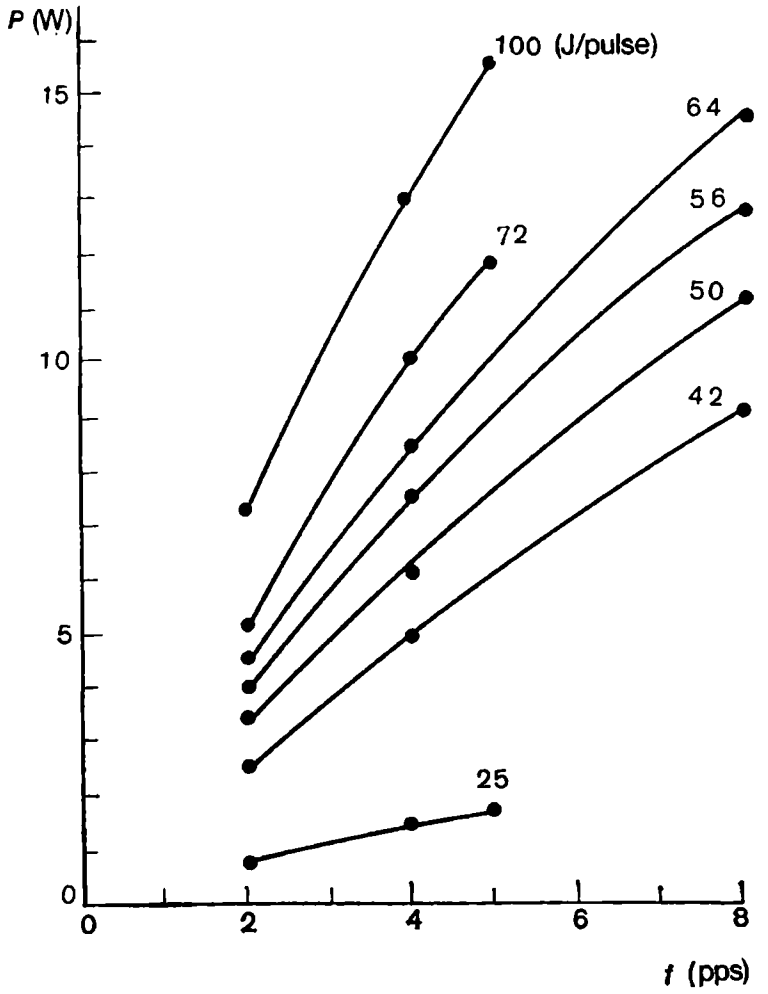

Fig. 8.9. The dependence of the average KNFS laser energy on the pulse repetition rate for different values of the pumping energy. The size of the active element is $\varnothing$ 5 × 70 mm; $n_{Nd} = 8 \times 10^{20}$ cm^{-3}.

microparameter does not exceed $C = (1\text{-}3) \times 10^{-41}$ cm^6/sec. (3) The distance between the neighbouring Nd^{3+} ions must not be less than 4.5 Å.

These rules were followed while synthesizing the Li-La-Nd phosphate glass (KNFS). Figure 8.6 shows the dependence of the quantum yield of the KNFS glass on the Nd^{3+} concentration. It can be seen that the Nd^{3+} concentrations up to 2.7×10^{21} cm^{-3} can be attained without any sharp decrease in the quantum yield [8.26]. The basic properties of the KNFS glass are presented in Tables 8.3 and 8.4.

The use of KNFS glass active elements in different lasers operating in various modes (from quasicontinuous to single-pulse mode and under free-running or self-synchronizing conditions) improved

Table 8.3. Spectroscopic and Optical Properties of KNFS Glass

Nd^{3+} ion concentration (cm^{-3})	up to 2.7×10^{21}
Lasing wavelength (μm)	1.0545 and 1.32
Luminescence bandwidth (Å)	185
Induced transition cross section, σ (cm^2)	3.8×10^{-20}
Lifetime of the excited state, τ (μsec)	330-80
Refractive index, n_D	1.555
Relative dispersion of the refractive index, $n_F - n_C$	870×10^{-5}
Nonlinear refractive index, n_2	1.35×10^{-13}
Thermo-optical coefficients:	
W ($°C^{-1}$)	31×10^{-7}
dW/dT ($°C^{-2}$)	0.18
P ($°C^{-1}$)	26×10^{-7}
Q ($°C^{-1}$)	6×10^{-7}
$B_{\parallel}$ ($\lambda = 448.8$ nm) (cm^2/kg)	2.5×10^{-7}
$B_{\perp}$ ($\lambda = 448.8$ nm) (cm^2/kg)	4.2×10^{-7}
dn/dT ($°C^{-1}$)	13×10^{-7}

Table 8.4. Physical and Chemical Properties of KNFS Glass

Density (gm/cm^3)	2.85
Young's modulus, E (kg/mm^2)	6000
Shear modulus, μ (kg/mm^2)	2386
Poisson's ratio, σ_P	0.259
Coefficient of thermal expansion, α, ($°C^{-1}$)	80×10^{-7}
Chemical stability (loss of weight per hour upon boiling in water) (%)	0.2

the energy parameters in the case of an effective utilization of the pumping radiation [8.18, 23].

Free-running Oscillations. This type of oscillations has been studied for single as well as repeating pulses. In the case of single pulses in a 70 mm long KNFS rod of 6.3 mm diameter, an absolute efficiency of 6.3 ± 0.25% and a slope efficiency of 8.4 ± 0.35% have been attained for pumping energies up to 20 J (Fig. 8.8). At a pulse repetition rate of 5 pps and a pumping energy of 100 J, the average output power exceeds 15 W (Fig. 8.9). The output power at a pulse repetition rate of 25 pps and a pumping energy of 10 J is 3.4 W (Fig. 8.10).

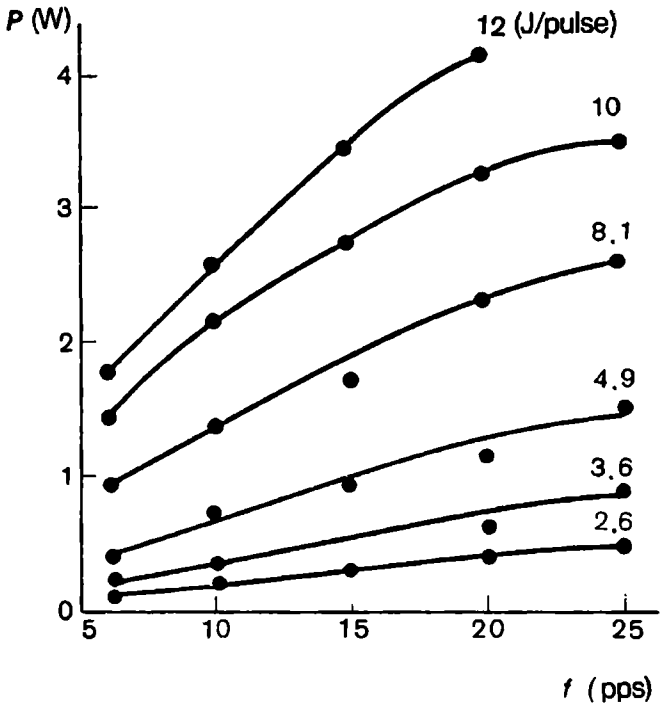

Fig. 8.10. The dependence of the average KNFS laser power on the pulse repetition rate for low pumping energy values. The size of the element is ⌀6.3 × 100 mm, and $n_{Nd} = 8 \times 10^{20}$ cm^{-3}.

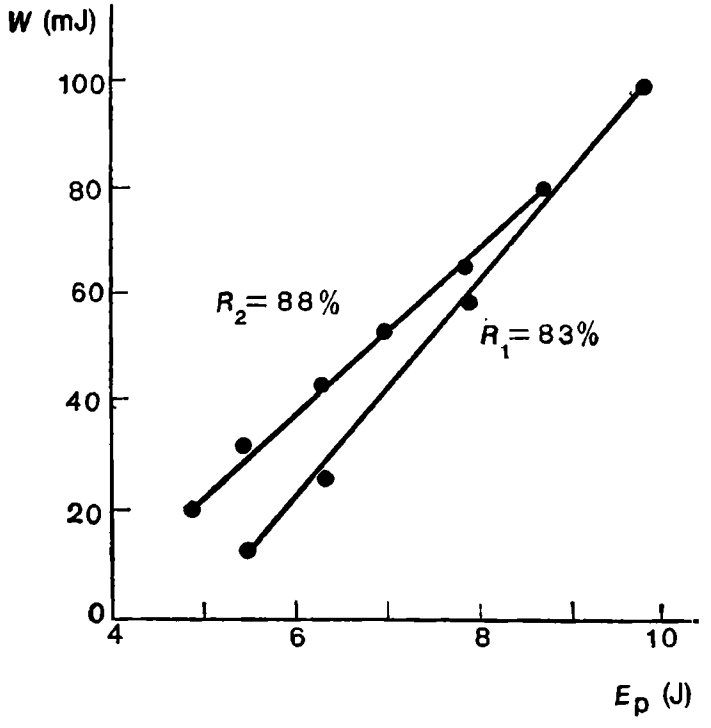

Fig. 8.11. The dependence of the KNFS laser energy on the *Q*-switched pumping energy. An electro-optical switch is used. The size of the active element is ⌀6.3 × 100 mm, and $n_{Nd} = 8 \times 10^{20}$ cm^{-3}.

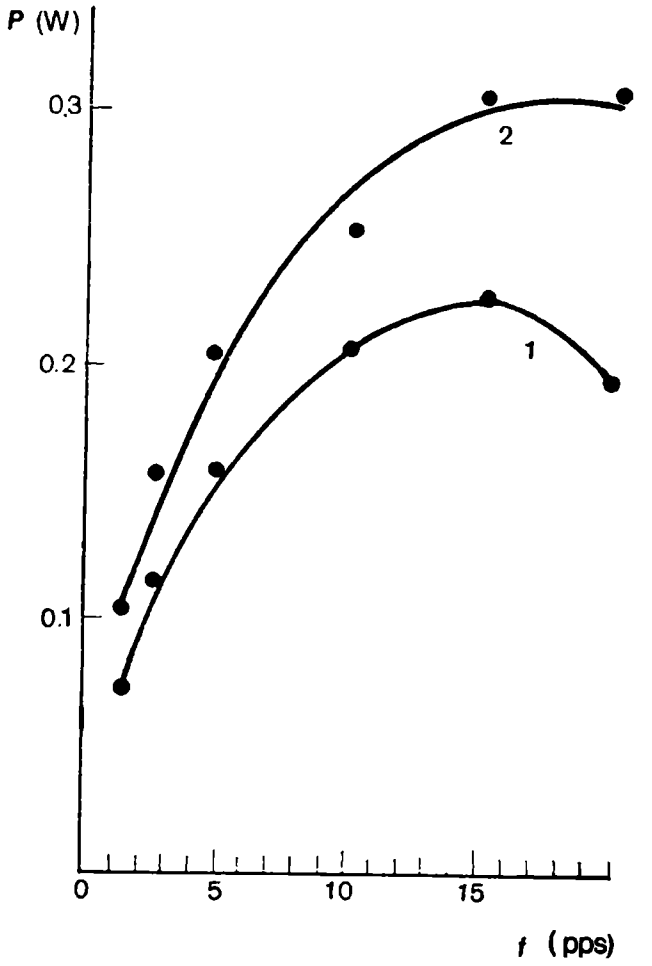

Fig. 8.12. Dependence of the average KNFS laser energy on the pulse repetition rate for a pumping energy of 9 and 10 J. The size of the active element is ⌀ 6.3 × 100 mm, and $n_{Nd} = 8 \times 10^{20}$ cm^{-3}.

***Q*-switched Mode.** In the case of traditional *Q*-switching with the help of a rotating prism, a pulse energy of 0.64 J is attained at a pumping energy of 65 J (Fig. 8.11). An efficiency of 1% is reached by using an electrooptic *Q*-switch based on deuterated KDP at a pumping power of 10 J. At a pulse repetition rate of 20 pps and at the same value of the pumping energy, the average power is equal to 0.3 W (Fig. 8.12). A lithium fluoride passive element with F_2^- colour centres has been used recently for *Q*-switching of a KNFS laser [8.27]. A pumping power of only 5.6 J was required to obtain an output energy of 30 mJ in a single TEM_{00} mode with the help of this element.

Quasicontinuous Operation. Quasicontinuous lasing was attained in KNFS glass through laser pumping by a Kr laser [8.28]. The active medium was the KNFS glass activated either by Nd^{3+} ions only (8×10^{20} cm^{-3}) or jointly by Nd^{3+} (8×10^{20} cm^{-3}) and

Cr^{3+} (8×10^{19} cm^{-3}). The duration of pumping pulses was 0.5 msec for a pulse-period to pulse-duration ratio of 1 : 100. The pumping was carried out either at the Nd^{3+} absorption line or the Cr^{3+} band. The efficiency in these cases was 18 and 8% respectively.

These results show that the efficiency of KNFS lasers is about twice as high as in lasers based on known crystals and glasses in the small and average energy pulsed pumping regions both in the case of free running oscillations and Q-switched mode. The main advantage of KNFS lasers is their high output parameters at relatively low pumping energies. This makes it possible not only to construct compact lasers, but also to considerably increase the reliability and the service life of laser equipment. In many fields of application, rare and expensive laser crystals, especially YAG-Nd^{3+}, which require rare-earths and precious metals like Ir and intricate technological equipment, can be replaced by cheaper and easily accessible elements made of KNFS glass. These elements have an additional advantage in that their laser properties are much better in many respects.

8.3.2. The Use of Sensitization Effect for Increasing the Efficiency of Neodymium Lasers with Nonselective Pumping

It is well known that the pumping band of doubly activated matrices is a superposition of the absorption spectra of the active impurity from the sensitizer. However, for this purpose it is essential that the excitation energy of the sensitizer be transferred to the upper laser level of the active impurity rapidly and without any losses. The first attempt to use the sensitization effect for increasing the efficiency of neodymium lasers was made as early as in 1964 [8.29]. This was a laser based on YAG-Cr^{3+}-Nd^{3+} crystals in which the Cr^{3+} ions served as sensitizers. A nearly two-fold increase in the efficiency in the CW mode was reported. However, this result was not exploited subsequently, and YAG crystals with neodymium alone are still used in many cases. It was only after a decade that the interaction mechanism in the Cr^{3+}-Nd^{3+} pair was explained. In 1978, Hattendorf *et al.* [8.30] described crystals of the chromium-neodymium-alumoborate compound. A rapid energy transfer from Cr^{3+} to Nd^{3+} (occurring in less than 100 nsec) was observed for the first time in this crystal. The power required to create a population inversion on the $^4F_{3/2}$ level of the Nd^{3+} was reduced by an order of magnitude in comparison with the Cr-free crystal. The high sensitization efficiency was attributed by the authors to the high Nd^{3+} concentration in the crystal under investigation, and hence to the fact that the distance between Cr^{3+} and Nd^{3+} ions is quite small. An important step towards the understanding of the energy transfer mechanism

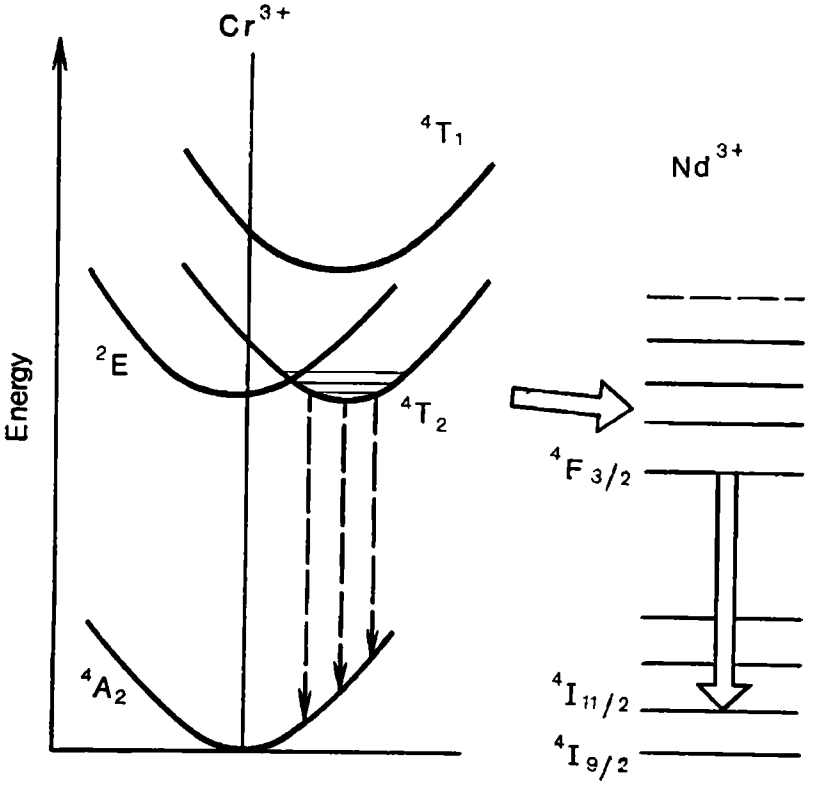

Fig. 8.13. The lower energy levels of Cr^{3+} and Nd^{3+} ions.

in the Cr^{3+}-Nd^{3+} pair was made in [8.31]. It was shown that the energy gap ΔE between ^2E and $^4T_2$ energy levels of the Cr^{3+} ion plays an important role (Fig. 8.13). The rapid energy transfer from Cr^{3+} to Nd^{3+} (i.e. rapid in comparison to the deactivation rate of the upper working level $^4F_{3/2}$ of Nd^{3+}) is possible only if

$$\Delta E \leqslant kT. \tag{8.1}$$

In particular, it was shown that the level diagram of Cr^{3+} ions in a YAG crystal do not satisfy this condition. Hence, the introduction of chromium into YAG-Nd^{3+} does not lead to a significant increase in gain. The search for crystals and glasses with the effective excitation energy transfer from chromium to neodymium resulted in the synthesis of Cr^{3+}-Nd^{3+} KNFS glass [8.32]. Later, gadolynium-gallium garnet with chromium and neodymium (GGG-Cr^{3+}-Nd^{3+}) was synthesized [8.33]. In this crystal, the energy transfer was effective, which resulted in an increase in the slope efficiency in comparison with YAG-Nd^{3+}. However, a number of technological drawbacks do not allow this crystal to replace YAG-Nd^{3+}. Further theoretical and experimental studies have led to the creation of a number of garnet-type crystals activated with Cr^{3+} and Nd^{3+} and satisfying the

condition (8.1). These are mainly complicated compounds belonging to the group of substituted gallium garnets. Among them, GSGG-Cr^{3+}-Nd^{3+} crystal has remarkable properties. This crystal is a complex gallium garnet which, in addition to gallium, contains gadolynium, scandium, chromium, and neodymium. The luminescence spectrum of Cr^{3+} in GSGG at 300 K is represented by a wide electronic-vibrational band with a maximum at 750 nm (Fig. 8.14) (the

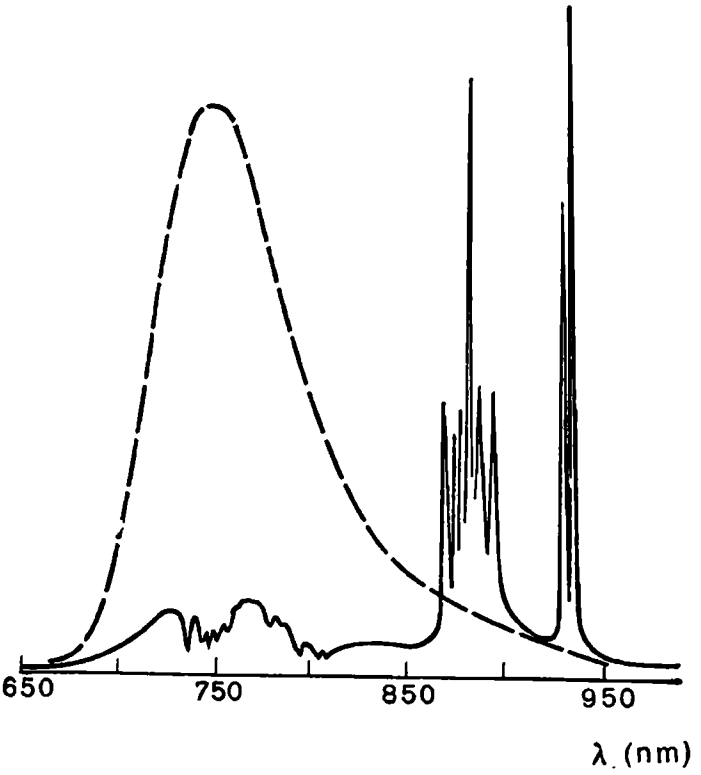

Fig. 8.14. Luminescence spectra of Cr^{3+} (dashed line) and Nd^{3+} (solid line) in GSGG crystals at 300 K.

$^4T_2 \rightarrow {}^4A_2$ transition on the diagram in Fig. 8.13) [8.34]. It is important that the luminescence from the ^2E-level, responsible for the R-lines of the Cr^{3+} luminescence spectrum, is completely absent due to a small energy gap ΔE between ^2E and $^4T_2$ ($\Delta E = 0$ cm^{-1}). A detailed analysis of the kinetics of the excited states of Cr^{3+} and Nd^{3+} has shown [8.34] that the $^4T_2Cr^{3+}$ level decays exponentially with a decay constant equal to 120 μsec and does not depend on the chromium concentration in a crystal up to 3×10^{20} cm^{-3} (Fig. 8.15). This fact is of considerable importance. It indicates that there is no concentration quenching of Cr^{3+} luminescence in GSGG. The introduction of the Nd^{3+} into the crystal leads to a sharp decrease in the decay time of $^4T_2$-level in Cr^{3+}. The decay becomes nonexponential

and can be described by the following expression:

$$I(t) = I_0 \exp[-(t/\tau_{Cr} + \gamma\sqrt{t} + \bar{w}t)], \quad (8.2)$$

where I_0 is the normalized luminescence intensity at the instant t_0,

$$\gamma = (4/3)\,\pi^{3/2} n_{Nd} \sqrt{C_{DA}} \quad (8.3)$$

is the $Cr^{3+} \rightarrow Nd^{3+}$ static interaction parameter, n_{Nd} the neodymium concentration, C_{DA} the $Cr^{3+} \rightarrow Nd^{3+}$ interaction microparameter, and $\bar{w} = 1/\tau_{meas} - 1/\tau_{Cr}$ the probability of the migration-induced relaxation of the $^4T_2$-state.

It was found that $\bar{w}$ increases linearly with the Cr^{3+} concentration. In accordance with formula (8.3), the parameter γ does not depend

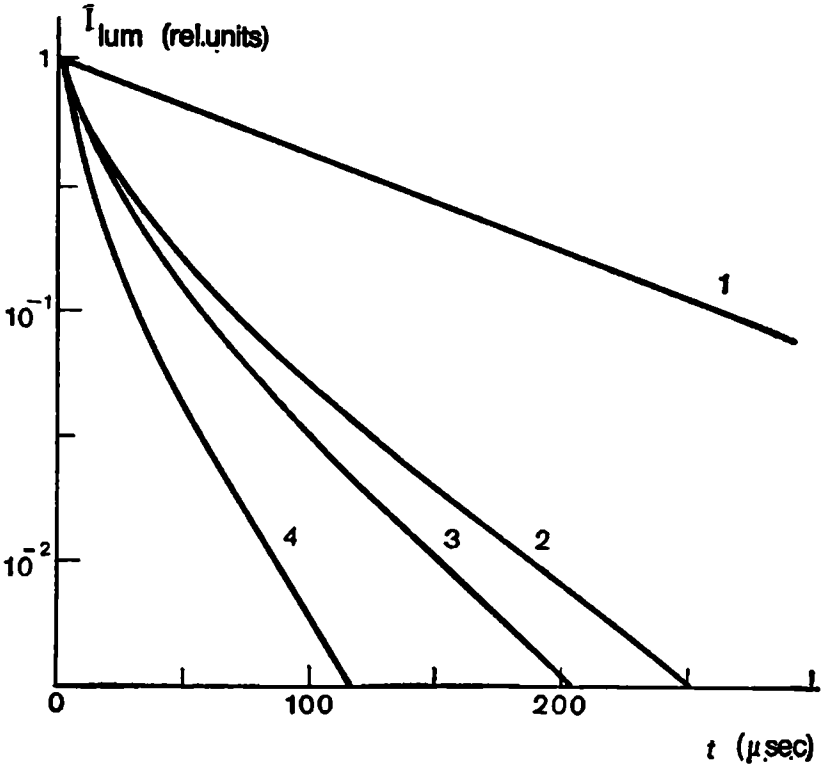

Fig. 8.15. Decay curves for the $^1T_2$ excited state of the Cr^{3+} ion in a GSGG-Cr^{3+} (*1*) and in a GSGG-Cr^{3+}-Nd^{3+} crystal with Cr^{3+} concentration 1×10^{20} and Nd^{3+} concentration 2×10^{20} (*2*), 3×10^{20} (*3*) and 6×10^{20} cm^{-3} (*4*).

on the Cr^{3+} ion concentration and is equal to 210 ± 20 sec^{-1}. This gives the value of 2×10^{-38} cm^6/sec for C_{DA}. A comparison of this value with the corresponding value for YAG-Cr^{3+}-Nd^{3+}, obtained in [8.35], shows that the value of C_{DA} for GSGG is 20 times higher than

for YAG and twice that for GGG. Thus, the energy transfer rate from Cr^{3+} to Nd^{3+} in a GSGG crystal is much higher than the activation rate for the upper working level $^4F_{3/2}$ in Nd^{3+}. The first experiments on lasing in GSGG-Cr^{3+}-Nd^{3+} were described in [8.36]. The discs cut from GSGG containing 1×10^{20} cm^{-3} Cr^{3+} and

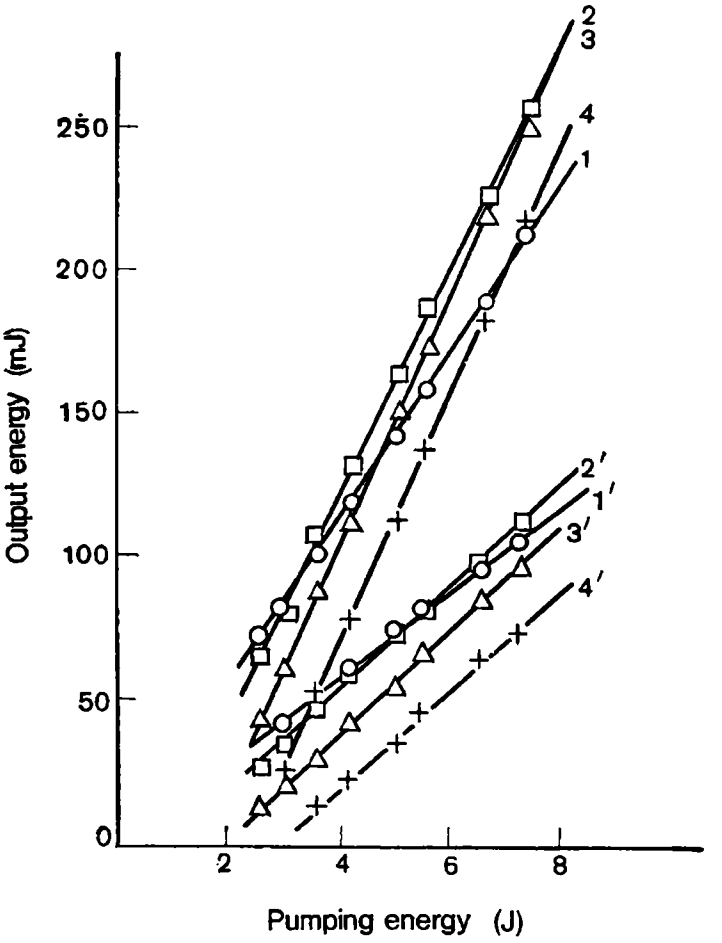

Fig. 8.16. Energy dependence for GSGG-Cr^{3+}-Nd^{3+} (*1*, *2*, *3*, *4*) and YAG-Nd^{3+} lasers (*1′*, *2′*, *3′*, *4′*) operating in free-running mode. The transmission of the output cavity mirror is 87% for *1* and *1′*, 66% for *2* and *2′*, 43% for *3* and *3′*, and 31% for *4* and *4′*.

2×10^{20} cm^{-3} Nd^{3+} were placed in a concentric resonator. The radius of curvature of the mirrors was 5 cm and their transmittivities 99 and 90% at $\lambda = 1.06$ μm. The pumping was carried out longitudinally by Kr laser radiation. The Kr 530.9 μm line was used for pumping to the Nd^{3+} band, while for the Cr^{3+} pumping, the 647.1μm line was used. CW lasing with the slope efficiencies $\eta_{Cr} = 41\%$ and $\eta_{Nd} = 36\%$ was observed in this case.

Lasing in GSGG-Cr^{3+}-Nd^{3+} crystals with nonselective single-pulse flash lamp pumping was investigated by Zharikov *et al.* [8.34, 37]. GSGG-Cr^{3+}-Nd^{3+} lasers operating on the frequency mode are described in [8.38]. The concentration of Cr^{3+} and Nd^{3+} ions was 2×10^{20} cm^{-3}. The element size was 5×50 mm^2. Plano-spherical resonator was used in this case. The 83 cm spherical mirror was opaque. The cavity was a silvered quartz monoblock with the outer diameter 20 mm. A xenon lamp with 3×45 mm^2 discharge gap was placed in it. The laser was cooled by running water. The pulse repetition rate was 20 pps. Figure 8.16 shows the dependence of the output energy on the pumping energy in the single-pulse free-running mode for different reflection coefficients of the plane output mirror for GSGG-Cr^{3+}-Nd^{3+} and YAG-Nd^{3+} lasers. It was not possible to obtain the pulse repetition rate of more than 20 pps with the help of the power supply used in this case. Significantly, the linearity of the output energy was not violated with increasing frequency. It can be seen from the figure that for the pumping energy of 7.3 J, the output energy of the GSGG-Cr^{3+}-Nd^{3+} laser was 255 mJ. In other words, the absolute efficiency of such a laser is 3.5%. At a pulse repetition rate of 20 pps, the average output power of 5 W was obtained for an average pumping power of 145 W. Under the experimental conditions, the slope efficiency of the GSGG laser was 4.5%, which is 2.4 times more than the efficiency of the YAG laser (Table 8.5). A consid-

Table 8.5. Comparison of Properties of Laser Crystals Containing Nd^{3+}

Crystal	Chemical formula	Nd^{3+} ion concentration, n (10^{20} cm^{-3})	Cr^{3+} ion concentration, n (10^{20} cm^{-3})	τ (μsec)	Initial gain, α (relative units)	Intracavity losses, $\varkappa$ (%)	σ (10^{-19} cm^2)	η (%)
YAC	$Y_3Al_5O_{12}$-Nd^{3+}	1.4	—	210	1	4.3	3.6	0.71
YAlO	$YAlO_3$-Nd^{3+}	5.7	—	60	0.5	6.3	1.4	1.3
SLM	$NaLa(MoO_4)_2$-Nd^{3+}	2.9	—	140	0.9	8.5	1.1	1.5
PGT	$KGd(WO_4)_2$-Nd^{3+}	1.8	—	140	2.5	3.0	4.3	1.4
GSGG	$(Gd,Nd)_3(Sc,Ga,Cr)_2Ga_3O_{12}$	2.0	2.0	240	1.9	10	1.4	2.5

erable increase in efficiency was also observed in the Q-switched mode (Fig. 8.17). An electrooptic Q-switch on the $LiNbO_3$ crystal cut at the Brewster angle was used in this case. A glass plate with interference coating was introduced into the cavity as a polarizer. The reflection coefficient of the plane output mirror was 43%. The

opaque spherical mirror and the pump had the same parameters as in previous experiments. The cavity length was 490 mm. A differential efficiency of 3% was attained under these conditions. For a pump-

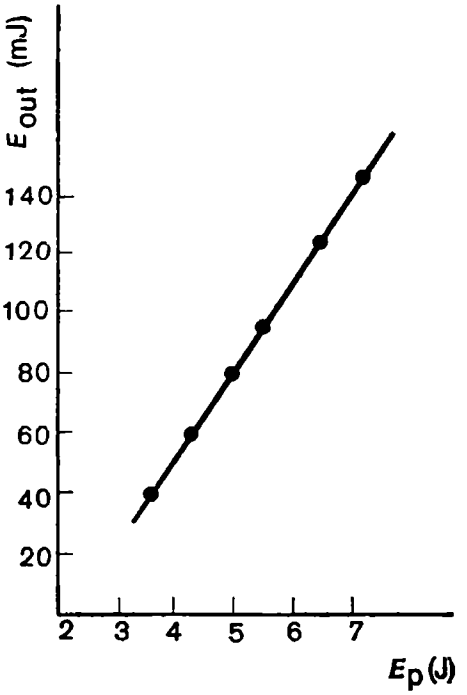

Fig. 8.17. Dependence of the energy of a giant pulse GSGG-Cr^{3+}-Nd^{3+} laser on the pumping energy.

ing energy of 7.3 J, the absolute efficiency amounted to 2%. This corresponds to an average output power of 2.9 W at a pumping energy of 145 W and a pulse repetition rate of 20 pps.

In conclusion, the authors express their gratitude to L. V. Kasatkina and E. O. Kirpichenkova for their help in preparing the manuscript.

References

8.1. B. Fritz and E. Menke, *Solid State Commun.*, 3, 61 (1965).
8.2. L. F. Mollenauer and D. H. Olson, Appl. Phys., 46, 3109 (1975).
8.3. R. Beigang, G. Litfin, and H. Welling, *Appl. Phys. Lett.*, 31, 381 (1977).
8.4. Yu. L. Gusev, S. N. Konoplin, and S. I. Marennikov, *Kvant. Electron.*, 4, 2024 (1977).
8.5. Yu. L. Gusev, S. I. Marennikov, and V. P. Chebotaev, *Pis'ma v Zh. Tekhn. Fiz.*, 3, 7, 305 (1977).
8.6. P. P. Feofilov and V. A. Arkhangel'skaya, *Izv. Akad. Nauk SSSR, Ser. Fiz.*, 45, 2, 302 (1981).
8.7. Yu. L. Gusev, S. I. Marennikov, and V. P. Chebotarev, *Izv. Akad. Nauk SSSR, Ser. Fiz.*, 44, 10, 2018 (1980).

8.8. I. A. Parfianovich, V. M. Khulugurov, B. D. Lobanov, and N. G. Maksimova, *Izv. Akad. Nauk SSSR, Ser. Fiz.*, 43, 6, 1125 (1979).
8.9. L. F. Mollenauer, *Opt. Lettr.*, 1, 164 (1977).
8.10. R. Beigang, G. Litfin, and H. Welling, *Opt. Commun.*, 22, 3, 269 (1977).
8.11. V. M. Khulugurov and B. D. Lobanov, *Pis'ma v Zh. Tekhn. Fiz.*, 4, 24, 1471 (1978).
8.12. T. T. Basiev, S. B. Mirov, and A. M. Prokhorov, *Dokl. Akad. Nauk SSSR*, 246, 72 (1979).
8.13. T. T. Basiev, Yu. K. Voron'ko, S. B. Mirov, V. V. Osiko, and A. M. Prokhorov, *Pis'ma v Zh. Tekhn. Fiz.*, 30, 661 (1979).
8.14. T. T. Basiev, Vu. K. Voron'ko, E. O. Kirpichenkova, S. B. Mirov, V. V. Osiko, M. S. Soskin, and V. B. Taranenko, *Kvant. Elektron.*, 8, 2, 419 (1981).
8.15. T. T. Basiev, N. S. Vorob'ev, S. B. Mirov *et al.*, *Pis'ma v Zh. Eksp. Teor. Fiz.*, 31, 5, 316 (1980).
8.16. T. T. Basiev, Yu. K. Voron'ko, S. B. Mirov *et al.*, *Proc. of the 3rd All-Union Conf. on Laser Optics, Abstracts*, Leningrad, 1982, p. 21.
8.17. G. B. Adbullaev, T. T. Basiev, Yu. K. Voron'ko *et al.*, *Proc. of the 10th All-Union Conf. on Lasers and Nonlinear Optics*, Kiev, 1980.
8.18. B. I. Denker, V. V. Osiko, P. P. Pashinin, and A. M. Prokhorov, *Vestnik Akad. Nauk SSSR*, 6, 75, (1982).
8.19. Yu. K. Voron'ko, V. V. Osiko, and I. A. Shcherbakov, *Zh. Eksp. Teor. Fiz.*, 55, 1598 (1968).
8.20. H. G. Danielmeyer and H. P. Weber, *IEEE J.*, QE-8, 805 (1972).
8.21. H. P. Weber, T. C. Damen, H. G. Danielmeyer, and B. C. Tofield, *Appl. Phys. Lettr.*, 22, 534 (1973).
8.22. I. A. Bondar', B. I. Denker, A. I. Domanskii *et al.*, *Kvant. Elektron.*, 4, 2, 302 (1977).
8.23. B. I. Denker, V. V. Osiko, P. P. Pashinin, and A. M. Prokhorov, *Kvant. Elektron.*, 8, 3, 469 (1981).
8.24. Yu. K. Voron'ko, B. I. Denker, A. A. Zlenko *et al.*, *Dokl. Akad. Nauk SSSR*, 227, 75 (1976).
8.25. S. Kh. Batygov, Yu. K. Voron'ko, B. I. Denker *et al.*, *Kvant. Elektron.*, 3, 2243 (1976).
8.26. B. I. Denker, V. V. Osiko, A. M. Prokhorov, and I. A. Scherbakov, *Kvant. Elektron.*, 5, 847 (1978).
8.27. K. L. Vodop'yanov, B. I. Denker, N. N. Il'ichev *et al.*, *Kvant. Elektron.*, 8, 1595 (1981).
8.28. A. G. Avanesov, Yu. K. Voron'ko, B. I. Denker *et al.*, *Proc. of the 2nd All-Union Conf. on Laser Optics*, Leningrad, 1980.
8.29. Z. T. Kiss and R. C. Duncan, *Appl. Phys. Lettr.*, 5, 200 (1964).
8.30. H. D. Hattendorf, G. Huber, and F. Lutz, *Appl. Phys. Lett.*, 34, 437 (1979).
8.31. V. V. Osiko, A. M. Prokhorov, and I. A. Shcherbakov, *Izv. Akad. Nauk SSSR, Ser. Fiz.*, 44, 1698 (1980).
8.32. A. G. Avanesov, Yu. K. Voron'ko, B. I. Denker *et al.*, *Kvant. Elektron.*, 6, 1583 (1979).
8.33. E. V. Zharikov, N. N. Il'ichev, V. V. Laptev *et al.*, *Kvant. Elektron.*, 9, 568 (1982).
8.34. E. V. Zharikov, N. N. Il'ichev, V. V. Laptev *et al.*, *Kvant. Elektron.*, 10, 1, 140 (1983).
8.35. A. G. Avanesov, B. I. Denker, V. V. Osiko *et al.*, *Kvant. Elektron.*, 9, 681 (1982).

8.36. D. Pruss, G. Huber, A. Beimowski, V. V. Laptev, I. A. Shcherbakov, and E. V. Zharikov, *Appl. Phys.*, **B28**, 1 (1982).
8.37. E. V. Zharikov, V. A. Zhitnyuk, G. M. Zverev *et al.*, *Kvant. Elektron.*, **9**, 12, 2531 (1982).
8.38. E. V. Zharikov, M. B. Zhitkova, G. M. Zverev *et al.*, *Preprint FIAN* No. 162, 1963.
8.39. T. Kulinksi, F. Kaczmarek, M. Ludwiczak, and Z. Blaszszak, *Opt. Com.*, **35**, 120 (1980).
8.40. T. T. Basiev, Yu. K. Voron'ko, V. D. Dmitriev *et al.*, *Proc. 10th All-Union Conf. on Lasers and Nonlinear Optics*, Kiev, 1980, part I, p. 278.

9 Etching of Polymers in Quantum- and Particle Flux

T. M. Makhviladze, A. M. Prokhorov, K. A. Valiev, and L. V. Velikov

9.1. INTRODUCTION

In the last few years, several authors have reported the effect of direct etching of polymer films by vacuum ultraviolet (VUV) [9.1, 2] and X-ray [9.3] radiation, as well as by electron [9.4, 5] and ion [9.6] beams. The VUV etching effect was independently observed by the authors of [9.7]. The photoetching of polymers in the radiation field of an excimer laser with wavelength 193 nm was reported in [9.8]. In an earlier work [9.9], the indirect results on the change in optical properties of exposed polymer films led to the conclusion on their degradation under the action of VUV radiation. The observed effects are of great practical importance in view of the possibility of using them in the submicron lithography and for a dimensional treatment of polymer films [9.1-3]. The main theoretical concepts on the direct etching of polymers were developed in [9.10] on the basis of VUV- and X-ray etching.

In any method of radiational treatment of a polymer, the observed effect is due to destruction of polymer molecules and diffusive and thermal processes occurring in the polymer film and involving molecular fragments. At large radiation intensities the thermal mechanism of etching dominates, when the film is heated as a result of absorption of radiant energy, leading to thermal decomposition of polymer molecules and evaporation of molecular fragments of the polymer from its surface. The diffusion mechanism which plays a dominating role at low intensities can be described as follows. The elementary acts of interaction of external radiation with polymer molecules lead to a scission of the molecular bonds and to a decrease in the molecular weight of the polymer. The destruction of a polymer (in the bulk of the film) is associated with the creation of fragments with lower molecular weight, which are capable of moving diffusively in the polymer. Having arrived at the surface of the film, these molecular fragments fly out to the surroundings. The diffusion of the fragment is limited by the reactions involving the recombination of fragments with other particles of the medium. Thus, at low radiation intensities, the final result of the absorption of the radiation energy is again a degradation of the film whose rate is determined by the balance between the diffusion and recombination processes.

The basic mechanisms of etching of polymers by electromagnetic and corpuscular fluxes of low intensity (diffusive etching) have been described in [9.10]. These results, however, correspond only to two limiting cases of surface and volume absorption of radiation. In the first case, $\alpha^{-1} \ll h_0$, while in the second case, $\alpha^{-1} \gg h_0$, where h_0 is the initial thickness of the film and α is the absorption coefficient (the reciprocal of the corpuscular mean free path). This complicates a qualitative comparison between the theory and the experiment, especially in the case of X-ray etching, since the inequality $h_0\alpha \gg 1$ was not always satisfied in our experiments. Besides, the authors of [9.10] employed the model of a semi-infinite layer, which does not take into account the real geometric parameters of the experiment, although it leads to qualitatively correct results under the limiting conditions mentioned above.

In this paper, we shall present the results of detailed theoretical and experimental investigations of diffusive etching of polymer films. The first part (Secs. 9.2-9.5) describes the theory of diffusive etching, generalizing the results given in [9.9] and permitting a detailed comparison with the experimental results. The theoretical results obtained in the approximation of a step functional dependence of the radiation intensity on the film thickness are equally applicable in the case of photoetching of polymer films as well as in the case of etching by corpuscular fluxes of low intensity. Section 9.2 contains the model assumptions and the initial boundary-value problems which form the basis of the theory. Next, the solution of these boundary-value problems has been given for a uniform (Sec. 9.3) and nonuniform (Sec. 9.4) exposure of polymer films. The basic expression for the etching rate, taking into account the real, geometric parameters of the experiment and the gradual modification of the polymer during exposure, is obtained in Sec. 9.5. The rate of the process for the final etching stage, when the film becomes thin, is also found in this section. The second part of this paper (Secs. 9.6 and 9.7) describes the experiments on diffusive etching and gives a comparison of the experimental results with the theory. The experimental results pertain to photoetching by X-ray (Sec. 9.6) and VUV radiation (Sec. 9.7), since these experiments do not involve any heating of the film. A discussion of the results concludes this review.

9.2. BASIC EQUATIONS OF DIFFUSIVE ETCHING

The destruction of molecules as a result of a scission of polymer bonds due to absorption of quanta of external radiation or an inelastic scattering of particles in an external corpuscular flux is the primary process behind etching. The number of volatile fragments of molecules per unit time in a unit volume of the polymer is

proportional to the density of the energy absorbed from an external source:

$$G_1(x) = g\alpha(x) I(x), \tag{9.1}$$

where $I(x)$ is the intensity of radiation J/(cm^2·sec), g the yield of volatile fragments, i.e. the number of fragments formed per joule of the absorbed energy. The quantities appearing in (9.1) depend only on the coordinate x which gives the position of the polymer layer parallel to the exposed polymer surface (the x-axis is directed into the polymer).

The linear relation (9.1) between $G_1(x)$ and $I(x)$ is valid for comparatively weak radiation fluxes, when the yield g of the fragments does not depend on $I(x)$. Besides, for small values of $I(x)$, the density n of volatile fragments is much lower than the density n_p of the polymer molecules. Hence, the main contribution to the absorption is made by the polymer molecules:

$$\alpha(x) = \sum_i n_i \sigma_i \simeq \sigma_p n_p, \tag{9.2}$$

where σ_i is the absorption cross section of the radiation by the i-th component of the medium (for example, by a polymer molecule, a volatile fragment, or one of the intermediate products of a radical reaction); and n_i the density of the i-th component. In view of the condition $n_p \gg n$, we can also neglect the effect of depolymerization on n_p leading to the formation of volatile fragments, as well as the effect of recombination processes (polymerization leading to annihilation of fragments), and consider n_p to be constant over the entire thickness of the film. Thus, $G_1(x)$ is a function of the coordinate x only due to the spatial dependence of the intensity $I(x)$, while the recombination rate constant G_2 for the volatile fragments, which determines the number $G_2 n$ of the fragments recombining per unit time per unit volume, is constant (see [9.10] for details). The quantities σ_p, $\alpha(x)$, I, G_1, g depend only on the radiation frequency (or energy in the case of corpuscular fluxes). Henceforth, by the values of these quantities we shall mean their average over the spectral distribution of the radiation source.

In the step dependence approximation of intensity on the film thickness,

$$I(x) = \begin{cases} I & \text{for } x_{sf} \leqslant x \leqslant x_{sf} + \delta, \\ 0 & \text{for } x_{sf} + \delta < x \leqslant x_{sb}, \end{cases}$$

where I is the input intensity, x_{sf} is the running coordinate of the exposed film surface, $\delta = \alpha^{-1}$ (α is the absorption coefficient determining the decrease in intensity with thickness according to the approximation (9.2)), x_{sb} the coordinate of the film surface adjoining

the substrate, the kinetic equations for the density of volatile fragments have the following form:

$$\frac{\partial n}{\partial t} = D\frac{\partial^2 n}{\partial x^2} + G_1 - G_2 n \quad (x_{sf} \leqslant x \leqslant x_{sf} + \delta), \tag{9.3}$$

$$\frac{\partial n}{\partial t} = D\frac{\partial^2 n}{\partial x^2} - G_2 n \quad (x > x_{sf} + \delta), \tag{9.4}$$

where D is the diffusion coefficient for the volatile fragments.

A peculiar feature of the problem under consideration is that the boundary conditions are formulated on the surfaces which move with a velocity equal to the etching rate $u(t)$:

$$D\frac{\partial n}{\partial x}\Big|_{x=x_{sf}} = v_0 n|_{x=x_{sf}}, \tag{9.5}$$

$$n|_{x=x_{sf}+\delta-0} = n|_{x=x_{sf}+\delta+0}, \tag{9.6}$$

$$D\frac{\partial n}{\partial x}\Big|_{x=x_{sf}+\delta-0} = D\frac{\partial n}{\partial x}\Big|_{x=x_{sf}+\delta+0}, \tag{9.7}$$

where the current coordinate x_{sf} of the exposed surface film is determined by the expression

$$x_{sf} = x_0 + \int_0^t u(t')\,dt',$$

x_0 is the position of the film surface at the initial instant of time, v_0 the velocity with which the volatile fragments cross the exposed surface. The relation (9.5) represents the continuity conditions for the flux of molecular fragments on the mobile etching surface. The relations (9.6) and (9.7) are the continuity conditions for the density of fragments and their diffusion fluxes on the lower boundary of the absorbing polymer layer. Besides, we can also use the condition that there is no diffusion flux at $x = x_{sb}$:

$$D\frac{\partial u}{\partial x}\Big|_{x=x_{sb}} = 0. \tag{9.8}$$

The additional condition for determining the rate of motion of the irradiated surface is the mass conservation law for the substance on the etching surface:

$$\rho u(t) = m v_0 n|_{x=x_{sf}}, \tag{9.9}$$

where ρ is the polymer density and m the mass of the molecular fragment.

Henceforth, we shall be interested in such solutions of the boundary-value problem (9.3)-(9.9) which describe the experimentally observed steady-state etching process. It was shown in [9.10] that in the semi-infinite layer model corresponding to the case $x_{sb} = \infty$,

such solutions in the limiting cases of surface- and volume absorption are the stationary solutions of the boundary-value problem (9.3)-(9.9) written in the coordinate system which moves along with the exposed surface. Steady-state solutions only exist for a moving system. In the laboratory coordinate system they correspond to the density waves of volatile fragments, which move at a constant velocity and retain their shape as they propagate. Hence, the boundary-value problem (9.3)-(9.9) with a finite value of x_{sb} should be formulated in a coordinate system fixed to the etching surface. A transition to this system with the help of the coordinate transformation

$$\xi = x - x_{sf} = x - \left(x_0 + \int_0^t u(t')\,dt'\right), \quad t' = t,$$

leads to the following equations:

$$\frac{\partial n}{\partial t} - u\frac{\partial n}{\partial \xi} = D\frac{\partial^2 n}{\partial \xi^2} + G_1 - G_2 n \quad (0 \leqslant \xi \leqslant \delta), \tag{9.10}$$

$$\frac{\partial n}{\partial t} - u\frac{\partial n}{\partial \xi} = D\frac{\partial^2 n}{\partial \xi^2} - G_2 n \quad \left(\delta \leqslant \xi \leqslant h_0 - \int_0^t u(t')\,dt'\right), \tag{9.11}$$

and the boundary conditions

$$D\frac{\partial n}{\partial \xi}\Big|_{\xi=0} = v_0 n|_{\xi=0}, \tag{9.12}$$

$$n|_{\xi=\delta-0} = n|_{\xi=\delta+0}, \tag{9.13}$$

$$\frac{\partial n}{\partial \xi}\Big|_{\xi=\delta-0} = \frac{\partial n}{\partial \xi}\Big|_{\xi=\delta+0}, \tag{9.14}$$

$$\frac{\partial n}{\partial \xi}\Bigg|_{\xi=h_0-\int_0^t u(t')\,dt'} = 0, \tag{9.15}$$

$$\rho u(t) = m v_0 n|_{\xi=0}, \tag{9.16}$$

where $h_0 = x_{sb} - x_{sf}$ is the initial thickness of the polymer film.

In the semi-infinite layer model ($h_0 = \infty$), stationary solutions of the boundary-value problem (9.10)-(9.16) exist at $\partial/\partial t \equiv 0$ and $u = \text{const}$. Such solutions are obtained after a certain transition time t_{tr} [9.10]. Strictly speaking, such solutions do not exist for a finite value of h_0, since time enters explicitly into the boundary condition (9.15). However, we can consider the quasistationary solution of this problem by putting $\partial/\partial t \equiv 0$ and $u = \text{const}$ in Eqs. (9.10)-(9.16). It follows from Eq. (9.15) that such solutions are valid under the condition $ut \ll h_0$, which means that the magnitude of the etched polymer layer is small in comparison to the initial film thickness. Thus, the quasistationary solutions describing the steady-state

etching are valid in the time interval

$$t_{tr} \ll t \ll h_0/u. \tag{9.17}$$

It will be seen later that under actual experimental conditions, such solutions are valid practically for the entire duration of the etching process with the exception of a negligible initial period, as well as final period of residual etching where the boundary-value problem (9.10)-(9.15) is no longer valid and new initial equations are required (see Sec. 9.5). Thus, the quasistationary solutions in which we are interested are valid in the time interval (9.17) and satisfy the following equations:

$$-u\frac{dn}{d\xi} = D\frac{d^2n}{d\xi^2} + G_1 - G_2 n \quad (0 \leqslant \xi \leqslant \delta), \tag{9.18}$$

$$-u\frac{dn}{d\xi} = D\frac{d^2n}{d\xi^2} - G_2 n \quad (\delta \leqslant \xi \leqslant h_0), \tag{9.19}$$

$$D\frac{dn}{d\xi}\Big|_{\xi=0} = v_0 n|_{\xi=0}, \tag{9.20}$$

$$n|_{\xi=\delta-0} = n|_{\xi=\delta+0}, \tag{9.21}$$

$$\frac{dn}{d\xi}\Big|_{\xi=\delta-0} = \frac{dn}{d\xi}\Big|_{\xi=\delta+0}, \tag{9.22}$$

$$\frac{dn}{d\xi}\Big|_{\xi=h_0} = 0, \tag{9.23}$$

$$\rho u = m v_0 n|_{\xi=0}. \tag{9.24}$$

Equations (9.18)-(9.24) are valid for $\alpha^{-1} < h_0$. For $\alpha^{-1} \geqslant h_0$, the generation of molecular fragments over the entire volume of the polymer film takes place at the same rate $G_1 = g\delta_p n_p I$. In this case, it can be easily shown that if the condition (9.17) is satisfied, the quasistationary solutions satisfy the following equations:

$$-u\frac{dn}{d\xi} = D\frac{d^2n}{d\xi^2} + G_1 - G_2 n \quad (0 \leqslant \xi \leqslant h_0), \tag{9.25}$$

$$D\frac{dn}{d\xi}\Big|_{\xi=0} = v_0 \cdot n|_{\xi=0}, \tag{9.26}$$

$$\frac{dn}{d\xi}\Big|_{\xi=h_0} = 0, \tag{9.27}$$

$$\rho u = m v_0 n|_{\xi=0}. \tag{9.28}$$

We shall begin our consideration of the solutions of the equations in the quasistationary approximation from the case when the absorption length α^{-1} is more than the film thickness h_0.

9.3. ETCHING UPON A UNIFORM EXPOSURE OF A POLYMER

In accordance with Eqs. (9.25)-(9.27), the distribution of the density of fragments has the form

$$n(\xi)=\frac{G_1}{G_2}\left\{1+A^{-1}\left[\exp(\lambda_1\xi)-\frac{\lambda_1}{\lambda_2}\exp((\lambda_1-\lambda_2)h_0)\right]\exp(\lambda_2\xi)\right\}, \tag{9.29}$$

where

$$\lambda_1=-\frac{u}{2D}\left(1-\sqrt{1+\frac{4DG_2}{u^2}}\right),$$
$$\lambda_2=-\frac{u}{2D}\left(1+\sqrt{1+\frac{4DG_2}{u^2}}\right). \tag{9.30}$$

The coefficient A defined as

$$A=\frac{D\lambda_1}{v_0}-1+\frac{\lambda_1}{\lambda_2}\left(1-\frac{D\lambda_2}{v_0}\right)\exp[(\lambda_1-\lambda_2)h_0], \tag{9.31}$$

is negative for any values of the parameters D, v_0, G_2, and u. Indeed, since $\lambda_1>0$, $\lambda_2<0$, and $\lambda_1-\lambda_2>0$, we get

$$A<\frac{D\lambda_1}{v_0}-1+\frac{\lambda_1}{\lambda_2}\left(1-\frac{D\lambda_2}{v_0}\right)=\frac{\lambda_1}{\lambda_2}-1<0. \tag{9.32}$$

It follows hence that the density $n(\xi)$ of the fragments for $0\leqslant\xi\leqslant h_0$ is a function which monotonically increases with thickness:

$$\frac{dn(\xi)}{d\xi}=\frac{G_1}{G_2}\lambda_1A^{-1}\exp(\lambda_1\xi)\{1-\exp[(\lambda_1-\lambda_2)(h_0-\xi)]\}\geqslant 0,$$

attaining its maximum value at $\xi=h_0$. The increase in the fragment density with the polymer thickness is given by the characteristic diffusion length

$$l_D=\frac{2D}{u}\left(1+\sqrt{1+\frac{4DG_2}{u^2}}\right)^{-1},$$

which has the sense of such a thickness of the diffusion layer from which the volatile fragments can arrive at the exposed surface during their lifetime limited by the recombination processes.

Considering the fragment density $n(\xi)$ as a function of the initial film thickness h_0, we can show that for any fixed value of ξ, the fragment density increases with h_0. Indeed, according to (9.29), (9.30), and (9.32), the sign of the derivative $dn(\xi)/dh_0$ is the same as the sign of the expression

$$B=\left(\frac{D\lambda_1}{v_0}-1\right)+\left(1-\frac{D\lambda_2}{v_0}\right)\exp[(\lambda_1-\lambda_2)h_0],$$

which is positive for any values of the parameters entering it:

$$B > \left(\frac{D\lambda_1}{v_0} - 1\right) + \left(1 - \frac{D\lambda_2}{v_0}\right) = \frac{D}{v_0}(\lambda_1 - \lambda_2) > 0.$$

A rise in the value of n (ξ) with h_0 is due to an increase in the diffusion flux towards the irradiated surface as a result of a uniform absorption of the incident radiation over the entire thickness of the film. In the limit of an infinite thickness of the film ($h_0/l_D \to \infty$), the formula (9.29) is transformed into the corresponding result for the semi-infinite layer model [9.10]:

$$n(\xi) = \frac{G_1}{G_2}\left[1 - \left(1 + \frac{D}{v_0 l_D}\right)^{-1} \exp\left(-\xi/l_D\right)\right],$$

which determines the maximum possible fragment density in each polymer layer for given values of G_1, G_2, D, and v_0. The n vs. ξ dependence for different initial thicknesses are shown in Fig. 9.1.

According to Eqs. (9.28) and (9.29), the etching rate u satisfies the equation

$$u = \frac{m}{\rho} v_0 \frac{G_1}{G_2}\left\{1 + A^{-1}\left[1 - \frac{\lambda_1}{\lambda_2}\exp\left((\lambda_1 - \lambda_2)\, h_0\right)\right]\right\}, \qquad (9.33)$$

where the dependences of λ_1, λ_2, and A on u are determined by the formulas (9.30) and (9.31).

Estimates show that the following inequalities are satisfied under experimental conditions:

$$u/\sqrt{4DG_2} \ll 1 \qquad (9.34)$$

and

$$\sqrt{DG_2}/v_0 \ll 1. \qquad (9.35)$$

From these inequalities, it follows that $u \ll v_0$. Indeed, according to (9.28),

$$\frac{u}{v_0} = \frac{m}{M}\left(n|_{\xi=0}/n_p\right),$$

where M is the mass of a polymer molecule. Since $M \gg m$ and $n_p \gg n$, we get $u \ll v_0$ (according the experimental data, $u \simeq 10^{-8}$ cm/sec, and v_0 is of the order of thermal velocity of the molecules).

Using the fact that parameter (9.34) is negligibly small, we can obtain an explicit expression for etching rate from Eq. (9.33):

$$u = \frac{m}{\rho} v_0 \frac{G_1}{G_2} \frac{D}{v_0 l_D + D}\left\{\left[\exp\left(2h_0/l_D\right) - \frac{D/l_D - v_0}{D/l_D + v_0}\right]^{-1} \times \left[\exp\left(2h_0/l_D - 1\right)\right]\right\}, \qquad (9.36)$$

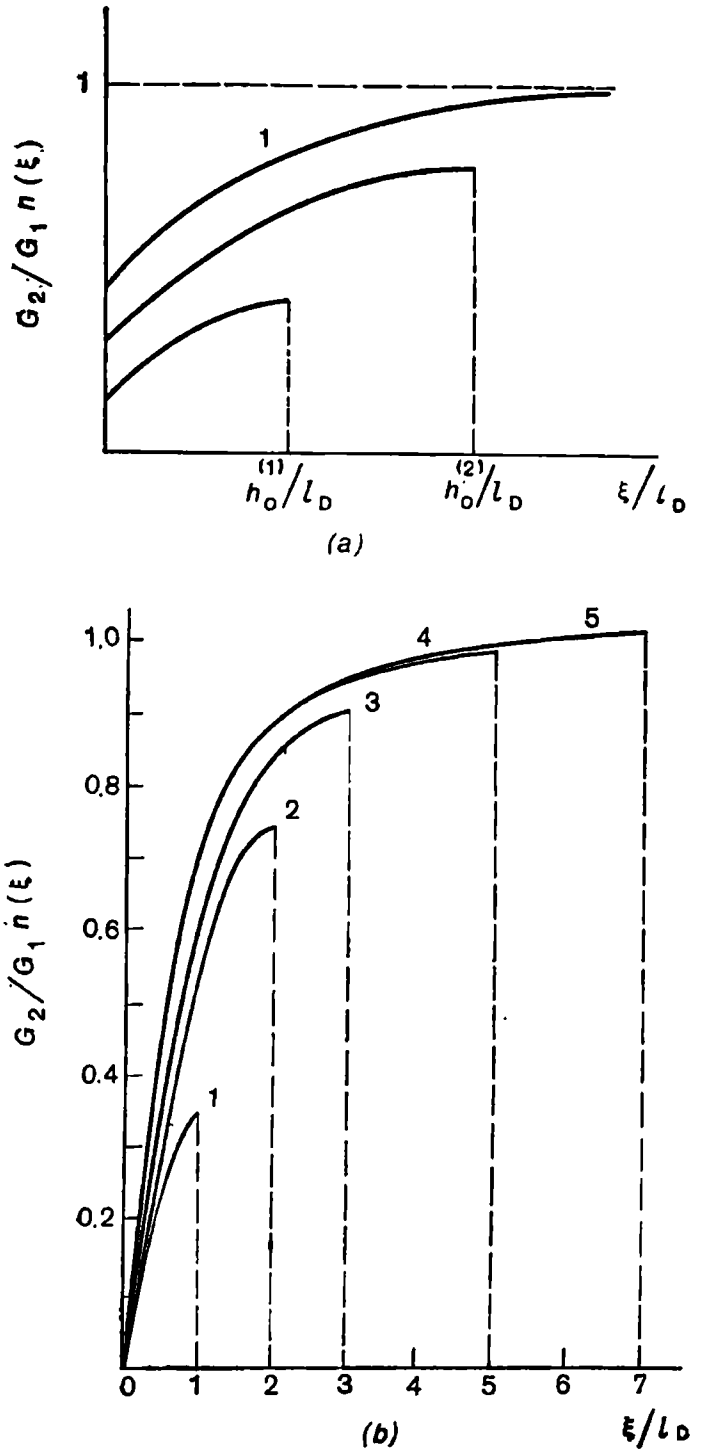

Fig. 9.1. Density distribution of low-molecular fragments for different thicknesses of the polymer film (uniform exposure):
(*a*) general form of the $(G_2/G_1)\,n$ vs. ξ dependence (curve *1* corresponds to the semi-infinite layer model $h_0/l_D = \infty$); (*b*) results of numerical calculations for the $(G_2/G_1)\,n$ vs. ξ distribution under the condition (9.35): curve *1*—$h_0/l_D = 1$, *2*—$h_0/l_D = 2$, *3*—$h_0/l_D = 3$, *4*—$h_0/l_D = 5$, *5*—$h_0/l_D = 7$.

where $l_D = (D/G_2)^{1/2}$. In the limit $h_0/l_D \to \infty$, the formula (9.36) gives the etching rate or a semi-infinite layer exposed to uniform radiation [9.10]:

$$u_0 = \frac{m}{\rho} v_0 G_1 \frac{\sqrt{D/G_2}}{v_0 + \sqrt{DG_2}}. \tag{9.37}$$

Hence, the expression in the parentheses in Eq. (9.36) takes into account the difference between the etching rate and the quantity u_0 for a polymer film of finite dimensions. It can be easily shown that this expression increases monotonically with h_0, attaining its maximum value of unity as $h_0 \to \infty$. Thus, the etching rate increases with the initial thickness of the film. This rise is due to the above-mentioned increase in the diffusion flux of volatile fragments with h_0 when the film is uniformly irradiated.

If the inequality (9.35) is satisfied, Eqs. (9.36) and (9.37) are reduced to the simple form

$$u = u_0 \tanh (h_0/l_D), \tag{9.38}$$

where

$$u_0 = \frac{m}{\rho} G_1 l_D. \tag{9.39}$$

It follows from the formulas obtained above that the fragment density $n|_{\xi=0}$ on the irradiated surface, and hence the etching rate u, increases linearly with G_1 (i.e. with the radiation intensity), decreases monotonically with an enhancement of the recombination processes, and increases with diffusion coefficient (or with the thickness of the diffusion layer).

9.4. ETCHING UPON A NONUNIFORM EXPOSURE OF A POLYMER

If the exposure is nonuniform ($\alpha^{-1} = \delta \leqslant h_0$), the distribution of fragment density is described by Eqs. (9.18)-(9.24). According to Eqs. (9.19) and (9.23), we get for the unexposed layer of the polymer ($\delta \leqslant \xi \leqslant h_0$)

$$n(\xi) = B_1 \left\{ \exp(\lambda_2 \xi) - \frac{\lambda_2}{\lambda_1} \exp(\lambda_1 \xi) \exp[(\lambda_2 - \lambda_1) h_0] \right\}, \tag{9.40}$$

where λ_1 and λ_2 are determined from the relation (9.30), and B_1 is a constant. In the exposed layer of the polymer, we get, in view of Eq. (9.28),

$$n(\xi) = C \exp(\lambda_1 \xi) + F \exp(\lambda_2 \xi) + \frac{G_1}{G_2} \quad (0 \leqslant \xi \leqslant \delta). \tag{9.41}$$

From the condition (9.20) of continuity of the diffusion flux on the exposed surface, and the conditions (9.21) and (9.22) for matching

the solutions, we can find the constants entering into Eqs. (9.40) and (9.41):

$$B_1 = \{\lambda_2 \exp(\lambda_2\delta) - \lambda_2 \exp(\lambda_1\delta) \exp[(\lambda_2 - \lambda_1) h_0]\}^{-1}$$
$$\times \left\{\frac{G_1}{G_2}\lambda_2\left(\frac{D\lambda_2}{v_0} - 1\right)^{-1} \exp(\lambda_2\delta)\right.$$
$$\left. + C\left[\lambda_1 \exp(\lambda_1\delta) + \lambda_2\left(1 - \frac{D\lambda_1}{v_0}\right)\left(\frac{D\lambda_2}{v_0} - 1\right)^{-1} \exp(\lambda_2\delta)\right]\right\}, \quad (9.42)$$

$$F = \frac{G_1}{G_2}\left(\frac{D\lambda_2}{v_0} - 1\right)^{-1}\left[1 + \frac{G_2}{G_1}\left(1 - \frac{D\lambda_1}{v_0}\right) C\right], \quad (9.43)$$

$$C = \frac{G_1}{G_2}\left\{1 + \left(\frac{D\lambda_2}{v_0} - 1\right)^{-1} \exp(\lambda_2\delta) - \left(\frac{D\lambda_2}{v_0} - 1\right)^{-1} \exp(\lambda_2\delta)\, g_1\right\}$$
$$\times \left\{\left[\frac{\lambda_1}{\lambda_2} \exp(\lambda_1\delta) + \left(1 - \frac{D\lambda_1}{v_0}\right)\left(\frac{D\lambda_2}{v_0} - 1\right)^{-1} \exp(\lambda_2\delta)\right] g_1\right.$$
$$\left. - \left[\exp(\lambda_1\delta) + \left(1 - \frac{D\lambda_1}{v_0}\right)\left(\frac{D\lambda_2}{v_0} - 1\right)^{-1} \exp(\lambda_2\delta)\right]\right\}^{-1}, \quad (9.44)$$

where

$$g_1 = \left\{\exp(\lambda_2\delta) - \frac{\lambda_2}{\lambda_1} \exp[(\lambda_2 - \lambda_1) h_0] \exp(\lambda_1\delta)\right\}$$
$$\times \{\exp(\lambda_2\delta) - \exp(\lambda_1\delta) \exp(\lambda_2 - \lambda_1) h_0]\}^{-1}. \quad (9.45)$$

According to Eq. (9.24), the etching rate u satisfies the condition

$$u = \frac{m}{\rho}\frac{G_1}{G_2} v_0 \left(1 - \frac{v_0}{D\lambda_2}\right)^{-1} g_2, \quad (9.46)$$

where

$$g_2 = 1 + \frac{\lambda_2 - \lambda_1}{\lambda_2}\left\{1 - \left(\frac{D\lambda_2}{v_0} - 1\right) \exp(\lambda_2\delta)\,(1 - g_1)\right\}$$
$$\times \left\{\exp(\lambda_1\delta)\left(\frac{\lambda_1}{\lambda_2} g_1 - 1\right)\right.$$
$$\left. - \left(1 - \frac{D\lambda_1}{v_0}\right)\left(\frac{D\lambda_2}{v_0} - 1\right)^{-1}(1 - g_1) \exp(\lambda_2\delta)\right\}^{-1}. \quad (9.47)$$

Since it is assumed that the condition (9.34) is satisfied, we can put

$$\lambda_1 = -\lambda_2 = 1/l_D \quad (9.48)$$

in formulas (9.42)-(9.44) and reduce them to a simpler form:

$$B_1 = \{\exp[-(2h_0 - \delta)/l_D] - \exp[-\delta/l_D]\}^{-1}$$
$$\times \left\{\frac{G_1}{G_2}\left(\frac{D}{v_0 l_D} + 1\right)^{-1} \exp(-\delta/l_D)\right.$$
$$\left. + C\left[\exp(\delta/l_D) + \left(1 - \frac{D}{v_0 l_D}\right)\left(\frac{D}{v_0 l_D} + 1\right)^{-1} \exp(-\delta/l_D)\right]\right\}, \quad (9.49)$$

$$F = -\frac{G_1}{G_2}\left(1+\frac{D}{v_0 l_D}\right)^{-1}\left[1+\frac{G_2}{G_1}\left(1-\frac{D}{v_0 l_D}\right)C\right], \tag{9.50}$$

$$C = \frac{G_1}{G_2}\left\{1-\left(\frac{D}{v_0 l_D}+1\right)^{-1}\exp\left(-\delta/l_D\right)+\left(\frac{D}{v_0 l_D}+1\right)^{-1}\right.$$
$$\times\exp\left(-\delta/l_D\right)\coth\left(\frac{h_0-\delta}{l_D}\right)\Big\}\Big\{\Big[\left(\frac{D}{v_0 l_D}-1\right)\left(\frac{D}{v_0 l_D}+1\right)^{-1}$$
$$\times\exp\left(-\delta/l_D\right)-\exp\left(\delta/l_D\right)\Big]\coth\left(\frac{h_0-\delta}{l_D}\right)-\exp\left(\delta/l_D\right)$$
$$\left.-\left(\frac{D}{v_0 l_D}-1\right)\left(\frac{D}{v_0 l_D}+1\right)^{-1}\exp\left(-\delta/l_D\right)\right\}^{-1}. \tag{9.51}$$

In the special case of a uniform absorption of the incident radiation, we can go over to the limit $h_0 \to \infty$ in Eqs. (9.41), (9.50), and (9.51). In accordance with the results obtained in Sec. 9.3, this gives the monotonic distribution for the fragment density in a polymer film, with its maximum at $\xi = h_0$ (Fig. 9.2, curve *1*). For $h_0 > \delta$, the density of fragments decreases monotonically in the interval $\delta \leqslant \xi \leqslant h_0$, since according to Eqs. (9.40) and (9.48), in this interval

$$n(\xi) = B_1\{\exp(-\xi/l_D) + \exp[-(2h_0-\xi)/l_D]\}.$$

The drop in the fragment density curve with the depth of the unexposed polymer layer is determined by the characteristic length $l_D = \sqrt{D/G_2}$. Since in view of the relation (9.22) the derivative $dn/d\xi$ is continuous at $\xi = \delta$ and does not vanish at this point, and since $dn/d\xi > 0$ at $\xi = 0$ (see Eq. (9.20)), the maximum of the fragment density for $h_0 > \delta$ lies inside the exposed layer ($0 \leqslant \xi \leqslant \delta$). Appropriate investigations show that with increasing h_0, this maximum shifts toward the exposed surface and decreases in absolute magnitude (see Fig. 9.2). In the limit $h_0/l_D \to \infty$, the distribution of the fragment density can be described, in accordance with formulas (9.48)-(9.51), by the following relations:

$$n(\xi) = \frac{G_1}{G_2}\left\{1-\frac{1}{2}\exp\left[(\xi-\delta)/l_D\right]+\exp\left(-\xi/l_D\right)\left[\frac{1}{2}\left(1-\frac{D}{v_0 l_D}\right)\right.\right.$$
$$\left.\left.\times\left(1+\frac{D}{v_0 l_D}\right)^{-1}\exp\left(-\delta/l_D\right)-\left(1+\frac{D}{v_0 l_D}\right)^{-1}\right]\right\} \quad (0 \leqslant \xi \leqslant \delta), \tag{9.52}$$

$$n(\xi) = B_1\exp\left(-\xi/l_D\right) \quad (\delta \leqslant \xi < \infty).$$

These formulas can be directly obtained by using the semi-infinite layer model and solving the boundary-value problem (9.18)-(9.24) for $h_0 = \infty$. Curve *2* in Fig. 9.2*a* corresponds to the distribution (9.52). At $h_0 = \infty$, the maximum of the density of volatile fragments is situated closest to the surface, and in accordance with (9.52), its position is determined by the relation

$$\xi_{max} = \frac{l_D}{2}\ln\left[2\left(1+\frac{D}{v_0 l_D}\right)^{-1}\exp\left(\delta/l_D\right)-\left(1-\frac{D}{v_0 l_D}\right)\left(1+\frac{D}{v_0 l_D}\right)^{-1}\right].$$

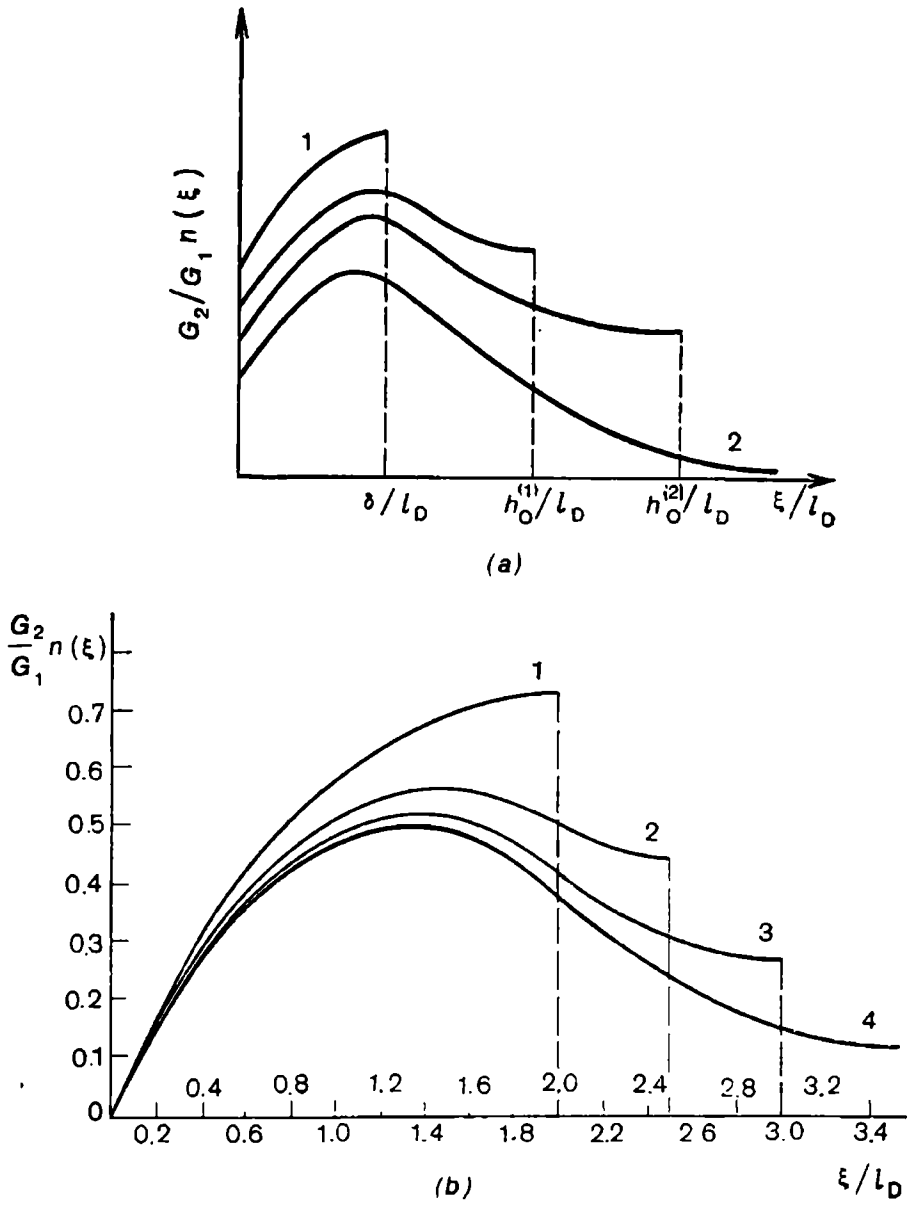

Fig. 9.2. Density distribution of low-molecular fractions for different thicknesses of the polymer film (nonuniform exposure):
(*a*) general form of the $(G_2/G_1)\, n$ vs. ξ dependence (curve *1* corresponds to the limit $h_0 \to \delta$, curve *2* to the semi-infinite layer model);
(*b*) results of numerical calculations for the $(G_2/G_1)\, n$ vs. ξ distribution for $\delta/l_D = 2$ (the condition (9.35) is assumed to be satisfied); curve *1*—$h_0/l_D = 2$, *2*—$h_0/l_D = 2.5$, *3*—$h_0/l_D = 3$, *4*—$h_0/l_D = 4$.

If the condition (9.34) is satisfied, Eq. (9.46) can be solved in u:

$$u = \frac{m}{\rho} G_1 \sqrt{D/G_2} \frac{v_0}{v_0 + \sqrt{DG_2}} \times \frac{2 \sinh(\delta/2l_D) \cosh[(h_0 - \delta/2)/l_D]}{\cosh(h_0/l_D) - \frac{D/(v_0 l_D)}{1 + D/(v_0 l_D)} \exp(-h_0/l_D)} \tag{9.53}$$

For $\delta \to h_0$, the formula (9.53) is transformed into (9.36) for uniform irradiation.

In the limit $h_0/l_D \to \infty$, we obtain the result for semi-infinite layer model:

$$u = \frac{m}{\rho} G_1 \sqrt{D/G_2} \frac{v_0}{v_0 + \sqrt{DG_2}} [1 - \exp(-\delta/l_D)]. \tag{9.54}$$

This case corresponds to the density distribution (9.52) for the volatile fragments.

In particular, if the absorption length is much less than the diffusion length, it follows from (9.54) that

$$u = \frac{m}{\rho} G_1 \delta \frac{v_0}{v_0 + G_2 l_D}. \tag{9.55}$$

Since $\delta \ll l_D$, in this case the density of fragments in the absorbing layer can be considered to be constant to within small corrections of the order of δ/l_D. According to (9.55) and (9.24), this quantity is given by

$$n^* = G_1 \delta (v_0 + G_2 l_D)^{-1},$$

whence

$$G_1 \delta = n^* v_0 + n^* G_2 l_D. \tag{9.56}$$

Following [9.10], we can show that Eq. (9.56) expresses a steady-state condition of the balance between the flux $G_1\delta$ of fragments resulting in the absorbing layer exposed to radiation, and the sum of the fluxes $n^*G_2l_D$ and n^*v_0. The first flux in this sum corresponds to a decrease in the number of fragments in the absorbing layer on account of their diffusion to an unexposed polymer while second flux appears on account of a transition of the fragments to the gaseous phase. Indeed, integrating Eq. (9.18) between the point $\xi = -0$ on the etching surface adjoining the gaseous phase and the point $\xi = \delta + 0$ on the lower boundary of the absorbing layer from the unexposed side of the polymer, we get

$$-u[n(-0) - n(\delta + 0)] = D \frac{dn}{d\xi}\Big|_{-0} - D \frac{dn}{d\xi}\Big|_{\delta+0} + \int_{\delta+0}^{-0} G_1 \, d\xi - G_2 \int_{\delta+0}^{-0} n \, d\xi. \tag{9.57}$$

Since the function $n(\xi)$ is constant within the interval $0 \leqslant \xi \leqslant \delta$ and continuous at the boundaries $\xi = 0$ and $\xi = \delta$ of the absorbing layer, the left-hand side of (9.57) is equal to zero, and we obtain the values $-G_1\delta$ and $G_2 n^*\delta$ respectively for the integrals on the right-hand side. In accordance with the boundary condition (9.20), we get

$$D\frac{dn}{d\xi}\Big|_{\xi=-0} = v_0 n^*$$

for the etching surface. In order to find the diffusion flux $D\frac{dn}{d\xi}\Big|_{\delta+0}$, we use the solution of Eq. (9.19) with the boundary conditions (9.21) and (9.23), putting $h_0 = \infty$ throughout:

$$n(\xi) = n^* \exp[\lambda_2(\xi - \delta)] \quad (\delta \leqslant \xi < \infty). \tag{9.58}$$

This equation is identical to (9.52). With the help of Eqs. (9.58) and (9.34), we can find

$$D\frac{dn}{d\xi}\Big|_{\delta+0} = -G_2 l_D n^*.$$

Finally, we get

$$G_1\delta = n^* v_0 + G_2 l_D n^* + G_2\delta.$$

This equation is equivalent to formula (9.56), since for $\delta \ll l_D$, the flux of fragments due to recombination in the absorbing layer can be neglected in comparison with the flux of fragments due to diffusion into the unexposed polymer. According to Eqs. (9.55) and (9.56), the quantity $p = v_0(v_0 - G_2 l_D)^{-1}$ gives the fraction of fragments leaving the polymer through the etching surface while $q = 1 - p$ is the fraction of fragments recombined in the polymer. It should be observed that the formula (9.55) corresponds to the model developed in [9.10] for explaining the VUV etching. This model, however, does not take into account the recombination of fragments in the unexposed polymer layer. In this case, obviously, l_D in the denominator of (9.55) must be replaced by δ (formula (20) in [9.10]).

According to (9.54), we get

$$u = \frac{m}{\rho} G_1 l_D \frac{v_0}{v_0 + G_2 l_D}$$

for the other special case when $\delta \gg l_D$. As expected, this result coincides with the formula (9.37) for the etching rate of a uniformly irradiated semi-infinite layer.

If the condition (9.35) is satisfied, i.e. if the velocity v_0 of the fragments leaving the polymer is much higher than the recombination "rate" $G_2 l_D$, Eq. (9.53) for the etching rate assumes the following form

$$u = \frac{m}{\rho} G_1 l_D \frac{2\sinh(\delta/2l_D)\cosh[(h_0 - \delta/2)/l_D]}{\cosh(h_0/l_D)}. \tag{9.59}$$

In this case, the fraction of fragments passing into the gaseous phase attains its highest value ($p = 1$) and the etching rate becomes maximum.

9.5. ETCHING RATE

According to (9.38), (9.39), and (9.59), the etching rate is equal to

$$u = u_0 f(h_0, \delta, l_D), \tag{9.60}$$

where

$$u_0 = \frac{m}{\rho} G_1 l_D \tag{9.61}$$

and

$$f(h_0, \delta, l_D) = \begin{cases} 2 \sinh(\delta/2l_D) \cosh[(h_0 - \delta/2)/l_D] \\ \qquad \times \cosh^{-1}(h_0/l_D) \quad \text{for} \quad h_0 \geqslant \alpha^{-1} = \delta, \\ \tanh(h_0/l_D) \quad \text{for} \quad h_0 \leqslant \alpha^{-1}. \end{cases} \tag{9.62}$$

The factor u_0 is determined by the intensity of the incident radiation and the properties of the exposed polymer (i.e. the density, the absorption cross section, the yield of volatile fragments, their diffusion coefficient, the recombination rate constant, and the average mass). This factor characterizes the etching ability of a given polymer for a fixed radiation intensity. The scaling factor $f(h_0, \delta, l_D)$ depends on the relation between the initial film thickness, the diffusion length, and the absorption length δ. It characterizes the penetrating power of the radiation used. Thus, in the approximation of a step dependence of the radiation intensity on the penetration depth, the dimensionless etching rate $u/u_0 = f(h_0, \delta, l_D)$ serves as a universal measure for the etching process in different polymers.

Figure 9.3 shows the dependence of the etching rate on the initial film thickness for radiation with a penetration depth δ. According to (9.60)-(9.62), the etching rate of thin films ($h_0 < \delta$) monotonically increases with h_0 and attains its maximum value $u/u_0 = \tanh(\delta/l_D)$ at $h_0 = \delta$ if δ exceeds the diffusion length l_D. This increase is caused by an increase in the diffusion rate of volatile fragments to the etching surface (see Sec. 9.3). Any further increase in h_0 leads to a monotonic decrease in the etching rate:

$$\frac{df(h_0, \delta, l_D)}{d(h_0/l_D)} = 2 \sinh^2(\delta/2l_D) \cosh^{-2}(h_0/l_D) < 0,$$

since a part of volatile fragments diffuses into the unexposed polymer layer and recombines in it. In accordance with (9.54), the asymptotic value of u/u_0 is equal to

$$f_{as} = 1 - \exp(-\delta/l_D).$$

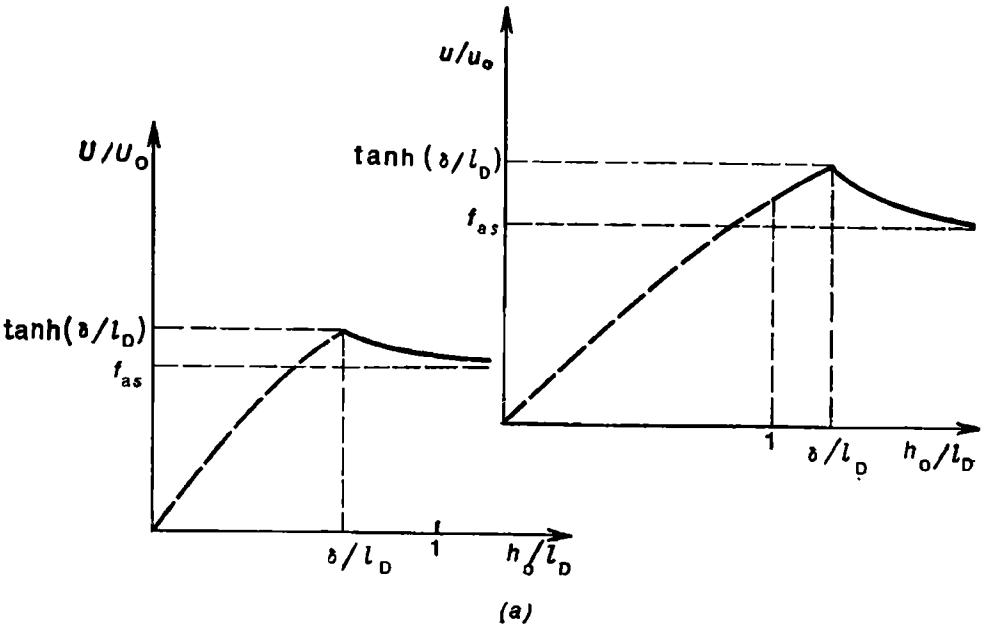

(a)

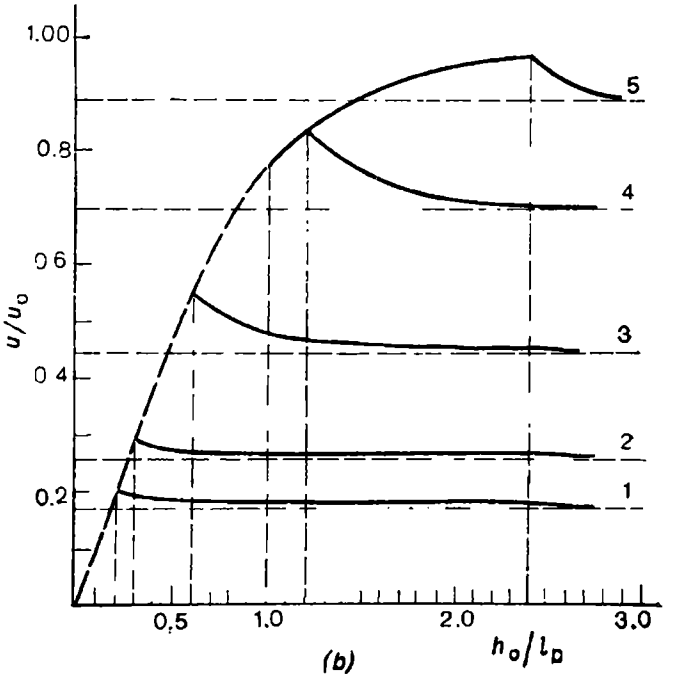

(b)

Fig. 9.3. Dependence of the dimensionless etching rate u/u_0 on the initial film thickness:
(*a*) general form of the u/u_0 dependence (left curve—$\delta < l_D$, right curve—$\delta > l_D$)
(*b*) results of numerical calculations: curve *1*—$\delta/l_D = 0.2$, *2*—$\delta/l_D = 0.3$, *3*—$\delta/l_D = 0.6$, *4*—$\delta/l_D = 1.2$, *5*—$\delta/l_D = 2.4$.

For $\delta < l_D$, the maximum etching rate also corresponds to the initial film thickness l_D (Fig. 9.3).

The initial segments of the curves in Figs. 9.3*a*, *b* are shown by dotted lines, since the process of etching of thin films whose initial thickness $h_0 < \min(\delta, l_D)$ cannot be described by the kinetic equations of Sec. 9.2, and so the formulas (9.60)-(9.62) become inapplicable. This case is similar to the final stage of etching of initially thick films, when their thickness h becomes comparable to the quantity $\min(\delta, l_D)$ [9.10]. The process of etching of thin films is described by the equation

$$\frac{dn}{dt} = G_1 - G_2 h - \frac{v_0}{h} n, \tag{9.63}$$

where the density n of fragments at any instant can be considered to be constant over the entire volume of the polymer. The process of residual etching is essentially of a transient nature and the etching rate in this case depends on time. Following [9.10], it can be easily shown that in view of the condition $u \ll v_0$, the etching rate can be described in this case by the following expression to within small corrections of the order of u/v_0:

$$u = \frac{m}{\rho} G_1 h v_0 (v_0 + G_2 h)^{-1}. \tag{9.64}$$

In other words, u depends on time only through the varying thickness h. In view of the condition (9.35), $v_0 \gg G_2 l_D > G_2 h$. Hence, the etching rate for a thin film is proportional to its current thickness:

$$u = \frac{m}{\rho} G_1 h, \tag{9.65}$$

and the process of etching gradually slows down.

Figure 9.4 shows the dependence of u/u_0 on the penetration depth α^{-1} of radiation. It can be seen from the curves that for a given radiation intensity, the maximum etching rate for a polymer film of thickness h_0 is ensured by radiation whose penetration depth is equal to or more than the initial thickness h_0. A comparison of this result with the dependences shown in Fig. 9.3 shows that the highest etching rate can be expected for a film with thickness $h_0 = \alpha^{-1}$.

The above results are directly applicable only if the polymer is almost unmodified upon exposure, i.e. if the parameters G_1, G_2, D, and δ remain practically unchanged with time.

In the time interval (9.17), the etching rate for an unmodifiable polymer film is constant, and the film thickness decreases linearly with time (or with the radiation dose $D_v = I_0 t$). The results of experiments on VUV etching (Sec. 9.7) show that such a situation is actually observed when a polymer film is exposed to an oxygen-containing atmosphere. This is due to the well-known fact [9.11]

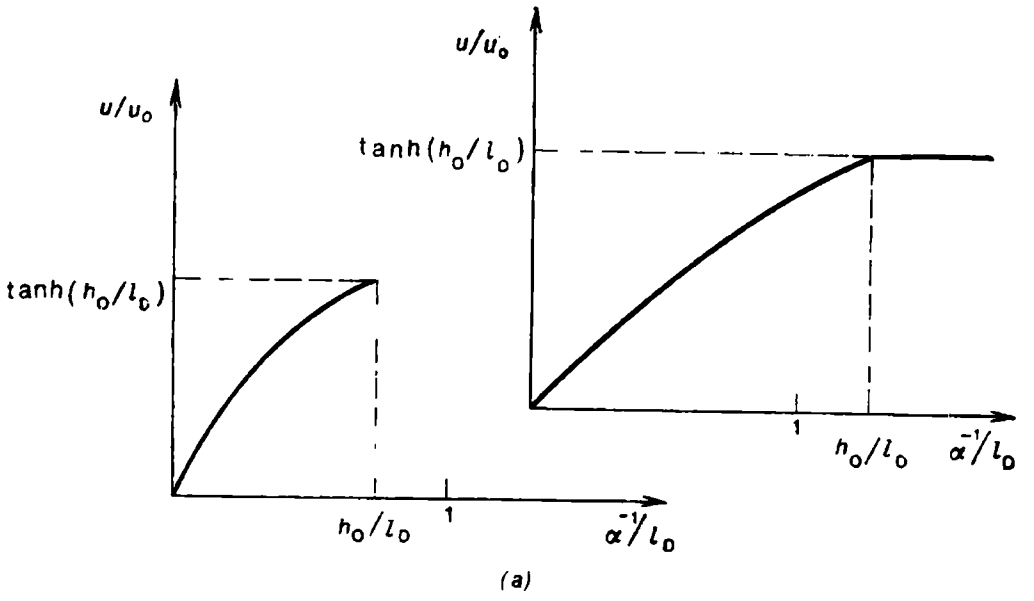

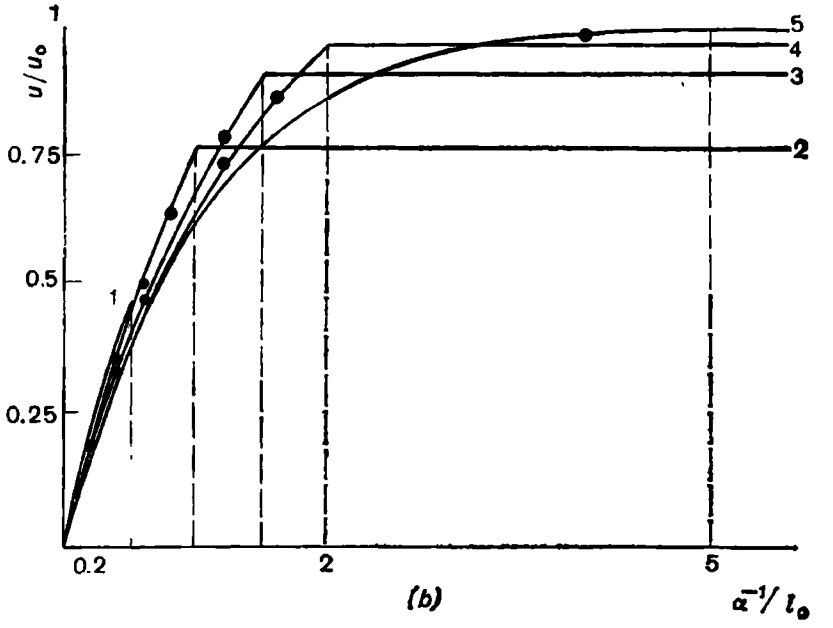

Fig. 9.4. Dependence of the dimensionless etching rate u/u_0 on the penetration depth:
(*a*) general form of the dependence of u/u_0 (left curve—$h_0 < l_D$, right curve—$h_0 > l_D$); (*b*) results of numerical calculations: curve *1*—$h_0/l_D = 0.5$, *2*—$h_0/l_D = 1$, *3* — $h_0/l_D = 1.5$, *4*—$h_0/l_D = 2$, *5*—$h_0/l_D = 5$.

that oxygen molecules suppress chemical reactions leading to a modification of the polymer (the "oxygen effect").

At the same time, the etching rate gradually decreases if the etching is carried out in vacuum or in an inert atmosphere. It can be assumed that in the case of volume absorption of radiation ($\alpha^{-1} > h_0$), such a dependence is caused by a gradual modification of the polymer under the action of penetrating radiation. This modification is caused by the appearance of cross-links between polymer molecules and their accumulation. However, even in the case of surface absorption ($\alpha^{-1} \ll h_0$), when the polymer layers lying below the absorbing layer of thickness $\delta = \alpha^{-1}$ are not directly influenced by the radiation, a modification of the polymer under the condition $l_D > \delta$ is caused by the diffusion of volatile fragments to the unexposed part of the film and by their recombination which also leads to the appearance and accumulation of cross-links. Thus, the parameters G_1, G_2, D, and δ which characterize the etching response of a polymer change during the exposure of the polymer film. Hence, in order to consider the effect of the polymer modification, we must proceed from the time-dependent version of the theory, assuming that the kinetic parameters in Eqs. (9.10)-(9.16) of the boundary-value problem depend explicitly on time. Consequently (assuming, of course, that the condition (9.17) is satisfied), we should replace Eq. (9.18) by, say, the following equation:

$$\frac{dn}{dt} = D(t)\frac{\partial^2 n}{\partial \xi^2} + u(t)\frac{\partial n}{\partial \xi} + G_1(t) - G_2(t)\,n \quad (0 \leqslant \xi \leqslant \delta(t)). \qquad (9.66)$$

It was shown in [9.10] that since the values of the characteristic time for the variation of the kinetic parameters $G_1(t)$, $G_2(t)$, $D(t)$, and of the parameter $\delta(t)$ are much larger than the values of the characteristic time for the elementary processes of depolymerization, recombination and diffusion, the solutions of the time-dependent equations in the quasi-stationary approximation are found to be satisfactory. In the present case, the quasistationary approximation means that at any instant of time in the interval (9.17), the algebraic sum of the fluxes on the right-hand side of Eq. (9.66) is equal to zero, i.e. a "flux equilibrium" sets in. In this case, $n(\xi, t)$ depends on time only through the parameters $G_1(t)$, $G_2(t)$, and $D(t)$. Formally, the solution of the quasistationary problem is reduced to the solution of the boundary-value problems considered in Secs. 9.3 and 9.4. However, in the final formulas obtained in this case, as well as in Eqs. (9.60)-(9.62), (9.64), and (9.65), the parameters G_1, G_2, D, and δ are found to be functions of time. The condition of applicability of the quasistationary solutions is given by the inequality

$$\left|\frac{\partial G_1(t)}{\partial t}\right| \ll \frac{G_1(t)}{\Delta t},$$

where Δt is the characteristic time for the variation of $G_1(t)$. Similar inequalities are applicable for the remaining kinetic parameters and parameter δ.

Thus, taking into account the polymer modification during exposure, the instantaneous etching rate will be given by

$$u(t) = u_0(t) f(h_0, \delta(t), l_D(t)), \tag{9.67}$$

where

$$u_0(t) = \frac{m}{\rho} G_1(t) \sqrt{D(t)/G_2(t)} \tag{9.68}$$

and the function f is defined by Eq. (9.62), where $\delta = \delta(t)$ and $l_D = l_D(t) = \sqrt{D(t)/G_2(t)}$. The process of polymer modification is quite complicated and is accompanied by a number of chemical and structural transformations. At present, it is hardly possible to obtain reliable theoretical dependences $G_1(t)$, $G_2(t)$, $D(t)$, and $\delta(t)$. It should be noted that it is also quite difficult to separately determine these dependences experimentally. Hence, we shall confine ourselves to the phenomenological introduction of the function $\varphi(t)$ which takes into account the modification of the polymer:

$$u(t) = u_0 f(h_0, \delta, l_D) \varphi(t). \tag{9.69}$$

Here, by u_0 and $f(h_0, \delta, l_D)$, we mean the quantities (9.61) and (9.62) for the unmodified polymer, and assume that $\varphi(0) = 1$. If etching is carried out in an oxygen-containing medium where no modification of the polymer takes place, we have $\varphi(t) \equiv 1$. In other cases, the modification function $\varphi(t)$ can be obtained from an analysis of the experimental data.

9.6. EXPERIMENTS ON THE PHOTOETCHING OF POLYMERS BY SOFT X-RAYS

Photoetching in the X-ray region was observed in polyolefinsulfones, polymethyl methacrylates (PMMA), its copolymers, and in several other polymers [9.3].

Polyolefinsulfones represent a large group of polymers which are used as positive electron resists [9.4, 5]. The general formula for such compounds is $(-R-SO_2-)_n$, where R can be butene, pentene, hexene, etc. These compounds have maximum sensitivity for positive electron resists, viz. $(1\text{-}4) \times 10^{-6}$ C/cm^2 [9.4]. This high electron sensitivity is the result of a large radiation-chemical efficiency of their destruction, the average number G of scissions of the principal chain per 100 eV of absorbed energy is equal to 10-12 [9.12]. Polyolefinsulfones allow a "dry" development of a film upon exposure to an electron beam. The kinetics of the radiative destruction of polyolefinsulfones, including "dry" development, was investigated in detail in [9.4, 5]. Bowden [9.13] studied the variation of infrared ab-

sorption spectra of poly (2-methylpentene-1)sulfone (PMPS) as a function of the absorbed energy (electrons having an energy 5-20 keV). He found that below 100°C, the aliphatic groups (presumably, 2-methylpentene-1) and the SO_2 groups evaporate from the film, their evaporation rates being different and temperature-dependent.

The radiative degradation of PMMA and other polymethacrylates has been investigated by several authors (see, for example [9.14, 18]). The irradiation of PMMA and other polymethacrylates and their copolymers by ultraviolet radiation, X-rays, gamma radiation, electrons or ions leads to a decrease in the molecular weight due to a scission of the principal polymer chain. This makes PMMA and other polymethacrylates suitable as electron- and X-ray resists, as well as resists for lithography in the far ultraviolet region [9.15, 16, 17]. At a temperature of 130-200°C and under the action of ultraviolet radiation with $\lambda < 260$ nm, polymethyl methacrylate films disintegrate as a result of radiative chain depolymerization, releasing a monomer which is practically the only gaseous product in this process [9.19]. The sensitivity of polymethyl methacrylate to electron radiation is $\sim 0.5 \times 10^{-4}$ C/cm^2, and the value of G is found to be 1.7.

We also investigated the copolymer of acidic allylic maleate and vinylethylene ester which is known to be a typical negative resist to electrons and X-rays [9.20].

The experiments on the photoetching of polymers under the action of soft X-rays with $\lambda = 0.7$-6.0 nm were carried out on the synchrotron FIAN S-60 (electron energy 580 MeV; orbital frequency of electrons 50 MHz, and radius of the orbit 2m [9.21]). Measurements were carried out in three spectral regions: 0.7-2.4 nm (Si filter), 0.8-2.8 nm (Al filter), and 2.4-6.0 nm (Sn filter). The polymer films were deposited on silicon and glass substrates by centrifugation of the polymer solution in ordinary organic solvents. The required film thickness was attained by choosing the optimal viscosity of the polymer solution and the rotational velocity of the centrifuge. The film was then dried in order to remove the solvent. The films deposited on the substrate were exposed to radiation in a vacuum chamber (under pressure of 5×10^{-6} mmHg) of the synchrotron channel through which the synchrotron radiation was extracted. The radiation intensity was obtained numerically [9.20, 21] from the number of electrons in the synchrotron orbit which was determined by a special detector (sensor). The computational parameters in this case are the electron energy and the radius of curvature of the electron orbit in the synchrotron channel. The conditions for synchrotron operation were as follows: quasicontinuous radiation with maximum electron energy was emitted for 0.5 sec, followed by a pause of 5.5 sec. The thickness of the polymer film subjected to photoetching was measured with the help of the microinterferometer

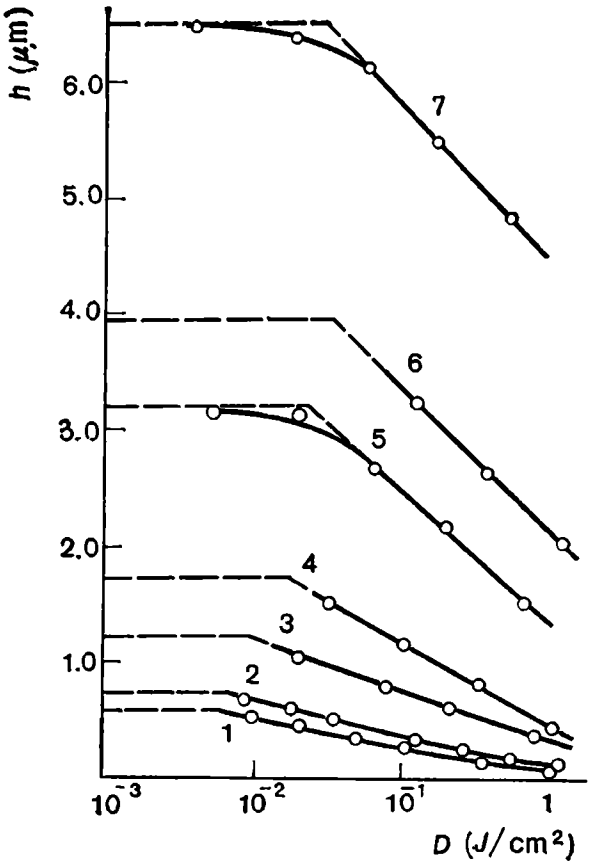

Fig. 9.5. Dependence of film thickness of polyhexene-1-sulfone on X-ray radiation dose for different initial thicknesses h_0: *1*—0.57 μm *2*—0.72 μm, *3*—1.2 μm, *4*—1.72 μm, *5*—3.20 μm, *6*—3.95 μm, *7*—6.90 μm.

MII-4 after spray-coating of a metallic layer (Cu, Au) of thickness ~50 nm.

Figure 9.5 shows on a semilogarithmic scale, the dependence of the residual film thickness of polyhexene-1-sulfone (PHS) films on X-ray radiation dose after irradiation for seven different values of initial thickness. Experimental curves show that the etching rate for polymer films is almost inversely proportional to the radiation dose on account of a gradual modification of the polymer properties. Consequently, we can write the following expression for the modification function:

$$\varphi(t) = \frac{1}{1+t/\tau} = \frac{1}{1+D_v/D_{v_0}}, \qquad (9.70)$$

where $D_{v_0} = I_0\tau$. The magnitude of τ indicates the time that elapses between the beginning of irradiation and the instant when the etching rate is reduced to half its initial value as a result of modification,

while the magnitude of the radiation dose D_{v_0} characterizes the modifiability of the polymer film. From the dependence $u = |dh/dt| \propto (1 + t/\tau)^{-1}$ it follows that the film thickness will decrease logarithmically (see Fig. 9.5). The shape of the experimental curves reveals that the etching attains a logarithmic form of dependence soon after the beginning of the irradiation (the time t_{tr} is small in comparison with the total duration of the process). Departures from the logarithmic (or near-logarithmic) dependence are observed at the termination of etching for film thicknesses of the order of 150-200 nm, when the etching rate diminishes even more rapidly. The quasistationary approximation can practically be considered to be valid for almost the entire duration of the process, and hence we can assume that the condition (9.17) is satisfied. According to our estimates, the absorption coefficient of PHS in the soft X-ray region is of the order of $\alpha \simeq 0.75\ \mu m^{-1}$, while $\delta = \alpha^{-1} \simeq 1430$ nm. Thus, the thickness of 150-200 nm at which the etching rate drops can be equated to the diffusion length $l_D = \sqrt{D/G_2}$. Taking the value $D \simeq 10^{-8}$ cm^2/sec [9.22], we find that $G_2 \simeq 10^2$ sec^{-1}. Since $v_0 \gg \sqrt{DG_2} \simeq 10^{-3}$ cm/sec, i.e. the inequality (9.35) is actually satisfied, we can use the expressions (9.69), (9.61), and (9.62) for the etching rate.

Integrating Eq. (9.69) and taking into account the relation (9.70) for the modification function, we obtain the following expression for the etching process:

$$h(D_v) = h_0 - \tilde{u}\tau \ln\left(1 - \frac{D_v}{D_{v_0}}\right), \tag{9.71}$$

where $\tilde{u} = u_0 f(h_0, \delta, l_D)$ is the etching rate for an unmodified polymer film with initial thickness h_0. At the initial stage of the process ($D_v \ll D_{v_0}$), the polymer is not modified and Eq. (9.71) leads to the following linear relation for etching:

$$h(D_v) = h_0 - \tilde{u}\tau\,(D_v/D_{v_0}).$$

When modification becomes significant ($D_v \gg D_{v_0}$), we obtain a logarithmic relation for the etching process:

$$h(D_v) = h_0 - \tilde{u}\tau\ \ln\ (D_v/D_{v_0}). \tag{9.72}$$

At the end of etching process, i.e. when $h \leqslant l_D$, the following expression should be used for the etching rate (see (9.65)):

$$u = \left|\frac{dh}{dt}\right| = \frac{m}{\rho} G_1 h \varphi(t).$$

Integrating under the initial condition $h = l_D$ at $t = t_1$, we get

$$h(D_v) = l_D \left(\frac{1 + D_v/D_{v_0}}{1 + D_{v_1}/D_{v_0}}\right)^{-\frac{m}{\rho} G_1 \tau},$$

where $D_{v_1} = I_0 t_1$. Since $D_v \gg D_{v_0}$, and $D_{v_1} \gg D_{v_0}$ in the final stage of the process, we obtain

$$h(D_v) = l_D (D_v/D_{v_1})^{-\frac{m}{\rho} G_1 \tau}, \tag{9.73}$$

i.e. the final stage of etching is described by a power law.

The relation (9.72) can be rewritten in the form

$$h(D_v) = h_0 + \frac{\tilde{u}\tau}{\log e} \log D_{v_0} - \frac{\tilde{u}\tau}{\log e} \log D_v. \tag{9.74}$$

This gives the following expression for the modification parameter D_{v_0}:

$$\log D_{v_0} = [h(1\ \text{J/cm}^2) - h_0]\ (-\gamma)^{-1}, \tag{9.75}$$

where γ is the slope of the linear parts of the curves in Fig. 9.5. According to (9.74), the parameter $\tilde{u}\tau$ is given by

$$\tilde{u}\tau = -\gamma \log e. \tag{9.76}$$

Table 9.1 shows the values of the parameters D_{v_0}, $\tilde{u}\tau$, and $\tilde{u}/I_0 = \tilde{u}\tau/D_{v_0}$ obtained from the curves in Fig. 9.5. It can be seen from

Table 9.1.

No.	h_0 (μm)	D_{v_0} (J/cm²)	$\tilde{u}\tau$ (μm)	$\tilde{u}/I_0$ $\left(\frac{\mu m/sec}{J/(cm^2 sec)}\right)$
1	0.57	$\left(6.3\pm^{1.9}_{2.0}\right)\cdot 10^{-3}$	0.11 ± 0.01	17.5 ± 5.6
2	0.72	$\left(6.7\pm^{1.5}_{2.0}\right)\cdot 10^{-3}$	$0.13\pm^{0.004}_{0.010}$	19.1 ± 5.6
3	1.20	$(1.0\pm0.3)\cdot 10^{-2}$	$0.19\pm^{0.01}_{0.02}$	19.0 ± 6.0
4	1.72	$(1.9\pm0.4)\cdot 10^{-2}$	$0.31\pm^{0.02}_{0.01}$	16.3 ± 4.0
5	3.20	$\left(2.6\pm^{0.2}_{0.1}\right)\cdot 10^{-2}$	$0.51\pm^{0.01}_{0.03}$	19.6 ± 3.1
6	3.95	$\left(3.5\pm^{0.1}_{0.3}\right)\cdot 10^{-2}$	$0.54\pm^{0.04}_{0.02}$	15.4 ± 1.6
7	6.90	$\left(3.3\pm^{0.9}_{0.5}\right)\cdot 10^{-2}$	$0.57\pm^{0.03}_{0.01}$	17.3 ± 4.8

Remark: The first column gives the number of the curve in Fig. 9.5.

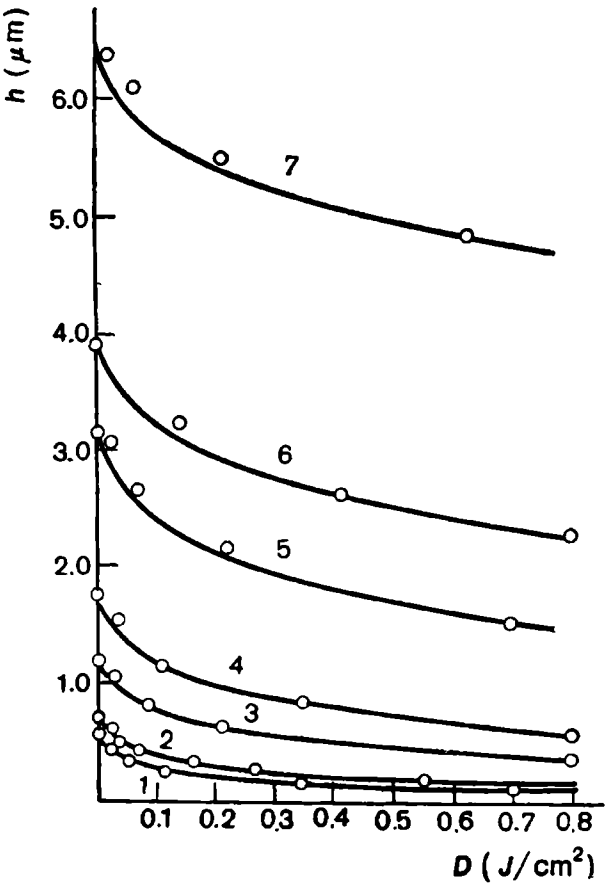

Fig. 9.6. Theoretical curves for photoetching in the X-ray region, calculated according to formula (9.74). The experimental values are shown by circles. The numbers on the curves correspond to those in Fig. 9.5

the table that within experimental errors the etching rate $\tilde{u}$ is independent of the initial thickness h_0 of the film. At the same time, the modification parameter D_{v_0} increases with h_0.

Figures 9.6 shows, on a linear scale, the theoretical etching curves obtained in accordance with the Eqs. (9.71) in which the values of the parameters D_{v_0} and $\tilde{u}\tau$ have been taken from Table 9.1. The experimental results are also shown in the same figure. The small deviations of the theoretical curves from the experimental results in the initial parts are apparently related to the onset of the quasi-stationary process. It is also possible that the initial modification process is not described quite accurately by the relation (9.70).

According to Table 9.1 (column 5), the magnitude of $\tilde{u}$ is independent of h_0. This fact is in accord with the theory developed above, since the scaling factor f (h_0, l_D, δ) in this case is practically equal to unity. Indeed, for $\delta = 1430$ nm and $l_D = 175$ nm, the ratio

$\delta/l_D = 8.17$. According to (9.62), we have

$$f(h_0, l_D, \delta) = \begin{cases} 2\sinh(4.085)\cosh(h_0/0.175 - 4.085) \\ \qquad \times \cosh^{-1}(h_0/0.175) \quad \text{for} \quad h_0 > 1.43\ \mu\text{m}, \\ \tanh(h_0/0.175) \quad \text{for} \quad h_0 \leq 1.43\ \mu\text{m}. \end{cases}$$

Since the ratio $h_0/l_D \gg 1$ for $h_0 = 0.57$, 0.72, and 1.2 μm, and $h_0/l_D \gg \delta/2l_D \gg 1$ for $h_0 = 1.72$, 3.20, 3.95, and 6.50 μm, this function is practically constant and equal to unity for all experimental values of h_0. Thus, the rate $\tilde{u}$ must coincide with u_0 within experimental error.

According to the data of Table 9.1, $\tilde{u}/I_0 = u_0/I_0 = 17.7$ μm/sec (where the intensity I_0 is measured in J/cm²·sec). Using the values $\rho = 1.2$ g/cm³ and $l_D = 175$ nm, we obtain an estimate for the generation rate of the low-molecular fragments in an unmodified polymer by using (9.61):

$$G_1 = \frac{\rho u_0}{m l_D} = 0.7 \times 10^{26} \frac{I_0}{m}\ (\text{cm}^{-3}\cdot\text{sec}^{-1}),$$

where m is measured in amu. The radiation intensity I_0 in our experiments was equal to about 10^{-3} J/cm²·sec. Hence $\tilde{u} \simeq 17$ nm/sec, and $G_1 \simeq 0.7 \times 10^{23} \frac{1}{m}$ (cm^{-3}·sec^{-1}). Taking the value $\delta = 1.43$ μm for PHS, we can estimate the quantum yield of low-molecular fragments in an unmodified polymer:

$$g = \frac{G_1 \delta}{I_0} = \frac{1.6}{m} \cdot 10^3 \text{ (particles per eV)}.$$

The kinetic etching curves for polymer films of different polysulfones are shown in Fig. 9.7. The results obtained from an analysis of the experimental data according to the formulas (9.75) and (9.76) are shown in Table 9.2. The same initial film thickness h_0 was taken

Table 9.2.

No.	Material	D_{v_0} (J/cm²)	$\tilde{u}\tau$ (μm)	$\tilde{u}/I_0$ (μm/sec / J/(cm² sec))	u_0 (rel. units)
1	polybutene-1-sulphone	0.17	0.063	0.36	1
2	polypentene-1-sulphone	$0.71\cdot10^{-1}$	0.076	1.3	4
3	polyhexene-1-sulphone	$0.59\cdot10^{-2}$	0.061	10.3	29
4	polyheptene-1-sulphone	$0.23\cdot10^{-2}$	0.067	28.8	80

Remark: The first column gives the number of the curve in Fig. 9.7.

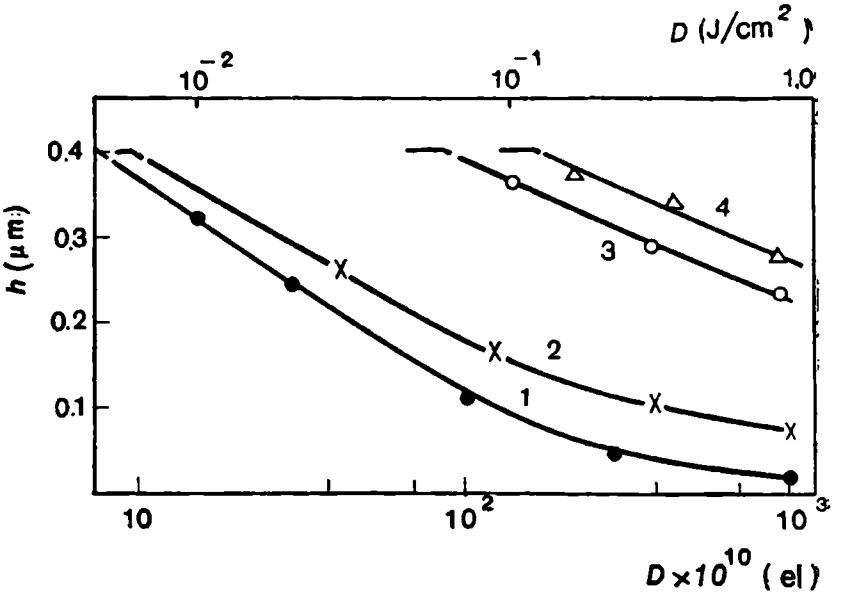

Fig. 9.7. Kinetic curves for etching of polyolefinsulfones in the X-ray region: *1*—polybutene-1-sulfone, *2*—polypentene-1-sulfone, *3*—polyhexene-1-sulfone, *4*—polyheptene-1-sulfone.

equal to 0.4 μm throughout. The radiation intensity was also the same in all cases. Since the thickness h_0 was less than δ, the scaling factor $f(h_0, l_D, \delta) = \tanh(h_0/l_D)$. It can be assumed that l_D is nearly the same for all films. Hence the values of $f(h_0, l_D, \delta)$ can be considered identical for all films. Therefore, the values of $\tilde{u}/I_0$, given in the penultimate column of Table 9.2, can be used for comparing the etching rates u_0 of unmodified films of different polysulfones (the values of $\tilde{u}/I_0$ have been obtained to within 30%). The relative values of etching rates u_0 have been shown in the last column of Table 9.2 (the etching rate of polybutenesulfone has been taken equal to unity). Assuming that δ and ρ are practically identical, the same quantities characterize the ratios of the products of the quantum yield and the average mass m of the volatile fragments for different polysulfones, i.e. the ratio of the quantities

$$gm = \frac{\rho\delta}{l_D I_0} u_0.$$

A clearly defined dependence between the etching rate (as well as the quantum yield) and the number n of the CH_2-groups in the side chains of the monomer link of polysulfone follows from Table 9.2. At the same time, the modification parameter D_{v_0} decreases with increasing n.

A comparison of the etching rates for polysulfones and polymethyl methacrylate (PMMA) can be made with the help of the experimen-

tal results shown in Fig. 9.8. The initial film thicknesses for PHS and PMMA were equal to 0.57 and 0.6 μm respectively (the difference in the initial thicknesses of films in this case does not have a noticeable effect on the values of the factor f (h_0, l_D, δ)). The values of $\tilde{u}/I_0$ are found to be equal to 16.8 μm/J·cm² for PHS and 0.09 μm/J·cm² for

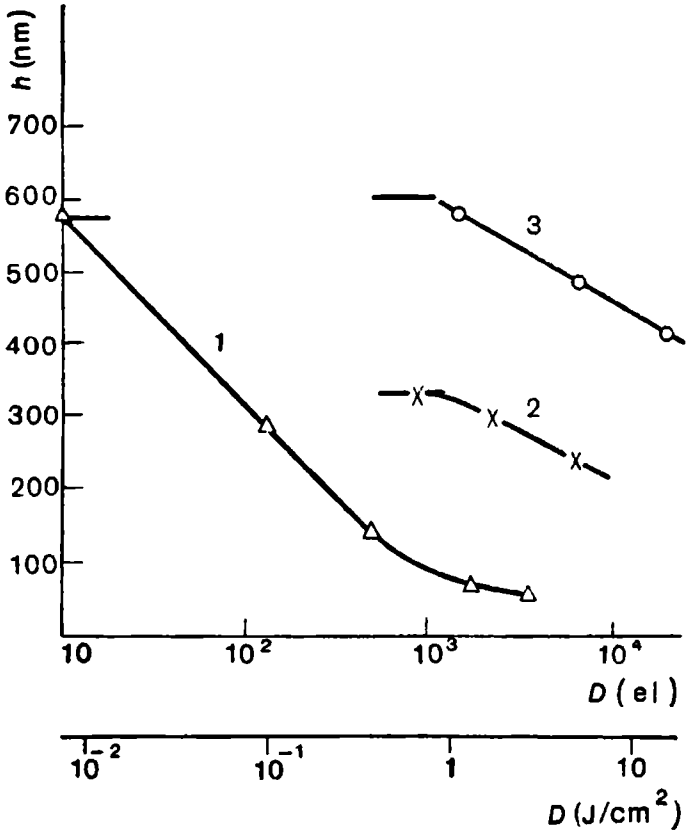

Fig. 9.8. Kinetic etching curves for PHS, negative resist, and PMMA films in the X-ray region: *1*—polyhexene-1-sulfone, *2*—copolymer of acidic allylic maleate and vinyl-ethyl ester, *3*—PMMA

PMMA. This leads to the following estimates for the ratio of the etching rates of unmodified PMMA and PHS: u_0 (PMMA)/u_0 (PHS) $\simeq$ 0.005.

We also discovered the etching effect for polymers which predominantly form cross-links when irradiated (i.e. for negative resists, see Fig. 9.8). The etching rate $\tilde{u}/I_0$ in this case was found to be equal to 0.077 μm/J·cm². Polymer etching upon exposure to X-rays is observed in cross-linking polymers as well as in polymers where scission of molecules predominates (negative as well as positive), and is thus a general property of polymers.

9.7. EXPERIMENTS ON PHOTOETCHING BY VUV-RADIATION IN VACUUM, NITROGEN, AND OXYGEN-CONTAINING MEDIA

Measurements of photoetching of polymers in the vacuum ultraviolet (VUV) region were carried out on films in vaccum, in pure nitrogen, and in air, i.e. in an oxygen-containing medium. The sources of radiation were scaled low-pressure hydrogen and deuterium tubes of 20-50 W power with MgF_2 output windows [9.23]. The radiation intensity in the spectral region of 110-220 nm up to 10^{15} quanta/(cm^2·sec) was attained. The fractions of energy in the spectral regions 110-135, 135-170, and 170-220 nm are equal to 23, 46, and 9% respectively [9.9]. In the 110-135 nm range, the energy is mainly determined by the radiation with wavelength 121.6 nm (L_α-line). In the 135-170 nm range, the highest intensity lines in the molecular hydrogen emission spectrum are concentrated around 160 nm. The construction of these tubes permits a metallic vacuum sealing of their output windows, thus considerably improving the conditions under which the radiation is introduced into the experimental vacuum chamber.

The samples to be irradiated were placed at an adjustable distance of 0.2-1.0 mm from the window of the tube. For such a gap, the absorption of radiation by oxygen (in an atmosphere with partial pressure of O_2 at about 150 mmHg) is significant in the spectral range of 135-170 nm and is determined by the dissociative continuum of the O_2 molecule. In the 110-135 nm range, oxygen absorbs to a lesser extent due to the existence of "transparency windows", one of which corresponds to the L_α line of the hydrogen emission spectrum [9.23]. In this case, the absorption may be affected by the formation of ozone (whose absorption cross section in this range is much higher than the absorption cross section of oxygen) and water vapour [9.23]. Hence, we investigated the dependence of the radiation intensity of the tube on the gap between the output window and the sample. The photodetector with a sunproof photocathode based on a niobium-tantalum alloy was placed in a chamber with LiF window. When a hydrogen (or deuterium) tube with MgF_2 window was used, the detector mainly registered radiation in the 115-125 nm range, i.e. in the region of the hydrogen spectrum that plays the dominating role in the photoetching of polymers [9.1, 2]. As the gap was increased from 0 to 0.5 mm, the radiation intensity dropped by 20-30%, i.e. the active molecules (for example, ozone) formed under the action of VUV, as well as the products of photodestruction of polymers, made a small contribution to the VUV absorption when the samples were irradiated in air, since radiation sources of

relatively low intensity were used and the products of photoreactions had time to leave the beam region and were not accumulated in it.

Experimental investigations of the kinetics of photoetching in vacuum were carried out in an oil-free pumping chamber at pressures $P \sim 10^{-6}$ mmHg. A low-pressure vacuum tube with a MgF_2 window was used as the source.

In some experiments a pulsed discharge creeping over a dielectric surface was used as the source [9.24]. This source has a linear spectrum which is determined to a considerable extent by the substrate material and contains a high-intensity shortwave component extending right up to the soft X-ray region [9.24]. In experiments carried out in air, the film of the polymer being irradiated was placed directly behind the MgF_2 output window of the discharge chamber. The experimental setup had the same geometry as in the case of a gas discharge tube. Investigations of photoetching in nitrogen atmosphere were carried out by placing the polymer films directly in the discharge chamber. In this case, high-quality N_2, which was transparent up to 100 nm, was used as the working medium.

According to our experimental estimates, the intensity of VUV radiation of the creeping discharge in the region 110-120 nm exceeds the intensity of tube sources by more than an order of magnitude.

The main experimental difficulties in the investigation of the kinetics of photoetching of polymers are associated with the measurement of the residual thickness of the polymer layer after irradiation. For this purpose, the interferometric method is usually employed. This method, used by us [9.1, 3], gives reliable values of the measured thickness right up to 30-50 nm. Measurement of smaller thicknesses may introduce considerable errors. The measurements are also hampered by the fact that after irradiation, the polymer layer must be spray-coated by a metal (Cu, Au) to a thickness not less than ~10 nm in order to obtain a good reflection of light.

In [9.25], we used the photometric method for measuring the polymer layer thickness. According to this method, the film thickness is measured by the transmission coefficient of the polymer film in the spectral range where the photoetching is being observed directly. The possibilities of this method in the case of thick films are limited by the fact that for absorption coefficients of $\sim 10^6$ cm^{-1} and above for the vacuum ultraviolet, it is difficult to measure thicknesses of more than 1 μm.

Besides, when thicknesses of the order of 100 nm are being measured, the diffusion of fragments in some polymers may cause chemical reactions to proceed in the entire layer, thus considerably changing the refractive index and leading to errors. However, it was shown by us [9.25] that the photometric method gives good results for the kinetics of photoetching of polymer films having thickness

less than 150 nm, if the irradiation does not cause a considerable change in the refractive index.

The difficulties encountered while using the interferometric and photometric methods for the measurement of small variations in thickness can be overcome with the help of the quartz microbalance method which was employed by us. Microbalances of different constructions are used to investigate the kinetics of thermal destruction of polymers (see, for example, [9.26]). Apparently, quartz microbalances were not used earlier for studying the kinetics of photoetching.

According to this method, a film of the polymer under investigation is deposited on a quartz resonator and is exposed either to radiation or to some other physical agency (for example, heating, or contact with a gas), thus bringing about a change in the mass of the film. Such a change in the mass is measured in terms of the variation of the natural frequency of the quartz resonator. This method is more sensitive than the methods described earlier in the literature, and can be used for studying other chemical and physical processes involving mass transfer, like diffusion from the gaseous phase into the polymer and from the polymer to vacuum, sorption and desorption, thermal destruction, etc.

Quartz discs of diameter 15 mm and thickness 200 μm were used as resonators. The natural vibrational frequency of the resonator was 3.33 MHz. One of the surfaces of the disc was polished and did not contain any inhomogeneity with a typical dimension more than ~30 nm. Obviously, the magnitude and number of these inhomogeneities determine the quality of the polymer layer in contact with the resonator surface. Hence, for a correct interpretation of the kinetic curves of photoetched ultrathin polymer films, it is extremely important that these inhomogeneities be small.[1] Silver layers of ~50 nm thickness, which served as the electrodes, were thermally sprayed on both sides of the disc and the polymer film was deposited on the polished side of quartz by centrifugation from a polymer solution in a specially selected organic solvent as described above. Films of different polymers were investigated. Photoetching by VUV radiation was observed in polymers which are predominantly crosslinked under the action of other types of radiation (gamma-rays, electrons, ultraviolet radiation), as well as in polymers whose bonds are predominantly ruptured under similar conditions (in particular, in negative- and positive electron resists and in X-ray resists). The experimental results on the kinetics of photoetching of PMMA, which were investigated in great detail by us, will be mainly described below. These results will also be compared with the theory developed above.

[1] For this reason, the use of standard resonators of quartz microbalances for studying the kinetics of photoetching of films with less than 100 nm thickness does not lead to correct results.

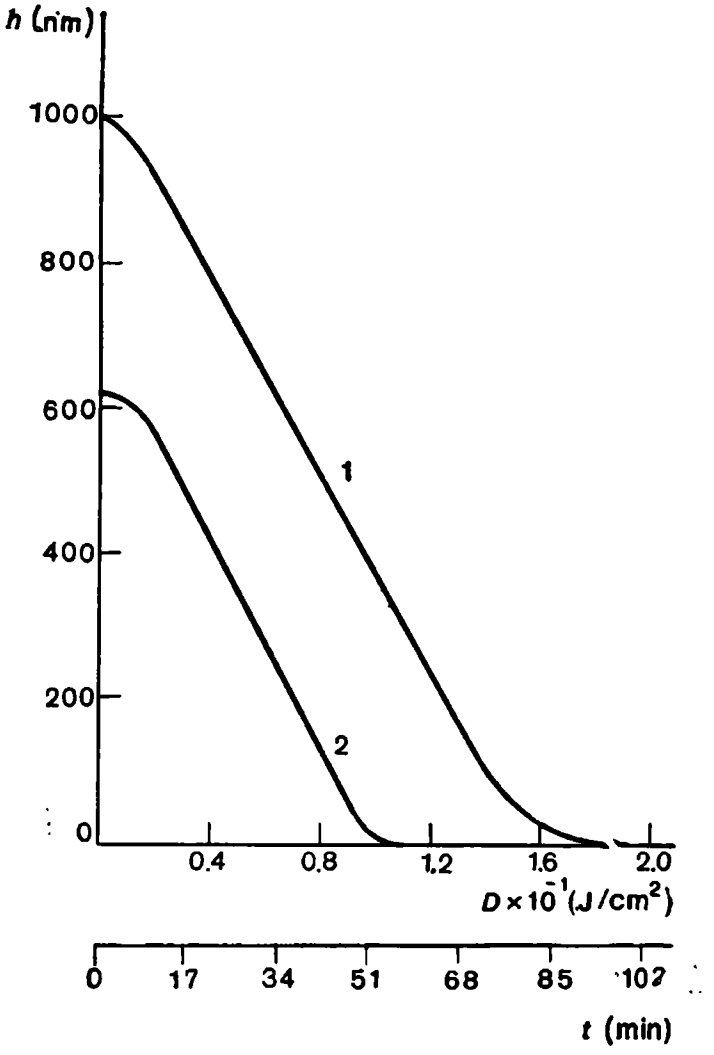

Fig. 9.9. Kinetic curves for VUV-etching of PMMA films in air at different inital film thicknesses.

Experimental results show that the process of photoetching in an oxygen-containing atmosphere strongly differs from etching in an oxygen-free atmosphere. This difference is due to the "oxygen effect" mentioned in Sec. 9.5, according to which the modification of a polymer is suppressed in an oxygen-containing atmosphere. The kinetic curves in Fig. 9.9 have been obtained for the same value of VUV-radiation intensity during etching in air. The same is the case for curves in Fig. 9.10 (the values of intensity in this case are different from those in Fig. 9.9). Curve *1* in Fig. 9.11 has been obtained for etching in nitrogen, while curve *2* corresponds to etching in air. The film thickness has a linear dependence on the exposure time if the etching is carried out in air. Figure 9.12 shows the same curves as

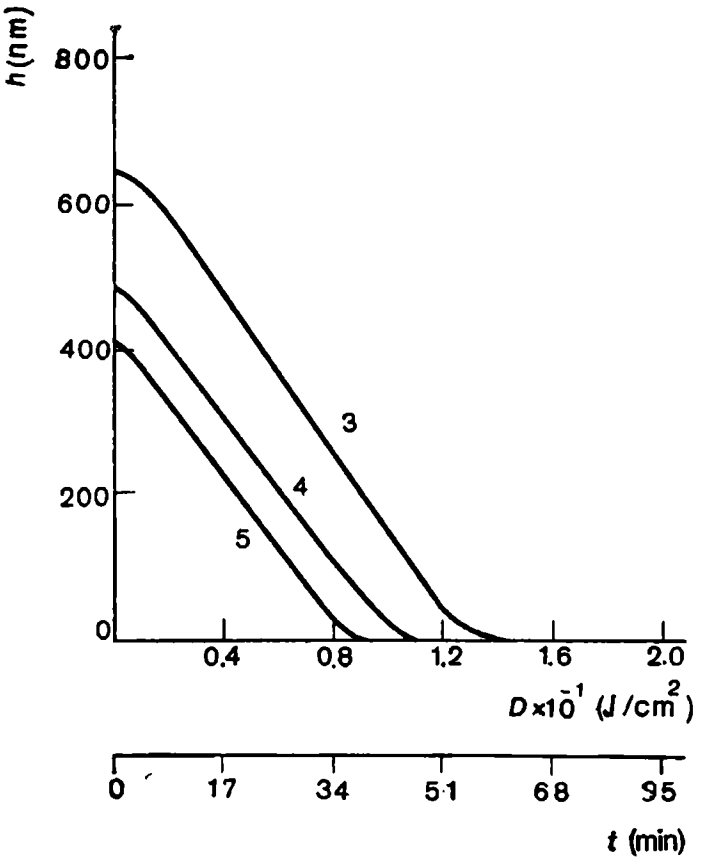

Fig. 9.10. Kinetic curves for VUV-etching of PMMA films in air (the radiation intensity is less than in Fig. 9.9) at different inital film thicknesses.

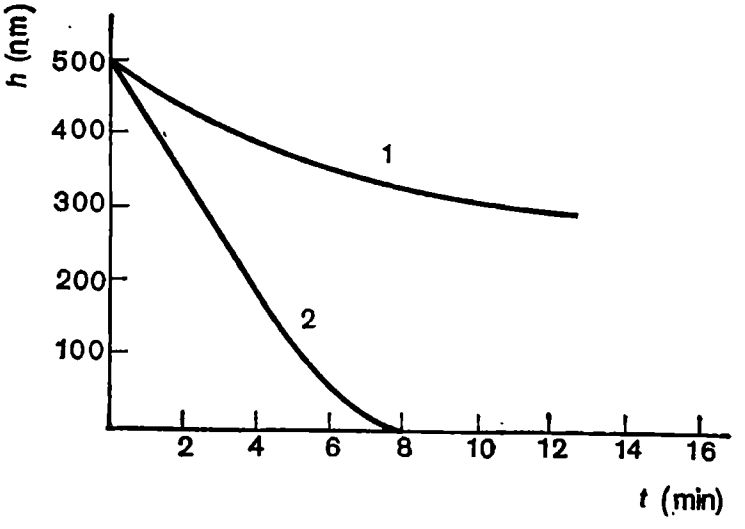

Fig. 9.11. Kinetic curves for VUV-etching in nitrogen (curve *1*) and in air (curve *2*), obtained by using an electric discharge creeping on the surface of a dielectric as the source of VUV-radiation.

in Fig. 9.9, but on a semilogarithmic scale. It can be seen from this figure that a change in the film thickness in nitrogen follows a logarithmic dependence. In other words, we can use the expression (9.70) for modification function in the same way as for their radiation in the X-ray region. At the same time, we can put $\varphi(t) = 1$ when considering etching in an oxygen-containing atmosphere, thus indicating that a polymer modification does not take place in this case.

From the experimental curves (Figs. 9.9-11), it follows that the quasistationary etching conditions (linear dependence for etching in air, and logarithmic dependence for etching in nitrogen) are attained rapidly. In all spectral regions of the VUV radiation employed for etching, deviations from these conditions are observed at film thicknesses of the order of 50 nm, when residual etching at a lower rate begins. Hence, the quasistationary condition (9.17) is satisfied practically throughout the process. The absorption coefficient for the VUV-radiation with a quantum energy of about 10 eV is found to be about (3-5) $\times 10^5$ cm^{-1} for PMMA, i.e. $\delta \simeq 50$ nm. Thus, a film thickness of 50 nm at which the residual etching sets in corresponds to the absorption length δ, and hence the diffusion length l_D is more than the absorption length. Since v_0 is of the order of thermal velocity, $D \sim 10^{-8}$ cm^2/sec [9.22] and G_2 is clearly less than 10^{12} sec, the inequality (9.35) must be satisfied and hence formulas (9.69), (9.61), and (9.62) are applicable. Since in all the experiments the initial film thickness exceeded the quantity $\delta \simeq 50$ nm, the following expression should be used for the scaling factor (9.62):

$$f(h_0, \delta, l_D) = 2 \sinh\left(\frac{\delta}{2l_D}\right) \cosh\left[\left(h_0 - \frac{\delta}{2}\right)\Big/ l_D\right] \cosh^{-1}(h_0/l_D).$$

Since $h_0 \gg \delta/2$ in all cases and $\delta < l_D$, it follows that

$$f(h_0, \delta, l_D) = 2 \sinh(\delta/2l_D) \simeq \delta/l_D, \tag{9.77}$$

in other words, $f(h_0, \delta, l_D)$ does not depend on h_0. Thus, in accordance with Eqs. (9.61), (9.69), (9.70), and (9.77), the expression for quasistationary etching rate in VUV-etching experiments has the following form:

$$u(t) = u_1 \varphi(t), \quad \text{where} \quad u_1 = \frac{m}{\rho} G_1 \delta. \tag{9.78}$$

The modification function $\varphi(t)$ for etching in an oxygen-containing atmosphere is equal to unity, while for etching in nitrogen we can take

$$\varphi(t) = \left(1 + \frac{t}{\tau}\right)^{-1}. \tag{9.79}$$

According to (9.78), the film thickness upon etching in air decreases linearly with the radiation dose:

$$h(D_v) = h_0 - \frac{u_1}{I} D_v.$$

At the end of the etching process, when $h \ll \delta$, the film thickness exponentially decreases in view of (9.65):

$$h(t) = \delta \exp\left[-\frac{m}{\rho} G_1 (t - t_0)\right].$$

If the etching takes place in an oxygen-free atmosphere, it can be easily shown in analogy with (9.71), (9.73) that the kinetic dependences are described by the following expressions:

$$h(D_v) = h_0 - u_1 \tau \ln\left(1 + \frac{D_v}{D_{v_0}}\right), \tag{9.80}$$

$$h(D_v) = \delta\,(D_v/D_{v_1})^{-\frac{m}{\rho} G_1 \tau}. \tag{9.81}$$

In formula (9.81) for the final stage of residual etching, $D_{v_1} = I_0 t_1$, where t_1 is the instant of time at which h becomes equal to δ.

Table 9.3.

Nos. of curves	*1* (Fig. 9.9)	*2* (Fig. 9.9)	*3* (Fig. 9.10)	*4* (Fig. 9.10)	*5* (Fig. 9.10)
u_1, nm/sec	0.24	0.24	0.20	0.21	0.20

Table 9.3 contains the estimates for the etching rates u_1 for curves in Figs. 9.9 and 9.10. It can be seen from the table that according to the theory, the etching rate does not depend on the initial film thickness h_0. Since in accordance with (9.78) $u_1 = \frac{m}{\rho} G_1 \delta$, where $G_1 = g\alpha I_0$, we obtain the following estimate for the quantum yield of low-molecular fragments in PMMA by using the values $\rho = 1.17$ g/cm^3, $u_1 = 0.24$ nm/sec, and $I_0 = 4 \times 10^{-4}$ J/cm^2 sec:

$$g = \frac{\rho u_1}{m I_0} = \frac{7}{m} \text{ (particles per quantum)},$$

where m is measured in atomic units. For $\delta = 1/\alpha = 50$ nm, the generation rate for fragments is given by

$$G = g\alpha I_0 = \frac{3.4}{m} \cdot 10^{21} \text{ cm}^{-3} \text{ sec}^{-1}.$$

We also have the experimental results on VUV etching of a PMMA film in vacuum. Using formulas (9.78) and (9.79) for describing the experimental curves, we get the following values from these results:

$$u_1 = (0.255 \pm 0.003) \text{ nm/sec}, \quad \tau = (204 \pm 3) \text{ sec}.$$

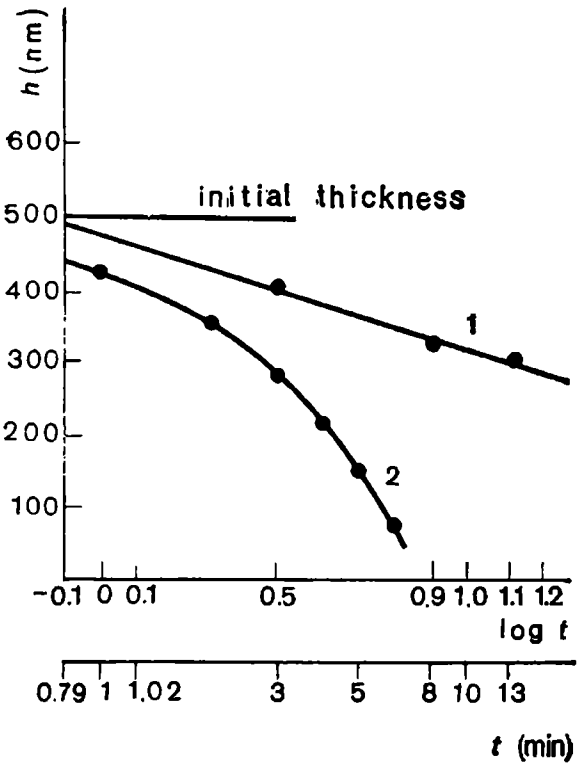

Fig. 9.12. Kinetic curves for VUV-etching; the same curves as shown in Fig. 9.11 have been plotted on a semilogarithmic scale.

The experimental points were found to fit on the theoretical curve to a high degree of accuracy. The value $u_1 = 0.24$ nm for the etching rate of a nonmodified film, obtained from the experiments on etching conducted in air, is in good agreement with the value obtained from experiments on etching in vacuum. The small discrepancy observed between these two values is due to a decrease in the intensity of VUV radiation as it passes through the air gap between the tube window and the film surface.

9.8. CONCLUSION

In this paper, we have carried out a detailed investigation of the etching of polymer films by electromagnetic and corpuscular radiation.

A theoretical model for this phenomenon, based on the concept of diffusion mechanism and applicable for describing etching by low-intensity radiation flux, has been proposed. In the step dependence approximation of the spatial distribution of radiation intensity on the penetration depth, solutions have been obtained for the appropriate boundary-value problems which describe the etching process for

any relation between the initial film thickness, absorption length, and the diffusion layer thickness of low-molecular fragments. The basic regularities for the final stage of the etching process have been revealed. On the basis of theoretical analysis, a general expression for the etching rate has been obtained. This expression is written in terms of the properties of the radiation (intensity, penetrability), the properties of the exposed polymer (density, yield of volatile fragments, and their average mass), and a universal function characterizing the geometrical parameters of the process. This expression also takes into account the modification of the properties of a polymer film during irradiation. The theory developed in this way has been used for a quantitative analysis of experiments on photoetching of polymer films.

Experimental methods have been worked out for investigating the process of direct etching of polymer films. The etching effect in VUV- and X-ray spectral regions has been discovered and analyzed in detail for several polymer materials. The basic kinetic relations for photoetching have been established. The experimental results obtained are in good agreement with theory on the whole.

It has been shown that both positive and negative polymers can be etched by X-ray radiation. It has been established that the X-ray etching in vacuum obeys a logarithmic law, which is explained by a gradual modification of the polymer properties. The etching rate of unmodified polymers, their modification parameters, and the quantum yields of low-molecular fragments have been obtained. The dependence of these quantities on the structure of monomer chains has been found for a number of polyolefinsulfones.

In the case of VUV-etching in an oxygen-containing atmosphere, etching is shown to be linear, thus signifying an absence of modification of the polymer ("oxygen effect"). At the same time, etching in an inert medium proceeds logarithmically. Quantitative characteristics have been obtained for VUV-etching, including the quantum yields of low-molecular fragments and the etching rate. The main differences between the VUV-etching, where the radiation is absorbed in a narrow surface layer of the film, and the etching by X-rays have been pointed out.

References

9.1. K. A. Valiev, L. V. Velikov, S. D. Dushenkov, A. V. Mitrofanov, and A. M. Prokhorov. *Pis'ma v Zh. T. F.* 8, 33, 48 (1982).

9.2. K. A. Valiev, L. V. Velikov, S. D. Dushenkov, A. V. Mitrofanov, and A. M. Prokhorov, in: *Proc. 3rd Microelectronics Conf. of the Socialist Countries*, 5-7 May, 1982, Siofoc, Hungary, p. 91.

9.3. Yu. M. Aleksandrov, K. A. Valiev, L. V. Velikov, S. D. Dushenkov, A. V. Mitrofanov, A. M. Prokhorov, and M. N. Yakimenko, *Pis'ma v Zh. T. F.*, 8, 577 (1982).

9.4. M. J. Bowden and L. F. Thompson. *Polymer Engineering and Science*, **14**, 525 (1974).
9.5. L. F. Thompson and M. J. Bowden. *J. Electrochem. Soc.*, **120**, 1722 (1973).
9.6. K. A. Valiev, V. A. Danilov, S. V. Peshekhonov, A. V. Rakov, and A. G. Shchuchkin. *Mikroelektronika*, **12**, 195 (1983).
9.7. N. Ueno., Sh. Kanishi, K. Tanimoto, and K. Sugita. *Jap. J. Appl. Phys.*, **20**, 709 (1981).
9.8. R. Shrinavasan and V. Mayne-Banton. *Appl. Phys. Lett.*, **41**, 576 (1982).
9.9. B. I. Khrushch, Yu. A. Ershov, A. N. Lyulichev, and V. F. Udovenko. *Khimiya Vysokikh Energii*, **11**, 332 (1977).
9.10. K. A. Valiev. L. V. Velikov, and T. M. Makhviladze. *Poverkhnost'*, **12**, 99 (1983).
9.11. D. E. O Hara and W. F. Beushel. *Polymer Engineering and Science*, **14**, 509, (1974).
9.12. E. Gipstein, W. Moreau, G. Chiu, and O. U. Need III. *J. Appl. Polymer Science*, **21**, 677 (1977).
9.13. M. J. Bowden. *J. Polym. Sci.*, **12**, 499 (1974).
9.14. H. Hiraoka, *IBM Journ. Res. Dev.*, No. 2, 121 (1977).
9.15. I. Haller, M. Hatzakis, and R. Shrinavasan. *IBM Journ. Res. Dev.*, **12**, 251 (1968).
9.16. D. L. Spears and H. L. Smith. *Electron. Lett.*, 8, 102 (1972).
9.17. Y. Mimura, T. Ohkubo, T. Takcuchi, and K. Sekikawa. *Jap. J. Appl. Phys.*, **17**, 541 (1978).
9.18. H. Sotobayshi, F. Asmussen, K. Thimm, W. Shnabel, H. Betz, and D. Einfield. *Polymer Bulletin*, **7**, 95 (1982).
9.19. P. R. E. J. Cowley and H. W. Melville. *Proc. Roy Soc.*, **A210**, 461 (1952); *ibid*, **211**, 320 (1952).
9.20. Yu.M. Aleksandrov, K. A. Valiev, L. V. Velikov, O. S. Glebova, B. G. Gribov, S. D. Dushenkov, D. D. Mozzhukhin, A. S. Pleshivtsev, G. K. Selivanov, and M. N. Yakimenko, *Mikroelektronika*, **126**, 3 (1983).
9.21. M. N. Yakimenko. *Usp. Fiz. Nauk*, **114**, Vyp. 1, 55 (1974).
9.22. P. A. Small, *Trans. Farad. Soc.*, **49**, 441 (1953).
9.23. A. N. Zaidel and E. Ya. Shreider, *Vacuum Ultraviolet Spectroscopy*, Nauka, Moscow, 1967.
9.24. K. A. Valiev, L. V. Velikov, S. D. Dushenkov, D. Yu. Zaroslov, E. R. Kanunov, N. V. Karlov, I. O. Kovalev, G. P. Kuzmin, and A. M. Prokhorov, *Pis'ma v Zh. Teor. Fiz.*, (1983).
9.25. K. A. Valiev, L. V. Velikov, S. D. Dushenkov, and A. V. Mitrofanov. *Poverkhnost'*, No. 6, (1983).
9.26. S. Madorsky, *Thermal Degradation of Organic Polymers*, New York, 1964.

10 Coil-Globule Transitions in Polymer Systems

A. Yu. Grosberg and A. R. Khokhlov

10.1. INTRODUCTION

Coil-globule phase transition is one of the most important phenomena in polymer physics, since its properties quite clearly reflect the basic specific aspects of polymer systems as such. This phenomenon first became the subject of experimental and theoretical investigations some 20 years ago in connection with the problem of denaturation of proteins. Denaturation of a protein consists in an abrupt loss of its native biochemical properties (for example, fermentative activity). At first, it was assumed that denaturation was associated with a transition of a protein chain from a dense globular state to a loose coil state. Although this hypothesis was not always found to be true, it stimulated investigations of main qualitative differences not only between the biochemical, but also between the physical properties of a coil and a globule.

It was first indicated by Lifshitz in what is now considered a classical work [10.1] that a coil and a globule are qualitatively different macroscopic phase states of a polymer chain, and that these phases primarily differ from each other in their fluctuational properties. According to [10.1], the difference boils down to the following: the spatial structure of a coil strongly fluctuates, while a globule has a clearly well-defined spatial structure.

The approach worked out by Lifshitz [10.1] turned out to be quite general and fruitful. Subsequently, it was further developed by several authors [10.8-9] and was found to be applicable for describing a wide range of polymer systems and the phenomena occurring in them. Due to limitation of space, we shall not describe all the applications of Lifshitz' theory in detail. We shall begin with the description of basic physical ideas and mathematical structure of the globule theory formulated by Lifshitz. After this, we shall consider in some detail the application of the general theory for describing the adsorption of ideal chains, the coil-globule transitions in linear uncharged homopolymer molecules, globular states of the simplest heteropolymers, and liquid-crystal ordering of polymer solutions. The latter is interpreted here as a special case of globule formation in the space of link orientations. We shall then briefly discuss coil-globule transitions in more complex polymer systems like polymer networks surrounded by a solvent; polyelectrolyte solutions; macromolecules

with a rigid chain or with mesogenic groups, which are capable of forming an intramolecular liquid-crystal phase in a diluted solution; comb-shaped polymers; individual macromolecules dissolved in another polymer; and DNA and protein macromolecules.

10.2. BASIC IDEAS OF LIFSHITZ' GLOBULE THEORY

The definiteness of spatial structure of a globule and the absence of strong fluctuations in it lead to the expectation that the self-consistent field approximation can be applied to the globular phase theory. This approximation forms the basis of Lifshitz' globule theory [10.1]. Before discussing the limits of applicability of this approximation, let us consider the constructive aspect of the theory.

As usual, the self-consistent field approximation problem is solved in two stages. Firstly, we must investigate the state of an ideal chain with a given form of linear memory, but without volume interactions, in an arbitrary external field. Secondly, we must find the average field acting on an individual link from the remaining links for a given conformation of the chain as a whole.

From a physical point of view, the first of these problems is interesting by itself, since it is the general problem of the adsorption of an ideal chain. Various specific aspects of the theory of adsorption were considered in [10.2-6]. An exhaustive general approach to the problem of homopolymer adsorption was, however, put forth in [10.1] (an equivalent approach has been proposed recently in [10.7]).

The following notation will be used here: ξ is the complete set of generalized coordinates of a single link, $\psi(\xi)$ the probability distribution function for the states of the terminal link in the chain, $n(\xi)$ the number density of links at the point ξ, $\varphi(\xi)$ the external field acting on the links, $g(\xi, \xi')$ the conditional probability that the next link in the chain will be in the state ξ provided the preceding link is in the state ξ', and $\hat{g}$ an operator with the kernel $g(\xi, \xi')$, i.e. $\hat{g}\psi = \int g(\xi, \xi')\, \psi(\xi')\, d\xi'$.

For an ideal chain, the random walk in an external field is a Markov process and can, therefore, be completely described by a diffusion-type linear equation. The corresponding Green function is the partition function for a chain with fixed ends and depends on the number N of links (which acts as time) and the coordinates ξ_1 and ξ_N of the ends. It can be easily surmised that (see [10.8] for details) this Green function is equal to

$$Z\left(\begin{matrix}1\\ \xi_1\end{matrix}\middle|\begin{matrix}N\\ \xi_N\end{matrix}\right) = \hat{Q}^N \delta(\xi_1), \quad \hat{Q} \quad \exp\left(-\frac{\varphi(\xi)}{T}\right) g(\xi, \xi'). \tag{10.1}$$

It follows hence that the state of a macromolecule is determined by the type of the spectrum of the operator $\hat{Q}$. If its highest eigenvalue belongs to a discrete spectrum, the distribution function of the terminal link exponentially tends to the corresponding eigenfunction of the operator $\hat{Q}$ with increasing length of the chain. In this case, the probability distribution functions for opposite ends become statistically independent. Moreover, the correlation along the chain decreases exponentially so that a long chain is actually split into portions of finite length, which are practically independent of each other. These portions make independent contributions to the density. The density distribution is therefore found to be thermodynamically well-defined and hence the discrete spectrum of the operator $\hat{Q}$ corresponds to the globular state of a polymer (some refinements are given in [10.8, 10]).

On the other hand, when the spectrum of the operator $\hat{Q}$ is continuous, the distribution functions for the chain ends are not independent. Naturally, this corresponds to the coil state.

Thus, the mathematical mechanism of the coil-globule transition in an external field, viz. adsorption transition, consists in the splitting of the discrete level from the edge of the continuous spectrum of the following equation:

$$\exp\left[-\varphi(\xi)/T\right]\hat{g}\psi = \Lambda\psi(\xi). \tag{10.2}$$

The difference in the free energies of the globular and the coil state is expressed in terms of Λ, viz. the highest eigenvalue of this equation, and is equal to $-TN\ln\Lambda$.

It was indicated in [10.1] that Eq. (10.2) is similar to the Schrödinger equation[1]. This similarity paves the way for a unified and systematic understanding of the concepts of temperature, type, and other characteristics of adsorption transitions of an ideal chain on the adsorbents of various shapes, symmetries, dimensionalities, etc. [10.7, 10].

The next step towards the construction of the general theory of globules was the computation of the conformational entropy of a chain in the state determined by the density distribution. For this purpose, we must simply expess the entropy of a globule in an external field in terms of density rather than in terms of the field φ.

---

[1] Other aspects of the similarity between polymer statistics and quantum mechanics, viz. the relation between the partition function for a chain and Feynman's continual representation for the Green function, between the function ψ and the creation (or annihilaton) operator, etc. are considered independently in [10.6, 11, 12].

This expression has the form

$$S = \int n(\xi) \ln \frac{\hat{g}\psi}{\psi} d\xi. \tag{10.3}$$

The following relation holds between $n(\xi)$ and $\psi(\xi)$:

$$\Lambda n(\xi) = \psi(\xi) \hat{g}\psi \tag{10.4}$$

(the factor Λ does not play any significant role here; it simply determines the most convenient form of normalization for the wave function ψ).

The last important aspect of Lifshitz' theory is the way in which volume interactions are taken into account. The main idea behind this is that the joining of monomeric links into a chain does not significantly alter the nature of volume interactions but simply deprives the links of the freedom of independent translational motion. In particular, when applied to the simplest polymer chain model, viz. the beads-on-a-filament model, this means that the free energy per unit volume for the system of links packed with a density n is equal to $f^*(n, T) = f(n, T) - f_{id}(n, T)$. Here, $f(n, T)$ is the free energy per unit volume of the system of disconnected links, and $f_{id} = Tn \ln(n/e)$ is the free energy of an ideal gas. Consequently, the self-consistent field acting on a given link from the surrounding links, i.e. the chemical potential $\mu^* = \partial f^*/\partial n$ of the link, is equal to

$$\varphi^{self}(\mathbf{x}) = \mu^*(n(\mathbf{x})) = \mu(n(\mathbf{x})) - \mu_{id}(n(\mathbf{x})), \tag{10.5}$$

where μ and $\mu_{id} = T \ln n$ are the chemical potentials of the gas of disconnected links and an ideal gas respectively. This expression solves the second of the problems formulated at the beginning of this section. Substitution of (10.5) into (10.2) leads to a nonlinear equation which, together with Eq. (10.4) and the normalization condition $N = \int n(\xi) d\xi$, completely determines the globule structure. The free energy of a globule can be calculated with the help of the following formula after solving the above system of equations:

$$F = \int f^*(n) d\xi - T \int n \ln \frac{\hat{g}\psi}{\psi} d\xi = -TN \ln \Lambda - \int p^*(n(\xi)) d\xi, \tag{10.6}$$

where $p^*(n) = n\mu^* - f^*$ is the osmotic pressure of the system of links.

The methods of solving Eqs. (10.2-6) in various limiting cases, viz. a large globule with a smooth density distribution, a large globule with a density bounded at the interface, a small globule, etc., have been discussed in [10.1, 8, 13, 14]. Here, we shall confine ourselves to qualitative considerations only.

10.3. COIL-GLOBULE TRANSITIONS IN THE SIMPLEST LINEAR UNCHARGED HOMOPOLYMER

A globule is a system with small fluctuations. The density fluctuations in a globule are small in comparison with the density itself, and the correlation radius is much smaller than the globule size. This means that from a localized point of view, a large globule on a scale of the order of correlation radius can be regarded as a solution of several independent chains which are actually different portions of the same chain. From this it primarily follows that the core of a large globule must be spatially homogenous and the link density in it must have a certain constant value n_0. Further, it also follows from here that for an equilibrium coexistence of a large globule with the surrounding solvent, the osmotic pressure created in the globule by independent subchains must be equal to zero. In other words, n_0 is determined by the condition

$$p^* (n_0) = 0 \tag{10.7}$$

For the homogeneous globule core, $\hat{g}\psi \simeq \psi$ i.e. the contribution from the entire volume of the globule core to the conformational entropy (10.3) is equal to zero. This is an indication of the fact that the portions of a chain inside a homogeneous core behave like Gaussian coils, i.e. like chains in a homogeneous melt [10.15, 16]. The equality of both the volume entropy and the pressure in a globule to zero leads to the following expression (see Eq. (10.6)) for the volume part of the free energy:

$$F = N\mu^* (n_0) \tag{10.8}$$

Formulas (10.7, 8) constitute the result of the volume approximation in the theory of a large globule. As the temperature, composition, or the state of a solvent change (see [10.8, 17] for the role of a solvent), the functions $p^* (n)$, $\mu^* (n)$, etc. evolve in a certain way. This is accompanied by a change in the volume $V = N/n_0$ and in the free energy F of a globule. When the quantity F is no longer negative, the globule disintegrates, and a coil-globule transition takes place.

The clearest visual interpretation of the above is provided by the curve describing the μ^* vs. n dependence. On this curve, Eq. (10.7) which defines the density or volume of a globule represents the condition that the shaded areas in Fig. 10.1 are equal. It can be seen from the figure that two cases are possible here (curves *I* and *II* in Fig. 10.1). These cases differ in the behaviour of the function $\mu^* (n)$

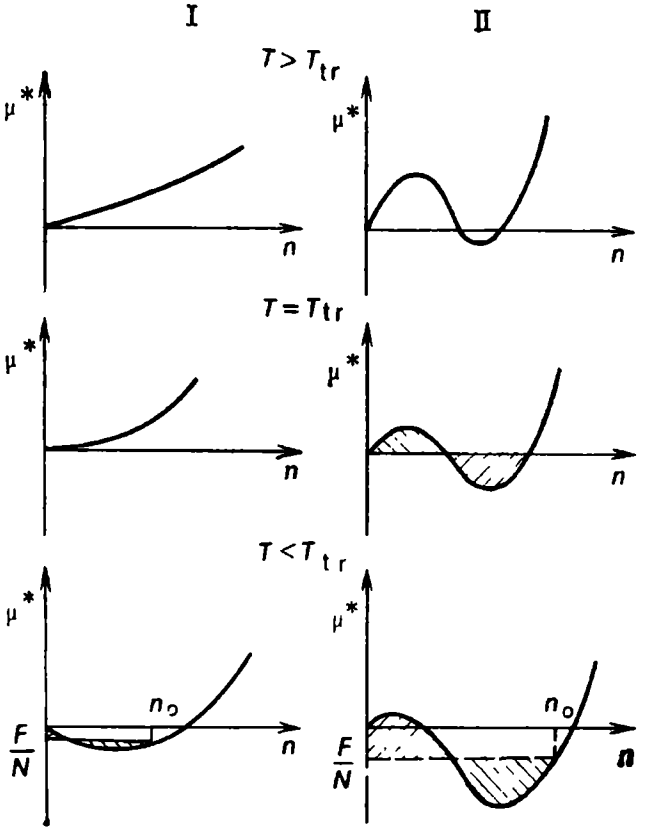

Fig. 10.1. Dependences of the chemical potential of a link on density as the temperature varies in the vicinity of the coil-globule transition point for both types of transition.

in the region of low densities, where the following virial expansion can be used:

$$\frac{\mu^*(n)}{T} \simeq 2Bn + 3Cn^2 + \dots . \tag{10.9}$$

In the original approach developed by Lifshitz [10.1], the quantities B, C, . . . should be interpreted as the second, third, etc. virial coefficients of interaction between monomers. In a more general case, these quantities represent the renormalized virial coefficients of interaction between quasimonomers [10.18, 19]. Thus, the two cases represented in Fig. 10.1 differ in the order in which the virial coefficients change sign upon a change in the temperature.

Curves *I* in Fig. 10.1 correspond to the first possible situation: when the second virial coefficient vanishes, the third and all subsequent virial coefficients are positive. This situation is typical of the simplest homopolymers, and in particular, for a chain of beads with any central interaction potential. In this case, the coil-globule tran-

sition is associated with a change in the sign of the second virial coefficient, i.e. with the θ point. It is accompanied by a significant pretransitional broadening (i.e. by a decrease in density and an increase in size) of the globule. In an infinite chain, for which the volume approximation is exact, the coil-globule transition occurs at the θ point and is a second-order phase transition.

In actual practice, for a molecule of real finite dimensions the thickness of the globule surface layer near the globule-coil transition point is comparable with its globule radius, and hence the volume approximation is no longer applicable. However, since the globule density in the pretransition region is low, we can confine the expansion (10.9) to just two terms.

Besides, the broadening of a globule allows us to consider only the ordinary coordinates **x** from among all generalized coordinates of the links and approximate the operator $\hat{g}$ in accordance with the relation

$$\hat{g} \simeq 1 + (a^2/6)\,\Delta. \tag{10.10}$$

Here, Δ is the Laplace operator and a the characteristic chain length per link. Hence, a complete description of the globule-coil transition for the case shown by curves *I* in Fig. 10.1 can be given in terms of the chain length a and the second and third virial coefficients of link interaction. In this respect, this description turns out to be universal.

An analysis shows that the free energy, the swelling factor, and other observable properties of a globule are expressed in terms of two dimensionless combinations of parameters[2]:

$$\sqrt{C}/a^3 \text{ and } q = +6^{3/4}BN^{1/2}a^{-3/2}C^{-1/4}. \tag{10.11}$$

Near the θ point, the parameter q is directly proportional to the temperature, since $B = b\tau$, where $\tau = (T - \theta)/\theta$. Numerical calculations carried out in [10.21, 22] show that the coil-globule transition takes place at $q = q_{tr} = -10.4$, i.e. slightly below the θ temperature:

$$\tau_{tr} \simeq -2.8\,(a^3C^{1/2}/b^2N)^{1/2}. \tag{10.12}$$

The free energy of a globule (for $|\tau| \ll 1$) is given by

$$\frac{F}{\theta} = 0.66\frac{a^3}{\sqrt{C}}\left[1 - \left(\frac{\tau}{\tau_{tr}}\right)^2\right]. \tag{10.13}$$

With decreasing temperature, i.e. with increasing q and $|\tau|$, the globule becomes denser, and at $q \gtrsim 3\theta$, the volume approxima-

---

[2] Three dimensionless combinations can be formed from the parameters N, a, B and C. The fact that only two combinations are left is a result of the general scaling law [10.20].

tion is applicable to within 10%. It can be easily seen from formulas (10.7-9) that in this region the globule radius changes[3] as $R \propto \propto |\tau|^{-1/3}$, while the free energy behaves as $F \sim -N\tau^2$. Thus, not very close to the transition point, i.e. when $1 \gg |\tau| \gg |\tau_{tr}|$, the system behaves in the same way as upon approaching the second-order phase transition point.

At the same time, the behaviour of the system in the close proximity of the transition point considerably depends on the second dimensionless parameter $\sqrt{C}/a^3$. If this parameter is small, i.e. if $\sqrt{C}/a^3 \ll 1$, the globule-coil transition is quite abrupt and similar to a first-order phase transition in many respects. Although the heat of transition $\delta Q = 0.45(b/\sqrt{C})\ (Na^3/\sqrt{C})^{1/2}$ remains small and of the order of $N^{-1/2}$ per particle, the transition is accompanied by a large jump in density and size. For example, the relative change in the swelling factor α^2 of a macromolecule, i.e. the ratio of its radius of gyration to the radius of gyration of a Gaussian coil is of the order of

$$\frac{\alpha^2_{coil} - \alpha^2_{glob}}{\alpha^2_{glob}} \sim \frac{a^3}{\sqrt{C}}. \tag{10.14}$$

The width of a transition is also an important factor characterizing its properties. As a matter of fact, the usual concept of a phase transition as the point of singularity of thermodynamic functions is strictly applicable only for an infinite system. Near the transition temperature, when the difference in the free energies of phases is less than or of the order of T per macromolecule, a macromolecule of real finite dimensions has equal (in the order of magnitude) probabilities of appearing in any of the competing states. Hence, it would be more appropriate to speak of a transition region of temperatures rather than the transition point. The width $\delta\tau$ of this transition region can be estimated from the condition $F(\tau_{tr} + \delta\tau) \sim T$:

$$\delta\tau \sim \tau_{tr}\sqrt{C}/a^3. \tag{10.15}$$

It is important to note that the transition width tends to zero as $N \to \infty$ (see Eq. (10.12)). It is this circumstance that leads us to the conclusion that the coil-globule transition is a phase transition.

Thus, for $\sqrt{C}/a^3 \ll 1$, the molecule collapses quite abruptly in a narrow region separated from the θ point. On the contrary, for $\sqrt{C}/a^3 \sim 1$, the globulization takes place smoothly over a wide interval including the θ point.

It should be noted that for a polymer, the parameter $\sqrt{C}/a^3$ is the Ginzburg number [10.23, 24, 8]. Consequently, for $\sqrt{C}/a^3 \ll 1$, the self-consistent field approximation, and together with it the entire

[3] This result was first obtained in [10.14].

theory described above, is asymptotically correct. For $\sqrt{C}/a^3 \sim 1$, the theory is true only in the order of magnitude.

It should be recalled that all the above description corresponds to the case shown in Fig. 10.1 (*I*). The second possible situation is shown in Fig. 10.1 (*II*): in the region of a good solvent, when the second virial coefficient is positive (i.e.when repulsion prevails during a binary contact of links), the many-particle contacts correspond to attraction, i.e. some higher-order virial coefficients are negative. We shall consider at a later stage the examples of systems in which such a possibility arises. It is obvious from the figure as well as from physical considerations that the coil-globule transition in this highly cooperative case is a first-order phase transition which is characterized by large values of the latent heat ($\sim T$ per link) and of jumps in the density (or volume).

Before concluding this section, let us give a brief resumé of other theoretical approaches to the problem of the coil-globule transition. At the very outset, it should be remarked that all these approaches are applicable only for the case shown in Fig. 10.1 (*I*). Chronologically, the first article on this subject [10.25] was published in 1965. The method proposed therein was improved in [10.26]. The widely cited papers [10.27] and [10.28] are in fact reproductions of [10.25] and [10.26]. The works [10.25-28] are based on a generalization of the well-known Flory method of calculating the swelling factor of a coil [10.29]. The generalization consists in that, firstly, the negative sign of the second virial coefficient below the θ point is taken into account; secondly, the contribution from triple interactions to the free energy of mixing is considered. Although the theory [10.25-28] correctly interprets certain qualitative properties of the globule-coil transition of the first type (Fig. 10.1 (*I*)), it is not possible to obtain correct quantitative results from it.

Some aspects of the theory of first type globule-coil transition in the volume approximation which, as has been shown above, is valid only for an infinite chain have been described in [10.30-32]. Such an approach naturally led Moore [10.32] to the conclusion that the globule-coil transition is a second-order phase transition. It has been mentioned above that while this conclusion is undoubtedly valid at the limit $N \to \infty$, it is essentially incorrect for real values of N.

Finally, the work of Sanchez [10.33], which appeared in 1979, does not differ significantly in the formulation of the problem or in the nature of results from earlier works [10.14, 8].

In [10.14], the example of the specific equation of state $\mu^*(n)$ for the case when the effective attraction between links is due to the saturating bonds (or the divalent cross-links present in the solution [10.34]) was considered in detail.

The theory of coil-globule transition was generalized in [10.35] to a space of arbitrary dimensionality.

It should be mentioned that the coil-globule transition of the type shown in Fig. 10.1 (*II*) was first considered in [10.1].

Various aspects of the theory of so-called small globules have been considered in [10.13, 17, 8, 36, 37].

10.4. A BRIEF COMPARISON OF THEORETICAL AND EXPERIMENTAL RESULTS

A direct observation of the collapse of an individual macromolecule in dilute solutions is very difficult, since the solutions must be of extremely low concentrations in order to avoid precipitation.[4] It is clear from the foregoing that a coil-globule transition can be considered to have taken place when the experimentally measured gyration radius of a molecule acquires a power dependence on temperature, i.e. $R \propto |\tau|^{-1/3}$. According to this criterion, a coil-globule transition was observed in [10.38-40, 108]. In other works on this subject (see [10.41-43]), only the initial stage of molecular collapse (a small contraction of the coil) was actually observed. Figure 10.2 represents the temperature dependence of the swelling factor of a molecule, i.e. ratio of its radius of gyration to the radius of gyration of a Gaussian coil. This dependence was theoretically obtained in [10.22] in the following way. The swelling factor of a macromolecule $\alpha^2_{\text{glob}}(q)$ in the globular state was calculated first. Then the swelling factor α^2_{coil} of a coil was taken in the form of the ordinary perturbation theory in which the first two terms in the series were taken into account. Finally, it was assumed that in the vicinity of the transition point, the measured value of the swelling factor is given by the formula

$$\langle\alpha^2\rangle = \left[1+\exp\left(\frac{F}{T}\right)\right]^{-1}\alpha^2_{\text{glob}} + \left[1+\exp\left(-\frac{F}{T}\right)\right]^{-1}\alpha^2_{\text{coil}}.$$

The experimental points from [10.39, 40, 108] are shown in Fig. 10.2 for the sake of comparison. The following estimates for the parameter $\sqrt{C}/a^3$ can be obtained for the systems investigated in [10.39, 40]: 0.12 for polystyrene in cyclohexane and 0.09 for polystyrene in dioctylphthalate.

Although polystyrene is flexible, it was found that for this polymer $\sqrt{C}/a^3 \simeq 0.1$, i.e. $\sqrt{C}/a^3 \ll 1$. Apparently, this means that in all real polymers, the coil-globule transition is rather abrupt.

A collapse of macromolecules above the θ temperature was reported

---

[4] An estimate of the concentration up to which globules remain in dissolved state is given in the review articles [10.8, 9]; see also the recent work of Post and Zimm [10.46].

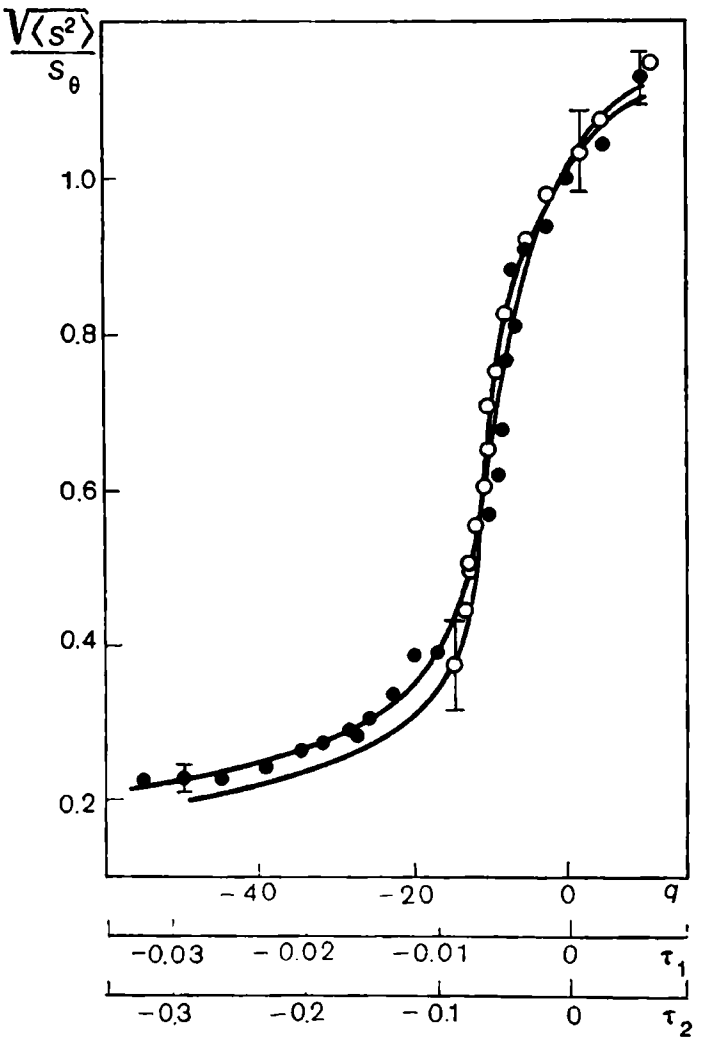

Fig. 10.2. Experimental dependences of the swelling coefficient of a macromolecule on relative deviation from the θ point $\tau_1 = (T - \theta_1)/\theta_1$ ($\theta_1 = 308.5$ K) for polysterene in cyclohexane [10.108] (dark circles) and $\tau_2 = (T - \theta_2)/\theta_2$ ($\theta = 295.1$ K) for polystyrene in dioctylphthalate [10.40] (light circles) and the corresponding theoretical curves.

in [10.47-49] for comb-shaped polymers with cholesteric groups in side chains were investigated in these works. According to [10.50-53], the transition observed in [10.47-49] should be interpreted as a coil-globule transition of type *II*. This also serves as a confirmation for the existence of two types of coil-globule transitions.

A large number of computer experiments on the coil-globule transition have also been reported [10.54-58]. All of them are in good qualitative agreement with the theory.

10.5. SOME RESULTS OF THE THEORY OF HETEROPOLYMER GLOBULES

Heteropolymers are chains consisting of several different types of links. For the sake of simplicity, we shall assume that only two different types of links are present, say, A and B. From a local point of view, heteropolymer globules are simply solutions of different types of links. Confining ourselves to the self-consistent field approximation, we must first write down the expressions for the effective fields acting on different types of links. This can be done easily by employing Lifshitz' idea of a gas of disconnected links. Indeed, let $f^*(n_A, n_B, T)$ denote the free energy of a unit volume of a solution of disconnected links with component densities n_A and n_B. Then, in complete analogy with the formula (10.2.4), we obtain the following relation for the self-consistent fields $\varphi_\alpha^{\text{self}}$ acting on links of the type A and B ($\alpha = A, B$):

$$\varphi_\alpha^{\text{self}}(\mathbf{x}) = \mu_\alpha^*(n_A, n_B, T) = \frac{\partial f^*}{\partial n_\alpha}. \tag{10.16}$$

Naturally, μ_α^* is the chemical potential of the links of type α.

The result (10.16) enables us to construct the theory of a large heteropolymer homogeneous globule in the volume approximation, since the conformational entropy of a chain in this approximation is equal to zero. As in a homopolymer, the volume and the total density $n_A + n_B = n_0$ of a globule is determined by the condition that the osmotic pressure of the polymer inside the globule must be equal to zero:

$$p^*(n_A, n_B, T) = n_A\mu_A^* + n_B\mu_B^* - f^* = 0. \tag{10.17}$$

Further, the densities n_A and n_B of the components are determined by the "bulk" composition of the primary structure: if c is the fraction of A links and $(1 - c)$ is the fraction of B links, we can write

$$n_A = cn_0, \quad n_B = (1 - c)\, n_0. \tag{10.18}$$

For the free energy of the globule, which is equal to $Vf^*(n_A, n_B)$ in the volume approximation, we obtain in accordance with (10.17) (see [10.59] for details)

$$F = N[c\mu_A^*(n_A, n_B) + (1 - c)\,\mu_B^*(n_A, n_B)] \tag{10.19}$$

cf. formula (10.8) for a homopolymer).

Formulas (10.17-19) show that in the volume approximation, a heteropolymer globule can be treated as a homopolymer globule with certain effective averaged thermodynamic functions. For example, according to (10.18), the expression within the brackets in Eq. (10.19) can be considered as the effective chemical potential of a one-component system with density n_0. Expanding this quantity in powers of

n_0, we can easily obtain the expressions for the virial coefficients of the effective homopolymer.

The physical consequences of the result obtained here have been analyzed in [10.60]. It is found that the averaging may lead to a change in the sequence of reversal of signs of virial coefficients with temperature. Hence, for example, the coil-homogeneous globule transition in a chain of a few strongly attracting links among weakly repelling ones must take place according to the mechanism represented in Fig. 10.1 (*II*), i.e. as an abrupt first-order phase transition.

The problem of calculating the conformational entropy of a heteropolymer globule is found to be far more complicated. The expression (10.1) for the partition function or the Green's function now contains the product of N noncommutative operators $\hat{Q}_A$ and $\hat{Q}_B$ instead of the N-th power of a single operator Q. The order of arrangement of these operators is determined by the primary structure.

At present, the complete solution of this problem is known to exist only for the simplest initial structures: (a) periodic structure when a whole period of a heteropolymer can be considered as a link of an effective homopolymer [10.34]; (b) large-block structure, when a heteropolymer essentially consists of several connected homopolymers (this situation has been investigated in detail in [10.61-63] dealing with the microdomain phase separation of heteropolymer melts).

The most interesting case, however, is that of a statistical primary structure in which the links A or B may appear at random and independently of their neighbours, with probabilities c and $(1 - c)$ respectively. In this case, the free energy and other thermodynamic properties of the globule, which are determined by the random structure, are themselves random quantities. Consequently, their statistical properties must be investigated. From the existing theory of products of random matrices [10.64], we can draw an important conclusion about the self-averaging of the globule free energy: for $N \to \infty$, the probability distribution of the random free energy per link concentrates[5] near a certain mean value. In other words, self-averaging makes the free energy behave like a thermodynamically well-defined quantity.

A complete solution of the problem on the globular state of a statistical heteropolymer has so far been obtained for two cases: (1) the regular method of expanding the free energy of a globule into a power series in the field difference $\varphi_A - \varphi_B$ is known [10.59] (this expansion is effective for heteropolymers whose links do not differ strongly); (2) the exact solution is known [10.65] for the case when both the fields φ_α have the form $\varphi_\alpha \propto k_\alpha (\mathbf{x} - \mathbf{b}_\alpha)^2$.

---

[5] Meaning thereby that its width tends to zero.

The globulization of the simplest heteropolymers has been modelled in [10.66-68] with the help of the Monte-Carlo method.

It is interesting to study separately the globulization of heteropolymers with a mobile primary structure, in which each link can reversibly change its state, $A \leftrightarrow B$. This model can be used for describing a homopolymer chain in the region of the helix-coil transition, as well as a homopolymer which can adsorb small molecules from the solution. Polymer systems of this type are widely investigated experimentally (see review [10.69]). The theory of such systems is based on the fact that the Green's function (10.1) for them has a "homopolymer" structure, but as a matter of fact, the operator $\hat{Q}$ is a matrix consisting of integral operators (see [10.34, 59] for details). The investigation of such systems has led to the prediction [10.34] of an interesting physical effect, viz. a sort of combination of the coil-globule transition and the $A-B$ transition (of the helix-coil type). Such a combined transition is found to be a first-order phase transition even when the transitions (globule-poly-A)-coil and (globule-poly-B)-coil take place according to Fig. 10.1 (I). The combined transition involves a collapse of the molecule and is accompanied by an abrupt change in its composition, i.e. its helicity or the number of adsorbed small molecules.

10.6. LIQUID-CRYSTALLINE ORDERING IN SOLUTIONS OF RIGID MACROMOLECULES

Rigid macromolecules are molecules whose persistence length l (i.e. the distance over which the polymer chain loses its orientational memory) is much larger than the characteristic thickness d of the chain. Since such macromolecules are highly asymmetric, they should easily form the liquid-crystalline (LC) phase in solution. This is actually the case and the investigation of LC polymer solutions constitutes a separate branch of the physics of macromolecules. This branch has recently aroused an especially large interest due to an important practical application of LC polymers in the production of high-strength artificial fibres.

In spite of this, very few theoretical works were carried out till the end of the seventies on the statistical physics of LC ordering in polymer solutions. Of all the theoretical problems in this field, only the problem of LC ordering in the solutions of long rigid rods could be essentially considered as solved (see the classical works of Onsager [10.70] and Flory [10.71, 72]). The shape of real rigid macromolecules, however, always differs from the rod-like form, since such macromolecules always have a finite flexibility. Systematic investigation of the LC ordering in solutions of macromolecules with a limited flexibility, carried out in a recent series of works [10.53, 73-80],

became possible only after the application of the Lifshitz formalism (described in Sec. 10.2 and reformulated for space of link orientations to this problem).

The LC ordering of macromolecules entails a loss in their orientation entropy S_1, but there is a gain in the free energy F_2 of their interaction. The properties of LC transition are determined by the balance of these two factors, $F = -TS_1 + F_2$. For rigid polymers ($l \gg d$), the quantity F_2 can be calculated with the help of the second virial approximation, since the LC transition always occurs at a quite low concentration of the polymer in solution. As regards the quantity S_1, the Lifshitz method was found to be very convenient for determining this quantity for polymer chains of different lengths with different flexibility mechanisms.

While considering the LC ordering, the unit vector $\mathbf{n}$ of link orientation plays the role of the generalized coordinate ξ of the link. Correspondingly, the orientational distribution function $f(\mathbf{n})$ for the links plays the role of density. The magnitude and nature of the flexibility of a polymer chain in this formalism is determined by the form of the operator $\hat{g}$.

Since the orientation space is compact, the spectrum of the operator $\hat{g} = \hat{Q}$ is known to be discrete. Hence, the solutions of semiflexible chains in which the total contour length L is much larger than the persistence length l, i.e. $L \gg l \gg d$, can be described directly by the formulas (10.3, 4) (formula (10.3) determines the entropy S_1). It should be noted that for $L \gg l$, the orientational distribution function for most links (separated from the ends by more than l) is independent of the link number.

The situation becomes much more complicated for $L \sim l$. In this case, the $f_t(\mathbf{n})$ distribution strongly depends on the link number t. This means that all the eigenfunctions of the operator $\hat{g}$ contribute to the partition function (10.1). In other words, the time-independent diffusion-type equation (10.2) must be replaced by a time-dependent equation which contains the differential operator $\partial/\partial t$ in addition to the integral operator $\hat{g}$. The corresponding calculations have been made in [10.77].

Without going into the details of the method used for calculations, let us briefly consider the results obtained in [10.73-80].

It was found that the nature of LC ordering in a solution of semiflexible chains depends significantly on the flexibility mechanism for the chain. Three most prevalent flexibility mechanisms were considered: the freely jointed mechanism (Fig. 10.3*a*), the persistent mechanism (Fig. 10.3*b*), and the rotational isomeric mechanism (Fig. 10.3*c*). For the freely jointed flexibility mechanism, i.e. in the solution of long chains of freely jointed rods, the LC transition takes

place in nearly the same way as in the corresponding solution of disconnected rods (with a somewhat broader region of phase separation and a somewhat larger order parameter in the appearing anisotropic phase; the difference between these two cases, however, does not exceed 10%) [10.53]. In a solution of semiflexible chains with persistent flexibility mechanism, the LC ordering takes place at much higher concentrations than in the solutions of freely jointed molecules with the same value of the ratio d/l, and is characterized by a relative narrowing in the phase separation region and considerable decrease in the order parameter at the transition point [10.76].

As regards the solution of semiflexible macromolecules with rotational-isomeric flexibility mechanism, the general tendency is such

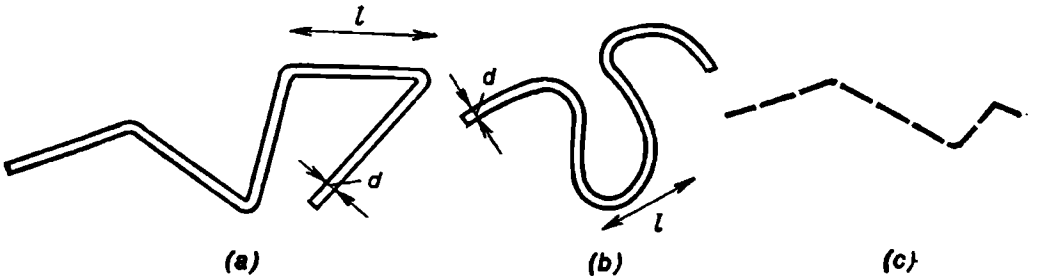

Fig. 10.3. Macromolecules with different flexibility mechanisms (schematic diagram): (*a*) freely jointed; (*b*) persistent; (*c*) rotational-isomeric.

that the homogeneous isotropic phase in this case becomes unstable at lower polymer concentrations in the solution. The appearing anisotropic phase has a higher concentration and a much larger ordering parameter than for the solutions of freely jointed or persistent chains with the same value of the ratio d/l. This tendency is most pronounced for a purely rotational-isomeric mechanism, and the anisotropic phase at the transition point in this case is found to be nearly completely ordered and extremely concentrated. However, the real rotational-isomeric chains always have a small component of persistent-type flexibility; the above-mentioned properties of the LC transition in this case are not pronounced in such an extreme form (although they to be quite significant). In addition to the parameters d and l, they also depend on the length of the second effective segment of the chain, characterizing the persistent flexibility component [10.77, 79].

An investigation of the LC ordering in persistent chain solutions with $L \sim l$ has shown [10.77] that only very short or very rigid macromolecules behave as rigid rods in the case of such a flexibility mechanism (in particular, only such molecules can have such large values of the order parameter at the transition point as in Onsager's theory of rigid rods, viz. $\eta = 0.84$). Even a low flexibility of

the chain ($L/l \simeq 0.1$) is sufficient to bring the properties of the LC transition closer to those for the semiflexible chain limit $L/l \gg 1$ than to the limit $L/l \ll 1$ for absolutely rigid rods (in spite of the fact that for $L/l \simeq 0.1$, the geometrical shape of a macromolecule is much closer to that of a rod-like molecule). In the case of rotational-isomeric or freely jointed flexibility mechanisms, the transition from $L/l \ll 1$ to $L/l \gg 1$ takes place at $L/l \simeq 1$ (and not at $L/l \simeq$ $\simeq 0.1$, as in the case of persistent mechanism), and no additional peculiarities are observed.

10.7. OTHER INVESTIGATED COIL-GLOBULE TYPE TRANSITIONS

The fruitfulness of the approach developed by Lifshitz is not limited to just the examples given above. It turned out that a very large number of phenomena in polymer physics can be theoretically described by coil-globule type transitions. We shall briefly describe some of these phenomena in this section.

A. On the collapse of polymer networks. Suppose that we have a sample of a polymer network swelling in an excess of a good solvent, and suppose that the quality of the solvent is made worse (say, by lowering the temperature). At a certain stage, each of the subchains constituting the polymer network must undergo a coil-globule transition. Consequently, the network sample must collapse as a whole. The collapse of polymer networks has actually been observed recently and investigated thoroughly [10.81, 82].

The theory of collapse of polymer networks was proposed in [10.44], and the influence of the collapse on the elastic properties of networks was considered in [10.45]. These investigations deal with the so-called networks of the second type, prepared in the presence of a large quantity of diluent, while the classical Flory theory [10.29] was shown to be applicable only to the first-type networks obtained in the dry state by vulcanization. Networks of the first type are known to swell without any abrupt collapse.

It was shown in [10.44] that the collapse of a network of the second type occurs abruptly if the network is composed of rigid chains (when $\sqrt{C}/a^3$ is small) and continuously if the network is formed by flexible chains. The stretching of a network practically does not change the coil-globule transition temperature but makes the transition more abrupt.

Interesting effects are also observed in the dependence of the equilibrium strain on the applied stress for the second-type networks. Upon a slow stretching of such networks in a poor solvent, the strain undergoes a discontinuity corresponding to the destruction of the globular structure, i.e. to the globule-coil transition induced by the stretching of the network subchains.

The role of charged groups in the collapse of a network has been considered in [10.83]. It has been shown that the presence of charges with opposite signs (polyampholytic network) leads to a considerable extension of the stability region of the globular state.

The observed experimental results can be fully explained by the theoretical conclusions drawn in [10.44, 45, 83].

B. Quite interesting results should be expected for the **coil-globule transitions in macromolecules of weakly charged polyelectrolytes,** i.e. polymers in which the main part of the links is not charged and interacts with ordinary van der Waals forces, although some rare links carry charge. The phase diagram for such a system has been studied in [10.84].

The theory of coil-globule transitions was constructed in [10.85] for an extremely dilute salt-free solution of a polyelectrolyte, when the screening of Coulomb interaction between links by counterions can be neglected. It was shown in [10.86] (see also [10.87]) that in this case, the macromolecule assumes a strongly elongated conformation (the root-mean-square radius of gyration $\sim N$). This conformation can be conveniently described by introducing the concept of blobs: the size of each blob is determined by the condition that the electrostatic energy of repulsion between two neighbouring blobs in a chain be of the order of temperature. Then, the chain inside a blob will be perturbed only slightly by the Coulomb interactions, and at the same time the system of blobs acquires a strongly elongated conformation.

It follows from the above description that the coil-globule transition occurs separately in each blob and somewhat below the θ point of the uncharged portions of the chain.

It should, however, be noted that as soon as the polyelectrolyte molecules in a salt-free solution assume a strongly elongated conformation, it becomes very difficult to obtain a dilute solution of nonoverlapping chains. Of greater interest and importance is the wide range of concentrations where the molecules strongly overlap, but the volume fraction of the blobs is still quite low. It was shown in [10.85] that the coil-globule transition in this region is accompanied by an avalanche-type condensation of counterions.

In order to understand the essence of this phenomenon, it should be recalled [10.88] that the charge on any one-dimensional structure in an electrically neutral system can be increased only to a certain critical value of the linear charge density. Any further charging of the line results in the condensation of counterions thus compensating the excess charge. In a good solvent region, the linear charge density on a chain of blobs never exceeds the critical value. As the quality of the solvent deteriorates, the globulization of blobs leads to an increase in the linear charge density and to the onset of condensation of counterions. It is essential that this condensation leads to

an increase rather than a decrease in the linear charge density, since the partial compensation of the charge is accompanied by the corresponding conformational changes of the macromolecule which becomes less and less elongated. The resulting avalanche-like process leads to a condensation of almost all the counterions and to the appearance of a spherical globule.

An experimental investigation of the collapse of a weakly charged polyelectrolyte has not been carried out so far, although we feel that it should offer interesting results.

C. Intramolecular liquid crystal. Macromolecules with a stiff chain or with mesogenic groups in the main or side chains globulize in a peculiar way. The segments of macromolecules are orientationally ordered inside the globule in this case; in other words, an intramolecular liquid-crystalline phase emerges.

From the theory of the liquid-crystalline state in the solutions of semiflexible chains [10.73, 76], we can easily draw a conclusion about the globulization of very long chains [10.34]. It is natural to consider two cases here: a persistent macromolecule and a macromolecule containing rigid rods in the main or side chains. The local asymmetry parameter p, viz. the ratio of the effective segment length l to the molecule thickness d, is assumed to be large: $p \equiv d/l \gg 1$.

The orientational ordering in a system of long rigid rods is associated with a comparatively small loss in entropy $\sim \ln p$ per rod [10.53]. Hence, a chain of connected rods globulizes quite cooperatively according to the mechanism shown in Fig. 10.1 (*II*), i.e. above the θ point and through a first-order phase transition. The globule in this case appears directly in the LC state (the apparent correlation between this result and the experimental results of [10.47-49] is worth noting).

The orientational entropy losses per effective segment due to ordering in the case of persistent chain mechanism is much more than $\ln p$ (of the order of p per segment [10.76]). Hence, a long persistent molecule globulizes according to the mechanism shown in Fig. 10.1 (*I*). Although the coil-globule transition is quite abrupt, on account of the fact that $\sqrt{C}/a^3 \sim 1/p \ll 1$, it leads to the formation of an isotropic liquid globule. If the chain is sufficiently long ($L/l \gg p^{5/2}$), a lowering of temperature to θ ($1 - \text{const} \cdot \ln p/p$) transforms the globule to LC state through a first-order phase transition. It should also be noted that a long chain of rods can form a metastable isotropic globule [10.53].

A large LC globule is spherical in shape [10.52, 53]. The shape of globules with relatively short chains may be quite peculiar—from a folded sheaf-like globule for chains consisting of rods [10.50, 51] to toroidal shape for a persistent chain [10.53, 89, 90]. It should be remarked that the existence of a cavity is a quite general property

of a small persistent globule (for $L/l \ll p^2$). In particular, this property does not depend on the nature of forces compressing a chain into a globule, and is exhibited during globulization in a poor solvent [10.53, 89], as well as during confinement of a chain in a microscopic cavity [10.90].

The results of the theory are in agreement with the data obtained from real experiments (see above), as well as from "computer" experiments [10.55-58]. It should be noted, however, that the formulation of problems in these papers differed from the formulation of problems in theoretical papers [10.50-53] in that the length of rigid portions was not fixed beforehand and could be varied depending on the external conditions and the resulting ternary structure (in other words, the mobile primary structure was considered; see Sec. 10.4).

D. Globulization of comb-like polymers was considered in [10.51, 91]. Obviously, for very long chains, where the globule size exceeds the length of the side chain, the specific nature of comb-like "architecture" may not be manifested. Small globules are the most interesting and important for comparison with the experiment. Such globules have been considered in [10.51] for rod-like side groups and in [10.91] for flexible side chains. The possibility of an intramolecular phase transition of the first kind due to a rearrangement of the packing in a sheaf from parallel to antiparallel has been indicated for the first case. A nonmonotonic dependence (with a maximum) of the coil-globule transition temperature on the length of the side chain has been predicted for the second case.

E. The ψ-condensation of DNA in polyethylene oxide (PEO) solution [10.92-94], which is important for biophysical phenomena, provides a very interesting example of a collapse caused by the fluctuations in the surrounding polymer solution. In order to explain the essence of this phenomenon, it should be mentioned at the very outset that the DNA double helix appears in it as a single-thread macromolecule which is quite close to the persistent model (see, for example, [10.89]). Further, the screening of interactions in a polymer solution [10.95, 16] is a well-known effect: a trial chain in a sufficiently concentrated solution of chemically identical chains behaves like a Gaussian coil. In other words, the effective interaction through a polymer medium compensates the forces of the excluded volume. It was shown in a series of articles [10.96-98], and more formally in [10.99], that for a rigid trial molecule the effective attraction of its segments through a strongly fluctuating polymer medium may exceed the forces in the excluded volume, thus resulting in a collapse. This type of collapse is similar to the well-known phenomenon of fluctuational instability [10.23].

The theory of the ψ-condensation of DNA, developed in [10.96-98] on the basis of the above-mentioned physical idea, provides a fairly complete explanation for the known experimental data.

It should be mentioned that this phenomenon was also considered in [10.100-103, 28]. A detailed critical analysis of the works [10.100, 101] is given in [10.98]. The globulization of a trial molecule in the melt of another polymer has been investigated by various methods in [10.102, 28] for the case when the ratio of Huggins constants corresponds to the separation of one polymer from another. Such an approach reduces the ψ-condensation to an ordinary coil-globule transition on account of the deterioration of the solvent and cannot claim to explain the interesting effects associated with the polymer nature of the solvent. Tanaka [10.103] has repeated some of the results of [10.96, 97] corresponding to an extremely dilute PEO solution.

F. Denaturation of globular proteins was considered for a long time to be a classical example of the globule-coil transition [10.104]. Recently, however, it has been established that globular proteins do not go over to the coil state for all types of denaturation [10.105, 106]. In particular, heating induces in many proteins a phase transition with the formation of denaturated compact state. This state should be interpreted as globular. The theory of this state and of the corresponding phase transition, which is quite similar to the Lifshitz theory of globules, has been constructed in [10.107]. According to this theory, the transition of a protein globule to the denaturated state is associated with the liberation of the rotational degrees of freedom of the side groups in the protein chain. The gain in entropy in this case compensates the loss in the energy of van-der Waals contacts, while the hydrophobic interactions practically remain unchanged and stabilize the globular state of the protein.

10.8. CONCLUSION

On the basis of the above consideration, it can be concluded that the approach proposed by Lifshitz [10.1] in the theory of polymer systems was found to be very fruitful. A large number of problems of practical importance and of general theoretical significance in the statistical physics of macromolecules were solved by using this approach and its various generalizations. A large body of experimental data available in literature pertaining at first sight to different branches of polymer physics was systematized within the framework of a single unified approach and explained theoretically. At the same time, the potentialities of Lifshitz' approach are, naturally, far from being exhausted and offer bright prospectives for further applications to various problems of the polymer theory including, for example, the theory of compactization of heteropolymers, block copolymers, the theory of high elasticity of globulized polymer networks, the theory of coil-globule transition in an LC solvent, etc.

In conclusion, the authors consider it a previlege to put on record

their profound respect to the memory of their teacher I. M. Lifshitz. Our understanding of the topics discussed in this article was considerably influenced by many years of association with him.

References

10.1. I. M. Lifshitz, *Zh. Eksp. Teor. Fiz.*, **55**, 6, 2408 (1968).
10.2. R. J. Rubin, *J. Chem. Phys.*, **43**, 7, 2392 (1965).
10.3. R. J. Rubin, *J. Chem. Phys.*, **44**, 5, 2130 (1966).
10.4. E. F. Cassasa and Y. Tagami, *Macromolecules*, 2, 1, 14 (1969).
10.5. E. A. Di Marzio and R. J. Rubin, *J. Chem. Phys.*, 55, 9, 4318 (1971).
10.6. P. G. de Gennes, *Rep. on Progr. in Phys.*, 32, 1, 187 (1969).
10.7. T. M. Birshtein, *Vysokomol. Soed.*, **24A**, 9, 1828 (1982).
10.8. I. M. Lifshitz, A. Yu. Grosberg, and A. R. Khokhlov, *Rev. Mod. Phys.*, **50**, 3, 683 (1978).
10.9. I. M. Lifshitz, A. Yu. Grosberg, and A. R. Khokhlov, *Usp. Phys. Nauk*, **127**, 3, 353 (1979).
10.10. A. Yu. Grosberg, *Vysokomol. Soed.*, **24A**, 6, 1194 (1982).
10.11. S. F. Edvards, *Proc. Phys. Soc.*, 85, 2, 613 (1965).
10.12. K. F. Freed, *Adv. Chem. Phys.*, **22**, 1 (1972).
10.13. I. M. Lifshitz and A. Yu. Grosberg, *Zh. Eksp. Teor. Phys.*, 65, 6, 2399 (1973).
10.14. I. M. Lifshitz, A. Yu. Grosberg, and A. R. Khohklov, *Zh. Eksp. Teor. Phys.*, **71**, 4, 1634 (1976).
10.15. P. J. Flory, *J. Chem. Phys.*, **17**, 1, 303 (1949).
10.16. P. G. de Gennes, *Scaling Concepts in Polymer Physics*, Cornell Univ. Press, Ithaca, 1979.
10.17. I. M. Lifshitz and A. Yu. Grosberg, *Dokl. Acad. Nauk SSSR*, **220**, 2, 468 (1975).
10.18. A. R. Khokhlov, *Journ. de Phys.*, 38, 7, 845 (1977).
10.19. A. R. Khokhlov, *Polymer*, **19**, 12, 1387 (1978).
10.20. M. Daoud, and G. Jannink, *J. de Phys.*, **37**, 7-8, 973 (1976).
10.21. A. Yu. Grosberg and D. V. Kuznetsov, *Vysokomol. Soed.*, **26A**, 4, 223 (1984).
10.22. A. Yu. Grosberg and D. V. Kuznetsov, *Vysokomol. Soed.*, **26A**, 4, 227 (1984).
10.23. A. Z. Patashinskii and V. L. Pokrovskii, *The Fluctuation Theory of Phase Transitions*, Moscow, Nauka, 1982 (in Russian).
10.24. E. S. Nikomarov and S. P. Obukhov, *Zh. Eksp. Teor. Fiz.*, **80**, 2, 650 (1981).
10.25. O. B. Ptitsyn and Yu. E. Eizner, *Biofizika*, **10**, 1, 3 (1965).
10.26. Yu. E. Eizner, *Vysokomol. Soed.*, **11A**, 2, 364 (1969).
10.27. P. G. de Gennes, *Journ. de Phys. Lettres*, **36**, 3, 55 (1975).
10.28. C. B. Post and B. H. Zimm, *Biopolymers*, 18. 6, 1487 (1979).
10.29. P. J. Flory, *Principles of Polymer Chemistry*, New York, Cornell Univ. Press, 1953.
10.30. N. Saito and M. Inoue, *Repts Progr. Polym. Phys. Jap.*, **17**, 17 (1974).
10.31. Y. Oono, *J. Phys. Soc. Jap.*, **41**, 787 (1976).
10.32. M. A. Moore, *J. Phys.*, A8, 237 (1975).
10.33. I. C. Sanchez, *Macromolecules*, **12**, 980 (1979).
10.34. A. Yu. Grosberg, D. Sc. Thesis, Institute of Chem. Physics, USSR Acad. Sciences, 1982.
10.35. A. R. Khokhlov, *Physica*, **1054**, 357 (1981).
10.36. A. Yu. Grosberg and B. D. Liberol', *Biofizika*, **21**, 4, 610 (1976).
10.37. A. Yu. Grosberg, *Biofizika*, **21**, 5, 820 (1976).

10.38. I. Nishio, S. T. Sun, G. Swislow, and T. Tanaka, *Nature*, **281**, 208 (1979).
10.39. G. Swislow, S. T. Sun, I. Nishio, and T. Tanaka, *Phys. Rev. Lett.*, **44**, 796 (1980).
10.40. P. Stepanek, C. Konak, and B. Sedlacek, *Macromolecules*, **15**, 4, 1214 (1982).
10.41. M. Nierlich, J. P. Cotton, and B. Farnoux, *J. Chem. Phys.*, **69**, 1379 (1978).
10.42. D. R. Bauer and R. Ullman, *Macromolecules*, **13**, 392 (1980).
10.43. T. Tanaka, *Polymer*, **40**, 99 (1979).
10.44. A. R. Khokhlov, *Polymer*, **21**, 4, 376 (1980).
10.45. A. R. Khokhlov, *Vysokomol. Soed.*, **22B**, 10, 736 (1980).
10.46. C. B. Post and B. H. Zimm, *Biopolymers*, **21**, 11, 2123 (1982).
10.47. Ya. S. Freidzon, V. P. Shibaev, I. M. Agranovich, V. D. Pautov, E. V. Anufrieva, and N. A. Plate, *Vysokomol. Soed.*, **20A**, 11, 2601 (1978).
10.48. Ya. S. Freidzon, V. P. Shibaev, V. D. Pautov, T. K. Bronich, G. D. Shelukhina, V. A. Kasaikin, and N. A. Plate, *Dokl. Akad. Nauk SSSR*, **256**, 6, 1435 (1981).
10.49. V. D. Pautov, E. V. Anufrieva, V. A. Kasaikin, and Ya. S. Freidson, *Abstracts of the 1st All-Union Simposium on Liquid-Crystal Polymers*, Suzdal', 1982, p. 36.
10.50. A. Yu. Grosberg, *Vysokomol. Soed.*, **22A**, 1, 90 (1980).
10.51. A. Yu. Grosberg, *Vysokomol. Soed.*, **22A**, 1, 96 (1980).
10.52. A. Yu. Grosberg, *Vysokomol. Soed.*, **22A**, 1, 100 (1980).
10.53. A. Yu. Grosberg and A. R. Khokhlov, *Adv. in Pol. Sci.*, **41**, 53 (1981).
10.54. A. Baumgarther, *J. Chem. Phys.*, **72**, 2, 871 (1980).
10.55. A. M. El'yashevich and A. M. Skvortsov, *Molek. Biol.*, **5**, 2, 204 (1971).
10.56. T. M. Birshtein, A. M. El'yashevich, and L. A. Morgenshtern, *Biophys. Chem.*, **1**, 1, 242 (1974).
10.57. P. G. Khalatur, *Vysokomol. Soed.*, **22A**, 10, 2050 (1980).
10.58. P. G. Khalatur, *Biofizika*, **25**, 4, 729 (1980).
10.59. A. Yu. Grosberg, *Some Problems in the Theory of Heteropolymers*, Preprint Nauch. Tsentra Biol. Issl., Pushchino, 1983 (in Russian).
10.60. D. V. Kuznetsov and A. R. Khokhlov, *Vysokomol. Soed.*, **23B**, 1, 59 (1981).
10.61. E. Helfand, in: *Recent Adv. in Pol. Blends, Grafts and Blocks*. Ed. by L. H. Sperling, New York, 1974.
10.62. E. Helfand, *Macromolecules*, **8**, 3, 552 (1975).
10.63. S. Krause, *Macromolecules*, **3**, 1, 84 (1970).
10.64. H. Furstenberg and H. Kesten, *Ann. Math. Statistics*, **31**, 2, 457 (1960).
10.65. A. Yu. Grosberg, E. M. Kaganova, and S. A. Molchanov, *Biofizika*, **29**, 1, 30 (1984).
10.66. T. M. Birshtein, A. M. Skvortsov, and A. A. Sariban, *Vysokomol. Soed.*, **17A**, **12**, **2558** (1975).
10.67. T. M. Birshtein, A. M. Skvortsov, and A. A. Sariban, *Macromolecules*, **9**, **4**, **888** (1976).
10.68. A. A. Sariban, T. M. Birshtein, and A. A. Skvortsov, *Vysokomol. Soed.*, **19A**, **10**, **1728** (1977).
10.69. V. A. Kabanov and A. B. Zezin, *Uspekhi Khimii*, **51**, 9, 1447 (1982).
10.70. L. Onsager, *Ann. N.Y. Acad., Sc.*, **51**, 627 (1949).
10.71. P. J. Flory, *Proc. Roy. Soc. (London)*, **234**, 60 (1956).
10.72. P. J. Flory, *Proc. Roy. Soc. (London)*, **234**, 73 (1956).
10.73. A. R. Khokhlov, *Phys. Lett.*, **68A**, 1, 135 (1978).
10.74. A. R. Khokhlov, *Vysokomol. Soed.*, **21A**, 9, 1981 (1979).
10.75. A. R. Khokhlov, *Vysokomol. Soed.*, **21B**, 3, 201 (1979).
10.76. A. R. Khokhlov and A. N. Semenov, *Physica*, **108A**, 2/3, 546 (1981).
10.77. A. R. Khokhlov and A. N. Semenov, *Physica*, **112A**, 3, 605 (1982).
10.78. A. N. Semenov and A. R. Khokhlov, *Vysokomol. Soed.*, **24B**, 7, 544 (1982).

10.79. A. R. Khokhlov and A. N. Semenov, *J. Phys. A: Math. Gen.*, 15, 1361 (1982).
10.80. A. R. Khokhlov and A. N. Semenov, *Macromolecules*, 15, 1272 (1982).
10.81. T. Tanaka, *Polymer*, 20, 1404 (1979).
10.82. T. Tanaka, *Phys. Rev. Let.*, 40, 820 (1978).
10.83. V. V. Vasilevskaya and A. R. Khokhlov, in: *Mathematical Methods for Investigation of Polymers*, Pushchino, 1982, p. 45 (in Russian).
10.84. A. R. Khokhlov and K. A. Khachaturyan, *Polymer*, 23, 11, 1742 (1982).
10.85. A. R. Khokhlov, *J. Phys. A: Math. Gen.*, 13, 979 (1980).
10.86. P. G. de Gennes, P. Pincus, R. M. Velasco, and F. Brochard, *J. Physique*, 37, 1461 (19).
10.87. P. Pfeuty, *J. Physique-Colloques*, 39, C-2, 149 (1978).
10.88. F. Oosawa, *Polyelectrolytes*, New York, 1971.
10.89. A. Yu. Grosberg, *Biofizika*, 24, 1, 32 (1979).
10.90. A. Yu. Grosberg and A. B. Zhestkov, *Biofizika*, 29, 2, 96 (1984).
10.91. A. Yu. Grosberg and E. M. Kaganova, *Vysokomol. Soed.*, 25A, 1185 (1983).
10.92. L. S. Lerman, *Proc. Nat. Acad. Sci. USA*, 68, 8, 1886 (1971).
10.93. L. S. Lerman, in: *Phys.-chem. properties of nucleic acids*, ed. by J. Duchesne, New York, Acad. Press, 1973, V. 3, p. 61.
10.94. V. I. Salyanov, V. G. Pogrebnyak, S. G. Skuridin, G. B. Lortkipanidze, Z. G. Chidzhavadze, A. I. Toryanik, and Yu. M. Evdokimov, *Molek. Biol.*, 12, 3, 485 (1978).
10.95. S. F. Edwards, *Proc. Phys. Soc.*, 88, 265 (1966).
10.96. A. Yu. Grosberg, I. Ya. Erukhimovich, and E. I. Shakhnovich, *Biofizika*, 26, 3, 415 (1981).
10.97. A. Yu. Grosberg, I. Ya. Erukhimovich, and E. I. Shakhnovich, *Biofizika*, 26, 5, 897 (1981).
10.98. A. Yu. Grosberg, I. Ya. Erukhimovich, and E. I. Shakhnovich, *Biopolymers*, 21, 12, 2413 (1982).
10.99. E. S. Nikomarov and S. P. Obukhov, *Zh. Eksp. Teor. Fiz.*, 80, 2, 650 (1981).
10.100. J. Naghizadeh and A. R. Massih, *Phys. Rev. Lett.*, 40, 19, 1299 (1978).
10.101. H. L. Frish, and S. Fesciyan, *J. Polym. Sci.: Polym. Let. Ed.*, 17, 2, 309 (1979).
10.102. J. F. Joanny and F. Brochard, *J. de Physique*, 42, 8, 1145 (1981).
10.103. F. Tanaka, *J. Chem. Phys.*, 78, 5, 2788 (1983).
10.104. M. Joly, *A Physico-Chemical Approach to the Denaturation of Proteins*, London, 1965.
10.105. K. Kawajima, *J. Molec. Biol.*, 114, 2, 241 (1977).
10.106. P. I. Gil'manshin, D. A. Dolgikh, O. B. Ptitsyn, A. V. Finkel'shtein, and E. I. Shakhnovich, *Biofizika*, 27, 6 (1982).
10.107. A. V. Finkel'shtein and E. I. Shakhnovich, *Dokl. Akad. Nauk SSSR*, 267, 5, 1247 (1983).
10.108. S. T. Sun, I. Nishio, G. Swislov, and T. Tanaka, *J. Chem. Phys.*, 73, 12, 5971 (1980).

AUTHOR INDEX

Abdulaev, G. B., 289
Abrahams, S. C., 106
Agaev, V. V., 234
Agafonov, V. G., 234f
Agranovich, I. M., 352
Akhiezer, I. A., 107
Akiba, S., 234
Akhmedov, D., 235
Aleksandrov, Yu. M., 328
Aleksandrova, N. Ya., 107ff
Alekseenko, Z. S., 54
Alexandrovich, S. V., 171
Alferov, Zh. I., 13, 201, 233f
Aliev, R. A., 55
Alimov, V. Kh., 169
Allakhverdiev, K. R., 55
Al'shin, B. I., 108
Ambrazyavichene, V. S., 55
Anderko, K., 170
Anderson, P., 55
Anderson, R. L., 233
Andreev, V. M., 233
Andreeva, G. T., 108
Antonov, V. E., 10, 109, 169f
Antonova, T. E., 169
Antypes, G. A., 233ff
Anufrieva, E. V., 352
Arkhangel'skaya, V. A., 288
Arsent'ev, I. N., 233f
Ascher, E., 107ff
Asmussen, F., 329
Aston, J. G., 170
Astrov, D. N., 108
Austin, A. E., 108
Avanesov, A. G., 289
Aven, M., 200

Bakay, A. S., 108
Balakhovskii, O. A., 169
Balakirev, M. K., 266
Balkarei, Yu. I., 107
Baranova, R. V., 169
Baranowski, B., 169f
Baryakhtar, V. G., 9f, 56, 79f, 107
Basiev, T. T., 289
Baturov, L. N., 108
Batygov, S. Kh., 289
Bauer, D. R., 352
Bauer, H. J., 171
Baumgartner, A., 352
Beigang, R., 288
Beimowski, 289
Belash, I. T., 10, 109, 169f
Belov, K. P., 80
Belov, N. V., 79, 107
Bel'skii, A. A., 234
Bennemann, K. H., 172
Benshel, W. F., 329
Berninger, G., 171
Berstein, I. L., 106
Bert, N. A., 234
Bertaut, F., 106
Besnus, M. J., 171
Betz, H., 329
Bielska-Landowska, 108
Bill, H., 108
Birshtein, T. M., 351f
Blackburn, L. D., 170
Blaszszak, Z., 290
Bloch, D., 170
Bobeck, A. H., 79
Bocheńska, K., 172
Bochkov, B. G., 108
Bogatov, A. P., 202, 233
Bogdanov, S. V., 266
Bohmhammel, K., 172
Bojarski, K., 170
Bokov, V. A., 106
Bondar', I. A., 289
Boritko, S. V., 266
Born, R. A. I. A., 108
Borovik, A. E., 79
Borzunov, V. N., 171
Bowden, M. J., 311, 329
Boyer, L. L., 171
Bozorth, R. M., 172
Brekhovskikh, L. M., 55
Brochard, F., 353
Brodale, G. E., 106
Brodowsky, H., 169
Bronich, T. K., 352
Brown, W. E., 107
Brunskill, J. H., 108
Brzhezina, B., 55
Bube, R. H., 200

Bugaev, A. S., 266
Bugakov, V. I., 108
Bujnowski, W., 169
Bulaevskii, L. N., 79, 107
Bundy, F. P., 170
Burell, G. J., 234
Burger, J. P., 172
Burrus, G. A., 235
Bystrov, V. P., 54

Cable, J. W., 171
Campbell, J. C., 235
Cannon, J. F., 170
Casey, H. C., 233
Cassasa, E. F., 351
Chai, Y. G., 235
Chalyi, V. P., 235
Chantry, G. W., 25, 55
Chebotarev, V. P., 288
Chernyshev, I. M., 55
Chidzhavadze, Z. G., 353
Chin, A. K., 234
Chin, G., 329
Chisdes, D. M., 172
Chupis, I. E., 10, 79ff
Cochran, W., 55
Cohen, M., 170
Coleman, J. J., 233f
Cook, L. W., 234
Cotton, J. P., 352
Cowley, P. R. E. J., 329
Cowley, R. A., 108
Cox, D. E., 108
Crangle, J., 171
Cross, L. E., 80

Damen, T. C., 289
Danielmeyer, H. G., 289
Danil'chenko, V. G., 235
Danilov, V. A., 329
Daoud, M., 351
Davydov, L. N., 107f
de Gennes, P. G., 79, 351
Degtyareva, V. F., 169f
Della-Tore, E., 79
Denker, B. I., 289
Dentai, A. G., 235
Dianov, E. M., 54
Di Marzio, E. A., 351
Dmitriev, V. D., 290
Dolgikh, D. A., 353
Dolginov, L. M., 233
Domanski, A. I., 289
Donneley, J. P., 233
Drakin, A. E., 233
Drobyshev, L. A., 108
Drozhdin, S. N., 108
Dubovka, G. T., 171
Duchesne, J., 353
Dudko, K. L., 79
Dumoulin, L., 172
Dunkan, R. C., 289
Dushenkov, S. D., 329
Dutta, N. K., 234
Dvorak, V., 55
Dzigasov, A. G., 233
Dzyaloshinskii, I. E., 79f, 87, 107

Economou, E. N., 171
Edwards, D. M., 171
Edwards, S. F., 351ff
Eibschutz, I. M., 108
Einfield, D., 329
Eizner, Yu. E., 351
Eliseev, P. G., 233
Ellis, B., 234
El'yashevich, A. M., 352
Eremenko, V. V., 79
Ershov, Yu. A., 329
Erukhimovich, I. Ya., 353
Evdokimov, Yu. M., 353
Evtikheev, V. P., 234

Fain, V. M., 107
Fang, P., 106
Farztdinov, M. M., 79
Faulkner, J. S., 171
Feldkamp, G. E., 55
Feng, M., 234
Feofilov, P. P., 288
Ferrari, J. M., 108
Fesciyan, S., 353
Filipek, S., 170
Finkel'shtein, A. V., 353
Fisher, R. A., 106
Flanagan, T. B., 171f
Flory, P. J., 343, 351
Fonstad, C. G., 234
Forrat, F., 106
Forrer, R., 172
Forrest, S R., 235
Fousek, J., 55
Fox, D. L., 102
Franoux, B., 352
Freed, K. F., 351
Freidzon, Ya. S., 352
Freeman, A. J., 171
Fridman, F. M., 79
Friedel, J., 171
Frish, H. L., 353

Fritz, B., 267
Fujimoto, A., 226, 235
Furstenberg, H., 352
Fujita, F. E., 171

Gagulin, V. V., 106
Galkin, A. A., 79
Galperin, Yu. M., 266
Gammel, J. C., 235
Ganguly, B. N., 172
Gantsevich, S. V., 266
Garbuzov, 13, 201, 233f
Garland, J. W., 172
Gatsoev K. A., 234
Gavrilova, N. D., 108
Gaydanskii, P. F., 79
Gel'mont, B. L., 234
Georgieva, I. Ya., 171
Ghez, R., 234
Gaingue, W. F., 106
Gil'manshin, P. I., 353
Ginzburg, V. L., 55, 79
Gipstein, E., 329
Glebova, O. S., 329
Gliksman, M., 266
Golant, M. B., 54
Goncharov, Yu. G., 55
Gorodetsky, A. E., 169
Gorelenok, A. T., 13, 201, 233
Gottehrer, Y., 171
Graham, T., 170
Grazhulis, V. A., 200
Gregora, I., 55
Gribov, B. G., 329
Grosberg, A. Yu., 17f, 330, 351
Gufan, Yu. M., 106
Gugenheim, H. I., 108
Gulyaev, Yu. V., 14, 236, 266
Gupta, M., 171
Gurevich, V. L., 14, 266
Gusev, Yu. L., 288
Gvozdev, A. A., 235

Hallam, G. C., 171
Haller, I., 329
Hansen, M., 170f
Hardcastle, K. I., 169
Hattendorf, H. D., 282, 289
Hatzakis, M., 329
Haufler, R., 172
Helfand, E., 352
Hicinbothen, W. A., 266
Hirao, M., 235
Hiraoka, H., 239
Hitchens, W. R., 235
Hoffman, V. G., 55
Holakowsky, J., 107
Holonyak, N., 202f, 226, 233
Hori, K., 235
Hornreich, R. M., 107
Hornung, E. W., 106
Hsieh, J. J., 202, 233
Huber, G., 289
Hubert, A., 79

Ibrakhimov, N., 233
Ilegems, M., 234
Il'ichev, N. N., 289
Imai, H., 235
Imamov, R. M., 169
Inoue, M., 351
Ioffe, V. A., 106
Irisova, N. A., 54
Ishibashi, Y., 55
Ishikawa, H., 235
Ismailzade, I. H., 106
Isupov, V. A., 106
Ivanov, N. R., 55
Ivanov, S. N., 266

Jannik, G., 351
Jashida, H., 235
Jinzo, K., 108
Joanny, J. F., 353
Joly, M., 353
Jones, D. M., 172

Kabanov, V. A., 352
Kaczmarek, F., 290
Kadomtseva, A. M., 80
Kagan, V. D., 266
Kaganova, E. M., 352f
Kajzar, F., 80
Kanishi, Sh., 329
Kanunov, E. R., 329
Kaplun, Z. F., 54
Karlov, N. V., 329
Kasatkin, V. A., 352
Kasatkina, L. V., 288
Katilyus, R., 266
Kaufmann, L., 170
Kawajima, K., 353
Kay, K., 108
Keitsiro, A., 106
Kennedy, G. C., 170
Kesten, H., 352
Keve, E. T., 106
Khabakhpashev, M. A., 107
Khachaturyan, K. A., 353

Khalatur, P. G., 352
Khalfin, V. B., 234f
Khalfina, A. A., 79
Khan, H. R., 169ff
Kharlamov, A. A., 199f
Khazanov, E. N., 266
Khodenko, G. E., 79
Khodyrev, Yu. P., 169
Khördler, A., 171
Khokhlov, A. R., 17f, 330, 351
Khrushch, B. I., 329
Khuchua, N. P., 108
Khulugurov, V. M., 289
Kiefer, B., 172
Kim, O. K., 235
King, A. R., 79
Kirichenko, L. G., 200
Kirpichenkova, E. O., 288
Kiselev, S. V., 106
Kiss, Z. T., 289
Klein, B. M., 171
Knödler, A., 169
Koehler, W. C., 171
Koichi, K., 106
Kolmykova, N. R., 79
Koltygin, V. M., 170
Komija, S., 234
Konak, C., 352
Konoplin, S. N., 288
Koptsik, V. A., 107f
Korotkova, Z. S., 54
Kovalev, O. V., 107f, 329
Kovner, S. N., 79
Kozlov, G. V., 8, 19, 54f
Krainik, N. N., 106ff
Kramer, J. J., 80, 106
Krasikov, V. S., 55
Krause, S., 352
Krukowski, 169f
Kryukova, E. B., 55
Kucab, M., 80
Kulakova, L. A., 266
Kulikov, N. I., 171
Kulinski, T., 290
Kusunoki, T., 234
Kutsenko, A. V., 50
Kuzmin, G. P., 329
Kuznetsov, D. V., 351f
Kveder, V. V., 199f

Laikhtman, B. D., 266
Landau, L. D., 9, 79, 107
Laptev, V. V., 289
Lebedev, S. P., 54f
Lee, M. H., 233
Lee, T., 235
Leger, J. M., 171
Leibler, K., 108
Leonov, A. S., 266
Lerman, L. S., 353
Liberol', B. D., 351
Liffin, G., 288
Lifshitz, E. M., 9, 79, 107
Lifshitz, I. M., 17f, 330, 335, 341, 350ff
Lobanov, B. D., 289
Loriers-Susse, C., 171
Lortkipanidze, G. B., 353
Ludwiczak, M., 290
Lutz, F., 289
L'vov, V. A., 56, 79f
Lyubimov, V. N., 106f
Lyulichev, A. N., 329
Lyukina, L. A., 54

Macksey, H. M., 233
Madorsky, S., 329
Maeland, A., 172
Majchrzak, S., 171
Makhviladze, T. M., 16, 291, 329
Maksimova, N. G., 289
Mal'ginova, S. D., 79
Malyshev, V. Yu., 170
Mandel'shtam, T. S., 54
Mansfel'd, G. D., 14, 236, 266
Marennikov, S. I., 288
Massih, A. R., 353
Matsumoto, Y., 233
Mayerfeld, A., 234
Mayne-Banton, V., 329
Mdivani, V. N., 234
Mekata, M., 172
Melville, H. W., 329
Menke, E., 267, 288
Miller, B. I., 235
Mil'ner, A. A., 79
Mimura, Y., 329
Minetaka, H., 108
Mirishli, F. A., 106
Mirov, S. B., 289
Mirzoev, G. I., 55
Mitrofanov, A. V., 328
Mitrofanov, K. P., 106
Mitsek, A. I., 79, 107
Mitsui, 46
Molchanov, S. A., 352
Mollenauer, L. F., 267, 288
Moon, R. L., 233
Moore, M. A., 338, 351
Moreau, W., 329
Moria, T., 79
Moret, J. M., 108

Morgenshtern, L. A., 352
Moss, T. S., 234
Mozzhukhin, D. D., 329
Mukhortov, Yu. P., 266
Mukhina, V. Yu., 200
Munschy, G., 171
Myl'nikova, I. E., 106

Nace, D. M., 170
Naghizadeh, J., 353
Nahory, R. E., 234
Nakajima, K., 234
Nash, F. R., 234
Nedellec, P., 172
Nedlin, G. M., 106
Need, O. U., 329
Negirev, A. A., 54
Nelson, R. J., 234f
Neronova, N. N., 79, 107
Nesterenko, N. I., 106
Newnham, 86, 106
Newton, R. C., 170
Nierlich, M., 352
Nikitov, V. A., 107f
Nikomarov, E. S., 351ff
Nishida, K., 235
Nishio, I., 352f
Novik, 108

Obukhov, S. P., 351ff
O'Hara, D. E., 329
Ohkubo, T., 329
Ohno, H., 172, 235
Oles, A., 80
Olson, D. H., 288
Onsager, L., 352
Oono, Y., 351
Oosawa, F., 353
Osiko, V. V., 15, 267, 289
Ossipyan, Yu. A., 12, 199f
Owen, E. A., 172
Ozerov, R. P., 106
Ozon, M., 235

Panish, M. B., 233f
Papaconstantopoulos, D. A., 171
Paquette, D., 79
Parfianovich, I. A., 289
Parilov, T. B., 54
Pashinin, P. P., 289
Patashinskii, A. Z., 351
Pautov, V. D., 352
Pearsall, T. P., 235
Pearson, W. B., 172
Perea, E. H., 234
Peshekhonov, S. V., 329
Petrenko, V. F., 200
Petrov, V. M., 108
Petrova, O. P., 54
Petzelt, J., 41, 54f
Pfeuty, P., 353
Pincus, P., 353
Plate, N. A., 352
Pleshivtsev, A. S., 329
Plyushko, N. Ya., 107
Poeschel, E., 172
Pogrebnyak, V. G., 353
Pokrovskii, V. L., 351
Pollack, M. A., 234
Polos'yants, B. A., 54
Polzikova, N. I., 266
Ponomarev, B. K., 170
Ponyatovskii, E. G., 10f, 109, 169
Popkov, Yu. A., 79
Popov, S. N., 106
Popov, V. A., 79
Popova, T. V., 108
Post, C. B., 35, 339
Prener, T. S., 200
Prokhorov, A. M., 8, 15f, 19, 55, 267, 289ff, 328
Prokopenko, V. M., 200
Pruss, D., 289
Ptitsyn, O. B., 351ff
Pustovoit, V. I., 266

Rado, G. T., 108
Raev, V. K., 79
Rakov, A. V., 329
Rashupkin, V. I., 169
Raub, Ch. J., 171
Razsukovannyi, B. N., 79
Rebrova, T. B., 54
Richards, P. M., 108
Rivera, J. P., 108
Roginskaya, Yu. E., 106
Rossi, J. A., 233
Rubin, R. J., 351
Rubtsov, A. A., 266
Rumyantsev, V. D., 233f

Saito, N., 351
Sakai, K., 234
Salyanov, V. I., 353
Samara, G. A., 108
Sanchez, I. C., 338, 351
Sariban, A. A., 352
Savchenko, M. A., 107
Savchenko, V. N., 108

Savel'ev, V. S., 54
Schenk, H. J., 171
Schmid, H., 108
Schroeter, W., 200
Schubert, K., 172
Scott, I. F., 55, 108
Sedlacek, B., 352
Sekikawa, K., 329
Selivanov, G. K., 329
Semenov, A. N., 352f
Semiletov, S. A., 169
Shakhnin, E. I., 353
Shakhnovich, E. I., 353
Shapiro, S. M., 108
Sharapov, V. M., 169
Shavrov, V. G., 107
Shcherbakov, I. A., 289
Shchuchkin, A. G., 329
Shekhtman, V. Sh., 169
Shelukhina, G. D., 352
Sher, E. S., 106
Shevchenko, S. A., 199f
Shibaev, V. P., 352
Shikhsaidov, M. Sh., 200
Shilshtein, S. Sh., 170
Shiryaev, V. I., 170
Shmaonov, T. A., 54
Shmid, H., 106
Shnabel, W., 329
Shreider, E. Ya., 329
Shrivasan, R., 329
Shuichi, I., 106
Shulze, W. A., 80, 106
Shuvalov, L. A., 55, 107
Shvorneva, L. I., 106
Sicora, W., 80
Skinner, S. M., 106
Skośkiewicz, T., 170, 172
Skuridin, S. G., 353
Skvortsov, A. M., 352
Small, M. B., 234
Small, P. A., 329
Smbatyan, Zh. E., 266
Smiałowski, M., 170
Smith, H. L., 329
Smolenskii, G. A., 10, 79, 81, 106ff
Sniadower, L., 172
Sohmura, T., 171
Sokolova, Z. S., 234
Solov'ev, S. P., 106
Somenkov, V. A., 170
Soskin, M. S., 289
Sotobyshi, H., 329
Spears, D. L., 329
Spector, H. N., 266
Sperling, L. H., 352
Spitsyn, V. I., 169
Spol'nik, Z. A., 107
Stefanovich, A. V., 107
Stepanek, 352
Stephanovskii, E. P., 79
Stock, A. D., 169
Stolypin, Yu. E., 106
Stopol'nik, Z. A., 107
Stössel, H., 108
Strikman, S., 107
Stritzker, B., 169f, 172
Sugimura, A., 234
Sugita, K., 329
Sun, S. T., 352f
Swislow, G., 352
Switendick, A. C., 171
Szafrański, A. W., 172

Tadashi, M., 108
Tagami, Y., 351
Taguchi, K., 235
Takcuchi, T., 329
Tal'yanskii, V. I., 199f
Tamari, N., 235
Tanaka, F., 350
Tanaka, T., 352
Tanimoto, K., 329
Taranenkov, V. B., 289
Tashiaki, M., 108
Tashima, M. H., 234
Temkin, H., 234
Terekhin, S. A., 54
Thiessen, V. G., 170
Thimm, K., 329
Thompson, L. F., 329
Timofeev, V. N., 54
Tkacz, M., 170
Tofield, B. C., 289
Tomashpol'skii, Yu. Ya., 106
Tonaka, F., 353
Toryanik, A. I., 353
Tsuji, S., 235
Tulina, N. A., 170
Turov, E. A., 79

Udovenko, V. F., 329
Ueno, N., 329
Uimin, G. V., 200
Ullman, R., 352
Usui, 233

Valiev, K. A., 16, 291, 328f
Van den Boomgaard, I., 108
Vasil'ev, M. G., 235
Vasilevskaya, V. V., 353

Vavilova, L. S., 233f
Vdovin, V. I., 234
Velasco, R. M., 353
Velichko, I. M., 55
Velikov, L. V., 16, 291, 328f
Venevtsev, Yu. N., 106
Veretin, V. S., 266
Verochek, V., 55
Vilenskaya, R. L., 54
Vinogradov, E. A., 54
Viskov, A. S., 106
Vitebskii, I. M., 77, 79f
Vodar, B., 171
Vodop'yanov, K. L., 289
Volkov, A. A., 8, 19, 55
Vonsovsky, S. V., 171
Vorob'ev, N. S., 289
Voron'ko, Yu. K., 289

Wada, O., 234
Wallace, W. E., 171
Wallan, E. O., 171
Weber, H. P., 289
Weiss, P., 172
Welling, H., 288
White, D. L., 266
Whitworth, R. W., 200
Wicke, E., 169, 172
Wilkens, M., 172
Wiśniewski, R., 169
Wohlfarth, E. P., 171
Wolf, G., 169, 172
Wood, E., 108
Wright, P. D., 235
Wühl, H., 170

Yablonskii, D. A., 56, 79f
Yakimenko, M. N., 328f
Yakupov, R. Ya., 108
Yamakoshi, S., 235
Yanke, J., 172
Yarmukhamedov, Yu. N., 108
Yudin, V. M., 106

Zabrodskii, A. G., 200
Zaidel, A. N., 329
Zakharov, A. P., 169
Zaretskii, A. V., 200
Zaroslev, D. Yu., 329
Zemon, S., 266
Zharikov, E. V., 287, 289
Zhdanov, G. S., 166
Zhdanova, V. V., 108
Zhebelev, V. P., 170
Zhestkov, A. B., 353
Zhitkova, M. B., 290
Zhitnyuk, V. A., 289
Zilberman, P. E., 266
Zimm, B. H., 339, 351
Zimmermann, G. J., 171
Zlenko, A. A., 289
Zorin, R. V., 108
Zucker, J., 266
Zverev, G. M., 289f
Zvonkov, A. D., 171
Zyulina, E. A., 54

SUBJECT INDEX

AFM ordering, 75
amplification,
  acoustic noise, 260
  acoustoelectron, 237
  acoustoelectric, 253
  multitransit, 236, 264ff
    of acoustic waves, 243f
    of fluctuations, 14
amplitudon, 47
antiferroelectric(s), 84f
antiferromagnetics, 71, 77, 84f
  with weak ferromagnetism, 85
antiferromagnetism vector, 78
approximation,
  isotropic magnetic, 59
  quadratic magnetization, 61
  quasistationary, 296, 310
  self-consistent field, 331, 341
  two-coupled oscillators, 50
  volume, 338, 341
Auger analysis, 209
avalanche photodiodes, 202

Backward-wave tube(s) (BWT), 8, 20
band magnetics, 11
blob, 347

Characteristic(s), current-voltage (CVC), 246
charge, dislocation, 195f
chemical potential, 335
coefficient,
  Auger recombination, 219
  diffusion, 300, 306
  transmission, 22
  virial, 335ff, 338, 342
coil, 330
  Gaussian, 334, 337, 339
collapse of polymer networks, 17, 346
colour centres, 268
  electronic, 267f
condensation,
  avalanche-type, 17
  ψ, 349f
condition(s),
  generation, 240f, 259
  synchronism, 238, 263, 265
conductivity,
  dislocation (DC), 173ff
  negative differential, 247
  superionic, 20
conformational entropy, 341
constant,
  recombination rate, 293, 306
Corbino disc, 14, 237, 257ff
  CVC, 261
crystal(s),
  with incommensurate phases, 8
  KDA, 43
  KDP-type, 42ff
  laser, 287
  magnetically ordered, 9
  RDP, 43
current,
  acoustoelectric, 246
  dark, 231
  diffusion, 231
  dislocation, 173, 187
  drift, 247, 254
  generation-recombination, 231
  threshold, density of, 222
  tunnel, 231
current-voltage characteristic(s), 14

Deformation, Luminescence (DL), 187
density, dislocation, 181
depolymerization, 310
detector, infrared, 22
devices, semiconducting optoelectronic, 13
diffusion, 310
diffusion layer thickness, 328
diode(s),
  light-emitting (LED), 13
  surface-emitting, 228ff
dislocation(s), 12, 173
  misfitting, 209
  mobile, 105
domain boundaries (DB), 9f
  of antiferromagnetic crystals, 67
  Bloch-type, 62f, 70, 73
  of ferromagnetic crystals, 67ff
  Néel-type, 10, 62f, 70, 73
  plane, 67

domain boundaries (DB), 9f
  quasi-Bloch, 75
  quasi-Néel, 75
double heterojunction(s) (DH),
  AlGaAs, 213
  InGaAsP/InP, 208
  N-n-N, 213

Effect,
  acoustoelectric, 254
  electroplastic (EPE), 13, 173, 187
    odd, 190
  injection plastic (IPE), 187
  magnetoelectric (ME), 9, 56, 104ff
    homogeneous, 56
    inhomogeneous, 56ff
    linear, 87, 99, 101
    nonlinear, 87
  nonlinear, 265
  "oxygen", 323, 328
  parasitic diffraction, 23
  photoplastic (PhPE), 13, 173, 184ff
    impurity (IPhPE), 187f
    infrared quenching, 186f
  piezoelectric, 260
  Raman, 19
  relaxation, 96
  sensitization, 282f
  short-circuiting (ShCE), 187f
  Stark, 60
  VUV etching, 291
  Zeeman, 88
EPR,
  dislocation, 173, 175
  photo-, 175, 177
  efficiency,
  absolute, 279, 287f
  differential, 288
    quantum, 223f
  of electroluminescence,
    external, 227, 229
    internal, 228
  external quantum, 210
  external PL, 213
  quantum, internal, 227
  of radiative transitions, 220
    internal, 215
  of radiative recombination,
    external, 213
    internal, 213
electroluminescence, 217, 220
  efficiency, 217
energy, of exchange magnetoisotropic ME, 87
epitaxy,
  vapour-phase (VPE), 224f
  liquid-phase (LPE), 203, 206, 208, 224
equation, continuity, for acoustic flux, 257
etching,
  diffusive, 292ff
  photo-, 292
  of polymers,
    upon uniform exposure, 297ff
    upon nonuniform exposure, 30ff
  VUV, 291, 305, 308, 323f, 327f
  X-ray, 291f
etching rate, 292f, 316, 318f
  quasistationary, 325, 328
exciton, 177

Factor,
  electromagnetic coupling, 241
  electron amplification, 240
  scaling, 306
  swelling, 336ff, 339f
Faraday phase inverter, 104
F-centre(s), 268ff, 273
Fedorov symmetry group, 78
ferroelectric(s), 84f
ferroelectromagnets, 10, 81ff
ferroelectromagnetic(s),
  applications, 103f
  high-frequency properties, 94
  Ni-I boracite, 98
ferromagnetics, 67, 77
ferromagnets, itinerant, 136
ferrimagnetic(s), 85
free energy of globule, 333f, 336
frequency synchronism, 239
function, orientation distribution, 344

Gain,
  electronic, 255f, 258f
  mean, 263
gain factor, 14
Gaussian coil, 349
generation,
  of acoustic signals, 263
  multitransit, 236, 244, 246, 252
    of acoustic flux, 14
generator, cyclic acoustoelectronic, 259
Ginzburg number, 337
glass(es)
  high-concentration, 277
  KNFS, 278f, 281f
  neodymium, 277
globule, 330, 334
  free energy, 342

heteropolymer, 341
homopolymer, 341
LC, 348
persistent, 349
globulization, 343
of comb-shaped polymers, 349
of heteropolymers, 17
Golay cell, 26
Goldstone waves, 47f
gyration radius, 339

Heterojunction(s), 13
InGaAsP, 201
In Ga-As-P systems, 201
lattice-matched, 233
InGaAsP/InP, 202, 213, 125
InGaAsP/GaAs, 213, 215
heterophotodetector(s), 233
holographic selector, 272
Hydrides, 10, 109ff

Index,
adsorption, 22
refractive, 22
instability, acoustic, 13, 236f
instruments, optoelectronic, 201ff
insulator, Mott-Habbard, 176
interaction,
of acoustic fluctuations in semiconductors, 14
acoustoelectron, 237, 252ff
collision-free, 237
Coulomb, 176, 343
dipole, 275
Dzyaloshinskii relativistic ME, 95, 97
electron-dislocation, 12, 173ff
exchange, 58f
ME, 89, 95, 97
magnetoelectric, 59, 87ff, 90ff
ME, anisotropic, 102
microparameter of, 285
nonlinear, 252, 263
acoustoelectronic, 236
non-Peierls, 252,
phonon-phonon, 19
relativistic, 58f
exchange, 58
strong, 61
volume, 333
interdomain potential difference, 74
interferometer,
Fabry-Perot, 33
Mach-Zehnder, 26
Rozhdestvenskii, 26

Laser, 209, 263
AlGaAs DH, 212, 216f, 226
buried-heterostructure, 224f
CW injection, 203, 226
continuously tunable, 15
cryogenic tunable, 269
double heterojunction (DH), 202f
dye, 16, 268, 273
excimer, 291
free-running, 273
GSGG-Cr^{3+}-Nd^{3+}, 286f
He-Ne, 271
heterojunction, 13
InGaAsP injection, 226
InGaAsP/InP DH, 212, 220, 222, 226
injection, 13, 202
KNFS, 15, 277, 280, 282
Kr, 213, 281, 286
LiF colour centre, 273
pulsed periodic, 274
tunable, 16, 272f
low-threshold infrared, 13
mesa-band grown, 225
neodymium, 15, 270ff, 275ff
efficiency, 282ff
rhodamin 6G, 270
room-temperature tunable, 267f, 273
ruby, 277
solid-state, 15
tunable colour centre, 268f
YAG:Nd^{3+}, 213, 277, 286f
laser crystals, 267ff
laser glasses, 267ff
laser matrices, 267
lasing threshold, 221
latent heat, 338
lattice matching, 222
lattice mismatching, 209ff, 223
law, Curie-Weiss, 46
length,
absorption, 296, 304, 328
diffusion, 298, 304, 314
persistence, 343f
lifetime,
band-to-band radiative, 217f
effective, 212f
radiative, 212
light-emitting diode (LED), 209, 214, 222, 227ff
AlGaAs/GaAs, 216, 229
InGaAsP/InP, 216, 220f, 227
liquid-crystal ordering, 343f
luminescence dislocation, 173

Magnetic symmetry classes, 73
magnetization, spontaneous, 135, 140, 151

Markov process, 331
Maxwell relaxation time, 240
meander, 237
method(s),
  of application of compensating bands, 194
  of compressing hydrogen, 110ff
  dislocation current, 189
  dislocation band, 192
  Flory, 338
  interferometric, 321
  Lifshitz, 344
  microwave waveguide, 36
  Monte-Carlo, 343
  photometric, 321
  quartz microbalance, 322
  resonator, in BWT spectroscopy, 31
  of stimulating acoustic activity, 237
  of two thicknesses, 23f
  T and φ, 23f
mode(s),
  Q-switched, 281
  rigid, 40
  dipole moment, 40
  soft, 41, 47, 50
mode locking, 272
model,
  Mitsui, 46
  rigid d-band, 11, 154ff
  of semiinfinite layer, 292, 294f, 299, 302ff
modification function, 313f, 325

Normalized luminescence intensity, 285

Ohmic contacts, 258
optical communication systems, 227
oscillations, free-running, 279
oscillator,
  acoustoelectronic, 14
  alternating drift-field, 250
  BWT, 20f
output power, 279

Parameter(s),
  local asymmetry, 348
  ME exchange interaction, 103
  modification, 315f, 318
  static interaction, 285
phase diagram, T-P, 11
phase shift, 22, 259
phase transition(s),
  coil-globule, 330ff
  in crystals, 8
  displacement type, 20, 49
  in external fields, 92ff
  first-order, 52, 61, 92, 105, 338, 342, 348
  intramolecular, 349
  LC, 17
  metal-insulator, 20
  orientational, 10
  second-order, 92, 105, 337
  temperature of, 10
  thermal, 90ff
phason, 47f
photodetector(s), 231ff
  avalanche (APD), 231 .
  heterojunction, 231
  IR, 13
  p-i-n, 232
photodiode,
  InGaAsP/InP DH, 229f
  p-i-n, 232
photoetching, 311, 316, 320ff
  of polymers, 11
photoluminescence (PL), 212, 227
photoresistor(s), 233
phototransistors, 231
principle, Pauli, 60
pyroelectric(s), 85

Quantum yield, 317f
  luminescence, 275f

Radiation, vacuum ultraviolet (VUV), 291f, 320
radiation dose, 325
radius, Debye screening, 240
rate,
  diffusion, 306
  etching, 301, 305ff, 309, 313
    instantaneous, 311
  generation, of low-molecular fragments, 317
recombination, 310
  Auger, 212, 214
    band-to-band, 219f, 222
  in InGaAsP DH, 212ff
  nonradiative, 212, 214, 218
reflectivity, 22
relaxation, migration-induced, 285
resonator, acoustic, 241

Scattering, neutron, 19
semiconductor(s), 8, 12, 173
  piezoelectric, 237
solid solutions
  InGaAsP, 203ff, 207
  quaternary, 208

spectrometer(s)
BWT, 8, 25, 27, 33, 37
Epsilon, 25, 27f, 30, 38
Fourier, 41
spectrum(a),
absorption, 271
dislocation, 174ff
generation, 246, 251
luminescence, 271, 284
Raman, 48
submillimetre dielectric, 48ff
vibrational, 19
spectroscopy,
BWT, 20ff
dielectric, 20
far-infrared, 23, 38
infrared, 19f, 38
Fourier, 36
monochromatic, 29
soft-mode, 38
submillimetre, 8, 19ff, 36ff, 43
Stokes shift, 268f
superlinearity of CVC, 260
system,
displacement, 44
optical communication, 202
order-disorder, 41, 44

Temperature,
Curie, 11
ferroelectric transition, 90
magnetic transition, 90
superconducting transition, 11
theory,
of acoustoelectron interaction, 239
linear, 263
nonlinear, 246, 252
of adsorption, 331
of DB electric polarization, 9, 56ff
phenomenological, 61
Flory, 346
Kane Band, 219
of LC state, 348
Landau, of second-order phase transitions, 89, 91
of large globules, 334
Lifshitz, 330ff
globule, 333, 350
linear, 250, 255, 259
of LC ordering, 17
of nonlinear amplification, 265
Onsager of rigid rods, 345
of orientational ordering, 17
of simple solution, 206
thermodynamic, 89ff
transducer, electroacoustic (EAT), 242
transistor(s), field-effect (FET), 232
transiton(s),
coil-globule, 17, 334, 336, 347
combined, 343
globule-coil, 343
helix-coil, 343
LC, 344f
transition probability, band-to-band radiation, 213
transition width, 337

TO THE READER

Mir Publishers would be grateful for your comments on the content, translation and design of this book. We would also be pleased to receive any other suggestions you may wish to make.

Our address is:
Mir Publishers
2 Pervy Rizhsky Pereulok
I-110, GSP, Moscow, 129820
USSR

OTHER BOOKS IN THE SERIES FOR 1984

Numerical Methods in Fluid Dynamics
Edited by N. YANENKO, Mem. USSR Acad. Sc.

This collection of articles edited by Academician N. Yanenko includes works devoted to the development of new models and methods for numerical solution of problems in fluid dynamics appearing in the investigation of various physical phenomena. The book gives a definite notion of the level of development of methods for solving problems in fluid dynamics and makes it possible to observe the dynamics of development of various trends in constructing numerical algorithms. For specialists working in the field of applied mathematics and mechanics.

Contents. Direct Statistical Simulation of Problems in Aerohydro dynamics. The Splitting Method for the Numerical Solution of Problems in Gas Dynamics. Simulation of Shock Waves in Rarefied Plasma. Nonregular Nets for Solving Two-Dimensional Nonstationary Problems in Gas Dynamics. The EGAC Method for Calculating Gas Flows of Heterogeneous Media in Eulerian Coordinates. The Numerical Solution of Spectral Problems of Thermal Radiation Transport by Iterative Correction Methods. Numerical Simulation of Tsunamis. Application of Characteristic Series to the Solution of Three-Dimensional Problems in Gas Dynamics. Investigation of the Dissipative Properties of Difference Schemes for the Gas-Dynamics Equations. On Complete Conservatism of Difference Schemes. Local and Nonlocal Stability Conditions for Calculating Gas-Dynamics Problems in Lagrangian Coordinates. A Modification of the Spectral Method for Investigating the Stability of Difference Schemes. On the Approximation of the Navier Stokes Equations for an Incompressible Fluid by Evolutionary-Type Equations. Towards a Theory of Variable-Type Nonlinear Equations.

Advances in Organometallic Chemistry
Edited by O. REUTOV, Mem. USSR Acad. Sc.

This volume under the general editorship of Academician O. Reutov contains articles on the chemistry of organometallic compounds, a field of science that has consistently maintained a leading place both in the development of the theoretical conclusions of chemistry, and in practical application (the production of polymer materials, antiknock compounds, etc. as raw materials of large-tonnage organic synthesis).

Problems are considered that relate to the organometallic chemistry of non-transition (iron, cobalt, nickel, platinum, palladium, gold) and transition metal compound; among the latter particular attention is given to the study of mercury, boron, silica, tin and germanium compounds. For scientific workers in the general field of organometallic chemistry.

Contents. On the Mechanism of Electrophilic Substitution in the Organometallic Chemistry of Non-Transition Elements. Carbon-Carbon Metallotropic Tautomerism. Solvent Effects on the Kinetics and Mechanism of Organomercury Reactions. Carbon-Group IVA Element Compounds with a Multiple $p\pi$-$p\pi$ Bond: New Approaches to Synthesis. A New Method for Synthesis of Cationic Arene Complexes of Group VII and VIII Metals. Ligand Exchange in Ferrocene. Organogold(I) Complexes. Optically Active Organometallic Compounds with Central and Planar Chirality. Homolytic Reactions of Addition to Unsaturated Tin, Germanium, and Silicon Derivatives. New Findings Concerning Liquid Phase Autoxidation of Organometallic Compounds. Summary Results of Studies into Organoaluminium Synthesis.